

Mariyamni Awang
Berihun Mamo Negash
Nur Asyraf Md Akhir
Luluan Almanna Lubis *Editors*

ICIPEG 2014

Proceedings of the International
Conference on Integrated Petroleum
Engineering and Geosciences

ICIPEG 2014

Mariyamni Awang · Berihun Mamo Negash
Nur Asyraf Md Akhir · Luluan Almannan Lubis
Editors

ICIPEG 2014

Proceedings of the International Conference
on Integrated Petroleum Engineering
and Geosciences

Editors

Mariyamni Awang
Universiti Teknologi PETRONAS
Perak
Malaysia

Nur Asyraf Md Akhir
Universiti Teknologi PETRONAS
Perak
Malaysia

Berihun Mamo Negash
Universiti Teknologi PETRONAS
Perak
Malaysia

Luluan Almanna Lubis
Universiti Teknologi PETRONAS
Perak
Malaysia

ISBN 978-981-287-367-5

ISBN 978-981-287-368-2 (eBook)

DOI 10.1007/978-981-287-368-2

Springer Singapore Heidelberg New York Dordrecht London

© Springer Science+Business Media Singapore 2015

This work is subject to copyright. All rights are reserved by the Publisher, whether the whole or part of the material is concerned, specifically the rights of translation, reprinting, reuse of illustrations, recitation, broadcasting, reproduction on microfilms or in any other physical way, and transmission or information storage and retrieval, electronic adaptation, computer software, or by similar or dissimilar methodology now known or hereafter developed.

The use of general descriptive names, registered names, trademarks, service marks, etc. in this publication does not imply, even in the absence of a specific statement, that such names are exempt from the relevant protective laws and regulations and therefore free for general use.

The publisher, the authors and the editors are safe to assume that the advice and information in this book are believed to be true and accurate at the date of publication. Neither the publisher nor the authors or the editors give a warranty, express or implied, with respect to the material contained herein or for any errors or omissions that may have been made.

Printed on acid-free paper

Springer Science+Business Media Singapore Pte Ltd. is part of Springer Science+Business Media
(www.springer.com)

Committee Members

Chairperson

Associate Professor Dr. Ismail Bin Mohd Saaid

Co-Chairperson

Associate Professor Dr. Abdul Hadi Bin Abdul Rahman

Technical Chair

Associate Professor Dr. Eswaran Padmanabhan

Dr. Sulaimon Aliyu Adebayor

Secretariat

Nor Sara Izzatti Bt Bashah (Leader)

Siti Sarah Bt Salehudin (Secretary 1)

M Aslam Bin Md Yusof (Secretary 2)

Salina Bt Mat Nawi (Assistant Secretariat)

Technical Program Committee

Professor Dr. R.P. Major

Professor Dr. Deva Prasad Ghosh

Associate Professor Dr. David Menier

Associate Professor Wan Ismail bin Wan Yusoff

Dr. Sonny Irawan

Dr. Syahrir Ridha

Dr. Masoud Rashidi

Dr. Ahmed Mohamed Ahmed Salim

Dr. M. Suhaili Ismail

Khor Wei Chung (EDAS-related matters)

Mohammad Amin Shoushtari

Noor Ilyana Ismail

Dr. Mohammed Abdalla Ayoub Mohammed

Associate Professor Dr. Muhannad Talib Shuker

Treasurer

Associate Professor Dr. Chow Weng Sum
Raja Rajeswary Suppiah

Sponsorship

Md Yazid Bin Mansor
Jasmi Bin Ab Talib
Publicity & Protocol
Ali Fikret Mangi
Saleem Qadir Tunio
Webmaster
Khairul Arifin Bin Mohd Noh

Publication

Professor Dr. Mariyamni Bt Awang
Berihun Mamo Negash
Nur Asyraf Md Akhir
Luluam Almanna Lubis

Registration

Che Rafidah Bt Abd Aziz
Nor Baizura Bt Mokhtar
Nur Hidayah Bt Abdul Karim

FnB

Mohamad Shaufi Bin Sokiman
Muhammad Aqram B. Shahidan

Event Management

Associate Professor Askury bin Abd Kadir
M. Ayyub Bin M. Syayuti

Logistic

Mohd Zairi Bin Zohaidi (Leader)

IT Media

Khairul Azhar
Munirah Bt Musa

Reviewers

Abdul Hadi Abd Rahman
Abeeb Awotunde
Akanji Lateef
Alain Mascle
Ali F. Mangi Alta'ee
Ali Zulfiqar
Aliyu Sulaimon
Askury Abd Kadir
Dr. Muhannad Shuker
David Menier
Deva Ghosh
Essam Ahmed
Eswaran Padmanabhan
Felix Tongkul
Halim Abdul
Hamzah Mohamad
Harry Doust
Jamaal Hoesni
Jasmi A. Talib
Joseph Lambiase
Khaled Elraies
Luluan Lubis
M. Suhaili Ismail
Manuel Pubellier
Mario Aurelio
Mariyamni Awang
Masoud Rashidi
Mazlin Idress
Mazuin Jasamai
Melissa Johansson
Mohamad Nasir Mohamad Ibrahim

Mohamed Jan
Mohammed Ayoub
Mohd Amin Shoushtari
Mohd Zaidi Jaafar
Mokhtar Awang
Mr. Khairul Arifin Mohd Noh
Muhammad Manan
Mustafa Onur
Noor Ilyana Ismail
Richard Paul Major
Raja Rajeswary Suppiah
Ralph Kugler
Sara Bashah
Sonny Irawan
Subramania Iyer
Sunday Isehunwa
Swapn Bhattacharya
Syahrir Ridha
Wan Ismail Wan Yusof
Weng Sum Chow

Preface

The articles in this book include the proceedings of the 3rd International Conference on Integrated Petroleum Engineering and Geosciences 2014 (ICIPEG2014). It was held under the banner of World Engineering, Science and Technology Congress (ESTCON2014) at the Kuala Lumpur Convention Centre from 19–22 May 2014. The theme for ICIPEG 2014, “Current Trends & Challenges in Petroleum Exploration & Production” reflects the present challenges we all are on. The theme was selected with the objective to continuously re-examine current practices, and identify challenges and limitations associated with the current technologies and the world energy demand.

The conference brought together academicians and industry experts from more than five countries and assisted the exchange of ideas and research findings on fundamental and applied researches related to the oil and gas industry. The papers in this proceeding were selected from more than 130 paper submissions of which 92 were selected for presentation during the conference. The selection was made based on input from peer reviews. The publication committee selected these papers for their perceived quality, originality, and appropriateness to the theme of the conference. Topics covered on the petroleum engineering side include reservoir modeling and simulation, enhanced oil recovery, production, and operation. Similarly, geoscience presentations cover diverse areas in geology, geophysics, paleontology, and geochemistry. The selected papers focus on current interests in petroleum engineering and geoscience. We hope that this book will be a bridge between engineering, geoscientists, academicians, and industry. The program schedule and all information regarding the conference may be accessed from the home page <http://www.utp.edu.my/icipeg2014/>.

Acknowledgments

We would like to express our gratitude to all who submitted papers. We also thank the colleagues who provided reviews of the submitted papers. The names of the reviewers are acknowledged in the following pages. We extend special thanks to Associate Professor Dr. Shari Dunn-Norman from Missouri University of Science and Technology, Prof. John Kaldi from University of Adelaide and James Stannard from PETRONAS for joining us as plenary speakers. All three are esteemed specialists in the field of Petroleum Engineering and Geosciences.

Contents

Part I Reservoir Numerical Simulation and Characterization

Pressure Transient Behavior of Immiscible Water Alternating Gas (IWAG) Injection with and Without Relative Permeability Hysteresis Effects	3
Azeb D. Habte, Mustafa Onur and Ismail M.B. Saaid	
Control of Paraffin Deposition in Production Operation by Using Ethylene–TetraFluoroEthylene (ETFE)	13
Mombekov Bagdat and Rashidi Masoud	
Investigation of Asphaltene Onset Pressure (AOP) in Low Asphaltenic Light Oil Samples	23
Teoh Wan Ru and Ali F. Alta’ee	
Porosity and Permeability Modification by Diagenetic Processes in Fossiliferous Sandstones of the Baram Delta, Sarawak Basin, Malaysia	47
J. Ben-Awuah and E. Padmanabhan	
Analytical Study on Gas Lift Optimization and Prediction of Production Life of Wells in Platform C, B-1 Field.	59
Muhammad Aslam Bin Md Yusof and Nurfuzaini Binti Abdul Karim	
Modeling Pressure Drop in Vertical Wells Using Group Method of Data Handling (GMDH) Approach	69
Mohammed A. Ayoub, Berihun M. Negash and Ismail M. Saaid	

Comparison of Critical Gas Flow Rate Equations to Prevent Liquid Loading	79
Pei Wen Lim, Mohd Amin Shoushtari, A.P. Ismail bin Mohd Saaid and Salahaldin Sh	
Use of Group Method of Data Handling Algorithms for Predicting Heated and Steamed Zone Volumes During Steam Flooding	89
Sami Abdelrahman Musa and Mariyamni Awang	
 Part II Enhanced Oil Recovery	
The Effect of Water Salinity and Reservoir Temperature on Silica Dissolution During ASP Flood: Static Model	99
F.A. Ahmed and A.K. Elraies	
Simulation Study of the Effect of Smart Water on Relative Permeability During WAG-CO₂ Injection for Light Oil Reservoir	109
Pui Mun Yip and Ali F. Alta'ee	
Hydroxypropylmethylcellulose as a Free Water and Settling Control Agent in Oil Well Cement Slurry	121
Ghulam Abbas, Sonny Irawan, Muhammad Khan Memon, Shuaib Ahmed Kalwar and Sandeep Kumar	
Static Adsorption of New CO₂ Philic Surfactant onto Berea Sandstone	129
Muhammad Sagir, Isa M. Tan, Muhammad Mushtaq and Seyda Hosna Talebian	
Comparison of MMP Between Slim Tube Test and Vanishing Interfacial Tension Test	137
Choon Lin Voon and Mariyamni Awang	
Investigating the Influence of Water Cut on Naphthenate Precipitation in Oil Production Facilities	145
Aliyu A. Sulaimon, Sathishkumar Arumugam and Bamikole J. Adeyemi	
Wax and Asphaltene Deposition Tendency of Malaysian Crude Oils	155
Aliyu Adebayo Sulaimon and Mohamad Hazwan Yusoff	

**Vapor-Liquid Equilibria for Hydrocarbon/Water Systems
Using Thermodynamic Perturbation Theory** 171
W.P. Yong and M. Awang

Part III Drilling, Well Completion, Production and Operation

**Technical and Economic Analysis of Hydraulic Pumps
in Deliquifying Gas Wells** 189
Yan Ching Lye and Mohd Amin Shoushtari

**Drilling Parameter Effects on Cuttings Transport
in Horizontal Wellbores: A Review** 199
T.N. Ofei, S. Irawan and W. Pao

**Flow Profile Distribution in Narrow Annuli Using Modified
Yield Power-Law Fluid Model** 209
T.N. Ofei, S. Irawan and W. Pao

Part IV Reservoir Monitoring and Management and Risk Assessment

**Quantification of Clay Mineral and Log Response
Toward Reservoir Rock Properties** 221
Nur Asyraf Md Akhir, Gamal Ragab Gaafar and Ismail Mohd Saaid

VTI Wave Modeling Using Weak Elastic Anisotropy Approximation 233
S. Y. Moussavi Alashloo, D.P. Ghosh and W.I. Wan Yusoff

**The Effect of Tar on the Petrophysical Analysis of FMI
in Asmari Fractured Reservoir** 239
Z. Movahed, R. Junin and H. Amiri Bakhtiari

Part V Advances in Geophysics and Reservoir Geoscience

**A Hybrid Approach for Subsurface Illumination Analysis
in Shallow Gas Region: A Case Study in Malay Basin** 249
A.H. Abdul Latiff and D.P. Ghosh

A New Fluid Factor Based on AVO Technique 257
Liu Changcheng

Geological Structures of the Kinta Valley Revisited Using Drainage Anomalies	267
Choong Chee Meng and Manuel Pubellier	
Geochemical Signatures of Some Devonian Black Shales	277
E. Padmanabhan and D. Jeffrey Over	
Variation in Surface Characteristics of Some Gas Shales from Marcellus Shale Formation in the USA	283
Shama Mohammed Balulla and E. Padmanabhan	
Preservation of Marine Chemical Signatures in Upper Devonian Carbonates of Kinta Valley, Peninsular Malaysia: Implications for Chemostratigraphy	291
Haylay Tsegab Gebretsadik, Chow Weng Sum and Aaron W. Hunter	
The Kati Formation: A Review	303
Hissein A. Alkhali and Chow Weng Sum	
Rock Physics Diagnostics and Effective Medium Model of Boonsville Field	313
Ida Ayu Purnamasari, Wan Ismail Wan Yusoff and Chow Weng Sum	
Geomechanical Brittleness Estimation Through Simultaneous Pre-stack Inversion	323
Maman Hermana, Chow Weng Sum and D.P. Ghosh	
Palynological Zonation of the Paleogene–Neogene Strata of the Kaikang Trough, Muglad Rift Basin, Republic of South Sudan . . .	331
Omer Babiker Abdelrahim, Mohd Suhaili bin Ismail and Aaron W. Hunter	
The Shallow Marine Succession of Begrih Formation (Pliocene), Mukah Area, Sarawak: Facies, Stratigraphic Characteristics, and Paleoenvironmental Interpretation	337
Muhammad Murtaza, Abdul Hadi Abdul Rahman and Chow Weng Sum	

Part VI Advanced Geological Concepts in Carbonates and Sedimentary Basins

Application of Wireline Logs in the Determination of Fluvial Deposits of the Reservoir Interval of Bentiu Formation (Albian–Cenomanian) Muglad Basin Sudan	365
Ahmed Ali Hassan Taha, Abdul Hadi Abd Rahman and Wan Ismail bin Wan Yusoff	
Construction in Terrain with Subsurface Karstic Limestone Bedrock . . .	373
Chow Weng Sum, A.H. bin Abdul Rahman, Khor Wei Chung and Solomon Kassa	
Evaluation of Pore Network Variation in a Carbonate Rock from Onshore Sarawak, Malaysia	379
S. Andriamihaja and E. Padmanabhan	
Comparison of Different Rock Physics Models to Evaluate the Impact of Pore Types on Velocity—Porosity Relationship in Carbonates of Central Luconia Sarawak.	387
Luluan A. Lubis, Sara Bashah and Deva P. Ghosh	
Presence of Oleanane in Oil also as Evidence of Contamination	395
Swapan Kumar Bhattacharya, Syed Mohammad Ibad Mahmoodi and Fawzia Hussein Ali Abdulla	

Part I
Reservoir Numerical Simulation
and Characterization

Pressure Transient Behavior of Immiscible Water Alternating Gas (IWAG) Injection with and Without Relative Permeability Hysteresis Effects

Azeb D. Habte, Mustafa Onur and Ismail M.B. Saaid

Abstract Pressure transient tests can provide useful information for characterization and evaluation of reservoirs under secondary and tertiary processes if properly designed and analyzed. There are a number of literature concerning the injectivity and falloff testing of water or gas injection wells. However, the information available on immiscible water alternating gas (IWAG) injection tests is limited to falloff tests without considering the effect of trapped gas. In this study, the pressure transient behavior of IWAG injection and falloff tests with and without relative permeability hysteresis effect is investigated using simulated pressure data. The saturation distribution shows that gas relative permeability hysteresis increases the recovery of oil in IWAG injection. At early times, the pressure response of gas injectivity test exhibits the properties of the gas zone which is in contrast to the water injectivity test. The pressure-derivative curve of gas falloff test exhibits a long transition period with a half-slope before the late time radial flow. The pressure and pressure-derivative curves of the water injectivity test display a unit-slope line at early times which can mislead to conclusion of wellbore storage effects. It is shown that the hysteresis has a significant effect on the pressure and pressure-derivative behavior of an injectivity test, but less effect on a falloff test.

Keywords Falloff test · Hysteresis effect · Immiscible water alternating gas injection (IWAG) · Injectivity test

A.D. Habte (✉) · I.M.B. Saaid
Department of Petroleum Engineering, Universti Teknologi PETRONAS,
31750 Tronoh, Perak, Malaysia
e-mail: azeb.habte@petronas.com.my

M. Onur
Petroleum and Natural Gas Engineering Department, Istanbul Technical University,
Buyuk Dere Caddesi, Istanbul, Masalak 34469, Turkey

Nomenclature

B	Formation volume factor, v/v
c	Isothermal fluid compressibility, psi^{-1}
h	Thickness, ft
k	Absolute permeability, md
p	Pressure, psi
r	Radial distance, ft
S	Saturation, fraction
t	Time, hrs
μ	Viscosity, cp
ρ	Density, lbm/ft
ϕ	Porosity, fraction
Δ	Difference operator

Subscript

f	Formation
g	Gas
i	Initial
o	Oil
r	Relative
w	Water

1 Introduction

Pressure transient analyses of injectivity and falloff data based on two-zone radial composite reservoir models have been extensively presented in literature for reservoirs which are under secondary and tertiary recovery, such as water, gas, and thermal injections. Similar to production well-test analysis, if the flow regimes from injection and falloff pressure responses can be clearly identified and analyzed, flood front location, effective permeabilities, fluid mobility profile in the fluid banks, average reservoir pressure from falloff test, wellbore storage, and skin effects can be estimated.

Using the analysis procedures of water/gas injection wells, which are presented in literature [1, 2], it may be possible to analyze injection and falloff pressure data for immiscible water alternating gas (IWAG) injection wells. However, due to the presence of three phases with different fluid properties, gas trapping, saturation gradients, and three or more fluid banks because of the injection of two fluids with different mobilities and compressibilities, the interpretation and analysis may be complex and can lead to inaccurate estimates of key parameters such as flood front location.

Stenger et al. [3] presented interpretation of pressure falloff test acquired from two vertical IWAG injection wells in a carbonate reservoir using the concept of radial composite model with two zones. They showed that at early times, the falloff pressure-derivative curve of gas injection shows a hump, and a straight line with slope of positive quarter (+1/4 slope line) is observed instead of a zero-slope on the falloff-derivative curve following water injection period which is an indication of a progressive mixing of injected water with gas (high mobility). They suggested the need of an investigation on the effects of hysteresis due to trapping of injected gas by water and three-phase relative permeabilities on IWAG injection pressure transient analysis.

Experimental studies show that the three-phase relative permeability is highly dependent on saturation history [4]. Due to the cyclic process during WAG injection which results in the presence of both imbibition and drainage, treatment of three-phase relative permeability hysteresis for gas (most non-wetting phase) is essential. Spiteri and Juanes [5] studied the effect of gas-phase relative permeability hysteresis on field-scale prediction of WAG injection in reservoir simulation. Their investigation shows that based on the three-phase relative permeability interpolation models used, reservoir simulations with hysteresis effects give higher recovery than without hysteresis effects. The increment can be as high as 15 %. In addition, they evaluated the commonly used three-phase relative permeability interpolation models (Stone I, Stone II, and Baker) by comparing their prediction with Oak's [4] experimental data. They showed that Stone I model predicts the residual oil saturation during water injection following gas injection well, making the model preferable for the cyclic IWAG injection simulation.

To the best of the authors' knowledge, pressure transient behavior of WAG injection with and without relative permeability hysteresis effects has not been studied in detail. Stenger et al. [3] presented only the falloff period behavior without considering hysteresis effects. In this study, the pressure transient behaviors of IWAG injection and falloff tests with and without three-phase relative permeability hysteresis effects are presented. A black oil numerical simulator (Eclipse 100) is used to generate the pressure and saturation data because there is no analytical solution suitable for WAG injection, except the composite system which ignores the saturation gradient due to injection of water and gas into the reservoir. Capillary effects are neglected in this paper, although preliminary results with capillary effects indicate that capillary pressure may have a significant effect on saturation profiles and hence pressure transient behavior especially in the presence of gas phase. Currently, we are investigating the effect of capillary pressure on the pressure transient behavior for the IWAG scheme considered in this study.

2 Numerical Simulation Model

It is assumed that a fully penetrating vertical well is located at the center of a cylindrical, homogeneous, isotropic, and no-flow outer boundary reservoir. The well is injecting water and lean gas (88 % CH₄ and 12 % C₂H₆) with specific

gravity of 0.612 alternately with a constant rate, and the flow is unidirectional. Water is injected first with 2000 STB/D rate then followed by gas with a 1:1 WAG ratio. Skin and wellbore storage effects are not considered in this study. Two WAG cycles for injection periods of 10 days followed by falloffs for 20 days are simulated on Eclipse 100. The modified Stone I three-phase relative permeability interpolation model is chosen to accurately simulate the three-phase flow in WAG [5].

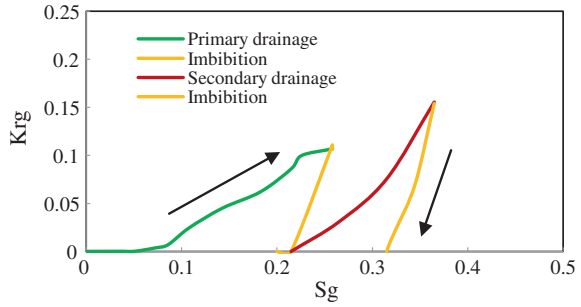
The process is immiscible and the hysteresis effect is activated using WAGHYSTR keyword in the PROP section. The hysteresis models used in the simulator for the non-wetting phase relative permeability are presented in Ref. [6].

Relative permeability data from the Oak's [4] experiments as presented by [5] are used. Table 1 presents fluid and rock properties used for the simulation. The land trapping coefficient of 0.78 and secondary drainage reduction of 0.01 were used in the simulation [5]. Figure 1 shows a representative of gas relative

Table 1 Fluid and rock properties at average reservoir conditions

Average reservoir conditions	
P , psi	2,000
T , °F	250
<i>Fluid and rock properties</i>	
B_o , rb/stb	1.0
B_w , rb/stb	1.0
B_g , rb/Mscf	1.65
μ_o , cp	2.0
μ_w , cp	1.0
μ_g , cp	0.02
c_o , psi ⁻¹	2.8×10^{-5}
c_w , psi ⁻¹	2.3×10^{-6}
c_f , psi ⁻¹	3×10^{-6}
ρ_o , lbm/ft ³	43.0
ρ_w , lbm/ft ³	62.4
h , ft	100
r_e , ft	10,000
ρ_g , lbm/ft ³	5.056
S_{wi} , fraction	0.31
S_{gc} , fraction	0.06
S_{orw} , fraction	0.373
S_{org} , fraction	0.125
$k_{rw}(@Sor)$	0.09
$k_{rg}(@Sor)$	0.45
$k_{ro}(@Swi)$	0.88
$k_{ro}(@Sgi)$	0.88
k , md	200
ϕ , fraction	0.2

Fig. 1 Gas relative permeability calculated from three-phase relative permeability hysteresis model [6]



permeability hysteresis following water and gas floods. It can be seen that trapping of gas phase during water injection (imbibition) reduces the relative permeability of gas and hence its mobility.

3 Results and Discussions

3.1 Saturation Profile

Figure 2 shows saturation distribution in the reservoir at the end of the 2nd water and gas injection and falloff periods with and without hysteresis effect. As can be seen from the figure, hysteresis has a significant effect in the recovery of IWAG injection. At the end of the 2nd water injection ($t = 70$ days) and the 2nd gas injection ($t = 100$ days), the gas saturation is higher and more oil is displaced near the wellbore region for the case with hysteresis effect. As expected, due to the reduction of gas mobility by injected water, the distance to the gas front is shorter when hysteresis effect is considered. For instance, at the end of the 2nd gas injection (at $t = 100$ days), the gas front reaches the 223rd grid block and 233rd for the case with and without hysteresis effects, respectively. In addition, despite the high compressibility of gas, the front movement is negligible during falloff period (see Fig. 1). Thus, the interface boundary in IWAG injection may be treated as stationary during falloff period. However, the saturation distribution in the flooded zone shows significant difference during the falloff period following the second water injection for the case with hysteresis effect.

3.2 Pressure and Pressure-Derivative Responses

In this section, the pressure transient behavior of injectivity and falloff test periods of gas injection following water injection and water injection following the gas injection are investigated with the help of pressure and pressure-derivative

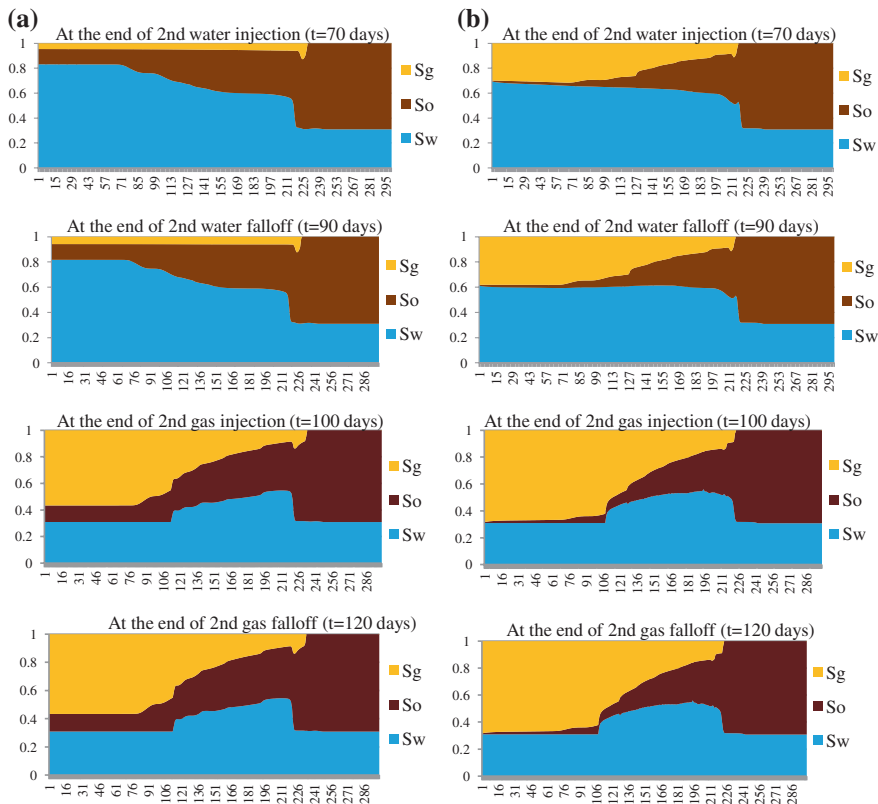


Fig. 2 Saturation distribution for IWAG process at $t = 70, 90, 100,$ and 120 days **a** without gas relative permeability hysteresis **b** with gas relative permeability hysteresis

curves. To reduce the effect of injecting time, Agarwal’s [7] equivalent time is used to calculate pressure derivative for the falloff periods. Study of pressure and pressure-derivative responses of water injection into an oil reservoir is presented in reference [1].

3.2.1 Gas Injection and Falloff Periods Following Water Injection

Figures 3 and 4 show the comparison of pressure and pressure-derivative behavior with and without hysteresis effects for the 2nd gas injection and falloff periods, respectively. Due to the high mobility contrast between gas and the reservoir fluids, the well starts detecting the injected fluid at early times and the pressure derivative exhibits a value inversely proportional to the total mobility around the flood front. The high compressibility and mobility of gas also cause an increase in injectivity of gas. Hence, the pressure change starts to decrease after some time which

Fig. 3 Pressure change and pressure-derivative responses for 2nd gas injection period with and without hysteresis effects

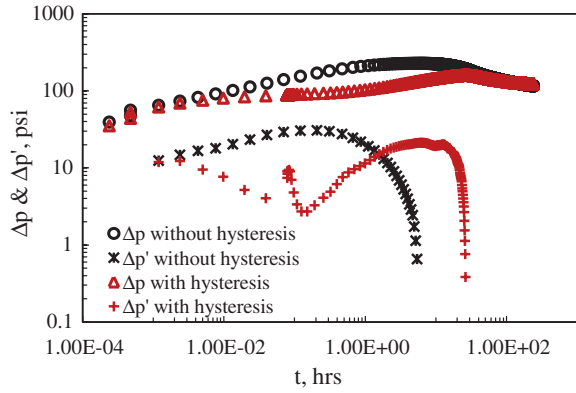
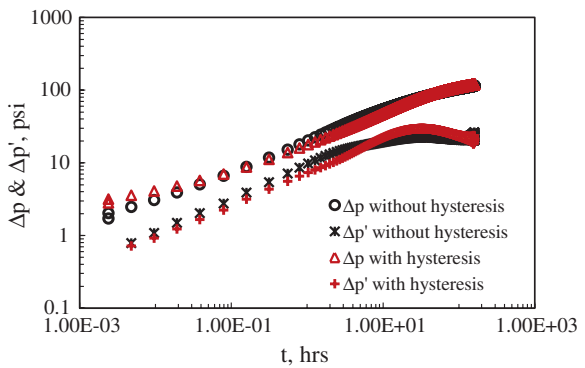


Fig. 4 Pressure change and pressure-derivative responses for 2nd gas falloff period with and without hysteresis effects



results in negative pressure-derivative values in both cases (see Fig. 3). In addition, because of the additional gas saturation from the trapped gas near the wellbore from the previous water injection, the mobility of gas in the gas zone for the case with hysteresis effect is higher than the one without hysteresis effect. This results in a lower pressure and pressure-derivative values at early times (see Fig. 3).

The falloff pressure-derivative curve on log–log graph is expected to show first radial flow reflecting gas zone property at early time if wellbore storage has no effect, then a long transition period because of the high mobility of gas, and a second radial flow (reflecting the unflooded zone property) if the test is long enough and the pressure has not been stabilized. For the case considered in this study, due to the high mobility of gas, the pressure propagates fast and the first radial flow has not been seen, rather a very long transition period is seen on Fig. 4. As expected, a short second radial flow regime is seen at late times which reflects the property of the oil zone.

The falloff period pressure response in Fig. 4 shows that the impact of hysteresis during the period is insignificant.

3.2.2 Water Injection and Falloff Period Following Gas Injection

Figures 5 and 6 show the comparison of pressure change and pressure-derivative responses with and without hysteresis effects for the 2nd water injection and falloff periods, respectively. In this injection period, it is expected to see the effect of hysteresis on the pressure behavior because the injected water will trap gas and reduce its mobility (see Fig. 2).

As is seen in Fig. 5, at early times, the pressure change and pressure derivative exhibit a unit-slope line on both with and without hysteresis effect cases. This is caused by the high compressibility and mobility contrasts between previously injected gas and the reservoir fluid. In the case of hysteresis effects, the water is trapping the gas around the wellbore which results in a reduction in the mobility and an increase in the pressure change and its derivative.

As discussed before, because of the high mobility of gas, the interface between oil zone and gas zone acts as a no-flow boundary; thus, a unit-slope line is seen at early times [8]. Following the unit-slope line, a flow period with pressure-derivative value inversely proportional to the average mobility profile near the wellbore is seen. As time increases, the pressure response reflects the average mobility profile away from the wellbore.

Fig. 5 Pressure change and pressure-derivative responses for 2nd water injection period with and without hysteresis effects

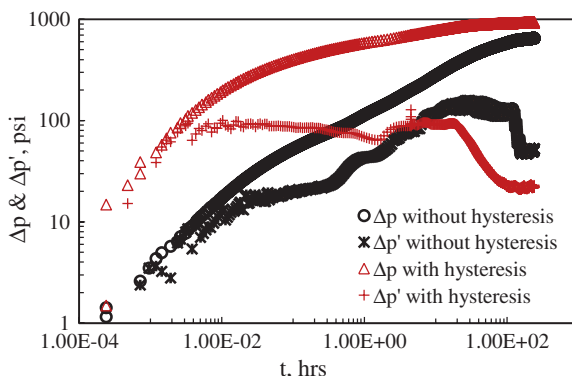
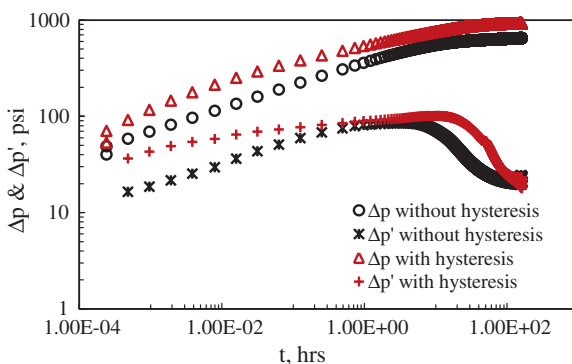


Fig. 6 Pressure change and pressure-derivative responses for 2nd water falloff period with and without hysteresis effects



In the case of with hysteresis, the mobility of gas is reduced by injected water which is also causing a reduction in water injectivity and an increase in pressure drop compared to the case without hysteresis which can be seen in Fig. 5. Similar to the case without hysteresis, after the unit-slope line, there is a radial flow period on the derivative curve which is inversely proportional to the total mobility profile near the wellbore and also as time increases, the pressure response reflects the average mobility profile away from the wellbore.

The falloff pressure-derivative curve for the case of without hysteresis in Fig. 6 exhibits a positive quarter-slope instead of a radial flow from the water zone. This is due to a progressive mixing of injected water with gas and has also been reported by [3]. For the case with hysteresis, the pressure-derivative curve exhibits a shorter quarter-slope line at early times and the pressure and pressure-derivative curves are higher than the case without hysteresis because of the reduction of mobility in the flooded zone.

4 Conclusions

Pressure transient behaviors of IWAG injection with and without hysteresis effect using simulated data were investigated. It is seen that hysteresis affects the displacement process in IWAG injection by reducing gas mobility which leads to an effective displacement.

Gas has a much higher mobility and isothermal compressibility compared to oil and water. This makes it easier to inject gas with less pressure drop as its volume increases near the wellbore. Hence, bottom-hole pressure during the gas injection period starts reducing after some time. The falloff pressure-derivative response shows a long transition zone with a half-slope line because of the high mobility contrast. Then followed by a second radial period which reflects the end point mobility ratio of the oil zone.

Pressure change and pressure-derivative curves of water injection period after gas injection exhibit a unit-slope line at early time based on the amount of gas trapped. Unless care is taken in the analysis, this might create confusion with the wellbore storage effect. At early times on the falloff curve, a positive quarter-slope line may be seen instead of the radial flow response from the flooded zone. This can be an indication of the progressive mixing of water with gas.

It is worth noting that the pressure behavior during falloff period has not been influenced by the hysteresis effect significantly as that of the injection period. This might be due to the fact that the fluids movement is negligible. Injection period is influenced by the hysteresis effect due to the change in mobilities of reservoir and injected fluids. Therefore, incorporation of gas relative permeability hysteresis effect in modeling and simulating pressure transient response of IWAG injection is necessary for accurate and reasonable parameter estimation.

Acknowledgments The authors would like to thank the Universiti Teknologi PETRONAS (UTP) for providing the necessary financial support and research facility to conduct this study.

References

1. M. Abbaszadeh and M. Kamal, "Pressure transient testing of water-injection wells," *SPE*, vol 4, no. 1, pp. 115-124, 1989, paper SPE 16744-PA.
2. A. Satman, M. Eggenschwiller, and H. J. Ramey, "Interpretation of injection well pressure transient data in thermal oil recovery," presented at the 1980 50th annual California meeting of SPE of AIME, Los Angeles, California, April 9-11, 1980, paper SPE 8908-MS.
3. A. B. Stenger, S. A. Al-Kendi, A. F. Al-Ameri, and A. B. Al-Katheeri, "Interpretation of immiscible WAG Pressure-Falloff Tests," presented at the Abu Dhabi International Petroleum Exhibition and conference, Abu Dhabi, UAE, 1-4 November 2010, paper SPE 137062.
4. M. J. Oak, "Three-phase relative permeability of Berea sandstone," presented at the SPE/DOE 17th symposium on EOR, Tulsa, Oklahoma, April 22-25, 1990, paper SPE/DOE 20183-MS.
5. E. J. Spiteri and R. Juanes, "Impact of relative permeability hysteresis on the numerical simulation of WAG injection," presented at the SPE annual technical conference and exhibition, Houston, Texas, September 26-29, 2004, paper SPE 89921-MS.
6. "Eclipse 100 Technical description," Schlumberger GeoQuest, 2010.
7. R. G. Agarwal, "A new method to account for producing time effects when drawdown type curves are used to analyze pressure buildup and other test data," presented at the 55th annual fall technical conference and exhibition of the society of petroleum engineers of AIME, Dallas, Texas, September 21-24, 1980, paper SPE 9289.
8. G. L. Messner and R. L. Williams, "Application of pressure transient analysis in steam injection wells," presented at the 1982 California Meeting of SPE, San Francisco, CA, March 24-26, 1982, paper SPE 10781-MS.

Control of Paraffin Deposition in Production Operation by Using Ethylene–TetraFluoroEthylene (ETFE)

Mombekov Bagdat and Rashidi Masoud

Abstract The physiochemical characteristics of the crude and deposited wax are two main issues associated to the flow assurance. They can provide useful estimates of the parameters and behavior required for operational engineering process developments and/or physical modifications to the processing of crude oils where the main objectives are to reduce costs of production and transportation. This study will attempt to determine and explain the new and effective way of eliminating paraffin depositions by utilizing a novel polymer which is called Ethylene–TetraFluoroEthylene (ETFE) with IUPAC name poly(ethylene-co-tetrafluoroethylene). Furthermore, this paper compares the known characteristics of three types of pipes—ETFE internal plastic pipe coating and rigid PVC plastic pipe coating and steel pipe. The paraffin deposition decreases as the effect of temperature increases from 5 to 25 °C and the flow rate increases from laminar to turbulent. The deposition reaches its peak at a fluid velocity value around 2.4 ft/s. The surface roughness of the three pipes steel, rigid PVC, and ETFE plastic pipe coated on paraffin deposition was evaluated. The ETFE plastic pipe with the least roughness recorded an appreciably good deposition (15 g/4 h) than the other two pipes. This study results show that ETFE internal plastic pipe coating is the most appropriate solution for paraffin deposition in the pipelines.

Keywords Cloud point • Ethylene–tetrafluoroethylene (ETFE) • Polyvinyl chloride (PVC) • Paraffin deposition • Precipitation

M. Bagdat · R. Masoud (✉)
Faculty of Geosciences and Petroleum Engineering, Universiti Teknologi Petronas,
31750 Tronoh, Perak, Malaysia
e-mail: masoud.rashidi@petronas.com.my

M. Bagdat
e-mail: bagdatbiz@gmail.com

1 Introduction

Paraffin deposition problems have been recognized as one of the main challenge in oil and gas industry during production and transportation of crude oil. Petroleum industry loses hundreds of millions of dollars yearly for controlling these problems. Paraffin wax has been defined as the organic compounds found in crude oil. Paraffin molecules are very complex with relatively high molecular weight, and it mainly contains carbon and hydrogen atoms. They are usually found in between the hydrocarbon chain of $C_{18}H_{38}$ and $C_{78}H_{142}$ with highest melting point [1]. In the oil industry, paraffin deposits are frequently a trouble for assured flow of oil from production site toward processing facilities and refineries. Paraffin could be deposited anywhere along the production system, from near the wellbore region to production tubing, flow lines, pipeline, and processing facilities such as separators and leading to the reduced production and transportation rate, equipment damage, and production shut down [2]. Hence, several methods such as mechanical, thermal, and chemical have been used to remove and prevent the formation of paraffin deposits. However, no perfect solution has been found to overcome this initial problem yet.

Steel pipe and rigid polyvinyl chloride (PVC) have been used in several oil and gas fields, and it has lots of advantages and disadvantages which still need to be improved for this reason Ethylene–TetraFluoroEthylene (ETFE) can be a better solution to overcome this problem.

ETFE is fluorine-based plastic which melts at high temperature (250–280 °C), and it was synthesized in order to be highly resistant to corrosion, high temperatures, and water absorption as well as excellent weather durability and resistance to oxidation. Moreover, it is considered as material with exceptional electrical and chemical properties, which is also resistant to high energy radiation [3–5]. The application of internal coating can be an efficient solution for mitigating the precipitation and paraffin deposition as well as corrosion and pressure drop.

The use of ETFE plastic pipe coating for solving and preventing paraffin deposition is going to be novel mitigation study in EOR production state.

1.1 Mechanism of Paraffin Wax Crystallization, Precipitation, and Deposition

Paraffin is completely dissolved in crude oil in equilibrium condition [6]. Changes in temperature and pressure disturb this equilibrium, which might result in paraffin precipitation and crystallization. It is known that the solubility of the paraffin wax is very sensitive to temperature changes [7]. For instance, if the temperature of pipe's surface is below the Cloud Point (The Cloud Point is the temperature at which paraffin starts to crystallize in the solution [1, 8]) of the oil, high molecular weight paraffin waxes are deposited. When crude oil temperature is lowered below

the Cloud Point, paraffin wax crystals precipitate and adhere by colliding with surface and deposits [6, 7, 10]. Besides, a mechanism such as shear dispersion, Brown diffusion, gravity, thermophoresis, and turbophoresis helps to drive the wax molecule particle to deposit on the pipeline wall [9, 11, 12].

There are three main factors that affect paraffin wax deposition in flow systems, which are flow rate, temperature deferential, and cooling rate, as well as surface properties [13].

2 Experimental Section

2.1 Characterization of Malaysian (Tapis) Crude Oil

Characterizations of crude oil were performed based on several ASTM methods. It should be carried out in order to determine the physiochemical properties of crude oil. The density of crude oil was determined by using DMA 35 N Standard Test Method, and the viscosity of crude oil was performed using an electromagnetic viscometer, EV 1000, by Vinci Technologies. Pour point measurement was carried out using ISL's CPP 5Gs Pour Point Analyzer, and the Carl Zeiss microscope equipped with Olympus BX51 camera was used to measure the WAT of crude oil. The Gas Chromatography Mass Spectrometer was used to determine carbon number distribution of crude oil. Surface roughness of the steel pipe, rigid PVC, and ETFE plastic coated pipe was measured by the Hommel T 1000®.

Experiments were carried out to characterize the crude oil sample studied in this paper. Rheological study results are reported in Table 1.

The result of compositionally characterized crude oil is shown in Fig. 1. The carbon number chain length of the n-alkane peaks is labeled in the chromatogram. The gas chromatogram indicates that the crude oil consists of mainly C14–C25 where the highest peak is at C14.

Table 1 Physical properties of the Tapis crude oil

Properties	Unit	ASTM method	Tapis crude oil
Density	g/m ³	DMA 35 N	0.82
Pour point	°C	D 97	18
Wax appearance temperature (cloud point)	°C	Cross polarized microscopy	27
Viscosity	cp	Electromagnetic viscometer	4.012
Carbon number distribution		GCMS	Refer Fig. 3

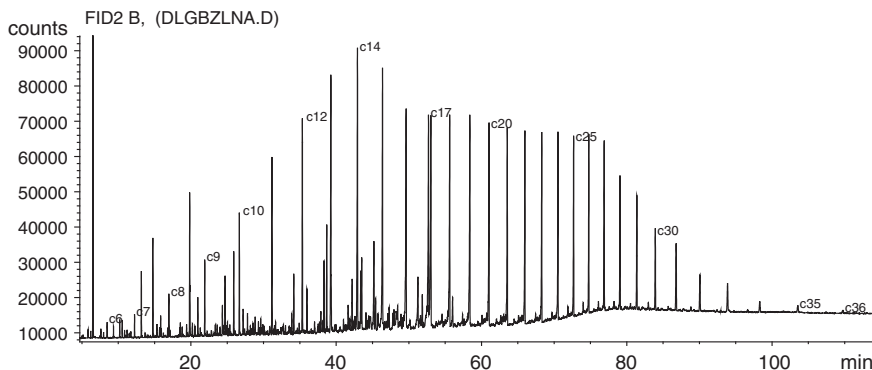


Fig. 1 Carbon number distribution of Tapis crude oil

2.2 Experimental Facility

The steel, rigid PVC plastic coated, and ETFE plastic coated pipes nominal diameter 2 in. and 12 m in length were used to determine the effect of velocity, temperature, and surface roughness on rates of deposition. The schematic diagram of the test device is shown in Fig. 2.

Paraffin deposition apparatus consisted of 4 major sections:

- Cooling section
- Heating section

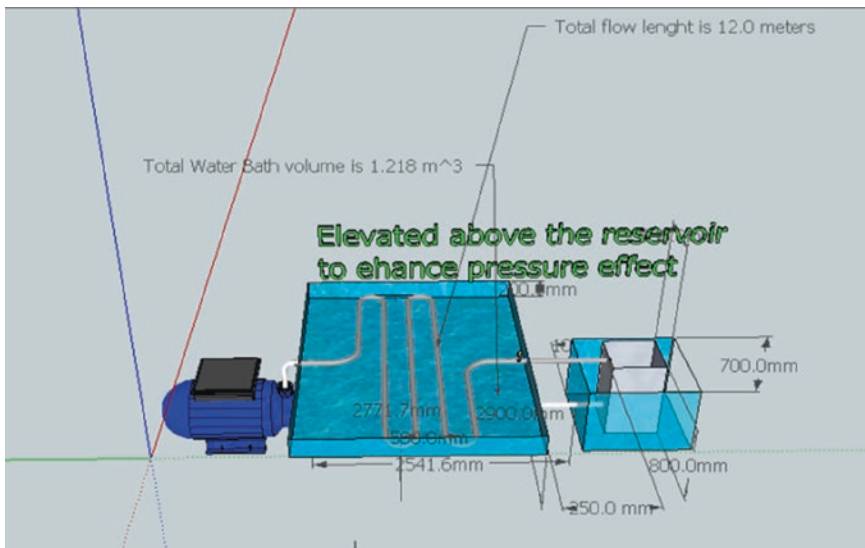


Fig. 2 Paraffin deposition apparatus

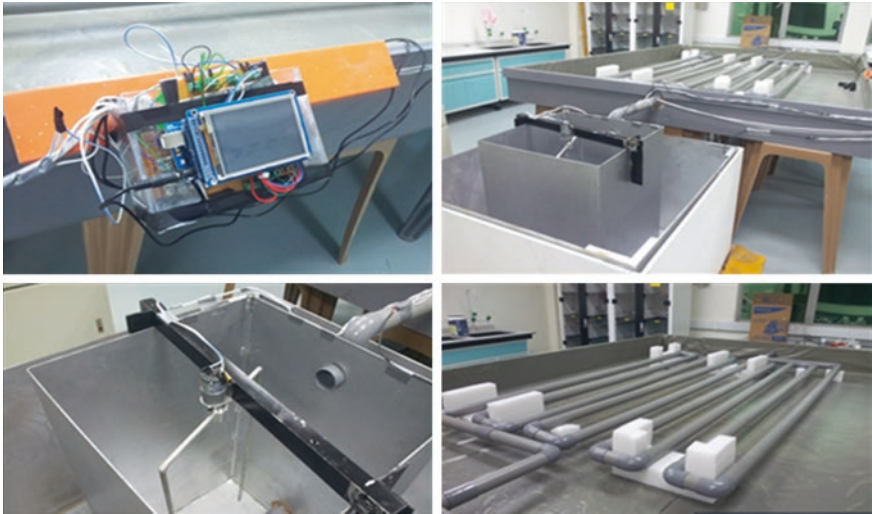


Fig. 3 Paraffin deposition apparatus

- Control and fluid flow section
- Stirring section

For the cooling section, a cold water bath of dimension $2.9 \text{ m} \times 2.1 \text{ m} \times 0.2 \text{ m}$ was designed to house a piping system that stretched 12 m long. This cold water bath causes deposition and precipitation of the paraffin wax on the test pipes' surface when the temperature is below the cloud point of the crude oil.

For the heating system, there are two parts, namely the hot water bath and the oil reservoir. The hot water bath has a dimension of $1.0 \text{ m} \times 1.0 \text{ m} \times 0.7 \text{ m}$, and the reservoir on the other hand has a dimension of $0.5 \text{ m} \times 0.5 \text{ m} \times 0.8 \text{ m}$. As it can be seen from Fig. 3, the hot water bath was equipped with electro heater, and a thermo regulator is used to maintain the temperature of the oil. The oil reservoir is to be place in the hot water bath.

For the control and fluid flow section, the first design element is the valve in between the hydrocarbon pump and the heating system. This valve is to allow the crude to be properly heated above its cloud point before actually flowing into the cooling system via pump. As it can be seen from Fig. 3, the cold water bath is elevated to a level higher than that of the hydrocarbon pump and also the heating system. This is to allow pressure to stabilize and facilitate the flow of crude from the cooling system to the heating system.

For the stirring section, the stirring system is placed in the oil reservoir to mix up the crude oil in order to avoid early stage of precipitation of crude oil. As it can be seen from Fig. 3.

2.3 Experimental Procedure

Paraffin deposition apparatus was used in order to investigate the paraffin wax formation mechanisms. Detailed experimental procedures as well as parameters are shown below.

2.4 Effect of Lowering Temperature on Paraffin Deposition

Effect of lowering temperature on the rate of paraffin deposition has been studied by performing experiments with various temperatures. The lowering temperature shall be tested at three different points which are 25, 15, and 5 °C. The crude oil temperature has been kept constant at 55 °C, which is above its cloud point. Firstly, test pipes have been submerged in a cold water bath in order to reduce the crude oil temperature below its cloud point. The gear pump was used to circulate the oil through the system, and the flow rate was controlled by valves A. Typically, one cycle of the experiment takes 4 h, and after this, the test pipe must be removed in order to clean it from paraffin deposits. This operation can be carried out by pushing a rod scraper through the pipes several times. The scraped paraffin is mixed with normal pentane in the beaker into standard ASTM 100-ml centrifuge tubes. It was centrifuged at 1,500 rpm for 20 min. As a result, it is expected that the solid precipitation will take place and it is considered as paraffin deposition at the bottom of the beaker. Inside and outside of the test pipes were totally cleaned by wiping with kerosene—saturated rag then dried with a clean, waterless cloth for the next run.

2.5 Effect of Velocity on Paraffin Deposition

This section will follow the experimental procedure performed in the above section. However, this part is concerned on changing of velocity of the flowing fluid in the pipe which is crude oil in this case. The velocity shall be varied gradually, and the quantity of wax deposit will be determined for each variation. The change of velocity will be performed so that it can change the flow characteristic from laminar to turbulence. The crude oil temperature and all the surfaces properties shall be maintained at fixed value.

2.6 Effect of Surface Roughness on Paraffin Deposition

Similar experimental procedure will be performed as discussed in the previous section with no change on coolant temperature and crude oil velocity. The roughness parameters of steel, PVC, and ETFE pipes were measured, and effect of wax deposition on their surfaces will be determined.

3 Results and Discussions

Malaysian (Tapis) crude oil has been used in performing experiments to obtain the effect of velocity, temperature, and surface roughness on rate of paraffin deposition.

Experiments have been conducted to investigate the effect of temperature on paraffin deposition by lowering temperature between 25 and 5 °C while oil temperature was set to 55 °C, which is above its cloud point at the constant velocity. The study concluded that the paraffin deposit was indeed increased as the temperature decrease. The data obtained from these experiments are illustrated in Fig. 4.

It can be seen from the experiment above that when temperature decreases more heat will be dissipated from the deposit reducing the temperature of the crude oil. As a consequence, solubility of wax in the crude oil was reduced and thus forming a network of solid wax. The growth of these paraffin deposits increases simultaneously with increasing temperature difference between the temperature of the pipe surface and temperature of the crude oil.

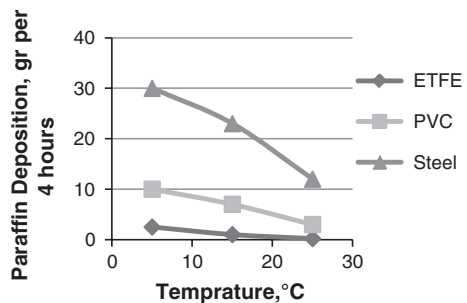
The rate of paraffin deposition increased gradually with increase in velocity whereas the maximum rate was obtained when flow changed from laminar to turbulent flow. At higher velocities, the rate of deposition decreases rapidly. Results of flow test are illustrated in Fig. 5.

This investigation results show that the rate of paraffin deposition on steel pipe also was higher than rigid PVC and ETFE plastic pipe coated. It can be explained by the longer residence time of the oil in the tubing, which leads to more heat loss and decreases the temperature of the oil, which results in paraffin deposition.

The least amount of paraffin accumulation was found in the surface of the ETFE plastic pipe coated due to its smooth surface rather than rigid PVC plastic pipe coated and steel pipe. The result of this investigation is shown in Table 2.

ETFE plastic pipe coating is distinguished by its ability to improve the surface smoothness and reduce surface energy which leads to a reduction in the adhesive ability of paraffin—crystals on the material's surface with its excellent insulation properties and a low dielectric constant. These properties make ETFE plastic pipe coating an outstanding choice for using in oil production to solve and prevent paraffin deposition.

Fig. 4 The effect of temperature on rate of paraffin deposition



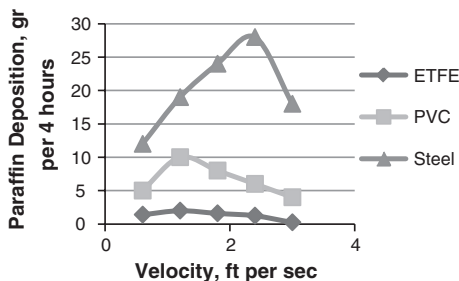


Fig. 5 The effect of velocity on rate of paraffin deposition

Table 2 The effect of surface roughness on paraffin deposition

Type of pipe	Surface roughness R_a (microns)	Paraffin deposition gram per 4 h
Steel	5.06	110
Rigid PVC	2.01	62
ETFE	0.10	15

4 Conclusions

The all experiment results show that the rate of paraffin deposition at all temperatures, velocity, and on the surface of the pipe was greatest in steel pipe but significant paraffin accumulation was found in rigid PVC plastic coated pipe. The lowest amount of paraffin deposition was observed in the ETFE plastic coated pipe.

It has been proven that the usage of ETFE plastic pipe coatings in a typical crude oil can potentially reduce down the paraffin deposition inside the pipelines, hence improving the whole system thoroughly.

The use of ETFE plastic pipe coating for solving and preventing paraffin deposition has proved to be an economically and technically feasible method.

Acknowledgments The authors wish to express their appreciation to Universiti Teknologi PETRONAS for permission to publish this paper. The authors also thanks for the respective Petroleum Engineering Department for helping us to complete our project in terms of venue, lab work assistance, and lab testing facilities. In addition, thank you for all those are involved directly and indirectly to make our project successful.

References

1. James B. Dobbs "A unique method od paraffin control in production operation", *SPE 55647*, *Unichem*, A division of BJ Services Company, Paper was presented at the 1999 SPE rocky Mountain Regional Meeting held in Gillette, Wyoming, 15-18 May, 1999;
2. V. Seredyuk and M. Psyuk, "The Method for Increasing the Efficiency of Asphalt-Resin-Paraffin Deposits Inhibitors", 2009, pp. 313-317.

3. Leslie A. Robinson, "Structural Opportunities of ETFE (ethylene tetra fluoro ethylene)", Civil Engineering, Massachusetts Institute of Technology, 2004;
4. Ge'rrard Calleja, Axel Houdayer, Sylvie Etienne-Calas, David Bourgogne, "Conversion of Poly(ethylene-alt-tetrafluoroethylene) Copolymers into Polytetrafluoroethylene by Direct Fluorination: A Convenient Approach to Access New Properties at the ETFE Surface" *Inge'nerie et Architectures Macromole'culaires*, Institut Charles Gerhardt-UMR(CNRS) 5253, Ecole Nat Sup de Chimie de Montpellier, 8 Rue de l'Ecole Normale, F-34296 Montpellier Cedex, France, January 2011.
5. Precisioncoating.com. the Teflon Coating Process: Benefits of Teflon Coatings [Online]. Available: <http://www.precisioncoating.com/industrial-coatings/teflon-coating-benefits.html>, 2014.
6. G. E. Addison, "Identification and treating of downhole organic deposits", *SPE 18894*, paper was presented at the SPE Production Operations Symposium held in Oklahoma City, Oklahoma, March 13-14, 1989;
7. D. C. Thomas, "Selection of Paraffin Control Products and Applications", *SPE 17626*, paper was presented at the SPE International Meeting on Petroleum Engineering held in Tianjin, China, November 1-4, 1988;
8. M. M. Santamaria, R. B. Roberts, S.K.J. Gill, "Evaluation of Paraffin Deposition Potential Using Drillstem Test Fluids", *SPE 21713*, paper was presented at the Production and Operations Symposium held in Oklahoma City, Oklahoma, April 7-9, 1991;
9. Lee, H., PhD. Thesis, University of Michigan, 2008;
10. Sanjay Misra, Simanta Baruah and Kulwant Singh, "Paraffin Problems in Crude Oil Production and Transportation: A Review", *SPE 28181*, Oil and Natural Gas Corp. Ltd., paper accepted for publication September 21, 1994;
11. Borghi, G.P., Corraera, S., and Merino-Garcia, D. "In-depth investigation of wax deposition mechanisms". Proceedings OMC 2005 Offshore Mediterranean Conference and Exhibition. Ravenna, Italy, March 16-18, 2005;
12. Merino_Garcia and Corraera S., "Cold Flow: A review of a Technology to Avoid Wax Deposition," *Petroleum Science and Technology* 26(4), 446-459, 2008; .
13. Bott T.R. and Gudmundsson, J. S., "Deposition of Paraffin Wax From Flowing Systems", Institute of Petroleum Engineering, Tech. *Paper IP-77-007*, 1977;

Investigation of Asphaltene Onset Pressure (AOP) in Low Asphaltenic Light Oil Samples

Teoh Wan Ru and Ali F. Alta'ee

Abstract Asphaltene precipitation is a common problem in reservoir field during natural pressure depletion and gas injection process for enhanced oil recovery (EOR). Extensive field and laboratory data have proven that asphaltene precipitated more easily from light oil rather than from heavy oil. This study concerns with both experimental and simulation investigations on asphaltene precipitation condition during pressure depletion and gas injection. A series of isothermal depressurization experiments have been carried out using light oil samples with low asphaltene content to investigate its asphaltene onset pressure (AOP). In addition, precipitation onset condition induced by different carbon dioxide (CO₂) concentration has been investigated over the pressure change. Besides, simulation studies have been carried out to understand asphaltene onset behavior over pressure change at reservoir temperature. Three light oil samples with low asphaltene content have been chosen to investigate precipitated asphaltene fraction induced by different CO₂ concentrations over the pressure change. The results of this study have shown that asphaltene starts to precipitate in oil when approaching bubble-point pressure during depressurization. The precipitated amount increases and reaches the maximum around bubble-point pressure. After bubble-point pressure, part of the precipitated asphaltene re-dissolved back to the oil. By injecting higher CO₂ mol percentage, bubble-point pressure increases and more asphaltenes precipitate in oil.

Keywords Asphaltene onset pressure • Light oil • CO₂

T.W. Ru · A.F. Alta'ee (✉)

Universiti Teknologi PETRONAS, 31750 Tronoh, Perak, Malaysia

e-mail: ali_mangi@petronas.com.my

1 Introduction

In recent years, offshore production system has been moving to deepwater and subsea environments which increased the importance of fluid properties related to flow assurance issues. One of these potential challenges is asphaltene precipitation and deposition problems from reservoir up to the production line, causing reservoir formation damage and plugging wells and flow lines. The impacts are usually catastrophic, while the remedial measures are expensive yet disruptive. Therefore, it is crucial to investigate the potential of asphaltene precipitation in reservoir prior to natural pressure depletion, especially before implementing a gas injection scheme, in order to build proper control and remediation strategies into the systems from the beginning.

Asphaltenes are heavy hydrocarbon molecules which are naturally existing as colloidal suspension in petroleum reservoir fluids and stabilized by resins adsorbed on their surface [6, 15, 21, 22]. Asphaltene precipitations are the common problems in reservoir field during natural pressure depletion [2, 4, 12], as well as during gas injection processes for IOR [18] or EOR [5, 20]. Extensive field and laboratory data have proven that asphaltene precipitates more easily from light oil rather than from heavy oil, even though the heavier oil might have much higher asphaltene content [4, 5, 15, 20].

Asphaltene precipitation during pressure depletion and oil recovery is a common problem occurring in many fields around the world. In reservoir, the precipitated asphaltenes can deposit onto the rock surface or remain as a suspended particle in the oil phase. The deposited asphaltenes may cause blockage of the pore throats and channels, which results in permeability reduction and porosity alteration and later leading to the formation of damage, furthermore plugging the wellbore and blocking the production line.

The review of asphaltene deposition in field situations indicates that asphaltene content in oil does not play a crucial role in the flocculation process. Asphaltene precipitation problems are more common in lighter oil which contains only minor amount of asphaltene in reservoir especially at pressure above the bubble point; therefore, the aim of this study was to determine the AOP for light crude oil samples with low asphaltene content and to investigate the tendency of asphaltene precipitation under reservoir conditions for different CO₂ concentrations.

In this project, three light oil samples with API gravity range within 31° to 42°, which are low in asphaltene content (less than 1.0 wt%) and have been used for reservoir simulation studies. One of the light oil samples has been recombined in laboratory for experimental investigation. With known amount of fluid composition and asphaltene weight content, at reservoir pressure and temperature, the light oil samples have been tested through simulation studies to investigate their AOP. This research focuses on the phase behavior and equilibrium studies of asphaltene precipitation in reservoir condition.

Static asphaltene test has been carried out with additional mole percentage of CO₂ gas injection, over isothermal pressure depletion to monitor asphaltene onset

precipitation condition. This investigation mainly simulated the reservoir condition which is away from the near wellbore region, while the dynamic flow within the reservoir will not be included here. Finally, these results have been related to the expected behavior of asphaltene in the deep reservoir and to address the uncertainties.

2 What Is Asphaltene?

2.1 Asphaltene Definition

Compositional studies separate petroleum reservoir fluids into SARA, namely saturates, aromatics, resins, and asphaltenes. Asphaltenes are complex organic components of reservoir fluids with no defined melting point, while having the highest molecular weight hydrocarbon fraction and highest polarity among the four. Generally, asphaltenes are characterized as soluble in aromatics (e.g., benzene and toluene), but insoluble in paraffinic compounds (e.g., *n*-pentane and *n*-heptane) to form dark color solid as shown in Fig. 1 [5, 8, 10, 21–23].

2.2 Asphaltene Precipitation

According to the first theoretical model of asphaltene precipitation as proposed by Liao and Geng [16], asphaltenes are believed to exist dissolved in oil under dynamic stable system and this is known as solubility model. With respect to the interactions of asphaltenes–resins, they suggested the second model—colloid model. Similarly, Hirschberg et al. [14] summarized that colloidal model is the most common model for asphaltenes–resins interactions. This colloidal model was further supported by Kokal and Sayegh [15], Buckley et al. [6] and Alta'ee et al. [5],

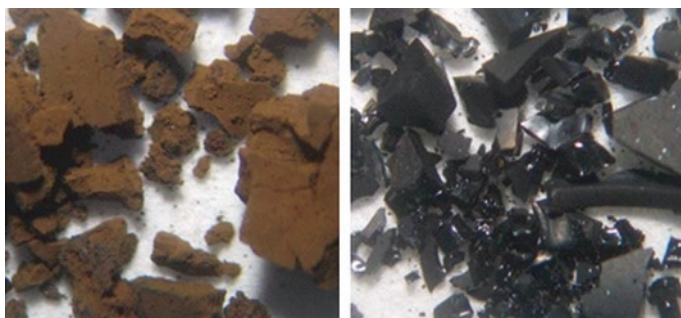
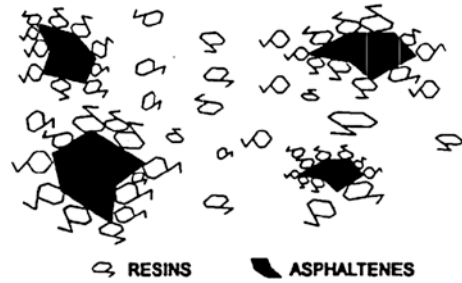


Fig. 1 *n*-Pentane asphaltene (*left*) and *n*-Heptane asphaltene (*right*) [11]

Fig. 2 Peptization of asphaltenes by resins [5, 15]



who also agreed that asphaltenes are heavy hydrocarbon molecules which exist naturally as dispersed colloidal suspension model in petroleum fluids.

As shown in Fig. 2, asphaltenes are finely dispersed in oil and stabilized by the highly polar peptizing agents—resins, which are adsorbed on their surfaces. The result of asphaltenes–resins interactions is generally termed as “micelles”. Hirschberg et al. [14] advocated that resins have a strong tendency to associate with asphaltenes. This statement was strengthened by Speight [21, 22] who regarded asphaltenes–resins interactions appear to be preferable over asphaltenes–asphaltenes interactions and resins–resins interactions when both asphaltenes and resins coexist in petroleum fluids. When incompatibility occurs among petroleum fluids, the loss of dispersability in colloidal suspension causes the higher molecular weight polar components (asphaltenes and resins) to precipitate.

Operational problems associated with asphaltene precipitation and deposition manifest in nearly all facets of petroleum production, processing, and transportation of petroleum [10, 12]. The precipitation of asphaltenes from reservoirs, to near wellbore, well tubing, up to the surface facilities have detrimental effects on the economics of well development as well as oil production. The chance for these problems to happen is expected to be even higher in offshore and into deepwater operations where the prevention and remediation costs increase dramatically [2, 13].

2.3 Mechanism of Precipitation

Alta'ee et al. [5] defined the terminology of asphaltene solidification in terms of three stages, namely precipitation, flocculation, and deposition. Firstly, asphaltenes precipitate from petroleum fluids when solid particles form a distinct phase as they come out of solution. During precipitation, the quantity and size of solid particles could be quite small and they are “swimming” along with the fluid flow. Then, the flowing polar solid particles coalesce and their sizes are growing larger during asphaltene flocculation. The quantity and size of particles are increasing. Finally, when the flocculated particles lump together as residue, they become so large until can no longer be supported by the fluid flow. These deposited asphaltenes will be settled out and adhered to solid surfaces.

Fig. 3 Asphaltene micellization (*left*) and precipitation (*right*) [16]

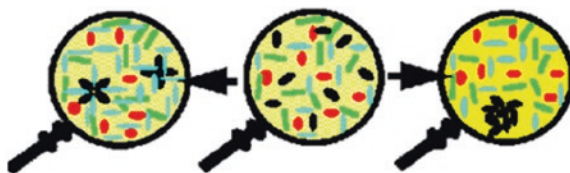
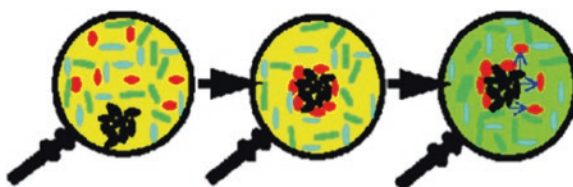


Fig. 4 Peptization by resins (*center*); change in chemical potential balance (*right*) [24]



Similarly, Hammami and Ratulowski [13] also emphasized the difference between both precipitation and deposition terminology, whereby precipitation is the formation of a solid phase out of a liquid phase, while deposition is the growth of the precipitated solids on a surface. However, as quoted by them, “Precipitation is, although a precursor to deposition, does not necessarily ensure deposition.”

Thou et al. [24] explained the mechanism of asphaltene deposition in terms of four effects—solubility, colloidal, aggregation and electrokinetic effects. As illustrated by Fig. 3, solubility effect is due to the content of crude oil. Micellization of asphaltenes is resulted by the increase in aromaticity in fluid composition, while addition of light paraffinic compounds will result in asphaltene precipitation. Due to colloidal effect, asphaltenes suspended in oil phase by the peptization of resins to form micelles. Increase in light paraffinic compounds in oil content results in migration of resins from asphaltene surface, thus breaking the micelle (asphaltene–resin) bond. Concentration variation of resins due to the addition of light saturates causes change in chemical potential balance, as illustrated in Fig. 4. Aggregation effect occurs as a result of insufficient resins coating around the entire surface of one asphaltene particle, causing asphaltene and asphaltene flocculate together due to their polarity [6], while electrokinetic effect is related to the electrical potential difference due to motion of charged while particles flowing in porous medium.

2.4 Major Destabilizing Factors

As summarized by most researchers based on field experience and experimental observations, the major destabilizing factors for asphaltene are pressure depletion, compositional change, as well as temperature variation [2, 13–15, 20]. The general consensus is that the effect of pressure and composition change on asphaltene precipitation is comparatively stronger than the effect of temperature.

2.4.1 Pressure Depletion

Asphaltene precipitation and deposition problems along the production system occur near wellbore region and along well tubing below the depth at which the oil becomes saturated [12, 13, 15, 24]. These are the impacts of pressure drop from near wellbore region up to the production line on surface, whereas at reservoir conditions, asphaltene precipitation happens in the oilfield which experiences natural pressure depletion throughout the production phase [2, 10]. This phenomenon is mainly related to the different compressibility of the light ends and the heavy components (e.g., resins and asphaltenes) of the under-saturated oil [13].

2.4.2 Compositional Change

Compositional change in reservoir fluids includes addition in light paraffinic compounds, increase in aromaticity, gas injection scheme, as well as change in gas–oil ratio (GOR), ratio of high to low molecular weight component, and asphaltene–resin ratio [20]. As reviewed by Hammami and Ratulowski [13], asphaltene precipitation can occur in situ during mixing of incompatible hydrocarbon fluids, miscible flooding, CO₂ flooding, and other solvent injection operations due to the effect of compositional change.

2.5 *Precipitation Over Pressure Depletion*

Experimental investigations and simulation studies on asphaltene precipitation in under-saturated petroleum fluids at reservoir conditions indicate that maximum amount of asphaltene precipitation is observed near the bubble-point pressure region [2, 12, 15, 18]. This bulk precipitation is due to maximum density difference between asphaltenes and bulk oil at bubble-point pressure before the first gas evolved from the under-saturated oil. When the gas mole percent is about to increase from zero, there is the highest asphaltene deposition mole percent [5].

According to Schlumberger Oilfield Glossary, AOP is defined as the pressure at a given test temperature which first causes asphaltenes to precipitate from reservoir fluid as pressure decreases. Utilizing the results from simulation studies, asphaltene precipitation envelope (APE) is generated as shown in Fig. 5, whereby the shaded area indicates asphaltene precipitation. When pressure is reducing, APE upper boundary is believed to be the onset pressure, while asphaltene precipitation increases with the reduction in pressure and reaches to a maximum near the bubble point [2]. Hence, according to Nghiem's model, asphaltene onset region is bounded by upper and lower AOP.

Fig. 5 Pressure–temperature APE [18]

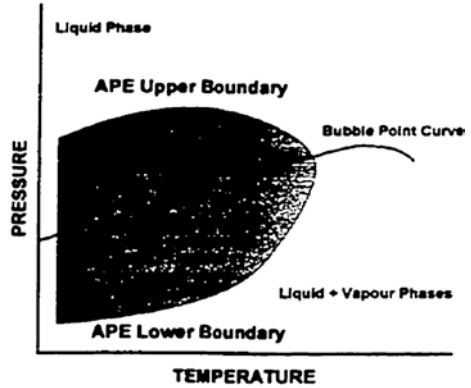
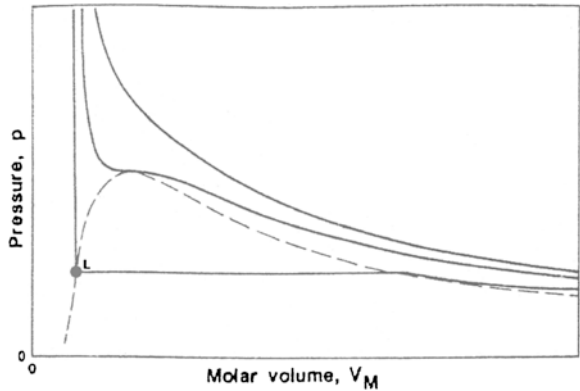


Fig. 6 Van der Waals loop [17]



2.5.1 Above Bubble-Point Pressure

Under very high reservoir pressure, the under-saturated single-phase oil is exerted by very high compressibility forces from the external pressure. According to the van der Waals loop [17] as shown in Fig. 6, at very high pressure along the liquid part of the isotherm before point *L*, the molar volume (V_m) is small. In terms of chemical potential, smaller V_m is having greater chemical potential, results in stronger van der Waals bond. Therefore, under very high pressure, the stronger van der Waals bond within colloidal model is believed to tighten the distance between asphaltenes and resins and thus stabilize the suspension micelles particles in oil [6, 13].

As reservoir pressure decreases, the weakening van der Waals bonds plus change in fluid properties disturb the stability of asphaltene–resin micelles. As the oil is depressured from reservoir pressure to bubble-point pressure, the mass and molar

composition keep constant, but the molar volume of the bulk oil is increasing, while the overall density is reducing. Due to the difference in compressibility, the volumes occupied by the C_6 components are increasing more rapidly than those of the C_{7+} fraction [6]. Hence, the reservoir fluids possess higher behavior of light oil and act more like lighter oil while pressure is decreasing.

With this increase in the volume of lighter hydrocarbon fraction, the solubility parameter between resins and evolving lighter ends decreases, meanwhile reduces the micelles solubility, and as such induces resin to dissolve constantly [5]. And later, this results in the reduced solubility of asphaltenes upon reaching bubble-point pressure, causing asphaltene precipitation [14]. Kokal and Sayegh [15] and Hammami et al. [12] have concluded that maximum difference in molar volume (density) between the asphaltenes and the bulk oil occurred at the bubble-point pressure before the first dissolved gas released.

2.5.2 Below Bubble-point Pressure

Below the saturated pressure, composition of reservoir fluids changes when the lighter hydrocarbon fraction evaporates from the oil as gas phase, thus changing the molar volume of the liquid phase and reestablishing some of its lost asphaltene solubility [12, 15]. As pressure is going down, light gas liberation leaves the heavier reservoir fluids with higher resins fraction, which is insufficient to peptize and stabilize the asphaltenes. Thus, the change in reservoir fluids composition will result in enhanced solubility with decreasing deposition upon pressure decreases below the bubble point [2, 14].

The review of asphaltene precipitation conditions over pressure depletion from reservoir pressure until below saturated pressure has explained the asphaltene field problems as addressed by Kokal and Sayegh [15]. After the bottom-hole pressure fell below the bubble-point pressure, asphaltene precipitation problems at the Ventura Field, Hassi-Messaoud Field, and Lake Maracaibo are diminishing. On the other hand, there was no deposition problem observed in Ula Field, Norway, below the bubble-point pressure. Evidence of asphaltene precipitation above the bubble-point pressure and asphaltene redissolution below the saturated pressure as observed by Hammami et al. [12] could be explained by the review as above.

2.6 *Precipitation in Light Oil*

Extensive field and laboratory data indicate that asphaltenes precipitate more easily from light oil as compared to from heavier oil, though the heavier oil consists of higher asphaltene content [4, 5, 15, 20]. Heavier oil consists of higher intermediate components with more resins and aromatics which make it a good solvent to stabilize asphaltenes, while lighter oil contains higher fraction of light hydrocarbon ends which have limited solubility on asphaltenes. The addition of light paraffinic compounds can alter the solubility of the asphaltene component in reservoir

fluids [12]. In accordance with the colloidal model of asphaltene behavior, resin molecules tend to desorb from the surface of the asphaltenes, thus breaking the micelles bond, in respond to the addition of light hydrocarbon fraction to reservoir fluids in order to reestablish thermodynamic equilibrium.

2.7 Effect of Asphaltene Content

The review of asphaltene deposition in field situations indicates that the quantity of asphaltene content in oil does not play a crucial role in asphaltene flocculation process [4, 15]. Asphaltene precipitation problems are often more common in lighter oil that contains minor amount of asphaltenes in reservoir at pressure above the bubble point. There are two field examples to prove the fact as discussed above. The Venezuelan Boscan heavy crude oil with 17.2-wt% asphaltenes was produced nearly trouble-free, whereas Hassi-Messaoud light crude oil in Algeria with only 0.15-wt% asphaltenes has numerous production problems due to asphaltene precipitation. As recognized by Alta'ee et al. [5], light oil with small amount of asphaltenes is more likely to cause production problems which are related to asphaltene precipitation, rather than the heavy oil with larger amount of asphaltene fraction.

2.8 CO₂ Injection

Field data have proven that asphaltene precipitation and deposition could have been exacerbated by gas injection, and coincidentally, light oil reservoirs are the more preferable candidates for gas injection processes [20, 23]. Most miscible solvents have the potential to cause asphaltene flocculation. The investigation result from Gholoum et al. [10] revealed that CO₂ is the most effective asphaltene precipitant followed by alkanes (C₁–C₇). Miscibility of CO₂ gas with the reservoir oil will contribute to the compositional change which favors the precipitation of asphaltenes. When injected CO₂ is in contact with the reservoir fluids, vaporizing gas drive process causes CO₂ gas vaporizes part of the light and intermediate components to the gas phase, which results in the loss of intermediate components (C₃₊) in reservoir fluids [11]. Meanwhile, resins are vaporized to the CO₂ gas phase as well. As a result, the reservoir oil phase is left with lesser resins content and lower molecular weight, acting as if light oil.

The loss of resins and the light oil characteristic destabilize asphaltenes in the reservoir fluids and then change the fluids behavior and equilibrium condition when CO₂ gas is in contact with the reservoir oil, which results in asphaltene precipitation [15, 20, 23]. Alta'ee et al. [5] and Srivastava and Huang [23] reported about their study on asphaltene precipitation at constant temperature over different CO₂ concentrations. The results proved that the amount of precipitated asphaltene increases with increasing CO₂ concentration as expressed in mole percentage. Besides, the results also showed that saturation pressure increases with increasing

CO₂ concentration. Experimental investigation by Gholum et al. [10] and Sarma [20] demonstrated that with the addition of CO₂ mol%, the power of transmitted light (PTL) is increasing until certain CO₂ concentration.

3 Methodology

The behavior of asphaltenes in light oil samples has been investigated through experimental and simulation studies. Low asphaltenic light oil samples were chosen to determine their AOP. In addition, the precipitation onset condition induced by different CO₂ concentrations has been investigated over the pressure change as well.

3.1 Sample Recombination

For experimental studies, dead oil sample obtained from one of the South China Sea oilfields has been recombined according to the desired ratio of methane gas and CO₂ gas.

3.2 Asphaltene Content Measurement

To determine the mass percentage of asphaltenes in an oil sample, asphaltene separation method (ASTM D3279) has been performed on oil sample which asphaltene weight content was unknown.

3.3 Static Asphaltene Test

A series of isothermal pressure depletion test has been carried out in a PVT cell with the recombined light oil sample from above reservoir pressure under reservoir temperature. CCE experiments were performed to investigate the saturation (bubble point) pressure.

3.4 Solid Detector System (SDS)

The light-scattering technique, also known as the solids detection system (SDS), is attached with the PVT cell during CCE experiments. A near-infrared (NIR) light

source on one side of the cell generates light at a specific transmittance power. When asphaltenes precipitate, they scatter light, reducing the transmittance power of the light detected by fiber-optic sensors on the other side of the cell.

3.5 Carbon Dioxide Injection

After undergoing one round of CCE experiment on the original oil sample, CO₂ gas will be added to illustrate CO₂ gas injection scheme. A total of 99.9 % purity CO₂ gas will be obtained from the CO₂ gas tank in laboratory. Applying the calculation suggested by Obeida and Heinemann [19], the concentration of CO₂ gas will be expressed in terms of mole percentage which will then be manipulated by the number of moles injected.

3.6 Data Gathering

To carry out simulation investigation, three low asphaltenic light oil samples have been selected to collect the parameters and input data. The first one is the recombined sample from experimental study, the second light oil sample data were obtained from an Iranian oilfield [9], and another one is obtained from South China Sea fields [1]. The oil properties for three oil samples studied are summarized in Table 1.

3.7 Simulation Modeling

The behavior of asphaltenes in both light and heavy oil was studied using a compositional simulator from the Computer Modeling Group (CMG) Ltd. The equation of state (EOS) applied in this simulation study is Soave-Redlich-Kwong (SRK).

Table 1 Oil properties for three (3) oil samples chosen for simulation studies

Oil properties	Oil samples		
	Oil sample 1 ^a	Oil sample 2	Oil sample 3
API gravity	37.8	34.3	41.4
Asphaltene (wt%)	0.12	0.66	0.07
Reservoir temperature (°F)	215	160	204
Reservoir pressure (psia)	1,800	6,000	2,900

^aRecombined sample used for laboratory studies

4 Results and Discussion

4.1 Experimental Studies

Laboratory experiment has been conducted on oil sample 1 using PVT cell attached with SDS. SDS transmittance is recorded over pressure depletion, while volume is recorded over the pressure change as well. When asphaltenes start to precipitate in oil sample, the transmittance power of the light detected reduced. As shown in Fig. 7, AOP is determined by the declining curve during depressurization, which is found to be at 4,200 psi for base case oil sample 1. Pressure depletion continued, and at one point, the transmittance power drops drastically, which is interpreted as maximum asphaltene precipitation at 1,660 psi. Besides, oil sample volume has been monitor throughout and presented in PV curve indicated by Fig. 11. From PV curve, bubble-point pressure (P_b) is found to be 1,900 psi for base case oil sample 1.

CO₂ gas has been injected to recombined oil sample 1 to illustrate 20, 40, and 60 mol% CO₂ gas injection. SDS transmittance and volume have been monitored over pressure reduction, as shown in Figs. 8, 9, 10, 11, 12, 13, and 14. The summary of experimental results is shown in Table 2.

4.2 Simulation Studies

Using the parameters and input data as from the literature, asphaltene precipitation model for each oil sample has been generated by the simulator. Two-phase (pressure–temperature) diagram and asphaltenes precipitated weight percentage versus

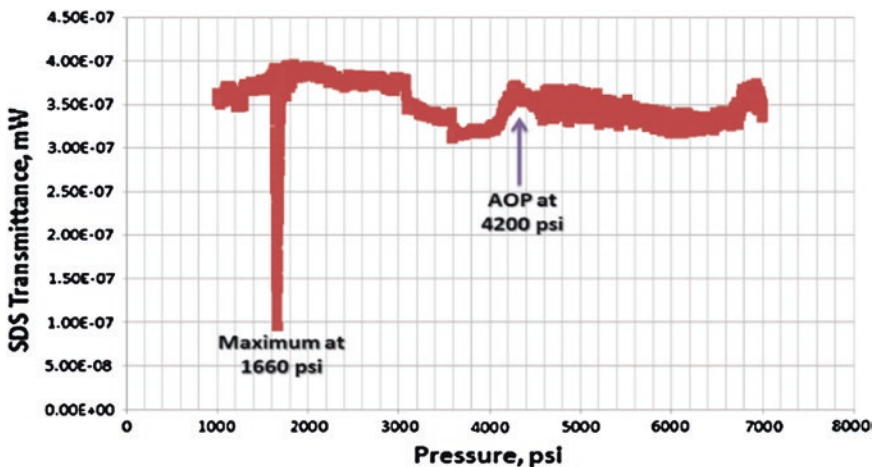


Fig. 7 SDS transmittance versus pressure for oil sample 1 (base case)

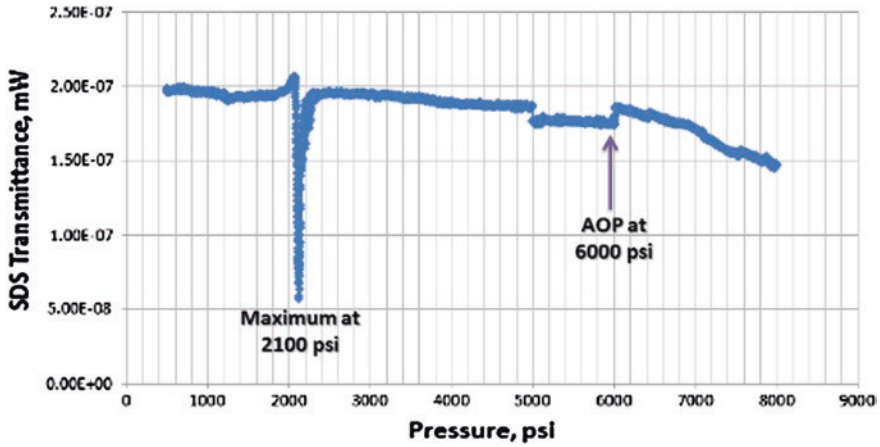


Fig. 8 SDS transmittance versus pressure for oil sample 1 (20 mol% CO₂)

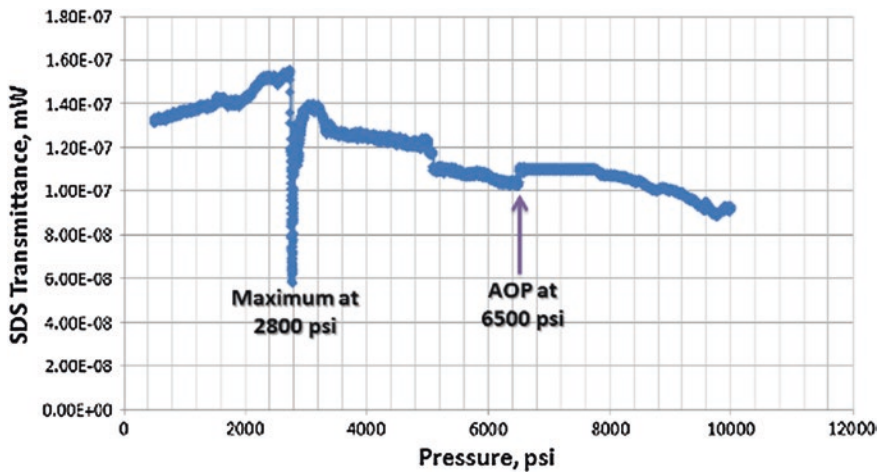


Fig. 9 SDS transmittance versus pressure for oil sample 1 (40 mol% CO₂)

pressure graph have been plotted with the simulator, as illustrated in Figs. 15 and 16, for three oil samples over different CO₂ mol% gas injection. P–T diagram as shown in Fig. 15 has been generated to find out the bubble-point pressure (P_b) at reservoir temperature.

Both P–T diagram and asphaltene precipitated weight percentage graphs have been generated for all three oil samples, over various CO₂ mol% gas injection. Tables 3, 4, and 5 summarize the lower and upper AOP, bubble-point pressure, and pressure at maximum asphaltene precipitation for different CO₂ mol% injection at reservoir temperature for oil sample 1, Iranian oil, and SCS oil 3, respectively.

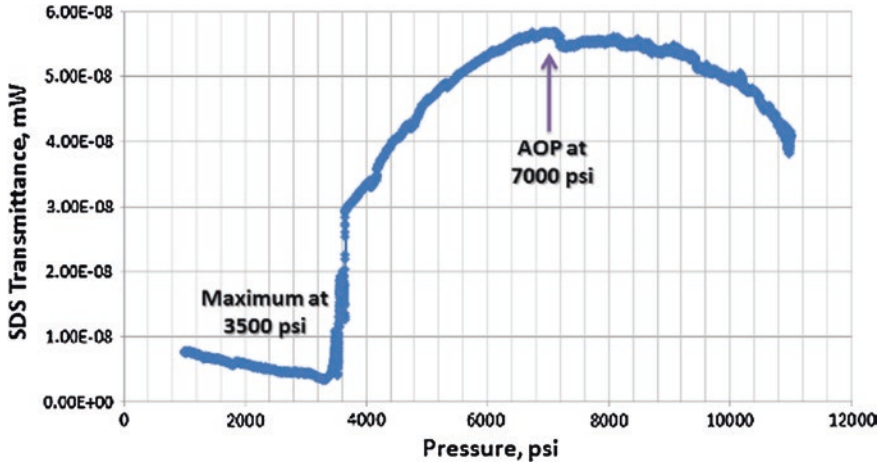


Fig. 10 SDS transmittance versus pressure for oil sample 1 (60 mol% CO₂)

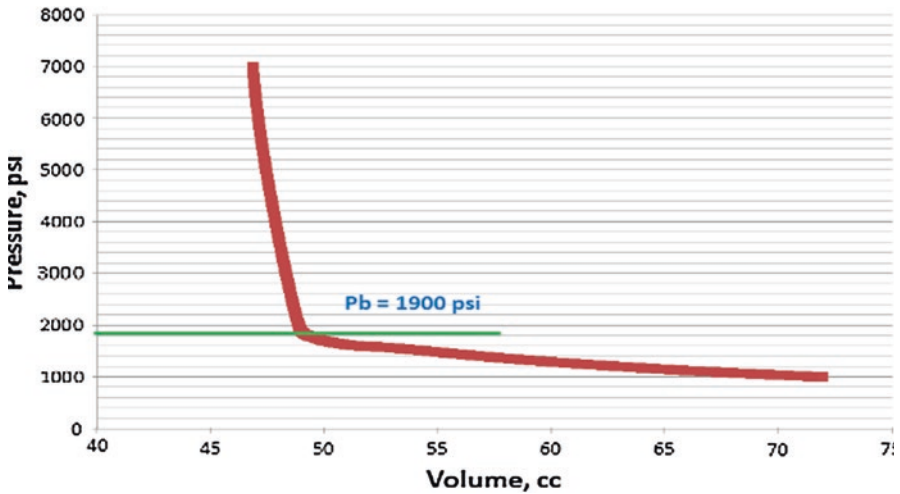


Fig. 11 PV curve for oil sample 1 (base case)

5 Discussion

According to Nghiem’s APE model [18] as shown in Fig. 5, asphaltene onset pressure is bounded within the upper and lower of the shaded region. Thus, in graph asphaltene precipitated wt% versus pressure, as shown in Fig. 16, the points where asphaltene start to precipitate from zero weight percentage are defined as the AOP, whereby the higher AOP is described as the “upper AOP,” while the lower one is defined as the “lower AOP.”

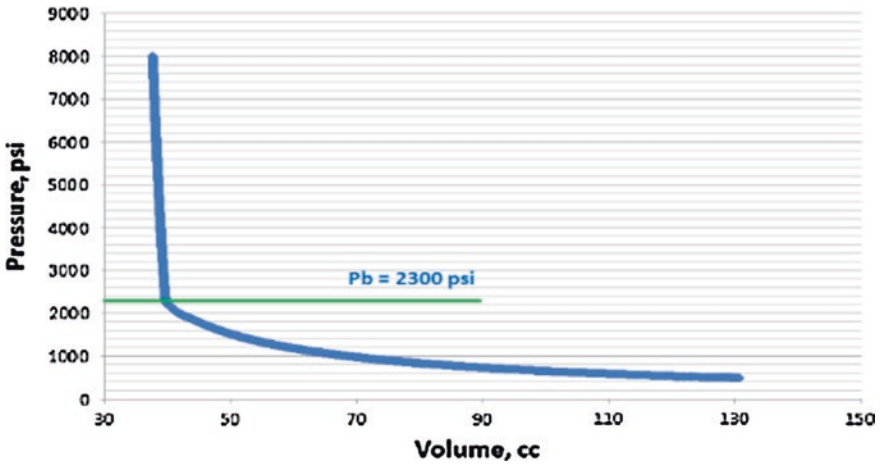


Fig. 12 PV curve for oil sample 1 (20 mol% CO₂)

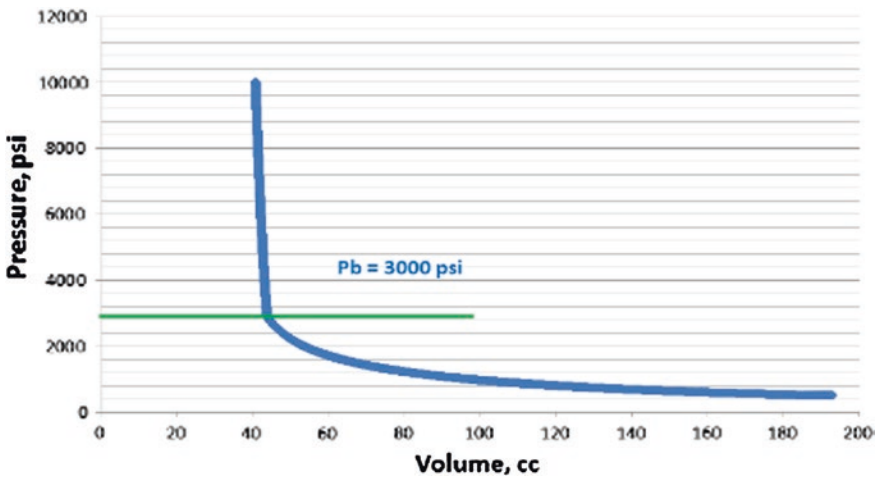


Fig. 13 PV curve for oil sample 1 (40 mol% CO₂)

Upon pressure depletion, asphaltenes start to precipitate when the van der Waals bonds within asphaltene colloidal model become weaker, in addition to the change in fluid properties which disturb the stability of asphaltene-resin micelles [5, 14]. At or very near to the bubble-point pressure, the graph shows maximum precipitated weight percentage of asphaltene, which is in accordance with the findings of Kokal and Sayegh [15], Hammami et al. [12], Afshari et al. [2], and Alta'ee et al. [5] who have claimed that asphaltene precipitation reaches maximum at bubble-point pressure. After crossing bubble-point pressure, evaporation of lighter

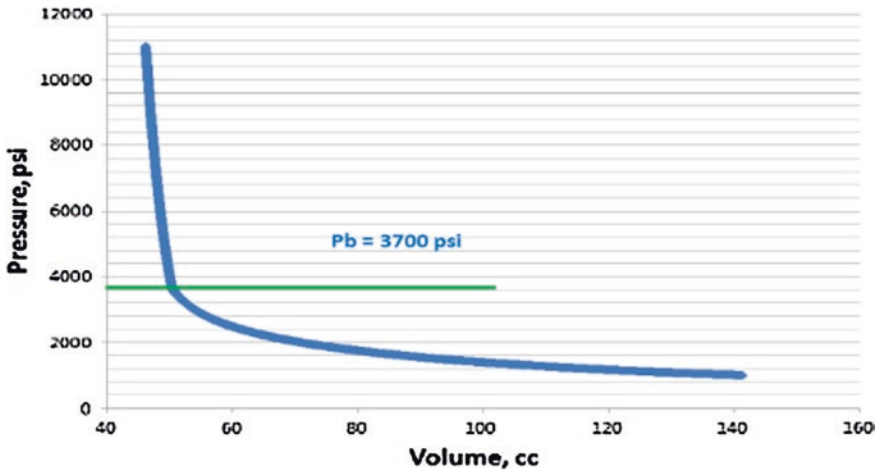


Fig. 14 PV curve for oil sample 1 (60 mol% CO₂)

Table 2 AOP, P_b , and maximum precipitation pressure for oil sample 1

Oil sample 1	AOP (psi)	P_b (psi)	Maximum precipitation (psi)
Base case	4,200	1,900	1,660
20 mol% CO ₂	6,000	2,300	2,100
40 mol% CO ₂	6,500	3,000	2,800
60 mol% CO ₂	7,000	3,700	3,500

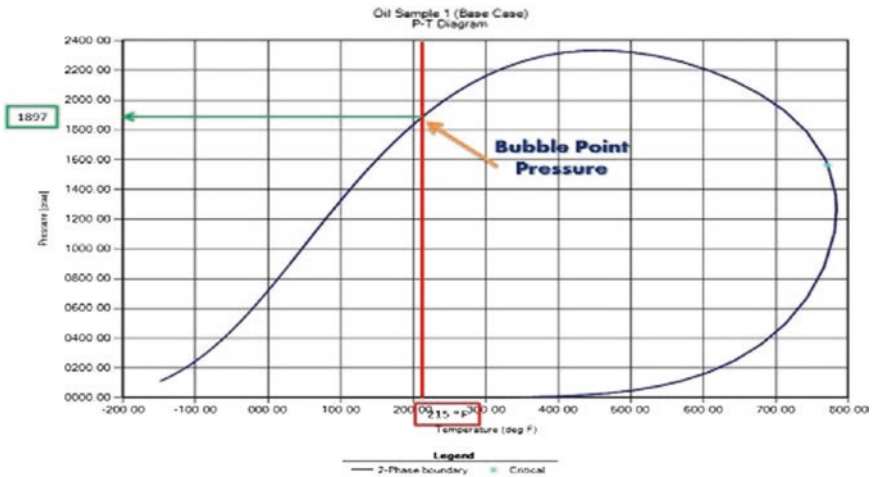


Fig. 15 Two-phase (pressure–temperature) diagram for oil sample 1 (base case)

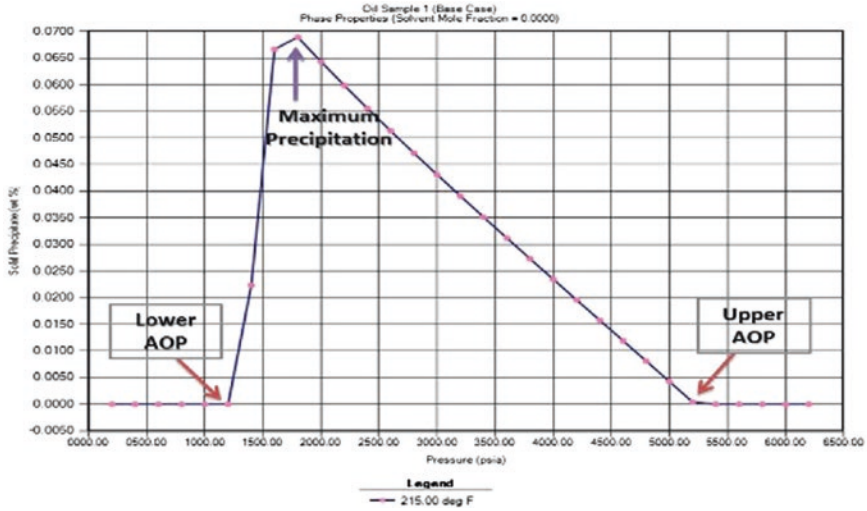


Fig. 16 Asphaltene precipitated wt% versus pressure for oil sample 1 (base case)

Table 3 Lower and upper AOP, P_b , and maximum precipitation pressure for different CO₂ mol% injection at reservoir temperature (215 °F) for oil sample 1

Injected CO ₂ (mol%)	Lower AOP (psi)	Upper AOP (psi)	P_b (psi)	Maximum precipitation (psi)
0	1,200	5,200	1,897	1,800
20	1,250	6,750	2,300	2,250
40	1,250	7,250	3,085	3,000
60	1,500	7,500	3,738	3,500

Table 4 Lower and upper AOP, P_b , and maximum precipitation pressure for different CO₂ mol% injection at reservoir temperature (160 °F) for oil sample 2

Injected CO ₂ (mol%)	Lower AOP (psi)	Upper AOP (psi)	P_b (psi)	Maximum precipitation (psi)
0	1,400	6,000	3,722	3,800
20	1,500	6,500	4,130	4,100
40	1,800	6,800	4,657	4,400
60	2,000	7,500	5,154	5,000
80	2,000	7,750	5,594	5,000

hydrocarbon fraction reestablishes the lost asphaltene solubility [2, 12, 15]. When asphaltene redissolve back to the oil, amount of precipitated asphaltene decreases. Thus, the “bell shape” graph generated has portrayed asphaltene precipitation phenomenon as described.

Table 5 Lower and upper AOP, P_b , and maximum precipitation pressure for different CO₂ mol% injection at reservoir temperature (204 °F) for oil sample 3

Injected CO ₂ (mol%)	Lower AOP (psi)	Upper AOP (psi)	P_b (psi)	Maximum precipitation (psi)
0	1,200	3,600	2,333	2,300
20	1,600	4,100	2,807	2,800
40	1,800	4,800	3,066	3,150
60	2,000	5,800	3,476	3,450
80	2,400	6,800	3,741	3,800

The results as summarized in Tables 3, 4, and 5 have been presented in pressure-composition diagram, as illustrated in Figs. 17, 19, and 21, whereas the graph of asphaltene precipitated wt% versus pressure for different CO₂ mol% gas injection for each oil sample has been combined, as shown in Figs. 18, 20, and 22. All the graphs have shown the similar increasing trend, where bubble-point pressure is always in between the upper and lower AOP. Additional CO₂ mol% gas injection increases the bubble-point pressure and thus raises up the upper and lower AOP values, i.e., AOP region is shifted upward.

During depressurization at reservoir temperature, asphaltene start to precipitate from upper AOP when approaching bubble-point region. Precipitation increases until it reaches maximum weight percentage at or very near to the bubble-point pressure. After that, precipitation reduces with decreasing pressure. By injecting more CO₂ mol%, the amount of peak precipitated asphaltene near bubble-point pressure is increasing.

For oil sample 1, the reservoir pressure is denoted by the yellow line as shown in Figs. 17 and 18. By assuming good work in initial reservoir pressure maintenance, both the figures have indicated that oil sample 1 reservoir would be affected by asphaltene precipitation problem from before CO₂ gas injection up to 80 mol% of CO₂ gas injection, as its reservoir pressure is sat within the AOP region in Fig. 17 and within all five “bell” in Fig. 18. However, it has been observed that asphaltene precipitation severity is decreasing with increasing mol% of CO₂ gas injection, due to the rising bubble-point pressure.

On the other hand, at reservoir temperature and pressure as indicated by the yellow straight line in Figs. 19 and 20 for oil sample 2, asphaltene precipitation problem takes affect from zero CO₂ mol% up to 80 mol% gas injection. While it has been observed that asphaltene precipitation is becoming serious with increasing mol% of CO₂ gas injection. Thus, oil sample 2 is not recommended for CO₂ gas injection scheme to avoid severe asphaltene precipitation problem.

As shown in Figs. 21 and 22 for oil sample 3, at reservoir pressure and temperature as prescribed, asphaltene precipitation occurred from zero up to 80 mol% CO₂ gas injection, while it reaches maximum while increasing from 20 to 40 mol%. From this observation, it is suggested that CO₂ gas injection should be avoided near 20–40 mol%. Besides, reservoir management scheme should be taken into account for handling asphaltene precipitation problem in such reservoir condition.

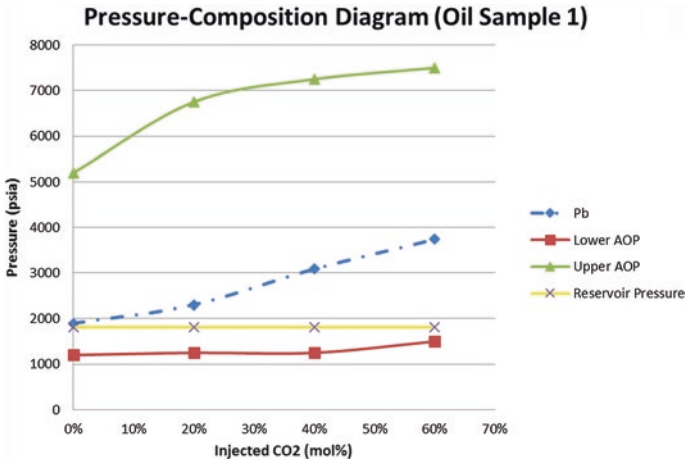


Fig. 17 Pressure-composition diagram at 215 °F for oil sample 1

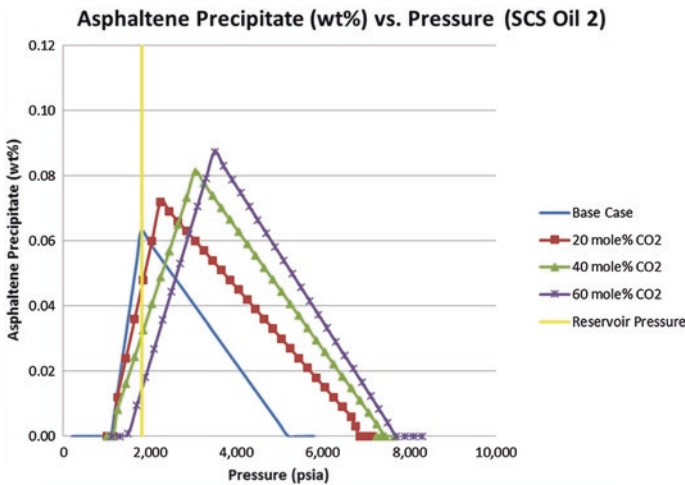


Fig. 18 Asphaltene precipitated wt% versus pressure at 215 °F for oil sample 1

From the findings as discussed, it has been found that additional CO₂ gas injection has altered the oil composition, contributing to higher bubble-point pressure as well as asphaltene onset pressure region. This compositional change also favors the precipitation of asphaltenes [15, 20, 23]. Injected CO₂ which is in contact with light oil-induced vaporizing gas drive process, where CO₂ gas vaporizes part of the light and intermediate components to the gas phase, results in the loss of intermediate components (C₃₊) as well as resins in reservoir fluids [11]. Hence, the more the CO₂ mol% injected, the more the loss in vaporized intermediate components and resins, which causes higher amount of asphaltene precipitation.

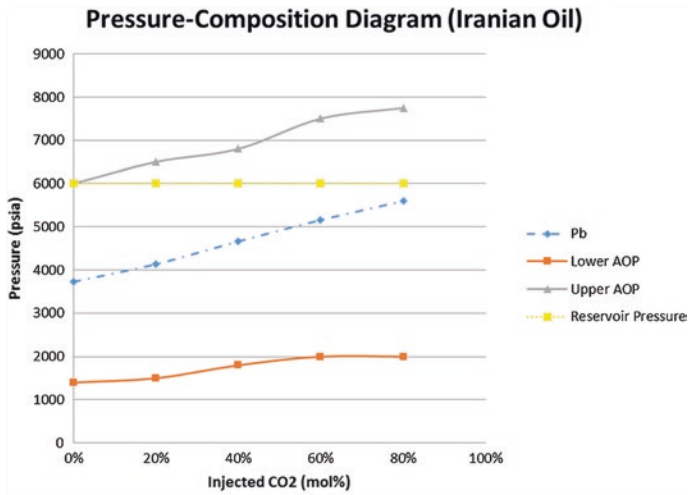


Fig. 19 Pressure-composition diagram at 160 °F for iranian oil sample

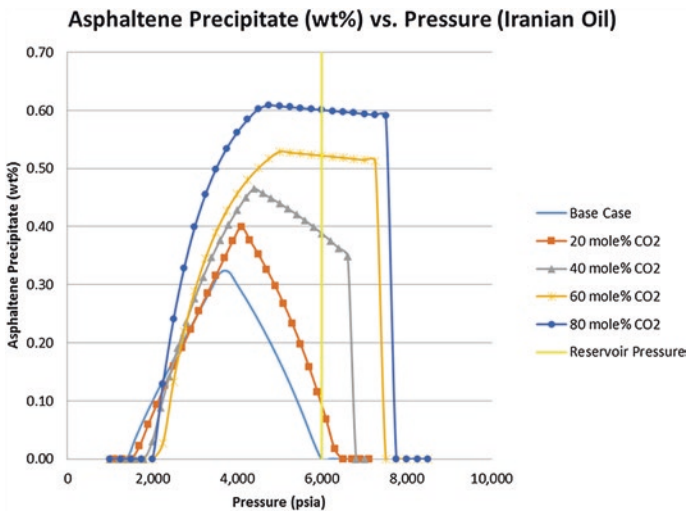


Fig. 20 Asphaltene precipitated wt% versus pressure at 160 °F for iranian oil

By assuming isothermal reservoir condition, the initial reservoir pressure is denoted as the yellow straight line crossing the graph. It has been observed that at reservoir temperature and pressure, the amount of asphaltenes precipitated may vary from before CO₂ gas injection up until increment to 80 mol% injection. Besides, the trend of the graph is different from sample to sample.

For planning for reservoir management strategy, it is crucial to know the initial temperature and pressure in reservoir condition, as well as the bubble-point

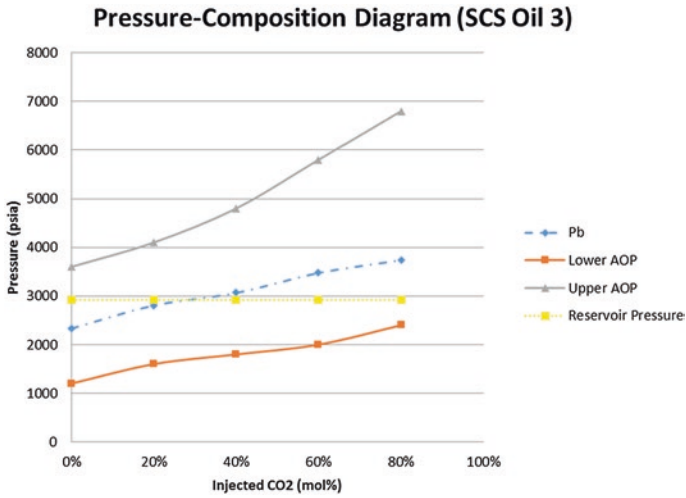


Fig. 21 Pressure-composition diagram at 204 °F for SCS oil 3

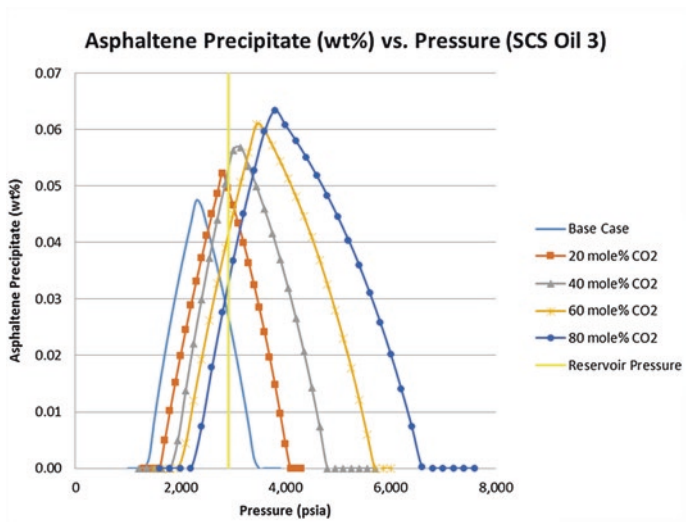


Fig. 22 Asphaltene precipitated wt% versus pressure at 204 °F for SCS Oil 3

pressure, prior to designing field development operation as to mitigate asphaltene precipitation problem in reservoir. By investigating asphaltene onset pressure for a reservoir oilfield over different mol% of CO₂ gas injection, optimum scheme for CO₂ gas injection could be designed in order to minimize problem of asphaltene precipitation and deposition in reservoir.

6 Conclusions

The results of this study have shown the tendency of asphaltene precipitation in low asphaltenic light oil reservoirs with different mole percentage of CO₂ gas injection. After data analysis and discussion in previous chapter, the results are concluded as below:

1. AOP is surrounding the bubble-point pressure, as bounded within asphaltene precipitation region range between the upper AOP and lower AOP.
2. Amount of precipitated asphaltenes increases when approaching bubble-point pressure, where it reaches maximum at or very near to bubble-point pressure.
3. With addition to injected CO₂ mol%, bubble-point pressure increases, and thus shifting up AOP region, whereby the amount of maximum precipitated asphaltenes increases with more CO₂ mol% injected near bubble-point pressure.
4. At specific reservoir temperature and pressure, the amount of precipitated asphaltenes in different CO₂ gas injection scheme (mol%) varies from one field to another field.

By understanding the asphaltene onset trend behavior of light oil in reservoir condition over different CO₂ gas injection scheme, the author concluded that the findings from this study can be applied as criteria for designing successful reservoir management strategy. To avoid the asphaltene onset region, pressure maintenance scheme should be planned and manipulated prior to oil production. Therefore, asphaltene precipitation problem could be mitigated and thus minimizing technical uncertainties and economical losses in light oil reservoir.

References

1. Adyani W.N., Daud W.A.W., Darman N., *et al.*, "A Systematic Approach to Evaluate Asphaltene Precipitation during CO₂ Injection," SPE Paper 143903, *SPE Enhanced Oil Recovery*, Kuala Lumpur, Malaysia, 2011.
2. Afshari S., Kharrat R. and Ghazanfari M.H., "Asphaltene Precipitation Study during Natural Depletion at Reservoir Conditions," SPE Paper 130071, *SPE International Oil & Gas Conference and Exhibition*, Beijing, China, 2010.
3. Ahmed T. H., *Equations of State and PVT Analysis: Applications for Improved Reservoir Modeling*, Houston, Texas, Gulf Publishing Company, 2007.
4. Akbarzadeh K., Hammami A. and Kharrat A., *et al.*, "Asphaltene—Problematic but Rich in Potential," *Oilfield Review (Summer 2007)*, **Vol. 19 (2)**: p.22-43, 2007.
5. Alta'ee A.F., Saaid I.M. and Masoudi R., "Carbon Dioxide Injection and Asphaltene Precipitation in Light oil Reservoirs," *the 11th Mediterranean Petroleum Conference and Exhibition*, Tripoli, Libya, 2010.
6. Buckley J.S., Wang J. and Creek J.L., "Solubility of the Least-Soluble Asphaltene," *Asphaltene, Heavy Oils, and Petroleomics*, **Vol. 16**: p.401-437, 2007.
7. Burke N.E., Hobbs R.E. and Kashou S.F., "Measurement and Modeling of Asphaltene Precipitation," *Journal of Petroleum Technology*, p.1440-1520, November 1990.

8. Cheng X., *Sorption of Athabasca Vacuum Residue on Acidic, Neutral and Basic Surfaces*, MSc. Thesis, University of Alberta, Canada, 2008.
9. Dahaghi A.K., Gholami V., Moghadasi J., and Abdi R., "Formation Damage Through Asphaltene Precipitation Resulting from CO₂ Gas Injection in Iranian Carbonate Reservoirs," SPE Paper 99631, *SPE Europec Conference and Exhibition*, Vienna, Austria, 2006.
10. Gholoum E.F., Oskui G.P. and Salman M., "Investigation of Asphaltenes Precipitation Onset Conditions for Kuwaiti Reservoirs," SPE Paper 81571, *SPE 13th Middle East Oil Show & Conference*, Bahrain, 2003.
11. Green D.W. and Willhite G.P., *Enhanced Oil Recovery*, Richardson, Texas, Society of Petroleum Engineers Book Series, 1998.
12. Hammami A., Phelps H. and Little T.M., "Asphaltenes Precipitation from Live Oils: An Experimental Investigation of the Onset Conditions and Reversibility," *Energy Fuels* 2000, **Vol. 14**: p.14-18, 2000.
13. Hammami A. and Ratulowski J., "Precipitation and Deposition of Asphaltenes in Production Systems: A Flow Assurance Overview," *Asphaltenes, Heavy Oils, and Petroleomics*, **Vol. 23**: p.617-660, 2007.
14. Hirschberg A., de Jong L.N.J., Schipper B.A., *et al.*, "Influence of Temperature and Pressure on Asphaltenes Flocculation," *Shell E&P Laboratorium*, 1984.
15. Kokal S.L. and Sayegh S.G., "Asphaltenes: the Cholesterol of Petroleum," SPE Paper 29787, *SPE Middle East Oil Show*, Bahrain, 1995.
16. Liao Z. and Geng A., "Asphaltenes in Oil Reservoir Recovery," *Chinese Science Bulletin*, **Vol. 45 (8)**: p.682-686, 2000.
17. McCain W. D. Jr., *The Properties of Petroleum Fluids*, (**Ed. 2**), Tulsa, Oklahoma, PennWell Publishing Company, 1990.
18. Nghiem L. X., *Phase Behavior Modeling and Compositional Simulation of Asphaltenes Deposition in Reservoirs*, Ph.D. Thesis, University of Alberta, Canada, 1999.
19. Obeida T. A. and Heinemann Z. E., "Accurate Calculations of Compressibility Factor for Pure Gases and Gas Mixtures," SPE Paper 37440, *SPE Production Operations Symposium*, Oklahoma, 1997.
20. Sarma H.K., "Can We Ignore Asphaltenes in a Gas Injection Project for Light-Oils?" SPE Paper 84877, *SPE International Improved Oil Recovery Conference in Asia Pacific*, Kuala Lumpur, Malaysia, 2003.
21. Speight J.G., "Petroleum Asphaltenes Part 1: Asphaltenes, Resins and the Structure of Petroleum," *Oil & Gas Science and Technology*, **Vol. 59 (5)**: p.467-477, 2004.
22. Speight J.G., "Petroleum Asphaltenes Part 2: Asphaltenes, Resins and the Structure of Petroleum," *Oil & Gas Science and Technology*, **Vol. 59 (5)**: p.479-488, 2004.
23. Srivastava R.K. and Huang S.S., "Asphaltenes Deposition During CO₂ Flooding: A Laboratory Assessment," SPE Paper 99631, *SPE Europe/EAGE Annual Productions Symposium*, Oklahoma, 1997.
24. Thou S., Ruthammer M. and Potsch K., "Detection of Asphaltenes Flocculation Onset in a Gas Condensate System," SPE Paper 78321, *SPE 13th European Petroleum Conference*, Scotland, U.K., 2002.

Porosity and Permeability Modification by Diagenetic Processes in Fossiliferous Sandstones of the Baram Delta, Sarawak Basin, Malaysia

J. Ben-Awuah and E. Padmanabhan

Abstract The main productive units in the Baram Delta are cycles V and VI Upper to Middle Miocene sandstones. Significant fossiliferous intervals have been identified within these units. The objective of this paper was to investigate the impact of diagenetic processes on fossiliferous sandstones and how such modifications to the fossils influence porosity and permeability. Two wells from two fields in the Baram Delta were evaluated using thin sections, CT scan imaging, SEM, EDX, spot permeability, and poro-perm. Intragranular pores have been formed within the fossils by diagenetic processes. The uplift of the Rajang Group accretionary prism to form the Rajang Fold-Thrust Belt facilitated the creation of these pores by bringing the reservoir sandstones into the telogenetic regime where dissolution by meteoric water is the major porosity-forming process. Spot permeability in the fossiliferous part of the sandstone ranges between 606 and 879 mD, whereas the relatively non-fossiliferous part has spot permeability values ranging between 305 and 521 mD. This represents a porosity and permeability enhancement of 50–60 % in the fossiliferous part. This enhancement is attributed to the intragranular porosity formed within the fossils by diagenetic processes. Porosity and permeability range between 18 and 30 % and 662 and 683 mD in fossiliferous horizons (FH) and 13 and 27 % and 10 and 529 mD in non-fossiliferous horizons, respectively.

Keywords Baram Delta · Fossils · Diagenesis · Porosity · Permeability

J. Ben-Awuah · E. Padmanabhan (✉)
Department of Geosciences, Faculty of Geosciences and Petroleum Engineering,
Universiti Teknologi PETRONAS, 31750 Tronoh, Perak, Malaysia
e-mail: eswaran_padmanabhan@petronas.com.my

1 Introduction

The measure of the void space in a rock is defined as the porosity of the rock, and the measure of the ability of the rock to transmit fluids is known as permeability [1]. Effective porosity refers to the percentage of the total rock volume that consists of interconnected pores [1, 2]. Porosity formed within grains is known as intragranular porosity, whereas intergranular porosity refers to porosity formed between grains [2]. Sandstones are normally dominated by intergranular porosity even though additional intragranular porosity may be formed in the sandstone during diagenesis normally as a result of dissolution of minerals such as feldspars. This study has been necessitated by recent advances in the studies on formation of secondary and intragranular porosity during diagenesis. Such studies have focused mainly on mineral dissolution and precipitation processes; however, this study focuses on the role of diagenetic processes on fossils in contributing to the total porosity of reservoir sandstones with examples from the Baram Delta, Sarawak Basin. Fossils are the preserved remains or traces of animals and plants. Fossils are a common feature in most marine and shallow marine sedimentary environments such as deltaic environments [3–5]. Significant fossiliferous intervals have been identified in some of the most productive siliciclastic hydrocarbon reservoirs in the world including the Middle Jurassic Brent Group in the North Sea [6, 7], the Jurassic Norphlet formation in the Gulf of Mexico [8], and Cycles VI and VI Lower to Middle Miocene reservoir sandstones of the Baram Delta, Sarawak Basin [9]. Fossils form an important part of rock fabric and are a vital form of rock heterogeneity that can induce textural and mineralogical variations in a rock. The concept of influence of some rock fabric elements such as texture and mineralogy on reservoir rock quality has been well investigated by [8, 10–14]. However, the influence of fossils as a rock fabric element on porosity and permeability in reservoir sandstones has not been exhaustively discussed.

At the time of deposition, sediments will have a primary mineralogical, chemical, and textural composition with the primary composition and sorting of clastic sediments related to provenance, climate, and sedimentary facies [15]. The deposited sediment composition is modified by diagenetic processes: surface process such as weathering on land, compaction (chemical and mechanical), and cementation on the seabed [11]. Three diagenetic regimes were originally proposed by Choquette and Pray [16] for limestone diagenetic processes: early diagenesis (eogenesis), burial diagenesis (mesogenesis), and uplift-related diagenesis (telogenesis). The objective of this paper was to investigate the impact of such diagenetic processes on fossils in fossiliferous sandstones of the Baram Delta and how such modifications to fossils influence porosity and permeability.

2 Geologic Setting

The Sarawak Basin is most widely believed to have originated as a foreland basin that formed after the collision of the Luconia Block with the West Borneo Basement, and the closure of the Rajang Sea during the Late Eocene [17]. Deformation and uplift of the Rajang Group accretionary prism to form the Rajang Fold-Thrust Belt provide the sediment supply to the Sarawak Basin [18, 19].

The Baram Delta is one of the seven geological provinces found offshore the Sarawak Basin and is the most prolific of all the geological provinces in the basin [9] (Fig. 1). The offshore stratigraphy of the Baram Delta is characterized by the occurrence of coastal to coastal-fluviomarine sands which have been deposited in a northwestwards prograding delta since the Middle Miocene (from Cycle IV onwards) (Fig. 2) [9, 17, 20].

3 Materials and Methods

Two wells from two fields in the Baram Delta were evaluated in this study. The depth of the wells ranges between 792 and 1,829 m. The studied reservoir sandstone intervals all belong to the cycles V and VI Upper to Middle Miocene sandstones [9]. Core logging was carried out for all wells. Fossiliferous intervals identified from the core logging were sampled for further analysis.

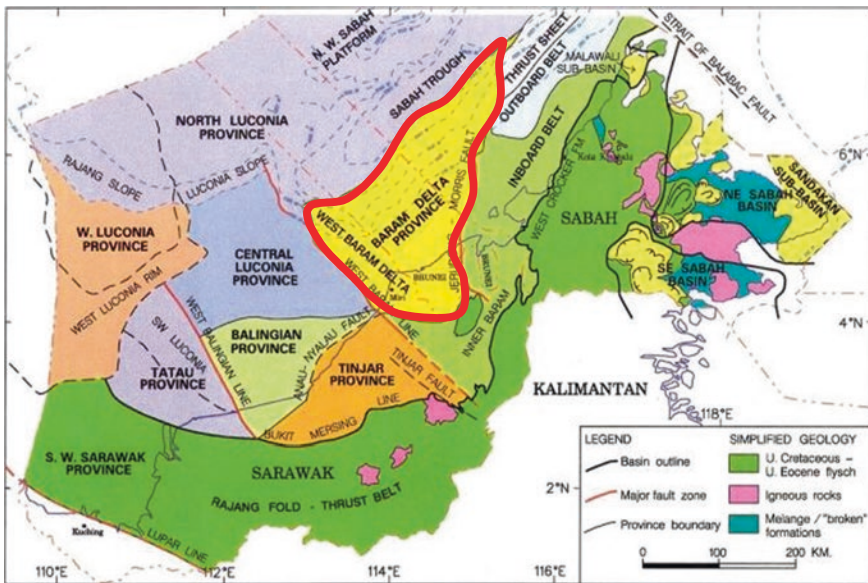


Fig. 1 Location map of Baram Delta in Sarawak Basin [18]

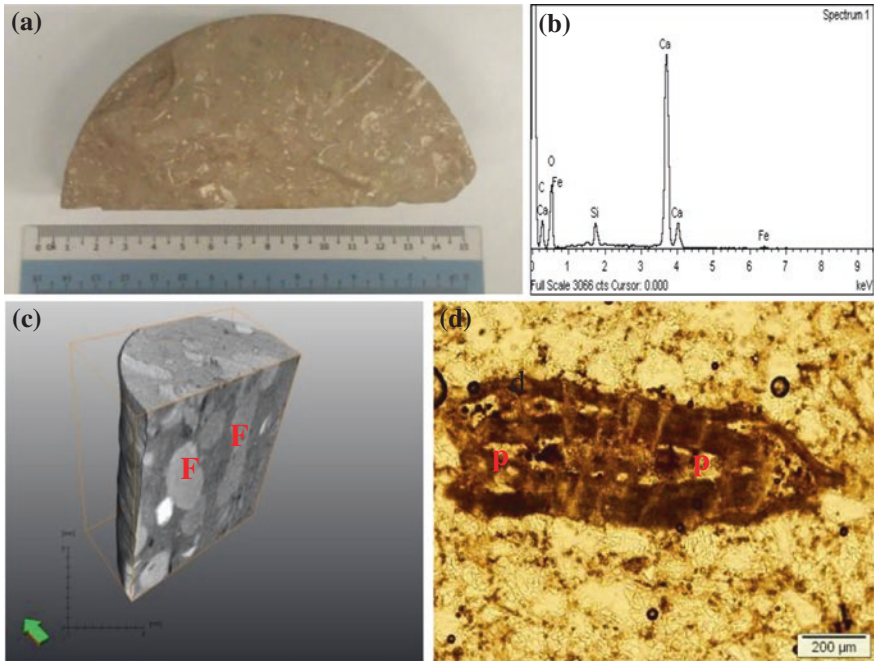


Fig. 2 **a** Hand specimen of fossiliferous sandstone. **b** EDX of fossiliferous sandstones showing high Ca. **c** CT scan showing internal rock structure. **d** Thin-section photomicrograph showing intragranular pore (P) in fossil fragment

2 cm × 4 cm slices of core were cut from the fossiliferous sandstone samples to make thin sections. Thin-section photographs were taken using Olympus SZX16 research stereomicroscope with attached digital camera.

Spot/probe permeability measurements were measured on the fossiliferous sandstone intervals using a CoreLab Profile Decay Permeameter (PDPKTM 300 system). To ensure accurate values as possible, 3–5 points were measured at each point on the grid and the average values were taken. A geometric factor (G_0) of 1.83 was used in this experiment [21].

Samples of 2 cm × 2 cm dimension of each core slab were taken for scanning electron microscopy (SEM). The SEM analysis was done using a Carl Zeiss Supra 55VP FESEM with variable pressure ranging from 2 to 133 Pa and probe current between 1 pA and 10 nA. Energy dispersive X-ray spectroscopy (EDX) of specific points in the samples was taken to determine the elemental composition at these points.

Core plug permeability was measured using a Vinci Technologies Coreval 30 poro-perm equipment. The core plugs used had a 1 in. diameter and 3 in. length.

Fossiliferous sandstone samples were selected for microcomputer tomography (CT) scan imaging. The micro-CT scan images were taken with an InSpeXio Microfocus CT system and processed with Avizo 7.1 imaging software. 511 image slices were taken at a voxel size of 0.045 mm/voxel, with an X-ray voltage of 130 kv and current of 100 μ A.

4 Results and Discussion

The dominant lithologies in the wells studied are sandstones and siltstones with rare intercalations of mudstones. Most of the sandstones are fined grained with a few sections of the well-being medium to coarse grained.

The fossiliferous sandstones are generally fine grained, moderately sorted, very pale orange (10YR8/2) with subangular grains (Fig. 2a, c). EDX data shows a predominantly quartz composition with some amount of iron oxide and calcite (Fig. 2b). CT scan images show that the fossils (F) make up a significant part of the internal structure of the rock fabric and are a vital form of heterogeneity in the rocks (Fig. 2c, d). From the CT scan image and thin-section photomicrographs, the fossils can be estimated to make up a significant percentage of the fossiliferous sandstones (10–20 %). Such fossil-induced heterogeneities may influence the rock texture and reservoir rock quality.

Modifications to the pore system in the fossiliferous sandstones are observed in the SEM and CT scan images (Fig. 3a–f).

Such modifications affect the fossils embedded in the rock. Additional pores and porosity have been formed within the fossils as a result of diagenetic processes that have affected the sandstones (Fig. 3b, c, d). As you move along the CT scan slices from one slice to another, the intragranular porosity formed within the fossils become very visible. For example, in Fig. 3e, f, open intragranular pores which were previously nonexistent in the slices begin to form in slice 420 and open up even further in slice 428. Diagenetic processes such as dissolution have been identified to be responsible for creation of such pores within fossils and mineral assemblages [22–24]. Diagenetic reactions involving carbonate minerals (dominant minerals in fossils) are kinetically faster and less dependent on temperature and may be important near the surface [11]. Such near-surface reactions are sensitive to climate (rainfall) controlling the flow of meteoric water, which may result in a geochemically open system [11].

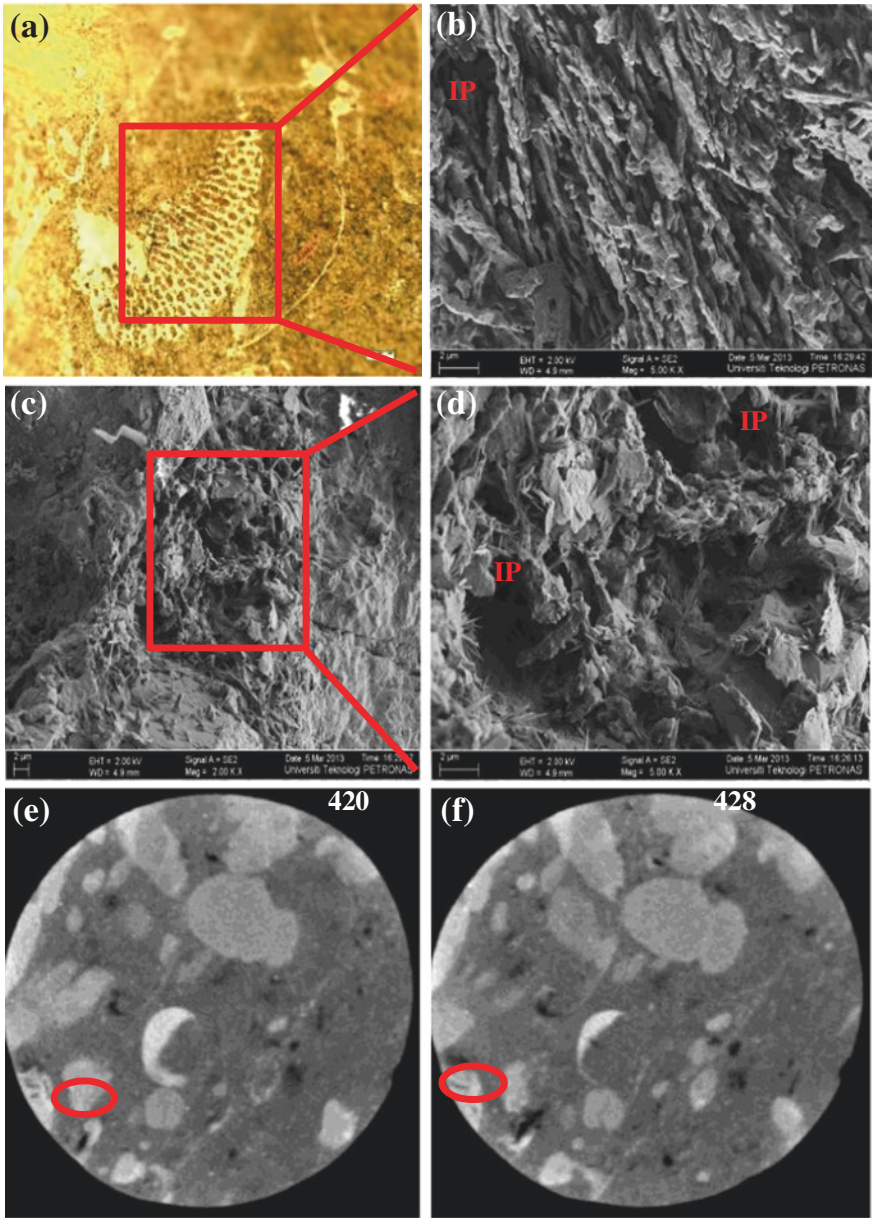


Fig. 3 a Photomicrograph of shell fragments. b SEM of shell fragment with solution porosity. c and d SEM of fossil showing intragranular porosity from fossil modification. e and f CT scan slices showing development of intragranular pores within fossils from slices 420 and 428

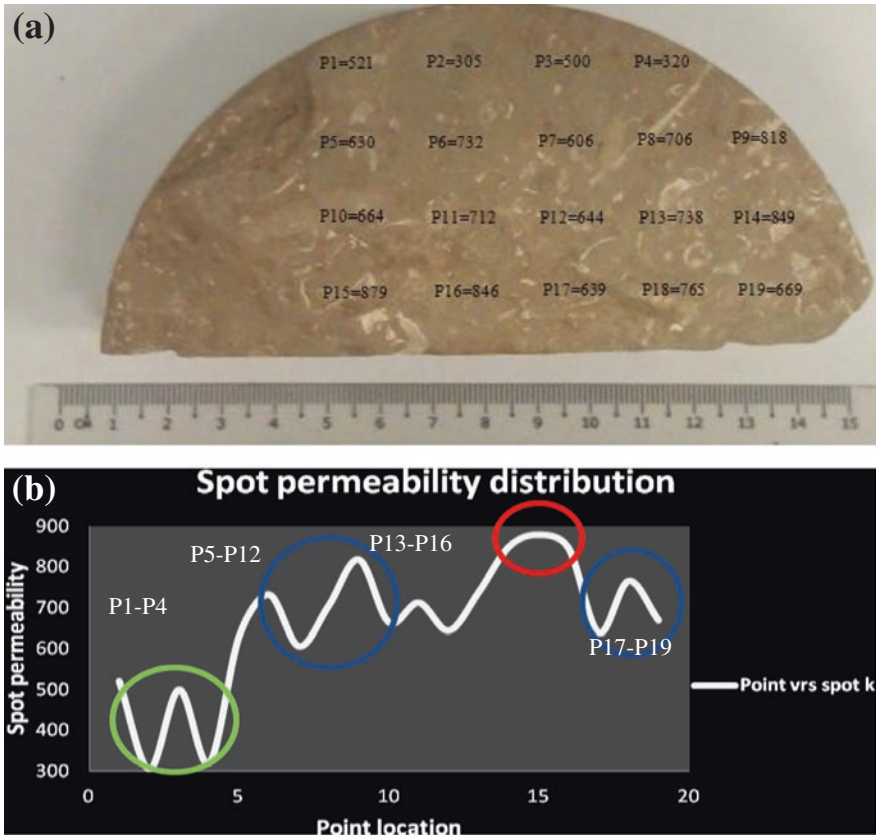


Fig. 4 a Spot permeability distribution in fossiliferous sandstone sample. b Graphical representation of spot permeability distribution in the sample

A review of the available literature shows that creation of such porosity normally occurs at shallow depth (<10–100 m) where the groundwater flux is high because this allows the pore water to remain constantly undersaturated and capable of leaching minerals [11, 12, 23].

Spot permeability values are 50–60 % higher in the highly fossiliferous part of the sandstones compared to the non-fossiliferous and low fossiliferous part. An example of the spot permeability measurement is shown in Fig. 4a. Spot permeability in the fossiliferous part of the sandstone ranges between 606 and 879 mD, whereas the relatively non-fossiliferous part has spot permeability values ranging between 305 and 521 mD. P1-P4 represents permeability in the non-fossiliferous part, P5-P12 and P17-P19 represent the moderately fossiliferous part, and P13-P16 represents the highly fossiliferous part of the sandstone (Fig. 4b) (Table 1). This

Table 1 Spot permeability distribution in sample

Points	Permeability (mD)	Point location
P1	521	Non-fossiliferous
P2	305	Non-fossiliferous
P3	500	Non-fossiliferous
P4	320	Non-fossiliferous
P5	630	Moderately fossiliferous
P6	732	Moderately fossiliferous
P7	606	Moderately fossiliferous
P8	706	Moderately fossiliferous
P9	818	Moderately fossiliferous
P10	664	Moderately fossiliferous
P11	712	Moderately fossiliferous
P12	644	Moderately fossiliferous
P13	738	Highly fossiliferous
P14	849	Highly fossiliferous
P15	879	Highly fossiliferous
P16	846	Highly fossiliferous
P17	639	Moderately fossiliferous
P18	765	Moderately fossiliferous
P19	669	Moderately fossiliferous

marked increase in porosity in the fossiliferous sandstones can be attributed to the intragranular porosity formed within the fossils as observed in the SEM, CT scan, and thin-section images. The formation of intragranular porosity is interpreted to have been facilitated by the Eocene uplift of the Rajang Group accretionary prism to form the Rajang Fold-Thrust Belt. This uplift is interpreted to have brought the reservoir sandstones into the telogenetic regime where dissolution by meteoric water is a major porosity-forming process [16, 24].

The poro-perm experiment was carried out to confirm the influence of fossils in enhancing the porosity and permeability in the fossiliferous sandstones. The results from the poro-perm experiment are summarized in Fig. 5a, b. The figures show that the fossiliferous horizons (FH) have a significantly higher porosity and permeability than the non-fossiliferous horizons. Core plugs from the FH in well B have porosity between 18 and 30 % and permeability ranging

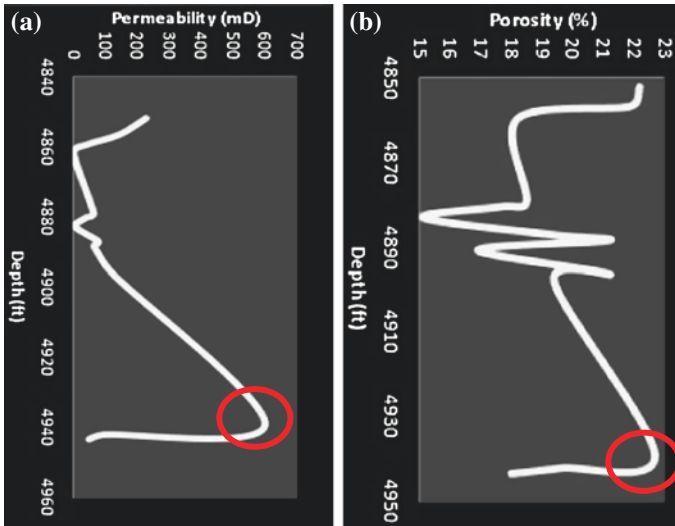


Fig. 5 **a** Graphical representation of core plug permeability in well B. **b** Graphical representation of core plug porosity in well B

between 662 and 683 mD, whereas the non-fossiliferous horizons have porosity between 13 and 27 % and permeability ranging between 10 and 529 mD. The significantly higher porosity and permeability recorded in the fossiliferous cores emphasize the importance of the fossils in enhancing the reservoir rock quality.

5 Conclusions

Evidence of creation of intragranular porosity within fossils was observed in SEM images, CT scan images, and thin-section photomicrographs. The uplift of the Rajang Group accretionary prism during the Eocene facilitated the intragranular porosity creation process by bringing the sandstones into the telogenetic regime where pore waters are mostly undersaturated with mineral phases. An increase in porosity and permeability is observed in both the spot permeability and core plug porosity and permeability measurements in the fossiliferous sandstones over the non-fossiliferous sandstones. Spot permeability in the fossiliferous part of the sandstone ranges between 606 and 879 mD, whereas the relatively non-fossiliferous part has spot permeability values ranging between 305 and 521 mD. This represents a porosity and permeability enhancement of 50–60 % in the fossiliferous part. This enhancement is attributed to the intragranular porosity formed within the fossils by diagenetic processes. This observation is confirmed by the core plug porosity and permeability measurements. Core plugs from the FH have porosity

between 18 and 30 % and permeability ranging between 662 and 683 mD, whereas the non-fossiliferous horizons have porosity between 13 and 27 % and permeability ranging between 10 and 529 mD.

References

1. Tiab, D. and Donaldson, E. C., 2012. *Petrophysics: Theory and practice of measuring reservoir rocks and fluid transport properties*. 3rd Edition. Gulf Professional Publishing, pp. 976.
2. Flugel, E. 2004. *Microfacies of carbonate rocks: Analysis, interpretation and application*. Springer. pp.996.
3. Selley, R.C. 2000. *Applied Sedimentology*, Academic Press, London, 2nd Edition, San Diego, 470 pp.
4. Reineck, H.E. and Singh, I.B. 1986. *Depositional Sedimentary Environments: with reference to terrigenous clastics*, (2nd Edition). Springer- Verlag, Berlin, 551 pp.
5. Elliot, T. 1989. Deltaic systems and their contribution to an understanding of basin-fill successions. In: Wheatley, M.K.G. and Pickering, K.T. (eds.), *Deltas: Sites and Traps for Fossil Fuels*, Geological Society Special Publication, No. 41, pp.3-10.
6. Fraser, S.I., Robinson, A.M., Johnson, H.D., Underhill, J.R., Kadolsky, D.G.A., Connell, R., Johannessen, P. and Ravnås, R., 2002, Upper Jurassic. In: Evans, D., Graham, C., Armour, A. and Bathurst, P. (eds.), *The Millenium Atlas: petroleum geology of the central and northern North Sea*, p. 157-189.
7. Goldsmith, P.J., Hudson, G. and Van Veen, P., 2003, Triassic. In: Evans, D., Graham, C., Armour, A. and Bathurst, P. (eds.), *The Millenium Atlas: petroleum geology of the central and northern North Sea*, p. 105-127.
8. Ajdukiewicz, J.M., Nicholson, P.H. and Esch, W.L. 2010. Prediction of deep reservoir quality using diagenetic process models in the Jurassic Nophlet Formation, Gulf of Mexico. *AAPG Bulletin*, 94, no.8, pp.1189-1227.
9. Tan, D.N.K., Rahman, A.H.B., Anuar, A., Bait, B. and Tho, C.K., 1999, West Baram Delta. In: Meng, L.K. (ed.), *The Petroleum Geology and Resources of Malaysia*, Petroliaam Nasional Berhad (PETRONAS), Kuala Lumpur, p. 291-341.
10. Maast, T.E., Jahren, J. and Bjorlykke, K. 2011. Diagenetic controls on reservoir quality in Middle to Upper Jurassic sandstones in the South Viking Graben, North Sea. *AAPG Bulletin*, v. 95, no. 11, pp. 1937-1958.
11. Bjorlykke, K. and Jahren, J. 2012. Open or closed geochemical systems during diagenesis in sedimentary basins: Constraints on mass transfer during diagenesis and the prediction of porosity in sandstone and carbonate reservoirs. *AAPG Bulletin*, v.96, no.12, pp.2193-2214.
12. Ehrenberg, S.N., Walderhaug, O. and Bjorlykke, K. 2012. Carbonate porosity creation by mesogenetic dissolution: Reality or illusion? *AAPG Bulletin*, v.96, no.2, pp.217-233.
13. Nguyen, B.T.T., Stuart, J.J., Gouly, N.R., Middleton, A.J., Grant, N. and Ferguson, A. 2013. The role of fluid pressure and diagenetic cements for porosity preservation in Triassic fluvial reservoirs of the Central Graben, North Sea. *AAPG Bulletin*, v.97, no.8, pp.1275-1302.
14. Mork, M.B.E. 2013. Diagenesis and quartz cement distribution of low permeability Upper Triassic-Middle Jurassic reservoir sandstones, Longyearbyen CO2 lab well site in Svalbard, Norway. *AAPG Bulletin*, v.97, no.4, pp.577-596.
15. Bjorlykke, K. 2010. *Petroleum Geoscience: From sedimentary environments to rock physics*, New York, Springer-Verlag, 508p.
16. Choquette, P.W. and Pray, L. (1970): *Geologic nomenclature and classification of porosity in sedimentary carbonates*. American Association of Petroleum Geologists Bulletin (AAPG.), 54, 207-250.

17. Hazebroek, H.P., Tan, D.N.K. and Swinburn, P. 1994. Tertiary evolution of the offshore Sarawak and Sabah Basins, NW Borneo. Abstracts of the American Association of Petroleum Geologists (AAPG) International Conference and Exhibition, Kuala Lumpur, Malaysia. American Association of Petroleum Geologists Bulletin, 78, 1144-1145.
18. Madon, M.B. Geological Setting of Sarawak. 1999. In: Meng, L.K. (ed.), The Petroleum Geology and Resources of Malaysia, Petroliaam Nasional Berhad (PETRONAS), Kuala Lumpur, p. 274-290.
19. Hutchinson, C.S., 2005, Geology of North West Borneo: Sarawak, Brunei and Sabah. 1st ed., Elsevier, New York, USA, 421 pp.
20. Ho, K.F., 1978, Stratigraphic framework for oil exploration in Sarawak. Bulletin of the Geological Society of Malaysia, 10, 1-13.
21. Ben-Awuah, J. and Padmanabhan, E., 2013. Impact of bioturbation on reservoir quality: A case study of biogenically reduced permeability of reservoir sandstones of the Baram Delta, offshore Sarawak Basin, Malaysia. International Oil & Gas Symposium & Exhibition, Sabah, Malaysia.
22. Boggs, S.Jr. 1992. Petrology of Sedimentary Rocks. Macmillan Publishing Company Ltd., New York, 707 pp.
23. Worden, R.H. and Burley, S.D. 2003. Sandstone diagenesis: The evolution of Sand to Stone. In: Burley, S.D. and Worden, R.H. (eds.); Sandstone Diagenesis: Recent and Ancient. Malden, Massachusetts, USA: Wiley-Blackwell Publishing, International Association of Sedimentologists Reprint Series, vol.4, p. 3-44.
24. Ali, S.A., Clarke, W.J., Moore, W.R. and Dribus, J.R. 2010. Diagenesis and reservoir quality. Schlumberger Oilfield Review, 22, no.2, 14-27.

Analytical Study on Gas Lift Optimization and Prediction of Production Life of Wells in Platform C, B-1 Field

Muhammad Aslam Bin Md Yusof and Nurfuzaini Binti Abdul Karim

Abstract Platform C has been idle since May 2008 due to high water cut production and no gas lift facilities to assist the wells to flow. Last wells flowing from Platform C were BY-1 and BY-9 which is flowing at 90 % water cut at high flowing tubing head pressure. Due to long shut-in of wells in B-1 field because of the high water cut in production, well modeling is crucial to optimize the production. Moreover, since it has been shut in for a long time, the well behavior cannot be predicted. Furthermore, the optimization problem is to optimize the daily production by choosing the optimal gas lift rates subject to pressure and properties of the wells. Thus, this project is initialized mainly to do the well modeling as well as reservoir dynamic modeling using the PROSPER and ECLIPSE software. This project focused on data from eight wells on the Platform C in B-1 field. In this project, gas lift has been selected for the production optimization. Gas is injected at high pressure from the casing into the wellbore and mixes with the produced fluids from the reservoir to reduce the fluid density to be brought up to surface. The production rate of eight wells in Platform C is optimized, and prediction of production life of the Platform C wells has been done by using ECLIPSE100 software. As a result, the proposed gas lift optimization showed significant increase in production rate of the wells and also successfully proven to sustain up to the time step 25 years of production in this project.

Keywords Gas lift optimization · Production optimization

M.A.B.M. Yusof (✉) · N.B.A. Karim
Petroleum Engineering Department, Universiti Teknologi PETRONAS,
Seri Iskandar, Malaysia
e-mail: aslam.myusof@petronas.com.my

1 Introduction

This project is based on the data from one of the field located in Sarawak named B-1 field. This project only focuses on the eight wells in the Platform C. The B-1 field is located 80 km northwest of Bintulu. The field is 14 km long and 6 km wide with water depth of 90 ft which is quite shallow.

In this project, simulations using PROSPER software will be done using the relevant data from B-1 field. Moreover, with the recent PROSPER well models, dynamic reservoir model will be created using the ECLIPSE 100 software in order to predict the production life of the wells in Platform C. To ensure the project is successful, three objectives are established which are

- To remodel the wells in B-1 field using the relevant data in PROSPER software.
- To optimize production of the wells in B-1 field using the gas lift optimization.
- To predict production life of the wells in B-1 field using ECLIPSE 100 software.

In this project, gas lift will be used for the production optimization. Gas will be injected at high pressure from the casing into the wellbore and mixes with the produced fluids from the reservoir to reduce the fluid density to be brought up to surface. Moreover, the project is then continues with the prediction of production life of the field by integrating the PROSPER well model in ECLIPSE 100.

The scopes of study will be divided into three simulation phases. The first phase and second phase include the well modeling, gas lift design, and gas lift optimization, where the simulation will be done using PROSPER software. The third phase is the dynamic reservoir modeling and prediction of production life of the wells by using the ECLIPSE 100 software.

2 Nodal Analysis and Gas Lift Optimization

Nodal analysis as explained by Bitsindou and Kelkar [1](#) involves calculating the pressure drop in individual components within the production system so that pressure value at a given node in the production system (e.g., bottom-hole pressure) can be calculated from both ends (separator and reservoir). The rate at which pressure is calculated at the node from both ends must be the same. This is the rate at which the well produces.

According to Guo et al. [2](#), Munoz and Quintero [3](#), the performance curves generated using a steady-state software will represent a very specific “operating point”, valid for one set of flowing well-head and bottom-hole pressures for a specific production rate, and under one casing head injection pressure and gas lift injection rate. Thus, from the performance curve, the production rate is known and can be optimized. By combining the principle of nodal analysis and gas lift design, the Inflow Performance Curve and Vertical Lift Performance curve are generated from the well modeling.

Since the B-1 field has a high water cut, according to Chia 8, gas lift becomes critical to sustain production as oil fields mature. Increasing water cut and decreasing reservoir pressure eventually cause wells to cease natural flow 4. Subsequently, gas lift is required to kick off and sustain flow from these wells. Thus, for gas lift optimization, the new setting of the gas lift valve is very important by considering the static fluid gradient, kick off injection pressure gradient and the wellhead tubing pressure 5.

3 Reservoir Modeling

In this project, the main focus of the reservoir simulation area is the construction of a reservoir model. This model is represented numerically in a 3D based on the data and parameter input which serves as the input for a numerical reservoir flow simulator 6. The output obtained from the reservoir simulation run represents the expected performance production curve given a particular production well pattern. Furthermore, through the reservoir simulations that are based on accurately developed reservoir characterization, it will be significant in predicting the production life of the field.

4 Methodology/Project Work

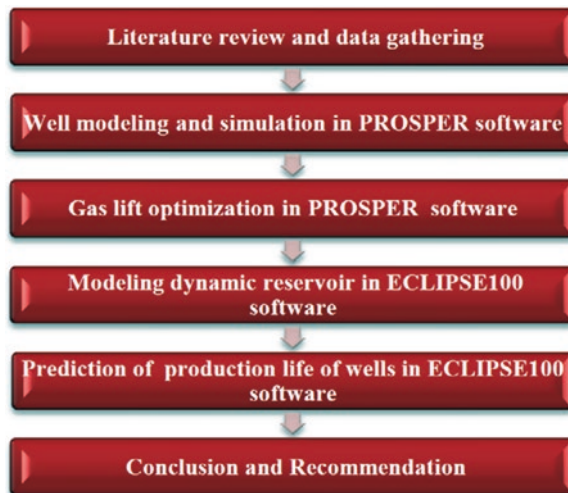


Figure 1 shows the workflow of the project. Firstly, data of all eight wells in Platform C which are the B-301, B-303, B- 304, B-305, B-306, B-307, B-308, and B-309 are collected and gathered. All the data and information needed include the well test, deviation data, well diagram, pressure profile, and PVT data. All these data need to be prepared at first place for the PROSPER and ECLIPSE 100 well modeling.

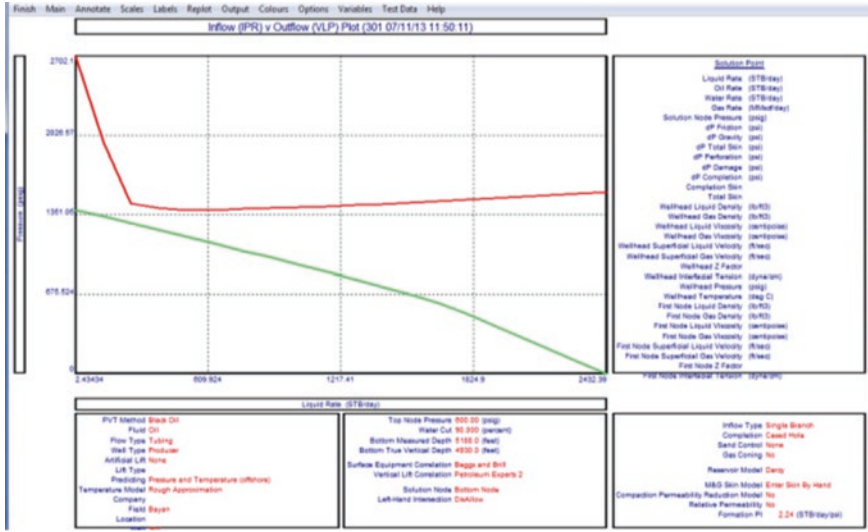


Fig. 1 IPR/VLP curve for BY-1 in base case

4.1 Well Modeling and Simulation in PROSPER Software

Well models in Platform C are matched with the relevant production data. This is executed by building single well model for each well in Platform C using PROSPER. The data to be input include PVT data, reservoir characteristic, well deviation, and well construction. Matching is done to ensure correct data, and well performance is matched with the model. This process mainly requires recent well test data and pressure profile.

After all the data have been key-in, matching is done to obtain the IPR/VLP curves. From the intersection point between the IPR and VLP curves, the operating point which is the point of the well start to flow with respect to the bottom hole flowing pressure can be obtained.

4.2 Gas Lift Optimization in PROSPER Software

This will be achieved by adding the gas lift facility in every well in the PROSPER software in the process of remodeling the wells. Thus, multiple cases on gas lift optimization are done. Two cases were run for field-wide optimization in this project which is

- i. Base case: the PROSPER model is run without gas lift facilities with relevant data from the field
- ii. Case 2: gas-lifted all wells with optimized gas lift parameters)

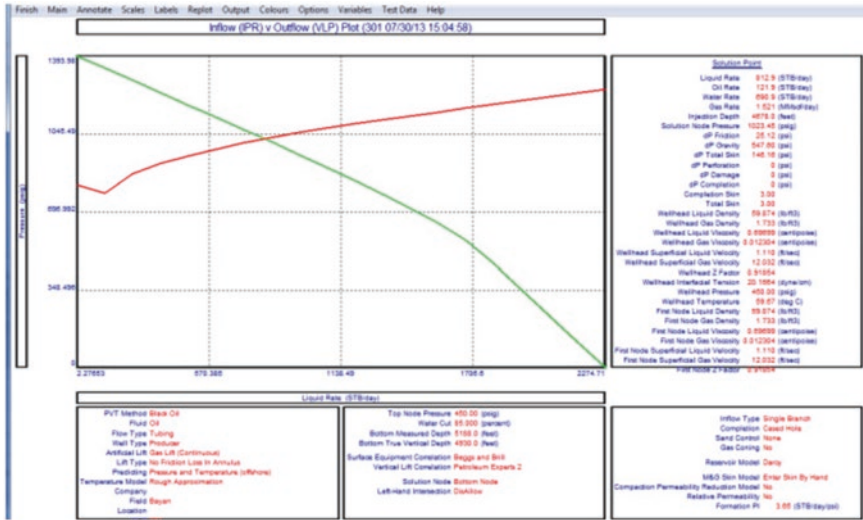


Fig. 2 IPR/VLP curve for BY-1

5 Results and Discussion

5.1 PROSPER Modeling-Base Case

The base case is the study on the wells in Platform C using PROSPER modeling without the gas lift injection. The IPR/VLP graph is obtained, and Fig. 1 is the example of the IPR/VLP graph for BY-1:

After the PROSPER modeling was completed for all wells, it is observed that all eight wells have zero production rate.

5.2 PROSPER Modeling-Case 2 (Gas-Lifted All Wells with Optimized Gas Lift Parameters)

Figure 2 shows the IPR/VLP curve for well BY-1. From the graph, the absolute open flow (AOF) can be observed. AOF is the maximum flow rate the well can achieve when the flowing bottom hole pressure is equal to zero. In this well, the AOF is 2,274.71. Moreover, the operating point is present at the rate of 812.9 bbl/day of liquid.

The Gas Lift Design-Performance Curve Plot for BY-1 in Fig. 3 shows an increasing oil rate with respect to the gas lift injection rate curve trend. Initially, when zero gas injection rate is applied, the oil rate is zero showing no flow in the reservoir but when the gas injection rate increases, the oil gain increases. From the graph, the optimum gas lift injection rate is 0.485 and the oil rate is 218.26 bbl/day.

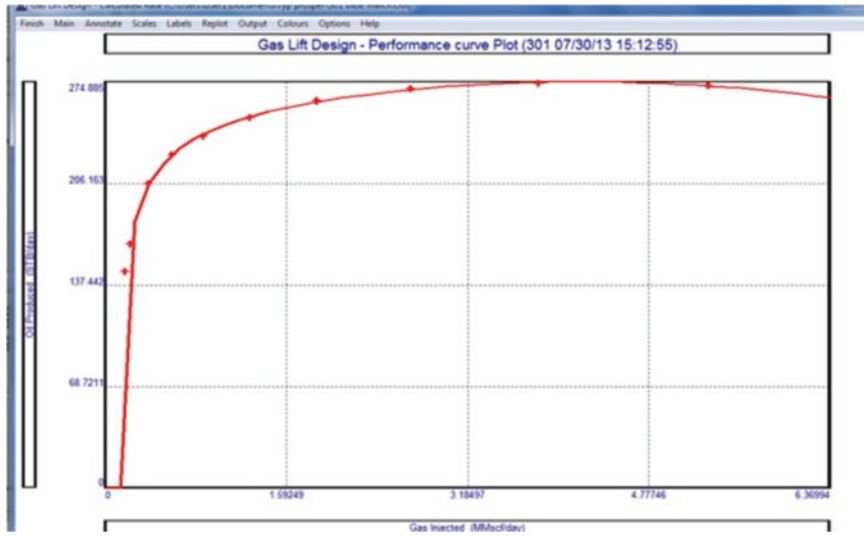


Fig. 3 Gas lift design-performance curve plot for BY-1

Table 1 Oil rate production from eight wells after gas lift injection

Well	Injection rate (MMscf/d)	Point of injection (MD-ft-THF)	Oil rate (bbl/d)
BY-1	0.49	4,678	218.26
BY-3	0.34	6,750	115.43
BY-4	0.48	4,773	148.17
BY-5	0.47	6,061	192.18
BY-6	0.49	5,057	290.58
BY-7	0.44	5,242	147.63
BY-8	0.38	4,693	117.68
BY-9	0.34	4,199	100.88
<i>Total</i>			1,330.81

From Table 1, the total oil production rate after the gas lift optimization is 1,330.81 bbl/day shows that it is possible for the wells in Platform C to flow with the gas lift aid. Moreover, the oil production rate shown is the optimize rate from the gas lift design done in the PROSPER software with respect to the optimum injection gas rate and depth of injection point.

Figure 4 shows the Field Oil Production Rate which shows that the field production can sustain up to 25 years based on the prediction period of the production of the wells in Platform C. Although the graph shows decreasing trend curve, the rate of production is still high approximately 1,000 STB/day up to 25 years of production.

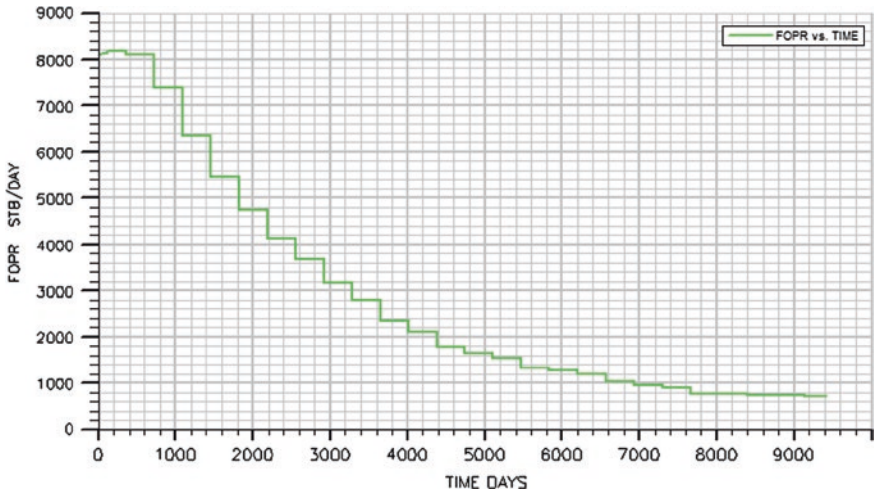


Fig. 4 Field oil daily production rate

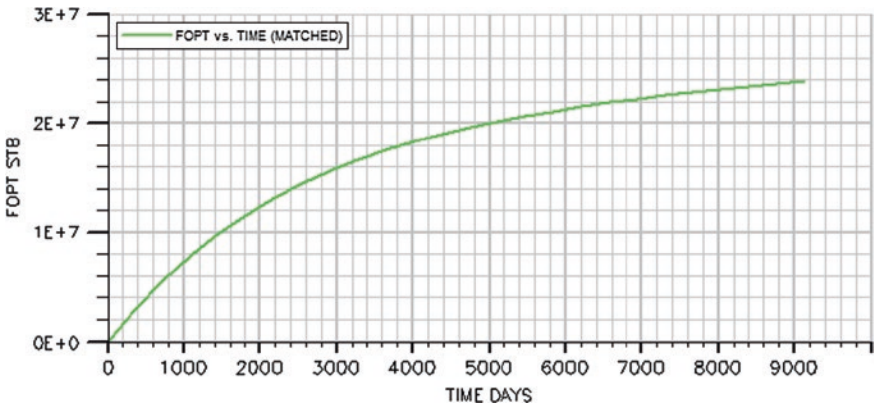


Fig. 5 Field oil total production rate

Figure 5 shows the Field Oil Production Total of Platform C production rate up to 9,125 days (25 years). The graph shows a linear increasing trend proving that the well will have increasing production rates in the 25 years production time.

In the base case study, the production rates for all wells are 0 bbl/day means that the wells in the field require an aid to flow. The reason for the wells cannot flow is because there is no intersection point between the Inflow Performance and Vertical Lift Performance of the well. This is because of insufficient differential pressure between reservoir pressure and inflow flowing pressure. In other words, the well has no operating point and thus cannot flow. Therefore, to flow the wells and to optimize the production of the wells in Platform C, this project is proposed.

Table 2 Comparison on the existing valve and the proposed design for BY-1

EXISTING VALVE				PROPOSED DESIGN			
VALVE TYPE	DEPTH (ft)	TEST RACK OPENING PRESSURE	PORT SIZE	VALVE TYPE	DEPTH (ft)	TEST RACK OPENING PRESSURE	PORT SIZE
Dummy	1175	N/A	N/A	Dummy	1175	N/A	N/A
Dummy	2027	N/A	N/A	Valve	2027	1263.3	8/64"
Dummy	2933	N/A	N/A	Dummy	2933	N/A	N/A
Orifice	3808	N/A	12/64"	Valve	3808	1258.11	8/64"
Dummy	4678	N/A	N/A	Orifice	4678	N/A	9/64"

Gas lift is chosen because one of the well in Platform C which is BY-10 has been identified as a natural gas reservoir and thus is very suitable to be the gas lift source for the project and on the other hand known as one of the efficient artificial lift method.

The production rate is analyzed from the IPR/VLP curves generated. From the IPR/VLP curve, the liquid rate and oil rate are known thus showing that there is an increase in the production for every well when gas lift is applied in the well to assist the production. Moreover, the production rate is basically known from the intersection point of the IPR and VLP curve, and in the other hand showing the relationship of the flow from the reservoir and the flow through the tubing up to the surface. Furthermore, the value of AOF is also known from the IPR/VLP curve which shows the maximum flow rate that can be obtained when the bottom hole flowing pressure is equal to zero. The production rate is the highest the well can achieve with the minimum rate of injection. Thus, the cost in gas lift injection can be reduced when the optimum volume of gas injection rate is known based on the gas lift design.

Furthermore, from the gas lift design, the new setting of the gas lift will be shown in the results pane. The information given in the results pane are the gas lift valve types with respect to its depth setting, transfer pressure, gas lift gas rate, port size, tubing head pressure, and casing pressure. This information is very useful in the gas lift design so that the proper well accessories can be installed, and thus, gas lift system can work properly in the well. Table 2 shows the example of comparison of the well’s existing valve and the proposed design for the well B-301 that can be done from the gas lift design results.

The existing valve is based on the wellbore diagram of well B-301. Based on the table, it is observed that the new proposed design gives more information than the existing design. Moreover, the injection point which is the Orifice is changing from the depth of 3,808 ft in the existing valve to the deepest point 4,678 ft in the new proposed design. The changes are made in order to optimize the production of the well based on the data input. The change of the gas lift injection point will require the gas lift change valve (GLVC) operation, where the type of valve is

change. For example, a dummy is changed to the gas lift valve so that the gas lift injection operation can be done at the selected depth.

The reservoir static and dynamic model is created using suitable keywords for the gas-lifted wells. Then, the reservoir model is run and the time step is set to be 9,125 days to observe the production of the well in 25 years. Based on the graph in the Fig. 1, it is shown that the wells in Platform C will be able to produce up to 25 years. The result is very useful because it gives the insight of the reservoir ability to produce in a long time for the economic benefits in the future.

6 Conclusion

All wells in Platform C, B-1 field have been successfully remodeled using relevant data in the PROSPER. For every well, matching is done and IPR/VLP curve is generated. Moreover, The wells significantly optimized by the addition of gas lift facility since the total flowing rate is increased up to 1,330.81 STB/day of oil. By designing the gas lift, the injection depth and injection gas rate are proposed to have the optimum oil production rates from the eight wells in Platform C, B-1 field.

References

1. Bitsindou, A., & Kelkar, M. (1999). Gas well production optimization using dynamic nodal analysis. Paper presented at the SPE mid-continent operations symposium.
2. Guo, B., Lyons, W. C., & Ghalambor, A. (2011). Petroleum production engineering, a computer-assisted approach: Gulf Professional Publishing.
3. Munoz, E. A., & Quintero, N. (1999). Production Optimization Using a Dynamic Gas-Lift Simulator History Case. Paper presented at the SPE Western Regional Meeting.
4. Economides, M. J., Nolte, K. G., Ahmed, U., & Schlumberger, D. (2000). Reservoir stimulation (Vol. 18): Wiley Chichester.
5. Lu, Q., & Fleming, G. C. (2012). Gas lift optimization using proxy functions in reservoir simulation. SPE Reservoir Evaluation & Engineering, 15(01), 109-119.
6. Cunha, L. (2004). Integrating static and dynamic data for oil and gas reservoir modelling. Journal of Canadian Petroleum Technology, 43(3), 8-11.
7. Lee, H., Liang, J., Ader, J., & Legget, R. (1993). Computer Design and Fieldwide Optimization for Gas-Lifted Wells. Middle East Oil Show.
8. Chia, Y. C., and Sies Hussain. "Gas lift optimization efforts and challenges."SPE Asia Pacific Improved Oil Recovery Conference. Society of Petroleum Engineers, 1999.

Modeling Pressure Drop in Vertical Wells Using Group Method of Data Handling (GMDH) Approach

Mohammed A. Ayoub, Berihun M. Negash and Ismail M. Saaid

Abstract An accurate estimation of the pressure drop in well tubing is essential for the solution of a number of important production engineering and reservoir analysis problems. Several empirical correlations and mechanistic models have been proposed in the literature to estimate the pressure drop in vertical wells that produce a mixture of oil, water, and gas. Although many correlations and models are available to calculate the pressure loss, these models were developed based on a certain set of assumptions and for particular range of data where it may not be applicable for use in different conditions. In this paper, group methods of data handling (GMDH) is used to build a model to predict the pressure drop in multiphase vertical wells. The developed GMDH model has shown the outstanding results, and it has outperformed all empirical correlations and mechanistic models, which have been compared to. The analysis of the results also confirmed that the testing set achieves accurate estimation of the pressure drop. Trend analysis of the model showed that the model is correctly predicting the expected effects of the independent variables on pressure drop.

Keywords Pressure drop estimation · Vertical multiphase flow wells · Group method of data handling · Empirical correlations · Mechanistic models

M.A. Ayoub (✉) · B.M. Negash · I.M. Saaid
Faculty of Geoscience and Petroleum Engineering, Petroleum Engineering Department,
Universiti Teknologi Petronas, Teronoh, Malaysia
e-mail: abdalla.ayoub@petronas.com.my

B.M. Negash
e-mail: bmamo.negash@petronas.com.my

I.M. Saaid
e-mail: ismailsaaid@petronas.com.my

1 Introduction

Multiphase flow in pipes is the process of concurrent flow of two phases or more. In oil or gas production wells, the multiphase flow usually consists of oil, gas and water. The estimation of the pressure drop in vertical wells is quite important for cost-effective design of well completions, production optimization and surface facilities. However, due to the complexity nature of multiphase flow, several approaches have been used to understand and analyze the multiphase flow behavior.

Oil and gas industry needs to have a general method for forecasting and evaluating the multiphase flow in vertical pipes [1]. Multiphase flow correlations are used to determine the pressure drop in the pipes. Although many pressure drop correlations and models have been proposed in literature to estimate pressure drop in vertical wells, but the debate about their accuracy persists. Numerous correlations and equations have been proposed for multiphase flow in vertical, inclined, and horizontal wells in the literature [2–9]. Early methods treated the multiphase flow problem as the flow of a homogeneous mixture of liquid and gas. This approach completely disregarded the well-known observation that the gas phase, due to its lower density, overtakes the liquid phase, which results in “slippage” between the phases. Another reason behind that is the complexity of multiphase flow in the vertical pipes. Many methods have been proposed to estimate the pressure drop in the vertical wells that produce a mixture of oil and gas. The study conducted by [11] concluded that none of the traditional multiphase flow correlations works well across the full range of conditions encountered in oil and gas fields. Besides, most of the vertical pressure drop calculation models were developed for average oil field fluids, and this is the reason for special conditions, such as emulsions, non-Newtonian flow behavior, excessive scale, or wax deposition on the tubing wall, can pose severe problems. Accordingly, predictions in such cases could be doubtful, [12].

The early approaches used the empirical correlation methods such as [2–4]. Then, the trend shifted into mechanistic modeling methods, which adopt the hydrodynamics principles such as [9, 10]. Lately, the researchers have introduced the use of artificial intelligence to the oil and gas industry by using artificial neural networks such as [13–16].

2 Group Method of Data Handling (GMDH)

In 1966, the Russian cyberneticist, Prof. Alexey G. Ivakhnenko in the Institute of Cybernetics in Kiev (Ukraine) introduced a technique for constructing an extremely high-order regression-type polynomial, [17]. The algorithm, the group methods of data handling (GMDH), builds a multinomial of degree in the hundreds, whereas standard multiple regression becomes bogged down in

computation and linear dependence. GMDH modeling can be an alternative to artificial neural networks approach since it helps overcome many of the artificial neural networks limitations due to its self-organizing nature. Based on the self-organizing GMDH, this technique uses well-proven optimization criteria for automatically determining the network size and connectivity, and element types and coefficients for the optimum model, thus reducing the modeling effort and the need for user intervention. The mechanism of model creation not only lessens the burden on the analyst but also safeguards the generated model from being influenced by human biases and misjudgments, [18]. The GMDH model automatically selects influential input parameters, and the input–output relationship can be expressed in polynomial form. This enhances explanation capabilities and allows comparison of the resulting data-based machine learning models with existing first principles or empirical models [19, 20]. In this study, GMDH polynomial neural networks technique is used to construct a mathematical model that can estimate the pressure drop in vertical wells.

3 Model Development

3.1 Data Gathering and Processing

During the data gathering and collection, the quantity and quality of the collected data have been considered to ensure sufficient information has been fed into the model. When it comes to estimate the pressure drop in multiphase vertical wells, there are so many parameters known to be contributing to it. However, not all these parameters might be significantly contributed to the final output. Besides that, some of these parameters cannot be available during the data collection process due to some technical problems. Although this insufficiency in the data can reduce the accuracy of the model, it also might not have significant effects as it will be discussed later.

A total number of 260 data sets had been used in this study. The input variables have been selected based on the most commonly used empirical correlations and mechanistic models used by the industry. These input variables are oil rate, water rate, gas rate, diameter of the pipe, length of the pipe “depth,” wellhead pressure, surface temperature, and oil gravity “API.” Data partitioning has also been carried out after randomization. The data were divided into three different sets: training sets, validation sets, and test sets. Although different partitioning ratios were tested (2:1:1, 3:1:1, and 4:1:1), the authors have chosen the 2:1:1 ratio because it is more popular and frequently used by researchers. According to the chosen partition ratios, 130 data sets have been reserved for training the model, while 65 data sets were utilized for validation purposes. The last 65 data set had been kept aside for testing the new model performance. Table 1 shows the statistical analysis of the used data.

Table 1 Statistical analysis of the used data

Flow parameter	Min	Max	Average	STD
Bottomhole pressure, (psi)	1,019	3,124	2,234	476
Oil rate, (bbl/D)	45	19,618	5,068	4,838
Water rate, (bbl/D)	0	7,900	1,757	2,309
Gas rate, (Mscf/D)	0	13,562	2,563	3,047
Depth, (ft)	2,726	8,070	5,829	1,039
Tubing diameter, (in)	2	4	3.75	0.33
Surface temperature, (°F)	70	160	113	27
Wellhead pressure, (psi)	5	800	249	159
Oil gravity, (API)	12.4	37	31	5.8

4 GMDH Model

The process of building the GMDH model started with selecting the input parameters, which have been discussed earlier. Free software has been used for this purpose [21]. This source code was tested with MATLAB version 8.1 (R2013a). Although all of the input parameters had been used in generating the model, just a few are used in the final equation to estimate the pressure drop. The selection process has been done automatically based on the parameter's contribution to the final output.

Out of the eight variables introduced to the software, five input variables had shown pronounced effect on the final pressure drop estimate, which were oil rate, length of the pipe “depth,” oil gravity, gas rate, and water rate. Those five input parameters were selected based on their mapping influence inside the data set on the pressure drop values.

This topology was achieved after a series of optimization processes by monitoring the performance of the network until the best network structure was accomplished. Figure 1 shows the schematic diagram of the proposed GMDH topology. The final output layer “pressure drop” is being formed from five variables from the input layer. The first three variables combined in one variable in the hidden layer and then with the other two variables used to build the output layer.

4.1 Summary of the Model's Equation

As described in the previous section, the model consists of two layers as follows:

Number of layers: 2

Layer #1

Number of neurons: 1

$$\begin{aligned}
 \mathbf{A} = & a_0 + a_1q_w + a_2L + a_3q_o + a_4q_w \cdot L + a_5q_o \cdot q_w + a_6q_o \cdot L + a_7(q_w)^2 + a_8(L)^2 \\
 & + a_9(q_o)^2 + a_{10}q_o \cdot L \cdot q_w + a_{11}L \cdot (q_w)^2 + a_{12}(L)^2 \cdot q_w + a_{13}(q_w)^2 \cdot q_o + a_{14}q_o \cdot (L)^2 \\
 & + a_{15}(q_o)^2 \cdot q_w + a_{16}(q_o)^2 \cdot L + a_{17}(q_w)^3 + a_{18}(L)^3 + a_{19}(q_o)^3
 \end{aligned}$$

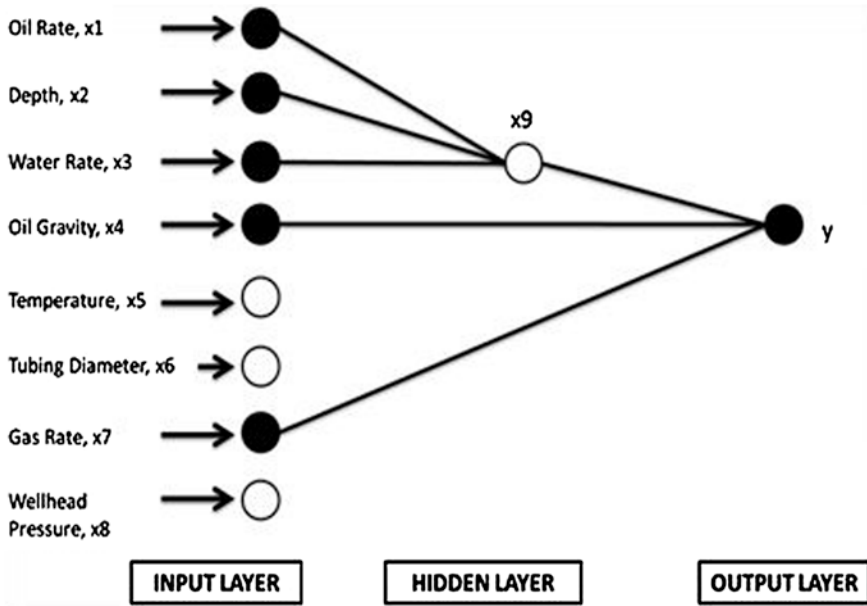


Fig. 1 Proposed GMDH topology

$$\begin{aligned}
 a_0 &= -2301.448 & a_5 &= -4.415E-005 & a_{10} &= 2.316E-009 & a_{15} &= 1.733E-009 \\
 a_1 &= -2.610 & a_6 &= 9.869E-005 & a_{11} &= -7.008E-009 & a_{16} &= 5.425E-009 \\
 a_2 &= 1.845 & a_7 &= 3.675E-005 & a_{12} &= -5.434E-008 & a_{17} &= 1.356E-010 \\
 a_3 &= -0.077 & a_8 &= -3.163E-004 & a_{13} &= 1.946E-009 & a_{18} &= 2.098E-008 \\
 a_4 &= 7.796E-004 & a_9 &= -2.645E-005 & a_{14} &= -1.542E-008 & a_{19} &= -1.839E-010
 \end{aligned}$$

$$\begin{aligned}
 \Delta P &= b_0 + b_1A + b_2q_g + b_3API + b_4q_g \cdot A + b_5API \cdot A + b_6API \cdot q_g + b_7(A)^2 + b_8(q_g)^2 \\
 &+ b_9(API)^2 + b_{10}API \cdot q_g \cdot A + b_{11}q_g \cdot (A)^2 + b_{12}(q_g)^2 \cdot A + b_{13}(A)^2 \cdot API + b_{14}API \cdot (q_g)^2 \\
 &+ b_{15}(API)^2 \cdot A + b_{16}(API)^2 \cdot q_g + b_{17}(A)^3 + b_{18}(q_g)^3 + b_{19}(API)^3
 \end{aligned}$$

Layer #2

Number of neurons: 1

$$\begin{aligned}
 b_0 &= 3415.957 & b_5 &= 1.667E-001 & b_5 &= -2.260E-006 & b_{15} &= -1.250E-002 \\
 b_1 &= -0.606 & b_6 &= -8.800E-003 & b_6 &= -8.033E-008 & b_{16} &= 1.209E-003 \\
 b_2 &= -1.046 & b_7 &= -2.304E-004 & b_7 &= 1.264E-008 & b_{17} &= -8.185E-007 \\
 b_3 &= -357.669 & b_8 &= 2.129E-004 & b_8 &= 1.593E-004 & b_{18} &= 1.670E-009 \\
 b_4 &= 2.621E-004 & b_9 &= 10.907 & b_9 &= -7.628E-006 & b_{19} &= 6.518E-002
 \end{aligned}$$

where

q_o = oil rate, bbl/d, L = length of the pipe, ft, q_w = water rate, bbl/d, and
 API = oil gravity, API
 q_g = gas rate, scf/d, ΔP = simulated pressure drop by GMDH model

5 Results and Discussion

A trend analysis was carried out to check whether the developed model is physically correct. Synthetic data sets were prepared where in each set only one parameter is changed, while other parameters are kept constant. Besides, statistical error analysis was used to check the accuracy of GMDH model and all investigated models. The statistical parameters used in this study are the average absolute percentage relative error (AAPE), the average percentage relative error (APE), the maximum absolute percentage error (MaxAE), the minimum absolute percentage error (MinAE), the root mean square error (RMSE), the coefficient of determination (R^2), and the standard deviation of error (STD). Cross-plots were also used to compare the performance of all GMDH model's data sets and all investigated models. A 45° straight line between the calculated pressure drop values and measured pressure drop values is plotted which represents a perfect correlation line. When the values go closer to the line, it indicates better agreement between the measured and the estimated values.

5.1 Trend Analysis

To test the developed model, the effects of gas rate, oil rate, water rate, and depth "pipe length" on pressure drop were determined and plotted on Fig. 2a–e. As expected, the developed model has achieved truthful trends that match the normal pressure trends. The pressure drop increases as the gas, water, and oil increases as justified by the general energy equation. The same goes to the increase in the pressure drop with depth. The increase in pressure drop when oil gravity increased is simply justified by the specific gravity equation, where specific gravity is proportionally direct to pressure.

5.2 Comparison of GMDH Against Other Models

Summary of statistical comparisons between all GMDH model's sets (training, validation, and testing) is presented in Table 2. However, Table 3 summarizes these statistical parameters of the proposed GMDH model and the other investigated models.

To demonstrate the success and superiority of the GMDH model against the other models, RMSE of each model has been plotted against the standard deviation (STD) of errors, as presented in Fig. 3a. The best model will be located at the lower most left corner, which is indicated by the intersection of both lower values of RMSE and STD. Also, average absolute relative error (AAPE) of each model is plotted against the coefficient of determination (R^2), as presented in Fig. 3b. However, this time the best model will be AAPE of each model is plotted against the coefficient of determination (R^2), as presented in Fig. 3b. However, this time the best model will be located at the uppermost left corner, which is indicated

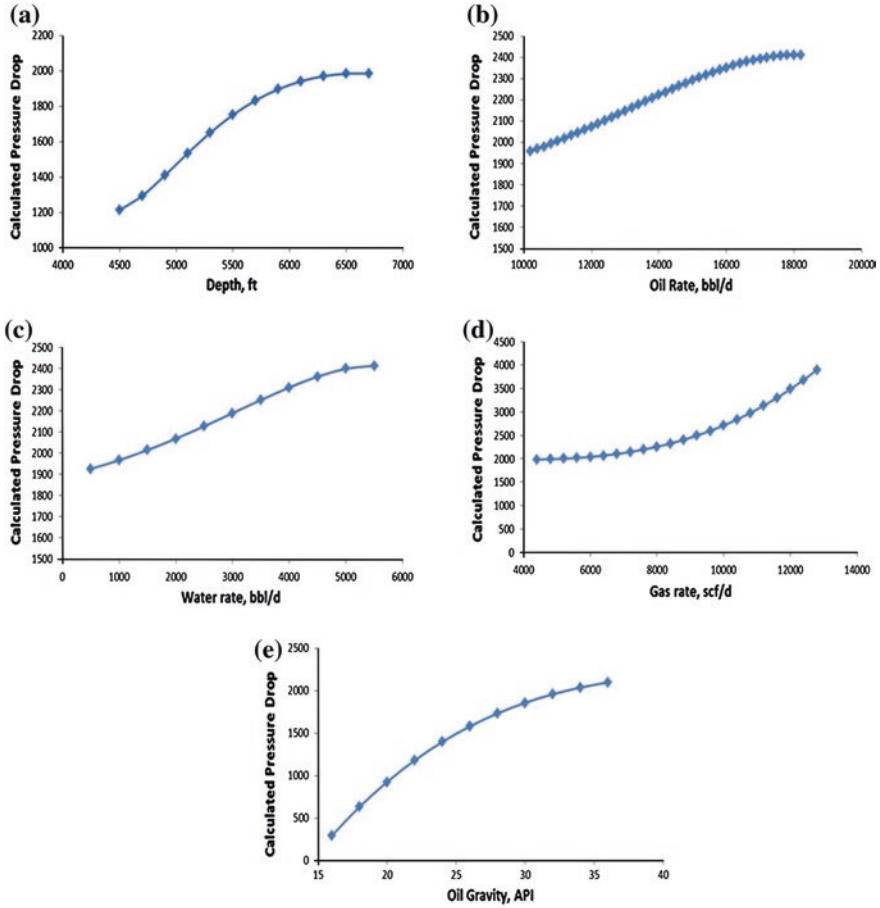


Fig. 2 Effect of different parameters on pressure drop

Table 2 Statistical analysis results of the proposed GMDH model

Statistical parameter	Training	Validation	Testing
AAPE	4.36	7.16	4.46
APE	0.13	1.45	-0.38
MaxAE	18.96	29.13	22.31491
MinAE	0.018	0.16	0.22
RMSE	5.63	9.62	5.86
R ²	0.933	0.723	0.923
STD	3.56	6.43	3.80

by the intersection of both low AAPE value with High R². In both cases, GMDH model has always fallen in the best corner of the graph, as compared to other models. This also indicates better quality performance of GMDH model when compared to other tested models.

Table 3 Statistical analysis results of GMDH model and other investigated models

Method	AAPE	APE	MaxAPE	MinAPE	RMSE	R ²	STD
Aziz et al	18.16	15.31	60.51	0.169	25.71	0.2044	18.20
Hagedron and Brown	11.97	10.89	25.64	0.28	13.71	0.7888	6.68
Gray	11.70	10.06	25.13	0.06	13.76	0.7346	7.23
Orkiszewski	11.51	10.14	28.15	0.50	13.43	0.7758	6.92
Mukherjee and Brill	9.69	5.56	39.36	0.45	11.70	0.8061	6.56
Ansari et al	7.90	4.94	30.09	0.09	9.51	0.8614	5.30
Duns and Ros	7.64	5.52	24.27	0.05	9.47	0.8362	5.60
Beggs and Brill	6.58	3.21	24.95	0.31	8.12	0.8710	4.76
Ayoub	4.53	-0.32	18.22	0.06	6.15	0.9052	4.16
This study, (GMDH)	4.46	-0.38	22.32	0.22	5.86	0.9233	3.80

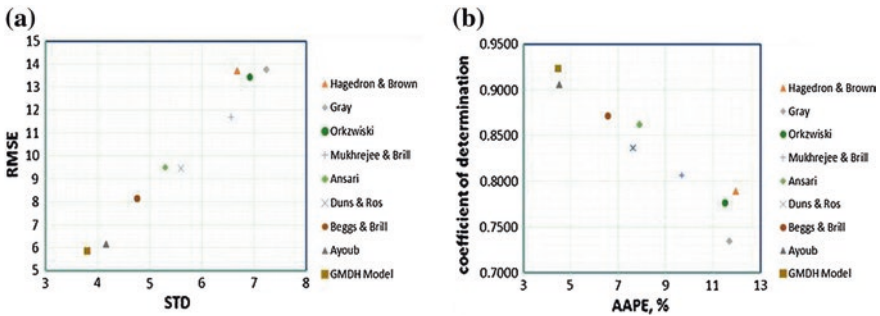


Fig. 3 Error analysis

6 Conclusion

The following conclusions can be drawn from the current study:

1. GMDH approach has been utilized to develop, for the first time, a model for estimating the pressure drop in vertical wells successfully.
2. This developed model showed better results when compared against the common used models in the industry. Comparison of the statistical error proves the GMDH model superiority over the existing correlations and models.
3. The developed model achieved the lowest AAPE (4.46), the lowest RMSE (5.86), the highest coefficient of determination (0.92), and the lowest STD (3.80).
4. The trend analysis of the model showed that the model is correctly predicting the expected effects of the independent variables on the pressure drop.

5. Five input parameters have been selected automatically based on their contribution to the final output by this smart regression procedure with minimal intervention by the authors. Tubing diameter is not one of them indeed. Meaning that the correlation is independent on the effect of tubing diameter. This is again a great sign of model robustness and in contrary to what has been believed since long time by multiphase scientists.
6. Fluid viscosity and density are well known for their interrelating functions, when viscosity is high, density is high, and fluid is harder to move. In this study, viscosity is not omitted, rather it is being considered implicitly.

Acknowledgment The authors would like to thank the Petroleum Engineering department at Universiti Teknologi PETRONAS for supporting this study.

References

1. Poettman, F. H., & Carpenter, P. G. The Multiphase Flow of Gas Oil and Water through Vertical Flow Strings with Application to the Design of Gas-lift Installations. *Drilling and Production Practice*. 1952.
2. Ros, D. J. Vertical flow of gas and liquid mixtures in wells. In *6th World Petroleum Congress*. 1963.
3. Hagedorn, A. R., & Brown, K. E. Experimental study of pressure gradients occurring during continuous two-phase flow in small-diameter vertical conduits. *Journal of Petroleum Technology*. 1965. 17(04). 475-484.
4. Orkiszewski, J. Predicting two-phase pressure drops in vertical pipe. *Journal of Petroleum Technology*, 1967. 19(06). 829-838.
5. Aziz, K., & Govier, G. W. Pressure drop in wells producing oil and gas. *Journal of Canadian Petroleum Technology*. 1972. 11(03).
6. Beggs, D. H., & Brill, J. P. A study of two-phase flow in inclined pipes. *Journal of Petroleum technology*. 1973. 25(05). 607-617.
7. Gray, H. E. Vertical flow correlation in Gas Wells: User's Manual for API 14B Subsurface Controlled Subsurface Safety Valve String Computer Program. 1978. 2nd Edition (Appendix B). American Petroleum Institute. Dallas. TX.
8. Mukherjee, H., & Brill, J. P. Pressure drop correlations for inclined two-phase flow. *Journal of energy resources technology*. 1985. 107(4). 549-554.
9. Ansari, A. M., Sylvester, N. D., Sarica, C., Shoham, O., & Brill, J. P. A comprehensive mechanistic model for upward two-phase flow in wellbores. *SPE Production & Facilities*. 1994. 9(02). 143-151.
10. Gomez, L. E., Shoham, O., Schmidt, Z., Chokshi, R. N., & Northug, T. Unified mechanistic model for steady-state two-phase flow: horizontal to vertical upward flow. *SPE journal*. 2000. 5(03). 339-350.
11. Pucknell, J. K., Mason, J. N. E., & Vervest, E. G. An Evaluation of Recent "Mechanistic" Models of Multiphase Flow for Predicting Pressure Drops in Oil and Gas Wells. *Offshore Europe*. 1993.
12. Takacs, G. Considerations on the selection of an optimum vertical multiphase pressure drop prediction model for oil wells. *SPE/ICoTA Coiled Tubing Roundtable*. 2001.
13. Ayoub, M. A. Development and testing of an artificial neural network model for predicting bottomhole pressure in vertical multiphase flow (Doctoral dissertation, King Fahd University of Petroleum and Minerals). 2004.

14. Mohammadpoor, M., Shahbazi, K., Torabi, F., Firouz, Q., & Reza, A. A New Methodology for Prediction of Bottomhole Flowing Pressure in Vertical Multiphase Flow in Iranian Oil Fields Using Artificial Neural Networks (ANNs). In *SPE Latin American and Caribbean Petroleum Engineering Conference*. Society of Petroleum Engineers. 2010.
15. Jahanandish, I., Salimifard, B., & Jalalifar, H. Predicting bottomhole pressure in vertical multiphase flowing wells using artificial neural networks. *Journal of Petroleum Science and Engineering*. 2011. 75(3). 336-342.
16. Ayoub, M. A. Development and Testing of Universal Pressure Drop Model in Pipelines Using Abductive and Artificial Neural Networks. Bandar Seri Iskander. Perak: PhD Thesis. Universiti Teknologi Petronas. 2011.
17. Ivakhnenko, A. G. Group Method of Data Handling a Rival of the Method of Stochastic Approximation. *Soviet Automatic Control*. 1966. 13, 43-71.
18. Ivakhnenko, A. G. Polynomial Theory of Complex Systemq. *IEEE Transections on System, Man and Cybernetics*. 1971. 364-378.
19. Farlow, S. J. The GMDH algorithm of Ivakhnenko. *The American Statistician*. 1981. 35(4), 210-215.
20. Farlow, S. J. The GMDH algorithm,” in *Self-Organizing Methods in Modeling: GMDH Type Algorithms*. New York: Marcel-Dekker. 1984.
21. Jekabsons, G. GMDH-type Polynomial Neural Networks for Matlab. from <http://www.cs.rtu.lv/jekabsons/2010>.

Comparison of Critical Gas Flow Rate Equations to Prevent Liquid Loading

Pei Wen Lim, Mohd Amin Shoushtari, A.P. Ismail bin Mohd Saaid
and Salahaldin Sh

Abstract Liquid loading is a common problem in mature gas wells that may cease production if the problem is prolonged. Thus, it is required to check for the occurrence of the liquid loading problem. This paper aims to develop a work flow that predicts critical gas flow rate (minimum required gas flow rate) to prevent liquid loading based on the published literature and to analyze effects of temperature, pressure, conduit size, producing depth, and inclination on the critical gas flow rate. Turner et al. model and Guo et al. model are selected to develop a work flow. Fluid characterization is performed using the necessary inputs of fluid properties based on that stated in this paper. This work presents a work flow with two functions, which are estimating critical gas flow rate and performing sensitivity study. It is found that prediction of critical gas flow rate by the Turner et al. model is lower than that of the Guo et al. model. Analyses from sensitivity studies show that critical gas flow rate will be increased if temperature is reduced; pressure is increased; conduit size is increased; producing depth is increased or inclination is reduced. For the set of inputs utilized, the critical gas velocity and flow rate calculated by the Turner et al. model (10.139 ft/s and 0.701 MMscf/d) is lower than that of the Guo et al. model (11.689 ft/s and 0.827 MMscf/d). The success of this project will yield a better insight on liquid loading problem, and it is hoped that the developed work flow can be applied in the industry.

Keywords Critical gas flow rate · Liquid loading

P.W. Lim (✉) · M.A. Shoushtari · A.P. Ismail bin Mohd Saaid · S. Sh
Universiti Teknologi PETRONAS, Tronoh, Malaysia
e-mail: peiwen.lim@petronas.com.my

M.A. Shoushtari
e-mail: amin.shoushtari@petronas.com.my

Nomenclature

A	Tubing cross-sectional area (ft ²)
$a_g, b_g, c_g, d_g, e_g, f_g, m_g, n_g,$	Parameters for Guo et al. model
D	Producing depth (ft)
E_k	Gas-specific kinetic energy (lb _f -ft/ft ³)
E_{km}	Minimum kinetic energy required to transport liquid drops (lb _f -ft/ft ³)
N_{Re}	Dimensionless Reynolds Number (–)
P	Pressure (lb _f /ft ²)
P_{av}	Average pressure (psia)
P_{hf}	Wellhead pressure (psia)
Q_c	Condensate make (bbl/d)
Q_g	Gas production day (scf/d)
Q_{gm}	Minimum required gas flow rate for liquid removal (MMscf/d)
Q_o	Condensate make (bbl/d)
Q_s	Solid make (ft ³ /d)
Q_w	Water make (bbl/d)
S_g	Gas-specific gravity (–)
S_o	Condensate gravity (–)
S_s	Solid-specific gravity (–)
S_w	Water-specific gravity (–)
T_{av}	Average temperature (°R)
T_{wf}	Surface temperature (°R)
T_{wh}	Wellhead temperature (°R)
V_g	Gas velocity required to transport liquid drops (ft/s)
Z	Gas compressibility factor (–)
γ_c	Condensate gravity (–)
γ_g	Gas-specific gravity (–)
γ_s	Solid-specific gravity (–)
γ_w	Water-specific gravity (–)
ε	Tubing wall roughness (ft)
θ	Hole inclination (rad)
ρ_g	Gas density (lb _m /ft ³)
ρ_l	Liquid density (lb _m /ft ³)
σ	Interfacial tension (dynes/cm)

1 Introduction

Liquid loading is a common problem for mature gas wells. Depleting reservoir pressure reduces gas flow velocity, and the gas flow does not have sufficient energy to carry liquids up to the surface [1, 2]. As the pressure drops to a critical

point, liquids tend to accumulate at the bottomhole [3]. The accumulated liquid (liquid hold up) in the wellbore will increase with time and affects the gas relative permeability. This causes additional backpressure on the formation and reduces gas production rate [4, 5]. The increased backpressure may increase the risk of formation damage [6, 7] and later may cease production and induces higher operating cost [8].

The ultimate objective of this paper is to present a work flow for predicting critical gas flow rate (based on the Turner et al. model and the Guo et al. model) and analyzing effects of temperature, pressure, conduit size, producing depth, and inclination on the critical gas flow rate.

An estimation of critical gas flow rate is important to enable the well to be continuously deliquified with its own energy without external aid [9]. A few models that predict critical gas flow rates were reviewed.

Turner et al. model [1, 10–13] was the first work in the area of predicting minimum gas flow rate to prevent liquid loading. The authors compared calculated results with field data. They proved that the model can be used for wells with surface pressure that is higher than 1,000 psi or as low as 5–800 psi. Coleman et al. extended Turner et al.'s work in their model [14–16]. Their equation is the same as the previous model but without 1.2 adjustment. This creates doubt as limitation of the droplet model and conditions to apply the 1.2 adjustment are not clearly defined [9]. For Nosseir et al. model [9, 10, 13], the authors considered flow regimes in a well and concluded that flow regime can be determined from dimensionless Reynolds number, N_{Re} . Leas and Nickens model is developed by modifying [10, 17] Turner et al. model by assuming some values into the Turner et al. model. For Li et al. model, a new assumption is added [13, 18] where a liquid droplet tends to change shape due to the pressure difference and that a flattened droplet can be lifted easier up to the surface compared to a spherical droplet. Guo et al. model [10, 12] is one of the recent works which is based on minimum kinetic energy criterion and four-phase mist-flow model in gas wells. The authors proposed that the minimum required gas flow rate can be calculated by comparing gas-specific kinetic energy, E_k with minimum kinetic energy required to transport liquid drops, E_{km} .

2 Methodology

The Turner et al. model and the Guo et al. model are selected to develop the work flow for prediction of minimum required gas flow rate for liquid removal. Comparisons of the result are made. All the assumptions and limitations used in both models and other equations to reach final results are applied in the developed work flow. If both water and condensate are present in a system, denser of the two should be used to proceed with determinations of surface tension and liquid density. Figure 1 shows the flowchart on how to use the developed work flow.

Turner et al. developed (1) and (2) to calculate minimum gas flow rate required for liquid removal.

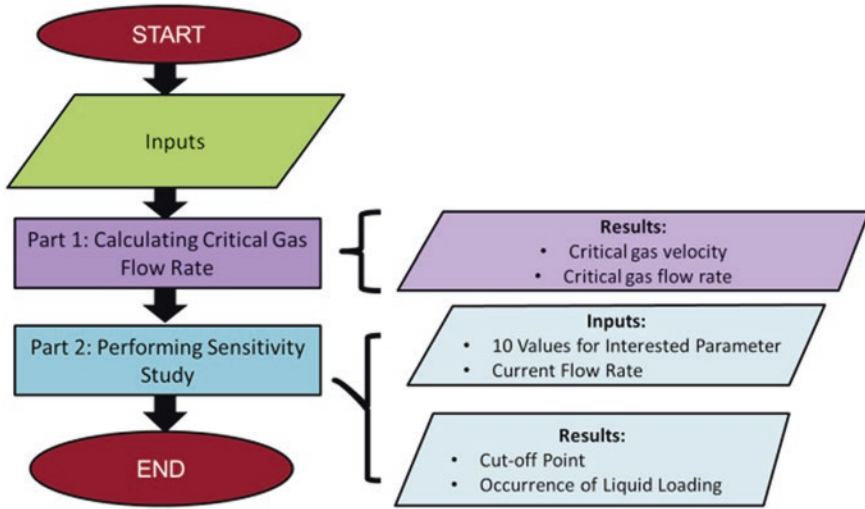


Fig. 1 Flowchart of the developed work flow

$$V_{gm} = \frac{1.3\sigma^{1/4}(\rho_l - \rho_g)^{1/4}}{C_d^{1/4} \rho_g^{1/2}} \quad (1)$$

$$Q_{gm} = \frac{3.06P_{av}AV_{gm}}{T_{av}Z} \quad (2)$$

Guo et al. developed the following equations to calculate minimum gas flow rate required for liquid removal:

$$\begin{aligned} & b_g(P - P_{hf}) + \frac{1 - 2b_gm_g}{2} \ln \left| \frac{(P + m_g)^2 + n_g}{(P_{hf} + m_g)^2 + n_g} \right| \\ & - \frac{m_g + \frac{b_g}{c_g}n_g - b_gm_g^2}{\sqrt{n_g}} \left[\tan^{-1} \left(\frac{P + m_g}{\sqrt{n_g}} \right) - \tan^{-1} \left(\frac{P_{hf} + m_g}{\sqrt{n_g}} \right) \right] \\ & = a_g(1 + d_g^2e_g)D \end{aligned} \quad (3)$$

$$P = 6.46 \times 10^{-13} \frac{S_g T_{av} Q_{gm}^2}{A^2 E_{km}} \quad (4)$$

$$V_{gm} = 4.71 \times 10^{-5} \frac{T_{av} Q_{gm}}{AP} \quad (5)$$

3 Result and Discussion

3.1 Development of Work Flow

The work flow is developed using Microsoft Excel based on the Turner et al. model and the Guo et al. model. The work flow is modified and updated from the work completed by Guo and Ghalambor [12]. The design and flow of the work flow is modified from ‘Sand Modelling SpreadSheet’ [19]. For both models, users can choose to proceed from the two functions equipped in the work flow, which are firstly, calculation of critical gas flow rate to prevent liquid loading problem and secondly, performing sensitivity study. Temperature, pressure, conduit size, producing depth, and inclination are the parameters chosen to be checked in sensitivity studies.

3.2 Critical Gas Flow Rate to Prevent Liquid Loading

A set of inputs is used to demonstrate results of Turner et al. model and Guo et al. model. Inputs used are shown in Table 1. Results calculated for both models are shown in the respective model page of the spreadsheet. In addition, a comparison page is created so that results of both models can be viewed in a single page in the

Table 1 Inputs of the Turner et al. model and the Guo et al. Model

Parameter	Symbol	Value	Unit
Surface temperature	T_{wf}	520	°R
Surface pressure	P_{wf}	500	psia
Wellhead temperature	T_{wh}	520	°R
Wellhead pressure	P_{wh}	500	psia
Gas-specific gravity	γ_g	0.6	–
Water-specific gravity	γ_w	1.08	–
Condensate gravity	γ_c	0.53764	–
Solid-specific gravity	γ_s	2.65	–
Liquid density (Heavy)	ρ_l	67.4	lbm/ft ³
Interfacial tension	σ	60	dynes/cm
Conduit outer diameter	d_{to}	1.995	inch
Conduit inner diameter	d_{ti}	0.000	inch
Tubing wall roughness	ϵ	1.50×10^{-5}	inch
Hole inclination	θ	0	degree
Producing depth	D	6,700	ft
Water make	Q_w	8.6	bbl/day
Solid make	Q_s	0	ft ³ /day
Condensate make	Q_c	0	bbl/day
Major liquid	–	1.000	–

spreadsheet. The calculated V_{gm} and Q_{gm} are: 10.139 ft/s and 0.701 MMscf/d by the Turner et al. model; 11.689 ft/s and 0.827 MMscf/d by the Guo et al. model. The later gives calculated bottomhole pressure of 589.756 psia. Bottomhole pressure calculation is not available for the Turner et al. model. Any flow rate for the well that is below the calculated Q_{gm} may lead to liquid loading problem. It was found that the results of the Guo et al. model are slightly higher than that of the Turner et al. model. The differences may be caused by differences physics and assumptions used. The Turner et al. model was developed from the droplet model while the Guo et al. model was developed from the minimum kinetic energy theory and the four-phase flow model. In the Turner et al. model, drag coefficient and Weber number may be the reasons that result in lower critical flow rate.

From the results, it is suggested that Guo et al. model should be used in predicting Q_{gm} . Guo et al. [10, 12] state that results of their model are more conservative than that of the Turner et al. model since comparison of results with field data is made. Hence, it is recommended that the Guo et al. model should be used to predict critical gas flow rate to prevent liquid loading problem in gas well. However, in the case when only minimum data are available, Turner et al. model that requires fewer inputs can be used to give a rough prediction of onset of liquid loading problem.

3.3 Sensitivity Study

Sensitivity studies on five parameters (temperature, pressure, conduit size, producing depth, and inclination) have been run to examine the effect of the parameters on critical gas flow rate to prevent liquid loading problem in gas wells. Note that sensitivity studies of producing depth and inclination can only be performed by using the Guo et al. model.

When value of one variable is altered, the other parameters are kept constant and the effect of the change of the variable on critical gas flow rate is analyzed. Thus, it is necessary to run base case (Table 1) before running the sensitivity studies. This is performed because inputs, such as specific gravity (of water, solid, and condensate), production rate (water, solid, and condensate), conduit wall roughness, liquid density, and surface tension, which are kept constant throughout the sensitivity studies, are needed to be carried forward from the input table into sensitivity study table.

In all sensitivity studies, input current flow rate is compared against the calculated minimum required gas flow rate for each parameter, in which current flow rate that is below the critical gas flow rate may lead to liquid accumulation in gas wells. A graph of current flow rate and critical gas flow rate is plotted in every sensitivity study section. The intersection point is the cutoff point where liquid loading problem may occur. Sets of inputs are used to run sensitivity study with the work flow developed.

For sensitivity study of temperature, the results of the Turner et al. model are varying from 0.724 MMscf/d to 0.387 MMscf/d while the results of the Guo et al.

model are ranging from 0.844 MMscf/d to 0.492 MMscf/d. Graph of sensitivity study of temperature is extracted to demonstrate the graph that will be obtained from the sensitivity study section in the work flow (Fig. 2). Blue line represents current flow rate; red line shows flow rate calculated by the Turner et al. model; and green line depicts flow rate calculated by the Guo et al. model.

From Fig. 2, the cutoff point is 880 °R for the Turner et al. model and 1,340 °R for the Guo et al. model. Both models give lower critical gas flow rates when temperature is increased. The differences of results are due to the inputs of differences temperatures in the respective correlations.

For sensitivity study of pressure, the results of the Turner et al. model are varying from 0.295 MMscf/d to 1.643 MMscf/d while the results of the Guo et al. model are varying from 0.387 MMscf/d to 1.595 MMscf/d. The cutoff point is 260 psia for the Turner et al. model and 180 psia for the Guo et al. model. Both models give higher critical gas flow rates when pressure is increased. The differences of results calculated by the two models are due to the difference pressures used in the respective correlations.

For sensitivity study of conduit size, the results of the Turner et al. model are varying from 0.305 MMscf/d to 7.735 MMscf/d while the results of the Guo et al. model are changing from 0.364 MMscf/d to 8.990 MMscf/d. The cutoff point used is 1.7 in. for the Turner et al. model and 1.5 in. for the Guo et al. model. Both models give higher critical gas flow rates when conduit size is increased. The differences of results calculated by the two models are due to the differences of uses of conduit sizes in the respective correlations.

For sensitivity study of producing depth, the calculated minimum required gas flow rates are ranging from 0.798 MMscf/d to 0.890 MMscf/d. Cutoff point is found to be 7,200 ft which shows that liquid loading problem may occur in the

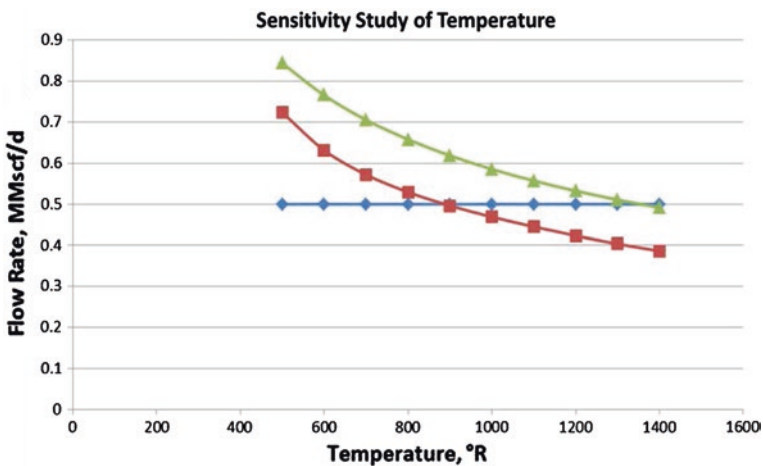


Fig. 2 Graph of sensitivity study of temperature

well if producing depth is larger than 7,200 ft. Critical gas flow rate is higher when producing depth is increased.

For sensitivity study of inclination, the calculated minimum required gas flow rates are ranging from 0.827 MMscf/d to 0.769 MMscf/d. Cutoff point is found to be 56°, which shows that liquid loading problem may occur in the well if inclination angle is smaller than 56°. Critical gas flow rate reduces when inclination is increased.

4 Conclusions and Recommendations

A work flow that predicts critical gas flow rate to prevent liquid loading and to conduct sensitivity study by Turner et al. model and Guo et al. model was developed. All the assumptions applied in the models by the respective authors and in the other equations used are applied in this work flow. For the set of inputs utilized, the critical gas velocity and flow rate calculated by the Turner et al. model (10.139 ft/s and 0.701 MMscf/d) is lower than that of the Guo et al. model (11.689 ft/s and 0.827 MMscf/d).

Through sensitivity studies, effects of parameters (temperature, pressure, conduit size, producing depth, and inclination) on the critical gas flow rate were obtained. Critical gas flow rate will be increased if temperature is reduced; pressure is increased; conduit size is increased; producing depth is increased, or inclination is reduced.

It is hoped that through this project, a better understanding of the prediction of liquid loading problem in gas wells can be yielded. The findings of this work provide insights on the effects of the five parameters studied on the critical gas flow rate and contribute to research development on predicting occurrence of liquid loading problem in gas wells.

Recommended actions for future are to include gas well deliquification techniques selectors and mathematical models of different techniques to check well performances after unloading by those techniques.

Acknowledgments The authors would like to express their appreciation to Universiti Teknologi PETRONAS, Malaysia for the directional guidance, valuable assistance, and constructive feedbacks in producing this paper.

References

1. J.F. Lea, H.V. Nickens, and M.R. Wells, Gas Well Deliquification, 2nd ed., Burlington, MA: Gulf Professional Publishing, 2008.
2. PCSPlungers. (2011, April 13). PCS FlowThru Plunger [Video file]. Retrieved on February 6, 2013, from <http://www.youtube.com/watch?v=4DJYv5pZr3E>
3. ABB Totalflow. (2009, May 11). Liquid Loading [PDF file]. Retrieved on February 24, 2013, from Arcadiana Flow Measurement Society Website: <http://www.afms.org/Docs/liquids/LiquidLoad.pdf>

4. J.Y. Wang, 2009. Novel Completion for Effective Deliquification of Natural Gas Wells. Paper SPE 120663 presented at the 2009 SPE Production and Operations Symposium, Oklahoma, 4-8 April.
5. A.V. Bondurant, B.D. Dotson, and P.O. Oyewole, 2007. Getting the Last Gasp: Deliquification of Challenging Gas Wells. Paper IPTC 11651 presented at the International Petroleum Technology Conference, Dubai, 4-6 December.
6. E.K. George, (2005, November 4). Deliquifying Mature Gas Wells. EP Magazine.
7. S.B. Coleman, H.B. Clay, D.G. McCurdy and L.H. Noris III, (March 1991). A New Look at Predicting Gas Well Loading-Up (SPE 20280). JPT.
8. G.K. Chava, G. Falcone, and C. Teodoriu, 2008. Development of a New Plunger-Lift Model Using Smart Plunger Data. Paper SPE 115934 presented at the 2008 SPE Annual Technical Conference and Exhibition, Denver, 21-24 September.
9. M.A. Nosseir, T.A. Darwich, M.H. Sayyouth and M.E. Sallaly, 2000. A New Approach for Accurate Prediction of Loading in Gas Wells under Different Flowing Conditions. Paper SPE 66540 presented at the 1997 SPE Production Operations Symposium, Oklahoma, 9-11 March.
10. B. Guo, A. Ghalambor, and C. Xu, 2005. A Systematic Approach to Predicting Liquid Loading in Gas Wells. Paper SPE 94081 presented at the 2005 SPE Production and Operations Symposium, U.S.A., 17-19 April.
11. R.G. Turner, M.G. Hubbard and A.E. Duckler, November 1969. Analysis and Prediction of Minimum Flow Rate for the Continuous Removal of Liquids from Gas Wells. Paper SPE 2198 presented at the SPE 43rd Annual Fall Meeting, Houston, 29 Sept – 2 Oct, 1968.
12. B. Guo and A. Ghalambor, Natural Gas Engineering Handbook, University of Louisiana at Lafayette: Gulf Publishing Company, 2005.
13. Y. Nallaparaju. (2012). Prediction of Liquid Loading [PDF file]. Retrieved on July 23, 2013, from SPG India Website: https://www.google.com.my/url?sa=t&rct=j&q=&esrc=s&source=web&cd=8&cad=rja&ved=0CH8QFjAH&url=http%3A%2F%2Fwww.spgindia.org%2Fspg_2012%2Fspgp446.pdf&ei=UL73UYq7Ic-qrAee1ICoBw&usg=AFQjCNH8XCRx1Z2L2Xb_P5Py2H9LXCnc3w&sig2=YN2xDNw9OjKDxKyFuGZhwQ&bvm=bv.49967636,d.bmk
14. Texas A&M University. (1999, July 16). Liquid Loading: Reference Summary of Selected Papers on Water Load-Up in Gas Wells [Word file]. Retrieved on July 22, 2013, from Department of Petroleum Engineering of Texas A&M University Website: https://www.google.com.my/url?sa=t&rct=j&q=&esrc=s&source=web&cd=1&cad=rja&ved=0CCwQFjAA&url=http%3A%2F%2Fwww.pe.tamu.edu%2Fwattenbarger%2Fpublic_html%2FSelected_papers%2FLiquid%2520Loading.doc&ei=nbr3UdOZjczRrQfQjCgAw&usg=AFQjCNG5KtmT70RLr55596M6c22wsxeSrg&sig2=crULi1DKqtue_Es8gId_RA&bvm=bv.49967636,d.bmk
15. Unknown. (n.d.): Gas Well Liquid Load-Up (Critical Rate for Gas Well Unloading) [Online]. Available: <http://www.peteng2.com/jmm/gw101.html>
16. Artificial Lift R&D Council (ALRDC). (n.d.). Guidelines and Recommended Practices for Selection of Artificial Lift Systems for Deliquifying Gas Wells [Word file]. Retrieved on January 31, 2013, from Artificial Lift R&D Council Website: <http://www.google.com.my/url?sa=t&rct=j&q=&esrc=s&source=web&cd=3&cad=rja&ved=0CEAQFjAC&url=http%3A%2F%2Fwww.alrdc.com%2Frecommendations%2Fgas%2520well%2520deliquification%2Fartificial%2520lift%2520selection%2FAL%2520Selection%2520Edited%2520-%2520Section%25202.2%2520-%2520Selection%2520Document.docx&ei=Dw4sUZPxA4TjrAfwp4HoDQ&usg=AFQjCNGyqO6ppRc-0rLBJ8Dh4qMvFk8p3g&sig2=HKxf8Y7ir0NVcCFxYTa2DA&bvm=bv.42965579,d.bmk>
17. J.F. Lea and H.V. Nickens, (April 2004). Solving Fas-Well Liquid-Loading Problems (Paper SPE 72092). SPE Prod. & Facilities.
18. M. Li, S.L. Li and L.T. Sun, 2002. New View on Continuous-Removal Liquids From Gas Wells. Paper SPE 75455 presented at the 2001 SPE Permian Basin Oil and Gas Recovery Conference, Midland, 15-16 October 2001.
19. P.W. Lim and W.C. Kan, 'Sand Modelling Handbook' (for SPT Group), unpublished

Use of Group Method of Data Handling Algorithms for Predicting Heated and Steamed Zone Volumes During Steam Flooding

Sami Abdelrahman Musa and Mariyamni Awang

Abstract The predictions of steamed and heated zone volumes are critical aspects of steam or hot water injection for enhanced oil recovery because they are used to calculate the expected oil recovery. There are a few models available to calculate steamed and heated zone volumes, but most of these models assume that the volumes of the steam and heat penetrated zones are the same. This assumption is incorrect in general. Furthermore, the available models are quite complex to use because of the difficulties in obtaining data for their required variables. In this study, new prediction models for calculating the steamed and heated zone volumes using regression analysis methods based on group method of data handling (GMDH) parametric and nonparametric algorithms are presented. The models are based on published experimental data. The GMDH algorithms considered to develop the new predictive models are full polynomials (FP) and polynomial neural networks (PNN). The new proposed and the existing models were evaluated and compared using rigorous statistical tools. The results show that both the FP- and PNN-based GMDH models have a better prediction performance compared to the existing models. In addition, the results show that the FP-based predictive model provides a better match with experimental data for the volume of heated zone than does the PNN-based predictive model. On the other hand, the PNN-based predictive model provides better match with the experimental data for the volume of steamed zone than the FP-based model. All these results suggest that the predictive methods based on the GMDH algorithms could be useful tools for determining the recoverable oil and analysis of thermal performance of a steam drive process.

Keywords Steam flooding · Polynomial neural networks · Full polynomials · Enhanced oil recovery · Predictive model

S.A. Musa (✉) · M. Awang
Geosciences and Petroleum Engineering Department,
Universiti Teknologi PETRONAS, Teronoh, Malaysia
e-mail: samiabc@yahoo.com

1 Introduction

Steam injection is one of the most significant enhanced oil recovery processes; its success depends on thorough analysis, design, and evaluation. Having the knowledge of the expected steamed zone is indispensable to determining the total volume of displaced oil during hot water and steam injection process. Several predictive models for calculating the volume of heat or steam zone are available. They include the following: Marx and Langenheim [1], Willman [2], Boberg and Lantz Method [3], Mandl and Volek Method [4], Farouq Ali [5], Neuman [6], Myhill and Stegemier [7], and Jones [8]. These models assume that when the steam has been injected in the reservoir, the steamed zone is the same as the heated zone volume or radius (i.e., they have same penetration through the reservoir). However, this assumption is generally not the case in reality.

Hosseini et al. [9] shows that the distance travelled by hot water saturation front is not the same as the distance travelled by the temperature front. They developed analytical model to obtain the heat zone radius from the radius of the hot water saturation zone. Baker [10] conducted an experimental study of heat flow in steam flooding with steam displacing water in a plane radial fluid flow model; he compared his results from the experiments of hot water flooding with several theoretical results, which showed a rather poor agreement. In our previous work [11], we developed a predictive model for determine the volume of steamed zone (V_{st}) and the volume of heated zone (V_h) using Barker [10] experimental data by applying the alternating conditional expectation (ACE) algorithm technique. The ACE predictive model for determining V_{st} and V_h shows better matching than pervious predictive models when it was compared to the experimental data.

As we mentioned above, several models have been proposed to calculate the steamed and heated zone volume or radius, these models required parameters for each model which are measured directly, and some of them are calculated from analytical models; hence, using of such models can lead to complex calculation of estimate of the (V_{st}) and (V_h). In our previous developed model (Sami et al. [11]), the required parameters are as following:

- Heat in steam zone H_s : calculated from analytical models
- Heat in hot water zone H_w : calculated from analytical models
- Heat lost to overburden and substratum H_L : calculated from analytical models
- Injected heat H_I : identified directly
- Steam injection rate Q_{inj} : identified directly
- Time t : identified directly

In this study, we will use the same required variables mentioned above to determine the V_{st} and the V_h .

Our work here is basically on using regression analysis algorithms to predict V_{st} and V_h during steam flood. Our study focuses on developing of highly accurate and efficient predictive model by using the GMDH parametric and nonparametric algorithms to predict the performances of steam flood enhanced oil recovery.

These prediction performances are extremely challenging to determine because of the complexity and accuracy of the available models.

2 Methodology

The group method of data handling (GMDH) algorithm, available in VariReg software ver. 0.10.2, is used in this study. VariReg is a software tool for general-purpose multidimensional regression modeling with the main emphasis on methods used in meta-modeling/surrogate modeling. This software tool provides means for creating full polynomial regression models and polynomial neural networks (PNN), for example, which were induced by GMDH [12].

The regression analysis algorithms based on GMDH modeling approach have been used for modeling and classification in a number of fields including water forecasting, medical diagnosis, create evaluation marketing, multivariate time series forecasting of energy consumption, vibration monitoring, soil and agriculture, spectrum analysis, evaluation of speed coders, electrical load forecasting and petroleum, and gas industry [13]. Examples of application of GMDH modeling approach in petroleum include Osman and Abdel-Aal [13] who developed two models for predicting oil pressure–volume–temperature (PVT) properties and also Semenov et al. [14] who have developed prediction model obtained rock porosity at deferent input GMDH parameter. Thus, motivated by application of GMDH modeling approach in petroleum industry, we proposed this approach to develop models to predict for V_{st} and V_h values.

The GMDH consist both parametric and nonparametric algorithms; in this paper, we applied the full polynomial regression models as parametric algorithm and PNN as nonparametric algorithms. More description of theoretical features of the two kinds of algorithms is discussed in reference [12].

3 Result and Discussion

Parametric and nonparametric algorithms are used to predict the V_{st} and V_h by using the experimental data published by Barker [10] for steam injection process. The full polynomials (FP) and PNN algorithms of GHMD which is implemented in VariReg software were used [12].

The multiple independent variables $(H_I, H_L, H_s, H_w, Q_{inj}, t)$ were prepared according to the procedure used by VariReg software manual. The data was recorded and inserted to the software. Following this, the testing data samples were divided with 25 % for the training data, the values of the complexity penalization criteria AICC are selected for model evaluation, and second degree of polynomial was adopted for all prediction models. Moreover, we selected 20 neurons as maximum number for each layer when implementing the PNN algorithms.

On the training data set analysis of V_{st} and V_h , we found that there is a significant positive correlation between predicted and experimental values, as shown in Figs. 1 and 2.

According to training data set analysis and after trying many selection options provided by VariReg software, the following new developed models are created to calculate heated and steamed zone volumes:

Equation developed using GMDH—FP for V_h calculation:

$$\begin{aligned}
 V_{h_FP} = & 511.819 + 5.098 t + 653.091 H_s \\
 & + 131.425 H_w - 28.215 H_L + 32.521 H_I \\
 & - 717.418 Q_{inj}
 \end{aligned} \tag{1}$$

Equation developed using GMDH—PNN for V_h calculation:

$$\begin{aligned}
 V_{h_PNN} = & -9519.747 + 19.938 t - 0.2549 t^2 \\
 & - (334.752 + 3.042 t) H_I - 9.217 H_I^2 \\
 & + (91159.348 + 235.943 t + 915.283 H_I) Q_{inj} \\
 & - 145111.005 Q_{inj}^2
 \end{aligned} \tag{2}$$

Fig. 1 GMDH—FP for V_h training; GMDH—PNN for V_h training

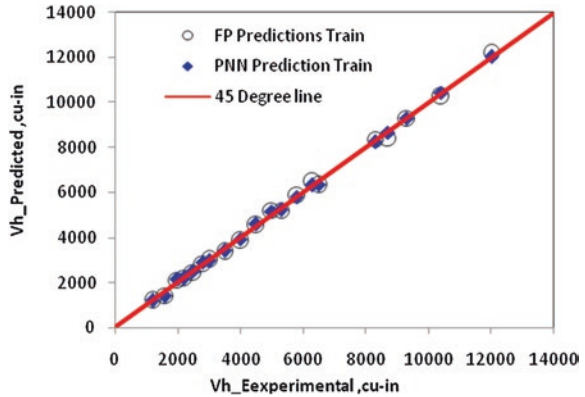
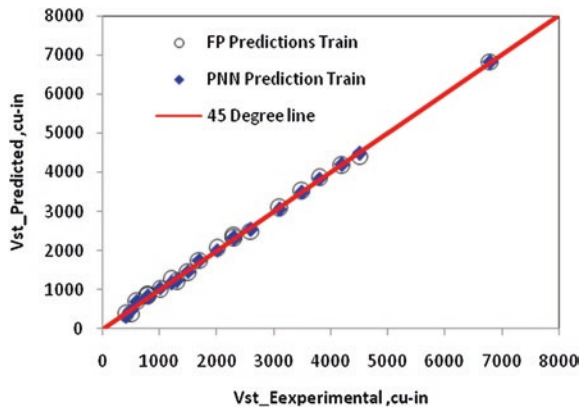


Fig. 2 GMDH—FP for V_{st} training; GMDH—PNN for V_{st} training



Equation developed using GMDH—FP for V_{st} calculation:

$$\begin{aligned}
 V_{st_FP} = & 120.271 - 7.182 t + 426.878 H_s \\
 & + 60.613 H_w + 90.463 H_L \\
 & - 27.570 H_I - 436.651 Q_{inj}
 \end{aligned}
 \tag{3}$$

Equation developed using GMDH—PNN for V_{st} calculation:

$$\begin{aligned}
 V_{st_PNN} = & -663.019 + 11.228 t + 0.083 t^2 \\
 & - (307.668 - 0.376 t) H_L - 2.439 H_L^2 \\
 & + (4983.973 + 98.212 t + 813.989 H_L) Q_{inj} \\
 & - 6678.166 Q_{inj}^2
 \end{aligned}
 \tag{4}$$

The new developed predictive models (1)–(4) are evaluated and compared to experimental data set. Figures 3 and 4 show the testing of the developed models, with satisfactory results.

Fig. 3 GMDH—FP for V_h testing: GMDH—PNN for V_h testing

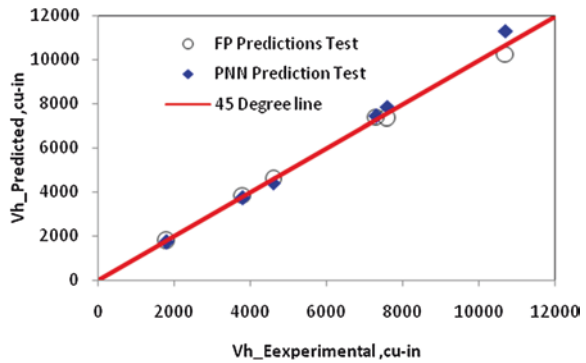


Fig. 4 GMDH—FP for V_{st} testing: GMDH—PNN for V_{st} testing

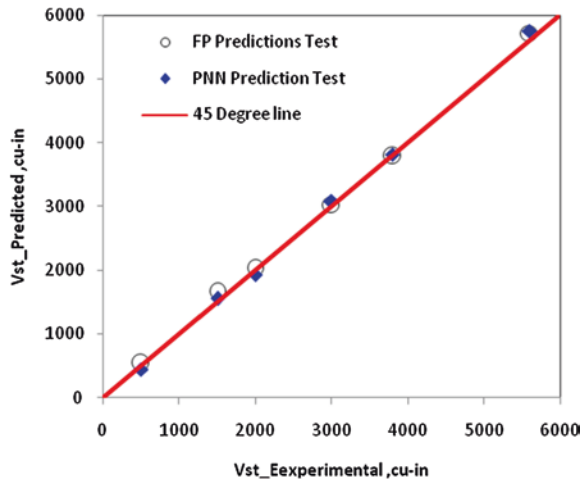


Fig. 5 Comparison of correlation V_h prediction using GMDH—FP and PNN, ACE model, and Marx Langenheim model with experimental data

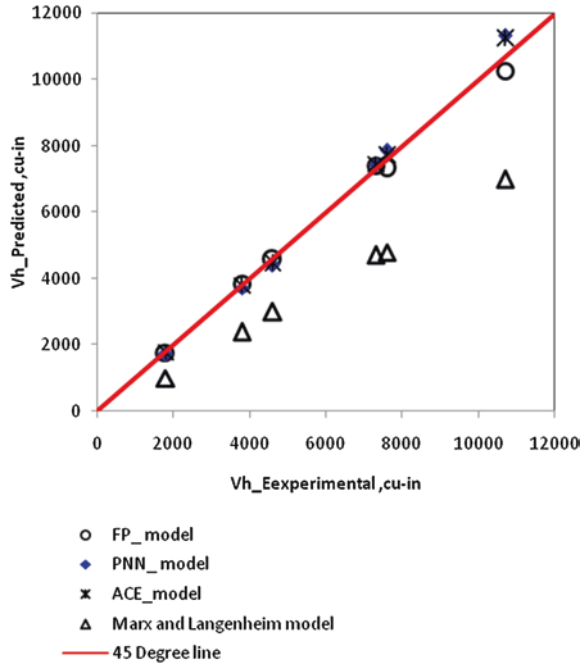


Fig. 6 Comparison of correlation V_{st} prediction using GMDH—FP and PNN, ACE model, and Marx Langenheim model with experimental data

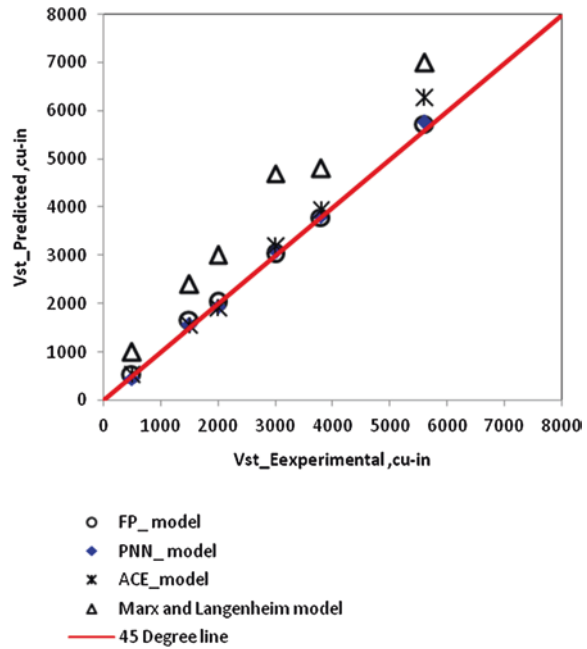


Table 1 General results of model predicted from GMDH—FP and PNN

Prediction model for	Applied method	Total input variable(X_i)	Used input variable(X_i)	$f(X_i)$	Test data		
					MSE	RRMSE	R^2
V_h	FP	6	6	$t, H_s, H_w, H_L, H_1, Q_{inj}$	46,595	0.074	0.994
V_h	PNN	6	3	t, H_1, Q_{inj}	87,699	0.101	0.989
V_{st}	FP	6	6	$t, H_s, H_w, H_L, H_1, Q_{inj}$	7,827	0.053	0.997
V_{st}	PNN	6	3	t, H_L, Q_{inj}	6,653	0.049	0.997

In this paper, the calculated values of V_{st} and V_h from the models developed using the GMDH algorithm, ACE algorithm, and available theoretical model are compared with experimental data. Figures 5 and 6 shows the compared results of the FP, PNN, ACE, and Marx and Langenheim prediction models. Prediction model performance of the FP and PNN shows better result than the Marx and Langenheim model compared to experimental data as observed in Figs. 5 and 6. Table 1 shows the comparison study parameters of the developed GMDH prediction models and also shows the statistical analysis performance for the developed GMDH prediction models. From Table 1, it can be said that based on the statistical measures (MSE, RRMSE, R^2), the FP prediction model for V_h is better than PNN prediction model. Besides, it can be said that PNN prediction model for V_{st} is better than FP prediction model.

4 Conclusions

In this paper, the volumes of the steamed and heated zones during steam injection process prediction models are developed and compared. The model formulations are developed according the GMDH algorithms, and a statistical error analysis is given to compare their prediction performances. The FP prediction model for V_h has the better match with experimental data than PNN prediction model, and the PNN prediction model for V_{st} is better than FP Prediction model. The results of this research support the idea that steamed and heated zone volumes or penetrations are not same; however, the pervious available models assumed they are same. GMDH (FP, PNN) developed models will be useful tools for determine the recoverable oil, analysis of thermal performance of steam drive process, and as accurate prediction model to validate the numerical simulation of steam injection process.

Acknowledgments The authors would like to thank Universiti Teknologi PETRONAS and the EOR Center Universiti Teknologi PETRONAS for their help and support.

References

1. Marx and Langenheim, "Reservoir Heating by Hot Fluid Injection," SPE 1266, 1959.
2. Willman, "Laboratory Studies of Oil Recovery by Steam Injection," SPE1537, 1961.
3. Boberg and Lantz, "Calculation of the Production Rate of a Thermally Stimulated Well," SPE 1578, 1966.
4. Mandl and Volek, "Heat and Mass Transport in Steam-Drive Processes," SPE 2049, 1969.
5. Faroug Ali et al, "Oil recovery by steam injection," Bradford PA: Producers Publication Co. Inc, 1970
6. C. H. Neuman, "A mathematical Model of the steam drive process--Derivation, SPE5495, 1975.
7. Myhill and Stegemeier, "Steam-Drive Correlation and Prediction," SPE 5572, 1978.
8. Jones, "Steam Drive Model for Hand-Held Programmable Calculators," SPE 8882, 1981.
9. Hosseini et al, "A new Analytical Approach to Investigate Heated Area in Thermal Recovery, CSUG/ SPE148836, 2011.
10. Baker, "An Experimental Study of Heat Flow in Steam Flooding.SPE2208, 1962.
11. Sami A.Musa Mariyamni Awang and Noaman El-Khatib, "Prediction of Heated and Steamed Zone Volume during Steam flood Using Alternating Conditional Expectation Algorithm," ICIPEG, Paper No.1569576011, 2012.
12. G. Jekabsons, "VariReg ver. 0.10.2. A software tool for performing regression modeling using various modeling method," 2010.
13. Osman, Abdel-Aal "Abductive Networks : A New Modeling Tool for the Oil and Gas Industry," SPE77882, 2002.
14. A.A. Semenov, et al "Application of Group Method Of Data Handling For Geological Modeling of Vankor Field," SPE128517, 2010.

Part II

Enhanced Oil Recovery

The Effect of Water Salinity and Reservoir Temperature on Silica Dissolution During ASP Flood: Static Model

F.A. Ahmed and A.K. Elraies

Abstract Silica scaling has been studied by many researchers in the last four decades, in order to identify the roots of the silica scaling problem, understand the process of scale formation, and find the possible ways to inhibit the scaling from occurrence. Silicate scaling occurs inside the production tubing, progressive cavity pumps and other surface equipment, causing continual work-overs, which increases the cost and non-productive time to the operator. Silicate scale is a multi-step process which involves silica dissolution, polymerization, and precipitation with other ions, and multiple factors including pH, temperature, and magnesium concentration affect the scaling tendency and the severity of the problem. This paper describes the results obtained from scanning electron microscopy (SEM), spectrophotometer DR/2800, and X-ray diffraction (XRD) techniques that addresses the impact of brine salinity and temperature on silica dissolution. Based on the results, the silica dissolution increased slightly with the salinity increase; 6.2 mg/L of silica has been dissolved in 20,000 ppm brine, while 60,000 ppm brine has dissolved 15.5 mg/L. Increase in temperature has a significant influence on silica dissolution. The 60,000 ppm brine solution dissolved 15.5 mg/L of silica at 25 °C, while the same solution dissolved 67.8 mg/L of silica when the temperature was elevated to 80 °C. It was also observed that by adding 250 ppm of Mg^{2+} and Ca^{2+} each to the 40,000 ppm brine solution, the silica dissolution increased from 8.3 to 19.1 mg/L.

Keywords Silica dissolution • Silicate scale

F.A. Ahmed (✉) · A.K. Elraies (✉)
Faculty of Geoscience and Petroleum Engineering, Petroleum Engineering Department,
Universiti Teknologi PETRONAS, Seri Iskandar, Malaysia
e-mail: ahmed9fatah@gmail.com

A.K. Elraies
e-mail: khaled.elraies@petronas.com.my

1 Introduction

Silica is a general term, which refers to silicon dioxide in all of its crystalline, amorphous, and hydrated or hydroxylated forms. It commonly implies that the silicon content is given in terms of weight of silicon dioxide (SiO_2) [1]. The common and simplest phase found in nature of silica is quartz, which is the main constituent of common sand [2, 3]. Many parts of the world including the western United States, Hawaii, Puerto Rico, Mexico, and the Middle East and Southeast Asia have reported silicate scaling issues as one of the most severe problems that occur due to silica/water interactions mainly during alkaline surfactant polymer (ASP) flood.

Quartz is the most thermodynamically stable phase of silica [4]. The potential for silica scaling exists when the concentration of the dissolved silica exceeds the solubility limit at given temperature and pH [1] that results in the precipitation and deposition of amorphous silica, which once formed is very difficult and costly to be removed [5]. The solubility of silica is dependent on many factors such as pH, temperature, particle size, particle hydration, and the presence of other ions such as iron and aluminum [4].

Divalent minerals such as magnesium lead to form magnesium silicate scale; magnesium can bridge the colloidal silicate particles and form an amorphous magnesium silicate scale [6]. In the field applications, the silica scaling can be found inside the production tubes, which leads to down-hole pumps failure, operational problems as well as a defect in pipeline systems [7]. Moreover, silicate scale results in serious formation damage by reducing the porosity and the permeability of the formation [8]. Many studies indicated that the observed change in permeability with temperature is associated with silica/water interactions [9–11].

Numerous excellent researchers were declared that silica scale formation is a highly complex process, which involves silica dissolution, polymerization, and precipitation with other multivalent ions [4, 5, 12–14]. The mechanism of silicate scale formation is very complex and poorly understood process that likely forms in the following stages [15]:

1. Silica dissolution: The alkaline creates high pH at the reservoir and around the wellbore; the high-pH water dissolves quartz in the formation which results in monomeric silica ($\text{Si}(\text{OH})_3\text{O}^- \text{Na}^+$).
2. Silica polymerization: As high-pH water mixed with the neutral-pH connate water near the wellbore, the dissolved silica begins to polymerize and form colloidal silica as the pH is partially neutralized.
3. Silica scale formation: This stage occurs due to the presence of magnesium in the solution. The remaining magnesium after water softening would precipitate and interact with the neutral-pH water, which causes the magnesium silicate scale.
4. Coprecipitation of silicate scale by other minerals: Calcium carbonate scale can occur if the calcium is introduced to the high-pH water, and it provides nuclei for the development of silicate scale [4].

2 Experimental Methodology

The amount of soluble silica dissolved from quartz was determined by using the silicomolybdate method with chemical reagent packets [14]. Series of static experiments were conducted to investigate the effect of brine salinity, brine composition, and temperature on silica dissolution based on the above method by using spectrophotometer DR/2800, X-ray diffraction (XRD), and scanning electron microscopy (SEM/EDX).

Silica powder, crush (Berea sandstone) core, and slide core samples were used to conduct the experiments; 15 ml was used to saturate each gram of silica powder, and 5 ml was used for each gram of crush and slide core samples. After saturation, the samples were kept for 3–5 days until equilibrium is achieved and then, the silica dissolution was measured using DR/2800. For the slide core samples, the samples were examined by SEM/EDX before and after saturation to confirm the silica dissolution into the brine solutions.

3 Results and Discussion

3.1 Basic Core Identification

The main components present in the core sample were measured by using XRD and scanning electron microscopy (SEM). The basic core mineralogy obtained by XRD is demonstrated in Fig. 1, which shows that quartz is the main dominant component of the core sample. The results obtained from SEM for multiple

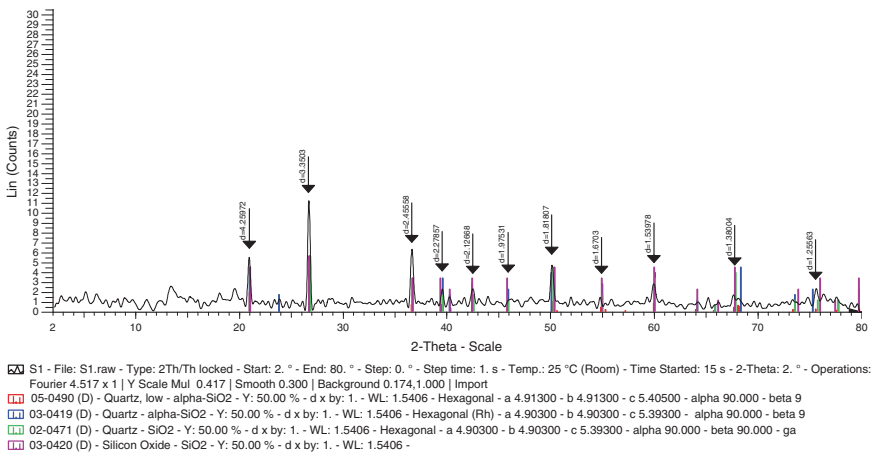


Fig. 1 Core composition obtained from XRD

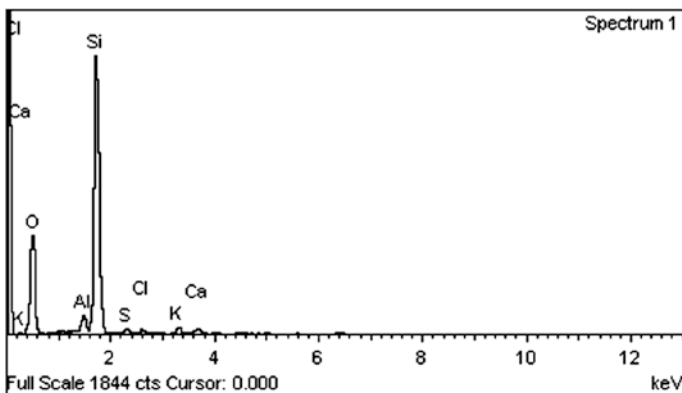


Fig. 2 Sample 1: main core components obtained from SEX/EDX

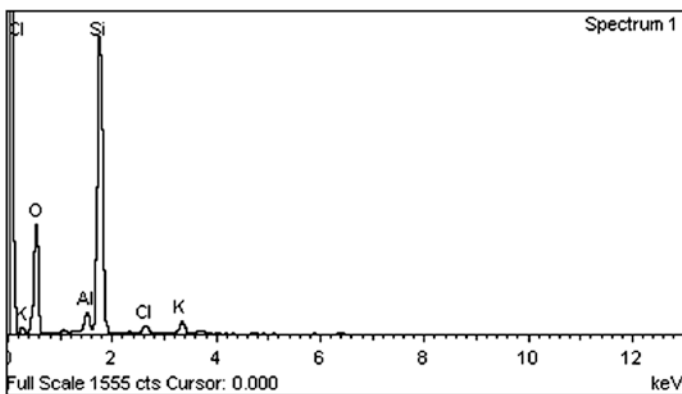


Fig. 3 Sample 2: main core components obtained from SEX/EDX

Table 1 Sample 1: basic core component concentration obtained from SEM/EDX

Component	Concentration %	Component	Concentration %
SiO ₂	96.31	CaO	0.43
Al ₂ O ₃	1.50	K ₂ O	0.65
FeS ₂	0.61	Fe ₂ O ₃	0.49

slide core samples confirmed the presence of the quartz as the highest component. Figures 2 and 3 show the X-ray spectrum for two samples. However, additional minerals such as aluminum oxide (Al₂O₃) and pyrite (FeS₂) were present but with lower concentrations compared with the quartz. Tables 1 and 2 show the concentration of each component as obtained from SEM/EDX where silica concentration corresponds to 96.31 and 96.33 % for samples 1 and 2, respectively.

Table 2 Sample 2: basic core component concentration obtained from SEM/EDX

Component	Concentration %	Component	Concentration %
SiO ₂	96.33	KCl	0.83
Al ₂ O ₃	1.44	K ₂ O	1.40

3.2 Brine Salinity and Temperature Test

Distilled water and three samples of synthetic soft brine with salinities ranged between 20,000 and 60,000 ppm were studied; the test was conducted at three different temperatures (25, 50, and 80 °C). To establish consistency of the results with literature ones, both silica powder and sandstone core samples were employed to measure the silica dissolution at different temperatures. Sodium chloride (NaCl) was used to prepare the brine solution without introducing any hard minerals at this stage.

Based on the findings, silica powder has high silica dissolution comparing with the sandstone core samples due to the absence of crystalline structure in the powder, as it dissolves as an amorphous silica. At constant temperature and pH, the silica powder can define the solubility limit of amorphous silica which is above 100 mg/L. However, at the same conditions, the crush and slide core samples have much lower silica dissolution due to the thermodynamic stability of quartz grains; the results are tabulated in Table 3 and illustrated graphically in Fig. 4. Crush core samples have a relatively higher dissolution than the slide core samples due to the size of the grain particles [16]. This indicates that the small silica particles are more soluble.

Silica dissolution increases with salinity increase, and this is due to the effect of degree of hydration factor. When the crystalline quartz grains contacted with the water, they contain this water inside the crystals, which is known as the water of hydration. When the silica starts to polymerize, the crystals can still contain the water and they can lose it stepwise. The amount of this water decreases with the increasing of salt contents such as Na⁺, Mg²⁺, and Ca²⁺, meaning that the high hydrated particles have low silica solubility which have the low salt contents as agreed by literature [16].

Reservoir temperature has an obvious effect on silica dissolution: as the temperature elevates, the silica dissolution increases, and the cause is the massive

Table 3 Silica dissolution obtained from salinity test at ambient temperature

Silica dissolution, mg/L				
Brine salinity, ppm	pH value	Silica powder	Crush core	Slide core
0	7	121.6	4.5	3.7
20,000	7.8	135.2	6.2	4.2
40,000	8	140.7	8.3	6.1
60,000	8.3	159.6	15.5	6.4

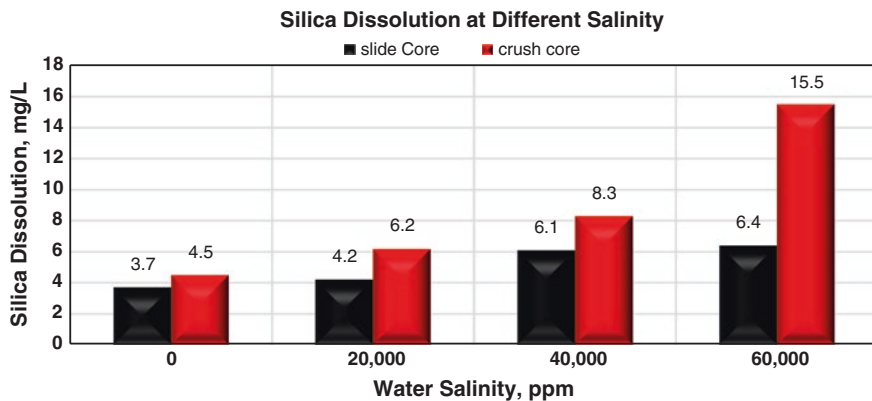


Fig. 4 Water salinity effect on silica dissolution from slide and crush core samples

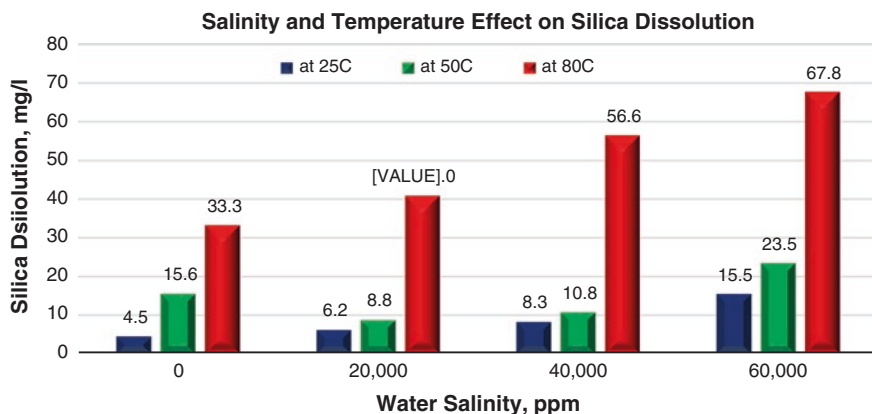


Fig. 5 Water salinity effect on silica dissolution at different temperatures

generation of silicate ions in addition to the monomer which is in equilibrium with the solid phase [16]. Crush core samples were used during this test, and the illustrated results in Fig. 5 show that the 60,000 ppm brine solution dissolved 15.5 mg/L of silica at 25 °C, while the same solution dissolved 67.8 mg/L of silica when the temperature was elevated to 80 °C.

3.3 Brine Composition Test

The effect of hard minerals on silica dissolution was investigated during this test. By adding 50, 150, and 250 ppm of Mg²⁺ and Ca²⁺ ions each to the 40,000 ppm

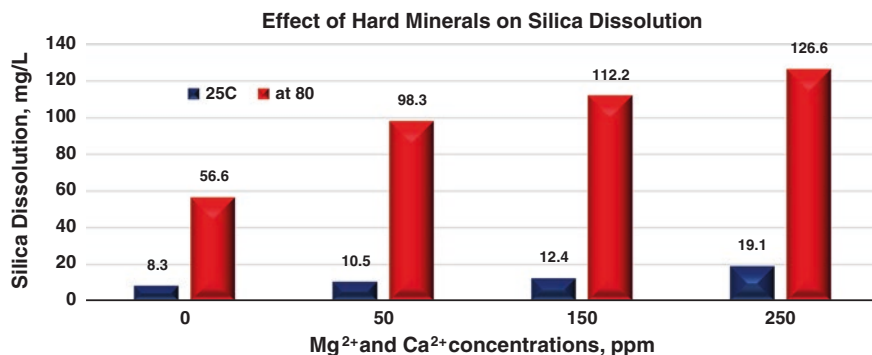


Fig. 6 The effect of Mg²⁺ and Ca²⁺ ions on silica dissolution

synthetic brine solution, the silica dissolution increased from 6.6 mg/L to (10.5, 12.4, and 19.1 mg/L), respectively, at 25 °C. At higher temperature of 80 °C, more silica has been dissolved as shown in Fig. 6.

Introducing Mg²⁺ and Ca²⁺ ions into the solution increases the potential for silica scaling by generating more ions of soluble silica. These hard minerals will lead to deplete the silicic acid, thus dissolving additional silica [13]. These results agreed with the literature which indicated that magnesium can bridge the colloidal silicate particles and form an amorphous magnesium silicate scale [17].

3.4 SEM/EDX Experiment

SEM/EDX was employed to further confirm and provide supporting evidence of the silica solubility measurements obtained from the crush core samples. Four slide core samples were placed under SEM/EDX before and after saturation. The samples were saturated into different brine salinities, based on the results obtained; dissolution of silica into the solution did occur due to silica/water interaction. Silica dissolution ratio (SDR) was calculated, and it is observed that this ratio is increasing with the increase in salinity. The results obtained from energy dispersive X-ray analysis (EDX) spectrum are shown in Table 4.

Table 4 Effect of brine salinity on silica dissolution ratio

Sample ID	Brine salinity, ppm	Silica concentration before saturation, %	Silica concentration after saturation, %	SDR, %
A-F 1	0	96.29	95.80	0.51
A-F 2	20,000	95.39	92.32	3.22
A-F 3	40,000	97.96	93.03	4.75
A-F 4	60,000	96.31	89.26	7.32

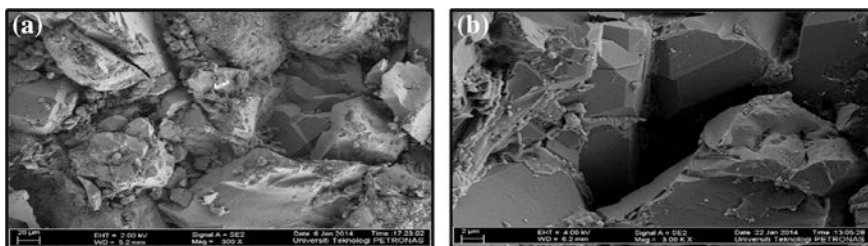


Fig. 7 a Original core sample before saturation. b Core sample after saturation

Figure 7a, b are typical SEM photographs that were obtained from the core sample that has been saturated with 60,000 ppm brine solution at 25 °C. Dissolution of silica into the solution did occur due to silica/water interaction; silica film around the quartz grains which appeared in Fig. 7a was removed, and the grains have a clean surface as appeared in Fig. 7b.

4 Conclusion

The results presented in this paper indicate that the water salinity, composition, and reservoir temperature have a significant effect on silica dissolution. Silica dissolution increased three times its original value when water salinity increased from 20,000 to 60,000 ppm. When 250 ppm of Mg^{2+} and Ca^{2+} ions has been presented into the 40,000 ppm brine solution, silica dissolution increased from 6.3 to 19.3 mg/L. Additionally, elevation of temperature from 25 to 80 °C has increased the silica dissolution dramatically. Lastly, SEM/EDX results have confirmed that the silica dissolution is affected by brine salinity and composition with 7.32 % reduction in silica contents with 60,000 ppm brine.

Acknowledgments The authors would like to thank the MOR-EOR at Universiti Teknologi PETRONAS for supporting this work. This research work was fully sponsored by Y-UTP grant no 0153AA-A69.

References

1. I. Bremere, M. Kennedy, S. Mhyio, A. Jaljuli, G. Witkamp, and J. Schippers, "Prevention of silica scale in membrane systems : removal of monomer and polymer silica," ELSEVIER, vol. 132, no. October, pp. 89–100, 2000.
2. R. K. Iler, *The Occurrence, Dissolution, and Deposition of Silica*. 1979.
3. J. Eikenberg, ON THE PROBLEM OF SILICA SOLUBILITY AT HIGH pH, no. July 1990. 1990.
4. J. S. Gill, "SILICA SCALE CONTROL," NACE, no. 226, 1998.
5. Z. Amjad, J. F. Zibrida, and R. W. Zuhl, "A New Antifoulant for Controlling Silica Fouling in Reverse Osmosis Systems *," vol. 16, no. 2, 2007.

6. J. Arensdorf, S. Kerr, K. Miner, and T. Ellis-toddington, "Mitigating Silicate Scale in Production Wells in an Oilfield in Alberta," SPE, 2011.
7. I. Gunnarsson and S. Arnórsson, "Silica scaling : The main obstacle in efficient use of high-temperature geothermal fluids," pp. 30–36, 2003.
8. W. Yupu, L. Junde, L. Bing, L. Yingping, W. Hongxing, and C. Gang, "Why Does Scale Form in ASP Flood? How to Prevent from It?—A Case Study of the Technology and Application of Scaling Mechanism and Inhibition in ASP Flood Pilot Area of N-1DX Block in Daqing," Proceedings of SPE International Symposium on Oilfield Scale, pp. 1–6, May 2004.
9. K. S. Udell and J. D. Lofy, "Permeability Reduction of Unconsolidated Media Caused by Stress-Induced Silica Dissolution," SPE, no. March, 1989.
10. R. M. Weinbrandt, H. J. R. Jr, and F. J. Casse, "The Effect of Temperature on Relative and Absolute Permeability of Sandstones," SPE, 1975.
11. W. E. Dibble Jr and J. M. Potter, "Porosity Reduction in Sandstone," SPE-AIME, 1983.
12. Z. Amjad and R. W. Zuhl, "AN EVALUATION OF SILICA SCALE CONTROL ADDITIVES," NACE, no. 08368, pp. 1–12, 2008.
13. A. E. A. Basbar, K. A. Elraies, and R. E. Osgouei, "SPE 164669 Formation Silicate Scale Inhibition during Alkaline Flooding : Static Model," SPE, vol. 4, 2013.
14. J. G. Southwick, "Solubility of Silica in Alkaline Solutions: Implications for Alkaline Flooding," SPE, 1985.
15. J. Arensdorf, D. Hoster, D. Mcdougall, and M. Yuan, "Static and Dynamic Testing of Silicate Scale Inhibitors," SPE, no. June, pp. 8–10, 2010.
16. J. S. Gill, "SILICA SCALE CONTROL," corrosion98, no. 226, 1988.
17. J. Arensdorf, S. Kerr, and K. Miner, "SPE 141422 Mitigating Silicate Scale in Production Wells in an Oilfield in Alberta," SPE, 2011.

Simulation Study of the Effect of Smart Water on Relative Permeability During WAG-CO₂ Injection for Light Oil Reservoir

Pui Mun Yip and Ali F. Alta'ee

Abstract Water alternating gas (WAG) injection with its first successful field pilot application on the North Pembina field in Alberta, Canada, in 1957, is one of the most prominent EOR methods that substantially prolong the lives of the otherwise depleted and uneconomical oil fields. This technique is well established, but the practical challenges are often of the occurrence of viscous fingering, gravity segregation, and gas channeling or override, and consequently lower oil recovery rates. Previous researches have focused almost exclusively on modifying the salinity and the ionic composition of the injected water, also termed as smart waterflooding which proved to further enhance the oil recovery obtained from waterflooding. However, obscurity exists on whether the deployment of smart water during WAG-CO₂ injection will be successful. This paper addresses the impacts of the implementation of a technique which combines smart waterflooding and WAG-CO₂ injection on the oil/water relative permeability curves for a light oil reservoir. An analysis on the two-phase relative permeability functions is essential as to predict the effectiveness of the displacement process or the performance of smart water injection applied during WAG-CO₂ injection. CMG STARS was used to simulate the effects of fine-tuning the salinity as well as varying the composition of Ca²⁺ and Mg²⁺ ions in brine on the oil recovery factor. The optimum brine salinity for maximum oil recovery was also determined. The slight shifting of the relative permeability curves to the right which can be observed proves the capability of the smart water to modify the rock wettability toward a more water-wet system. Yet the findings from the simulation study suggest that the use of smart waterflooding is not ideal or has low potential in increasing the oil recovery during WAG-CO₂ injection.

Keywords Smart water · WAG-CO₂ · Light oil reservoir

P.M. Yip · A.F. Alta'ee (✉)
Universiti Teknologi PETRONAS, Tronoh, Perak, Malaysia
e-mail: ali_mangi@petronas.com.my

1 Introduction

WAG injection is a combination of the two conventional secondary recovery techniques, waterflooding, and gas injection. It is a conventional EOR process in which slugs of water and gas are injected alternately to sweep the residual oil not recovered by the primary and the secondary phases of production [6]. The CO₂ gas works to reduce the viscosity of oil, cause oil swelling, and increase the relative permeability so the trapped oil is mobilized and can flow more easily through the rock. Due to the low gas density, the unfavorable high mobility ratio leads to poor sweep efficiencies. Thus, after a period of time, the injection switches to water to improve the macroscopic sweep efficiency and these alternate CO₂ gas and water injection repeat until the oil production drops below a profitable level.

1.1 Problems Associated with the WAG Process

The ultimate recovery from WAG is relatively low with about incremental recovery of 5–10 % [6]. Christensen et al. [6] presented a comprehensive literature of the WAG processes in about 59 fields and commented on several severe problems which caused the decrease in displacement efficiency when performing WAG-CO₂ injection. The major problems of WAG injection are the water and gas breakthrough and decrease in injectivity [6, 7] due to challenges such as viscous instabilities/fingering, gravity segregation, gas override, and gas channeling through high permeability streaks/thief zone.

1.2 Smart Waterflooding

For over 100 years, waterflooding has been widely implemented to accomplish the dual objectives of reservoir pressure maintenance as well as a water drive to displace oil from the injector wells to the producer wells. In the 1990s, the idea of the influences of brine composition on the oil recovery as introduced in the papers published by Jadhunandan and Morrow [10] and Yildiz and Morrow [27] began to shift the industry's focus to adjusting the ion composition and salinity of the injected fluid. This chemically altered water is termed as "smart water". Since then, there have been numerous researches done to advance the concept of smart waterflooding and to demonstrate the tremendous potential of this technology.

There is an increasing evidence from the laboratory that reduction in the concentration of salinity leads to higher oil recovery factor than conventional waterflooding in sandstone reservoirs [24] and in carbonate reservoirs [28]. Research done by Tang and Morrow [25] indicated an improvement in the oil recovery efficiency when the salinity of the injection brine was reduced from 15,000 to 1,500 ppm. Apart from corefloods, several field single-well tests and field trials

demonstrated the potential of low-salinity waterflooding to improve oil recovery [15, 18, 23]. Webb et al. [26] reported a decrease in the residual oil saturation, S_{or} as the salinity of the injection brine is varied from 100 to 20 % and finally 5 % of the salinity formation water. The low salinity effect is believed to significantly impact the ultimate oil recovery as a result of different mechanisms acting together. Although there is still no consistent mechanistic explanation of the low-salinity waterflooding phenomenon in sandstone reservoirs, the possible mechanisms which have been proposed up to now are migration of fines [20], pH increase [18], and the multi-ions exchange (MIE) between the clay mineral surfaces and the injected brine [14] triggered by the expansion of the electrical double layer [16].

1.3 Smart Water Applications in WAG

To the best of our knowledge, there are only two prior researches concerning the applications of smart water in WAG. Kulkarni and Rao [13] published their work on the impacts of brine composition on the tertiary oil recovery through an experimental study using 5 % NaCl brine and 0.5815 % NaCl reservoir brine during WAG. They concluded that the WAG recoveries are highly dependent on the brine composition, and the explanation for the decrease in oil recovery at lower brine salinity is because of the rise in the solubility of the gas in the brine.

Jiang et al. [12] progressed the research on the impact of salinity of the injection brine by conducting experiments using two oil models, one of which is a mixture of 50 wt% n-decane and 50 wt% n-hexadecane, and the other is a crude oil from the Cottonwood Creek. According to [12], an increase in the salinity of the injection brine is accompanied by an increase in the tertiary recovery and oil recovery factor of both model oil and crude oil. Their reasoning was similar to that of [13] which is as the salinity of the brine increases, the solubility of CO₂ gas in the brine decreases; thus, more CO₂ gas are available for the miscible flooding followed by an increase in the WAG recoveries.

1.4 Relative Permeability

The computation of relative permeability is necessary for understanding the crude–brine–rock (CBR) interactions, reservoir performance prediction, finding out the factors contributing to low productivity, and reducing formation damage [9]. The relative permeability can be generally defined as the property of the porous media which can be estimated from the ratio of the effective permeability of a fluid at a given saturation to the permeability of the fluid at 100 % saturation [1, 2]. It corresponds to the ability of the porous media to transmit one fluid when one or more fluids are present [3]. The relative permeability curves are representative of

flow characteristics through the formation in the reservoir which is affected by the mechanism by which the reservoir is depleted [21].

Relative permeability is a reservoir dynamic property that is largely affected by several factors including the pore geometry, saturation history, and wettability. The changes in the shape of the relative permeability can be justified due to the uncertainties in rock wettability, saturation history, pore geometry, and fluid distribution in the reservoir [3, 19]. From the curves of relative permeability, the wettability of the reservoir system, whether oil wet or water wet, can be determined. Most of the studies suggested that the oil recoveries from oil-wet reservoirs are generally less than from water-wet reservoirs.

2 Methodology

2.1 Synthetic Reservoir Model

The reservoir simulation model has a dimension of $11 \times 11 \times 6$ with a total of 726 grid blocks with the Norne oil field reservoir rock and fluid properties. The length, width, and height of the reservoir simulation model are 550, 550, and 60 m, respectively. The data gathered were first input using the CMG Builder to be simulated or modeled by CMG STARS [4, 8, 17]. Due to the data availability constraints and processing time considerations, only a sector model of the formation with sufficient data was simulated. However, the static model is adequate to model the effects of smart water injection during WAG- CO_2 on the relative permeability and oil recovery factor. A quarter five spot injection pattern between the injector and the producer wells was employed. The water and CO_2 injector is located at the same position to enable alternate injection of high-salinity water or smart water and CO_2 gas.

2.2 Workflow of Smart WAG- CO_2 Modeling

The simulated reservoir was first depleted and waterflooded for 6 years before WAG is applied for 9 years. The secondary recovery using waterflooding stops at beginning of the year of 1997 because of the economical limit set using the percentage of water cut of higher than 80 %. The duration of the simulation run is for 15 years from January 1, 1991, up to January 1, 2006. For optimized production, a WAG ratio of 1:1 is used.

The conventional brine was set to have water components of 35,000 ppm, whereas the smart water is of different salinities of about 1,000, 3,000, and 7,000 ppm. This is because low salinity effects take place when the injected concentration is below 25 % of the salinity of the connate water with approximate values of 1,000–7,000 ppm for the lower and upper salinity threshold as suggested in

the literature [11]. The ion components dissolved in the water are Na^+ , K^+ , Ca^{2+} , Mg^{2+} , Cl^- , HCO_3^{2-} , and SO_4^{2-} . The composition of the Na^+ cations and the Cl^- anions defines the salinities of the injection water. The total dissolved solids (TDS) in the water at different salinities are as summarized in Table 1.

Simulation runs were performed for 3 different injection scenarios comprising of conventional WAG- CO_2 injection, proposed smart water assisted WAG- CO_2 injection, and smart WAG- CO_2 injection as presented in Fig. 1.

For the base case study which is the conventional WAG- CO_2 , alternate injection of high-salinity water of 35,000 ppm and CO_2 gas was used. Then, the second injection scenario which is smart assisted WAG- CO_2 involving the alternate injection of high salinity and smart waterflooding with CO_2 gas was simulated. There are 3 simulation runs which were conducted for this smart water assisted WAG- CO_2 injection whereby 3 different salinities of smart water including 1,000, 3,000, and 7,000 ppm were deployed. The next injection scenario is the smart WAG- CO_2 injection in which smart waterflooding follows every CO_2 gas injection and also runs at 3 different salinities similar to the smart assisted WAG- CO_2 case studies.

The interactions between the crude oil and brine are sensitive to the ionic compositions. Tuning the composition of divalent ions, specifically Ca^{2+} and Mg^{2+} ions in brine during smart WAG- CO_2 injection, plays an essential role in escalating the oil recovery factor. There are 7 simulation runs conducted in order to

Table 1 The total dissolved solids (TDS) in the brine at different salinities

TDS	35,000 ppm brine/mol/L	7,000 ppm brine/mol/L	3,000 ppm brine/mol/L	1,000 ppm brine/mol/L
Na^+	0.4703	0.1117	0.0408	0.01596
K^+	0.009873	0.0008440	0.0008696	0.0001279
Ca^{2+}	0.01003	0.005240	0.0008484	0.0001248
Mg^{2+}	0.05205	0.008640	0.004526	0.0001646
Cl^-	0.5349	0.1085	0.04632	0.01551
HCO_3^{2-}	0.002409	0.007523	0.0001967	0.001082
SO_4^{2-}	0.02753	0.0002498	0.002394	0.00003123

Adapted from McGuire et al. [18]

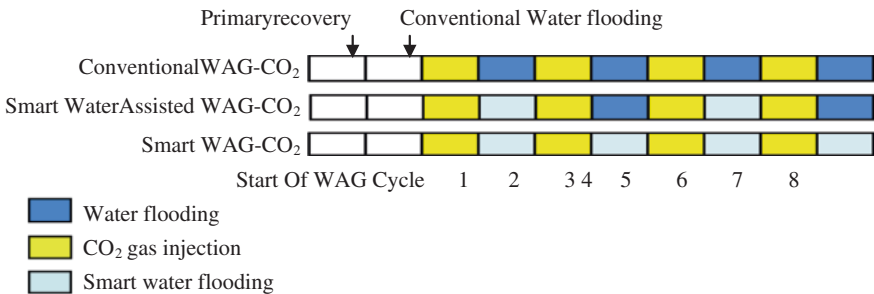


Fig. 1 Simulation design of 3 different injection scenarios

simulate the effects of the composition of these divalent cations on the oil recovery during smart WAG-CO₂ injection. The effects of the composition of Ca²⁺ and Mg²⁺ ions in brine on the oil recovery during WAG-CO₂ injection are simulated by varying the mole fractions of these divalent ions contained in the brine ranging from 0 up to 300 ppm at 50 ppm intervals.

3 Results and Discussion

3.1 The Effects of Smart Water Injection on the Relative Permeability

The effects of the smart water injection during WAG-CO₂ flooding are evident from the results of the relative permeability curves of k_{RO} and k_{RW} versus S_w as presented in Fig. 2. The relative permeability curves are shifted to the right when smart WAG-CO₂ injection with lower salinity from 35,000 ppm to 7,000 ppm is applied on the sandstone reservoir with light oil. Unlike waterflooding, the relative permeability to oil during smart WAG-CO₂ injection decreases instead of increase in relative to the relative permeability to oil during the base case conventional WAG-CO₂ injection when lower salinity brine is used. The lower relative permeability to oil implies that smart water injection during WAG-CO₂ flooding delays the oil displacement process and results in lower incremental oil recovery and higher residual oil saturation.

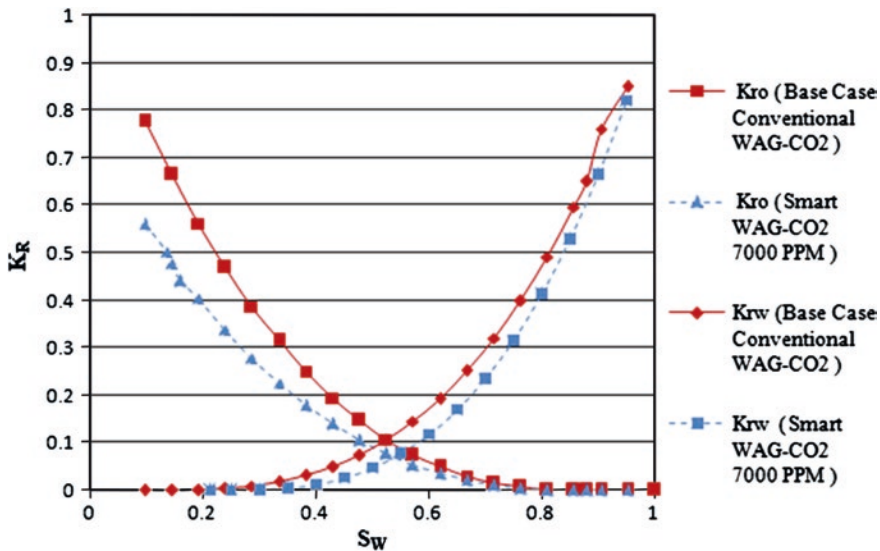


Fig. 2 Relative permeability curves of k_{RO} and k_{RW} versus S_w

At the same time, the relative permeability to water during smart WAG-CO₂ also decreases in relative to the relative permeability to water during base case conventional WAG-CO₂ injection when lower salinity brine is utilized. This is evident by the fact that solubility of CO₂ gas in brine increases with a decrease in the salinity of the brine [5] causing an increase in the viscosity of the water. Subsequently, the mobility of the water decreases and less percentage of water cut because of the reduction in the relative permeability to water during smart WAG-CO₂ injection. However, the effects of the dissolved CO₂ gas in water on the viscosity of the water are not very drastic [22] which clarifies the small reduction in the relative permeability to water as compared to the larger reduction in the relative permeability to oil during smart WAG-CO₂ injection.

The gradual shifting of the intersection point between the relative permeability to oil and to water curves to the right when lower salinity brine is used signifies the change in the wettability toward a more water-wet system induced by the smart water injection. The influence of the smart water injection on the relative permeability is related to the few smart waterflooding mechanisms including the MIE mechanism and expansion of the electrical double layer [14, 16]. The formation of a layer of multivalent cations during smart water injection increases the electrostatic repulsion and thus eases the desorption of oil components from the negatively charged clay.

3.2 The Effects of the Composition of Ca²⁺ and Mg²⁺ Ions in Brine

The results are represented as a plot of the cumulative oil produced versus Ca²⁺ and Mg²⁺ ions composition in brine as shown in Fig. 3. An increase in the composition of the Ca²⁺ and Mg²⁺ ions in the brine yields a higher oil recovery. The observed incremental recovery behavior as the concentration of Ca²⁺ and Mg²⁺

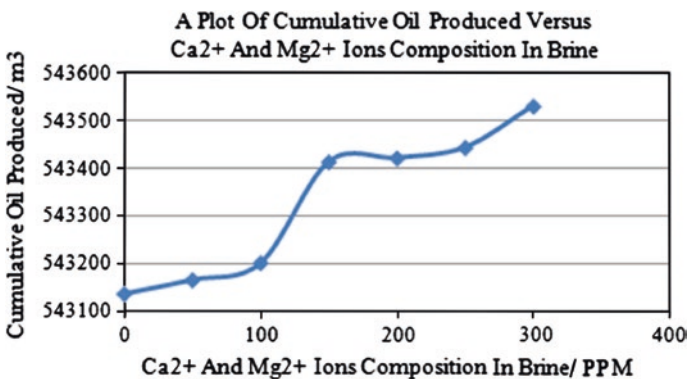


Fig. 3 A plot of cumulative oil produced versus Ca²⁺ and Mg²⁺

ions in the brine increases from 0 up to 300 ppm is ascribed to the presence of more divalent ions available for the cations exchange reaction between the clay minerals and the injected brine which further reduces the ion binding between the crude oil and rock surface. These divalent ions act as potential determining ions that are reactive and have the capability of changing the rock surface charges and thus allow the release of the negative carboxylic oil component from the rock surface. This eventually alters the rock wettability toward a more water-wet system and improves the ultimate oil recovery.

3.3 The Optimum Brine Salinity for Maximum Oil Recovery

In this simulation study, 7 different WAG-CO₂ injection schemes with the same injection rate are simulated for a sandstone reservoir with light oil. As illustrated in the Fig. 4, the injection timeline of the oil reservoir is mainly divided into 2 stages which are the secondary recovery via pre-waterflooding and the post-waterflooding or EOR. The pre-waterflooding stops early 1997 due to percentage of water cut of 81.5768 % exceeding the economic constraint of 80 %. To obtain a clearer picture of the difference in oil recovery between the 7 injection scenarios, the cumulative oil recovery plot is magnified to the comparison plots from year 2005 to 2006 as in shown in Fig. 5. The oil recoveries from waterflooding are the same for all the case studies which is 456,942 m³ or 2,874,029.81 bbl. The conventional WAG-CO₂ injection gives the highest oil recovery followed by smart

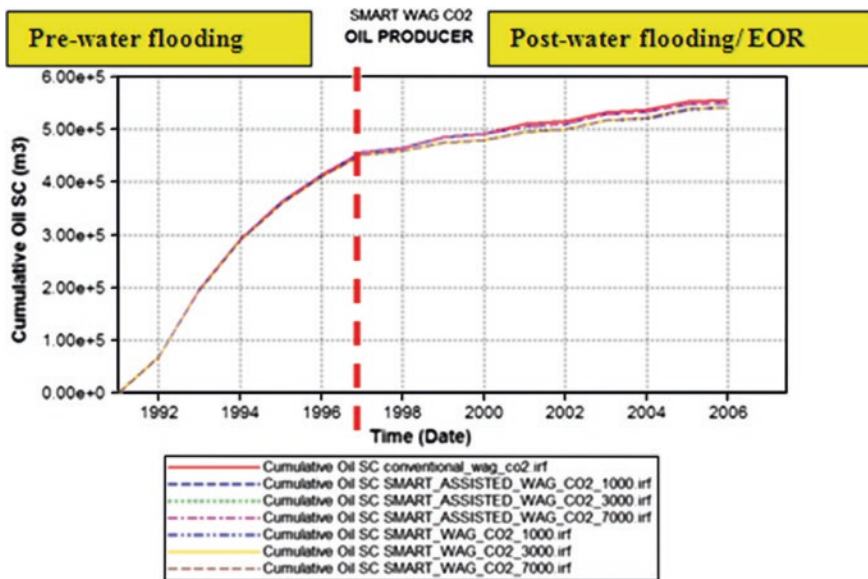


Fig. 4 A plot of cumulative oil produced for 7 different injection scenarios

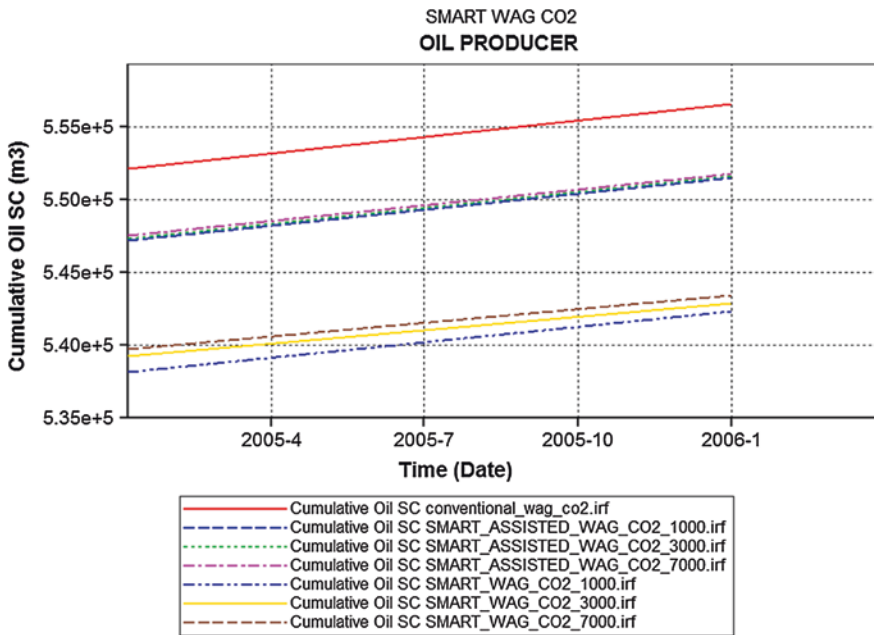


Fig. 5 Comparison of the cumulative oil produced from 2005 to 2006

assisted WAG-CO₂ using 7,000, 3,000, and 1,000 ppm and then smart WAG-CO₂ using 7,000, 3,000, and 1,000 ppm.

Although there is a no very significant difference in oil recovery in the various approaches, the correlation between salinity and oil recovery that can be observed is that as the salinity of the injected brines decreases, the oil recovery decreases. This means that the decrease in the salinity of the injection brine during WAG-CO₂ injection has adverse effects on the oil recovery. This is obviously very different from the smart water injection during secondary waterflooding whereby a decrease in the salinity contributes to a higher oil recovery [14, 24].

The proposed reason for the lower oil recovery during smart WAG-CO₂ injection is because of the decrease in solubility of CO₂ gas in oil but increase in solubility of CO₂ gas in water when the salinity of the brine decreases. The CO₂ gas solubility in water increases with pressure but decreases with a decrease in the temperature and salinity of water [5]. Thus, there is less amount of CO₂ gas available for mixing with the hydrocarbons to form a zone of miscible CO₂ and light hydrocarbons which works to reduce the viscosity of oil and cause oil swelling [12]. The increase in solubility of CO₂ gas in the smart water consequently hinders the oil displacement efficiency and reduces the ultimate oil recovery during WAG-CO₂ injection.

However, as compared to the smart WAG-CO₂ injection, the smart water assisted WAG-CO₂ injection achieves a higher oil recovery. Based on the Table 2 and Fig. 5, it is also obvious that the smart water assisted WAG-CO₂ has higher oil recovery

Table 2 Cumulative oil produced for 7 different injection scenarios

Case studies	Injection scenarios	Cumulative oil produced/m ³	Cumulative oil produced/MMbbl
1	Base case: conventional WAG-CO ₂	556 554	3.5006
2	Smart assisted WAG-CO ₂ using 7,000 PPM brine	551 745	3.4703
3	Smart assisted WAG-CO ₂ using 3,000 PPM brine	551 662	3.4698
4	Smart assisted WAG-CO ₂ using 1,000 PPM brine	551 483	3.4687
5	Smart WAG-CO ₂ using 7,000 PPM brine	543 428	3.4180
6	Smart WAG-CO ₂ using 3,000 PPM brine	542 895	3.4146
7	Smart WAG-CO ₂ using 1,000 PPM brine	542 346	3.4112

than the smart WAG-CO₂ but lower oil recovery than the conventional WAG-CO₂ injection. These occurrences may be due to the approach of alternate injection of conventional brines and smart water after each CO₂ gas injection. The first conventional brine injected after the first cycle of gas injection functions to increase the macroscopic efficiency through better gas–oil mobility control and stabilized displacement of oil. On the other hand, the smart water injection which follows the second cycle of gas injection aims to increase the microscopic sweep efficiency via altering the wettability of the reservoir rocks toward more water wet. Therefore, this combined approach makes a perfect scheme in increasing the overall sweep efficiency, yielding a lower water cut as well as higher oil recovery factor than the smart WAG-CO₂ injection. Besides that, the smart water assisted WAG-CO₂ injection may reduce the required expenses for the desalination of the brines.

All in all, the conventional WAG-CO₂ injection yields the highest oil recovery factor. Hence, the optimum brine salinity for maximum oil recovery in this simulation study is 35,000 ppm. This suggests that the potential use of smart water injection is low during WAG-CO₂.

4 Conclusions and Recommendations

From the simulation study conducted, the following conclusions and recommendations can be drawn:-

1. During WAG-CO₂ injection, the smart water injection causes both the relative permeability to oil and relative permeability to water to decrease in relative to that of conventional brine injection. In another words, smart water injection during WAG-CO₂ hinders the flow of oil through the porous medium resulting

in a lower oil recovery factor and also percentage of water cut. A slight shifting of the intersection point between the relative permeability to oil and to water curves to the right suggests that the smart water injection during WAG-CO₂ flooding modified the rock wettability toward a more water-wet system.

2. An increase in the composition of Ca²⁺ and Mg²⁺ ions in brine yields a higher oil recovery factor via reducing the ion binding between the negative carboxylic oil component and the rock surfaces.
3. A decrease in the brine salinity during WAG-CO₂ injection has unfavorable effects on the oil recovery factor. Therefore, the optimum brine salinity for maximum oil recovery during WAG-CO₂ injection in this simulation study is 35,000 ppm. All these findings are significant as to evaluate the performance of smart water injection applied during WAG-CO₂ injection which is mainly characterized by the relative permeability.
4. It is recommended that further research be undertaken to examine the effects of smart water on the three-phase relative permeability models which is much more complicated. Further works might explore or concentrate on experimental or laboratory works to compare and prove the results obtained from the simulation runs in this research. It is also imperative to determine the optimum WAG ratio to maximize oil recovery and optimize fluid injection.

References

1. Ahmed, T. 2001. Principles Of Waterflooding. In *Reservoir Engineering Handbook*, second edition. Houston, Texas: Gulf Professional Publishing.
2. Amyx, J. W., Bass, D. M. and Whiting, R. L. 1960. *Petroleum reservoir engineering: physical properties*, 174-209. New York City: McGraw-Hill.
3. Anderson, W. G. 1987. Wettability literature survey part 5: The effects of wettability on relative permeability. *Journal of Petroleum Technology*, 39(11), 1453-1468.
4. Awolola, K. A. 2012. Enhanced Oil Recovery For Norne Field (Statoil) C-Segment Using Alkaline-Surfactant-Polymer Flooding. PhD diss., Norwegian University of Science and Technology.
5. Chang, Y. B., Coats, B., and Nolen, J. 1998. A compositional model for CO₂ floods including CO₂ solubility in water. *SPE Reservoir Evaluation & Engineering*, 1(2), 155-160.
6. Christensen, J. R., Stenby, E. H., and Skauge, A. 2001. Review of WAG field experience. *SPE Reservoir Evaluation & Engineering*, 4 (2), 97-106.
7. Gorell, S. B. 1990. Implications of water-alternate-gas injection, for profile control and injectivity. In *SPE/DOE Enhanced Oil Recovery Symposium*.
8. Hasanov, B. 2010. Application of low salinity water injection to NORNE field E-segment.
9. Honarpour, M.M. and Maloney, D.R. 1990. Relative Permeability Technology And Applications. Paper NIPER 9008 presented at the 4th Annual SCA Conference.
10. Jadhunandan, P. P., and Morrow, N. R. 1995. Effect of wettability on waterflood recovery for crude oil/ brine/rock systems. *SPE Reservoir Engineering*, 10 (1), 40-46.
11. Jerauld, G.R., Lin, C.Y., Kevin J. Webb, and Jim C. Seccombe. 2008. Modeling Low-Salinity Waterflooding, Paper SPE 102239 presented at Conference and Exhibition, San Antonio, Texas, 24–27 September.
12. Jiang, H., Nuryaningsih, L., and Adidharma, H. 2010. The Effect of Salinity of Injection Brine on Water Alternating Gas Performance in Tertiary Miscible Carbon Dioxide Flooding: Experimental Study. SPE Western Regional Meeting. Anaheim, California, USA.

13. Kulkarni, M. M., and Rao, D. N. 2004. Experimental investigation of various methods of tertiary gas injection. SPE Annual Technical Conference and Exhibition. Houston, Texas, USA.
14. Lager, A., Webb, K.J., Black, C.J.J., Singleton, M., and Sorbie, K.S. 2006. Low Salinity Oil Recovery- An Experimental Investigation, Paper SCA 2006-36 presented at the International Symposium of the Society of Core Analysis, Trondheim, Norway.
15. Lager, A., Webb, K., Collins, I., and Richmond, D. 2008. LoSal enhanced oil recovery: Evidence of enhanced oil recovery at the reservoir scale. *SPE/DOE Symposium on Improved Oil Recovery*, Tulsa, Oklahoma, USA.
16. Ligthelm, D.I., Gronsveld, J., Hoffman, I.P., Brusse, N.J., Marcelis, F. and Van Der Linde, H. 2009. Waterflooding Strategy by Manipulation of Injection Brine Composition. Paper SPE 119835.
17. Maheshwari, Y. K. 2011. A Comparative Simulation Study of Chemical EOR Methodologies (Alkaline, Surfactant and/or Polymer) Applied to Norne Field E-Segment, PhD diss., Master thesis, NTNU.
18. McGuire, P.I., Chatman, J.R., Paskvan, F.K., Sommer D.M., and Carini F.H. 2005. Low Salinity Oil Recovery: An Exciting New EOR Opportunity for Alaska's North Slope. Paper SPE 93903 presented at 2005 SPE Western Regional Meeting, Irvine, CA.
19. Molina, N.N.1980. A Systematic Approach To The Relative Permeability Problem in Reservoir Simulation. Paper SPE 9234 presented at the 55th Annual Fall Technical Conference and Exhibition of the SPE, Dallas, Texas, 21 – 24 September.
20. Morrow, N. R., Tang, G. Q., Valat, M., and Xie, X. 1998. Prospects of improved oil recovery related to wettability and brine composition. *Journal of Petroleum science and Engineering*, 20 (3), 267-276.
21. Osoba, J. S., Richardson, J. G., Kerver, J. K., Hafford, J. A., and Blair, P. M. 1951. Laboratory measurements of relative permeability. *Journal of Petroleum Technology*, 3(2), 47-56.
22. Sayegh, S. G., and Najman, J. 1987. Phase behavior measurements of CO₂-SO₂-brine mixtures. *The Canadian Journal of Chemical Engineering*, 65 (2), 314-320.
23. Seccombe, J., Lager, A., Webb, K., Jerauld, G., and Fueg, E. 2008. Improving Waterflood Recovery: LoSalTM EOR Field Evaluation. In *SPE/DOE Symposium on Improved Oil Recovery*.
24. Tang, G. Q., & Morrow, N. R. 1997. Salinity, temperature, oil composition, and oil recovery by waterflooding. *SPE Reservoir Engineering*, 12 (4), 269-276.
25. Tang, G. Q., & Morrow, N. R. 1999. Influence of brine composition and fines migration on crude oil/brine/rock interactions and oil recovery. *Journal of Petroleum Science and Engineering*, 24(2), 99-111.
26. Webb, K. J., Black, C. J. J., and Edmonds, I. J. 2005. Low salinity oil recovery—The role of reservoir condition corefloods. In *13th European Symposium on Improved Oil Recovery*.
27. Yildiz, H. O., and Morrow, N. R. 1996. Effect of brine composition on recovery of Moutray crude oil by waterflooding. *Journal of Petroleum Science and Engineering*, 14(3), 159-168.
28. Yousef, A., Al-Saleh, S., Al-Kaabi, A., and Al-Jawfi, M. October. Laboratory investigation of novel oil recovery method for carbonate reservoirs. In *Canadian Unconventional Resources and International Petroleum Conference*.

Hydroxypropylmethylcellulose as a Free Water and Settling Control Agent in Oil Well Cement Slurry

Ghulam Abbas, Sonny Irawan, Muhammad Khan Memon,
Shuaib Ahmed Kalwar and Sandeep Kumar

Abstract Free water and sedimentation of particles are considered as severe problems for cementing operation. The sedimentation of particles alters the density of designed cement slurry and reduces hydrostatic pressure that becomes the cause of gas migration. Different additives and polymers have been used for prevention of free water and sedimentation. However, the mineralogy, chemical reaction, and increasing temperature affect the properties of additives and polymers. At high temperature, polymers suffer high thermal thinning problem and loss of viscosity that become incapable of controlling free water. This study presents hydroxypropylmethylcellulose (HPMC) polymer that works as viscosifying agent at high temperature. The inclusion of HPMC polymer in cement slurry eliminates the free water separation and sedimentation of solid particles at high temperature. Laboratory experiments were performed to determine the viscosity of 2 wt% of HPMC solution at various temperatures 30–100 °C. Further API properties of HPMC-based cement slurries were determined in terms of rheology, free water, and fluid loss with other additives at 90 °C. It was observed that HPMC polymer was stable at high temperature. In cement slurry, HPMC polymer completely prevents the free water separation and sedimentation of solid particles and decreases the fluid loss through cement slurry at high temperature.

Keywords Cement slurry · Free water · Sedimentation · Additives · Hydroxy propylmethylcellulose

G. Abbas (✉) · S. Irawan · M.K. Memon · S.A. Kalwar · S. Kumar
Petroleum Engineering Department, Universiti Teknologi PETRONAS,
Bandar Seri Iskandar, Perak Darul Ridzuan, Malaysia
e-mail: Engr_abbas27@live.com

1 Introduction

Separation of water and settling of particles are cause of primary cementing job failure. The excessive free water separation and sedimentation of solid particles through cement slurry leads to non-uniform density of cement slurry. As the water is separated from cement slurry, the viscosity of slurry increases and the solid particles settle down at bottom [1]. The sedimentation of particles builds the bridge inside the cement slurry and creates two phases of different densities. In this condition, high density at bottom creates fractures that become the cause of loss circulation. The low density at top of slurry decreases hydrostatic pressure that creates permanent channels and become the cause of gas migration through permeable zone [2].

Previously, the extender such as bentonite was used to control free water and sedimentation of solid particles. Bentonite prevents the breakthrough of formation and loss of circulation and has better yield to cement by remarkable amount of water. But the effectiveness of extender decreases tremendously in the presence of strong electrolytes such as CaCl_2 and NaCl [3]. Polysaccharides are extremely used as fluid loss control agent in oil well cement slurry. Allen states that the use of polysaccharides in cement slurry also controls the free water separation and shows more uniform density in cement slurry [4]. The polysaccharides such as hydroxyethylcellulose (HEC), hydroxypropylguar (HPG), and carboxymethylhydroxyethylcellulose (CMHEC) show limitation at high temperature. In oil well cementing operations, these polymers are unstable in cement slurry at high temperature. The viscosity of these polymers sharply reduces with respect to temperature, and polymers lose their desired properties in cement slurry [5]. Currently, polysaccharides were modified with some other chemicals to increase the stability of polymers at high temperature [6]. The utilization of chemicals to enhance the performance of polymers increased the operational cost and also affects the properties of cement. Therefore, it was necessary to use such type of polymer that could work effectively as a free water control agent and enhance the viscosity with increasing temperature without addition of any chemical.

Hydroxypropylmethylcellulose (HPMC) is a long chain cellulose water-soluble polymer that acts as thickener, film foamer, solid suspension agent and a surfactant. The rheology of HPMC polymer shows that it is stable at high temperature and will increase viscosity at gelation temperature. The application of HPMC in oil industry has been investigated as a permeability-reducing agent for profile modification and has long thermal stability through experimental analysis [7].

This paper presents the experimental study of HPMC polymer to control free water in the cement slurry. The objective of this study is to design HPMC-based cement slurry with other additives that control the free water, sedimentation, and fluid loss through cement slurry at high temperature. On the base of laboratory experiments, rheology of 2 wt% HPMC polymers in terms of viscosity was determined. Furthermore, the API properties of cement slurries in terms of rheology, free water, fluid loss, and settling of solid particles are determined by changing the concentration of HPMC solution at 90 °C temperature.

2 Experimental Procedure

2.1 Preparation of HPMC Polymer Solution

HPMC polymer was in the form of white fine powder. Commercial HPMC polymer was used for experiments. The concentration 2 wt% of HPMC polymer solution was prepared with distilled water to determine the properties of HPMC solution at different temperatures.

2.2 Viscosity of HPMC Polymer

High-pressure high-temperature viscometer (OFITE 1,100 model) was used to determine the viscosity of HPMC solution at different temperatures. The viscosity was determined at different shear rates from 1 to 1,000 s^{-1} . All viscosity measurements were performed at various temperatures from 30 to 100 °C to analyze the effect of temperature on HPMC polymer.

2.3 Preparation of Cement Slurry

The density of 16.5 pounds per gallon (ppg) was used to evaluate the effect of HPMC polymer on cement slurry at high temperature. Various cement slurries were prepared by changing the concentration of HPMC polymer from 0.20 to 0.65 gallon per sack (gps). The mixing process of cement, water, solution of HPMC polymer, and other additives was performed using constant high-speed mixture at 4,000 and 12,000 rpm according to API RP10B-2 procedure [8].

2.4 Conditioning of Cement Slurry

The preheating of cement slurry is very important for performing the rheology, fluid loss, and free fluid test. The rheology and free fluid test were performed at elevated temperature. Therefore, it was necessary to preheat the slurry at 90 °C. In order to determine the properties at 90 °C, the designed cement slurries were heated at 90 °C for 20 min using atmospheric consistometer.

2.5 Rheology Measurement

The rheology of designed cement slurry was determined using Fann rotational viscometer at different dial reading according the API standard. The preheated

cement slurry poured in the slurry cup of rotational viscometer. The rheology of slurries was determined in terms of shear stress by giving shear rate in terms of rpm.

2.6 Fluid Loss Testing

The API fluid loss of slurries was determined by using HPHT filter press. According to API standard, the cement slurry was conditioned at 90 °C for 20 min using atmospheric consistometer. The preheated cement slurry was poured into the slurry cup of filter press. The fluid loss of slurries was determined for the time duration of 30 min according to API criteria.

2.7 Free Water and Slurry Sedimentation Test

The separation of fluid through cement slurry was determined by free water test using 250-ml graduated cylinder. The preheated cement slurry was poured into the cylinder for two hours. According to API standard, the graduated cylinder was placed at an inclination of 45° to observe the effect in deviated condition. The settling of solid particles was analyzed based on visual observations made after examining the slurry in viscometer cup and the graduated cylinder after the free water test.

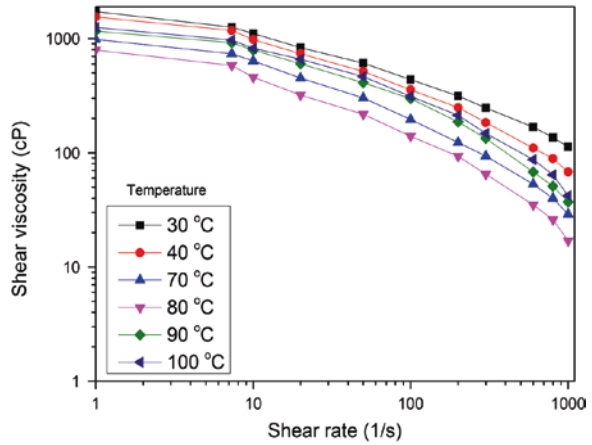
3 Results and Discussion

3.1 Rheology of HPMC Polymer

The viscosity of 2 wt% HPMC solution was determined at various temperatures from 30 to 100 °C to examine the effect of temperature on viscosity. HPMC solution shows maximum viscosity at low shear rate 1 s^{-1} and minimum viscosity at high shear rate $1,000 \text{ s}^{-1}$. The viscosity of 2 wt% HPMC solution is shown in Fig. 1. HPMC polymer shows high viscosity at 30 °C. On the other hand, the viscosity of HPMC solution was decreasing with increasing temperature. Like other polymer, the HPMC polymer has thermal thinning behavior by increasing temperature. The thermal thinning at elevated temperature was imposed by thermal fluctuation on the body of ether molecules [9].

On the other hand, it was observed that when the temperature was increased from 80 to 90 °C, the viscosity of solution increased. First, at 80 °C, HPMC showed minimum viscosity 17 cP at 1 s^{-1} and 793 cP at $1,000 \text{ s}^{-1}$. After this, above 80 °C, it was observed that viscosity of solution increased at 90 °C.

Fig. 1 Shear rate versus viscosity of HPMC solution at different temperatures



The viscosity of HPMC polymer was 37 cP at 1 s^{-1} and 1,160 cP at $1,000 \text{ s}^{-1}$. This was the property of HPMC polymer that above gelation temperature it will start to increase gel strength and viscosity. Increasing viscosity at $90 \text{ }^\circ\text{C}$ proves that HPMC polymer act as a viscosifying agent. The amplified viscosity at gelation temperature is a unique property of HPMC polymer and has not been observed in other cellulose-type polymers [10]. Further, it was also observed that at $100 \text{ }^\circ\text{C}$ the viscosity of both HPMC solutions was greater than the viscosity at $90 \text{ }^\circ\text{C}$. The stability of HPMC polymer at high temperature made it possible to use in cement slurry for prevention of free water.

3.2 Formulation of HPMC-Based Cement Slurry

The formulation of HPMC-based cement slurries is given in Table 1. The free water, rheology, sedimentation, and fluid loss of different cement slurries were determined by changing the concentration of polymer and other additives.

3.3 Characteristics of HPMC-Based Cement Slurry

The API properties of HPMC-based cement slurries were determined at $90 \text{ }^\circ\text{C}$. The density of all designed cement slurries was 16.5 ppg. The rheology, free water, visual sedimentation, and fluid loss of cement slurries at $90 \text{ }^\circ\text{C}$ are given below in Table 2.

It was clear that slurry 1 (without HPMC) showed high free water, fluid loss, and heavy sedimentation of particles. The solid particles settled down in the bottom of graduated cylinder. The remaining cement slurries 2–11 that contain

Table 1 Formulation of cement slurries

Slurry	Cement BWOC	FP9-LS gps	CD-33L gps	FL-66L gps	HPMC gps
1	100	0.02	–	–	–
2	100	0.02	–	–	0.65
3	100	0.02	–	–	0.50
4	100	0.02	–	–	0.30
5	100	0.02	–	–	0.20
6	100	0.02	0.03	0.40	0.30
7	100	0.02	0.04	0.30	0.50
8	100	0.02	0.05	0.40	0.30
9	100	–	0.05	0.40	–
10	100	0.02	0.05	0.40	0.40
11	100	0.02	0.05	0.40	0.50

Table 2 API properties of HPMC-based cement slurry

Slurry	Viscometer reading (rpm)						Free water ml	Fluid loss ml /30 min	Sedimentation comments
	600	300	200	100	6	3			
1	190	110	74	52	25	15	21	740	Heavy
2	+300	270	210	140	95	58	00	196	None
3	+300	257	198	127	81	47	04	288	None
4	281	233	164	107	57	37	11	484	Medium
5	257	206	147	97	42	32	15	548	Heavy
6	245	225	196	132	98	65	01	27	None
7	272	213	187	143	110	272	00	39	None
8	142	93	64	39	19	10	00	24	None
9	113	86	47	31	12	06	03	39	None
10	157	107	73	51	26	18	00	22	None
11	169	118	81	63	38	25	00	15	None

HPMC polymer shows low free water separation and very low settling of solid particles. Slurry 2 contains high-concentration 0.65 gps of HPMC showed zero free water separation within 2 h, and the fluid loss of this slurry was 196 ml in 30 min observed in slurry 2. It was also observed that as the concentration was decreasing from 0.65 to 0.20 in slurries 3–5, the free water and fluid loss was increasing. The sedimentation was analyzed by visual observation of cement slurry during free water test.

The high concentration of HPMC solution completely prevents the sedimentation of particles. HPMC polymer was viscosifying agent, and it increases the viscosity of slurry. HPMC-based cement slurries produce high viscosity and have better suspending properties. HPMC polymer has the property to act as particle suspension agent. In cement slurry, HPMC increases the cohesive force between particles that restrict the sedimentation of cement particles and control the separation of free water.

The high concentration of polymer was improving the properties of cement slurry in terms of fluid loss, free water, and sedimentation. On the other hand, high concentration of HPMC in cement slurry was increasing the rheology of cement slurry. The rheology of cement slurries is a very important property of oil well cementing operation during displacement of slurry. The high rheology of cement slurry requires high pump pressure at the time of displacement. High rheology of cement slurry will become the cause of fracture during displacement and loss of cement slurry. It was necessary to use dispersant in cement slurry that adjusts the rheology of cement slurry. Therefore, in order to maintain the rheology of cement slurries, 0.02–0.05 gps dispersant was used in slurry. On the basis of rheology of cement slurries, 0.30–0.50 gps HPMC was used for remaining cement slurries.

HPMC polymer had positive impact on cement slurry for controlling fluid loss. The increase in concentration of HPMC polymer decrease. It was also possible to decrease fluid loss further by increasing the concentration of HPMC polymer than 0.65 gps. But high concentration again becomes the cause of slurry viscosification and requires high pump pressure. Therefore, small quantity of fluid loss additive was used in cement slurry to maintain rheology and control fluid loss. The quantity 0.20–0.50 gps of fluid loss was used to obtain the fluid loss of less than 50 ml. The addition of dispersant in cement slurry has no effect on the properties of HPMC for controlling free water. For optimized cement slurries, the fluid loss and dispersant additives were used in cement slurries.

The addition of dispersant reduces the rheology in terms of viscometer dial reading, and fluid loss additive improves the properties of HPMC polymer for controlling fluid loss. The aim of dispersant is to reduce the rheology. The high concentration of HPMC increased the viscosity and rheology. Therefore, it was necessary to observe the effect of high concentration of HPMC for rheology. The concentration 0.05 gps of dispersant, 0.50 gps of fluid loss additive and 0.30–0.50 gps of HPMC solution was used to prepare cement slurry. The designed cement slurry improve the rheology, fluid loss control, free water separation and sedimentation of solid particles through cement slurry. The visual observation of optimized cement slurries were without sedimentation of solid particles.

4 Conclusions

- The solution of HPMC polymer shows enhanced viscosity at 90 and 100 °C. It proves that HPMC polymer can be used in cement slurry at high temperature for improving the properties of cement slurry.
- Increasing viscosity of HPMC polymer at high temperature controls the sedimentation of particles as well as prevents the separation of free water at high temperature.
- HPMC polymer acknowledged as a multifunctional material that control the free water separation and improve the property of fluid loss additive at high temperature in cement slurry.

- HPMC polymer eliminates the free water completely, thus diminishing the formation of channels through cement column, and can minimize the fluid migration through permeable formation.

Acknowledgments The authors wish to acknowledge Universiti Teknologi PETRONAS (Malaysia) for granting permission to present and publish this paper. The authors also wish to thank Yillong Chemical Group Limited (China) and Baker Hughes Oil field Services (Kemaman, Malaysia) for the supply of materials for this research.

References

1. K. Ganguli, "Biopolymers as free water and settling control agent," SPE Production Operations Symposium, 1993.
2. T. Allen and F. Sands, "Why Control Cement Slurry Density?," SPE Asia Pacific Oil and Gas Conference, 1993.
3. W. G. Jr, J. Rutledge, and C. Gardner, "Quality of bentonite and its effect on cement-slurry performance," SPE Production Engineering, no. November, pp. 411–414, 1990.
4. F. L. Allen, G. H. Best, and T. A. Lindroth, "Welan gum in cement compositions." Google Patents, 1990.
5. C. F. Parks, B. L. Gall, and P. E. Clark, "Evaluation of Polymers for Oilfield Use: Viscosity Development, Filterability and Degradation," 1988.
6. B. Reddy, R. Patil, and S. Patil, "Chemical Modification of Biopolymers to Design Cement Slurries with Temperature-Activated Viscosification," in SPE International Symposium on Oilfield Chemistry, 2011.
7. H. He, Y. Wang, M. Zhao, L. Cheng, and P. Liu, "Laboratory Evaluation of Thermoreversible Gel for In-Depth Conformance Control in Steam-Stimulated Wells," Proceedings of SPE Heavy Oil Conference Canada, Jun. 2012.
8. R. API, "10B, Recommended Practice for Testing Well Cements, 22nd," Washington, DC: API, vol. 2, no. July 2005, 2009.
9. G. Abbas, S. Irawan, S. Kumar and Ahmed A. I. "Improving Oil well Cement slurry Performance using Hydroxypropylmethylcellulose polymer". Journal of Advanced Materials Research, Volume (787) 2013, pp 222-227.
10. G. Abbas, S. Irawan, S. kumar, Nisar Khan and S. Memon, " Gas Migration Prevention Using Hydroxypropylmethylcellulose as a Multifunctional Additive in Oil Well Cement Slurry," proceeding of SPE Annual technical Conference, Pakistan, November 2013.

Static Adsorption of New CO₂ Philic Surfactant onto Berea Sandstone

Muhammad Sagir, Isa M. Tan, Muhammad Mushtaq
and Seyda Hosna Talebian

Abstract The adsorption of newly synthesized surfactant on Berea core is reported here. The static adsorption surfactant named UTP surfactant was found 0.91 mg/g. The adsorption of the surfactant followed a typical four-region adsorption isotherm. The critical micelle concentration of surfactant was found 2,075 ppm, and the point of zero charge (PZC) of Berea sandstone determined by potentiometric mass titration method (PMT) was at pH 8. The comparison of the adsorption of surfactant with commercial alpha olefin sulfonate (AOS) surfactant was also studied and reported. The newly developed surfactant performed better than AOS. The adsorption behaviors of both surfactants are explained by considering the factors such as the difference in structure, chain length, purity, and critical micelle concentration (CMC).

Keywords Surfactants • Adsorption • EOR

M. Sagir (✉)

Department of Chemical Engineering, Universiti Teknologi PETRONAS,
Tronoh, Malaysia
e-mail: sagir.utp@gmail.com

I.M. Tan

Department of Fundamental and Applied Sciences, Universiti Teknologi PETRONAS,
Tronoh, Malaysia

M. Mushtaq

Department of Petroleum Engineering, EOR Center, Universiti Teknologi PETRONAS,
Tronoh, Malaysia

S.H. Talebian

Department of Petroleum Engineering, Universiti Teknologi PETRONAS,
Tronoh, Malaysia

1 Introduction

Crude oil plays an important role in the world's economy, as it is the major source of energy especially for transportation, heat, and domestic purposes. Global energy demand has continued to rise because of enormous urban and industrial developments in recent years. This ever-increasing demand for oil has directed many researchers to find ways to maximize the oil recovery from existing resources. It is generally believed that only 30 % of oil in place is recovered by conventional methods. After primary and secondary oil recovery process, enhanced oil recovery methods (EOR) aim to recover the remaining 70 % of trapped oil in the reservoir. EOR processes are classified into gas, thermal, microbial, and chemical flooding processes. Chemical flooding includes the addition of various chemical compounds to reduce interfacial tension between reservoir oil and the injected fluid or to improve sweep efficiency of the injected fluid [1, 2].

Surfactants are the unique molecules with a water soluble part (head) and an oil soluble part (tail). Surfactants are not only present in consumer products (such as shampoos, soaps, and detergents) but are also one of the most important classes of industrial chemicals. According to a market research study by Ceresana Research, the surfactant market revenue was over US\$28 billion in 2011 and it will be more than US\$41 billion in 2018 with an average growth rate of 4.5 %. Anionic surfactants, which are about 70–75 % of the total surfactants produced worldwide, with a world demand of 6.5 million tons in 2010, are also the main class of surfactants used for EOR applications [3].

From foam generation to IFT reduction, surfactants can play pivotal roles for enhancing the oil recovery. The CO₂ philic surfactants are new type of surfactants employed for the generation of stable foam for CO₂ mobility control application. Like the typical surfactants, these surfactants have two distinct parts, head and tail, but the tail of these surfactants has the affinity with CO₂ gas in order to stabilize the foam [4, 5].

These surfactants act on a water–CO₂ interface, and due to their unique chemical structure, they orient themselves at the interface in such a way to stabilize the CO₂ foam. This remarkable capability of foam stability is used to control the CO₂ mobility problems as a result CO₂ mobilizes the trapped oil [3–5].

Despite the advantages of surfactants, these are expensive chemical agents and tend to adsorb on surface of rocks in oil reservoirs hence reducing its concentration in injected fluid [6, 7]. Surfactant adsorption is a process in which there is transfer of surfactant molecules from the bulk solution phases to solid–liquid interfaces [7, 8]. Surfactant adsorption depends upon numerous factors, which include salinity, pH, ionic strength, temperature, type, and composition of surfactants and divalent ions [7–10].

In this study, we reported static adsorption of synthesized surfactant onto Berea sandstone core sample. The adsorption of the newly developed surfactant was compared with alpha olefin sulfonate (AOS), a commercial surfactant.

2 Experimental

2.1 Materials

The surfactant was synthesized in UTP laboratory. The anionic surfactant AOS and Hyamine 1,622 were purchased from Fisher Scientific. Berea cores were purchased from Cleveland Quarries.

2.2 Analytical Methods

Titration method was used for the determination of surfactant concentration using Titrand 888 autotitrator. Hyamine 1,622 was used as titrant. High-purity deionized water was used after boiling for all solution preparations [9, 10].

2.3 CMC of Surfactant

Spinning drop surface tension method was employed to measure the CMC of surfactant. The IFT (surface tension) of different concentrations of surfactant solutions was determined by using the spinning drop tensiometer Data physics SV-20. Surfactant concentration against IFT was plotted, and CMC was identified.

2.4 Point of Zero Charge (PZC)

PZC of core sample was determined using potentiometric mass titration (PMT) method. In this method, a fixed amount of sodium solution (100 mL) was transferred into three flasks. Known amounts of 0.2, 0.4, and 0.6 g of crushed Berea were transferred to each flask, respectively. A blank solution without core sample was also prepared [11, 12].

After the solutions reach equilibrium, 0.1 M NaOH (5 mL) was added to all flasks. All these solutions were titrated against HCl. The PZC value was identified by recording the pH values after regular intervals of 30 s [6].

2.5 Adsorption Studies

The specific amount of surfactant, alkali, and salinity was added in surfactant solutions. Mixtures were agitated for 24 h on a horizontal shaker at room

temperature. The mixtures were centrifuged for 30 min at 3,000 rpm. The supernatant was analyzed for surfactant concentration. The amount of surfactant adsorbed was judged by depletion method. The amount of surfactant adsorbed Q_o (mg/g) on the crushed core samples is calculated by the following equation: [1, 2];

$$Q_o = (C_o - C_e) \cdot \left(\frac{V}{M} \right) \quad (1)$$

where

C_o is the initial surfactant concentration

C_e is surfactant concentration at equilibrium

V is volume of surfactant solution, and

M is the mass of core sample (g) [3].

3 Results and Discussion

3.1 Core Properties

The compositions of the core sample were determined by XRF analysis. Silica and alumina have the highest fractions 60.77 and 23.77 %, respectively. Therefore, their presence will influence the surface chemistry of the core.

3.2 CMC of Surfactant

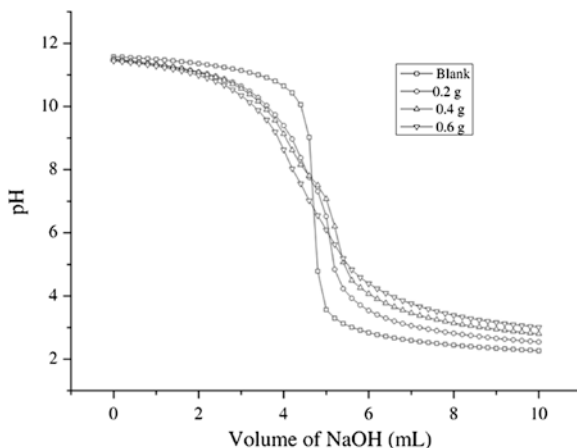
The CMC of synthesized surfactant sample was measured by surface tension method by using Data physics spinning drop tensiometer instrument. The IFT decreases linearly with increasing surfactant concentration until a specific point beyond which the effect was prominent. The CMC for available anionic surfactant was found to be 2,075 ppm.

The CMC of commercial anionic surfactant (AOS) is reported previously at 8 mM (~1,750 ppm).

3.3 Point of Zero Charge

The PZC results are shown in Fig. 1. It was found that the PZC value of crushed Berea sandstone core sample is pH 8.0 as shown in Fig. 1.

Fig. 1 PZC plot by potentiometric mass titration analysis



3.4 Adsorption Isotherm

The adsorption isotherm of anionic surfactant onto Berea sandstone is shown in Fig. 2. The adsorption isotherm is the plot of surfactant concentration against the adsorption density (mg/g). A typical isotherm usually shows four regions. Region 1 occurs at low surfactant concentrations in which the monomers are adsorbed onto the substrate. The adsorption values in this region increase by increasing the concentration of the surfactant. Formation of surface aggregates produces second region of the isotherm where sharp increase in adsorption was observed. In third region, the increase in adsorption of surfactants was low as the surface of the solid particles became electrically neutralized. As the surfactant concentration approaches CMC in region 4, therefore, no increment in adsorption was observed [4, 5].

Maximum adsorption of synthesized surfactant was found 0.91 mg/g. A typical adsorption isotherm for adsorption of synthesized surfactant is shown in Fig. 3.

Fig. 2 Adsorption isotherm of synthesized anionic surfactant

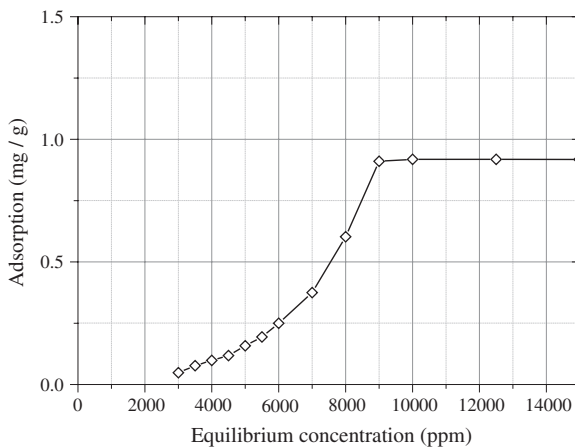
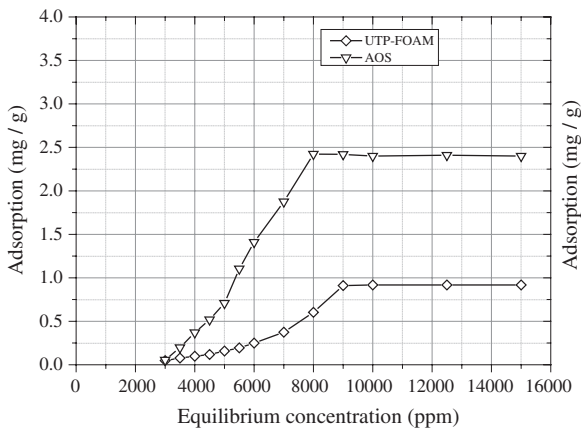


Fig. 3 Adsorption isotherm of synthesized anionic surfactant and AOS on Berea sandstone



3.5 A Comparative Study

The static adsorption of synthesized surfactant was compared to AOS, a commercially available surfactant. The depletion method was used to measure the static adsorption of AOS. The maximum static adsorption of AOS was found 2.40 mg/g. The adsorption of synthesized anionic surfactant is low, i.e., 0.91 mg/g compared to (AOS) commercial anionic surfactant. Figure 3 compares the adsorption of AOS with synthesized anionic surfactant.

The decrease in adsorption density of synthesized anionic surfactant is attributed to the following reasons:

1. The CMC of surfactant shows a marked influence on the adsorption of surfactant: Higher the CMC value, lower will be the adsorption. Critical micelle concentration (CMC) of AOS is 1,750 ppm (~8 mM), whereas the CMC of synthesized anionic surfactant (UTP) is 2,075 ppm. The CMC of UTP is higher than AOS surfactant, and hence, solubility of UTP is higher than AOS surfactant.
2. The branches in the surfactant structure also affected the adsorption; linear structure was adsorbed more when compared to the branched structures. The synthesized anionic surfactant have branched structure where AOS is linear in structure. Due to denser packing ability of AOS chain as compared to synthesized UTP surfactant, AOS have higher adsorption.
3. The presence of impurities may cause the higher adsorption value found in AOS compared to UTP surfactant. The UTP surfactant is synthesized in UTP EOR center using special purifying treatment, whereas AOS is commercially available and produced in bulk quantities.

4 Conclusions

The PZC of Berea sandstone was at pH 8. The static adsorption of surfactants follows a normal four-region adsorption isotherms trend. In region 1, the adsorption follows Henry's Law. In region 2 and 3, a higher adsorption was occurred. There was no increase in adsorption density in region 4 as it was beyond the surfactants CMC values. The adsorption of synthesized surfactant and AOS was 0.91 and 2.40 mg/g, respectively. AOS has comparatively higher adsorption because of its lower CMC, linear structure, and longer chain length. For surfactant applications in EOR, synthesized surfactant will perform better than AOS. The in-house developed novel CO₂ philic surfactant possessing low adsorption properties has a great potential for EOR applications.

Acknowledgments Authors acknowledge the financial support of UTP and PETRONAS Research Sdn. Bhd. (PRSB) through PRF Project 158200042 and the usage of CEOR Centre of excellence facilities.

References

1. Q. Feng, *et al.*, "Adsorption of lead and mercury by rice husk ash," *Journal of Colloid and Interface Science*, vol. 278, pp. 1-8, 2004.
2. R. J. Mazen Ahmed Muherei "Equilibrium Adsorption Isotherms of Anionic, Nonionic Surfactants and Their Mixtures to Shale and Sandstone," *Modern Applied Science*, vol. Vol. 3, No. 2, 2009.
3. A. Mohamed, *et al.*, "Hybrid CO₂-philic Surfactants with Low Fluorine Content," *Langmuir*, vol. 28, pp. 6299-6306, 2012/04/17 2012.
4. J. Eastoe, *et al.*, "Design and Performance of Surfactants for Carbon Dioxide," in *Supercritical Carbon Dioxide*. vol. 860, ed: American Chemical Society, 2003, pp. 285-308.
5. A. V. Yazdi and E. J. Beckman, "Design of Highly CO₂-Soluble Chelating Agents. 2. Effect of Chelate Structure and Process Parameters on Extraction Efficiency," *Industrial & Engineering Chemistry Research*, vol. 36, pp. 2368-2374, 1997/06/01 1997.
6. M. Farooq, *et al.*, "Physiochemical Properties of γ -Al₂O₃-MgO and γ -Al₂O₃-CeO₂ Composite Oxides," *Journal of Chemical Engineering*, vol. 57, pp. 26-32, 2012.
7. P. Somasundaran and L. Zhang, "Adsorption of surfactants on minerals for wettability control in improved oil recovery processes," *Journal of Petroleum Science and Engineering*, vol. 52, pp. 198-212, 2006.
8. S. Paria and K. C. Khilar, "A review on experimental studies of surfactant adsorption at the hydrophilic solid-water interface," *Advances in Colloid and Interface Science*, vol. 110, pp. 75-95, 2004.
9. M. Sagir, I.M. Tan, M. Mushtaq, L. Ismail, M. Nadeem, M.R. Azam, *et al.*, "Novel surfactant for the reduction of CO₂/Brine Interfacial tension," *Journal of Dispersion Science and Technology*, vol. 35, pp. 463-70, 2013.
10. M. Sagir, I.M. Tan, M. Mushtaq, S.H. Talebian, "FAWAG using CO₂ philic surfactants for CO₂ mobility control for enhanced oil recovery applications" in SPE saudi arabia section technical symposium and exhibition, Society of Petroleum Engineers, Al-Khobar, Saudi Arabia, 2014.
11. M.R. Azam, I.M. Tan, L. Ismail, M. Mushtaq, M. Nadeem, M. Sagir, "Kinetics and equilibria of synthesized anionic surfactant onto berea sandstone," *Journal of Dispersion Science and Technology*, vol. 35, pp. 223-30, 2013.
12. M. Mushtaq, I.M. Tan, M. Nadeem, C. Devi, S.Y.C. Lee, M. Sagir, *et al.*, *Grasas y Aceites*, vol. 64, pp. 103-114 2013.

Comparison of MMP Between Slim Tube Test and Vanishing Interfacial Tension Test

Choon Lin Voon and Mariyamni Awang

Abstract There are many tests used for determination of crude oil–CO₂ MMP, but there is no test that is taken as the standard for MMP measurement. However, there are two tests that are widely used which are vanishing interfacial tension (VIT) test and slim tube test. VIT test is fast but it is not accurate while slim tube test is exactly vice versa, it takes a lot of time for one MMP point; however, the result is much more accurate. This paper is going to discuss the accuracy of the MMP measurement for both tests at various scenario and observe the trends. Both tests are found to have very different principle in measuring MMP, and their results vary quite a bit. However, they are both very useful in proving the effectiveness of additives in reducing MMP.

Keywords VIT test · S lim tube test · Dulang · MMP · CO₂

1 Introduction

The injection of gas above the minimum miscibility pressure (MMP) is one of the ultimate goals in enhanced oil recovery. MMP [1] is defined as the lowest pressure when multi-contact miscibility can be achieved [2] at constant pressure and composition. The pressure of the CO₂ being pumped into the reservoir must constantly above the MMP pressure in order to have multi-contact miscibility. Any pressure below that will only result in immiscible displacement and hence much lower oil recovery [3].

C.L. Voon (✉) · M. Awang
Department of Petroleum Engineering, Universiti Teknologi PETRONAS,
Tronoh, Perak, Malaysia
e-mail: choonlin.voon@gmail.com

M. Awang
e-mail: mariyamni_awang@petronas.com.my

Miscibility occurs via either a vaporising process, or a condensing process. Occasionally, both previously mentioned processes will be developed at the same time [2] when the pressure at or higher than MMP. In the crude oil, the intermediate molecular weight hydrocarbons moved to the borderline of the gas throughout the vaporising process; hence, the carbon dioxide and the crude oil will be miscible [4].

On the other hand, the gas injected is highly saturated with crude oil's light component in the condensing process. The reservoir oil that comes in contact with the gas front is enhanced through the relocation of light component of the hydrocarbon from gas phase to the oil [2]. The process of enrichment of the crude oil will continue until it is miscible with the enriched injected gas.

Apart from the 2 previously mentioned processes, miscibility will also develop in a mixture of process between vaporising and condensing processes. The condensing process will be similar to the single condensing process where light-intermediate components that are in the injected gas will combine with the crude oil. Meanwhile, the middle intermediate components of the crude oil will vaporise into gas phase [2].

The simultaneous process of condensation and vaporisation causes the miscibility failed to develop which translates to low residual oil saturations.

Presently, many parts of the world are implementing miscible gas injection projects due to their capability to reach higher rate of recovery. Among the most standout industrial experience has been with United States for using CO₂ gas injection, while Canada has been very skilled with enriched hydrocarbon gas injection projects [3].

Oil displacements experiments are done using slim tube test. It involves the use of slim tubes with various length packed with either fine sand or glass beads. The fluids are injected into the cores at constant rate and at constant pressure during flooding. The produced fluid is collected at the outlet of the apparatus [5].

There is another experimental method called vanishing interfacial tension (VIT) test [6]. It has been gaining traction among the industry due to the immensely short time it requires and requires very low cost in estimating MMP. It measures the interfacial tension between the gas and oil at various set pressures and then calculates the MMP by extrapolation [7].

As mentioned before, the two laboratory methods for measurement of MMP are VIT test and slim tube test. Even though there are a lot of different types of slim tube apparatus offered in the market due to the accuracy of the test, majority of the MMP measured in the literature were measured with VIT test. This may be due to the short period of time it requires to obtain results. Slim tube test is just too troublesome and consumes a lot of time.

The aim of this paper was to differentiate the pros and cons between slim tube test and VIT test for measuring MMP. We have to understand the factors that might affect the result and keep it constant as possible to avoid any discrepancies. The oil used will be specifically for Dulang, and it will be a simple test compared to other studies which uses up to 12 different types of oil [2]. The goal of this

study was to publish the measured MMP for Dulang using slim tube test since this information is absent in the literature now while at the same time do a simple comparison with the MMP measured using VIT test.

2 Methodology

2.1 Material

2.1.1 Crude Oil: Dulang

Dulang crude has been selected due to the easy availability at the university. Besides that, it is waxy, hence we can see the difficulties that both methods might face when conducting the experiment.

2.1.2 Carbon Dioxide

Industrial grade carbon dioxide with 99.99 % purity is used in the experiment to eliminate other external factors that may affect the result of the experiment [8]. MMP is known to be affected by several factors such as reservoir temperature, oil composition and CO₂ impurities [9].

2.1.3 Alcohol

Apart from comparing the measured MMP, both methods will also be tested the trends that it might have when oleophilic chemical is added into the CO₂-crude oil mixture. Alcohol with 10 % concentration is added into the CO₂-crude oil mixture. The reason alcohol is chosen among all the other oleophilic chemicals is because alcohol has been proven [10] to be able to lower the MMP of CO₂-crude oil. If both methods show trend of decreasing MMP when alcohol is added, then both methods can be used for impact oleophilic chemicals have on the reduction of MMP.

2.2 Methodology

2.2.1 Slim Tube Test

Slim tube test has long been taken as the “industry standard” for measurement of MMP; however, there is no standard design or unified industry-set operating procedure nor any predetermined criteria for measuring MMP [2]. Slim tube test is a

much more accurate way to measure CO₂-crude oil MMP although its technique of measuring is different from IFT measurement.

2.2.2 Vanishing Interfacial Tension (VIT) Test

VIT test was first mooted in the early 1980s. The most important thing about the apparatus is its mounted upright flat glass tube that is capable to withstand high pressure and temperature while providing a sight gage for the researcher [2]. Near the sight gage, there is a syringe positioned at the top. The tip of the syringe extends into the middle of the glass tube. There is an allowance of 1–2 in. space kept between the ends of the syringe with the bottom of the glass tube. The interfacial tension (IFT) between CO₂ and crude oil is measured using the equipment IFT-700, and the same is done with the addition of alcohol.

3 Results

The MMP measured between VIT test and slim tube test is expected to vary greatly due to the difference of principle behind both techniques. However, both methods are able to correctly predict the trends of the MMP when alcohol is added.

3.1 Slim Tube Test

The data in Tables 1 and 2 are those obtained using slim tube test.

Table 1 Pressure versus percentage recovered for crude oil–CO₂ mixture

Pressure (psi)	Percentage recovered (%)
2,200	5.3
2,500	28.9
3,100	63.2
3,800	94.7
4,200	97.4
4,500	97.4

Table 2 Pressure versus percentage recovered for crude oil–CO₂–alcohol mixture

Pressure	Percentage recovered (%)
2,700	47.4
2,900	65.8
3,100	81.6
3,600	94.7
3,900	94.7
4,200	100.0

Based on the data from Tables 1 and 2, the MMP of both mixtures can be obtained by finding the intersection points between the 2 trend lines as shown in Figs. 1 and 2 in Appendix.

Then from those 2 graphs, we find that the MMP for crude oil–CO₂ mixture is 3,575.35 psi while the MMP for crude oil–CO₂–alcohol is 3,197.16 psi. There is a MMP reduction of 378.19 psi when alcohol is introduced into the mixture.

3.2 Vanishing Interfacial Tension (VIT) Test

For the data obtained in VIT test, it is much different from the way it is collected for slim tube test. For VIT test, the IFT between the solvent or solvent plus co-solvent with the solute is measured at various pressure and then from there, the MMP is obtained by extrapolating the trend line.

From the data in Table 3, the graphs of pressure versus IFT are plotted in Figs. 3 and 4. Based on the graphs in Figs. 3 and 4, the MMP we obtained for crude oil–CO₂ is 3,117.51 psi. For the crude oil–CO₂–alcohol mixture, the MMP is 3,003.90 psi. From both results, we can see that with the introduction of alcohol into the system, the MMP is reduced by 113.61 psi.

In summary, the results from both tests can be compared as shown in Table 4.

While all the results obtained from both tests vary to a certain degree, however, the two tests are very useful when observing trend. One very clear example is the one in this paper where both tests register the same trend which is the reduction in MMP when alcohol is introduced into the system. The two tests are suitable to be conducted together when testing other possible additives that might be able to reduce MMP just like what alcohol did.

Table 3 Interfacial tension of mixtures at different pressure

Pressure (psi)	Crude oil (dynes/cm)	Crude oil with ALFOL 1214 (dynes/cm)
800	14.47	11.89
1,200	11.68	8.88
1,600	8.98	6.85
2,000	6.64	4.70
2,400	4.77	3.73

Table 4 Comparison of slim tube test and VIT test results

Test	Crude oil + CO ₂ (psi)	Crude oil + CO ₂ + alcohol (psi)	Reduction (psi)
Slim tube test	3,575.35	3,197.16	378.19
VIT test	3,117.51	3,003.90	113.61

4 Conclusion

1. The VIT test is a much faster way in measuring the MMP compared to slim tube test. VIT test requires a maximum of 1 day to determine one MMP while slim tube takes at least two weeks for one MMP measurement.
2. The cost of purchase of VIT test apparatus which is the Vinci Technologies IFT-700 is much cheaper than the slim tube test apparatus which is the Slim Tube-100 by Core Lab Laboratories.
3. VIT test is able to measure the MMP for asphaltene crude while doing so for slim tube test will cause the equipment to malfunction. This is due to the blockage of filter at the inlet of the slim tube. VIT apparatus has no such problem.
4. Slim tube test and VIT test complement each other in tests that involve examining the effect of introducing additives into the mixture. The additive will be proven effective when both tests show result that there is a reduction of MMP with the introduction of additive.

Acknowledgments The author would like to thank the Malaysian Ministry of Education for providing the fund for this project via MyRA. Authors would also like to thank Universiti Teknologi PETRONAS for providing all the essential equipment to enable both methods to be tested in the university. On top of that, we would like to thank PETRONAS for providing the crude oils used in this study.

Appendix

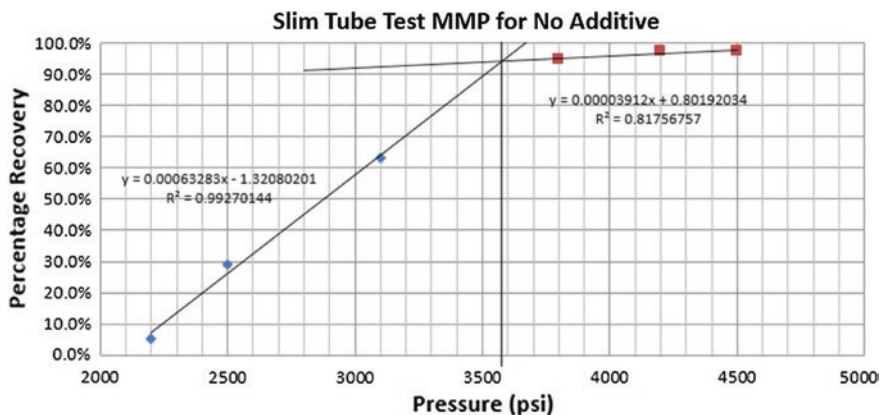


Fig. 1 MMP measurement using slim tube test for crude oil-CO₂ mixture

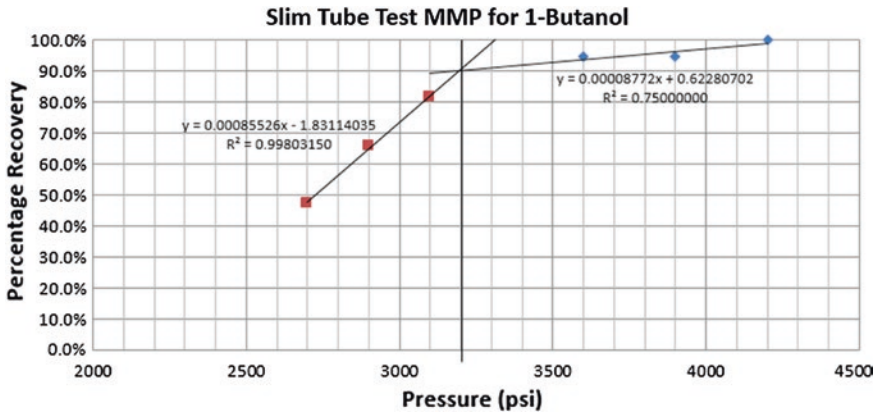


Fig. 2 MMP measurement using slim tube test for crude oil–CO₂–alcohol mixture

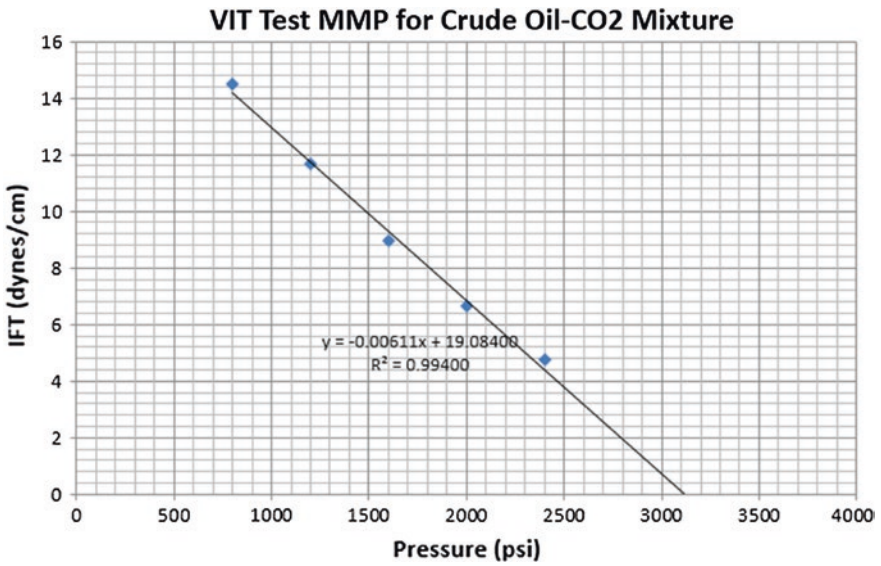


Fig. 3 MMP determination using VIT test for crude oil–CO₂ mixture

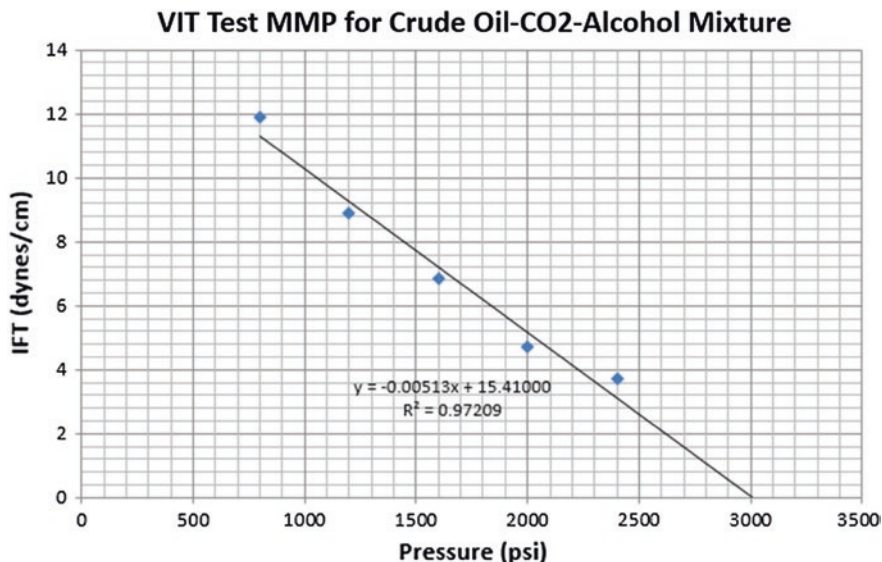


Fig. 4 MMP determination using VIT test for crude oil–CO₂–alcohol mixture

References

1. Ayirala, S.C. and D.N. Rao, *Miscibility Determination from Gas-Oil Interfacial Tension and P-R Equation of State*. The Canadian Journal of Chemical Engineering, 2007. **85**(3): p. 302-312.
2. A.M. Elsharkawy, F.H.P., and R.L. Christiansen, *Measuring Minimum Miscibility Pressure: Slim-Tube or Rising-Bubble Method?*, in *SPE/DOE Eighth Symposium on Enhanced Oil Recovery* 1992: Tulsa, Oklahoma.
3. Rao, S.C.A.a.D.N., *Miscibility Determination From Gas-Oil Interfacial Tension and P-R Equation of State*. The Canadian Journal of Chemical Engineering, 2007. **85**: p. 302- 312.
4. Benham, A.L., W.E. Dowden, and W.J. Kunzman, *Miscible Fluid Displacement - Prediction of Miscibility*, Society of Petroleum Engineers.
5. Holm, L.W. and V.A. Josendal, *Mechanisms of Oil Displacement By Carbon Dioxide*.
6. Rao, D.N., *A new technique of vanishing interfacial tension for miscibility determination*. Fluid Phase Equilibria, 1997. **139**(1): p. 311-324.
7. Saini, D. and D. Rao. *Experimental Determination of Minimum Miscibility Pressure (MMP) by Gas/Oil IFT Measurements for a Gas Injection EOR Project*. in *SPE Western Regional Meeting*. 2010.
8. Randall, T.E. and D.B. Bennion, *Laboratory Factors Influencing Slim Tube Test Results*.
9. Gardner, J.W. and J.G.J. Ypma, *An Investigation of Phase Behavior-Macroscopic Bypassing Interaction in CO₂ Flooding*. Society of Petroleum Engineers Journal, 1984. **24**(5): p. 508-520.
10. Djabbarah, N.F., *Miscible Oil Recovery Process using Carbon Dioxide and Alcohol*, U.S.P.a.T. Office, Editor 1990: US.

Investigating the Influence of Water Cut on Naphthenate Precipitation in Oil Production Facilities

Aliyu A. Sulaimon, Sathishkumar Arumugam and Bamikole J. Adeyemi

Abstract Naphthenic acids occur naturally in crude oils and can under certain conditions react with metal ions from produced water to form naphthenates. Precipitation of naphthenates can lead to serious problems in oil production facilities. Prediction of naphthenate precipitation is an important step toward early detection and resolution of their associated problems. Developing a method that will accurately predict precipitation of naphthenates in surface facilities and separators is of great value to the industry. In this paper, the principle of metal naphthenate formation is discussed. Experiments were conducted to investigate the effects of synthetic brine on naphthenic crude oil. The results were used to establish the relationship between produced water and the amount of naphthenate deposits. The experiments used a crude oil that has been classified as containing naphthenic acid and a laboratory-prepared synthetic brine. The pH of the brine was adjusted to suit the condition required for the experiment. Results show that increased water cut greatly influences the amount of precipitates. pH of subsequent mixtures increases as the volume of the brine is increased for each successive experiment. Precipitation of naphthenates occurs due to chemical reactions between the ions in both the brine and the naphthenic acid. It is established that as the produced water from reservoir increases, the amount of precipitates formed also increases since there are more ions made available for the chemical reaction. Maximum deposition of naphthenate precipitates occurred at 67 % water cut. The mass of precipitate measured at this water cut was 88 mg from 10 ml of crude oil and 136 mg from 20 ml of the same oil.

Keywords Precipitation · Naphthenates · Oil production facilities · Naphthenic acid · Produced water

A.A. Sulaimon (✉) · S. Arumugam · B.J. Adeyemi
Department of Petroleum Engineering, Universiti Teknologi Petronas,
31750 Tronoh, Perak, Malaysia
e-mail: alisulal1@yahoo.com

Nomenclature

Ca^{2+}	Calcium ion
Na^{+}	Sodium ion
V_o	Volume of crude oil
V_w	Volume of brine

1 Introduction

Naphthenic acid is a non-specific mixture of several cyclopentyl and cyclohexyl carboxylic acids with molecular weight ranging between 120 and 700 atomic mass units. The main fractions are carboxylic acids containing 9–20 carbon atoms. Presence of naphthenic acids in crude may cause corrosion and deposition problems in production facilities. When crude oil contains high content of naphthenic acids, it is said to have high total acid number (TAN). It can also be referred to as high acid crude oil (HAC). The oil industry has seen a trend toward producing more highly acidic oils since the early 1990s. This trend increases the potential for unexpected corrosion problems, but may extend the economic life of some existing production facilities.

The oil and gas industry has witnessed increased production of acidic crude oils containing naphthenic acids in large amounts. Studies [1, 3, 9] have shown that production of highly acidic crude oils will continue to increase. The corrosive nature of naphthenic acids is well known in the industry. However, the mechanism of its formation, characteristics, associated problems, and effective mitigation method require further investigation [9].

1.1 Naphthenic Acid Assessment in Crude Oil

Predicting crude oil corrosivity is critical, and it is a challenging aspect of production operations. Generally, the naphthenic acid content in oils is assessed in terms of TAN which is the amount of potassium hydroxide (KOH) in milligram required to neutralize a gram of oil sample. Values of TAN in the range of 0.1–3.5 mg KOH/g are common, but particularly severe situations (approx. 10 mg KOH) have been reported [4].

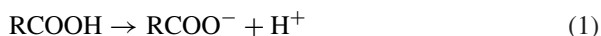
The complexity of the situation is evident considering that organic acid components in crude oils can vary considerably with their source [4]. Crude oils with TAN greater than 0.3–0.5 and refined crude oil fractions with a TAN higher than 1.5 are generally considered to be potentially corrosive due to the presence of naphthenic acid. The difference in these two values is due to the concentration of naphthenic acid in some hydrocarbon fractions during refining. However, such simple rules do not always indicate which hydrocarbon fractions and at what locations in the process the concentration of the corrosive acids will occur.

1.2 Formation of Naphthenates

Naphthenic acids, under certain conditions, react with metal ions contained in produced water to form metallic soaps. The metallic soaps formed are mainly calcium naphthenates and are insoluble in neither water nor oil. The soaps accumulate at the crude oil–water interface in separators due to their density [10]. Naphthenates cause a lot of problems as their deposits eventually clog the pipeline and cause delay and long shutdown periods. They also cause formation damage which leads to well productivity loss in petroleum reservoirs [11].

Rousseau et al. [7] presented a general review of naphthenate formation mechanism. In addition, a more comprehensive mechanism of naphthenate precipitation in the two end member naphthenate types (NaN and CaN) was described by Mohammed et al [6]. Later studies adopted the conceptual mechanism to study naphthenate precipitation in both model naphthenate systems and actual oil field production facilities. Due to the hydrophilic nature of the naphthenic acid group, naphthenates tend to congregate at the oil–water interface.

Due to pressure drop, carbon dioxide is lost from the solution during production. This increases the pH of brine, thereby leading to the dissociation of naphthenic acids as given below.



However, naphthenic acid is only fairly soluble in water except for the lower molecular weight naphthenic acids. The dissociated surface active naphthenate (RCOO^-) anion at the oil–brine interface reacts with either the calcium or the sodium ion in the brine to form either a soft (sodium) emulsion-type naphthenate or a hard (calcium) naphthenate at the oil–brine interface [11].

1.3 Case Studies

In many oil producing regions of the world, naphthenate deposition has resulted in blockage of surface equipment, increase in cationic content of crudes, extensive shutdown periods of offshore installations, and entrapment of oil in sludges [5]. Other severe problems during the separation of oil and water formation of very stable emulsions and/or insoluble deposits in separators or crude dehydration/desalting vessels have also been reported [2].

1.4 Naphthenic Acid Detection in Crude Oil

Many recently discovered fields produce oil with a high acid content. Identification of most individual members of the complex mixtures of carboxylic acids found in petroleum (naphthenic acids) has eluded chemists for over a

century; they remained unresolved by conventional gas chromatographic methods. Recently, two-dimensional comprehensive gas chromatography/mass spectrometry was developed to identify numerous individual diamondoid acids in the naphthenic acids of oil sands process water. Results confirmed that oil sands process water and refined petroleum contain very different distributions of acids [8].

2 Methodology

Produced water contains salts which when dissociate will leave their metal ions to react with naphthenic acid. The method adopted in this work was to reproduce the phases of reservoir fluids where the amount of produced water is increased with time. Two experiments were conducted to investigate the effect of water cut on naphthenate precipitation. The first experiment carried out was the “base case” naphthenate experiment where the specific crude sample that contained a certain amount of naphthenic acid was mixed with brine.

A volume of oil (V_o) was mixed with a synthetic brine of volume (V_w). This synthetic brine contained about 20,000 ppm of sodium ion (Na^+) and 15,000 ppm of calcium ion (Ca^{2+}). The pH of synthetic brine was also adjusted to nine. For the base case experiment, V_w was considered to be equal to V_o . The mixture was mixed in a bottle and left for precipitation to take place. Final pH of the mixture and the mass of precipitate were measured at the end of the experiment.

The second experiment was similar to the base case experiment, but the volume of synthetic brine, V_w , was varied. Amounts of precipitate were measured along with the final pH of the resulting mixture. The order of the experiments is highlighted here. A crude sample that contains some percentage of naphthenic acid was prepared.

Synthetic brine that contains 20,000 ppm of Na^+ and 15,000 ppm of Ca^+ with a pH value of nine was also prepared. Both the crude oil and synthetic brine were mixed together in a small laboratory bottle. The solution was left for 1 day, and any changes to the mixture in the bottle were observed. The pH value of the mixture was taken, and the mass of any precipitates was measured. This experimental procedure was repeated seven times varying the volume of synthetic brine while keeping the volume of crude oil constant. The other sets of experiments carried out used double amount of constant crude oil volume (V_o) and also double amount of the brine used in the first experiment.

3 Results and Discussions

The volume of crude oil used in the first set of experiments is 10 ml, and it was kept constant throughout the entire experiments. The original pH of the crude oil was 2.11. No naphthenates were present in the original crude oil before the experiment. The volume of brine used was varied at 1.25 ml interval starting from zero (at no water cut). Water cut values were calculated and the change in pH was

Table 1 Mass of naphthenate precipitated, water cut and pH for different brine concentrations with 10 ml crude oil

Volume of brine (ml)	Water cut (%)	pH of final mixture	Mass of precipitate (mg)
0.00	0.00	2.11	0.00
1.25	11.11	2.32	10.00
2.50	20.00	3.11	38.00
5.00	33.33	3.35	51.00
7.50	42.86	3.50	62.00
10.00	50.00	3.81	69.88
20.00	66.67	4.21	88.00
50.00	83.33	4.98	71.00

Table 2 Mass of naphthenate precipitated, water cut and pH for different brine concentrations with 20 ml crude oil

Volume of brine (ml)	Water cut (%)	pH of final mixture	Mass of precipitate (mg)
0.00	0.00	2.11	0.00
2.50	11.11	2.30	17.00
5.00	20.00	3.15	65.00
10.00	33.33	3.33	90.00
15.00	42.86	3.60	105.00
20.00	50.00	3.86	128.88
40.00	66.67	4.19	136.00
100.00	83.33	4.93	124.00

measured. The mass of naphthenate precipitates was also measured and recorded. These results are shown in Table 1. The fixed volume of crude oil used in the second experiment is 20 ml. The procedure for the first set of experiments was also followed in the second set. The volume of brine used was varied at twice the previous value. The results are presented in the following paragraphs (Table 2).

3.1 Naphthenates Precipitation at 10 ml Crude Oil

At 11.11 % water cut when 1.25 ml of brine was added to 10 ml base crude oil, the amount of naphthenate precipitated was 10 mg. In another step, the volume of brine in the mixture was increased to 2.5 ml at 20 % water cut. More naphthenates were precipitated increasing the amount to 38 mg. When the water cut was made 33.33 % (5 ml of brine in the mixture), naphthenate accumulation amounted to 51 mg. The volume of brine was raised to 7.5 ml at 42.86 % water cut, and the amount of naphthenate precipitate increased to 62 mg. A condition where equal amounts of crude oil and water are produced was also simulated.

When the water cut increased to 50 %, 69 mg of naphthenate precipitated out of the mixture. Two more steps were taken by increasing the volume of brine in

Fig. 1 Plot of mass of precipitate against water cut (10 ml crude oil in the mixture)

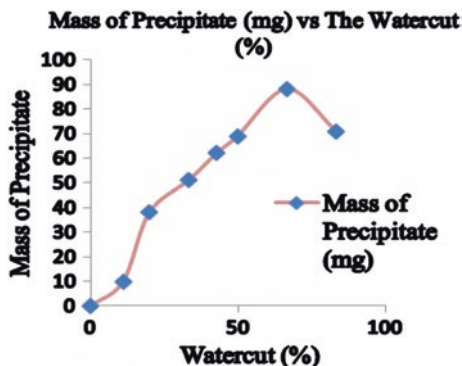
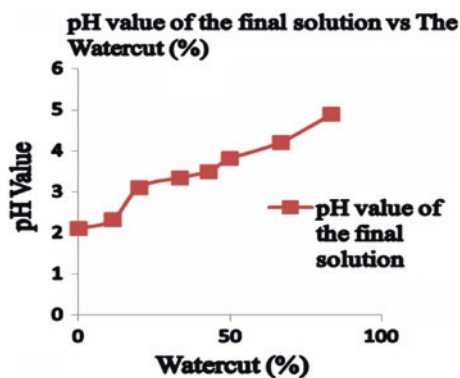


Fig. 2 Plot of pH versus water cut (10 ml of crude oil in the mixture)



the mixture to 20 ml (66.67 % water cut) and 50 ml (83.33 % water cut) successively. 88 mg of naphthenate and 71 mg of naphthenate precipitated, respectively. Figure 1 shows the plot of mass of precipitate against water cut.

Figure 2 shows the trend obtained for change in pH as water cut increased during the experiments. An increase in pH was observed throughout the experimental process. This shows the neutralization reaction between the naphthenic acid contained in the crude and the brine. Even at 83.33 %, the pH of the mixture was still 4.89 confirming the mixture being acidic.

3.2 Naphthenate Precipitation at 20 ml Crude Oil

The volume of the base crude oil was made 20 ml. The same amount of water cut as observed in experiment 1 was tested. 17 mg of naphthenates was precipitated at 11.11 % water cut. A significant increase in amount of precipitate was observed, and then, the water cut was increased to 20 %. 65 mg of naphthenates was measured. The amount of precipitates that was measured at 33.33 % water cut was 90 mg

Fig. 3 Plot of mass of precipitate against water cut (20 ml crude oil in the mixture)

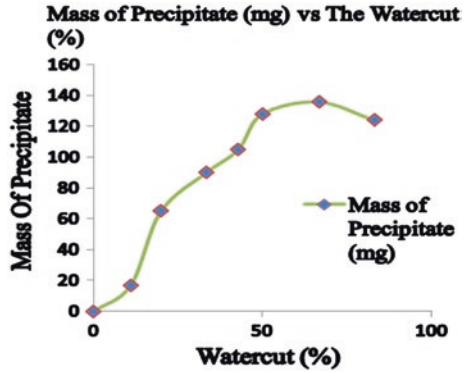
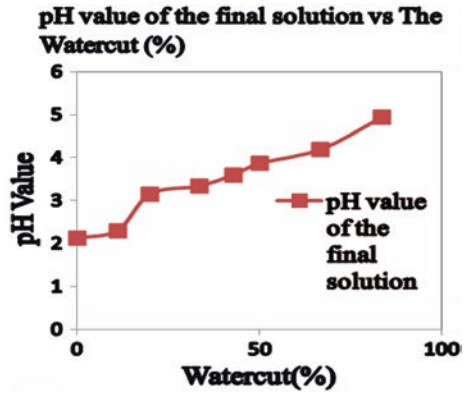


Fig. 4 Plot of pH versus water cut (20 ml crude oil in the mixture)



of naphthenates. For 42.86 % water cut, the precipitated amount was 105 mg. Further addition was made to bring the water cut to 50 %. The naphthenate precipitate measured was 128 mg, while 66.67 % water cut was also achieved by adding 40 ml of brine to the mixture. The amount of precipitated naphthenates was 136 mg.

Finally, the volume of brine (100 ml) was made five times the volume of the crude oil (20 ml) in the mixture. A reduction in the mass of naphthenate precipitate was observed. The measured precipitate was 124 mg. The plot of mass of naphthenate precipitate against water cut is shown in Fig. 3. Figure 4 shows the trend obtained by change in pH as brine was added to the mixture. This is similar to the trend obtained in experiment 1.

3.3 Additional Naphthenate Precipitation

Figures 1 and 2 show that naphthenate precipitation begins when brine is introduced into the system. The amount of precipitates also increases as further addition is made to a water cut of approximately 67 % and then reduces. This trend

can be explained by taking the amount of naphthenic acid in the crude oil into consideration. When brine is mixed with crude oil, a chemical reaction occurs between the acidic contents of the crude oil and the brine. This leads to precipitation of naphthenates. As more brine is added, the remaining acid in the crude oil reacts. After sufficient addition, the chemical reaction experiences retardation and the amount of naphthenate precipitate therefore reduces. It would be correct to say that if the addition continued, precipitation of naphthenates would eventually stop.

Analysis of the results presented for the first experiment shows that 10 mg of naphthenate precipitated when 1.25 ml of brine was added to the crude oil. An increase of 28 mg of naphthenate was observed when another 1.25 ml of brine was added to the mixture. After this, a drop in subsequent precipitate addition was recorded. When the volume of brine was increased to 5 ml, only 13 mg additional naphthenate precipitated. The reduction continued as more brine was added to the mixture. At approximately 67 % water cut, the amount of additional precipitate increased from 7 to 19 mg. This point was the peak of the reaction between the naphthenic acid and the brine. After that, the reduction in the additional precipitate continued and occurred at steeper rates.

The same scenario was experienced in experiment 2. The sudden increase in additional naphthenate precipitate occurred at 50 % water cut. Thereafter, there was an accelerated reduction in additional naphthenate precipitates. The pH of the mixture also increased with respect to addition of brine as shown in Figs. 2 and 4.

4 Conclusion

Experiments have been conducted to investigate the relationship between water cut and naphthenate precipitation. Amount of naphthenate precipitation and change in pH values with respect to water cut have also been observed. It has been shown that naphthenate precipitation increases with water cut. The maximum amount of naphthenates was measured at 67 % water cut. It has also been observed that even when the water cut approached 85 %, naphthenates can still precipitate in large amount. As the produced water from reservoir increases, the amount of precipitates formed will also increase since there are more ions made available to react with the naphthenic acid particles. Earlier preparations should be made to handle crude oil with naphthenic acid content before high water cut is experienced.

References

1. Alec Groysman, Naphtali Brodsky, Joseph Pener and Dmitry Shmulevich, 2007. Low Temperature Naphthenic Acid Corrosion Study, 07569, NACE International.
2. Bretherton, N., Smith, R., Keilty, G., and S. Ubbels, S., 2005. Naphthenates Control: Is Acetic Acid Injection the Answer? Paper SPE 95115 presented at SPE International Symposium on Oilfield Corrosion held on 13 May, Aberdeen, United Kingdom.

3. Goldszal, A., Hurtevent, C. and Rousseau, G., 2002. Scales and Naphthenates Inhibition in Deep-Offshore Fields. Paper SPE74661 presented at SPE Oilfield Scale Symposium, held on 1st Nov., in Aberdeen, UK.
4. Kane, R.D. and Cayard, M.S., 2002. A Comprehensive Study on Naphthenic Acid Corrosion. Paper 02555. CORROSION 2002, NACE International.
5. Mohammed, M. A., 2010. Characterization, Modeling, Prediction and Inhibition of Naphthenate Deposits in Oilfield Production. Thesis. Heriot-Watt University.
6. Mohammed, M.A., Sorbie, K.S and Shepherd, A.G., 2009. Thermodynamic Modeling of Naphthenate Formation and Related pH Change Experiment. SPE Production & Operation Journal (August) 466–472.
7. Rousseau, G., Zhou, H., Hurtevent, C., 2001. Calcium Carbonate and Naphthenate Mixed Scale in Deep-Offshore Fields. Paper SPE 68307 Presented at SPE Oilfield Scale Symposium held in Aberdeen, UK.
8. Rowland, S.J., West C.E., Scarlett, A.G. and Jones, D., 2011. Identification of Individual Acids in a Commercial Sample of Naphthenic Acids from Petroleum by Two-Dimensional Comprehensive Gas Chromatography/Mass Spectrometry, PMID: 21598334 [PubMed - indexed for MEDLINE], June.
9. Slavcheva, E., Shone, B. and Turnbull, A., 2002. Review of Naphthenic Acid Corrosion in Oil Refining, Br Corrosion Journal, 34(2) (1999) 125-131.
10. Trond E. H., 2002. Formation of Calcium Naphthenates in Water/Oil Systems, Naphthenic Acid Chemistry and Emulsion Stability, October.
11. Sarac, S., and Civan, F., 2007. Experimental Investigation and Modeling of Naphthenate Soap Precipitation Kinetics in Petroleum Reservoirs. Paper SPE 106074 presented at the International Symposium on Oilfield Chemistry, Houston, TX, USA.

Wax and Asphaltene Deposition Tendency of Malaysian Crude Oils

Aliyu Adebayo Sulaimon and Mohamad Hazwan Yusoff

Abstract Flow assurance is a term generally used to describe the processes that may lead to fluid flow restriction in production, processing and transportation systems, and also the comprehensive management of the processes and operations to ensure effective and efficient production and delivery of oil and gas from the reservoir to the refinery. Often, the flow assurance issues are largely associated with hydrates, organic waxes and asphaltenes deposition due to changes in fluid composition, pressure and temperature conditions. Organic wax starts to precipitate from oil when temperature falls below the cloud point. The focus of this research is to characterize Malaysian crude oils from Dulang, Tapis, Miri, Dubai, and Arab fields to evaluate their tendency to precipitate wax and/or asphaltene. The oils were characterized by conducting SARA analysis with high-performance liquid chromatography (HPLC), while carbon distribution of the oils was determined by gas chromatography mass spectrometry (GC-MS). Differential scanning calorimetry (DSC) and density meter were used to measure the WAT of waxy oils and the colloidal instability index (CII) was calculated to evaluate asphaltene deposition potential. The effect of continuous carbon dioxide (CO₂) injection on WAT was also investigated. Results show that crude oils with higher paraffinic content exhibit higher WAT and precipitated wax. Continuous gas injection was found to lower the WAT, thus reducing the risk of wax precipitation. Tapis oil with highest CII (5.05) is the most susceptible to asphaltenes deposition, while Arab oil with CII of 1.21 has the least tendency to cause asphaltenes deposition problems.

Keywords Wax appearance temperature · SARA · Colloidal instability index · Asphaltenes

A. A. Sulaimon (✉) · M.H. Yusoff
Department of Petroleum Engineering, Universiti Teknologi Petronas,
Perak, Malaysia
e-mail: alisulal1@yahoo.com

1 Introduction

Crude oil is composed of complex compounds containing hundreds to thousands of organic and inorganic components from simple low molecular weight *n*-alkanes to high molecular weight waxes and asphaltenes. Crude oil is colloidal in nature due to the content of high molecular weight substances.

The oil in reservoir exists in thermodynamic equilibrium, but during production, composition, pressure, and temperature change, thereby altering the equilibrium leading to phase separation and hence precipitation of waxes and asphaltenes. Wax is a normal alkane group that has 16 or more carbon atoms that will change to crystalline solid substances at about 20 °C [1]. The wax in crude oil is a mixture of normal hydrocarbons with different carbon number distributions which can be identified by using gas chromatography (GC). Macrocrystalline wax (C₁₈–C₃₆) and microcrystalline wax (C₃₀–C₆₀) are two different types of wax that can be found in crude oil. Both of them are made up of aligned paraffinic and naphthenic molecules [1]. Macrocrystalline waxes are mainly composed of straight-chain paraffins (*n*-alkanes) with different chain length while microcrystalline waxes contain high amount of isoparaffins and naphthenes [2]. The straight-chain structure of macrocrystalline waxes causes it to be more sensitive to temperature changes. Wax deposition occurs in crude oil that generally has *n*-paraffin as constituents; when the wellbore temperature falls below the cloud points. Wax crystallization forms and contributes to increase in pressure drop, reduction in productivity, and subsequently choking the production lines, causing emergency shutdown [3]. In subsea completion (where flow line temperature on the ocean floor ranges from 1.5 to 5 °C), each wax component becomes less soluble until the higher molecular weight components solidify [3].

The onset of crystallization is known as the wax appearance temperature (WAT) and as the temperature drop below WAT, the crude's flow properties change from a simple Newtonian fluid to a two-phase dispersion non-Newtonian fluid. This results in gelation of crudes and loss in flow-ability [3]. In practice, the WAT can be determined experimentally by using several methods such as differential scanning calorimetry (DSC), cross-polar microscopy (CPM), light transmittance (LT), viscometry, cold finger (CF), filter plugging (FP), Fourier transform infrared spectroscopy (FTIR), and ASTM D2500-88 [4].

Saturate, Aromatic, Resin and Asphaltene (SARA) analysis is used to characterize the crude oil. This area of study was first introduced by Jewell et al. [5]. The basis for SARA fractionation was developed [5]. It is the method that categorizes crude oil components based on their polarity and polarizability. Saturates are a non-polar hydrocarbon components such as paraffin, while aromatics are slightly more polarisable, but resins and asphaltenes have polar substituents. Precipitation of organic waxes and asphaltene flocculation has been identified as the main equipment fouling precursors. Though standard procedure ASTM D2007 for SARA fractionation is readily available, the method is tedious, lengthy, laborious, expensive and requires more solvents [6]. A high-performance liquid chromatography (HPLC)

method is an efficient alternative to the ASTM D2007-73 since the separation process is faster [7]. It is also automated as well as more reproducible.

In this work, a number of techniques were used to characterize crude oil samples from five main fields for analysis. The WAT was measured by DSC and density meter, while the Universal Oil Products (UOP) 46-64 method was used to measure the wax content. The HPLC and GCMS were used for SARA analysis and determination of carbon distribution, respectively.

2 Experimental Details

2.1 Samples

Five crude oil samples were used in this study, namely Dulang, Tapis, Miri, Dubai, and Arab. Dulang crude oil was reported to have severe problems of wax precipitation and deposition during its production and transportation. The samples were preheated to 80 °C for 8 h in water bath to achieve homogenous mixture of the crudes as well as to eliminate the thermal history which can affect the results.

2.2 SARA Fractionation

ASTM D3279 was used to remove asphaltene from the crude oil samples. The de-asphalted crude oil (maltenes) was reduced to saturates, aromatics, and resins using Agilent 1260 Infinity HPLC [8]. The HPLC unit was set up using volatile organic compounds (VOC) standards provided by Agilent for various conditions. The mixture comprises 100 $\mu\text{g mL}^{-1}$ each of *n*-pentadecane, *n*-decane, *n*-octadecane, *n*-tridecane, toluene, 1-methylnaphthalene, 1,3-diisopropylbenzene, and phenanthrene dissolved in *n*-pentane. Two 9.4×250 mm Zorbax NH₂ columns with 5- μm packing were used in series with a UV detector operating at a wavelength of 254 nm [9].

Dichloromethane (DCM), *n*-hexane, and iso-propanol (IPA) were used as solvents. The maltenes were filtered using a 0.2- μm PTFE syringe filter into 1.5-inch glass vial. During HPLC separation, saturates and aromatics were firstly eluted and dichloromethane was used to extract the resins being retained in the column. The system was then cleaned for the next analysis by flushing with IPA and *n*-hexane for 15 min.

2.3 Differential Scanning Calorimetry

The DSC method has been used to measure WAT of crude oil due to its accuracy, simplicity, reliability, and fast response. The WAT of the crude oil samples was measured using Setaram μDSC7 Evo. It allows the experiment to be run from

subambient temperature of $-45\text{ }^{\circ}\text{C}$ up to $120\text{ }^{\circ}\text{C}$ and under high pressure up to 400 bars. The cell used in this method is standard Hastelloy. In this study, approximate 50 mg of samples were tested at atmospheric pressure. Each sample was first heated to $70\text{ }^{\circ}\text{C}$ and held for 3 min before being cooled to $-20\text{ }^{\circ}\text{C}$ at a rate of $2\text{ }^{\circ}\text{C}/\text{min}$. The WAT was determined as the onset of the exothermic peak during the cooling process corresponding to the liquid–solid transition.

2.4 Density Meter

Anton Paar density meter was used to determine the density of the sample. The equipment was set up for a temperature scan by cooling the samples from 50 to $0\text{ }^{\circ}\text{C}$ at atmospheric pressure. Temperature step of $2\text{ }^{\circ}\text{C}$ was selected. The measurements by Anton Paar density meter were carried out according to ASTM Standard D5002-99. The density meter gives fast, reliable, and accurate measurement, and it requires small amount of sample.

2.5 Gas Chromatography Mass Spectrometry

A GC mass spectrometry (Agilent 5975C/7890A) was used to identify different carbon number in the crude oil samples. DB-5 silica capillary column was set up, and oven temperature was programmed from $120\text{ }^{\circ}\text{C}$ (hold 3 min) to $270\text{ }^{\circ}\text{C}$ (hold 40 min) at $10\text{ }^{\circ}\text{C}/\text{min}$. Splitless injection was carried out when the temperature reaches $300\text{ }^{\circ}\text{C}$. Constant flow rate mode was set at $2\text{ cm}^3/\text{min}$, while mass spectrometry (MS) transfer line is set at $300\text{ }^{\circ}\text{C}$. The ion source was kept at $230\text{ }^{\circ}\text{C}$.

2.6 Wax Content

Wax content for each crude oil sample was measured by using UOP46-85 method. The collected wax was weighed to calculate the wax content in the crude oil samples.

3 Results and Discussion

3.1 SARA Fractionation

SARA fractionation was successfully quantified using ASTM D 3279-97 and modified ASTM D 6591-06 methods. The results of the analysis for all samples are summarized in Table 1. Colloidal instability index (CII) is one of the methods

Table 1 SARA analysis of five crude oils

Component	Dulang	Arab	Tapis	Miri	Dubai
	(wt%)				
Saturates	82.15	51.36	83.03	66.05	77.80
Aromatics	15.41	38.16	15.09	22.78	17.66
Resins	2.26	7.16	1.75	10.83	4.42
Asphaltene	0.18	3.33	0.13	0.34	0.12
CII	4.66	1.21	5.05	1.98	3.53

used to analyze crude oil system with asphaltene deposition problems [13, 14]. It is the ratio of the total asphaltenes and saturates to the total of aromatics and resins. CII below 0.7 is considered as stable, while CII higher than 0.9 is considered as unstable. The presence and abundance of asphaltenes and high carbon number paraffins typically, but not always, indicates the potential for asphaltene and/or paraffin deposition during oil recovery.

The relative abundance of aromatics and resins reduces the tendency of paraffins and asphaltenes to drop out of solution during petroleum production. Hence, the entire petroleum composition must be taken into account and not only the presence of asphaltenes and paraffins, but also the relative abundance of aromatics and resins [10–12]. If there are no asphaltenes and high carbon number paraffins present in a crude oil, no asphaltene and/or paraffin deposition could be expected. Their presence, however, does not necessarily imply problematic organic deposition.

Table 1 shows the result of SARA analysis conducted on five Malaysian crude oil samples—Dulang, Arab, Tapis, Miri, and Dubai. Observation shows that all the oils are susceptible to asphaltene deposition problems since the colloidal instability indices are greater than 0.9. The weight percentage of asphaltene in Arab crude oil is high, but the average value of CII is 1.21, while Tapis crude oil with the lowest asphaltene content has a higher CII value (5.05). Therefore, Tapis, Dulang, and Dubai crude oils have higher tendency to precipitate asphaltenes, while Miri and Arab crude oils that are more stable would require adequate production management measures to prevent deposition of asphaltenes in production facilities.

3.2 Wax Analysis

The WAT and wax content of crude oil samples have been measured using DSC and UOP-46 methods respectively. Figures 1, 2, 3 and 4 show the plots of heat flow against furnace temperature for Dulang, Tapis, Miri, and Dubai, respectively. It represents the cool down portion of the heat flow curve. The WAT is denoted by the section of the curve where the steep rise in heat flow begins.

The result for WAT is shown in Table 2. WAT measurement for each sample was repeated three times with different weight, and the result shows that the WAT is approximately constant. Therefore, the weight of sample does not affect the magnitude of WAT.

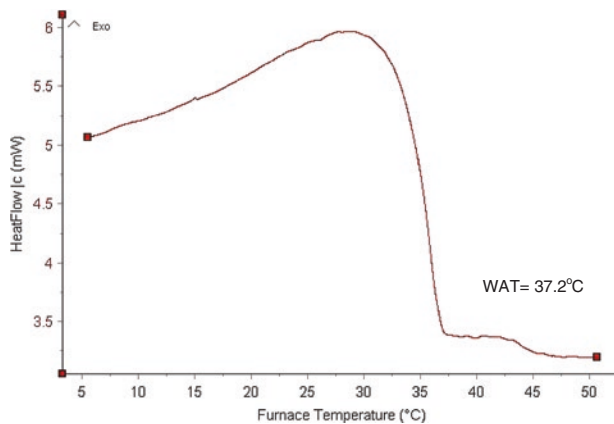


Fig. 1 Heat flow versus furnace temperature for Dulang crude oil

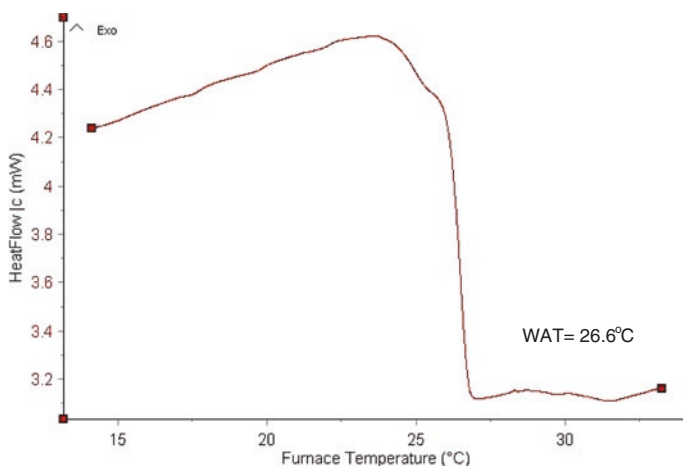


Fig. 2 Heat flow versus furnace temperature for Tapis crude oil

The density against temperature plots obtained during cooling process for the crude oil samples are as shown in Figs. 5, 6, 7 and 8. The WAT was determined by drawing a straight line over density data. A slight change in the slope of the line indicates the WAT of the sample. As observed, the plot for Dulang, Tapis, and Miri crude oil samples shows a clear and significant change in the slope. However, for Dubai crude oil, there is no significant change in the slope for the whole density data. This is due to the low wax content in Dubai crude oil. Perhaps, density meter method is suitable only for crude oil samples with high wax content.

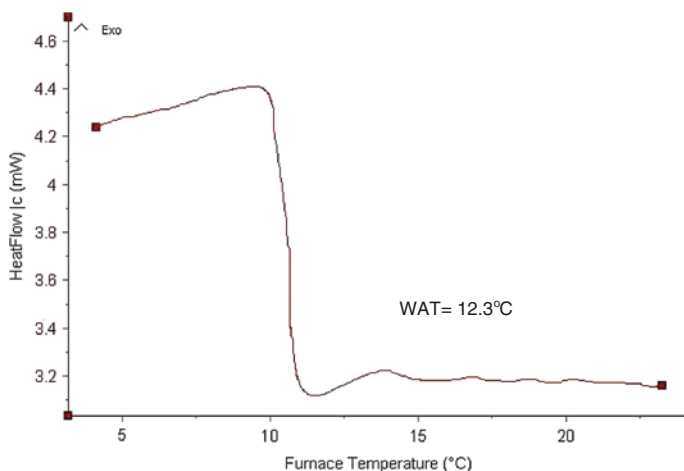


Fig. 3 Heat flow versus furnace temperature for Miri crude oil

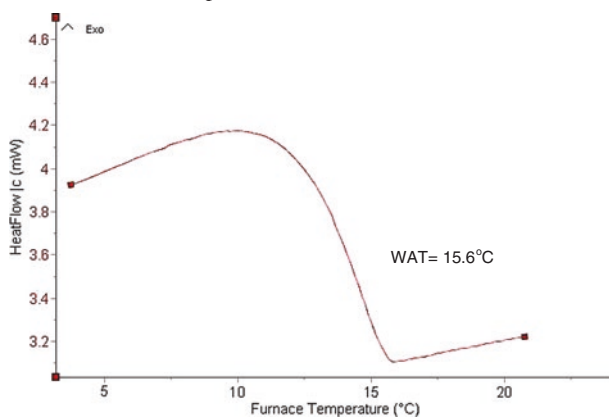


Fig. 4 Heat flow versus furnace temperature for Dubai crude oil

Table 2 WAT measurement by DSC and density meter

Sample	Weight(mg)	WAT (°C) by DSC	WAT (°C) by density meter
Dulang #1	60	37.52	37
Dulang #2	79	36.97	–
Dulang #3	118	36.99	–
Tapis #1	52	26.36	25
Tapis #2	61	26.69	–
Tapis #3	130	26.86	–
Miri #1	65	12.34	12
Miri #2	75	12.30	–
Miri #3	101	12.44	–
Dubai #1	49	15.62	–
Dubai #2	81	15.41	–
Dubai #3	126	15.88	–

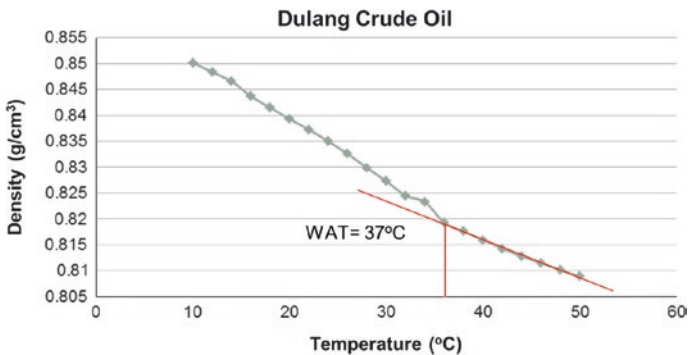


Fig. 5 Density versus temperature for Dulang crude oil

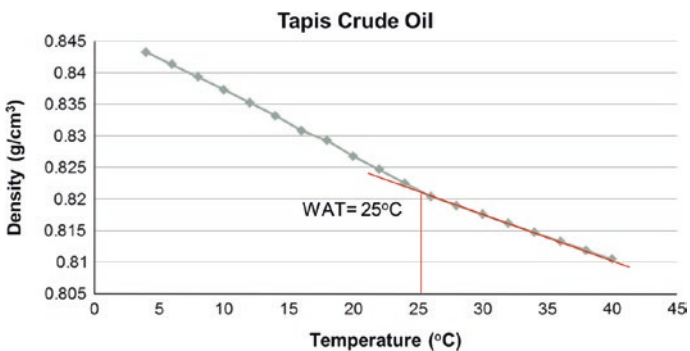


Fig. 6 Density versus temperature for Tapis crude oil

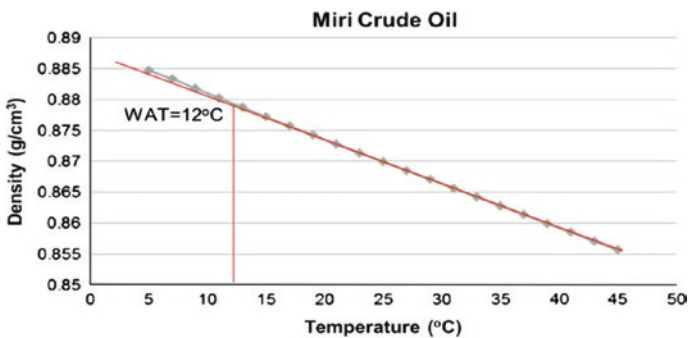


Fig. 7 Density versus temperature for Miri crude oil

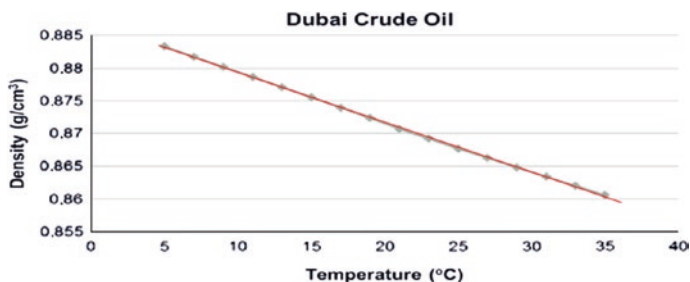


Fig. 8 Density versus temperature for Dubai crude oil sample

3.3 Wax Content

Tables 3 and 4 show the wax content and the total area percentage (area %) for carbon numbers ranging from C₂₀ to C₄₀, respectively. Total area percentage (Figs. 9, 10, 11 and 12) is obtained from the GCMS. Considering the Dulang, Tapis, and Dubai crude oil samples, comparative analysis of results shows that there is a relationship between paraffinic components, WAT, and wax content. Dulang oils with highest content of paraffinic components exhibit higher WAT and wax content, while Dubai oils with lowest content of paraffinic components have lower WAT and wax content. The straight-chain structure of macrocrystalline waxes makes it more sensitive to temperature changes hence increasing the WAT. This relationship is important for the development of wax deposition prediction models. Dulang, Tapis, Miri, and Dubai were sorted by API gravity to compare wax content with increasing specific gravity. Intuitively, heavier oil should contain more wax than lighter oil strictly based on the definition of wax. However, the API gravity of the crude oils does not have sufficient effect on the wax content.

Table 3 Wax content

Sample	°API	Wax content (wt%)
Dulang	37.60	28.5
Tapis	39.39	17.1
Miri	31.33	4.7
Dubai	30.95	6.2

Table 4 Total area percent (C₂₀–C₄₀)

Samples	Dulang	Tapis	Dubai	Arab
Total area percent (%)	24.599	24.291	8.514	8.017

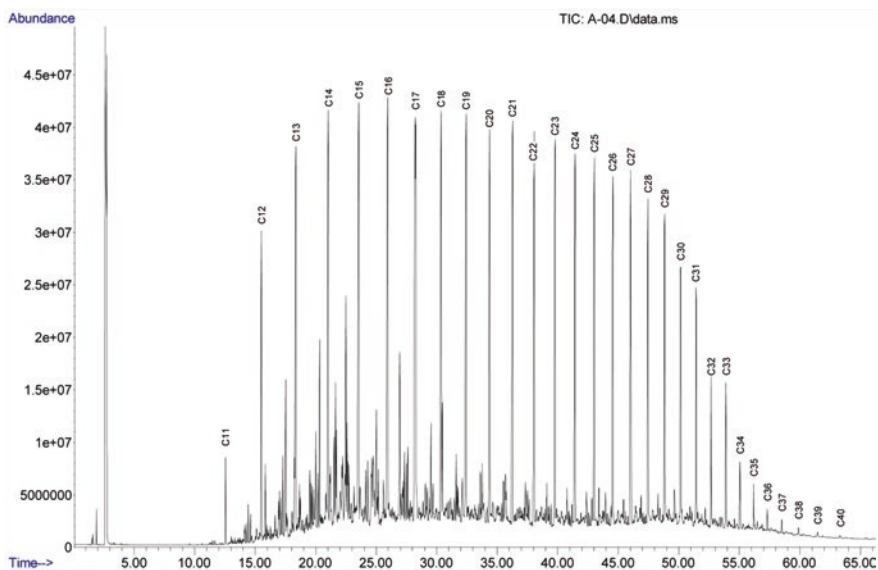


Fig. 9 Chromatogram for Dulang crude oil

3.4 Effect of CO₂ Injection on WAT

An experiment was also conducted to study the effect of CO₂ injection on WAT. Dulang crude oil was run through continuous CO₂ flooding at 98 °C and 3,000 psia. The sample was later run through differential scanning to measure the WAT. The result shows that the WAT for Dulang crude oil after CO₂ injection decreased to 32.4 from 37.2 °C. The reduction in WAT was discovered to have been the effect of supercritical carbon dioxide which must have dissolved the wax [15]. Supercritical carbon dioxide occurred when the carbon dioxide was held above its critical temperature and critical pressure which is 30 °C and 1,070 psia, respectively. Figure 13 shows the plot of heat flow against furnace temperature for Dulang crude oil after CO₂ injection.

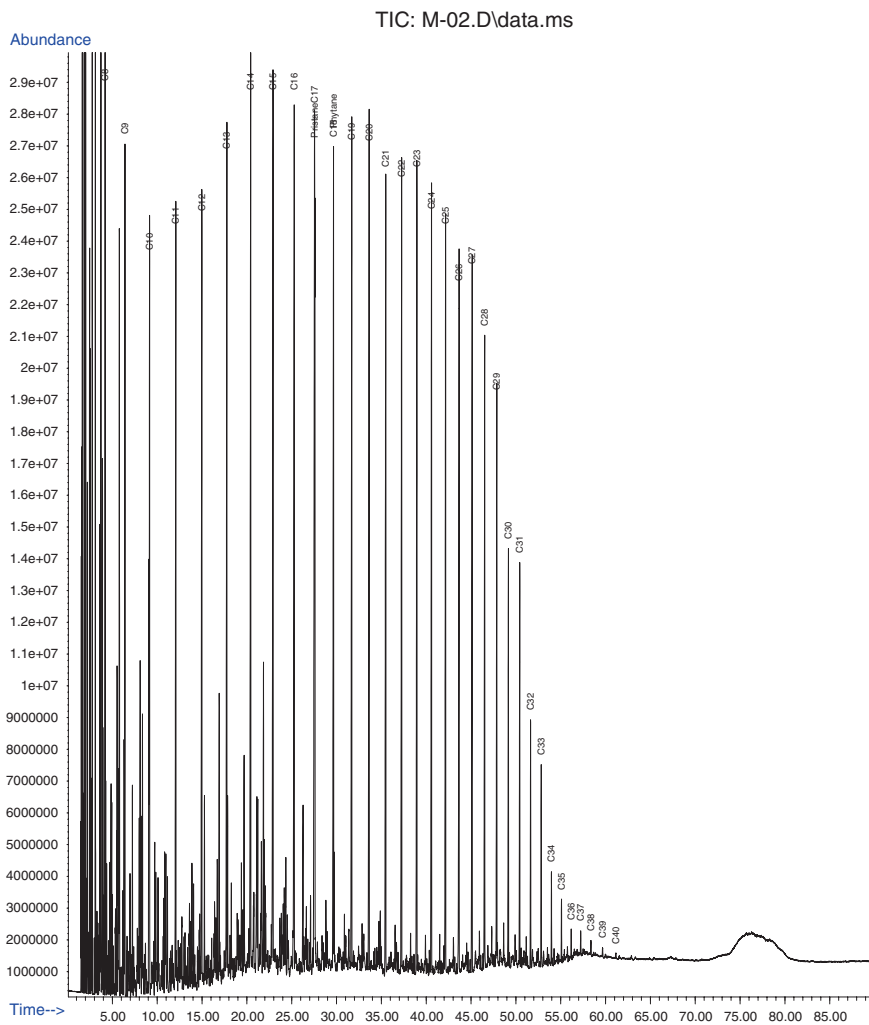


Fig. 10 Chromatogram for Tapis crude oil

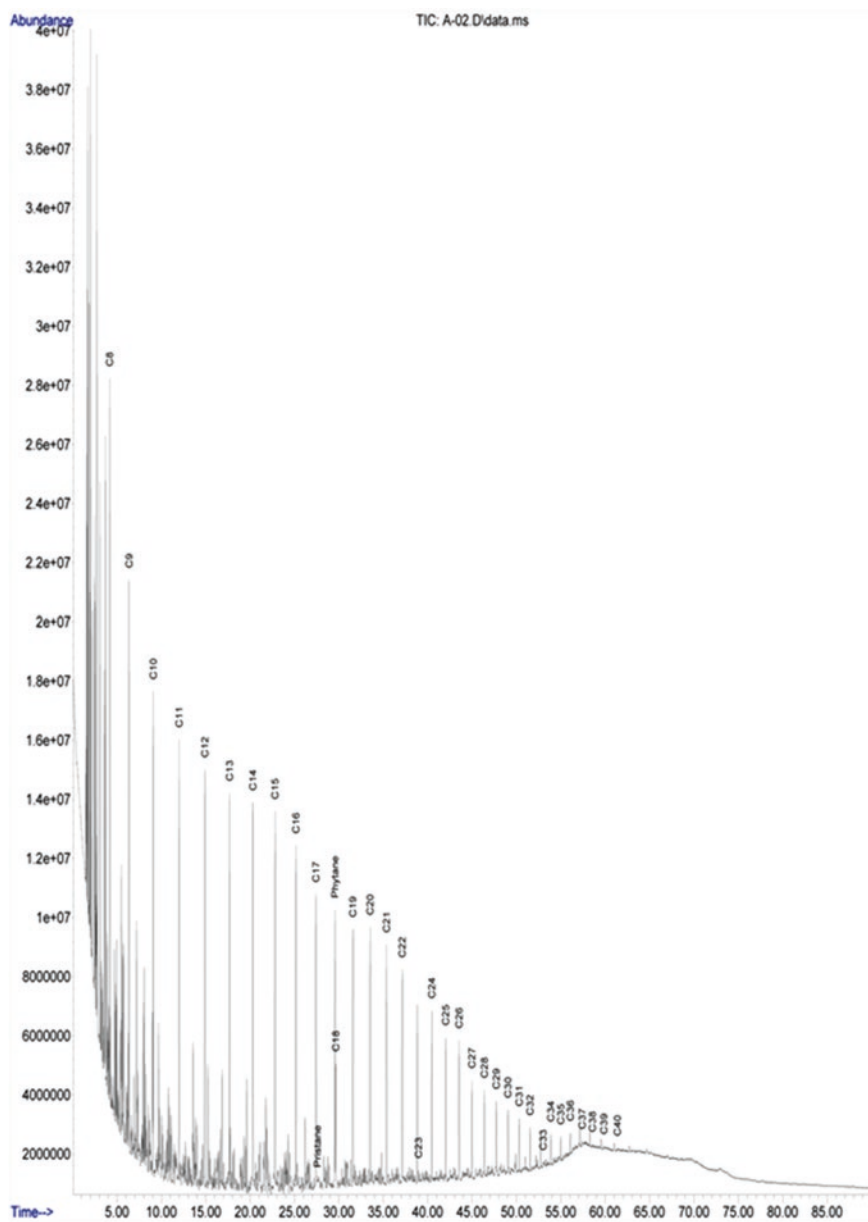


Fig. 11 Chromatogram for Dubai crude oil

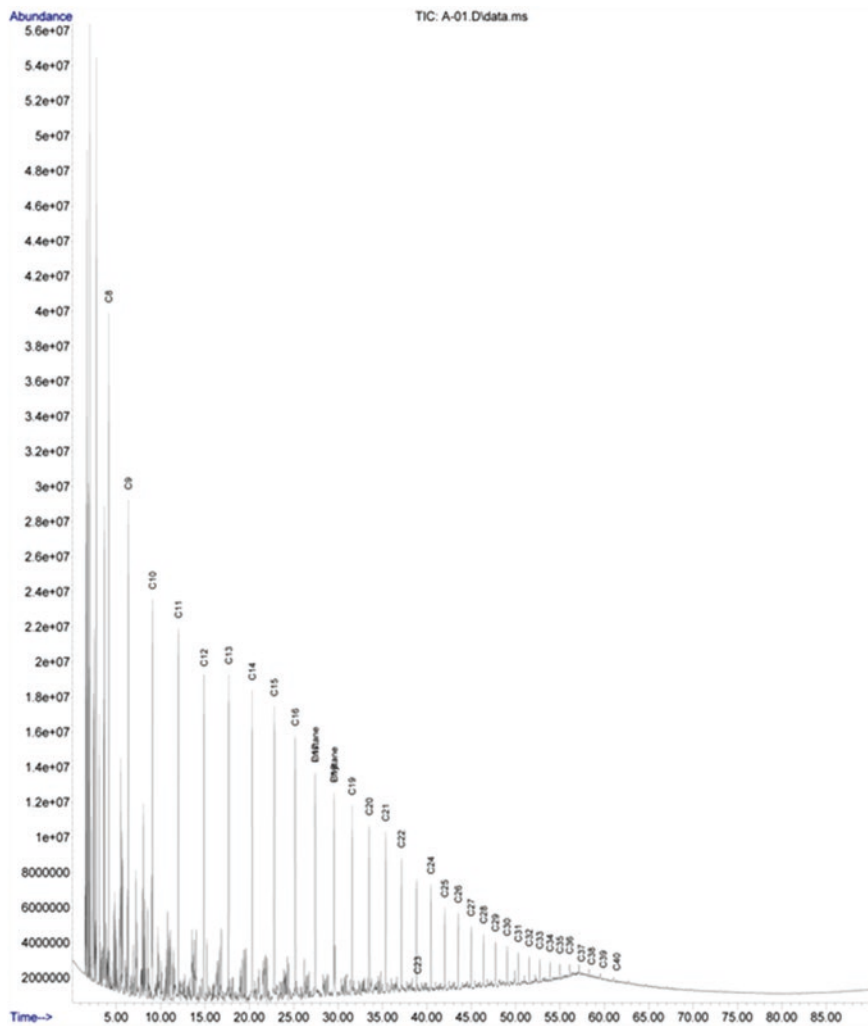
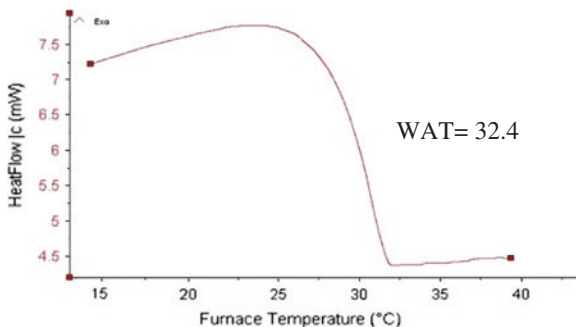


Fig. 12 Chromatogram for Arab crude oil

Fig. 13 WAT of Dulang crude oil After CO₂ injection



4 Conclusions

SARA analysis has been used to characterize crude oil samples. The results of WAT obtained from both DSC and density meter are similar particularly for oils containing high wax content. Observation shows that the WAT is sensitive to the amount of wax in the oil. Therefore, crude oils with higher paraffin content will precipitate at a higher WAT than oils containing less paraffinic components. Continuous CO₂ injection also affects wax precipitation by lowering the WAT as shown for Dulang oil. Analyses have also shown that crude oils with high CII exhibit the highest risk for asphaltene precipitation.

Acknowledgments The authors wish to appreciate the PETRONAS Carigali for providing the crude oil samples used for the study.

References

1. Kok, M.V. & Saracoglu, O. 2000. Mathematical modelling of wax deposition in crude oil pipeline systems. Report Number SPE 64514, Middle East Technical University, Ankara-Turkey.
2. Elsharkawy, A.M., Al-Sahhaf, T.A., Fahim, M.A., & Al-Zabbai, W. 1999. Determination and prediction of wax deposition from Kuwaiti crude oil. Report Number SPE 54006, Kuwait University, Safat, Kuwait.
3. Li, H., & Zhang, J. 2003. A generalized model for predicting non-newtonian viscosity of waxy crudes as a function of temperature and precipitated wax. *Fuel*, 82, 1387–1397.
4. Hammami, A., Ratulowski, J. & Coutinho, J.A.P. 2003. Cloud points: Can we measure or model them?
5. Jewell, D.M., Weber, J.H., Bunger, J.W., Plancher, H. & Latham, D.R. 1972. Ion-exchange, coordination and adsorption chromatographic separation of heavy-end petroleum distillates. *Anal. Chem.*, 44: 1391-1395
6. ASTM D2007, 1993. 11 Standard test method for characteristic group in rubber extender and processing oils by the clay-gel adsorption chromatographic method. ASTM International, USA.
7. Suotani, J.C. & Swab, R.E. 1975. Rapid hydrocarbon group-type analysis by high performance liquid chromatography. *J. Chromatogr. Sci.*, 13: 361–366.

8. ASTM D3279, 1997. 2001. Standard test method for n-heptane insoluble. ASTM International, USA.
9. Mansoori, G.A., Vazquez, D. & Shariaty-Niassar, M. 2007. Polydispersity of heavy organics in crude oil and their role in oil well fouling. *J. Petroleum Sci. Eng.*, 58: 375–390.
10. Wieha, I.A. 2008. Processing chemistry of petroleum macromolecules (chemical industries). CRC Press, USA., ISBN: 978-1574447873, Pages: 456.
11. Mansoori, G.A., Vazquez, D. & Shariaty-Niassar, M. 2007. Polydispersity of heavy organics in crude oil and their role in oil well fouling. *J. Petroleum Sci. Eng.*, 58: 375–390.
12. Sinnathambi, C.M., Nor, N.M., & Ahmad, M.Z. 2011. Fouling characteristics and tendencies of Malaysian crude oil processing. *J. Applied Sci.*, 11: 1815–1820.
13. Yen, A., Yin, Y.R., & Asomaning, S. 2001. Evaluating asphaltene inhibitors: Laboratory tests and field studies.
14. Choiri, M. 2010. Study of CO₂ effect on asphaltene precipitation and compositional simulation of asphaltenic oil reservoir.
15. Stauffer, T.C., Venditti, R.A., Gilbert, R.D., Kadla, J.F., Chernyak, Y. & Montero, G.A. (2000). Supercritical carbon dioxide dewaxing of old corrugated containers.

Vapor–Liquid Equilibria for Hydrocarbon/Water Systems Using Thermodynamic Perturbation Theory

W.P. Yong and M. Awang

Abstract Complex phase equilibrium prediction for hydrocarbon systems containing polar compounds such as water and alcohols is essential in oil and gas industry. Conventional thermodynamic model such as cubic equation of state (EoS) provides quick and often reliable phase equilibrium predictions in many inert compound systems. However, cubic EoS often cannot be satisfactorily extended to predict multi-component systems that contain polar compound. In this work, the well-known cubic EoS and association EoS are applied to predict hydrocarbon/water systems. The association EoS, cubic plus association equation of state (CPA EoS), and statistical associating fluid theory equation of state (SAFT EoS) are based on advanced molecular theory. Vapor–liquid equilibria (VLE) data for ethane/water system, *n*-hexane/water system, and *n*-decane/water system at various temperatures have been collected and modeled. Based on the results, association models are capable of predicting near critical points and yield very satisfactory predictions for aqueous systems. Among the selected EoS, CPA EoS yields much better predictions with average absolute relative error (AARE) 10.88 % for ethane/water system, 7.39 % for *n*-hexane/water system, and 10.41 % for *n*-decane/water water system.

Keywords Equation of state · Statistical associating fluid theory · Cubic plus association

1 Introduction

In oil and gas industry, phase behavior studies are important throughout field production periods when the reservoir fluids are in reservoir, production line, surface facilities, transportation line, and processing line. For decades, cubic EoS such

W.P. Yong (✉) · M. Awang
Department of Petroleum Engineering, Universiti Teknologi PETRONAS,
31750, Tronoh, Perak, Malaysia
e-mail: yong.wen.pin@gmail.com

as Soave–Redlich–Kwong equation of state (SRK EoS) [1] and Peng–Robinson equation of state (PR EoS) [2] are commonly applied for phase equilibrium calculations. Cubic EoS are well developed for hydrocarbon mixtures, but they are inaccurate for liquid densities unless a volume correction is used. In addition, cubic EoS has volume deficiencies which can reduce their efficiency to predict systems near critical points.

Water is always present in the reservoir as connate water. Water saturation will increase rapidly when water break through during water flooding process. With the presence of water (polar compound with hydrogen bonding) as the additional aqueous phase in the reservoir, cubic EoS no longer satisfactorily describes the phase behavior of the systems. Although one can argue that water is an inert phase under low temperatures and pressures, water mutual solubility with reservoir fluids under high pressure and high temperature is crucial to phase equilibrium calculation.

Extensive studies and investigations have been carried out to develop models that can represent systems containing polar compounds. For example, two or more adjustable parameter mixing rules or complex density-dependent mixing rules have been applied together with cubic equation of state in modeling associating fluids, but the prediction results are sometimes doubtful as the mixing rules are semiempirical modified. Besides the semiempirical methods, investigations in terms of theoretical insights of EoS have been derived based on the following:

1. Chemical theory [3]
2. Perturbation theory [4, 5]
3. Lattice/quasi-chemical theory [6]

Based on these theories, thermodynamic models such as CPA EoS [7] and SAFT EoS [8] were developed with the consideration of associating effect from polar compounds. Since the development of CPA EoS, it has been applied with success to phase equilibrium of systems that contain alcohols, glycols, water, and alkanes with very satisfactory results [9]. As for SAFT EoS, it has been used to describe phase equilibrium of complex fluids and mixtures including aqueous mixtures, polymers, petroleum fluids, and high-pressure PE with a significant improvement over the empirical EoS [10]. CPA EoS and SAFT EoS are currently available commercially in simulation software by Infochem Ltd. and Calsep International Consultants [9, 11].

In this study, SRK EoS, PR EoS, SAFT EoS, and CPA EoS are applied to model VLE in binary mixtures of hydrocarbon (alkane) and water. Water is assumed to have four association sites, while hydrocarbons are treated as inert compounds. The performance of EoS are examined and compared. The paper covered a brief description of SAFT EoS and CPA EoS followed by the discussion of results and conclusions.

2 Theory

2.1 Statistical Associating Fluid Theory Equation of State (SAFT EoS)

Statistical associating fluid theory equation of state (SAFT EoS) was developed by Huang and Radosz [5] by incorporating Wertheim chemical association theory [12–16]. In general, SAFT EoS can be expressed in terms of different contributions to the residual Helmholtz free energy a^{res} due to different intermolecular forces as

$$a^{\text{res}} = a^{\text{ideal}} + a^{\text{seg}} + a^{\text{chain}} + a^{\text{assoc}} \quad (1)$$

The segment Helmholtz free energy a^{seg} , per mole of molecules, is expressed as

$$a^{\text{seg}} = ma_0^{\text{seg}} \quad (2)$$

where

m segment number

a_0^{seg} residual Helmholtz energy of non-associated spherical segments (per mole of segments) and the summation of hard sphere and dispersion parts with

$$a_0^{\text{seg}} = a_0^{\text{hs}} + a_0^{\text{disp}} \quad (3)$$

where the hard sphere term, a_0^{hs} is proposed as

$$\frac{a_0^{\text{hs}}}{RT} = \frac{4\eta - 3\eta^2}{(1 - \eta)^2} \quad (4)$$

with

η reduced fluid density

T system temperature, °R

R gas constant, 10.73 psi-ft³/lb-mole °R

The dispersion term is a power series fitted by Alder et al. [17], and it is given by

$$\frac{a_0^{\text{disp}}}{RT} = \sum_i \sum_j D_{ij} \left[\frac{u}{kT} \right]^i \left[\frac{\eta}{\tau} \right]^j \quad (5)$$

where

τ 0.74048

$\frac{u}{k}$ temperature-independent dispersion energy of interaction between segments, K

D_{ij} universal constants

Based on association fluid theory [4], both chain and association terms are given by

$$\frac{a^{\text{chain}}}{RT} = (1 - m) \ln \frac{1 - \frac{1}{2}\eta}{(1 - \eta)^3} \quad (6)$$

$$\frac{a^{\text{assoc}}}{RT} = \sum_A \left[\ln X^A - \frac{X^A}{2} \right] + \frac{1}{2}M \quad (7)$$

where

M number of association sites on each molecule

X^A fraction of A -sites of molecule i that are not bonded with other active sites

\sum_A a sum over all associating sites on the molecule

SAFT EoS requires five pure compound parameters:

- the chain length number or number of segments, m ;
- the segment diameter, σ ;
- a segment energy parameter, ε ;
- the volume (κ^{AiBi}) of association;
- the energy ($\varepsilon^{\text{AiBi}}$) of association.

The last two parameters are needed for self-associating molecule such as water. For association compounds, the number and type of association sites are decided based on association scheme as proposed by Huang and Radosz [8] (shown in Figs. 1, 2). For both SAFT EoS and CPA EoS association term, water is modeled as (4C) molecules based on terminology of Huang and Radosz [8].

2.2 Cubic Plus Association Equation of State (CPA EoS)

The cubic plus association equation of state (CPA EoS) was developed by Kontogeorgis et al. [7] with the combination of cubic SRK EoS and an advanced association term which is similar to SAFT EoS. In the absence of hydrogen-bonding compounds, CPA EoS can be reduced to SRK EoS, where the association term is equal to zero. The CPA EoS can be expressed in terms of pressure by

$$p = \frac{RT}{V - b} - \frac{a\alpha}{V(V + b) + b(V - b)} - \frac{1}{2} \left(\frac{RT}{V} \right) \left(1 + \frac{1}{V} \frac{\partial \ln g}{\partial \left(\frac{1}{V} \right)} \right) \sum_i x_i \sum_{A_i} (1 - X_{A_i}) \quad (8)$$

where

p system pressure, psi

T system temperature, °R

R gas constant, 10.73 psi-ft³/lb-mole °R

V molar volume, ft³/mole

Type	Δ approximations	X^A approximations	X^A
1	$\Delta^{AA} \neq 0$		$\frac{-1 + \sqrt{1 + 4\rho\Delta}}{2\rho\Delta}$
2A	$\Delta^{AA} = \Delta^{AB} = \Delta^{BB} \neq 0$	$X^A = X^B$	$\frac{-1 + \sqrt{1 + 8\rho\Delta}}{4\rho\Delta}$
2B	$\Delta^{AA} = \Delta^{BB} = 0$ $\Delta^{AB} \neq 0$	$X^A = X^B$	$\frac{-1 + \sqrt{1 + 4\rho\Delta}}{2\rho\Delta}$
3A	$\Delta^{AA} = \Delta^{AB} = \Delta^{BB} = \Delta^{AC} = \Delta^{BC} = \Delta^{CC} \neq 0$	$X^A = X^B = X^C$	$\frac{-1 + \sqrt{1 + 12\rho\Delta}}{6\rho\Delta}$
3B	$\Delta^{AA} = \Delta^{AB} = \Delta^{BB} = \Delta^{CC} = 0$ $\Delta^{AC} = \Delta^{BC} \neq 0$	$X^A = X^B$ $X^C = 2X^A - 1$	$\frac{-(1 - \rho\Delta) + \sqrt{(1 + \rho\Delta)^2 + 4\rho\Delta}}{4\rho\Delta}$
4A	$\Delta^{AA} = \Delta^{AB} = \Delta^{BB} = \Delta^{AC} = \Delta^{BC} = \Delta^{CC}$ $= \Delta^{AD} = \Delta^{BD} = \Delta^{CD} = \Delta^{DD} \neq 0$	$X^A = X^B = X^C = X^D$	$\frac{-1 + \sqrt{1 + 16\rho\Delta}}{8\rho\Delta}$
4B	$\Delta^{AA} = \Delta^{AB} = \Delta^{BB} = \Delta^{AC} = \Delta^{BC} = \Delta^{CC} = \Delta^{DD} = 0$ $\Delta^{AD} = \Delta^{BD} = \Delta^{CD} \neq 0$	$X^A = X^B = X^C$ $X^D = 3X^A - 2$	$\frac{-(1 - 2\rho\Delta) + \sqrt{(1 + 2\rho\Delta)^2 + 4\rho\Delta}}{6\rho\Delta}$
4C	$\Delta^{AA} = \Delta^{AB} = \Delta^{BB} = \Delta^{CC} = \Delta^{CD} = \Delta^{DD} = 0$ $\Delta^{AC} = \Delta^{AD} = \Delta^{BC} = \Delta^{BD} \neq 0$	$X^A = X^B = X^C = X^D$	$\frac{-1 + \sqrt{1 + 8\rho\Delta}}{4\rho\Delta}$

Fig. 1 Unbonded site fractions X^A for different bonding types [8]

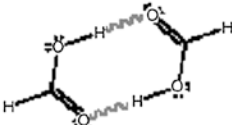
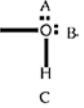
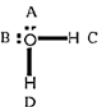
Species	Formula	Rigorous	Assigned type
Acids		1A	1A, 2B
Alcohols		3B	2B/3B
Water		4C	3B/4C

Fig. 2 Types of bonding in real associating fluids [8]

- a* “attraction” parameter from SRK EoS
- b* “repulsion” parameter from SRK EoS
- α temperature correction parameter from SRK EoS
- X_i^A fraction of *A*-sites of molecule *i* that are not bonded with other active sites
- x_i mole fraction of component *i*

3 Methodology

3.1 Literature Data

Ethane/water, *n*-hexane/water, and *n*-decane/water VLE experimental data were collected from reference [18–20]. Table 1 summarizes the collected literature data for this study.

3.2 EoS Parameters

The required EoS parameters for SRK EoS and PR EoS are critical pressure, critical temperature, and acentric factor. CPA EoS and SAFT EoS account for associating inert compounds with specific parameters such as u_0/k , v_{00} , m , ε^A , κ^A , and η/k for SAFT EoS and a_0 , b , c_1 , ε^A , and β for CPA EoS. Tables 2, 3 and 4 summarize the SRK EoS, PR EoS, SAFT EoS, and CPA EoS parameters for the associating compound and inert compounds in this study.

Table 1 Collected literature data for the study

System	T/K	P_{\min}/MPa	P_{\max}/MPa	References
C2/H ₂ O	523.15	20	200	Danneil et al. [18]
	573.15	20	200	
	623.15	20	350	
	629.15	120.5	350	
	643.15	160	350	
	651.15	199	350	
	658.15	219	350	
	673.15	321.5	370	
C6/H ₂ O	473.15	1.96	3.63	Lotter [19]
	493.15	2.94	5.23	
C10/H ₂ O	573.2	1.30	9.27	Wang and Chao [20]
	593.2	1.95	7.05	
	613.2	2.30	2.80	

Table 2 SRK EoS and PR EoS pure component parameters

Compound	MW/g/mol	T _b /K	T _c /k	P _c /MPa	Ω
H ₂ O	18.02	373.11	647.3	22.120	0.344
ethane	30.07	184.56	305.33	4.8714	0.088
<i>n</i> -hexane	86.177	341.89	507.43	3.0123	0.3046
<i>n</i> -decane	142.285	447.33	618.45	2.1229	0.4873

Table 3 SAFT EoS pure component parameters [8]

Compound	u_0/k	v_{00}	m	ε^A	κ^A	η/k
H ₂ O	431.69	0.01	1.236	1368.1	0.03647	1
ethane	191.44	0.01446	1.941	–	–	10
<i>n</i> -hexane	202.72	0.012475	4.724	–	–	10
<i>n</i> -decane	205.46	0.011723	7.527	–	–	10

Table 4 CPA EoS pure component parameters [21]

Compound	a	b	c	ε	β
H ₂ O	1.2277	0.0145	0.6736	2003.25	0.0692
ethane	5.485	0.0424	0.573	–	–
<i>n</i> -hexane	23.681	0.10789	0.8313	–	–
<i>n</i> -decane	47.389	0.17865	1.13243	–	–

3.3 Modeling Procedure

For the modeling work, software Phase Equilibria (PE) [22] has been applied to predict the hydrocarbon/water phase equilibria. The input data required are experimental data, pure components parameters, and EoS parameters. During the calculation, binary interaction parameters (BIPs) are required for mixture parameter calculations. Among the EoS parameters, BIPs were regressed based on optimization algorithm as proposed by Simplex–Nelder–Mead [23]. Finally, prediction error can be calculated based on average absolute relative error (AARE) as given by

$$\% \text{ AARE} = \frac{1}{n} \sum_i \left| \frac{x_i^{\text{cal}} - x_i^{\text{exp}}}{x_i^{\text{exp}}} \right| \times 100 \quad (9)$$

where

- x_i^{cal} mole fraction calculated from EoS
- x_i^{exp} mole fraction from experimental data
- n number of experimental data point

4 Result and Discussion

4.1 *N*-Ethane/Water System

The binary system ethane/water was modeled at eight high-temperature systems between 573.15 and 673.15 K. All experimental data are in vapor–liquid equilibria (VLE). At temperature greater than critical temperature of water (647.3 K), water is major component in both vapor and liquid phases.

Figures 3, 4, 5, 6, 7, 8, 9 and 10 present the experimental data points and modeling results predicted by all the selected EoS from 573.15 K until 673.15 K. Based on the plots, all EoS fairly predicted systems from 573.15 K until 643.15 K and all EoS poorly predicted systems with temperature beyond critical point of water ($T_c = 647.3$ K, $P_c = 22.12$ MPa).

Table 5 presents the error analysis of the prediction by AARE%. At 523.15, 573.15 and 623.15 K, SAFT EoS and CPA EoS performed better than cubic EoS with less than 7.5 AARE%, 8 AARE%, and 24 AARE%, respectively. At 643.15 and 651.15 K, PR EoS and SRK EoS predicted better than the association EoS with less than 10.5 AARE% and 13 AARE%, respectively. At 629.15 and 673.15 K, all EoS predicted with error around 14 AARE%.

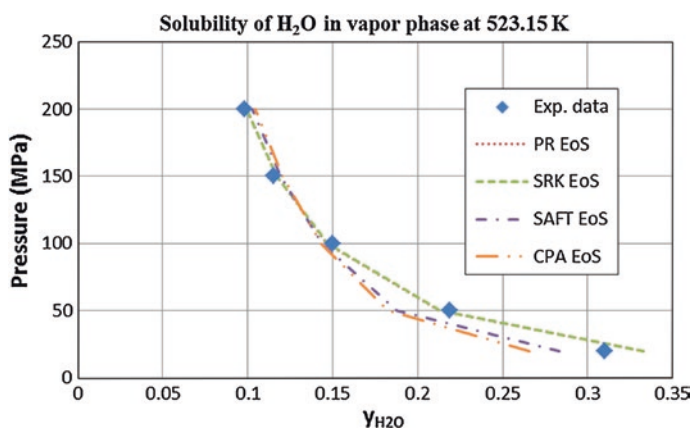


Fig. 3 Isothermal (p - y_i) phase diagram for C2/H₂O system at $T = 523.15$ K

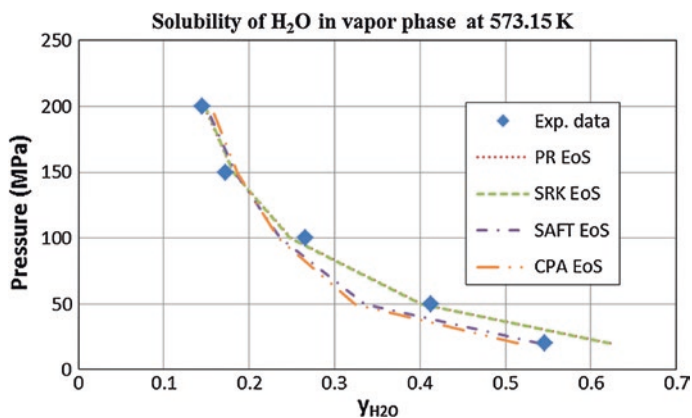


Fig. 4 Isothermal (p - y_i) phase diagram for C2/H₂O system at $T = 573.15$ K

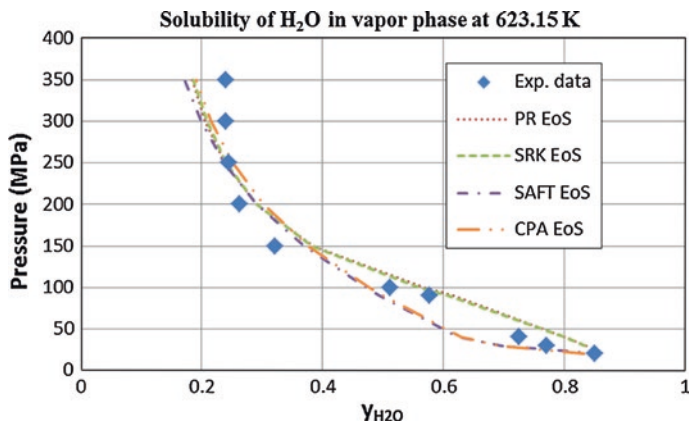


Fig. 5 Isothermal (p - y_i) phase diagram for C2/H₂O system at $T = 623.15$ K

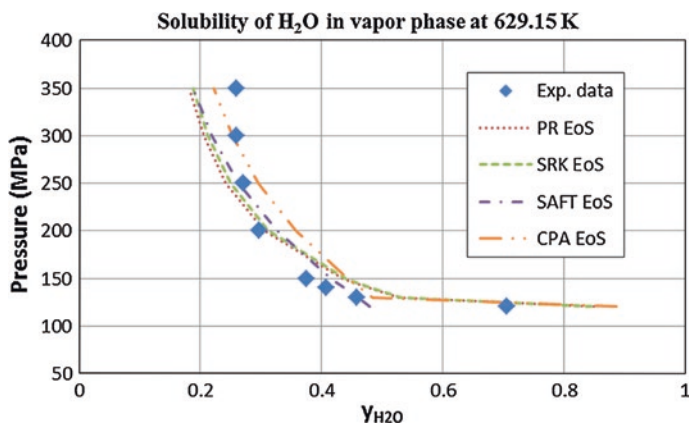


Fig. 6 Isothermal (p - y_i) phase diagram for C2/H₂O system at $T = 629.15$ K

4.2 *N*-Hexane/Water System

The binary system *n*-hexane/water was modeled at two high-temperature systems at 473.15 and 493.15 K. All experimental data are in vapor–liquid equilibria (VLE). *N*-hexane is the major component in both vapor and liquid phases. An increase in temperature produces a decrease in water solubility in both vapor and liquid phases. Meanwhile, an increase in pressure produces an increase in water solubility in both vapor and liquid phases. This phenomenon might be due to near-boiling point similarity between *n*-hexane and water.

Figures 11 and 12 present the experimental data points and modeling results predicted by all the selected EoS from 473.15 to 493.15 K. Based on the plots,

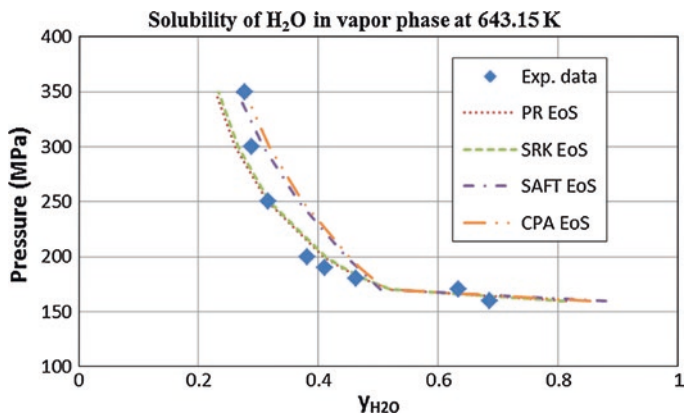


Fig. 7 Isothermal (p - y_i) phase diagram for C2/H₂O system at $T = 643.15$ K

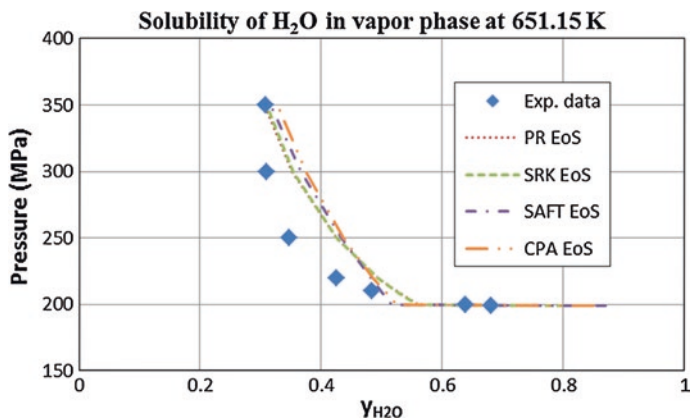


Fig. 8 Isothermal (p - y_i) phase diagram for C2/H₂O system at $T = 651.15$ K

SAFT EoS and CPA EoS gave better prediction than cubic EoS (PR EoS and SRK EoS).

Table 6 presents the error analysis of the prediction in terms of AARE%. At 473.15 K, PR EoS and SRK EoS performed better than the association EoS with less than 4.2 AARE%. At 493.15 K, SAFT EoS and CPA EoS performed better than the cubic EoS with less than 8.5 AARE%.

The overall AARE for *n*-hexane/water system are CPA EoS (7.391 AARE%), SAFT EoS (7.695 AARE%), PR EoS (8.005 AARE%), and SRK EoS (8.083 AARE%). Based on the results, all EoS based on optimized BIP predicted with almost similar performance at around 8 AARE%. It proved that BIP optimization can enhance the accuracy of cubic EoS prediction.

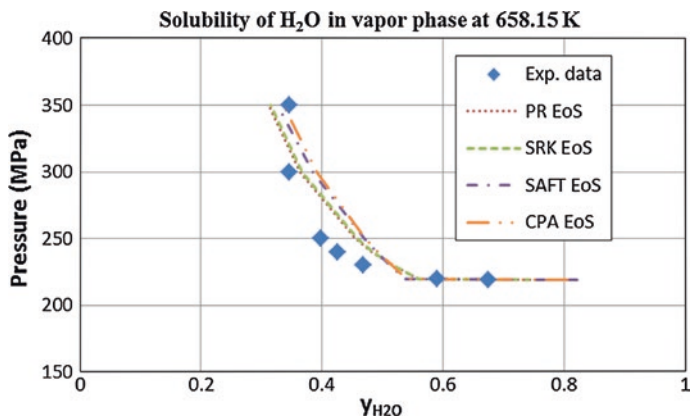


Fig. 9 Isothermal (p - y_i) phase diagram for C2/H₂O system at $T = 658.15$ K

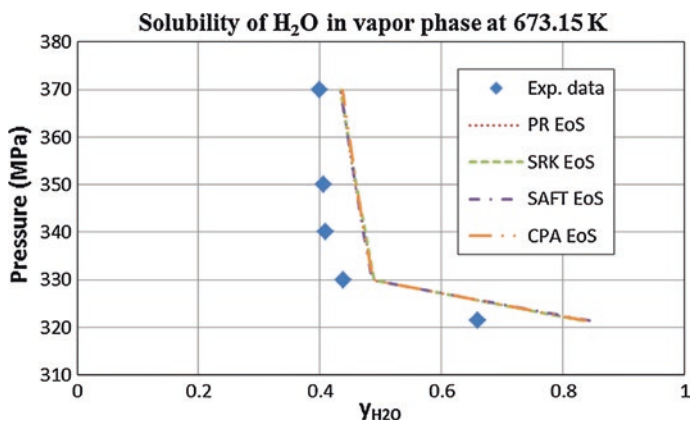


Fig. 10 Isothermal (p - y_i) phase diagram for C2/H₂O system at $T = 673.15$ K

Table 5 AARE% for C2/H₂O system

System	T/K	Average absolute relative error (AARE) (%)			
		PR EoS	SRK EoS	SAFT EoS	CPA EoS
C2/H ₂ O	523.15	4.208	4.352	4.922	5.769
	573.15	5.937	6.447	6.830	6.452
	623.15	18.601	18.890	14.236	9.804
	629.15	13.429	13.580	12.808	11.236
	643.15	10.406	10.382	14.883	13.615
	651.15	13.034	13.093	16.214	15.466
	658.15	9.583	9.719	11.974	10.913
	673.15	13.598	13.617	13.806	13.784

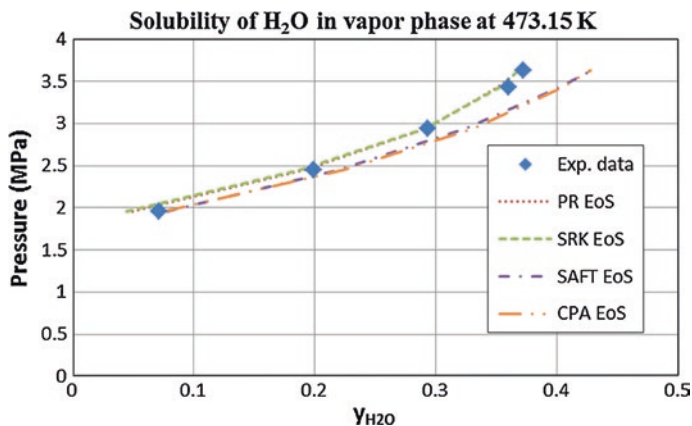


Fig. 11 Isothermal (p - y_i) phase diagram for C6/H₂O system at $T = 473.15$ K

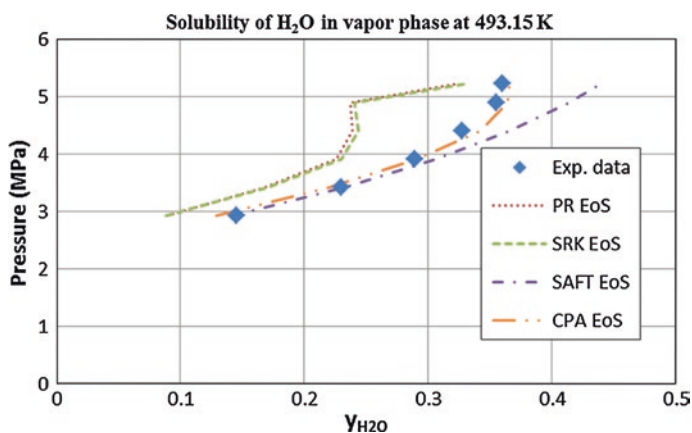


Fig. 12 Isothermal (p - y_i) phase diagram for C6/H₂O system at $T = 493.15$ K

Table 6 AARE% for C6/H₂O system

System	T/K	Average absolute relative error (AARE) (%)			
		PR EoS	SRK EoS	SAFT EoS	CPA EoS
C6/H ₂ O	473.15	3.276	4.126	9.109	6.285
	493.15	12.734	12.040	6.282	8.497

4.3 *N*-Decane/Water System

The binary system *n*-decane/water was modeled at three high-temperature systems at 573.2, 593.2 and 613.2 K. All experimental data are in vapor–liquid equilibrium. At low pressure, *n*-decane is the major component in both vapor and liquid phases and water is the main component in both vapor and liquid phases at high pressure.

Figures 13, 14 and 15 present the experimental data points and modeling results predicted by the selected EoS at 573.2, 593.2 and 613.2 K. From the plots, it can be observed that all EoS fairly satisfactorily predicted the 573.2 and 593.2 K systems. All EoS also poorly predicted systems at near critical point of *n*-decane ($T_c = 618.45$ K, $P_c = 2.123$ MPa).

Table 7 presents the error analysis of the prediction in terms of AARE%. At 573.2 K, all EoS predicted with AARE% around 20 AARE% and high AARE% were observed at high pressures. At 593.2 K, SAFT EoS and CPA EoS performed better than the cubic EoS with less than 6.6 AARE%. At 613.2 K, CPA EoS and SRK EoS outperformed the other EoS with less than 8 AARE%, while PR EoS and SAFT EoS predicted with 20 AARE%.

The overall AARE for *n*-decane/water systems are CPA EoS (10.412 AARE%), SRK EoS (11.9 AARE%), SAFT EoS (14.845 AARE%), and PR EoS

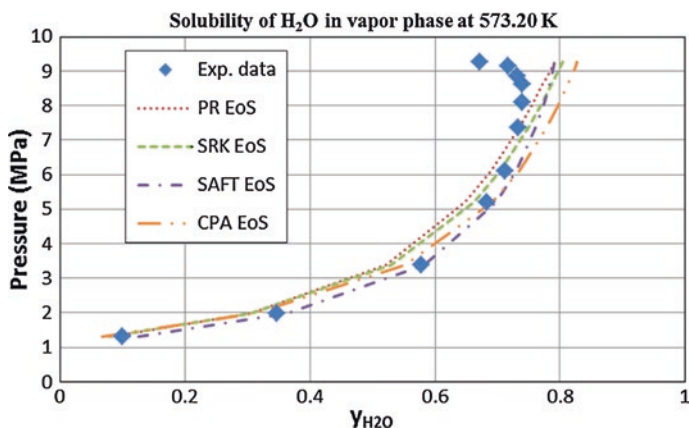


Fig. 13 Isothermal (*p*-*y_i*) phase diagram for C6/H₂O system at $T = 573.20$ K

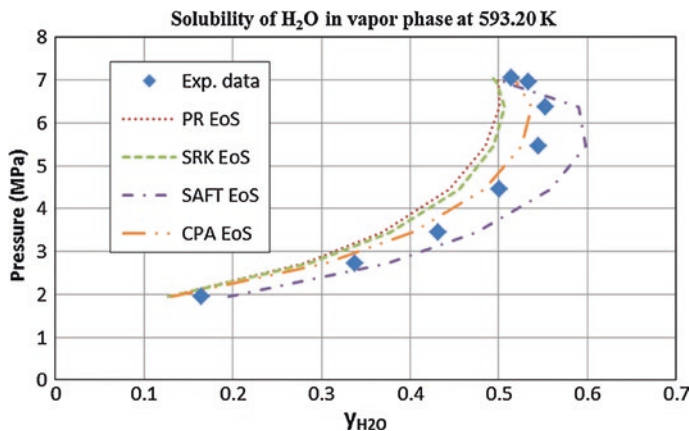


Fig. 14 Isothermal (*p*-*y_i*) phase diagram for C6/H₂O system at $T = 593.20$ K

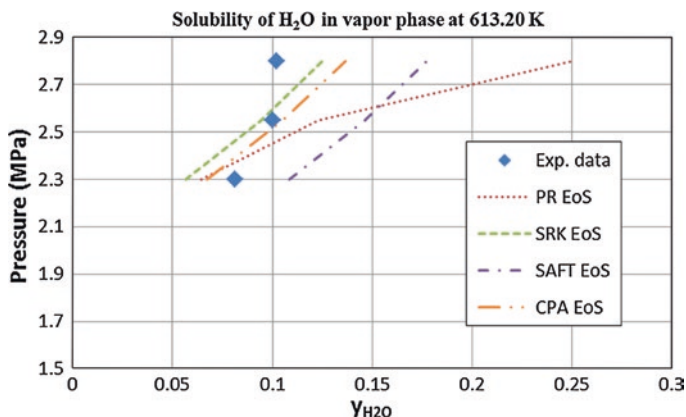


Fig. 15 Isothermal (p - y_i) phase diagram for C6/H₂O system at $T = 613.20$ K

Table 7 AARE% for C10/H₂O system

System	T/K	Average absolute relative error (AARE) (%)			
		PR EoS	SRK EoS	SAFT EoS	CPA EoS
C10/H ₂ O	573.2	18.762	19.516	18.745	20.877
	593.2	9.293	8.338	6.586	2.999
	613.2	20.685	7.845	19.203	7.359

(16.247 AARE%). Based on the results, it can be observed that PR EoS did not predict well for system with the presence of polar compound.

5 Conclusion

The VLE for ethane/water, *n*-hexane/water, and *n*-decane/water systems have been predicted using cubic EoS (PR EoS and SRK EoS) and association EoS (CPA EoS and SAFT EoS). PR EoS and SRK EoS cannot satisfactorily predict systems at conditions close to criticality. CPA EoS successfully modeled VLE for the studied systems with the least error. The association EoS has proven to have greater improvement over cubic EoS by having a firmer basis with the inclusion of association effects in the equation.

References

1. G. Soave, "Equilibrium constants from a modified Redlich-Kwong equation of state," Chem. Eng. Sci., vol. 27, 1197 (1972)
2. D. Y. Peng, and D. B. Robinson, "A new two-constant equation of state," Ind. Eng. Chem. Fundam., vol. 15, 59 (1976)

3. G. D. Ikonou, and M. D. Donohue, "Thermodynamics of hydrogen-bonded molecules: the associated perturbed anisotropic chain theory," *AIChE J.*, vol. 32, 1716 (1986)
4. W. G. Chapman, K. E. Gubbins, G. Jackson, and M. Radosz, "New reference equation of state for associating liquids," *Ind. Eng. Chem. Res.*, vol. 29, 1709 (1990)
5. S. H. Huang, and M. Radosz, "Equation of state for small, large, polydisperse, and associating molecules," *Ind. Eng. Chem. Res.*, vol. 29, 2284 (1990)
6. C. Panayiotou and I. C. Sanchez, "Hydrogen bonding in fluids: equation of state approach," *J. Phys. Chem.*, vol. 95, 10090 (1991)
7. G. M. Kontogeorgis, E. C. Voutsas, I. V. Yakoumis, and D. P. Tassios, "An equation of state for associating fluids," *Ind. Eng. Chem. Res.*, vol. 35, 4310 (1996)
8. S. H. Huang, and M. Radosz, "Equation of state for small, large, polydisperse, and associating molecules. extension to fluid mixtures," *Ind. Eng. Chem. Res.*, vol. 30, 1994 (1991)
9. G. M. Kontogeorgis, M. L. Michelsen, G. K. Folas, S. Derawi, N. von Solms, and E. H. Stenby, "Ten years with CPA (Cubic-Plus-Association) equation of state. Part 1. Pure compounds and self-associating systems," *Ind. Eng. Chem. Res.*, vol. 45, 4855-4868 (2006)
10. E. A. Muller and K. E. Gubbins, "Molecular-based equations of state for associating fluids: A review of SAFT and related approaches," *Ind. Eng. Chem. Res.*, vol. 40, 2193-2211 (2001)
11. Calsep International Consultants, "Advanced Modeling: Next generation equation of state. Retrieved January 3, 2014, from www.calsep.com/graphics/PCSAFT.pdf (2014)
12. M. S. Wertheim, "Fluids with highly directional attractive forces: I. statistical thermodynamics," *J. Stat. Phys.*, vol. 35, 19 (1984a)
13. M. S. Wertheim, "Fluids with highly directional attractive forces: II. thermodynamic perturbation theory and integral equations," *J. Stat. Phys.*, vol. 35, 34 (1984b)
14. M. S. Wertheim, "Fluids with highly directional attractive forces: III. multiple attraction sites," *J. Stat. Phys.*, vol. 42, 459 (1986a)
15. M. S. Wertheim, "Fluids with highly directional attractive forces: IV. equilibrium polymerization," *J. Stat. Phys.*, vol. 42, 477 (1986b)
16. M. S. Wertheim, "Fluids of dimerizing hard spheres, and fluid mixtures of hard spheres and dispheres," *J. Chem. Phys.*, vol. 85, 2929 (1986c)
17. B. J. Alder, D. A. Young, and M. A. Mark, "Studies in molecular dynamics. X. Corrections to the Augmented van der Waals theory for the square well fluid," *J. Chem. Phys.*, vol. 56, 3013 (1972)
18. A. Danneil, K. Todheide, and E. U. Franck, "Evaporation equilibria and critical curves in the systems ethane/water and n-butane/water at high pressure," *Chem. Ing-Tech*, vol. 13, 816-821 (1967)
19. Yu. G. Lotter, "Phase equilibria in hydrocarbon-water systems at high temperatures," *Viniti*, 1-13 (1976)
20. Q. Wang, and C. Chao, "Vapor-liquid and liquid-liquid equilibria and critical states of water + n-decane mixture," *Fluid Phase Eq.*, vol. 59, 207 (1990)
21. G. M. Kontogeorgis, and G. K. Folas, *Thermodynamic Models for Industrial Applications: From Classical and Advanced Mixing Rules to Association Theories* John Wiley & Sons Ltd (2010)
22. O. Pfohl, S. Petkov and G. Brunner, "Usage of PE- A program to calculate phase Equilibria. Herbert Utz Verlag; Munchen," ISBN 3-89675-410-6 (1998b)
23. J. A. Nelder, and R. Mead, "A simplex method for function minimisation," *The Computer Journal*, vol. 7, pp. 308 (1965)

Part III
Drilling, Well Completion,
Production and Operation

Technical and Economic Analysis of Hydraulic Pumps in Deliquifying Gas Wells

Yan Ching Lye and Mohd Amin Shoushtari

Abstract Liquid loading is the inability of produced gas to remove liquids produced together from the wellbore. This is a well-known phenomenon in mature gas wells. As production depletes, the reservoir loses energy and therefore allowing liquids to accumulate at bottomhole. The back pressure created can reduce gas production and kill the well eventually. Deliquification or liquid unloading—the process of removing associated liquids from produced gas—is therefore vital. This project is to compare and contrast the requirements and characteristics of hydraulic pumps and gas lift system, from technical specifications to power requirements and the economics involved. Both hydraulic pumps and gas lift system are few of the pioneer methods used in the industry to unload liquid in gas wells. To validate system feasibility, the author generated a mechanism for technical and economic analysis, generating minimum system power requirement from production projection. Power requirement is crucial to assess viability of system to be installed and operated. Economic analysis is essential in the project since operational benefits must be in balance with the economic value so that the system is economically viable. Sensitivity studies were conducted based on the results developed, to explore the relationships between technical and economic parameters.

Nomenclature

AOF	Absolute open flow (maximum flowrate)
CPF	Closed fluid system
FYP	Final year project
GL	Gas lift system
GLR	Formation gas–liquid ratio

Y.C. Lye (✉) · M.A. Shoushtari
Faculty of Geosciences and Petroleum Engineering,
Universiti Teknologi PETRONAS (UTP), Tronoh, Malaysia
e-mail: lyeyanching@gmail.com

HHP _{req}	Minimum required hydraulic horsepower
HJP	Hydraulic jet pump
HPP	Hydraulic piston pump
J	Desired productivity index
OPF	Open fluid system
V _t	Terminal/critical velocity

1 Introduction

Dort [14] proved in his study that approximately 90 % of 775,000 active gas wells globally suffer from liquid loading. This project puts focus on one of the major problems faced in gas production, especially in mature gas wells. Lea et al. [9] explained that liquid loading is caused by the erratic, slugging flow, decreased production and hydrostatic weight, thereby exerting back pressure on formation, choking the flow and consequently stops the production.

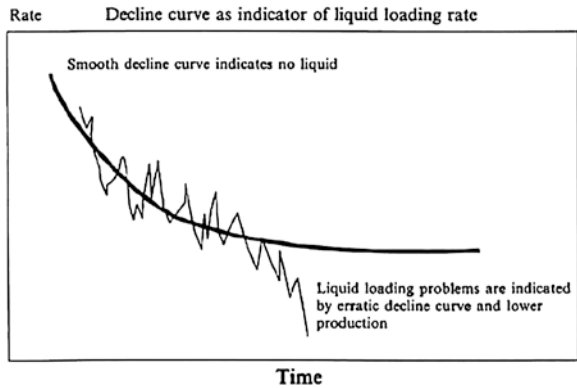
Since liquid loading can cause such severity in depleting gas production, liquid unloading techniques are relatively important. Bondurant et al. [1] defined deliquification as the process of removing associated liquids, which could be water, oils or condensates, from wellbore and reservoir to the surface. Deliquifying techniques were vastly developed since the history of gas well drilling started. For this paper, the author scopes down to hydraulic pumping and gas lift, and few techniques that have been practiced since 1800s because the application theory and principles are more or less similar and were widely misused in the production industry. Gas lift was first used in 1846, while hydraulic pumping which was first used in 1930 is hence a relatively new method of artificial lift [9]. Gas lift has been vastly in use since the interventions involved are relatively less expensive, reliable and closely matches the well natural production characteristics.

1.1 Gas Well Deliquification

Liquid loading of gas well is the incapability of the produced gas to remove the liquids from the wellbore [15]. The liquid accumulated downhole, where it increases the hydrostatic back pressure on the reservoir, destabilizes the multiphase flow in the well, decreases gas production rate and, in severe cases, kills the wells. The greatest engineering challenge to this operation is to unload liquids entering the wellbore. Eventually, the back pressure will increase until the well is killed by the water column overbalance. This back pressure or bottomhole pressure could be consists of hydrostatic pressure of the producing fluid column, friction pressure by fluid movement through the tubing, wellhead and surface equipment, and kinetic or potential losses due to diameter restrictions, pipe bends or elevation changes.

Liquid loading happens when the velocity of the produced gas decreases to a velocity until liquids were unable to be lifted. As gas production decreases, liquid

Fig. 1 Decline curve showing onset of liquid loading [8]



loading is more likely to occur. This phenomenon will cause resulting flow patterns to be annular or slug flow [6]. The bottomhole flowing pressure then increases due to an increase in liquid holdup in the tubing. The relative permeability of gas and gas mobility in near wellbore region will also be impaired since water saturation increased. This acts like skin damage to the reservoir, known as ‘liquid block’ [2]. Lea and Nickens [10] wrote that critical velocity is the minimum gas velocity in the production tubing required to move liquid droplets upward (Fig. 1).

Earlier this year (2013), A.D. Suhendar and his team from VICO Indonesia summarized that there are three most common ways to recognize liquid loading [6]:

- (i) Observing well’s production symptoms (fluid rate and pressure).
- (ii) Calculating critical velocity and monitor from there.
- (iii) Doing standard nodal analysis.

Currently, there are a few published papers, including Weatherford International® Unloading Selector [13] which proposed several types of decision matrix to screen the possible remedial options available to the operator; some are based on an assessment algorithm used in conjunction with a decision tree [3]. However, depending merely on technical analysis is not very useful for selecting best options for long-term deliquification of the well. Because the well productive characteristics vary so widely, the current and future productive potential of the well are not quantitatively considered in these methods. Hence, economic analysis is utmost crucial [16].

1.2 Hydraulic Pumping System

Lea [6] described hydraulic pumping as the hydraulically powered downhole pumps, powered by a stream of high-pressure water or power fluid. The major advantage of hydraulic pumping is that it can operate over a wide range of well conditions, such as setting depths of as much as 18,000 feet and production rates

of as much as 50,000 barrels per day. Moreover, no rig is needed to retrieve pumps. Hydraulic pumping is a very flexible system in adjusting to changing production rates. Chemicals can be added into the power fluid to control corrosion, paraffin and etcetera.

There are two types of hydraulic pumps: the hydraulic piston pump (HPP) and hydraulic jet pump (HJP). The summary of comparisons will be tabulated in the section below. Park et al. [16] addressed the efficiency of HJP system in his recent paper. Given that sandstone formation has solid problem, rig mobilization and operations are very costly, high deviated well construction, so HJP became the obvious choice. Currently, 43 active oil wells in Sembakung are producing with the aid of HJP as artificial lift, contributing 2,200 BOPD productions in year 2000–2010. The HJP brings additional advantages apart from the fundamental benefits such as high solid resistance and high tolerance to deviated wells. As compared to gas lift, downhole pumps are normally more effective, since it will be physically located below the bottom perforation and liquid will be mechanically removed with outside energy source. J.A. Babbit and F.K. Kpodo presented their innovations in jet pump design and applications in field. The field data and net cash flow were then used in the research [7, 11].

1.3 Gas Lift System

Gas lift is a popular artificial lift method in which gas is injected into the production tubing to reduce the hydrostatic pressure of the fluid column. The resulting reduction in bottomhole pressure allows the reservoir liquids to enter the wellbore at a higher flow rate [13]. The injection gas is typically conveyed down the tubing—casing annulus and enters the production train through a series of gas lift valves. The gas lift valve position, operating pressures and gas injection rate are determined by specific well conditions.

1.4 Economic Analysis

There is increasing demand for reliable and effective deliquification solutions since most of the wells are mature gas wells and were not originally completed with the purpose of deliquification in mind. Gas well deliquification is an operation which requires high amount of money as investment. Hence, the income by average gas net production per well has to be calculated. Amani [4] made the remark that in order to evaluate the economics of a particular artificial lift system, costs such as installation, power, repair, maintenance and operating labour costs have to be included in analysis. He also presented a case study where he concluded capital cost of the gas lift system is much higher than that of hydraulic gas pump, due to the cost of casing installation involved in gas lift system. In a

hydraulic pump system, there is no need for new casing string installation. He also tabulated a list of major equipment and costs estimated to illustrate the economic viability of the hydraulic pumping system. Approximately \$130,000 was needed for the cost of major equipment [5]. In order to quantify the benefits of a pump compared to other methods, production scenario for the pump must be projected and gas recovery has to be calculated to economic limit.

In order to generate computer coding for economic analysis, inputs were gathered from various studies. P.R. Newendorp listed the indicators to be taken into account when computing the economics of projects. For instance, payout period, net present value (NPV), internal rate of return (IRR), profit-to-investment ratio, time value of money, discounted profit-to-investment ratio (to today's value), etc. [12].

All values are brought to present to increase result accuracy in author's work.

2 Analysis and Modelling

2.1 Comparative Analysis

See Table 1.

Table 1 Comparisons between hydraulic pumps and gas lift system

Comparisons	Hydraulic pump		Gas lift
	Piston	Jet	
Maximum operating depth, TVD	17,000 ft	15,000 ft	18,000 ft
	5,182 m	4,572 m	4,878 m
Minimum operating depth, TVD	5,000 ft	5,000 ft	8,000 ft
	1,524 m	1,524 m	2,438 m
Maximum operating volume (BFPD)	8,000	20,000	50,000
Maximum operating temperature	550 °F	550 °F	450 °F
	288 °C	288 °C	232 °C
Corrosion handling	Good	Excellent	Good to excellent
Gas handling	Fair	Good	Excellent
Solids handling	Fair	Good	Good
Fluid gravity (°API)	>8 (extra heavy crude)	>8 (extra heavy crude)	>15 (heavy crude)
Servicing	Hydraulic or wireline		Wireline or workover rig
Prime mover	Multicylinder or electric		Compressor
Offshore application	Good	Excellent	Excellent
System efficiency	45–55 % less mechanical work, less problem	10–30 % more sophisticated mechanical components	10–30 %

2.2 Mechanism for Technical and Economic Analysis

For technical analysis, Kpodo [7] defined a few parameters which can validate viability of an energy adding system, in the liquid unloading application. In this project, minimum required hydraulic horsepower (HHPreq) is used as a ruler, to determine system feasibility. This is achieved by comparing system required horsepower and the readily available horsepower onsite. In order to compute this HHPreq, desired productivity index (J) and maximum flow rate, or absolute open flow (AOF). Several inputs are compulsory, power fluid rate—capacity of pump, system efficiency, and required surface operating pressure (wellhead P), reservoir pressure, desired production rate, and required producing pressure, AOF affected by desired productivity index (J).

The second part of the analysis is to economically analyse the deliquification projects using gas lift and hydraulic pump. According to M. Amani, to quantify the benefits of a pump compared to gas lift, one must project a production scenario for the pump and calculate gas recovery to economic limit [4]. P.D. Newendorp and Campbell suggested that to obtain a good measure of value, suitable for comparing and ranking the profitability of investment opportunities, we should consider the following indicators, payout, NPV and IRR. The 3 factors are crucial and most widely used to rank desirability of projects. Details will be analysed and discussed in the following section.

2.3 Development of Model

This is Step 2 in the whole process of validating feasibility of gas well deliquification method. The final output from Step 1 is selection of either 1 system from the 3 considered, HPP, HJP or gas lift. However, since gas lift is feasible with the presence of high-pressure gas source nearby, technical analysis will not be done on the system. Hence, only hydraulic pumping system will be analysed here. The outcomes of this step are desired productivity index (J), maximum flow rate or AOF and required minimum hydraulic horsepower (HHPreq). Users should then compare these 3 outcomes with initial production condition, production profile and readily available power source (Fig. 2).

According to data extracted from Kpodo's paper [7], the resulting HHPreq is 24.06 hp for HPP and 15.23 hp for HJP. Parameters such as power fluid rate, system efficiency and required surface operating pressure, or wellhead pressure affect the resulting HHPreq. As for the desired productivity index, it is very much affected by reservoir pressure, desired production rate and required producing pressure. The technical specifications of both the hydraulic pumping systems have to be abided at all times where range of operating temperature, depth and pressure was set. The generated outcome and processes below are based on values extracted from References [4, 5, 11].

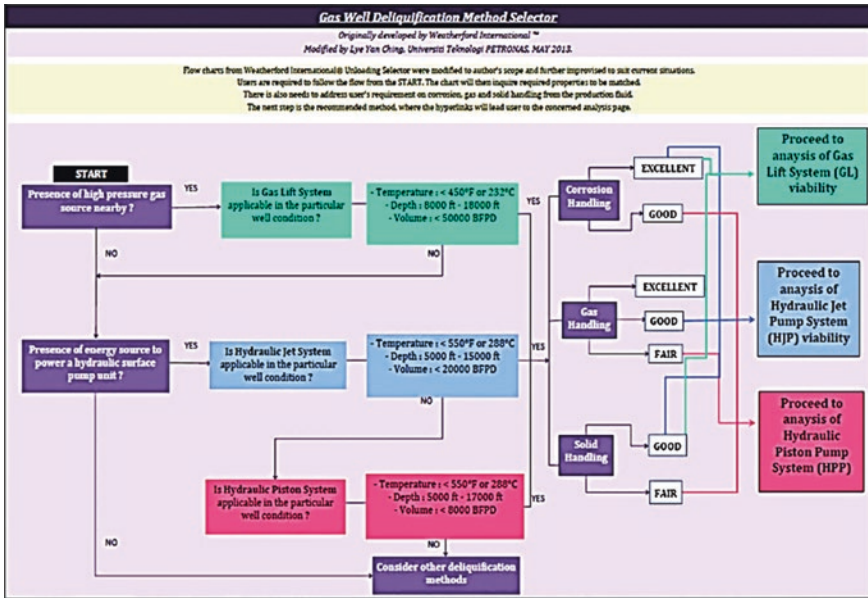


Fig. 2 Gas well deliquification method selector and general workflow (STEP 1)

2.4 Economic Analysis

As mentioned, there are several indicators that can differentiate profitable projects from the rest: payout period, NPV and IRR. For hydraulic pumping system, Amani [4, 5] proposed the total of \$129,549, around \$ 130,000, for installation of piston pump system, in year 1993. If we bring it to present, year 2013, assuming inflation rate as 4.5 % per year, it would be total of \$313,522.82. When the pump was installed in Year 3, the production rate was only 1,250 mcf/D. After installation of pump, the recovery was 2.42 BCF. The increment was 1.19 BCF. Given the gas price in 1993 was around \$8.26/thousand cubic feet, the increment brought in profit of around \$1.5 million. Compared to installation costs of \$313,000, the pump was perfectly viable. On the same ground, gas lift recovered 0.60 BCF, bringing in \$1.2 million. Although it is also economically viable, the difference of 1.82 BCF incremental recovery of a pump over gas lift is significant.

The present value of net cash flow occurring at some point in the future or happened in the past is referred to NPV of that cash flow. Sum of money received now is worth more than the same sum of money received several years later in the future. In this project, the discount factor is the inflation rate, which is assumed to be 4.5 % per year. Moreover, NPV is calculated, or brought forward to the present (year 0).

$$\text{Present Value} = \text{Net Cash Flow} \times \text{Inflation Rate (4.5\%)}$$

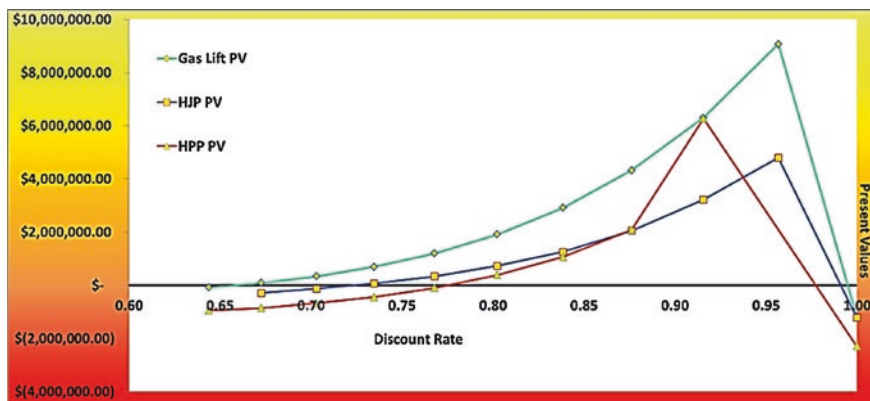


Fig. 3 IRRs identified in spreadsheet using graphical method

Result summary for NPV, summation of 10 years' present values:

- Hydraulic piston pump: NPV = \$19,541,526.69
- Hydraulic jet pump: NPV = \$22,915,124.02
- Gas lift system: NPV = \$25,608,269.59

NPV is a single measure showing the value in excess of capital expenditure (CAPEX), and it takes time into account. Gas lift system has the highest NPV of all 3 projects.

Generally speaking, the higher a project's IRR, the more desirable it is to undertake the project. From the data extracted from researches and papers published, author managed to generate detailed cash flow which includes present value, which can then lead to computations of IRRs for all 3 systems. Below are the generated outcome and process, based on values extracted from Reference [4, 5, 11] (Fig. 3).

We can observe that there are multiple rates of return as there is more than one intersection with the x -axis, which means the cash flow changes sign twice, since at high discount rates, even the discounted positive cash flow is not large enough to offset the negative cash flow at Year 0; hence, NPV becomes negative again. To relate this situation with real case, lower IRR is taken. Result summary for IRR is as follows:

- Hydraulic piston pump: IRR = 77.5 %
- Hydraulic jet pump: IRR = 72.5 %
- Gas lift system: IRR = 65.5 %

3 Conclusions and Recommendations

The detailed comparative studies concluded that for different situations, different methods should be used. For extra heavy crude wells with economic constraint, HPP should be opted since it has higher system efficiency. For deviated offshore

wells with high solid contents, HJPs should be chosen. Gas lift is elected when the operating volume is very high in deep offshore wells.

The sensitivity analysis on several technical and economic parameters was done to study the relationships between parameters. The minimum required hydraulic horsepower can be an indicator to validate operation feasibility of systems. For economic viability, the net profit has to exceed a threshold for the system to be practical.

The author has identified several improvements to be recommended in gas well deliquification future studies. This project only focused on 3 methods. Further studies can include more methods in the analysis. Further studies can embrace the field of petroleum economics and relevant latest innovations. Further improve the mechanism developed to include more systems, simplifies the commands, inputs required and made user friendly for suitability of the operation purposes.

References

1. A.V. Bondurant B.D. Dotson, P.O. Oyewole, *Getting the Last Gasp: Deliquification of Challenging Gas Wells*, IPTC 11651, 2007, p. 10.
2. Ade Diar Suhendar, Risdiyanto Kurniawan, Eder Lizacano, *Gas Well Deliquification for Maximizing Recovery from Mature Gas Assets*, VICO Indonesia, IPTC 16915, 2013.
3. Adjusting Cash Flow Projections for Inflation [Online] // <http://zinkpulse.com/inflation/>, Accessed on 3rd July 2013.
4. Amani Mahmood, *Gas Well De-Watering System and Hydraulic Gas Pump, New Designs and a Discussion on Their Economics*, 1994.
5. Amani Mahmood, *Hydraulic Gas Pump and Has Well De-Watering System: Two New Artificial-Lift Systems*, 1993.
6. Dotson, E. Nunez-Paclibon, *Gas Well Liquid Loading From the Power Perspective*, BP America Production Co., SPE 110357, 2011.
7. F.K. Kpodo, *Optimizations in the Design and Operation of an Offshore Hydraulic Pumping System*, SPE, 1988, pp459 – 462.
8. G.B. Stephenson, R.P Rouen, M.H. Rosenzweig, Schlumberger, *Gas Well Dewatering: A Coordinated Approach*, SPE 58984, 2000.
9. James F. Lea Henry V. Nickens, Mike R. Wells, *Gas Well Deliquification*, 2008, pp. 4-11.
10. James F. Lea Henry V. Nickens, *Solving Gas-Well Liquid-Loading Problems*, 2004.
11. Jess A. Babbit, *Hydraulic Pumping Units Proving Very Successful in Deliquifying Gas Wells in East Texas*, SPE 159346, 2012.
12. Kermit E. Brown, H. Dale Beggs, *The Technology of Artificial Lift Methods*, 1977, pp 262.
13. Rick D. Haydel, Donald J. Brink, William K. Acker, Gary J. Gassiot, *Gas Well De-Watering Method Field Study*, SPE 141036, 2011.
14. Roland van Dort, *Deliquification Technology Maximises Gas Well Production*, 2009.
15. William Hearn, *Gas Well Deliquification*, 2010.
16. Y. Park, Falcone, G. Teodoriu, *Decision Matrix for Liquid Loading in Gas Wells for a Cost/Benefit Analysis of Lifting Options*, Journal of Natural Gas Science and Engineering, Volume 1, Issue 3, September 2009, pp 72 – 83.

Drilling Parameter Effects on Cuttings Transport in Horizontal Wellbores: A Review

T.N. Ofei, S. Irawan and W. Pao

Abstract Extensive studies on cuttings transport have been conducted by many researchers over the years. In an attempt to better understand the factors influencing cuttings removal in the wellbore, the behaviour of drill-cuttings in the annulus has been simulated and measured under various conditions in the laboratory using mainly water-based and oil-based muds. Furthermore, empirical and semi-empirical correlations as well as mathematical models have also been developed under specific conditions by other investigators to ease the difficulties and complexities encountered by field engineers during drilling operations. In addition, qualitative hydraulic programmes have also been outlined to provide field guidelines for improved hole cleaning. In recent times, the use of computational fluid dynamics (CFD) in parametric study of cuttings transport has gained popularity due to its ability to handle unlimited number of physical and operational conditions as well as eliminating the need for expensive experimental set-ups. This paper seeks to review the factors or combination of factors affecting cuttings transport as well as the various hydraulic programmes applicable to solving the prevailing field drilling problems in horizontal wellbores.

Keywords Cuttings transport · Drill-cuttings · Hydraulic programmes

T.N. Ofei (✉) · S. Irawan

Department of Petroleum Engineering, Universiti Teknologi Petronas,
Seri Iskandar, Malaysia

e-mail: titus.ifei@petronas.com.my; titusofei@hotmail.com

W. Pao

Department of Mechanical Engineering, Universiti Teknologi Petronas,
Seri Iskandar, Malaysia

1 Introduction

There are huge amount of literature available on the study of cuttings transport due to its interest and complexity in understanding the transport behaviour. Till date, more research are being conducted as the well-known conventional rotary drilling method used in drilling onshore reservoirs are now replaced by coiled tubing drilling, casing drilling, etc., due to the challenging frontiers encountered in recent deep and ultra-deep offshore reservoirs. To better understand the various mechanisms affecting cuttings transport in horizontal wellbores, many investigators have conducted various studies under varying conditions by employing different approaches as follows: experimental, numerical simulation, mathematical modelling and field case study. The factors affecting cuttings transport in horizontal wellbores have been critically reviewed and addressed. It is believed that cuttings transported in the annulus are not always affected by a single parameter but a combination of parameters to ensure efficient hole cleaning. This study is aimed at reviewing all available literature on two-phase cuttings-liquid transport in horizontal annular wellbores where conventional drilling fluids such as pure water, water-based muds and oil-based muds are used in the drilling process.

2 Factors Affecting Cuttings Transport

Cuttings transported through the annulus (hole–pipe geometry) are affected by series of drilling parameters. The study of the effects of these parameters has been a subject of research by several investigators over the decades. According to these investigators, the factors affecting cuttings transport in the wellbore can be summarised as but not limited to: annular fluid velocity (flow rate), drill pipe eccentricity, wellbore size (annular size), drilling fluid rheology (density, viscosity, yield point, gel strength), cuttings size, drill pipe rotation, drilling rate (rate of penetration), hole inclination, mud type, temperature and drilling fluid density. Overestimation or underestimation of these parameters may result in hole problems such as cavings, enlargements, closures, mud cake formation and excessive cuttings bed as depicted in Fig. 1. Therefore, there is the need to optimise these parameters for effective hole cleaning.

Reference [1] has illustrated in Fig. 2 that the practical use of these factors in controlling cuttings transport is much dependent on their controllability in the field.

2.1 *Effect of Annular Velocity (Flow Rate)*

Figure 2 indicates that flow rate has the most significant influence on cuttings transport and hence could be easily controlled. Both experimental studies and numerical simulations of cuttings transport have shown that higher flow rates result

Fig. 1 Hole problems in high-angled wellbores

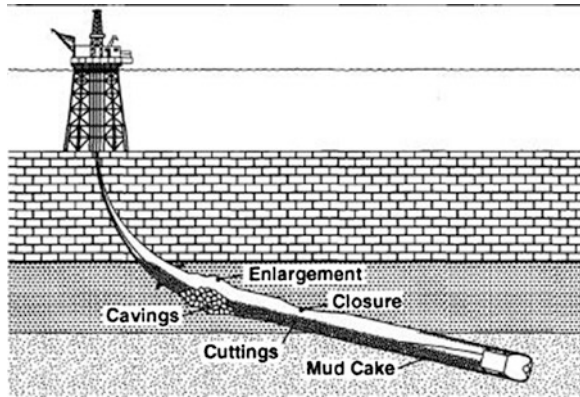
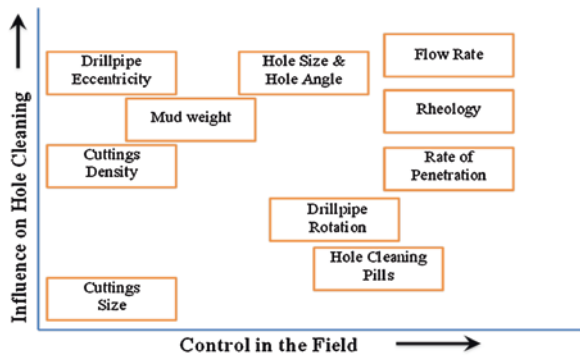


Fig. 2 Key variables controlling cuttings transport (modified after [1])



in drastic cuttings bed erosion [1–11]. Reference [12] observed that increasing flow rate of high-viscosity high-density sweep or high-viscosity sweep has no significant improvement on cuttings bed erosion. In addition, [13] observed a decrease in the critical flow rate required to reduce cuttings bed height as the open flow area decreases.

2.2 Effect of Drilling Fluid Density

Drilling fluid density or mud weight determines the cuttings carrying capacity. Mud weight is illustrated in Fig. 2 as one of the influential parameters on hole cleaning which could be moderately controlled on the field. Studies [5, 6, 14, 15] have shown that increase in fluid density enhances cuttings bed erosion and also prevents borehole collapse [16]. At high mud weight, the frictional effect of cuttings on rotating drill pipe also reduces [17]. Reference [18] indicated that fluid density is only a secondary factor in cuttings transport at constant critical flow rate.

2.3 Effect of Drilling Fluid Rheology

Fluid rheology also plays great role on hole cleaning as observed from Fig. 2. Experimental studies [19, 20] have shown that cuttings bed formation in high-viscosity fluids in laminar flow is slow compared low-viscosity fluids in laminar flow. On the contrary, other investigators [21, 22] have also observed that low-viscosity muds perform better than high-viscosity muds, whereas low-viscosity muds which are pumped in turbulent flow are more effective in hole cleaning than high-viscosity muds in laminar flow [23]. Furthermore, low-viscosity muds transport more large-sized cuttings than small-sized cuttings [24]. In addition, [12] noted that high-viscosity sweeps in the absence of drill pipe rotation is ineffective in cuttings bed erosion and cuttings removal, whereas low-viscosity sweeps with drill pipe rotation and improves 'sweep' efficiency at high flow rates. The effect of mud viscosity on cuttings transport however diminishes as drill pipe rotation speed increases [10].

On the other hand, a decrease in flow behaviour index, n , results in a decrease of stationary bed, whereas moving bed layer increases [25]. Reference [1] also observed that the increase in the ratio of flow behaviour index to consistency index (n/K) reduces cuttings bed height. Less gel strength formation in muds also helps minimise cuttings bed consolidation [16]. The mud yield point (YP) and plastic viscosity (PV) also influence cuttings removal. Further study [12] has shown that increase in YP at constant flow rate without drill pipe rotation results in negligible cuttings bed erosion, while a reduction in PV and YP results in a better hole cleaning at reduced flow rates [22].

2.4 Effect of Cuttings Size

The size of cuttings is mostly dependent on the type of formation being drilled as well as the type of drill bits. This parameter, as shown in Fig. 2, is very difficult to control. A general observation made by previous studies [3, 6, 23] shows that large-sized cuttings result in an increase in cuttings bed height. However, smaller-sized cuttings are observed to be more difficult to clean when using water as drilling fluid [8, 23] and, thus, require a higher flow rate to reach the critical transport fluid velocity (CTFV) due to their high interface interaction coefficient when using non-Newtonian fluids [21, 26, 27].

2.5 Effect of Drill Pipe Rotation

The rotation of drill pipe during drilling operations is shown to moderately influence hole cleaning and can be controlled as well (see Fig. 2). According to [19], drill pipe rotation has minor influence on cuttings transport when flow is turbulent. Higher drill pipe rotation speed is also observed effective in decreasing

annular cuttings concentration at low flow rates and diminishes at high flow rates [9, 24, 28]. Cuttings bed erosion is greatly improved by drill pipe rotation once drilling operation is stopped [24]. Reference [29] observed that drill pipe rotation enhances better hole cleaning when high-density sweep is used, whereas at low-viscosity sweep, a considerable decrease in cuttings bed erosion is noted as drill pipe rotation increases [12]. Another investigator [30] also noticed greater impact of drill pipe rotation in transporting smaller cuttings sizes. However, other studies [9, 28] observed a slight decrease in cuttings moving velocity; hence, a negligible change in cuttings bed height as drill pipe rotation increases.

2.6 Effect of Drill Pipe Eccentricity

Eccentricity shows how drill pipe is displaced either towards the upper or lower part in horizontal wellbores. The influence on cuttings transport is extremely high, but it is also very difficult to control as depicted in Fig. 2. Studies [14] have shown that concentric annuli promote more cuttings bed erosion than eccentric annuli. In addition, others [3, 5, 15] also confirmed that an increase in eccentricity increases cuttings bed.

2.7 Effect of Annular Size

Annular size shows huge influence on cuttings transport as illustrated in Fig. 2. Experimental studies [31] have shown that increase in diameter ratio (a ratio of drill pipe diameter to hole diameter) improves hole cleaning due to the increase in annular velocity and wall shear stress.

2.8 Effect of Fluid Type

Reference [13] noticed that water, as a drilling fluid, is more effective for cuttings bed erosion, while PAC fluid is more effective in preventing cuttings bed formation. Meanwhile, PAC solution is also seen to improve the transport of small-sized cuttings than large-sized cuttings [8].

2.9 Effect of Drilling Rate (Rate of Penetration, ROP)

Several investigators [6, 9, 30] and [32] have illustrated that higher drilling rates generate more cuttings in the wellbore and hence results in higher cuttings bed height. This effect further increases the hydraulic requirement for effective hole cleaning [19, 24].

2.10 Effect of Temperature

Very few experimental studies [12, 33] have been conducted in recent times under elevated temperature to analyse its effect on cuttings transport. It can be ascertained from these studies that an increase in temperature results in a decrease in cuttings bed height with time when using both water and non-Newtonian fluids. Other observation is that the rheology of drilling fluids changes significantly with temperature, which affects the viscous drag forces applied on drilled cuttings [33].

3 Drilling Hydraulic Programmes

The complexity of cuttings transport, which involves the combination of interacting variables, would not make it prudent to solely rely on predictive models with limited boundary conditions. In this regard, many investigators have recommended some general operational guidelines based on the results from laboratory study as well as field experience and observations. Appendix A summarises these operational guidelines in Tables 1 and 2.

4 Conclusion

A comprehensive study on the factors affecting cuttings transport in horizontal wellbores has been presented. The most important factor controlling cuttings transport or hole cleaning is annular velocity as illustrated in Fig. 2. Fluid rheological properties and density have moderate influence, while cuttings size, annular gap, drilling rate, drill pipe eccentricity and rotation have slight effect on cuttings transport. It is evident that different authors had different opinions on specific drilling parameter effects. This could be attributed to the range of composition of parameters as well as experimental and numerical set-up range used in their respective studies. This review clearly shows that effective hole cleaning is not dependent only on a single drilling parameter but also on a combination of parameters. Qualitative hydraulic programmes for ensuring efficient hole cleaning and wellbore stability as proposed by other investigators are also presented.

Appendix

See Tables 1 and 2.

Table 1 Drilling hydraulic programme (modified after [34])

1.	Monitoring the torque and drag trends, the rate of cuttings returned and volume reduction of the active mud system as the hole is drilled provide a good understanding of how well the hole is being cleaned. This, in turn, helps improve drilling performance
2.	When penetration rate exceeds 100 fph (average), 24-h wellsite drilling engineering support is needed
3.	Monitoring the rate of cuttings return over the shaker is a simple but effective way to enhance the understanding of how the hole is cleaned under various operating modes
4.	Monitoring the reduction in the volume of the active mud system as the hole is being drilled is means of determining how the hole is cleaned under various operating modes
5.	Convergence and divergence trends of pickup and slack-off drill string weight can be used as a means to determine hole cleaning over a period of time
6.	A reduction in off-bottom rotating torque, under some conditions, may be an indication that the hole is loading up with cuttings
7.	Predicted and actual drill string weight may not be close if there is significant formation ledging

Table 2 Drilling hydraulic programme (modified after [35])

1.	Design the well path so that it avoids critical angles in possible
2.	Use top drive rigs, if possible, to allow pipe rotation while tripping
3.	Maximise fluid velocity, while avoiding hole erosion, by increasing pumping power and/or using large diameter drill pipes and drill collars
4.	Design the mud rheology so that it enhances turbulence in the inclined/horizontal sections, while maintaining sufficient suspension properties in the vertical section
5.	In large diameter horizontal wellbores, where turbulent flow is not practical, use muds with high suspension properties and muds with high metre dial readings at low shear rates
6.	Select bits, stabilizers and bottom hole assemblies (BHAs) with minimum cross-sectional areas to minimise ploughing of cuttings while tripping
7.	Use various hole cleaning monitoring techniques including a drilled cuttings retrieval rate, a drilled cuttings physical appearance, pressure while drilling and a comparison of pickup weight, slack-off weight and rotating weight
8.	Perform wiper trips as the hole condition dictates

References

1. R.B. Adari, S. Miska, E. Kuru, P. Bern, and A. Saasen, "Selecting Drilling Fluid Properties and Flow Rates for Effective Hole Cleaning in High-Angle and Horizontal Wells" SPE 63050, presented at SPE Annual Technical Conference and Exhibition, Dallas, Texas, (2000).
2. A.L. Martins, M. Santana, E. Gaspari, and W. Campos, "Evaluating the Transport of Solids Generated by Shale Instabilities in ERW Drilling" SPE 50380, presented at the SPE International Conference on Horizontal Well Technology held in Calgary, Alberta, Canada, (1998).
3. A.M. Kamp, and M. Rivero, "Layer Modeling for Cuttings Transport in Highly Inclined Wellbores" SPE 53942, presented at the SPE Latin American and Caribbean Petroleum Engineering Conference held in Caracas, Venezuela, (1999).
4. L. Zou, M.H. Patel, and G. Han, "A New Computer Package for Simulating Cuttings Transport and Predicting Hole Cleaning in Deviated and Horizontal Wells" SPE 64646, presented at the International Oil and Gas Conference and Exhibition held in Beijing, China, (2000).

5. M.E. Ozbayoglu, S.Z. Miska, T. Reed, and N. Takach, "Analysis of the Effects of Major Drilling Parameters on Cuttings Transport Efficiency for High-Angle Wells in Coiled Tubing Drilling Operations" SPE 89334, presented at the SPE/ICoTA Coiled Tubing Conference and Exhibition held in Houston, Texas, USA, (2004).
6. Y. Li, N. Bjorndalen, and E. Kuru, "Numerical Modeling of Cuttings Transport on Horizontal Wells Using Conventional Drilling Fluids" Paper 2004-227, presented at the Petroleum Society's 5th Canadian International Petroleum Conference (55th Annual Technical Meeting), Calgary, Alberta, Canada, (2004).
7. M.E. Ozbayoglu, A. Saasen, M. Sorgun, and K. Svanes, "Estimating Critical Velocity to Prevent Bed Development for Horizontal-Inclined Wellbores" SPE/IADC 108005, presented at the SPE/IADC Middle East Drilling Technology Conference and Exhibition held in Cairo, Egypt, (2007).
8. M. Duan, S. Miska, M. Yu, N. Takach, R. Ahmed, and C. Zettner, "Transport of Small Cuttings in Extended-Reach Drilling" SPEJ 104192, (2008), pp. 258-265.
9. M.E. Ozbayoglu, R.O. Ettehadi, A.M. Ozbayoglu, and E. Yuksel, "Very-Difficult-to-Identify" Data for Hole Cleaning, Cuttings Transport and Pressure Drop Estimation in Directional and Horizontal Drilling" SPE/IADC 136304, (2010)
10. M. Sorgun, I. Aydin, and M.E. Ozbayoglu, "Friction Factor for Hydraulic Calculations Considering Presence of Cuttings and Pipe Rotation in Horizontal / Highly-Inclined Wellbores" Journal of Petroleum Science and Engineering 78 (2011) pp. 407-414.
11. J.O. Ogunrinde, and A. Dosunmu, "Hydraulic Optimization for Efficient Hole Cleaning in Deviated and Horizontal Wells" SPE 162970, (2012).
12. S.G. Valluri, S.Z. Miska, R. Ahmed, M. Yu, and N. Takach, "Experimental Study of Effective Hole Cleaning Using "Sweep" in Horizontal Wellbores" SPE 101220, presented at the SPE Annual Technical Conference and Exhibition held in San Antonio, Texas, USA, (2006).
13. M. Duan, S. Miska, M. Yu, N. Takach, R. Ahmed, and C. Zettner, "Critical Conditions for Effective Sand-Sized-Solids Transport in Horizontal and High-Angle Wells" SPEJ 106707, (2009), pp. 229-239.
14. A.L. Martins, C.H.M. Sa, A.M.F. Lourenco, and W. Campos, "Optimizing Cuttings Circulation in Horizontal Well Drilling" SPE 35341, presented at the International Petroleum conference and Exhibition of Mexico held in Villahermosa, Mexico, (1996).
15. D. Nguyen, and S.S. Rahman, "A Three -Layer Hydraulic Program for Effective Cuttings Transport and Hole Cleaning in Highly Deviated and Horizontal Wells" SPEJ 51186, (1998).
16. I. Kjosnes, G. Loklingholm, A. Saasen, S.O. Syrstad, A. Agle, and K.A. Solvang, "Successful Water Based Drilling Fluid Design for Optimizing Hole Cleaning and Hole Stability" SPE/IADC 85330, presented at the SPE/IADC Middle East Drilling Technology Conference and Exhibition held in Dhubai, UAE, (2003).
17. T.E. Becker, and J.J. Azar, "Mud-Weight and Hole-Geometry Effects on Cuttings Transport While Drilling Directionally" SPE 14711, SPE Manuscript, (1985).
18. T. Hemphill, and T.I. Larsen, "Hole-Cleaning Capabilities of Water-and-Oil-Based Drilling Fluids: A Comprehensive Experimental Study" SPEJ 26328, (1996) pp. 201-207.
19. P.H. Tomren, A.W. Iyoho, and J.J. Azar, "Experimental Study of Drilled Cuttings Transport in Directional Wells" SPEJ 12123, (1986), pp. 43-56.
20. T.E. Becker, J.J. Azar, and S.S. Okrajni, "Correlations of Mud Rheological Properties with Cuttings-Transport Performance in Directional Drilling" SPEJ 19535, (1991), pp. 16-24.
21. T.I. Larsen, A.A. Pilehvari, and J.J. Azar, "Development of a New Cuttings-Transport Model for High-Angle Wellbores Including Horizontal Wells" SPEJ 25872, (1997), PP. 129-135.
22. M. Mohammadsalehi, and N. Malekzadeh, "Optimization of hole Cleaning and cuttings Removal in Vertical, Deviated and Horizontal Wells" SPE 143675, presented at the Asia Pacific Oil and Gas Conference and Exhibition held in Jakarta, Indonesia, (2011).
23. S. Walker, and J. Li, "The Effects of Particle Size, Fluid Rheology, and Pipe Eccentricity on Cuttings Transport" SPE 60755, presented at the SPE/ICoTA Coiled Tubing Roundtable held in Houston, TX, (2000).

24. R.A. Sanchez, J.J. Azar, A.A. Bassal, and A.L. Martin, "Effect of Drillpipe Rotation on Hole Cleaning During Directional-Well Drilling" SPEJ 56406, (1999) PP. 101-108.
25. H. Cho, S.N. Shah, and S.O. Osisanya, "A Three-Segment Hydraulic Model for Cuttings Transport in Horizontal and Deviated Wells" SPE/PSCIM 65488, presented at the SPE/Petroleum Society of CIM International Conference on Horizontal Well Technology held in Calgary, Alberta, Canada, (2000).
26. Y. Masuda, Q. Doan, M. Oguztoreli, S. Naganawa, T. Yonezawa, A. Kobayashi, and A. Kamp, "Critical Cuttings Transport Velocity in Inclined Annulus: Experimental Studies and Numerical Simulation" SPE 65502, presented at the SPE/Petroleum Society of CIM International Conference on Horizontal Well Technology held in Calgary, Alberta, Canada, (2000).
27. S.A. Mirhaj, S.R. Shadizadeh, and M. Fazaelizadeh, "Cuttings Removal Simulation for Deviated and Horizontal Wellbores" SPE 105442, (2007).
28. M.E. Ozbayoglu, A. Saasen, M. Sorgun, and K. Svanes, "Effects of Pipe Rotation on Hole Cleaning for Water-Based Drilling Fluids in Horizontal and Deviated Wells" IADC/SPE 114965, presented at the SPE/IADC Asia Pacific Drilling Technology Conference and Exhibition held in Jakarta, Indonesia, (2008).
29. T. Hemphill, and K. Ravi, "Pipe Rotation and Hole Cleaning in an Eccentric Annulus" IADC/SPE 99150, presented at the IADC/SPE Drilling Conference held in Miami, Florida, USA, (2006).
30. H.I. Bilgesu, N. Mishra, and S. Ameri, "Understanding the Effects of Drilling Parameters on Hole Cleaning in Horizontal and Deviated Wellbores using Computational Fluid Dynamics" SPE 111208, presented at the SPE Eastern Regional Meeting held in Lexington, Kentucky, USA, (2007).
31. R. Ahmed, M. Sagheer, N. Takach, R. Majidi, M. Yu, S. Miska, C. Rohart, and J. Boulet, "Experimental Studies on the Effect of Mechanical Cleaning Devices on Annular Cuttings Concentration and Applications for Optimizing ERD Systems" SPE 134269, presented at SPE Annual Technical Conference and Exhibition held in Florence, Italy (2010).
32. S.S. Costa, S. Stuckenbruck, S.A.B. da Fontoura, and A.L. Martins, "Simulation of Transient Cuttings Transportation and ECD in Wellbore Drilling" SPE 113893, presented at the SPE Europec/EAGE Annual Conference and Exhibition held in Rome, Italy, (2008).
33. M. Yu, and N.E. Takach, "An Experimental Study of Hole Cleaning under Simulated Downhole Conditions" Paper SPE 109840, presented at the SPE Annual Technical Conference and Exhibition, Anaheim, California, 11-14 November, 2007.
34. G.J. Guild, I.M. Wallace, and M.J. Wassenborg, "Hole Cleaning Program for Extended Reach Wells" SPE/IADC 29381, presented at the SPE/IADC Drilling Conference held in Amsterdam, (1995).
35. A.A. Pilehvari, J.J. Azar, and S.A. Shirazi, "State-of-the-Art Cuttings Transport in Horizontal Wellbores" SPEJ 57716, (1999), pp. 196-200

Flow Profile Distribution in Narrow Annuli Using Modified Yield Power-Law Fluid Model

T.N. Ofei, S. Irawan and W. Pao

Abstract Drilling fluids are mostly non-Newtonian and can be accurately modeled by Herschel–Bulkley model, also known as yield power-law (YPL) fluid model. There are very little studies in literature on the flow behaviors of YPL fluid relative to cuttings transport in annular wellbores. However, in narrow annuli of diameter ratio, $\kappa > 0.7$, the flow behaviors of YPL fluids are still unknown. This study predicts the flow patterns of YPL fluid using CFD finite volume method in narrow annuli. The flow is considered fully developed, laminar, and steady state. The effects of bulk fluid velocity, diameter ratio, inner pipe rotation speed, and eccentricity on flow profiles are discussed and results presented. The singularity problem associated with the classical YPL viscosity function at vanishing shear rates is alleviated by using the proposed YPL viscosity model by Souza Mendes and Dutra (SMD) which is numerically stable and devoid of discontinuity. Simulation results compared excellently to experimental data.

Keywords CFD · Yield power-law fluid · Narrow annuli

Nomenclature

e Offset distance (m)
 D_1 Inner pipe diameter (m)
 D_2 Outer pipe diameter (m)

T.N. Ofei (✉) · S. Irawan
Petroleum Engineering Department, Universiti Teknologi PETRONAS,
Tronoh, Malaysia
e-mail: titus.ifei@petronas.com.my; titusofei@hotmail.com

W. Pao
Mechanical Engineering Department, Universiti Teknologi PETRONAS,
Tronoh, Malaysia

K	Consistency index (Pa s ⁿ)
m	Regularization parameter (1/s)
n	Flow behavior index
R	Radial distance (m)
r	Radial direction
p	Fluid pressure (Pa)
κ	Diameter ratio (D_1/D_2)
τ_0	Yield stress (Pa)
τ	Shear stress (Pa)
η_0	Zero shear rate viscosity
η	Apparent viscosity
ε	Eccentricity
ρ	Density (kg/m ³)
\vec{U}	Velocity vector
ω	Angular speed
$\dot{\gamma}$	Shear rate (1/s)

1 Introduction

Accurate modeling of drilling fluids for drilling operations is very essential for the design of hydraulic programs, cuttings transport, and drilling optimization. Drilling fluids are generally polymer-based shear-thinning non-Newtonian fluids whose shear stress strain rate behavior can be best described by the Herschel–Bulkley [1] (HB) fluid model, also known as yield power-law (YPL) fluid model. The YPL model has been used to accurately correlate the rheological data of several drilling fluids in some experimental studies [2, 3]. The classical constitutive equation governing the stress–deformation behavior of HB fluid (YPL fluid) in 1D is given as [1, 4]

$$\begin{cases} \tau = \tau_0 + K\dot{\gamma}^n, & \text{if } \tau > \tau_0 \\ \dot{\gamma} = 0 & \text{otherwise} \end{cases} \quad (1)$$

It can be seen that Eq. 1 will predict an infinite viscosity at limiting zero rate of strain leading to a discontinuity and numerical difficulties, a behavior that leads to poor curve fittings to data pertaining to viscoplastic fluids. Overcoming these setbacks, Mitsoulis et al. [5] proposed a new YPL stress function based on Papanastasiou [6] idea on Bingham-type materials for a finite apparent viscosity value at vanishing shear rate as

$$\bar{\tau} = \left(K|\dot{\gamma}|^{n-1} + \tau_0 \frac{1 - \exp(-m|\dot{\gamma}|)}{|\dot{\gamma}|} \right) \bar{\gamma} \quad (2)$$

A careful analysis [7] on the flow instabilities of Eq. 2 revealed that for a typical shear-thinning fluid, that is, when the flow behavior index $n < 1$, the apparent

viscosity tends to infinity when the shear rate approached zero. They argued further that Eq. 2 does not follow Papanastasiou's idea that the apparent viscosity should be a finite value at vanishing shear rate. Souza Mendes and Dutra [8] proposed a modified YPL model akin to Eq. 2 but devoid of discontinuity and numerical difficulties. They expressed the function as

$$\bar{\tau} = \left(1 - \exp\left(\frac{-\eta_o|\dot{\gamma}|}{\tau_o}\right)\right) \left(\frac{\tau_o}{|\dot{\gamma}|} + K|\dot{\gamma}|^{n-1}\right) \bar{\dot{\gamma}} \quad (3)$$

This study focuses on a CFD simulation of a fully developed, laminar, and steady-state flow of YPL fluid in concentric and eccentric narrow annuli with and without inner pipe rotation. To avert numerical singularity problems, the SMD viscosity model in Eq. 3 is adopted. The study addresses the effects of drilling parameters on the flow profiles of YPL fluid in narrow annuli.

2 Materials and Methods

Laminar flow of the proposed viscoplastic fluid properties by Souza Mendes and Dutra (SMD) [8] flowing through concentric and eccentric narrow annuli is considered. The inner cylinder is either stationary or rotating about its own axis.

2.1 Governing Equations

The yield viscoplastic fluid flow in pipe or annulus is usually modeled based on the assumptions such as (a) fluid is incompressible and isothermal and (b) flow is laminar, steady state, and fully developed. The governing continuity and momentum equations may be generally expressed, respectively, as

$$\nabla \cdot \vec{U} = 0 \quad (4)$$

$$\vec{U} \cdot \nabla(\rho \vec{U}) = -\nabla p + \nabla \cdot \tau \quad (5)$$

However, the stress tensor is nonlinearly related to the rate of strain for non-Newtonian fluids as

$$\tau = \eta \left[(\nabla \vec{U}) + (\nabla \vec{U})^T \right] \quad (6)$$

The proposed modified YPL flow equation is obtained by incorporating Eqs. 3 into 5. The above governing sets of equations were discretized using finite volume technique. The discretized equations together with initial and boundary conditions are solved iteratively for each control volume using ANSYS CFX solver [9].

2.2 Boundary Conditions and Meshing

At the inlet, a mass flow rate is specified, while a zero gauge pressure specified at the outlet boundary. The inner and outer walls were imposed with no-slip boundary conditions. In addition, the inner pipe can either be stationary or rotating at a specified angular speed. The concentric and eccentric annular geometries were meshed into tetrahedral cells resulting in grids of approximately 0.8×10^6 to 1.4×10^6 elements depending on the diameter ratio and eccentricity. Grid independence studies were conducted on the 3D geometry to optimize the mesh sizes until results were no more dependent on mesh size (see Fig. 1). Inflation layers covering about 20 % of the inner and outer pipes radii were created near the walls to accurately account for the high gradients in variables in that region as shown in Fig. 2.

2.3 Model Validation

Experimental data [10] for shear-thinning fluid obeying the Herschel–Bulkley fluid model flowing in a concentric annulus were adopted and compared with the current simulation model setup. The fluid is composed of 0.2 % Carbopol (940) solution. The rheological and operating parameters are shown in Table 1.

Fig. 1 Grid independence study

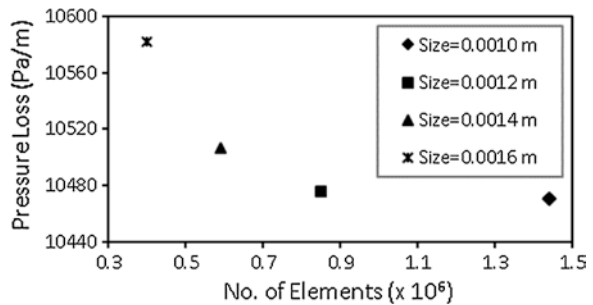


Fig. 2 3D meshed section of concentric and eccentric geometry

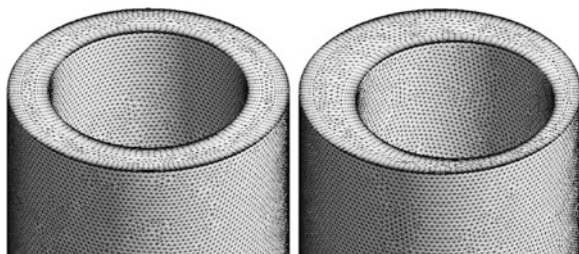
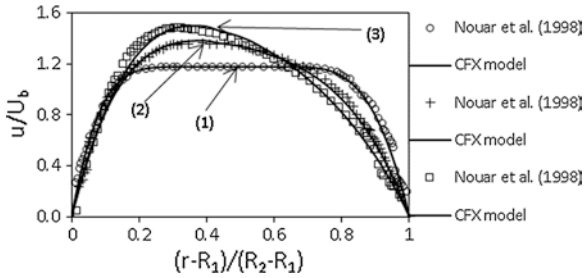


Table 1 Rheological and operating parameters [10]

	U (m/s)	ω (rpm)	τ_o (Pa)	K (Pa · s ⁿ)	n (–)
(1)	0.0740	0	26.54	20.93	0.34
(2)	0.0728	131.8	32	12.09	0.43
(3)	0.0728	268.15	32	12.09	0.43

Fig. 3 Experimental and simulation results for velocity profiles in concentric annular gap: (1) 0 rpm, (2) 131.8 rpm, and (3) 268.15 rpm



As shown in Fig. 3, there is excellent agreement between simulation and experimental axial velocity profile data with or without inner rotating cylinder, confirming the validity of the current model setup.

2.4 Simulation Study

The viscosity function in Eq. 3 is currently not available in the library of variables of ANSYS CFX-14.0; hence, it is modeled as expression language and coupled with the momentum equations. This study is carried out in concentric and eccentric annular geometries modeled with three diameter ratios, 0.70, 0.80, and 0.90, and flowing with bulk fluid velocities from 0.10 to 0.50 m/s. Pipe eccentricities are 0 and 0.50, while inner pipe rotation speed varies from 0 to 300 rpm. Table 2 summarizes the simulation setup data including fluid rheological properties, and operating and solver parameters.

3 Results and Discussion

3.1 Effect of Fluid Velocity on Velocity Profile

In Fig. 4a, b, it is evidenced that an increase in bulk fluid velocity results in an increase in axial fluid velocity profiles. In concentric annulus, fluid profiles are uniform, whereas in the eccentric annulus, there is a preferential flow in the wider gap as compared to the narrow gap due to the resistance to flow as a function of fluid viscosity in the narrow gap.

Table 2 Simulation data for rheological properties, and operating and solver parameters

Simulation data	$\kappa = 0.7$	$\kappa = 0.8$	$\kappa = 0$
Flow behavior index (n)	0.31	0.31	0.31
Consistency index, $K(\text{Pa} \cdot \text{s}^n)$	6.3	6.3	6.3
Yield stress, $\tau_o(\text{Pa})$	8.0	8.0	8.0
Zero shear rate viscosity, $\eta_o(\text{Pa} \cdot \text{s})$	1,100	1,100	1,100
Fluid density, $\rho(\text{kg/m}^3)$	1,200	1,200	1,200
Bulk fluid velocity, $V_b(\text{m/s})$	0.1–0.5	0.1–0.5	0.1–0.5
Inner pipe rotation speed, $\omega(\text{rpm})$	0–300	0–300	0–300
Eccentricity, ($\varepsilon = 2e/(D_2 - D_1)$)	0–0.5	0–0.5	0–0.5
Isothermal condition, ($^{\circ}\text{C}$)	25	25	25
Flow regime	Laminar	Laminar	Laminar
Advective scheme	High resolution	Same	Same
Convergence criteria	1×10^{-5}	1×10^{-5}	1×10^{-5}
Maximum iteration	300	300	300

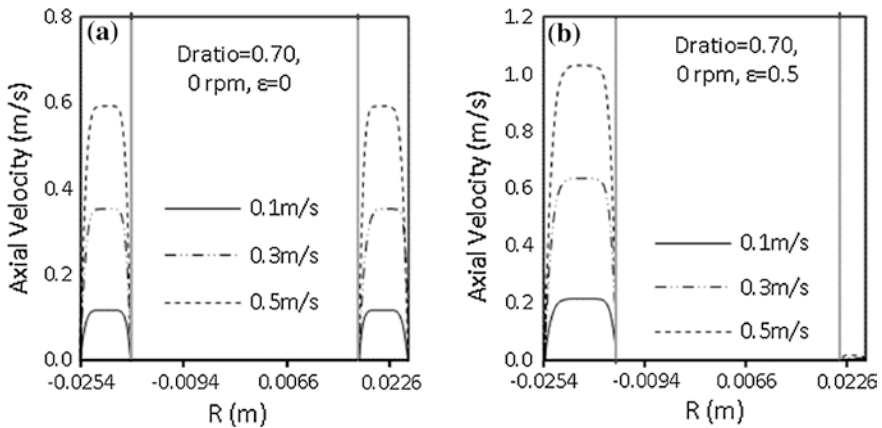


Fig. 4 Varying bulk fluid velocity **a** concentric annulus **b** eccentric annulus

3.2 Effect of Diameter Ratio on Velocity Profile

In concentric annulus of varying diameter ratios, the axial velocity profiles have similar magnitudes, an indication of similar carrying capacities of the drilling fluid for all varying diameter ratios. On the contrary, in eccentric annulus, as diameter ratio increases, fluid velocity profile increases in the wider gap, indicating a better cuttings transport. These are shown in Fig. 5a, b, respectively.

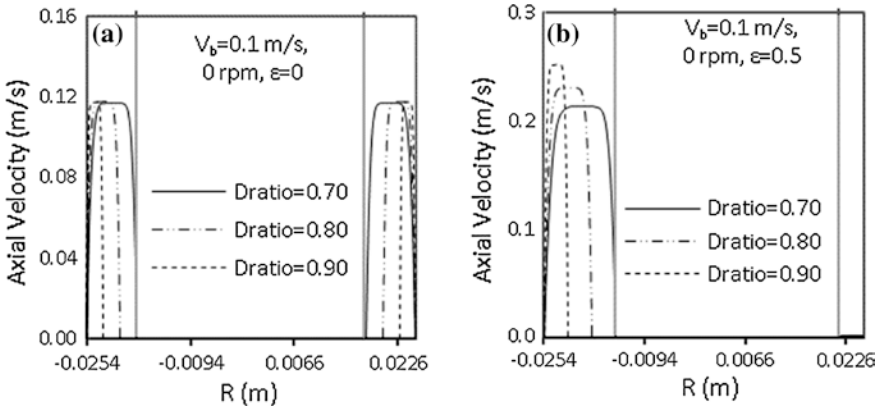


Fig. 5 Varying diameter ratios **a** concentric annulus **b** eccentric annulus

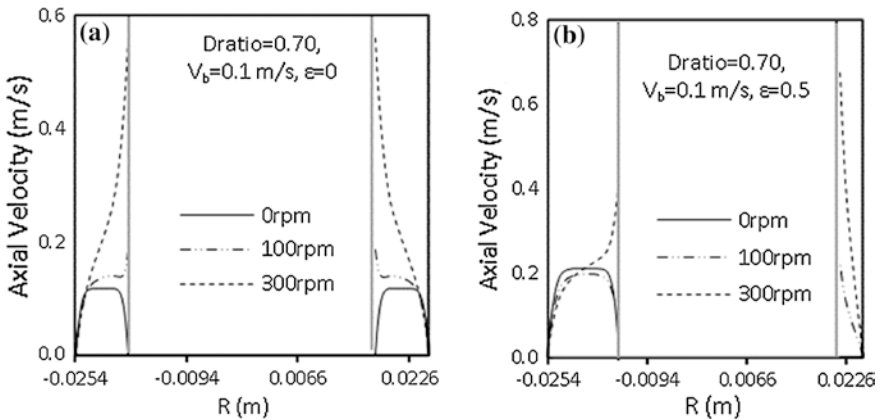


Fig. 6 Varying pipe rotation speed **a** concentric annulus **b** eccentric annulus

3.3 Effect of Inner Pipe Rotation Speed

The influence of pipe rotation speed on fluid profiles is greater at increasing rotation speed. The fluid profile increases near the pipe and dissipates with increasing distance across the annular gap. This indicates that cuttings transport is significantly enhanced by rotating the drill pipe (see Fig. 6a). In eccentric annulus, it is noticed that in the absence of pipe rotation (0 rpm), the fluid flows preferentially through the wider annular gap due to the difficulty to flow in the narrow annular gap. However, as the pipe rotation speed increases, the gelled fluid in the narrow annular gap is removed, an indication of better cuttings transport in the narrow annular gap (see Fig. 6b).

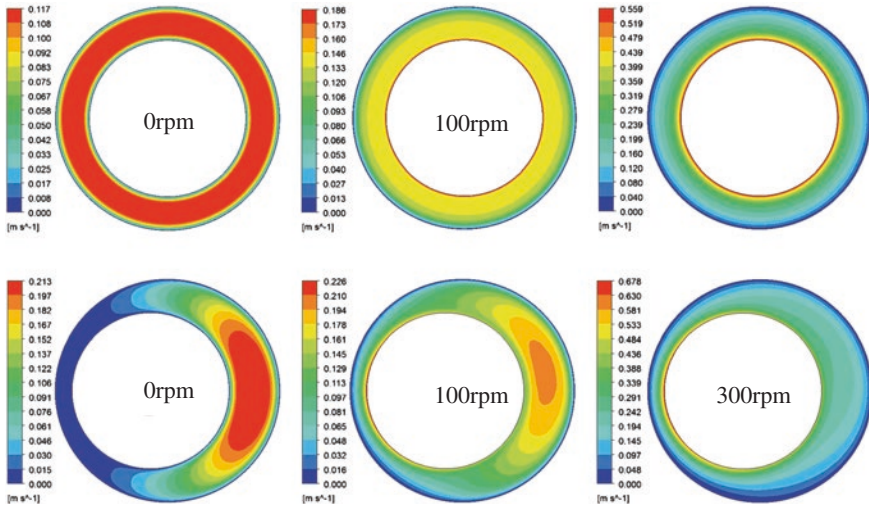


Fig. 7 Velocity contours in concentric and eccentric annuli

3.4 Velocity Contours

Figure 7 shows velocity contours in concentric and eccentric annuli varying from 0 to 300 rpm for constant diameter ratio of 0.70 and flowing at 0.1 m/s. The effects of eccentricity and inner pipe rotation are seen to play important roles in the flow distributions in the annular gaps.

4 Conclusions

The following could be inferred from the above study:

1. Increasing bulk fluid velocity results in an increase in fluid velocity profiles in both concentric and eccentric annuli.
2. In concentric annulus of varying diameter ratios, the velocity profiles have similar magnitudes. On the contrary, in eccentric annulus, as diameter ratio increases, fluid velocity profile increases in the wider gap, indicating a better cuttings transport.
3. The influence of increasing inner pipe rotation speed shows significant improvement in the fluid velocity in both concentric and eccentric annuli.

Acknowledgments The authors are very grateful to the Universiti Teknologi PETRONAS in Malaysia for sponsoring this article for publication.

References

1. W.H., Herschel and R. Bulkley, "Konsistenzmessungen Von Gummi-Benzollosungen," *Kolloid Z.* **39** (1926) 29-300
2. V.C., Kelessidis, R. Maglione, C. Tsamantaki and Y. Aspirtakis, "Optimal Determination of Rheological Parameters of Herschel-Bulkley Drilling Fluids and Impact on Pressure Drop, Velocity Profiles and Penetration Rates During Drilling," *J. Petrol. Sci. Eng.* **53**, (2006) 203-224.
3. R., Ahmed and S. Miska, "Experimental Study and Modeling of Yield Power-Law Fluid in Annuli With Drillpipe Rotation," Paper IADC/SPE2604 presented at the IADC/SPE Drilling Conference held in Orlando, Florida, U.S.A, 4-6 March (2008).
4. R.B., Bird, O. Hassager and R.C. Armstrong, "Dynamics of Polymeric Liquids," Vol. **1**: Fluid Mechanics, 2nd Edition, Wiley, New York (1987).
5. E., Mitsoulis, S.S. Abdali and N.C. Markatos, "Flow Simulation of Herschel-Bulkley Fluids Through Extrusion Dies," *Can. J. Chem. Eng.*, **71** (1993) 147-160.
6. T.C., Papanastasiou, "Flow of Materials with Yield," *J. Rheol.*, **31** (1987) 385.
7. H., Zhu, Y.D. Kim and D. De Kee, "Non-Newtonian Fluid with a Yield Stress," *J. Non-Newtonian Fluid Mech.*, **129** (2005) 177-181.
8. P.R., Souza Mendes and S.S.E. Dutra, "A Viscosity Function for Viscoplastic Liquids," *Annual Trans. of the Nordic Rheol. Soc.*, **12** (2004)
9. ANSYS CFX Release 14.0—"Solver Modelling Guide," ANSYS, Inc., USA (2011)
10. C., Nouar, C., Desaubry and H. Zenaïdi, "Numerical and Experimental Investigation of Thermal Convection for Thermodependent Herschel-Bulkley Fluid in an Annular Duct with Rotating Inner Cylinder," *Eur. J. Mech.*, (1998) B 17:875-90

Part IV
Reservoir Monitoring and Management
and Risk Assessment

Quantification of Clay Mineral and Log Response Toward Reservoir Rock Properties

Nur Asyraf Md Akhir, Gamal Ragab Gaafar and Ismail Mohd Saaid

Abstract Clay minerals are fine grained which compose of complex aluminum silicate with definite crystalline structure. They are divided into four major important groups which are kaolinite, illite, montmorillonite (smectite), and chlorite. The effect of clay minerals on formation evaluation and reservoir performance depends on its morphology, cation exchange capacity, and swelling properties. The occurrence of clay minerals leads to inaccurate values of porosity, water saturation, and permeability. In addition, the impacts of clay minerals during drilling, water injection, and acid stimulation are investigated as it leads to formation damage near wellbore or deep into formation. The current study aims at investigating the effect of clay minerals on log response and reservoir characteristics and to compare its impact on reservoir performance against reported works. Methodology used in the present research involves log interpretation, clay mineral characterization and to analyze the effect of clay on water relative permeability, water saturation, and capillary pressure curve. Results were discussed and benchmarked against selected literatures. Based on the effects of clay minerals, there are reduction in water relative permeability due to fine migration and swelling of clays. In addition, it was found that accurate value of water saturation can be obtained by using Waxman–Smits model. Moreover, it is shown that capillary pressure curve is reflected by the heterogeneity and bimodality of the reservoir. In this project, it is shown that the effect of clay minerals on reservoir can lead to the inaccuracy of determining reservoir characterization and its effect on reservoir productivity.

N.A.M. Akhir (✉) · I.M. Saaid
Universiti Teknologi PETRONAS, Tronoh, Malaysia
e-mail: Asyraf.akhir@petronas.com.my

G.R. Gaafar
PETRONAS Carigali Sdn. Bhd., Kuala Lumpur, Malaysia

Keywords Clay minerals · Logging tools · Water relative permeability · Water saturation

1 Introduction

Clay minerals are known as phyllosilicates due to its plasticity property. They have a very high surface area and fine-grained structure. Clay minerals can be classified into allogenic (detrital) and authigenic clays based on its occurrence during deposition [1]. In addition, clay minerals can be distinguished into three modes of distribution which are laminar, structural, and dispersed. Laminar and structural clay distribution are affecting the overall average effective porosity of the formation, meanwhile dispersed clay distribution can reduce permeability and porosity of the formation. The mode of occurrence of dispersed clay mineral can be subdivided into discrete, lining, and bridging. Based on the study on porosity and permeability relationship for dispersed clay mineral, pore bridging gives the lowest permeability and porosity relationship compared to discrete clay distribution and pore-lining [2].

The main properties of clay minerals are its cation exchange capacity (CEC) and swelling properties. The presence of clay minerals in the formation will leave negative charge on clay surface. This negative charge tends to balance the charge with positively charge cations in soil such as magnesium and potassium [3]. Meanwhile, swelling of clays happen when the exchangeable cations are hydrated and water molecules enter the space between clay structural layers and expands the volume of clay. There are several effects of clay minerals in the shaly reservoir which are further reduction in permeability due to migration of loose and fine clay minerals, water sensitivity, acid sensitivity and influence logging tool responses [4].

The mixing of incompatible drilling fluid with clay minerals in drilling operation leads to swell of clays hence the stuck pipe problem. In addition, mud viscosity can affect the dispersion and swelling of shales and decreases the diffusion velocity in porous media [5]. Meanwhile, during water injection, the effect of clay minerals can be due to the incompatible mixing fluids and difference in pH between injection and formation water, and difference in salinity and shear by moving pore water [6, 7]. In addition, clay minerals, siderite, and ankerite can release iron that will precipitate in the form of ferric hydroxide gel that will block the pore throats when it dissolved into acid [8].

In formation evaluation and log interpretation, the existence of clay minerals in the formation leads to inaccurate values of porosity, water saturation, and permeability. The presence of clay-bound water affects porosity and electrical properties of the formation by overestimating the porosity value due to significant amount of hydrogen and underestimating the resistivity value due to presence of excess of conductivity in the formation. Inaccuracy in reservoir properties leads to wrong interpretation of reservoir volume and hydrocarbon-in-place.

2 Methodology

Research methodology is divided into log interpretation, clay mineral characterization and to analyze the effect of clay mineral on water relative permeability, water saturation, and capillary pressure curves. In log interpretation, the volumes of shale are calculated and the types of clay minerals are identified. Next, the characteristics of clay mineral samples taken from Balingian Sub-basin, Mukah, and Sarawak have been identified by using thin section, polarize microscope, and field-emission scanning electron microscope/energy dispersive X-Ray (FESEM/EDX). Some of the field data such as scanning electron microscope (SEM) data for clay minerals characterization and the data on water relative permeability, water saturation, capillary pressure, logs response, and formation damage are used for the investigation of the effects of clay minerals [9].

2.1 Log Interpretation

The volume of shale is calculated based on gamma ray, density, neutron, and resistivity logs' reading taken from the case study done on the shaly reservoir in Palouge-Fal Oilfield, Sudan [10].

- Gamma Ray Log

The volume of shale is calculated by using the following equation [10]:

$$V_{sh} = (GR_{log} - GR_{min}) / (GR_{max} - GR_{min}) \quad (1)$$

where, GR_{log} = gamma ray log reading (zone of interest), GR_{min} = minimum value of gamma ray log, GR_{max} = maximum value of gamma ray log. Next, the types of clay minerals are identified using the plot of thorium (ppm) versus potassium (%)—these data are taken from spectral gamma ray reading. Then, this plot will be compared with thorium versus potassium cross-plot.

- Neutron–Density Log

The volume of shale is determined based on the equation below [11]:

$$V_{sh} = (\varnothing_N - \varnothing_D) / (\varnothing_{NSH} - \varnothing_{DSH}) \quad (2)$$

where, \varnothing_N = neutron porosity in the sand, \varnothing_D = density porosity in the sand, \varnothing_{NSH} = neutron porosity in adjacent shale, \varnothing_{DSH} = density porosity in adjacent shale.

- Resistivity Log

The calculation of volume of clay minerals is based on the following equation [11]:

$$V_{sh} = \frac{[\log(RES D) - \log(RES D_{CLN})]}{[\log(RES D_{SHL}) - \log(RES D_{CLN})]} \quad (3)$$

where, RESD = resistivity log reading from zone of interest, RESD_CLN = resistivity log reading from clean sand, RESD_SHL = resistivity log reading from shale.

2.2 Clay Minerals Characterization

Clay mineral characterizations are analyzed by using thin section, polarized microscope, SEM, and FESEM/EDX. The purposes of thin section analysis are to study of texture, sorting, and porosity of clay minerals. Then, the thin section is analyzed underpolarized microscope in order to detect the amorphous substance and distinguish crystalline structure in the samples. In addition, SEM is used to analyze the morphology, structure, and crystal size of the clay minerals. Next, FESEM/EDX is used in determining the surface structure and chemical elemental analysis of the clay minerals.

2.3 Effect of Clay Minerals

In this part, the effect of clay minerals on water relative permeability, water saturation, capillary pressure curve, log responses, and formation damage is analyzed based on the field data [9]. The purposes of these analyses are to examine the effects of clay minerals toward these parameters and how to identify its impact and to eliminate the problem associated with the clay minerals.

3 Results and Discussion

3.1 Log Interpretation

Natural gamma ray reading shows overestimate value of gamma ray, hence the volume of shale. It is because natural gamma ray can only measure the total radioactive in the formation regardless the sources of radioactive. The volume of shale calculated is 0.75. The reading from spectral gamma ray gives lower gamma ray compared to natural gamma ray. The plot of thorium versus potassium reading shows that the formation is mainly consists of mixed layer clay, followed by glauconite and potassium feldspar. Meanwhile, the volumes of shale calculated from neutron–density and resistivity logs are 0.45 and 0.50, respectively. The lower gamma ray volumes show that the use of combination logging tools and resistivity logs can give better indication of volumes of shale. However, with the presence of clay minerals in the formation, these tools will give inaccurate values of porosity and water saturation.

3.2 Scanning Electron Microscope (SEM) Analysis

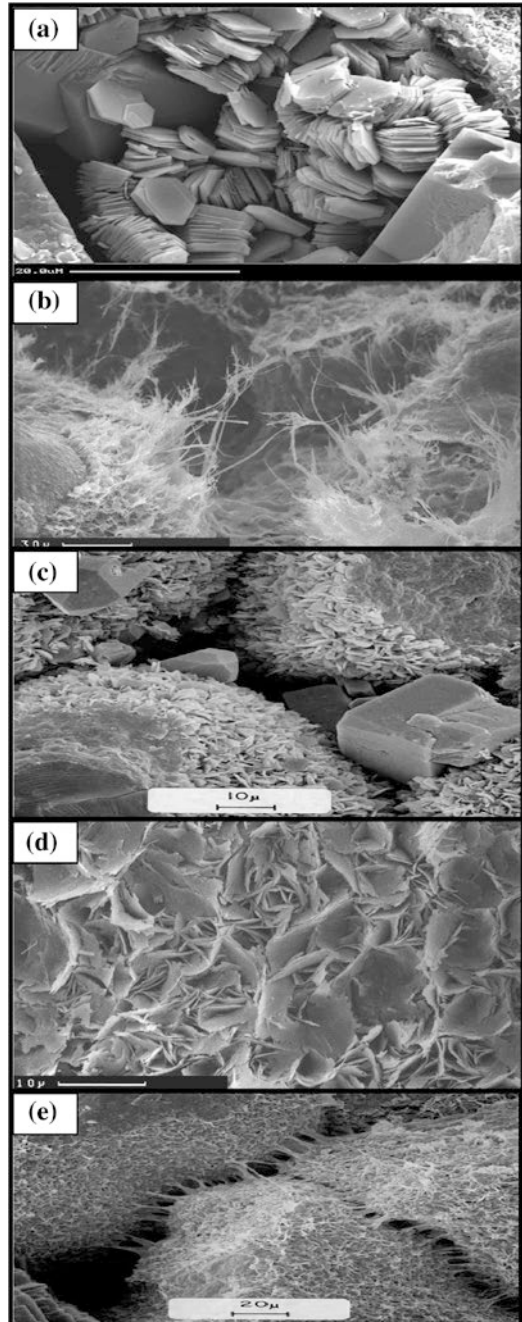
Figure 1a shows pseudo-hexagonal plates or booklet structure of kaolinite stack above each other. Next is illite group of clay minerals as shown in Fig. 1b. Illite has fibrous structure growing and coating the grain. Furthermore, the structure of chlorite group is shown in Fig. 1c. Chlorite group has platelets and honeycomb structure, and it is coating on sandstone grains. Based on the result, the structure of kaolinite and chlorite can easily break and lead to the potential of fine migration. Figure 1d shows the structure of honeycomb and cornflake of smectite group. Smectite group has the swelling properties, and its expansion during swells can lead to fine migration. In addition, clay minerals can also occur as mixed layer, for example, mixed layer of illite–smectite as shown Fig. 1e; coating of smectite and bridging of illite on the rock grains.

3.3 Combination of Thin Section and Field-Emission Scanning Electron Microscope/Energy Dispersive X-Ray (FESEM/EDX)

Figure 1 shows the result from thin section and FESEM/EDX analysis for five different samples. Figure 2a shows microporosity of the clay minerals structure, and FESEM analysis shows dissolution of potassium feldspar and flocculation of kaolinite clays; its plates are arranged in edge-to-face toward each other. This indicates the separation of the charges at surface and edge of clay particles. Meanwhile, Fig. 2b shows lamination of shale and sand formation. Clay minerals' thin beds show microporosity distribution, while sandstone laminations show bigger porosity with interconnected pore space. The FESEM image for this sample shows flocculation of kaolinite. Figure 2c shows sandstone lamination located next to clay minerals. The thin section shows the grain sizes are located close to each other. Meanwhile, FESEM image shows the platelets structure of kaolinite. This can be the reason of poor porosity and permeability of the sample as the kaolinite leads to fine migration and block the pore space. Furthermore, Fig. 2d shows the invasion of clay minerals next to sandstone lamination, with the area near to clay minerals formation has poorer porosity. In addition, the images from thin section and FESEM show the dissolution of chlorite clays. Finally, Fig. 2e shows the result from sandstone sample. The thin section shows greater grain size with good porosity and permeability. Meanwhile, the quartz overgrowth and precipitation of pyrite (cementation) are found in FESEM analysis.

The result from EDX shows atomic percentage of chemical elements in these samples. Based on the result, Fig. 2a–d has high percentage of aluminum, silicon, and oxygen. This confirms the presence of clay minerals in these samples. In addition, the traces of magnesium and iron indicate the presence of chlorite groups especially from the result in Fig. 2a and d. Meanwhile, traces of potassium can be

Fig. 1 Images of **a** kaolinite, **b** illite, **c** chlorite, **d** smectite and **e** mixed layer (illite–smectite) under SEM analysis [9]



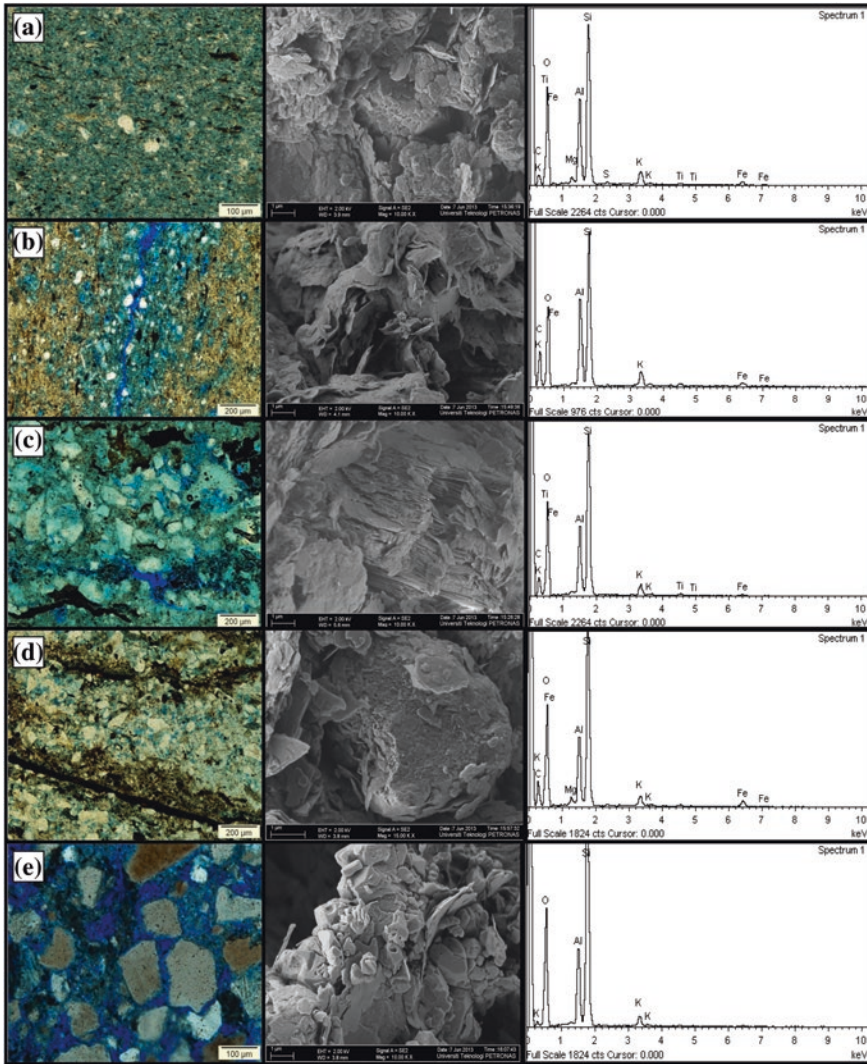


Fig. 2 Images of clay minerals samples under thin section and FESEM/EDX

due to the occurrence of illite group and potassium feldspar mineral in the formation. Moreover, the present of carbon element is due to the traces of hydrocarbon in the formation as it can also be seen as a black spot in the thin section. In addition, there are also small percentages of sulfur and titanium elements, in which the traces of titanium indicate heavy metal component. Finally, the result from Figure E shows high percentage of silicon and oxygen, and this is due to the composition of quartz mineral in the sandstone.

3.4 Effect of Clay Minerals on Water Relative Permeability

The effect of clay minerals on water relative permeability can be due to fine migration and clay swelling. From the study, water relative permeability decreases as water saturation increases. The point before the reduction of water relative permeability is known as the point of interstitial velocity. When the interstitial velocity is reached, the fine minerals will start to lose its bonding and migrate through the formation until its particles are supersaturated. Then, it will strand at the pore space and block the pore throats hence reduce the permeability of the formation. In addition, the presence of clay minerals can also lead to the increase in irreducible water saturation. It is due to the increase of capillary trapping by the invasion of drilling fluid near the wellbore, as a result, the relative permeability will reduced substantially.

In addition, the effect of clays swelling on water relative permeability is more severe as it can reduce the pore volume and permeability. High absorption of water by clay minerals lead to smaller mobility ratio of water adjacent to mineral surface, therefore, reduces relative permeability of water. Furthermore, pseudo-immobile water content separates zones of greater water relative permeability value from others presenting a restricted flow. Moreover, the reduction in water relative permeability drops substantially at maximum water saturation because of the reduction of residual oil saturation due to the effects of viscosity reduction.

3.5 Effect of Clay Minerals on Water Saturation

In this study, the effect of clay minerals on water saturation is investigated by using three different approaches: Archie equation (clean sand), laboratory data, and Waxman–Smits. The basic calculations for water saturation are based on different value of constant value (a), cementation factor (m), and saturation exponent (n). Based on the results, the values of water saturation calculated using Archie equation are higher compared to other methods. Even the result from laboratory data also gives overestimate values of water saturation. It is because the values are not corrected to the effect of excess water conductivity due to clay-bound water. Moreover, the calculation of water saturation using Waxman–Smits method is more accurate as it uses the corrected values of laboratory data, adjusted with CEC values of clay minerals. In this method, the extra conductivity is assumed to be independently in pore spaces of reservoir rock [12].

3.6 Effect of Clay Minerals Distribution on Capillary Pressure

The effects of clay minerals on capillary pressure are examined based on the distribution of clay minerals in thin section and its bimodal distribution behavior.

The permeability of the formation can be specified based on its distribution in the thin section. From the result, the good porosity is indicated by the coarser grain size and bigger space between the grains. Meanwhile, smaller grain size indicates poor porosity, and it is deteriorated by the filling of fine particles in the void space. Moreover, the changes of pore geometry under the thin section indicate high heterogeneity of the reservoir rock. In addition, the effects of clay minerals can be investigated base on the relationship between capillary pressures versus water saturation. From the result, the graph of capillary pressure is shifted to the right (upward) for the poorer permeability; this will give higher irreducible water saturation. Higher capillary pressure is also shown in this zone as it is needed to invade the fluid into smaller pores. Furthermore, discontinuity of the capillary curve can be an indication of bimodal distribution effect, in which it is associated with the decrease in reservoir quality due to smaller grain size.

3.7 Effect of Clay Mineralogy on Log Response

Gamma ray log response is affected by radioactive minerals such as k-feldspar and pore-filling of kaolinite. The presence of k-feldspar gives overestimate value of gamma ray. Thus, the use of spectral log is more feasible in determining the volume of shale as it can break natural radioactive reading into thorium, potassium, and uranium elements. Meanwhile, kaolinite will give a slightly underestimated volume of shale as it has lower gamma ray response compared to other clay minerals, and cemented kaolinite is not detected by the gamma ray response. Next is the effect of resistivity log toward laminar and structural clays, and glauconite. In the presence of clay minerals, the net matrix of resistivity decreases and gives overoptimistic value on neutron porosity due to high value of hydrogen atom in clay-bound water. In addition, undistinguishable dispersed clay in the formation leads to underestimation of porosity and permeability values as it coats and fills intergranular space of grains. Moreover, the presence of siderite in the formation can also affect the log response as it has higher than normal grain density; hence, it will give underestimation value of total porosity.

3.8 Potential Formation Damage from Diagenetic Components

In this section, the type of clay minerals associated with formation damage and its treatments are investigated. Smectite is the most sensitive mineral due to its swelling properties. Hence, the use of freshwater should be avoided. As a solution, potassium chloride solutions can be used as shale-swelling inhibitors in drilling fluids as potassium ion shows lower tendency to swell compared to sodium ion [13]. However, if the formation damage has occurred, the acid stimulation

(hydrochloric and hydrofluoric acids) with correct pre- and post-flushes is needed in order to prevent water blockage and improve flow back performance after the stimulation job. The second highest magnitudes of sensitive minerals are siderite, chlorite, and pyrite. These minerals lead to iron hydroxide precipitation with the presence of oxygen-rich system. Hence, oxygen scavenger is needed in order to lower the dissolved oxygen content in the solution. Acid system, stimulation work, and chelating agents can be used in order to eliminate the formation damage.

Moreover, kaolinite and illite groups can also lead to formation damage even though its magnitude is low. The problem is severe when high transient pressure and high flow rate of hydrocarbon production is used as this will lead to additional reason of fine migration. Hence, low transient pressure and flow rate, and clay stabilizer are needed. In addition, illite group has the ability to “mush” microporosity in the formation with the presence of freshwater. Hence, potassium chloride solutions and acid stimulation are more feasible to be used in eliminating formation damage.

4 Conclusion

The presence of clay minerals has a great impact on reservoir characterization and performance. The effects of clay minerals on logs response need to be corrected using various types of models and methods in order to obtain more accurate value of porosity, water saturation, and permeability. Based on calculated volumes of shale in log interpretation, natural gamma ray log gives overestimated volume of shale compared to neutron–density and resistivity logs. Furthermore, based on the analysis of the effects of clay minerals in the reservoir, it is shown that there are reduction in water relative permeability due to fine migration and swelling of clays. In addition, more accurate value of water saturation can be obtained by using Waxman–Smit model. Moreover, in the analysis of capillary pressure curve, there is a reflection of capillary pressure curve due to heterogeneity and bimodality of the reservoir. Next by examining the potential problem of formation damage, its mitigation plan and treatment have been introduced.

Acknowledgments The authors would like to thank the Petroleum Engineering Department, Universiti Teknologi PETRONAS and PETRONAS Carigali Sdn. Bhd. for their cooperation in providing the data and support.

References

1. Ali, S. A., Clark W. J., Moore, W. R., and Dribus, J. R., “Diagenesis and Reservoir Quality”, *Oilfield Review* Summer 2010: 22, no. 2, Schlumberger, 2010
2. Naesham, J., W., “The Morphology of Dispersed Clay in Sandstone Reservoirs and Its Effect on Sandstone Shaliness, Pore Space and Fluid Flow Properties”, *Society of Petroleum Engineers of American Institute of Mining*, 1977.

3. Ketterings, Q., Reid, S., and Rao, E., "Cation Exchange Capacity (CEC)", Agronomy Fact Sheet Series, Department of Crop and Soil Sciences, Cornell University Cooperative Extension, 2007.
4. Kurniawan, "Shaly Sand Interpretation Using CEC-Dependent Petrophysical Parameters", Dissertation of Doctor of Philosophy, Petroleum Engineering, Graduate Faculty of Louisiana State University and Agricultural and Mechanical College, 2005.
5. Khodja, M., Kodja-Saber, M., and Canselier, J. P., "Drilling Fluid Technology: Performances and Environmental Considerations", Products and Services; from R&D to Final Solutions, Intech, 2010.
6. Kantorowicz, J. D., Lievaart, L., Eylander, J. G. R., and Eigner, M. R. P., "The Role Of Diagenetic Studies In Production Operations", Clay Minerals (1986), 21, 769-780, The Mineralogical Society, 1986.
7. Krueger, R. F., "An Overview of Formation Damage and Well Productivity in Oilfield Operations", Journal of Petroleum Technology, Society of Petroleum Engineers, 1986.
8. Pittman E. D., and Thomas, J. B., "Some Applications of Scanning Electron Microscopy to the Study of Reservoir Rock", Journal of Petroleum Technology, Society of Petroleum Engineers of AIME, 1979.
9. Petronas Carigali Sdn Bhd (PCSB), Internal Reports and Training Materials.
10. Hussein, R. A. M., and Ahmed, M. E. B., "Petrophysical Evaluation of Shaly Sand Reservoirs in Palouge-Fal Oilfield, Melut Basin, South East of Sudan", Engineering and Computer Sciences (ECS), Journal of Science and Technology, Volume 13, No. 2, 2012.
11. Adeoti, L., Ayolabi, E. A., and James, P. L., 2009, "An Integrated Approach to Volume of Shale Analysis: Niger Delta Example, Orire Field", World Applied Sciences Journal 7 (4): 448-452, 2009, International Digital Organization for Scientific Information (IDOSI) Publications.
12. Waxman, M. H., and Smits, J. M., "Electrical Conductivities in Oil-Bearing Shaly Sands", Journal of SPE, American Institute of Mining, Metallurgical, and Petroleum Engineers, Inc, 1968.
13. Hensen, J. M., and Smit, B., "Why Clays Swell", Journal of Physics, Chemical, 106,12664-12667, American Chemical Society, 2002.

VTI Wave Modeling Using Weak Elastic Anisotropy Approximation

S.Y. Moussavi Alashloo, D.P. Ghosh and W.I. Wan Yusoff

Abstract Geological structures commonly exhibit anisotropic behavior which needs to be considered in seismic imaging not only to avoid distortions in imaging, but also to provide valuable information about lithology and fracture networks. Effects of seismic anisotropy in imaging can be studied by employing an anisotropic wave equation. Forward modeling of waves is a fundamental component in both migration and inversion algorithms to study the physics of wave propagation. In this study, we present the role of Thomsen parameters for elastic wave propagation in vertical transverse isotropy (VTI) using weak anisotropy approximation. Wavefield modeling revealed the influence of anisotropy parameter δ in controlling anisotropic features. Moreover, both phase velocity and group velocity are studied which can be employed for ray tracing.

Keywords Seismic anisotropy · Elastic wave propagation · VTI

1 Introduction

Hydrocarbon and geothermal reservoirs and overlying strata are often composed of anisotropic rocks. Considering anisotropy into account is necessary not only to avoid distortions in imaging, but also provides valuable information about lithology and fracture networks. To account for the effects of seismic anisotropy in imaging, an anisotropic wave equation must be employed. Forward modeling of waves is a fundamental component in both migration and inversion algorithms to study the physics of wave propagation and to test hypotheses inferred from observational data [1].

S.Y. Moussavi Alashloo (✉) · D.P. Ghosh · W.I. Wan Yusoff
Department of Petroleum Geoscience, Universiti Teknologi PETRONAS,
Seri Iskandar, Malaysia
e-mail: y.alashloo@gmail.com

Since there is no general analytic solution to the anisotropic elastic wave equation, various approximate approaches are employed. These are often based on physically motivated arguments specific to the problem under study [2, 3].

Most of the publications on seismic anisotropy present the effect of velocity variation with angle on the amplitudes and travel times of seismic waves [2, 4–6]. Backus [4], using averaging, illustrated that fine layering causes elastic anisotropy. Subsequently, transverse isotropy was parameterized using the “Thomsen” parameters for weak elastic anisotropy. The weak anisotropy approximation is an extremely powerful tool in understanding the behavior of seismic wavefields in anisotropic media [7]. Weak anisotropy approximation provides simpler equations compared to strong anisotropy. These equations indicate that anisotropy parameter δ controls most anisotropic phenomena of importance in exploration geophysics, some of which are non-negligible even when the anisotropy is weak [2]. Perturbation theory is another technique which applied to study attributes of elastic waves propagating in weakly anisotropic media. The approximated formula demonstrates that all studied attributes rely on elements of a matrix linearly dependent on parameters of a medium [3].

Since petroleum geophysicists are particularly interested in layered sedimentary rocks, the analysis of events at a planar horizontal interface between two media is given special attention. The principal objective of this research is to provide an approach offering a better understanding of physics of anisotropic media as observed through elastic waves. We present the role of Thomsen parameters for elastic wave propagation in vertical transverse isotropy (VTI) using weak anisotropy approximation. In this study, both phase velocity and group velocity are studied which can be employed for ray tracing [8].

2 Theory

When the wave velocity propagation depends on the angle between the wave vector and the vertical anisotropy symmetry axis, the medium is called VTI. Since most of rocks have anisotropy in the weak to moderate range (anisotropy parameters < 0.2), one can use the approximation of weak anisotropy and applying Taylor series to obtain a set of equations for phase and group velocities [2]. In order to obtain the P , vertical shear wave (SV) and horizontal shear wave (SH) velocities which depend on the phase angle θ , the phase velocity for weak anisotropy VTI is given by

$$v_P(\theta) = \alpha_0(1 + \delta \sin^2 \theta \cos^2 \theta + \varepsilon \sin^4 \theta) \quad (1)$$

$$v_{SV}(\theta) = \beta_0 \left[1 + \frac{\alpha_0^2}{\beta_0^2} (\varepsilon - \delta) \sin^2 \theta \cos^2 \theta \right] \quad (2)$$

$$v_{SH}(\theta) = \beta_0(1 + \gamma \sin^2 \theta) \quad (3)$$

where α_0 and β_0 are the vertical velocity for P and S waves, phase angle θ is the angle between the wavefront normal and the vertical axis, and Thomsen parameters ε , δ , and γ are defined by

$$\varepsilon \equiv \frac{C_{11} - C_{33}}{2C_{33}} \quad (4)$$

$$\delta \equiv \frac{(C_{13} + C_{44})^2 - (C_{33} - C_{44})^2}{2C_{33}(C_{33} - C_{44})} \quad (5)$$

$$\gamma \equiv \frac{C_{66} - C_{44}}{2C_{44}} \quad (6)$$

C_{ij} is elastic modulus tensor which characterizes the elasticity of the medium.

Group velocity, which is computed in ray direction (\emptyset), is a key element in driving anisotropy ray tracing equations. The exact scalar magnitude V_g of the group velocity is given in terms of the phase velocity magnitude v [9] by

$$V_g = v \sqrt{1 + \left(\frac{1}{v} \frac{dv}{d\theta} \right)^2} \quad (7)$$

Replacing (1) in (7) is given the quasi P wave group velocity in terms of its phase velocity for the case of weak anisotropy is as follows:

$$V_P(\emptyset) = v_P(\theta) \left[1 + \frac{1}{2v_P^2} \left(\frac{\partial v_P}{\partial \theta} \right)^2 \right] \quad (8)$$

The relationship between group angle \emptyset and phase angle θ for P , SV , and SH is in the linear approximation,

$$\tan \emptyset_P = \tan \theta_P \left[1 + 2\delta + 4(\varepsilon - \delta) \sin^2 \theta_P \right] \quad (9)$$

$$\tan \emptyset_{SV} = \tan \theta_{SV} \left[1 + 2 \frac{\alpha_0^2}{\beta_0^2} (\varepsilon - \delta) (1 - 2 \sin^2 \theta_{SV}) \right] \quad (10)$$

$$\tan \emptyset_{SH} = \tan \theta_{SH} (1 + 2\gamma) \quad (11)$$

These Eqs. 1–3 and 7–11, define the group velocity, at any angle, for each wave type.

3 Numerical Modeling and Examples

The theory, described in the previous section, is implemented in MATLAB. To solve the equations, some MATLAB's built-in functions are applied to calculate and plot the results. Elliptical anisotropy is given by the equality $\varepsilon = \delta$. Figure 1 shows the comparison of wavefields, for phase and group velocities, in a VTI and an isotropic medium. Since $\varepsilon = \delta$, the wavefield for anisotropic P wave is elliptical; however, the S wave wavefield for both media is spherical which can be directly realized from (2). Also, no difference can be seen between phase and group velocity in this condition.

In next example, to study the effect of parameter δ , we change the parameter δ and keep ε and γ fixed. It can clearly be seen that parameter δ along with parameter ε control the propagation of P and SV wave in VTI medium (Fig. 2). However, the Eq. (1) indicates that, for near-vertical P wave propagation, the δ contribution entirely dominates the ε contribution [2].

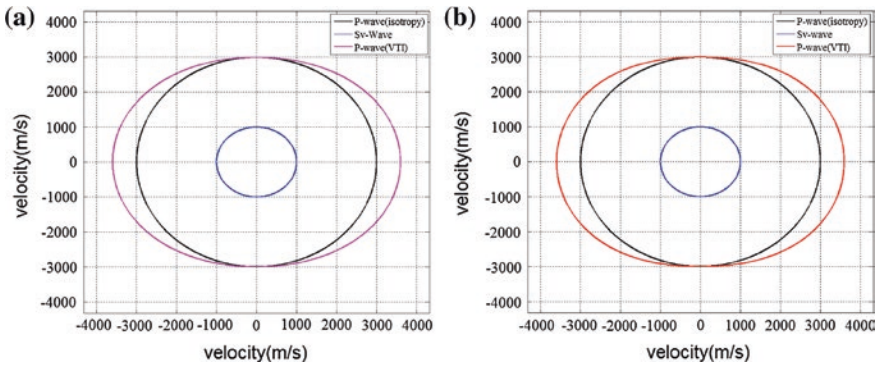


Fig. 1 Comparison of wave propagation in a VTI medium specified by $\varepsilon = 0.15$, $\delta = 0.15$ and $\gamma = 0.2$ and an isotropy medium. **a** Phase velocity modeling and **b** group velocity modeling

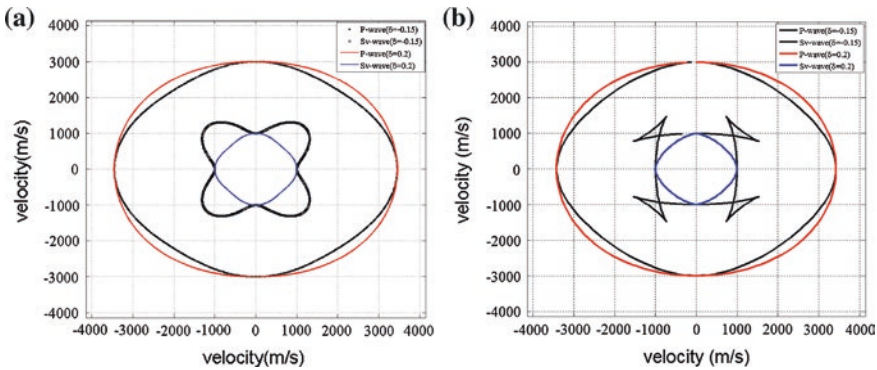


Fig. 2 Wave propagation in a VTI medium for different $\delta = -0.15$ and $\delta = 0.2$ ($\varepsilon = 0.15$ and $\gamma = 0.2$). **a** Phase velocity modeling and **b** group velocity modeling

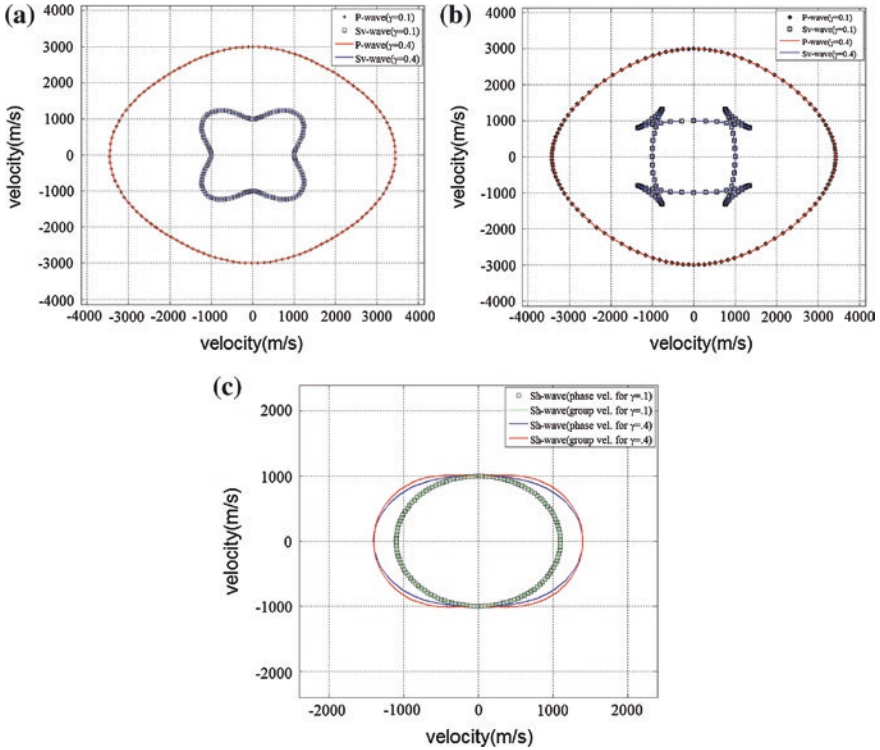


Fig. 3 Wavefield snapshots for different parameters $\gamma = 0.1$ and $\gamma = 0.4$ ($\epsilon = 0.15$, $\delta = -0.1$). **a** Phase velocity modeling of *P* wave and *S_v* wave, **b** group velocity modeling of *P* wave and *S_v* wave, and **c** group and phase velocity wavefields of *S_H* wave

Parameter γ is another anisotropy parameter, influencing elastic wave propagation, which is studied in this step. To achieve our goal, we keep ϵ and δ unchanged in both plotting, and only parameter γ is altered. As it is illustrated in Fig. 3, there is no difference in wavefields of both figures and wavefields are overlapped each other. Hence, γ does not affect the propagation of *P* and *SV* waves, and it only corresponds to the conventional meaning of *S_H* anisotropy (Eq. 3) [2]. For small value of γ , phase velocity and group velocity of *S_H* almost propagate similarly, although increasing γ causes the distinct wavefields of *S_H*.

4 Conclusions

I presented an elastic wave equation for VTI media with the weak anisotropy approximation. Solving exact elastic anisotropy equations are certainly more expensive in terms of computing time and memory requirement. A simplification of the phase velocity and group velocity formula under the assumption of

weak anisotropy allows one to express clearly the propagation of wave in anisotropy media. This yields a straightforward method for calculating phase and group velocity. Equation (1) shows that, for weakly anisotropic media, the anisotropy parameter δ , for near-vertical P wave propagation, completely dominates the ε contribution. Because of this, δ (rather than ε) controls the anisotropic features of most situations in exploration geophysics. Nevertheless, the parameter γ does not influence the P and SV wave wavefronts since it does not appear in their wave equations. In addition, S_H wave propagation is only affected by parameter γ . Another achievement of this study is the ability to compute P and S wave velocities as functions of the ray direction which is demanding for the implementation of ray tracing in anisotropic media.

Acknowledgments We gratefully acknowledge members of Centre of Seismic Imaging (CSI) at UTP for their helpful discussions. The support for this work is provided by PETRONAS on the project Seismic Anisotropy Imaging for Deep Reservoir and Fractured Basement.

References

1. J. Carcione, *et al.*, "Seismic modeling," *Geophysics*, vol. 67, pp. 1304-1325, 2002.
2. L. Thomsen, "Weak elastic anisotropy," *Geophysics*, vol. 51, pp. 1954-1966, 1986.
3. V. Farra and I. Pšenčík, "Properties of the zeroth-, first-, and higher-order approximations of attributes of elastic waves in weakly anisotropic media," *The Journal of the Acoustical Society of America*, vol. 114, pp. 1366-1378, 2003.
4. G. E. Backus, "Long-wave elastic anisotropy produced by horizontal layering," *Journal of Geophysical Research*, vol. 67, pp. 4427-4440, 1962.
5. T. Alkhalifah, "Efficient synthetic-seismogram generation in transversely isotropic, inhomogeneous media," *Geophysics*, vol. 60, pp. 1139-1150, 1995.
6. I. Tsvankin, *et al.*, "Seismic anisotropy in exploration and reservoir characterization: An overview," *Geophysics*, vol. 75, pp. 75A15-75A29, 2010.
7. I. Tsvankin, "P-wave signature and notation for transversely isotropic media: An overview," *Geophysics*, vol. 61, pp. 467-483, 1996.
8. V. Grechka, "Ray-direction velocities in VTI media," *Geophysics*, vol. 78, pp. F1-F5, 2013.
9. J. G. Berryman, "Long-wave elastic anisotropy in transversely isotropic media," *Geophysics*, vol. 44, pp. 896-917, 1979.

The Effect of Tar on the Petrophysical Analysis of FMI in Asmari Fractured Reservoir

Z. Movahed, R. Junin and H. Amiri Bakhtiari

Abstract Historically, in Iran, the borehole imaging tools as the FMI/FMS are acquired to locate major structural features, such as faults and fractures and sedimentary environment interpretation, and it has more advantages to the conventional methods for reservoir characterization. Petrophysicists and geologists by using this new method and suitable software (Geoframe) do a credible characterization in oil reservoirs. Prediction of the index permeability is a distinct advantage of image logging, because of the addition of orientation and dip data provided. Significant heterogeneity in these bitumen reservoirs is found in all dimensions, and predicting reservoir continuity is challenging. The textural heterogeneity corresponds to an extreme permeability variation that is the controlling cause in reservoir production. Because of the large vertical resolution, contrast amid cores (actual scale), and conventional logs (averaged responses over a few meters), extrapolation of small-scale heterogeneity into uncured wells using a traditional approach is unreliable. In this well, after comparison, image log average resistivity recognized that formation resistivity is particularly high (dolomite) in the porous layer and fracture zones.

Z. Movahed (✉) · R. Junin
Department of Petroleum Engineering, Faculty of Petroleum
and Renewable Energy Engineering, Universiti Teknologi Malaysia (UTM),
Skudai, Malaysia
e-mail: zmovahed@gmail.com

R. Junin
e-mail: radzuan@petroleum.utm.my

Z. Movahed
Schlumberger, Kuala Lumpur, Wilayah Persekutuan, Malaysia

H. Amiri Bakhtiari
National Iranian South Oilfield Company, Ahwaz, Iran

1 Introduction

The study of the fractures in the Asmari reservoir is a serious subject up to now [1]. Generally, in the fractured reservoir, the fractures control the reservoir behavior [2]. If the fractures are open, it is the conduits to petroleum migration, so resulted to develop a highly production zone; with the permeability more than 10,000 mD [3, 4]. Asmari reservoir attributes including medium to high porosity dolomite layers, complex lithology, presence of tar and organic-rich shale, and compartmentalization pose a challenge in understanding the production behavior. The presence of dissolution channels and fractures adds to this complexity. Additionally, formation heterogeneity is quite important, because almost carbonate formation evaluation methods rely on traditional resistivity and porosity logs. On the other hand, firstly, we do not have enough knowledge that how we get formation heterogeneity by using FMI. For many carbonate reservoirs, the correlation between amid hydrocarbon production and density-neutron logs has been inconsistent. Secondly, good production has been obtained from intervals where logs show low porosity, whereas zones having higher porosity have not produced. In old carbonate oil fields, the total production is often more in comparison with what we interpret by using standard porosity logs alone. Our study illustrates an approach to improve the reservoir characterization of the Asmari by quantifying small-scale heterogeneity using FMI and petrophysical logs.

2 Methodology

By using FMI logs the orientations of carbonate and shale beds in the well, as well as the orientations of faults and fractures in these Image logs are displayed using bright colors for resistive units, and lower resistivity conductive units are displayed using dark colors and the interpretation typically started with hand picking dips using sinusoid techniques on oriented images presented at 1:20 or 1:10 scale that the geological features are easily visualized in Borview (Geoframe). Once dips have been picked, it is classified into bed boundaries and fractures. The structural dip data are imported into the Bortex and the heterogeneity analysis of reservoirs from borehole images is carried out by the software used to extract heterogeneities and layer details from images. In conjunction with open-hole logs, the FMI images are used to examine the internal organization or rock fabric of the beds or reservoir units. In addition to formation heterogeneities, the software also computed connections for the connected-conductive heterogeneities of a formation.

3 Result and Discussion

3.1 Geological Interpretation as Input Data for Heterogeneity Analysis

Bedding over the entire interpreted interval shows dip inclinations of 46° to S20W. In addition, the reservoir is heavily fractured in the RS-55. In the azimuth view, all open fractures with 430-dip inclination toward N7W. The open fractures show a dominant, striking trend of N83E–S83W. When studied in the bedding dip data, it is found that open fractures tend to strike parallel to the bedding strike. It indicates that open fractures are longitudinal types (Fig. 1). Almost fractures have aperture near 0.01 cm (1 mm). Zones 6 and 7-1 have the highest fracture aperture (Fig. 3). In this reservoir, porosity is mainly secondary, the distribution of porosity and permeability is irregular, production varies greatly, and possibly, it does not have common hydrocarbon content.

3.2 Heterogeneity Analysis by Using Layering from FMI

The main cause contributing to the heterogeneity of a reservoir is patchy caused by areas of different porosity and permeability caused by diagenetic processes or/and change in a litho-facies. The heterogeneity analysis of reservoirs to extract heterogeneities and layer details (structural dip and azimuth) from FMI and it provided five heterogeneity indexes. The results of heterogeneity analysis are continuous depth-indexed channels or curves for the proportion and size of each form of formation heterogeneity. Such curves are averaged over any window length and output at any sampling rate. Average high resolution synthetic resistivity from FMI as resistivity, i.e., proportion of resistive and conductive heterogeneities are used as input to neural-network program to identify different rock-types or litho-types through classification software. It involved more iteration that is used for extraction of formation heterogeneities to optimize the parameters. The results of each iteration are validated by visual examination of the FMI image to see if all heterogeneities are identified and contoured or not. The resistive heterogeneities are contoured in dark blue despite the large resistive events are contoured in cyan. The conductive events are classified into three types: large patches, connected spots, and isolated (across each image) spots. These are shown in different colors on the images: The patches are shown in dark magenta, connected spots in red, and the isolated spots in orange (Fig. 2).

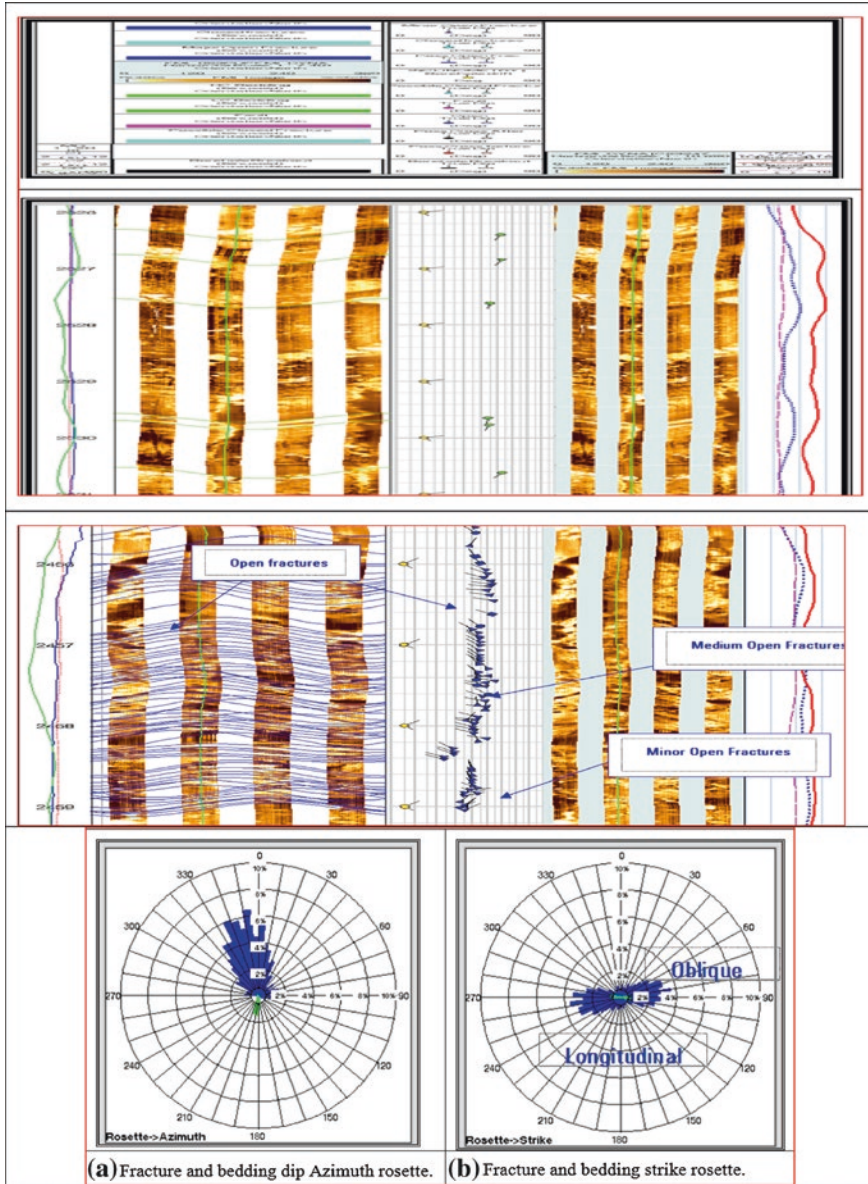


Fig. 1 FMI image showing layering and open fractures within the Asmari formation. Statistical plots of dips of all fractures and bedding dip attribute showing most longitudinal fractures in the Asmari interval

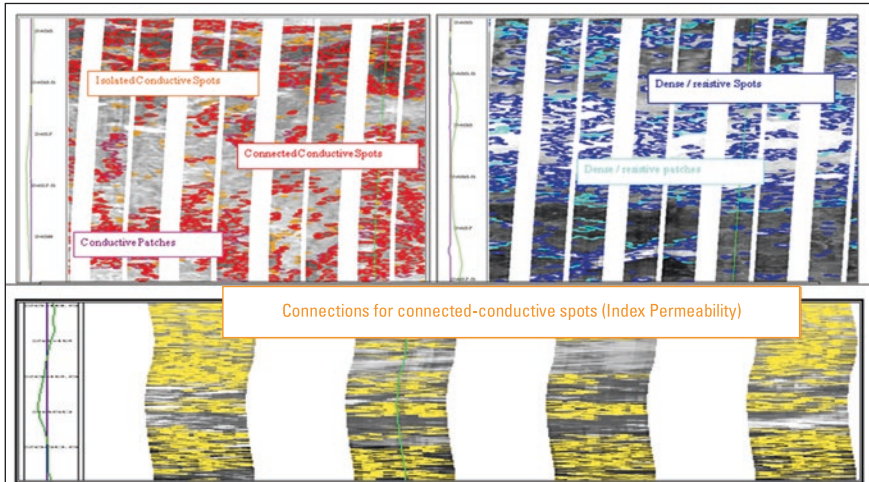


Fig. 2 Heterogeneity analysis from FMI

3.3 Permeability Analysis and the Effect of Tar on Permeability Computation

The connections correspond to the conductive links at the matrix level between the conductive events. They are shown as thin yellow lines on the FMI/FMS images (Fig. 2). By computing the amount of additional conductivity due to such thin conductive routes, a connectedness coefficient (henceforth called raw FMI/FMS permeability indicator) is computed, which can be transformed into absolute permeability after comparing it with the cores over some short intervals. Since FMI image has absolute shallow depth investigation, then the appearance of oil over the image is depending on that oil is un-flushed or flushed by the mud. If the mud hydrostatic pressure is few to contrast with formation pressure, then we assume to see oil smearing over the static image as white appearance because of oil is more resistive surrounding rock matrix (unflushed oil) and vice versa. A comparison within tradition and new processing through image log, this borehole is extra-heavy oil, so the oil signal is located at the early times or components, first we observe the gamma functions to identify new areas of tar. In this well, after comparison between image log average resistivity and log resistivity, we identify that formation resistivity is particularly high (dolomite) in the porous layer and fracture zones. Generally, if image log resistivity curve is reading greater than the log resistivity curves, this is an indication of the enhanced oil fluid invasion resulting from fractures, borehole breakouts and associated borehole wall damage, or heavy oil in the porous layers (Tar). There are zones with relatively moderate to high raw permeability index (>5), i.e., zones 4, 5, 6, 7-1, and 7-2 (Figs. 3 and 4).

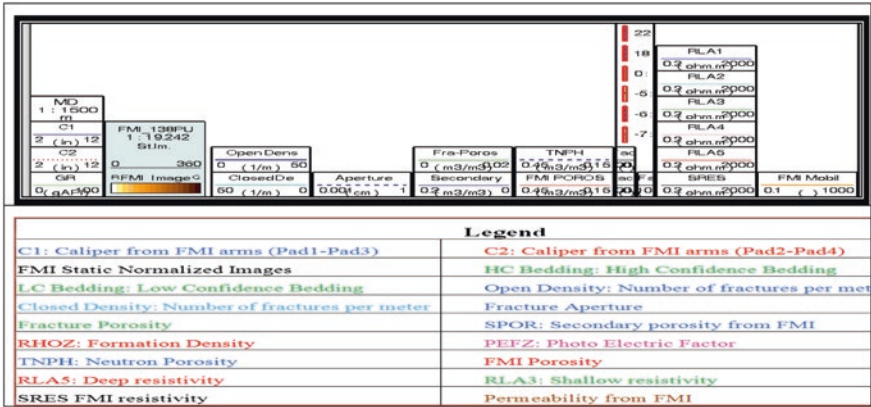


Fig. 3 Header detail for Fig. 4

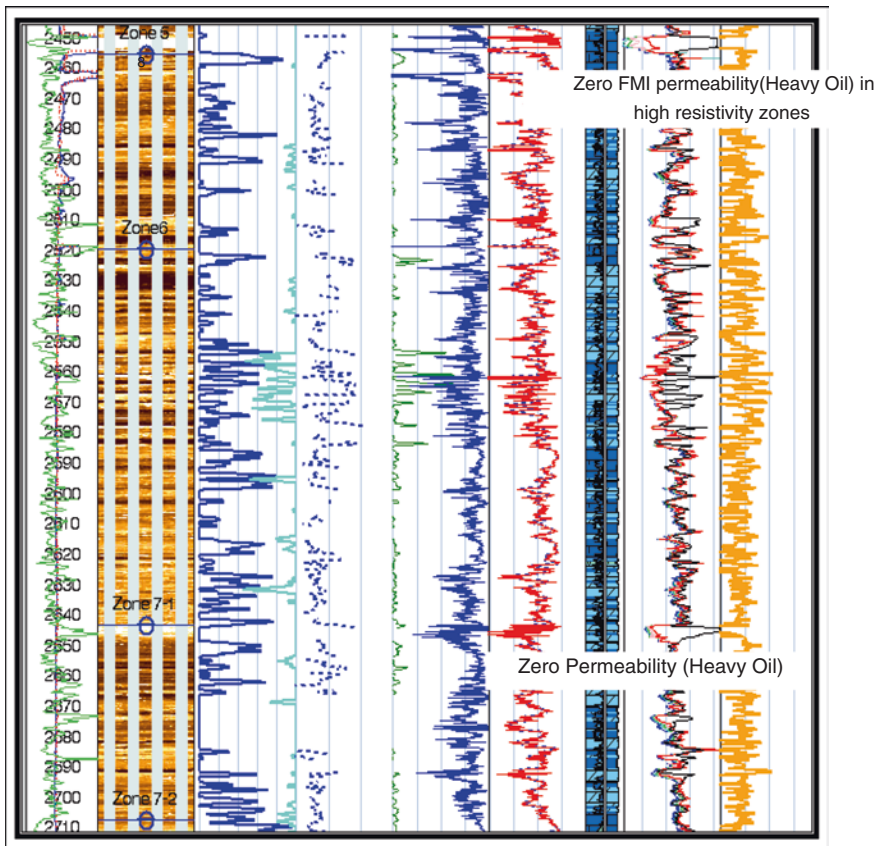


Fig. 4 Composite plot of orthogonal calipers (C1 and C2), GR, FMI static normalized images, open fracture density, aperture, porosity, resistivity curves, PHIT, TNPH curves, lithology, FMI and log porosity, and FMI raw permeability indicator across Asmari formation (header details in Fig. 3)

4 Conclusion

FMI images provided critical information if the rock structure and sedimentary features are significant determinants of formation productivity. Fractures related to the Rag e Safid fault which corresponds to permeability enhancement, because those are widely open, and their cementation is partial, but in this well, tar reduced the permeability of fractures. Subsequently, this study helped to understand the reservoir structure, identify and evaluate fractures, visualize the rock texture, and optimize coring and saving project drilling costs and at the same time allowing more wells to be drilled in the field.

References

1. Khoshbakht F, Memarian H, Mohammadnia M; 2009; Comparison of Asmari, Pabdeh and Gurpi formation's fractures, derived from image log. *Journal of Petroleum Science and Engineering*, p. 65-74.
2. Nelson, R.A., 2001, *Geologic Analysis of naturally fractured reservoirs*, Gulf publishing, Houston, Texas, Contr. In petrol. Geology & Eng., 2nd Ed., 332p.
3. Haller, D., Porturas, F., 1998. *How to Characterize Fractures in Reservoirs Using Borehole and Core Images: Case Studies*. Geological society, vol. 136. Special Publications, London, pp. 249–259.
4. Rezaeei, M.R; 2006, the book of petroleum Geology, Alavi propagation; 472p.

Part V
Advances in Geophysics and Reservoir
Geoscience

A Hybrid Approach for Subsurface Illumination Analysis in Shallow Gas Region: A Case Study in Malay Basin

A.H. Abdul Latiff and D.P. Ghosh

Abstract The existence of shallow gas accumulation disrupts the propagation of seismic wave from source to receivers, thus creating un-illuminated reflector image. In the previous years, several methods have been studied and applied in order to improve the subsurface data by restoring true reflectivity, with certain degree of success. Two ways of seismic enhancement can be carried out: either by applying complex migration algorithm or by reacquisition of survey area to bypass the shallow anomaly. However, both methods require plenty of time and effort before illumination analysis can be done. With this constraint in mind, geoscientists had developed two techniques for illumination studies: wave extrapolation using focal beam and counting reflected rays at the target subsurface. Since both methods are producing different results and might lead to wrong analysis, a new hybrid method was needed and consequently developed by integrating both techniques and producing new illumination measurement called illumination factor analysis. The hybrid technique then was applied to one of the shallow gas fields in offshore Malaysia. From the result obtained, it should help proposing new survey design by focusing to place source and receiver positions at the high illuminating zone.

Keywords Illumination analysis · Shallow gas clouds · Focal beam · Ray tracing

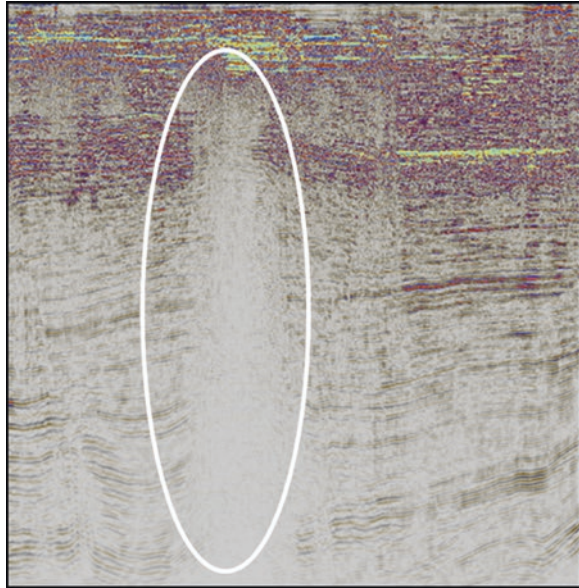
1 Introduction

Near-surface anomaly such as shallow gas cloud and salt diapir always produces blur image underneath its anomaly. Although both geological features exert contrasting influence toward wave propagation phenomena, the presence of both gas

A.H. Abdul Latiff (✉) · D.P. Ghosh
Center for Seismic Imaging, Universiti Teknologi PETRONAS, 31750
Bandar Seri Iskandar, Perak, Malaysia
e-mail: abdulhalim.alatiff@petronas.com.my

D.P. Ghosh
e-mail: drdeva@petronas.com.my

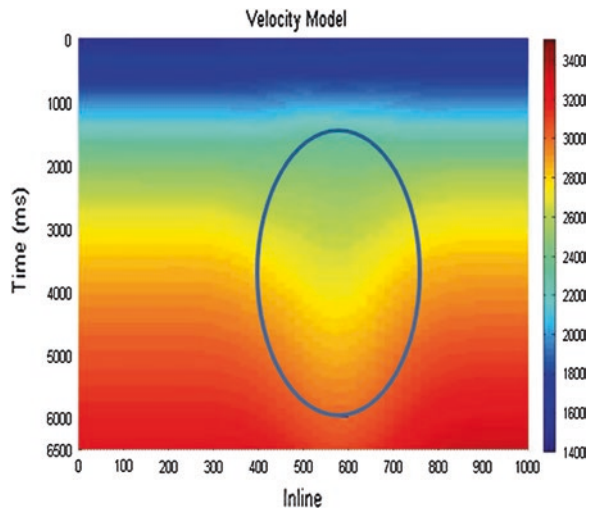
Fig. 1 A subsurface seismic section of shallow gas cloud field located in offshore Malaysia. The low illumination zone (indicated in *white circle*) was formed due to gas accumulation at shallow layer



clouds, as shown in Fig. 1, and salt domes causes severe distortion of wave propagation path due to abrupt change in velocity value.

In shallow gas cloud area as shown in Fig. 1, due to slower velocity of its composition compared to their surroundings as demonstrated in Fig. 2, wave tends to travel toward the center of the gas zone. However, in the salt dome zone, the faster velocity causes the wave to avoid the normal ray path. As a consequence, both phenomena produce poor data quality particularly at the edge of the anomaly as insufficient data unable to recover once the signals are detected at the receiver.

Fig. 2 The corresponding velocity model of seismic data shown in Fig. 1. The pull-down effect can be seen between inline 500–700 (circled in blue), and it indicates slower velocity of shallow gas anomaly



To enhance this poor-quality image, there are two ways to restore true subsurface data. First is by reacquisition of the survey area, using better configuration and finer and longer receiver cables, with the aim to bypass the anomaly zone, especially in gas/salt zone. If the reacquisition was conducted in shallow gas area, the most suitable configuration is by using ocean bottom cable [1] with four-component devices to record converted shear waves that unaffected by slower gas zones. Another option for improving seismic image underneath anomaly is by applying state-of-the-art technologies such as Q-migration, reverse-time migration [2], and downward continuation migration [3].

However, there is a shortcoming in determining poor illumination in subsurface seismic data. According to seismic value chain [4], the earth's depth section can be obtained after proper acquisition, following suitable processing and migration techniques before an illumination analysis can be carried out. To overcome this drawback, a method called focal beam analysis was developed [5–9], which allows us to perform a quick illumination analysis once a velocity model of the subsurface has been known. Another popular method commonly used for illumination analysis is hit count in ray tracing method [10].

Although both focal beam and ray tracing techniques are relatively known for developing an optimized survey design [11], each of these techniques has their own strength and weaknesses. For example, focal beam analysis will only give information for specific target point (also known as local method); hence, illumination analysis of the other location surrounding the target is relatively unknown. On the other hand, ray tracing method is solely based on the number of ray hits on the reflector. Disadvantage of this method is the inability of rays to incorporate true amplitude information during illumination analysis. With these constraints in mind, this study proposes a hybrid method of combining both ray tracing and wave propagation, thus creating a new function of analysis, called illumination factor analysis.

2 Methodology

In order to incorporate both techniques into one analysis, an integrated workflow containing both illumination techniques is required. Before the analysis begins, a comprehensive velocity model will be built using the field velocity information obtained from previous seismic data processing sequences. Starting at the reflector depth of interest, a wave is sent toward the surface level where source and receiver are placed according to full 3D acquisition design. The up-going wave then convolved with source and receiver positions before being propagated back toward the target reflector.

Once the focal beam process is finished, ray tracing analysis was carried out by using the same acquisition setup as in focal beam. For multiple source positions on the surface, a fan of rays will be shot toward target depth reflector. However, all the rays will travel through the layers and anomalies and will only get reflected

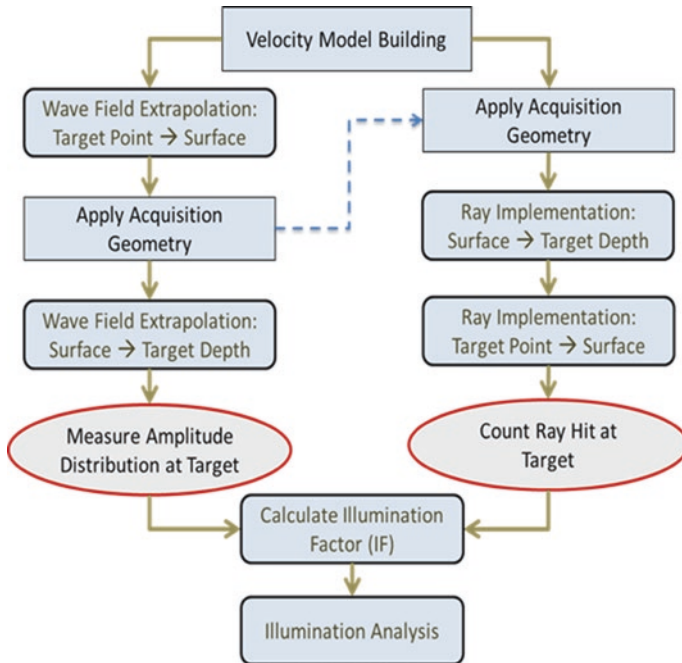


Fig. 3 Summary of the workflow used in developing integrated illumination analysis for shallow gas cloud area

back toward surface once it reaches the depth target and obeys certain rules. The reflected rays detected back at the surface level are the only rays that will be used for ray hit count.

Using both numerical solutions obtained from separate methods, we use a mathematical manipulation to calculate the illumination factor. The outcome from this factor will be used as a basis for new illumination analysis. The summary of methodologies used for this work is simplified in Fig. 3.

3 Wave Extrapolation Using Focal Beam

As explained in the previous section, focal beam analysis propagates a unit wave upward from target reflector until the signals reach the surface level. The wave is in the form of monochrome frequency (single frequency) and contains information from a single point, thus creating a local illumination analysis. To expand the concept to the whole reflector, a continuous simulation was run for the whole inline of a single crossline within the depth reflector. Once the signal reaches the surface,

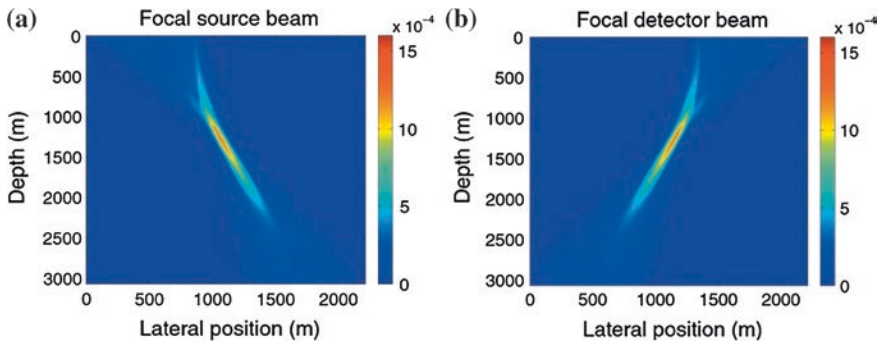


Fig. 4 The figures illustrate the focal beam using wave extrapolation from source at the surface to target reflector (a) and receiver at the surface to target reflector (b)

two separate downward signals were sent downward (source and receiver beams) as the result of surface and up-going wave multiplication (Fig. 4, [7]).

On the target subsurface, the focal beam analysis can be carried in two ways: spatial domain and radon domain. As our objective is to get the true subsurface amplitude analysis from this focal beam method, only spatial domain analysis was carried out which resulting in the resolution function. From Fig. 6a, the resolution function from focal beam analysis indicated that reflector within the depth of 6,500 ms zone, produce uniform amplitude distribution throughout the layer, indicating the shallow gas anomaly did not affect the seismic wave travelled past through.

4 Ray Trace Interpolation

Looking into different aspects of illumination, ray interpolation through a complex model may or may not follow with the wave extrapolation analysis. For better understanding of our subsurface, multiple ray fans were interpolated toward reflector and reflected back and a number of rays detected at receiver location were recorded and analyzed. As shown in Fig. 5a, more rays will be reflected if the source was located directly above the anomaly or source place further away from such anomalies. However, if a source was place at the edge of the gas anomaly, as demonstrated in Fig. 5b, there will be fewer ray signals that are able to pass through the gas zones and reflected to surface level.

Combining all the rays hit for each location within the reflector depth, a hit count map was produced as in Fig. 6b. Clearly, from this map, most of the rays will be reflected at the area directly beneath the gas zones (i.e., at coordinate [600 1,000]). The number of rays reflected in this region reaches maximum of 25 hits before decreasing toward the edge of gas zone.

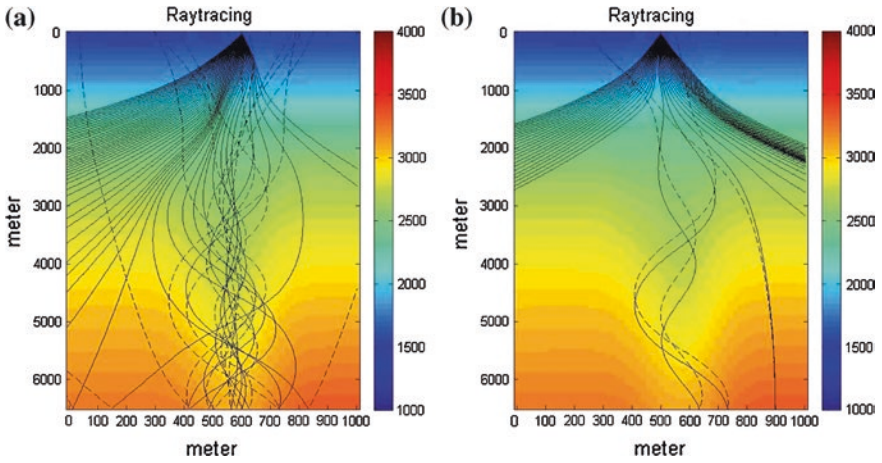


Fig. 5 Ray interpolation from two positions: **a** [600, 1,000, 0] and **b** [500, 1,000, 0]. More rays detected and reflected at **a** location which is approximately above the gas zone. **b** Position is located at the edge of the gas area which pushed away most of the rays passing through

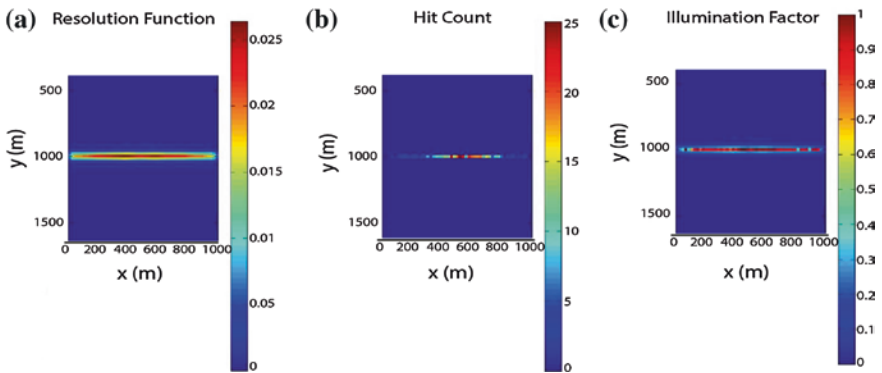


Fig. 6 Result from focal beam method as shown in **a** indicated that uniform amplitude distribution was achieved throughout the reflector, albeit with lower amplitude value. However, in ray tracing method **b**, the number of hit counts is scattered with higher rays detected at the middle of the reflector. By integrating both methods, the illumination factor produced in **c** gives better indication of illumination distribution of target subsurface

5 Illumination Factor

From Fig. 6a and b results, it is easier to understand why a comprehensive study of integrated rays and wave analysis is needed. Although the focal beam result indicates uniform amplitude distribution at reflector 6,500 ms depth, ray tracing interpolation method indicates only area directly underneath the shallow gas zone is having

greater illumination. These results are not contradicting, but more complementing each other, albeit it may be misleading and difficult for survey design justification.

By incorporating these two techniques using a mathematical formulation, an illumination analysis was obtained as shown in Fig. 6c. Normalizing the scale from 0 to 1, illumination of target subsurface reflectors can be explained within a single analysis. From the result, it is safe to say that the zone stretching from 400 to 700 m is experiencing a better illumination, provided the full 3D source and receiver setup was used throughout the simulation. Further outside this zone, a moderate illumination quality is achievable and it continues until 50 m before the survey ends.

6 Conclusion

The new method used in this research significantly improves our understanding in discovering the subsurface seismic quality compared to previous stand-alone methods of ray tracing or focal beam. With the same computing power and cost, the revised methodology will increase the efficiency of the illumination analysis. From the analyses conducted, hybrid illumination analysis enables higher confidence level during a survey design validation before a new acquisition took place in this area. The separate outcomes from wave and ray illumination techniques also confirmed that individual analysis of ray tracing and focal beam might yield different conclusions compared to real seismic data evaluations.

Acknowledgment The author would like to thank PETRONAS for financial support and Delft University of Technology for their permission to use part of their codes in this research.

References

1. T. Ishiyama, G. Mercado, and K. Belaid, "3D OBC Seismic Survey Geometry Optimization," *First Break*, vol. 30.
2. C. Yongping and H. Yan, "Use Q-RTM to Image Beneath Gas Hydrates in Alaminos Canyon, Gulf of Mexico," presented at the SEG Denver Annual Meeting, Denver, USA, 2010.
3. A. J. Berkhout, *Seismic Migration: Imaging of Acoustic Energy by Wave Field Extrapolation*. The Netherlands: Elsevier Scientific Publishing Company, 1980.
4. A. J. Berkhout, "The data-driven seismic value chain, providing a business context for the velocity issue," *Geophysical Prospecting*, vol. 52, pp. 481-487, 2004.
5. A. J. Berkhout, L. Ongkiehong, A. W. F. Volker, and G. Blacquièrè, "Comprehensive assessment of seismic acquisition geometries by focal beams - Part I: Theoretical considerations," *Geophysics*, vol. 66, pp. 911-917, 2001.
6. A. W. F. Volker, G. Blacquièrè, A. J. Berkhout, and L. Ongkiehong, "Comprehensive assessment of seismic acquisition geometries by focal beams -Part II: Practical aspects and examples," *Geophysics*, vol. 66, pp. 918-931, 2001.
7. E. J. Van Veldhuizen, G. Blacquièrè, and A. J. Berkhout, "Acquisition Geometry Analysis In Complex 3D Media," *Geophysics*, vol. 73, pp. Q43-Q58, 2008.
8. E. J. Van Veldhuizen, "Integrated approach to 3D seismic acquisition geometry analysis," PhD Thesis, Delft University of Technology, The Netherlands, 2006.

9. A. H. Abdul Latiff, D. P. Ghosh, and Z. Z. Tuan Harith, "Seismic Illumination Analysis in Poor Oil & Gas Field Data by Using Focal Beam Method," *IOP Conference Series: Earth and Environmental Science*, vol. 19, p. 012013, 2014.
10. R. Laurain, L. J. Gelius, V. Vinje, and I. Lecomte, "A Review Of 3D Illumination Studies," *Journal of Seismic Exploration*, vol. 13, pp. 17-37, 2004.
11. A. H. Abdul Latiff, D. P. Ghosh, Z. Z. Tuan Harith, and S. N. F. Jamaludin, "Seismic Illumination Analysis in Poor Quality Data Using Focal Beam Method: Full 3D vs. Conventional 3D Acquisition Design," *Journal of Applied Sciences*, vol. 14, pp. pp.1139-pp.1146, 2014.

A New Fluid Factor Based on AVO Technique

Liu Changcheng

Abstract AVO technique is already widely used in petroleum exploration and proved itself in many cases. There are a few AVO attributes presented based on Shuey's approximation. This paper is attempted to present a new AVO attribute, J , for fluid detection which is different with existed ones. The J attribute is focused on Poisson reflectivity instead of the difference between V_p and V_s . We compared the performances of J and one of the existed fluid factors in models, well logs, and seismic. From the result, J attribute provides a new way to detect gas reservoir and has better performance than existed fluid factor in some cases.

Keywords New fluid factor · AVO

1 Theory

Amplitude varies with offset (AVO) is an important tool for quantity interpretation as it can predict lithology from seismic. The reflection coefficient for plane elastic waves as a function of reflection angle at a single interface is described by the Zoeppritz equations in 1919. Shuey made further approximation which could be written as

$$R(\theta) \approx R(0) + G \sin^2 \theta + \frac{1}{2} \frac{\Delta V_p}{V_p} (\tan^2 \theta - \sin^2 \theta) \quad (1)$$

where

$$\begin{aligned} R(0) &= \frac{1}{2} \frac{\Delta V_p}{V_p} + \frac{1}{2} \frac{\Delta \rho}{\rho}; & G &= \frac{1}{2} \frac{\Delta V_p}{V_p} - 2 \frac{V_s^2}{V_p^2} \left(\frac{\Delta \rho}{\rho} + 2 \frac{\Delta V_s}{V_s} \right); \\ \Delta \rho &= \rho_2 - \rho_1; & \rho &= (\rho_2 + \rho_1)/2; \\ \Delta V_p &= V_{p2} - V_{p1}; & V_p &= (V_{p2} + V_{p1})/2; \\ \Delta V_s &= V_{s2} - V_{s1}; & V_s &= (V_{s2} + V_{s1})/2; \end{aligned}$$

L. Changcheng (✉)

Geoscience Department, University Technology PETRONAS, Tronoh, Ipoh, Malaysia
e-mail: lccgreatwall@gmail.com

When we have angle stack seismic, Eq. 1 could be written as

$$R(\theta) = \frac{1}{2} \left(\frac{\Delta V_p}{k} + \frac{\Delta \rho}{\rho} \right) + \begin{bmatrix} \sin^2 \theta_{\text{near}} \\ \sin^2 \theta_{\text{mid}} \\ \sin^2 \theta_{\text{far}} \end{bmatrix} \cdot \left[\frac{\Delta V_p}{V_p} - 2 \frac{V_s^2}{V_p^2} \left(\frac{\Delta \rho}{\rho} + 2 \frac{\Delta V_s}{V_s} \right) \right] \quad (2)$$

$$+ \frac{\Delta V_p}{V_p} \begin{bmatrix} \tan^2 \theta_{\text{near}} - \sin^2 \theta_{\text{near}} \\ \tan^2 \theta_{\text{mid}} - \sin^2 \theta_{\text{mid}} \\ \tan^2 \theta_{\text{far}} - \sin^2 \theta_{\text{far}} \end{bmatrix}$$

If we treat $2 \frac{V_s^2}{V_p^2} \left(\frac{\Delta \rho}{\rho} + 2 \frac{\Delta V_s}{V_s} \right)$ as an item, then $\frac{\Delta V_p}{V_p}$, $\frac{\Delta \rho}{\rho}$, and $2 \frac{V_s^2}{V_p^2} \left(\frac{\Delta \rho}{\rho} + 2 \frac{\Delta V_s}{V_s} \right)$ are solvable as stack angles are known.

If V_p/V_s is a constant in all layers, then

$$\frac{\Delta V_s}{V_s} = \frac{V_{s2} - V_{s1}}{V_{s2} + V_{s1}} = \frac{\frac{V_{p2}}{V_{s2}} * V_{s2} - \frac{V_{p1}}{V_{s1}} * V_{s1}}{\frac{V_{p2}}{V_{s2}} * V_{s2} + \frac{V_{p1}}{V_{s1}} * V_{s1}} = \frac{\Delta V_p}{V_p} \quad (3)$$

Thus, we can assume a V_p/V_s value, called v . Then, I present an attribute named J :

$$J = J_p - J_s$$

where

$$J_p = 2 \left(\frac{\Delta \rho}{\rho} + 2 \frac{\Delta V_p}{V_p} \right) / v^2$$

$$J_s = 2 \frac{V_s^2}{V_p^2} \left(\frac{\Delta \rho}{\rho} + 2 \frac{\Delta V_s}{V_s} \right)$$

J is supposed to be sensitive to fluid as V_p/V_s changes. When both V_p/V_s we assumed and real one are equal to two, J equals to $(R + G)/2$ exactly. The attribute J will show peaks (troughs) corresponding to the bottom (top) of the layer which has a lower V_p/V_s . And it could be regarded as gas reservoir.

2 Model

In order to verify this attribute, 25 sets of brine sands, gas sands, and shales are used which are shown in Table 1. As Fig. 1 shows, brine interfaces (blue) have different slope between gas interfaces (red) in this cross-plot. The specific value of the slope depends on the v we assumed and real V_p/V_s . Theoretically, when slope equals to one, v can be thought equal to real V_p/V_s .

In most models of 25, gas and brine can be separated clearly by cross-plot of J_p versus J_s . We analyze sand top interfaces for each model (Fig. 2a). We can find that gas sand has less J in most models except models 8, 12, and 17. From their petrophysical parameter, V_p/V_s differences between gas sand and brine sand

Table 1 *P*-wave and *S*-wave velocities and densities for 25 sets of brine sands, gas sands, and shales [1]

Model	Brine sand			Shale			Gas sand		
	α (km/s)	β (km/s)	ρ (g/cm ³)	α (km/s)	β (km/s)	ρ (g/cm ³)	α (km/s)	β (km/s)	ρ (g/cm ³)
1	3.28	1.68	2.19	3.27	1.65	2.20	3.04	1.74	2.05
2	4.06	2.03	2.40	4.69	2.61	2.49	3.70	2.06	2.26
3	3.85	2.24	2.24	2.77	1.52	2.29	3.08	2.34	2.14
4	4.06	2.34	2.30	4.06	2.18	2.58	3.62	2.58	2.30
5	3.21	1.79	2.22	3.05	1.69	2.34	2.91	1.85	2.01
6	4.55	2.61	2.44	3.21	1.60	2.39	3.96	2.80	2.41
7	3.05	1.56	2.40	2.77	1.27	2.45	2.69	1.59	2.25
8	3.42	1.78	2.53	2.77	1.45	2.67	3.39	1.79	2.50
9	2.52	0.90	2.11	2.31	0.85	2.18	1.58	0.94	1.94
10	3.44	1.94	2.52	2.75	1.26	2.43	3.19	1.98	2.45
11	3.55	1.54	2.38	3.51	1.85	2.46	3.47	1.75	2.21
12	5.03	3.32	2.61	3.60	1.85	2.63	4.91	3.30	2.59
13	2.07	0.81	2.10	1.94	0.77	2.10	1.54	0.98	2.05
14	2.69	1.38	2.13	2.67	1.13	2.29	2.07	1.29	2.02
15	2.19	1.21	2.15	2.10	1.03	2.10	1.68	1.15	2.10
16	2.52	1.20	2.24	2.59	1.39	2.30	1.86	1.16	2.09
17	3.81	2.30	2.25	3.81	2.26	2.40	3.45	2.02	2.10
18	2.66	1.25	2.23	2.38	0.94	2.27	2.25	1.30	2.06
19	2.84	1.47	2.08	2.74	1.39	2.06	2.84	1.76	2.08
20	2.13	0.67	1.90	1.83	0.40	2.02	1.44	0.53	1.53
21	3.05	1.46	2.30	3.35	1.72	2.36	2.18	1.37	2.19
22	3.46	1.85	2.26	2.31	0.94	1.90	3.04	1.92	2.09
23	2.11	0.93	2.11	2.10	0.64	2.14	1.42	0.97	1.97
24	3.21	1.85	2.17	2.87	1.30	2.27	2.93	1.79	1.96
25	4.35	2.34	2.40	2.77	1.52	2.30	4.05	2.38	2.32

are very tiny; even brine sand has a smaller V_pV_s than gas sand (model 17). That causes J of brine and gas are close in model 8 and 12, and J of brine is smaller in model 17. When above and below surrounding layers have same petrophysical parameters, these values will be reversed in the base of sand.

There is an existing attribute for detecting fluid which is called fluid factor [2] or ΔF . ΔF is defined as the difference between observed $\frac{\Delta V_p}{V_p}$ and predicted $\frac{\Delta V_p}{V_p}$ from $\frac{\Delta V_s}{V_s}$.

$$\Delta F = \frac{\Delta V_p}{V_p} - 1.16 \frac{\Delta V_s}{V_s} / v$$

where 1.16 is a local background trend we obtain from Mudrock line (Relationships between compressional-wave and shear-wave velocities in clastic silicate rocks, [3]) and v is a predicted background V_p/V_s .

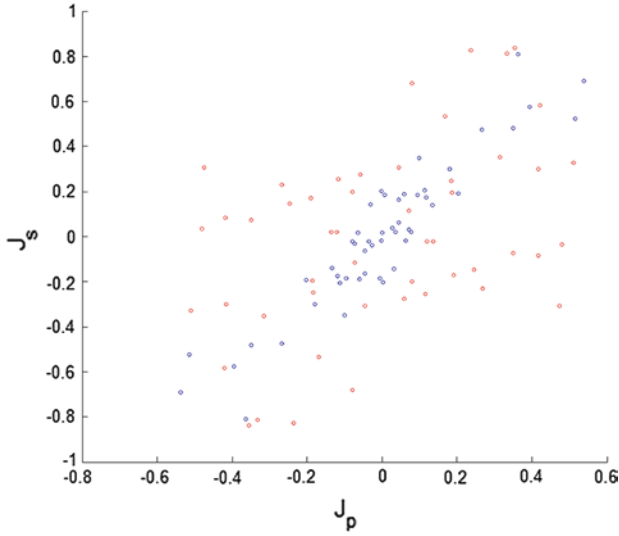


Fig. 1 Cross-plot: J_p versus J_s of 25 models. *Blue* is brine–shale interface (or shale–brine), and *red* is gas–shale interface (or shale–gas)

The constant term in fluid factor is based on Mudrock line [3], which refers to $V_p = 1.16 V_s + 1.36$ (where 1.36 could have local values). This formula is considered as a trend in brine-saturated sandstones. When gas exists in sand, ΔF will show an anomaly compared with brine.

$$\frac{\Delta V_s}{V_s} = \frac{(V_{P_2} - V_{P_1})/1.16}{V_{P_2} + V_{P_1}/1.16 + 2C/1.16}$$

We obtain the ν term in fluid factor, which is a replacement of C . Mathematically; ν is an approximation of V_p/V_s .

For comparison, the response of ΔF which ν is set to two for same model sets is given in Fig. 2b. It shows FF has similar responding to gas and brine in models 4, 6, 8, 10, 11, 12, 22, and 25. A reverse result existed in model 19, in which brine shows a lower value than brine. In addition, gas has lower value than brine.

Figure 2c compared the ability of distinguishing type of fluid in J and fluid factor. As a kind of seismic attribute, we hope it can work on both top and bottom interfaces, which means the absolute value for gas and brine is supposed to be different. Otherwise, we will be confused by top of gas or base of brine. So we use residual of absolute value in Fig. 2c to eliminate this potential confusion. J and fluid factor behavior could be close in models 9, 13, 20, and 23, where both J and FF have good result. It shows clearly residuals of J show large negative values in model 3 and 6 whereas residual of FF is close to zero.

From the result of the comparison, we found the new attribute J has a better performance than FF in some models. When analyzing models, we can see when the difference of V_p/V_s contrast has a larger value and J performs better, such as

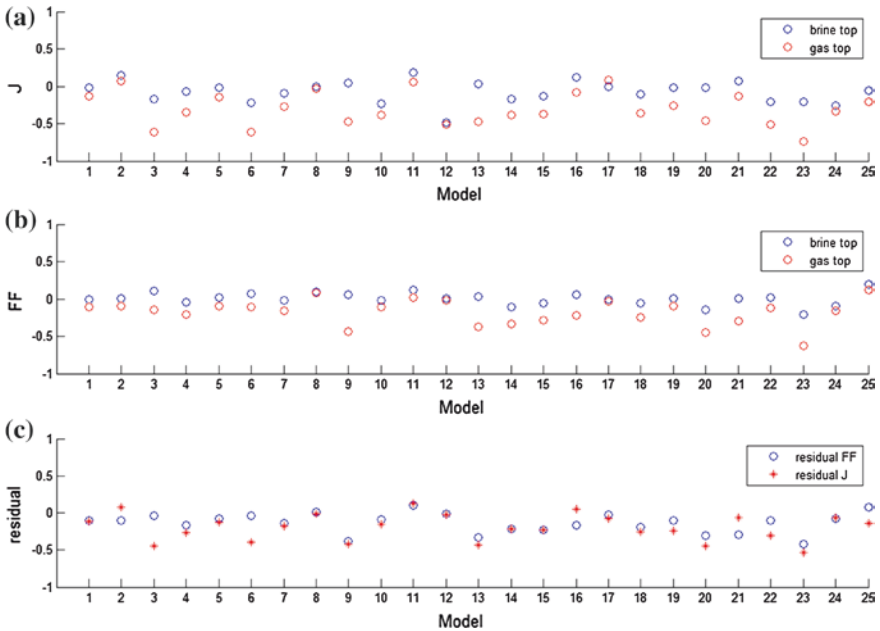
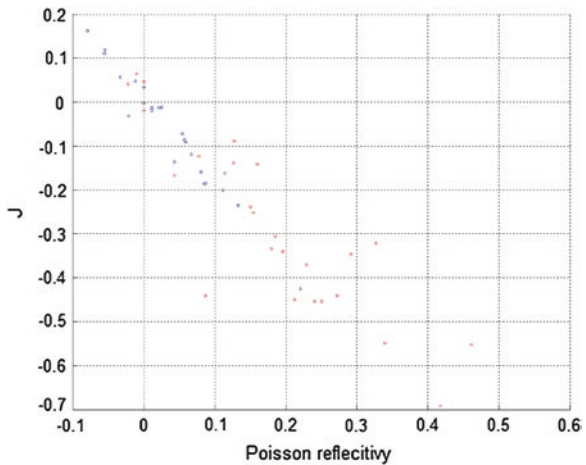


Fig. 2 a Top sand responding on J ; b top sand responding on fluid factor; c residual between brine and gas in J and fluid factor, in which residual is the difference of absolute value between gas and top

models 3,6,9,13,20, and 23. In other words, J and Poisson reflectivity are highly correlated, as shown in Fig. 3.

In addition to these three models, there are some models; J can be separated from the oil and gas, but the difference is not great. As a kind of seismic attribute, it is hard to regard J as indicator of lithology or fluid. Figure 3 shows the

Fig. 3 Cross-plot: Poisson reflectivity versus J



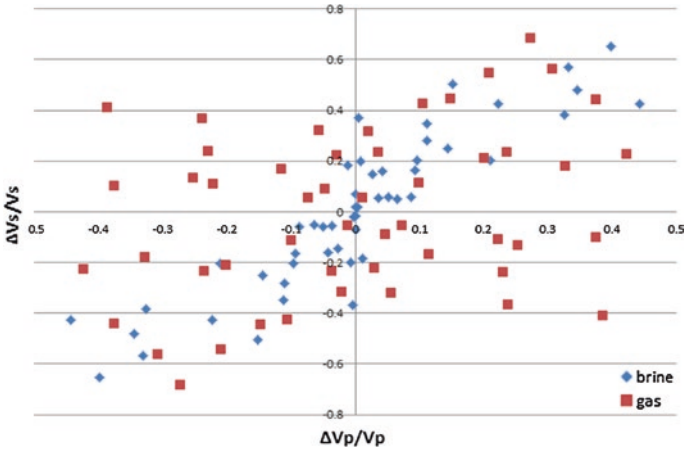


Fig. 4 Cross-plot: V_p contrast versus V_s contrast

relationship between J and Poisson reflectivity where strong correlation exists. When J is less than -0.2 or Poisson reflectivity is greater than 0.1 , gas and brine are separated very well, and J can be used to detect fluid in these cases.

In these model sets, we plot V_p contrasts and V_s contrasts as ΔF is focused on them in Fig. 4. Both top and bottom interfaces are plotted in the figure. We obtain that V_p and V_s contrasts have a same background trend line except about ten models. From this figure, it is difficult to distinguish gas from brine sand by V_p contrast and V_s contrast.

3 DATA

3.1 Well

As validation, well data will be applied, in which log contains V_p , V_s , and density. J_p and J_s are derived from these logs and are cross-plotted (Fig. 5).

The trend line is clearly shown in figure. Background $V_p V_s$ could be estimated from the gradient of trend line. Besides this, there are abnormal points plotted outside the trend line. According to above theory, these points can be considered abnormal reaction from gas sand. The well section of two wells is given in Fig. 6.

Combined with the existing data; we know that there are three main gas reservoirs which are 1,250, 1,435, and 1,448 m in Well-1. Brine sand is not always clear; it depends on surrounding layer. Generally, “box” shape logs will be more sensitive on J attribute as lithology changes rapidly and clearly. In Well-1 case, we see J attribute has a good response with gas sand and coal bed, and ΔF shows a very close result with J .

In Well-2 case, the only two reservoirs are at 1910 and 2085 m depth. For reservoir in 1910 m, ΔF and J both work well. But for the reservoir in 2085 m depth,

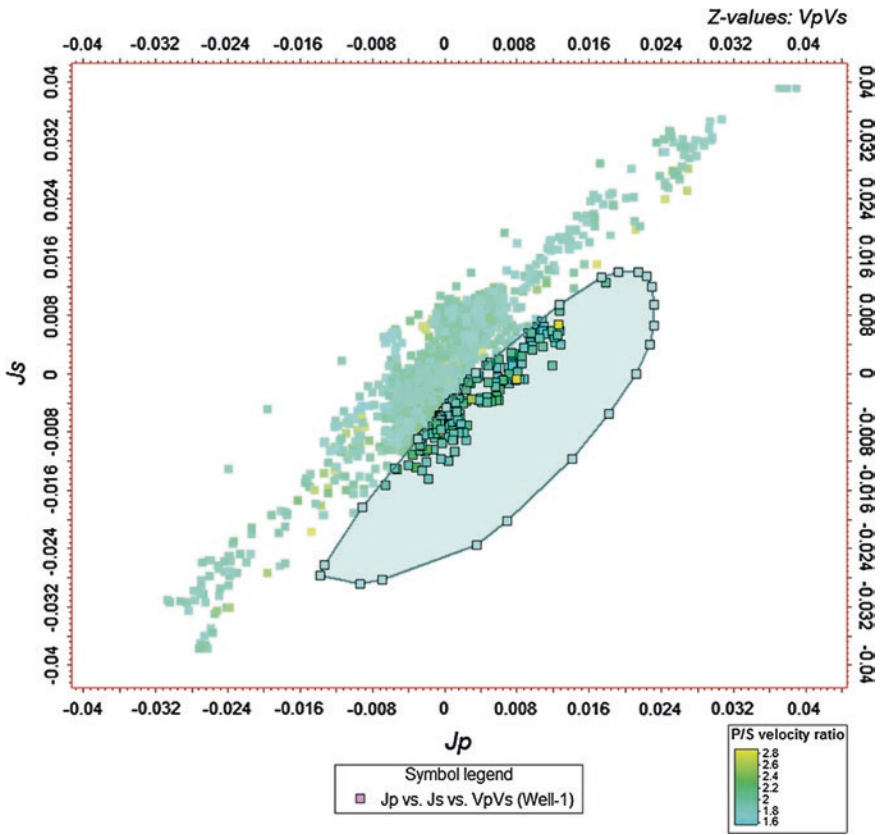


Fig. 5 Cross-plot on Well-1: J_p versus J_s

ΔF behavior is like brine sand, but J shows a very high value. It proved J performs better in some cases though in most situations their results are similar.

3.2 Seismic

Figure 7 is a comparison between J and ΔF seismic section cross-Well-1 in 3D seismic data (left is J , and right is ΔF). Structure is simple in this area, in which fault is not developed. The main gas reservoirs distribute in 1220, 1350, 1390, and 1550 ms in time domain. From this figure, we can see J anomalies spread at 1220, 1400, 1480, and 1580 ms. They cover most of the reservoirs except the one at 1350 ms and have response to the coal bed at 1480 ms.

As an indicator attribute for fluid, we will compare J with the fluid factors (ΔF) mentioned above, and ΔF (background v is set equal to two) shows higher value at 1220, 1380, and 1480 ms which are gas, sand, and coal. We can see ΔF works

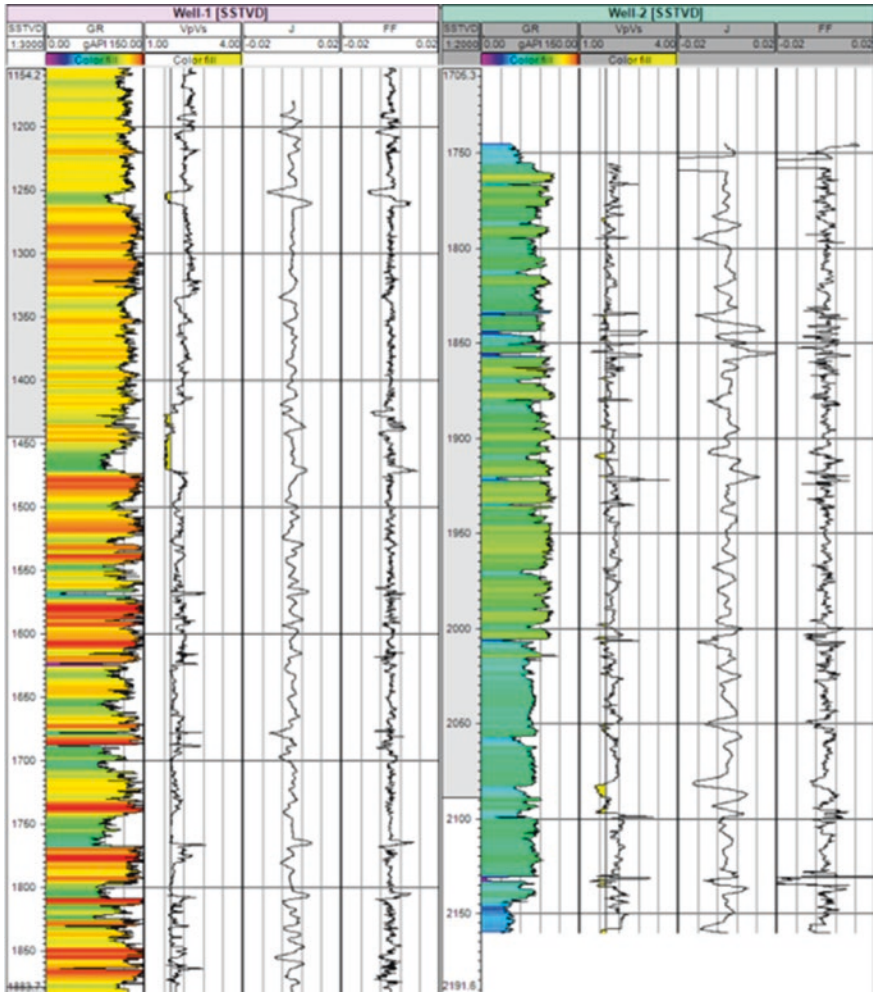


Fig. 6 Well section with J and FF

better in reservoir at 1350 ms and J performs better at 1380 ms. Different fluid factor result is based on the situation of lithology.

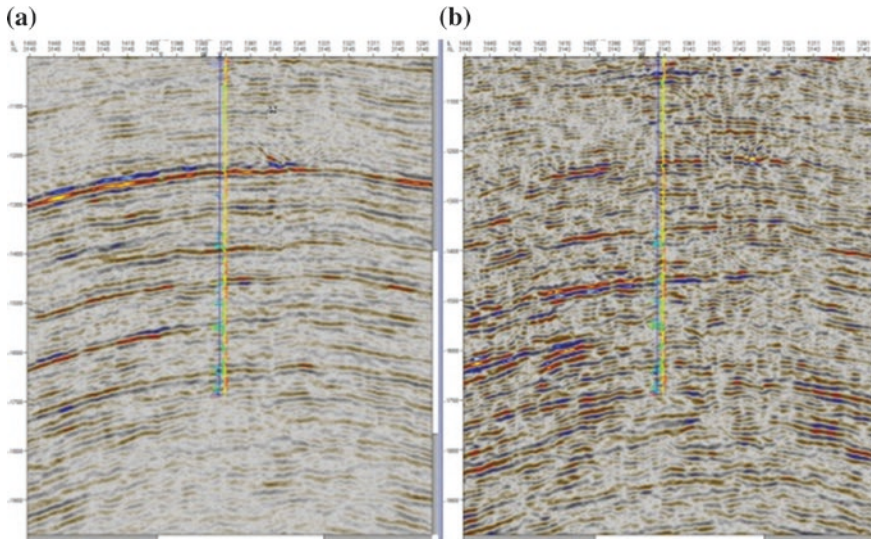


Fig. 7 a J attribute seismic section cross-Well-1; b ΔF seismic section cross-Well-1

4 Conclusion

1. In this paper, we presented a new fluid factor which is based on Shuey’s approximation for improving the ability of detecting fluid type. As the results from comparison in modeling and real data, new fluid factor has better performance in some cases. It provides a new method for the prediction of gas reservoirs, especially as gas reservoir has a larger Poisson reflectivity.
2. However, we need to pay attention that coal beds also show strong reflection on J as they have larger V_p/V_s ratio. Some of anomalies come from gas sand, and some come from coal bed. Furthermore, the impact of the coal cannot be theoretically eliminated. It usually shows larger values than gas sand because of its petrophysical parameter. This makes the results confusing. To remove this effect, we need to use other techniques, such as AVO classification or spectral decomposition.

References

1. Useful approximations for converted-wave AVO, Antonio C. B. Ramos and John P. Castagna, 2001
2. Weighted stacking for rock property estimation and detection of GAS, G. C. Smith and P. M. Gidlow, 1987
3. Relationships between compressional-wave and shear-wave velocities in clastic silicate rocks, J. P. Castagna, M. L. Batzle, and R. L. Eastwood, 1985

Geological Structures of the Kinta Valley Revisited Using Drainage Anomalies

Choong Chee Meng and Manuel Pubellier

Abstract More than 50 % of the surface of Kinta Valley is covered by alluvium overlying Paleozoic sequences and Late Triassic granitic intrusions. The alluvium of the valley is thin (mostly less than 30 m thick). Limestone and shale are the dominant lithologies cropping out in the valley, and they have been severely deformed. Unfortunately, these rocks are restricted to small areas of the valley and they are highly weathered, thus making the correlations between outcrops and structural interpretation commonly speculative. In this paper, we make use of drainage pattern anomalies of rivers, streams, and dry thalwegs that commonly reflect subsurface structures or variation of thickness of sediments and may help regional interpretation. Two main anomaly sets have been identified; NE–SW and N–S. These anomalies might reflect slight or large normal faults, and they formed sigmoid-shaped structure after interpolation. Three hypotheses are proposed to illustrate the extensional process in terms of reactivation of faults, transtension, and shear partitioning. Shear partitioning is most likely to occur by distributing the oblique extensional stress into normal faults and strike-slip faults. The valley is shallower and narrower to the north, suggesting more intense shortening than in the southern part. Both shortening by thrust faults and subsequent extension may be rooted in the lower ductile crust beneath the large granitic plutons.

Keywords Kinta Valley • Drainage anomalies • Deformation • Cross section

C.C. Meng (✉)

South East Asia Carbonate Research Laboratory, Department of Geoscience,
Universiti Teknologi PETRONAS, Seri Iskandar, 31750 Tronoh, Perak, Malaysia
e-mail: cheemeng.choong@yahoo.com

M. Pubellier

Department of Geoscience, Universiti Teknologi PETRONAS, Seri Iskandar,
31750 Tronoh, Perak, Malaysia
e-mail: manuel.pubellier@petronas.com.my

1 Introduction

The Kinta Valley is bounded by mountain ranges to the east and west and widens toward the south (Fig. 1). Rivers and streams which originated from the highland converge into the valley (lowland) by flowing following the regional slope forming a dense drainage system which carries the weathered materials of the mountain basement rocks. This drainage system is partially influenced by structures of the bedrocks such as fractures and folds. Several cores and wells drilled in the valley for ore exploration provide information concerning the thickness of the shallow sedimentary layers, which are generally less than 30 m (70 ft) thick [1]. As a result, the thin alluvium is likely to reflect the bedrock morphostructures caused by either differential compaction of sedimentary layers at the footwall and hanging walls of faults or to their reactivation.

In the past, deformation in Kinta Valley has been studied using multi-scale analysis that mainly focused on the dominant outcrops, limestone, and granite, whereas in fact, most of the valley is covered by alluvium. Thus, drainage anomalies analysis may help to extract geological information from the bedrock underneath the thin alluvium where data were previously lacking, resulting in revised interpretations. Basing on surface geological data, satellite imagery, and drainage anomalies, we present a map of the hidden structures of the Kinta Valley and two E–W cross sections from the Kledang Range to main range in order to better illustrate the structural setting.

2 Geological Setting

Various lithologies have been identified in the Kinta Valley. Some authors [1] have grouped them into a few geological successions, which are calcareous and arenaceous series, granite and alluvium. In terms of structural evolution, an early extension has been identified, followed by compression and a late extension [2]. The early extension is represented by small brittle conjugate fractures in the Paleozoic platform, which formed when the carbonate sediments deposited and started hardening by diagenesis during basin infilling, and fractured due to overburden. It was followed by a regional compressional regime, which led to the formation of conjugate strike-slip faults and a series of thrusts within the carbonate strata. It seems that the shortening propagated toward the east and increased approaching the contact with the granite of the main range. It is not clear if compression also affected the granite [3]. However, not far from the formerly hot granite contact, the limestone deformed in a ductile manner, as illustrated by localized flow structures and ductile pure shear. The ductile structures indicate both reverse and normal movement, suggesting a late gravitational collapse of the limestone parallel to the granite contact. The process would be similar to “roof-pendant” formation, but with high temperature (HT) conditions, and suggests the concomitance of the late stage of

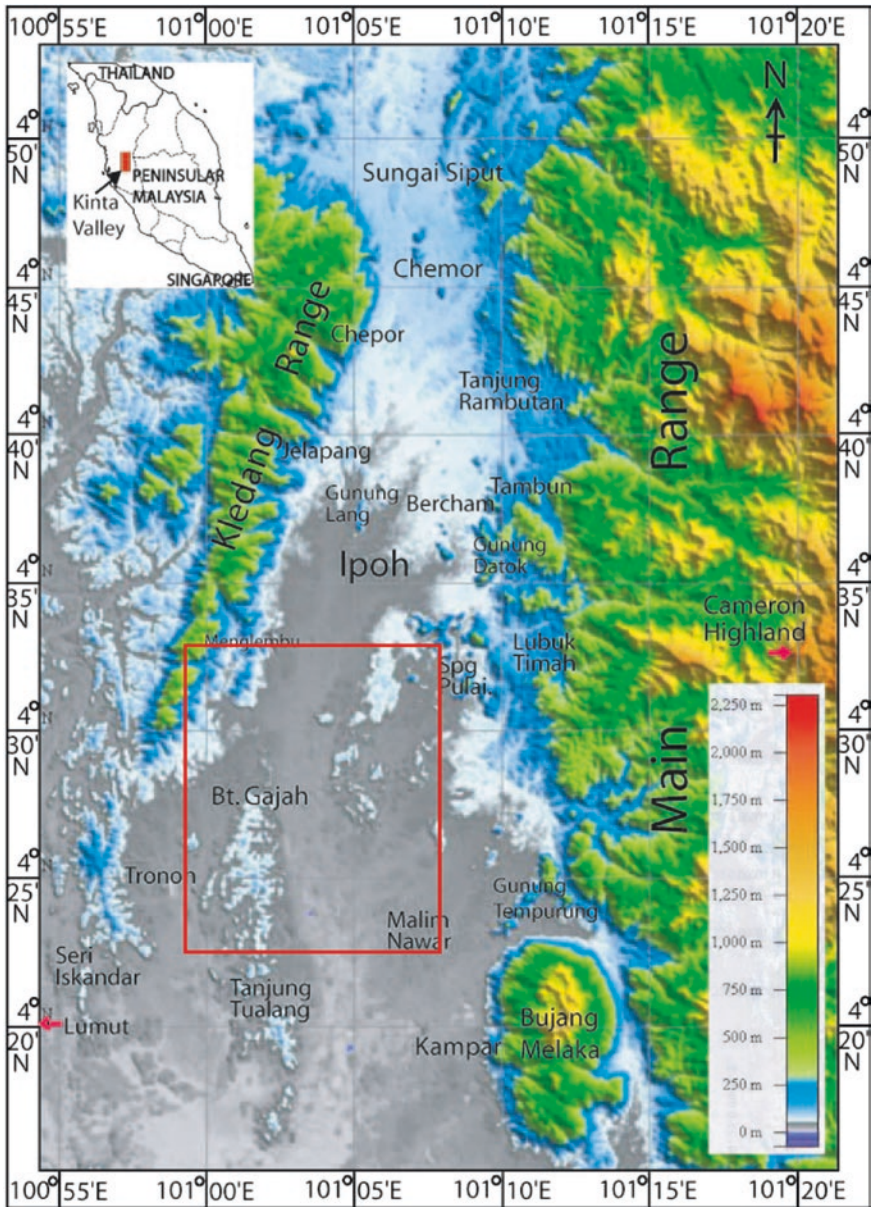


Fig. 1 Morphology and localities of Kinta Valley. The area between granitic intrusions (green and yellow) is mainly composed of alluvium (white and gray). The detailed drainage anomalies of Fig. 2 are shown in the red frame. Note the narrowing of the valley toward the North

granitic intrusion and the shortening. This region became extensional again as illustrated by large normal faults visible on the digital elevation model (DEM) [4] and satellite image. We correlate the late extensional event with the Tertiary horsts and grabens formation of the Strait of Malacca [5], the Mergui basins of the Sumatra, and other onshore Tertiary basins of Peninsular Malaysia, based on their similar orientation and structure.

3 Methodology

Rivers tend to flow naturally in the shortest path to the shoreline following the regional slope [6]. It is assumed that if it behaves in different way, it forms drainage anomalies which result from anthropogenic activities or local geological structures, topographic anomalies, or other external factors [7].

The drainage network of the Kinta Valley has been digitized and overlain on the DEM. The anomalies have been selected based on criteria [7] such as:

- Local modifications of the drainage pattern: The drainage locally appears in a pattern that differs from the dominant one. We identify, for example, radial drainage patterns including centrifugal and centripetal [8].
- Wide angle of river's convergence (the normal convergence is usually 60°), or divergence of the streams triggered by a subsurface topographic high.
- Stream directions not following the regional slope or marking a bayonet shape.

Anomalies are analyzed and interpreted in terms of potential geological structures such as bedding traces, faults, sagging zones, or underlying basement highs such as karst relicts or plutonic bodies. Based on structures inferred from drainage anomalies, and previous surficial geological information, a geological structural map was constructed, from which geological cross sections were constructed. The interpretation provides support for a discussion of the geological setting of the valley in terms of geodynamics and tectonics.

4 Results and Discussions

4.1 Drainage Anomalies

Analysis of drainage anomalies focused on the middle part of the valley (alluvium) where outcrops and therefore geological information were lacking or poor (Fig. 2). Two major sets of anomalies have been identified: NE–SW and N–S.

The NE–SW anomalies have a specific orientation, which may have some local deviations. These anomalies have been observed in the northern (e.g., Chemor) and southern ends (e.g., Batu Gajah–Gopeng) of Kinta Valley. They are commonly a few kilometers long and regularly spaced.

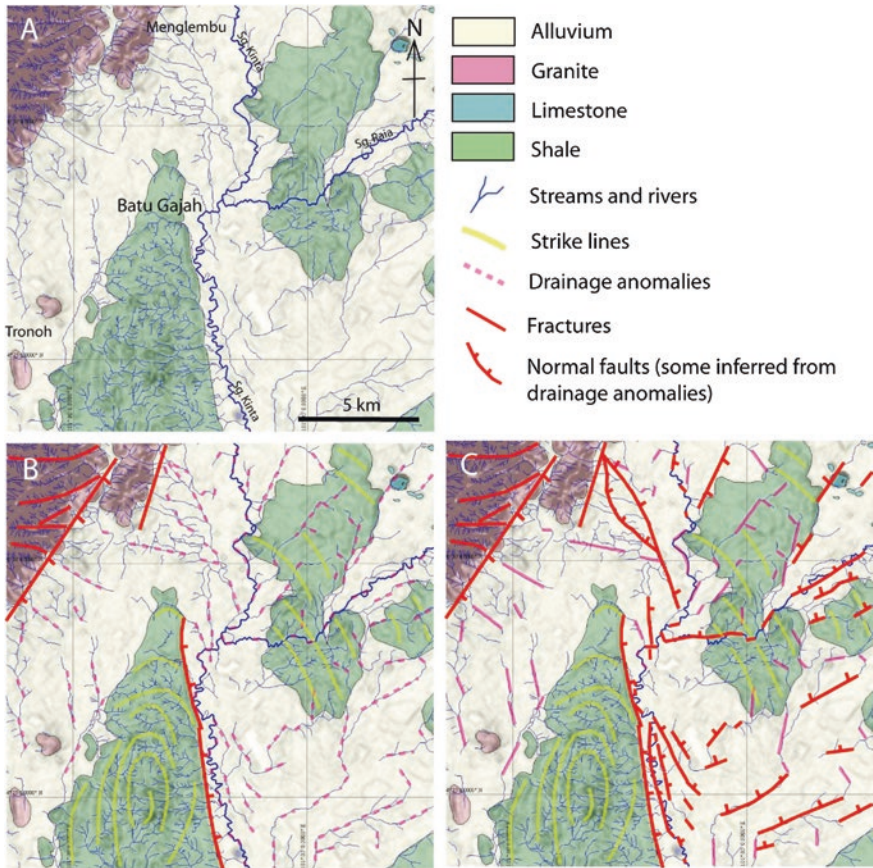


Fig. 2 a–c showing the steps followed in analysis and interpretation of drainage anomalies. **a** Detail map showing the drainage system and lithologies in the vicinity of Batu Gajah. **b** Drainage anomalies have been traced, together with fractures, normal faults, and strike lines of the beddings. **c** Some of the prominent the drainage anomalies have been correlated and interpreted as normal faults based on their curvilinear shape and their location at the edge of uplifted areas

The NE–SW anomalies are found in alluvium of the northern end of the valley, which includes north of Ipoh city, Tanjung Rambutan, and Chemor. They are totally absent in the valley flanks or granitic mountain ranges (Fig. 3). Parts of the major rivers such as Sg. Pari and Sg. Kinta have been included as large drainage anomalies. The average lengths of the anomalies (~5 km) suggest they are large faults. These faults are likely to result from a late deformation, because they crosscut other fractures. The NE–SW anomalies are also found in the southern part of the valley (Gopeng—Gunung Tempurung area next to the mountain range) (Fig. 3). Moving away from mountain range toward the Malim Nawar—Tanjung Tualang area in the west, the orientations of the anomalies are slightly deviated to ENE–WSW. Because of their curvilinear shape, these anomalies can be extended

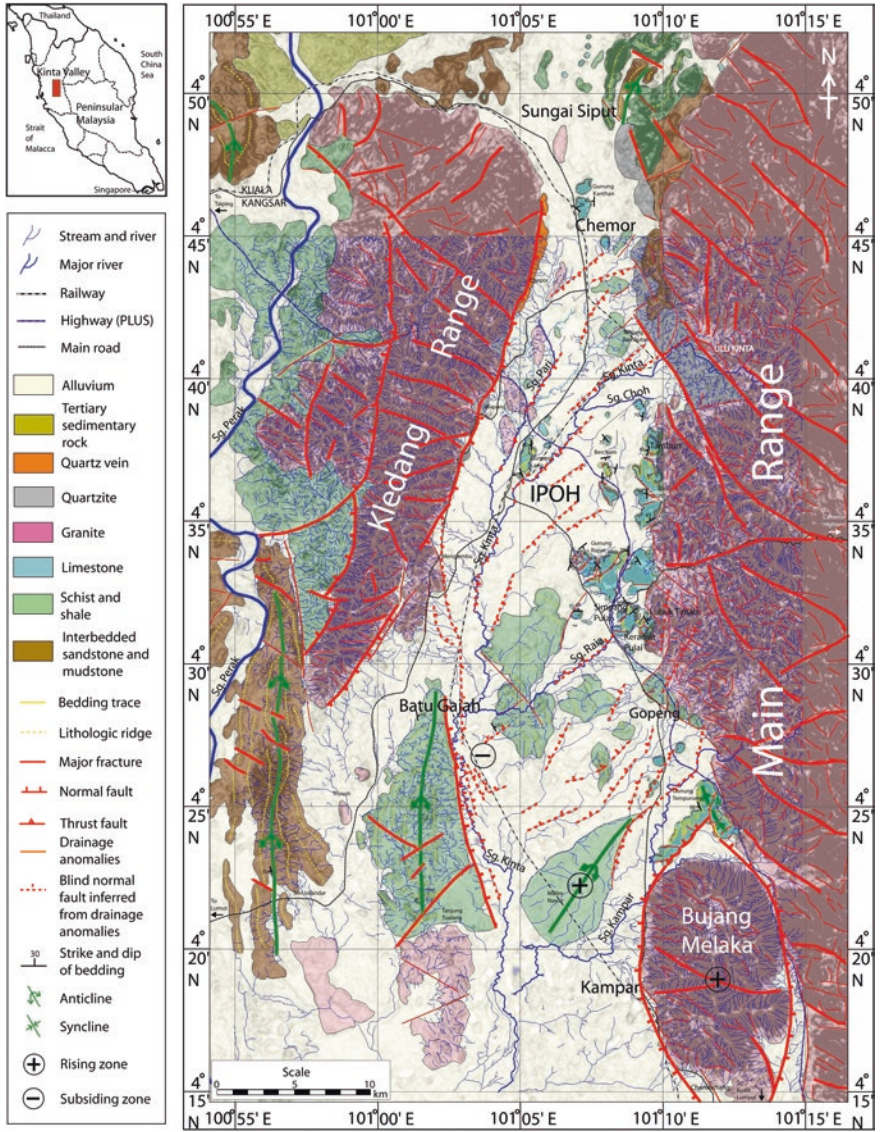


Fig. 3 Geological and structural map of the Kinta Valley, including the subsurface information deduced from the drainage anomalies

and connected to the N-S striking fractures to the granitic mountain range next to Gopeng town.

N-S anomalies are found near Sg. Kinta next to Batu Gajah and the southeast part of the Menglembu (Fig. 3). They are locally oriented NNW-SSE near the Tanjung Tualang area. They are closely spaced and localized. A normal fault near

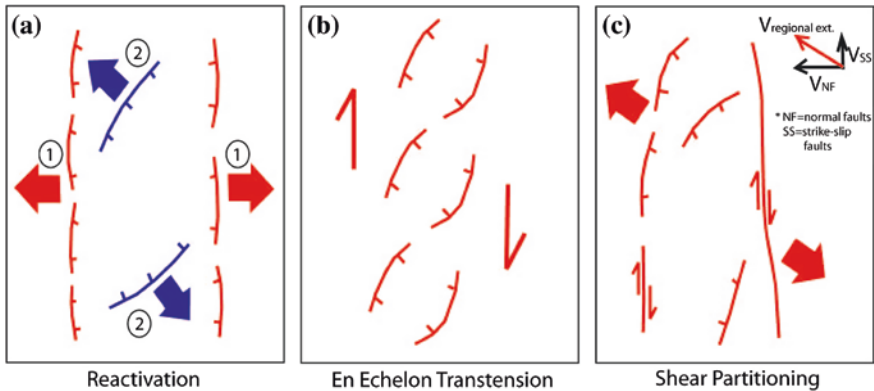


Fig. 4 Models illustrating the extension events that initiated the numerous normal faults in Kinta Valley. *Board arrow sets* indicate the extensional directions

Sg. Kinta, interpreted on DEM based on the change of the surficial texture, has an azimuth similar to this anomaly set.

A subsiding zone has been discovered at the intersection of the Sg. Kinta and Sg. Raia near Batu Gajah and labeled with a “-” symbol. The drainage disappears here and may connect to a groundwater system. These anomalies are likely to correspond to a late extensional event. Several additional structures have been observed in the valley, and these may be related to the late extension. They are namely, spoon-shaped normal faults (e.g., eastern part of the Batu Gajah), low-angle normal faults along granite (e.g., Simpang Pulai), and strike-slip faults (e.g., Lubuk Timah, Simpang Pulai). The geometry of the system encompassing these faults, close to a large pull-apart, suggests a component of strike-slip, which is not easy to see in the field. We propose three hypotheses to describe their occurrences (Fig. 4): (i) normal faults reactivated as strike-slip faults; (ii) a transtensional event consisting of faults that have both dip-slip and strike-slip components; or (iii) shear partitioning which distributed the oblique extensional stress into normal faults and strike-slip faults. Among these hypotheses, we favor shear partitioning as the initial extensional event because of the common existence of pure strike-slip and pure dip-slip faults in the valley.

4.2 Kinta Valley Cross Sections

The previous mapping using satellite imagery, DEM, and field observation has revealed that Kinta Valley is composed of few major lithologies (i.e., interbedded sandstone and mudstone, shale, limestone, and granite) with different geological structures. In order to illustrate the regional deformation of Kinta Valley, two large-scale E–W cross sections across valleys have been constructed (Fig. 5). As

mentioned above, Kinta Valley underwent an early extension in the Paleozoic platform, a syn-intrusive compression (Early Jurassic?) and late Tertiary extension. The early extension occurred at outcrop scale and is not represented on the sections. Thus, the structures observed in the valley are mainly the compression and late extension.

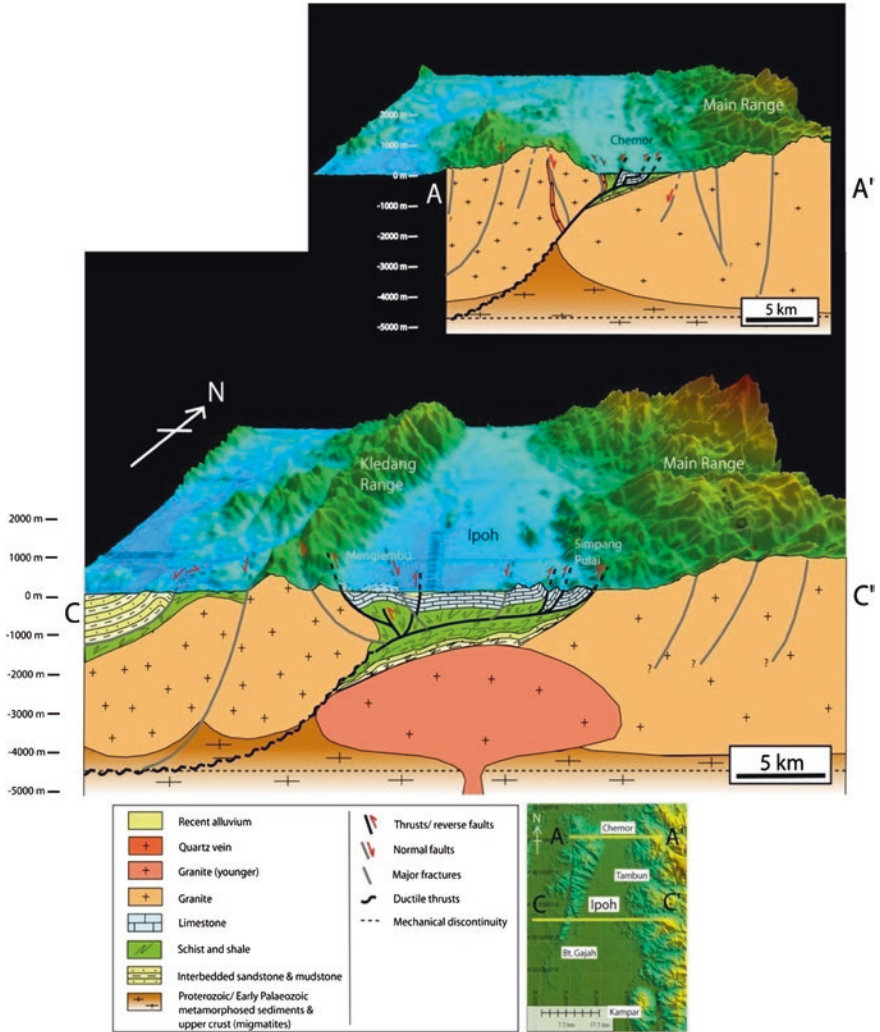


Fig. 5 Two E–W geological cross sections (A–A' and C–C') combined with DEM across Kinta Valley from the Kledang Range to the main range [9]. The sections illustrate that shortening affected the deep structures (including the basement and the granites) via deeply rooted thrusts propagating toward the surface into the thick black shale and the stacking of Paleozoic limestone. *Note* the increase of shortening from the south to the north of Kinta Valley

The compressional event occurred together with the granitic intrusion during Late Triassic to Early Jurassic time. All the preexisting rocks (interbedded sandstone and mudstone, schist and shale, limestone, and granite) were affected. The limestone close to the granite–limestone contact was shortened by folding. Thrust faults and tight folds are the main structure in this area, which contribute to the folding and tilting of the strata (Fig. 5). The important shortening of the limestone unit implies an effective decollement within the underlying lithologies, which are represented by over-thickened black clay. The deformation in the clay is severe at the scale of the outcrop but also visible for the first time on the map, in the form of a broad anticline. We propose that this geometry results from the shortening between the large granitic bodies of the Kledang Range and the main range, which in turn suggests that the thrust may be deep-seated and connected to the mechanical discontinuity at a few kilometers depth. The crustal thrust faults would ramp up to the shallow level (black shale) and then serve as a decollement for the Paleozoic limestone.

The granitic areas in the valley flanks are intensely fractured. As the granitic intrusions were cooling, they recorded the deformation as brittle fractures, which may have recorded the E–W compression as conjugate fractures. An extensional regime followed the compression, and this is evidenced by the propagation of normal faults reactivating existing discontinuities, e.g., fractures, thrust faults, or granite–limestone contacts.

5 Conclusions

Alluvium covers most of Kinta Valley and obliterates the main structures. They are thin (commonly less than 30 m thick) and accommodate a dense drainage system. Two major drainage anomaly sets, NE–SW and N–S, have been identified. Blind normal faults have been inferred from these anomalies and can be interpolated as large curvilinear structures. Three hypotheses have been proposed to illustrate the extensional event: (1) normal faults reactivated as strike-slip faults, (2) en echelon normal faults, and (3) shear partitioning dividing the extensional forces into pure strike-slip faults and pure normal faults, respectively. Based on field observations, shear partitioning is the most likely explanation for the occurrence of numerous blind faults marked by drainage anomalies. Two cross sections have been constructed based on the information extracted from field, satellite imagery, DEM, and drainage anomalies. The sections illustrate that the rock sequences of the valley are mainly affected by thrust faults, which accommodated the shortening and transferred the deformation from the deep crustal layers to the Paleozoic platform. The subsequent late extension led to formation of large normal faults, which may have reactivated the earlier structures at the contact between sediments and granite.

Acknowledgments This paper benefitted from discussions of many experts at Universiti Teknologi PETRONAS and was improved by remarks provided by our reviewers. This investigation was conducted in the facilities and under the auspices of the South East Asia Carbonate Research Laboratory, which is funded by Sarawak Shell Berhad.

References

1. F. T., Ingham, and E.P., Bradford, "Geology and Mineral Resources of the Kinta Valley, Perak," Federation of Malaya Geological Survey District Memoir 9, Malaya: Government Press, 1960.
2. C.M. Choong, M. Pubellier, Abdelaziz Abdeldayem, W.S. Chow, "Deformation Styles and Structural History of the Paleozoic Limestone: Kinta Valley, Perak, Malaysia", National Geoscience Conference, Kinta Riverfront Hotel, Ipoh, Perak, 2013.
3. D. J., Gobbett, "Joint Pattern and Faulting in Kinta, West Malaysia", Geol. Soc. Malaysia, Bulletin, No. 5, 1971, 39-48 pp. Art Printing Works, KL.
4. A. Jarvis, H.I. Reuter, A. Nelson, E. Guevara, "Hole-filled seamless SRTM data V4", International Centre for Tropical Agriculture (CIAT), available from <http://srtm.csi.cgiar.org>, 2008.
5. K.K., Liew, "Structural patterns within the Tertiary basement of the Strait of Malacca", Geological Society of Malaysia Bulletin, Vol. 38, 1995, 109-126 pp.
6. B. Deffontaines, P., Chotin, L., AitBrahim, and M., Rozanov, "Investigation of active faults in Morocco using morphometric methods and drainage pattern analysis.," Geol. Rundsch., vol. 81 (1), 1992, 199-210 pp.
7. M., Pubellier, B., Deffontaines, R., Quebral, and C., Rangin, "Drainage network analysis and tectonics of Mindanao, southern Philippines," Geomorphology, vol. 9, 1994, 325-342 pp.
8. A.D., Howard, "Drainage Analysis in Geological Interpretation: A Summary", The American Association of Petroleum Geologists Bulletin, Vol. 51, No. 11, 1967, 2246-2259 pp.
9. C.M., Choong, 2014. *Structural History of the Kinta Valley*. MSc Thesis, Geoscience Dept., Faculty of Geoscience and Petroleum Engineering, Universiti Teknologi PETRONAS. (Unpublished).

Geochemical Signatures of Some Devonian Black Shales

E. Padmanabhan and D. Jeffrey Over

Abstract Shales from two geographical locations but of the same age (Devonian) were compared in this study. Given that the depositional geochemical environment may be similar, it remains to be seen in if there is a possible unique geochemical signature that can globally unite all black shales of similar origin. Samples from the Oatka Creek Formation (USA) and Batu Gajah Shale (Malaysia) showed similar trends in terms of their absorbance at 465 and 665 nm. Since the E_4 and E_6 absorbance values are similar, it is believed that the supply of organics and the diagenetic history could have been very similar. The preliminary results suggest further that the similarity in the individual values of the E_4 and E_6 absorbances as well as the E_4/E_6 ratios may well serve as a unique geochemical signature for such black shales from the Devonian.

Keywords Black shales · Devonian · FTIR · Geochemical signatures

1 Introduction

Black shales have always been associated with their potential as a hydrocarbon source rock. The accumulation of such organic-rich deposits can be attributed to variations in rates of subsidence and relative sea level changes with subsequent changes in particle size and sedimentation rate [1–5]. Research on black shales spanning the last six decades or so has been focused on a few critical issues, one of which is the origin of these rocks itself.

E. Padmanabhan (✉)

Department of Geoscience, Faculty of Geoscience and Petroleum Engineering,
Universiti Teknologi PETRONAS, Tronoh, Perak, Malaysia
e-mail: eswaran_padmanabhan@petronas.com.my

D. Jeffrey Over

Department of Geological Sciences, State University of New York at Geneseo,
Geneseo, NY, USA

The Oatka Creek Formation is considered to have been deposited in a stagnant, euxinic basin [6]. The Batu Gajah shale is Paleozoic in age and believed to be deposited in a similar stagnant basin. Both of these formations are Devonian in age. It is recognized that most geochemical processes are influenced by more than one process. It is evident the development of black shales is possible in areas where the conditions favor the retention and preservation of organic fractions. The quality of the organic fraction may differ from location to location. However, what remains unclear is whether the black shales have a unique geochemical signature that typifies their geochemistry of the environment of deposition, organic matter diagenesis with subsequent preservation processes. In this chapter, one modern technique is explored as a possible tool to identify a unique geochemical signature for these rocks.

2 Materials and Methods

Several sets of samples were used for this study. The first batch of samples comes from surface exposures in western New York State, USA (Oatka Creek Formation of the Marcellus subgroup). Batch 2 is from a borehole near Geneseo, western New York State, USA, in the Marcellus subgroup (Union Springs Formation and Oatka Creek Formation). Batches 3 and 4 come from the Devonian beds at Batu Gajah, Perak, Malaysia.

Samples were treated with Dichloromethane (DCM) and the supernatant solution was decanted after 24 h. The solutions were analyzed using a Shimadzu UV-3150 UV Vis Spectrophotometer. E_4 was determined at an absorption frequency of 465 nm, E_5 at 550 nm, and E_6 at 665 nm.

3 Results and Discussion

The results show that for samples 1-1 until 1-4 of Batch 1, there are approximately equal proportions of aromatics and aliphatics as evidenced by the E_4 and E_6 values. All samples are black in color. This suggests a high content of carbon. Sample 1 had low amounts of E_4 and E_6 compared to the other samples. The E_4/E_6 ratios suggest a fairly constant distribution of carbon (Table 1).

The E_4/E_6 results from Batch 2 (Table 2) show generally an increase with depth. All samples from Batch 2 are black in color indicative of high organic contents.

Table 1 UV-visible results for middle Devonian shales from Batch 1

Sample	Member	E_4	E_6	E_4/E_6
1-1	Oatka Creek	0.25	0.24	1.04
1-2	Oatka Creek	1.13	1.09	1.04
1-3	Oatka Creek	1.11	1.08	1.03
1-4	Oatka Creek	1.09	1.06	1.03

Table 2 UV-visible results for middle Devonian shales from Batch 2

Sample	Member	E ₄	E ₆	E ₄ /E ₆
2-1 (254.9 m)	Oatka Creek	0.26	0.23	1.13
2-2 (255.6 m)	Oatka Creek	0.06	0.04	1.50
2-3 (257.3 m)	Oatka Creek	0.21	0.17	1.24
2-4 (263.2 m)	Oatka Creek	0.42	0.28	1.50
2-5 (264.1 m)	Oatka Creek	0.06	0.03	2.00
2-6 (264.8 m)	Union Springs	0.04	0.03	1.33

Table 3 UV-visible results for Devonian shales from Batch 3

Sample	Member	E ₄	E ₆	E ₄ /E ₆
3-1 (T1 – 0 m)	Dark gray (bottom)	1.32	1.03	1.28
3-1 (T1 – 0 m)	Dark gray (top)	1.24	0.99	1.25
3-2 (T1–2 m)	Dark gray (bottom)	1.33	1.04	1.28
3-3 (T1–4 m)	Dark gray (bottom)	0.43	0.29	1.48
3-4 (T1–6 m)	Dark gray (bottom)	1.44	1.11	1.30
3-5 (T1–8 m)	Light gray (bottom)	0.82	0.55	1.49
3-6 (T1–10 m)	Light gray (bottom)	0.45	0.24	1.88
3-7 (T1–12 m)	Light gray (bottom)	0.19	0.14	1.36
3-8 (T1–14 m)	Dark gray (bottom)	0.92	0.78	1.18
3-9 (T1–16 m)	Light gray (bottom)	0.26	0.20	1.30

This indicates a dominance of aromatic compounds over aliphatic compounds. However, the erratic distribution of the E₄/E₆ values suggests an irregular supply of carbon to the sedimentary basin before the onset of diagenesis. In terms of absolute values, all samples from Batch 2 have similar E₄ and E₆ values as sample 1-1 from Batch 1.

The E₄/E₆ ratios of shales from a transect (Batch 3) show quite similar results despite differences in the color or the rock (Table 3). There is a dominance of aromatic compounds. The dark gray shales tend to have more absolute values for E₄ and E₆ compared with the light gray units. This is to be expected since the dark gray units have more carbon content in them compared with the light gray units.

All samples from Batch 4 show dominance of aromatic compounds except for sample 4-5 that has a dominance of aliphatic compounds. However, only sample 4-1 shows high absolute values for E₄ and E₆ (Table 4). The light gray samples from this transect have low absolute values for E₄ and E₆.

Despite the E₄/E₆ ratios being similar, it is difficult to assign a particular value to any one facies (light gray or dark gray).

Table 4 UV-visible results for Devonian shales from Batch 4

Sample	Member	E ₄	E ₆	E ₄ /E ₆
4-1 (T2–0 m)	Dark gray	1.04	0.79	1.32
4-2 (T2–5 m)	Light gray	0.44	0.34	1.29
4-3 (T2–10 m)	Light gray	0.31	0.29	1.07
4-4 (T2–15 m)	Light gray	0.56	0.47	1.19
4-5 (T2–20 m)	Light gray	0.33	0.63	0.52

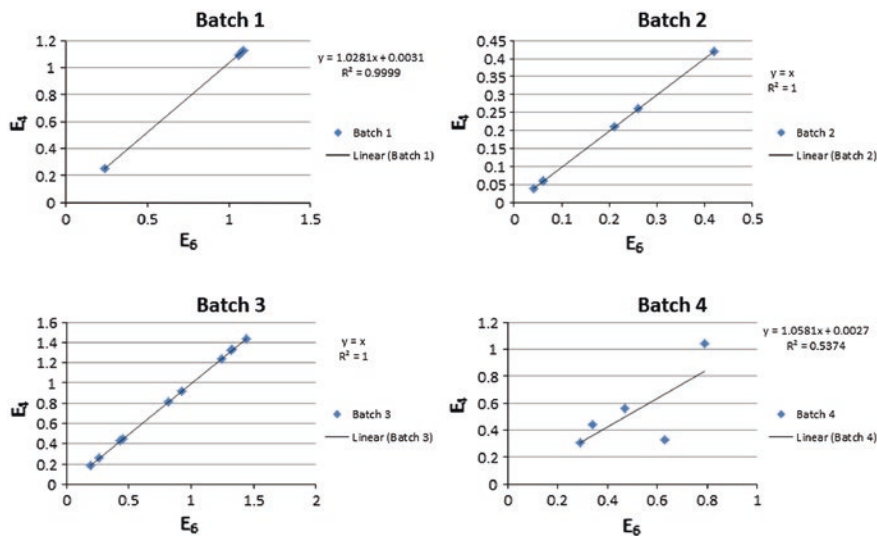
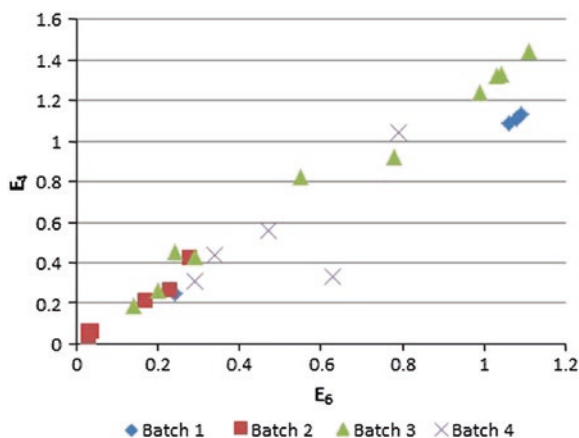


Fig. 1 Plot of E_4 against E_6 values for the different batches

Figure 1 shows that in most cases, the E_4 values increase almost in equal proportions to the E_6 values. This has been observed for Batches 1–3. However, Batch 4 shows a slightly more dispersed relationship between these two values. This could be due to an interrupted and inconsistent supply of carbon during deposition. It remains to be seen if the relationship observed for Batches 1–3 would hold for a larger population size.

The plot of E_4 against E_6 for all samples (Fig. 2) suggests a linear relationship between these two parameters in black shales of Devonian age. The results suggest that the supply of carbon during deposition was fairly consistent and in appreciable amounts. This also suggests that the organic matter diagenetic history could

Fig. 2 Plot of E_4 against E_6 for all samples



have been very similar. The equal proportions of E_4 and E_6 may also point out to the presence of type II kerogen. It appears that the signals given by E_4 and E_6 may be useful as a geochemical signature for Devonian black shales. This theory will have to be tested with a larger population size of Devonian black shales and shales from other geological periods.

4 Conclusions

It is concluded that the E_4/E_6 ratios probably indicate a unique geochemical signature for the Devonian black shales from both localities. This uniqueness is attributed to the depositional styles as well as post-depositional diagenesis and preservation mechanisms that by and large are unique to environments that create black shales.

References

1. Tyson, R.V. and Pearson, T.H. 1991. Modern and ancient continental shelf anoxia: An overview. *In* (Tyson, R.V. and Pearson, T.H., Eds., Modern and Ancient continental Shelf Anoxia). Geological Society Special Publication 58. P 1-24.
2. Arthur, M. A. and Sageman, B.B. 1994. Marine black shales: A review of depositional mechanisms and significance of ancient deposits: *Annual reviews in Earth and Planetary Science*, v. 22, p. 499-551.
3. Hedges, J.I. and Keil, R.G. 1995. Sedimentary organic matter preservation: an assessment and speculative synthesis: *Marine Chemistry*. V. 49. P. 81-115.
4. Ingall, E.D. and Jahnke, R. 1997. Influence of water-column anoxia on the elemental fractionation of carbon and phosphorus during sediment diagenesis: *Marine Geology*. v. 139. P. 219-229.
5. Murphy, A.E., Sageman, B.B. and Hollander, D.J. 2000. Eutrophication by decoupling of the marine biogeochemical cycles of C, N, and P: A mechanism for the Late Devonian mass extinction. *Geology*. v.28. p. 427-430.
6. Eddensohn, F.R., 1992. Controls on the origin of the Devonian-Mississippian oil and gas shales, east-central United States: *Fuel*, v. 71, p. 1487-1492.

Variation in Surface Characteristics of Some Gas Shales from Marcellus Shale Formation in the USA

Shama Mohammed Balulla and E. Padmanabhan

Abstract This study is to discover the variety of some surface characteristics in some gas shale samples from three different members from Marcellus shale formation. The X-ray powder diffraction (XRD) and field emission scanning electron microscope (FESEM) results show the presence of two types of clay minerals i.e. type 1:1 and type 1:2 with a variety of concentrations in the four samples from Chittenango member. Fourier transform infrared (FTIR) was done for the all samples from Chittenango member, East Berne member, and Bakoven member. The spectra showed the variation in the distribution of the hydrocarbon functional groups. C–H bonds occur as dominant peaks in the spectra. The four samples from the Chittenango member were used to measure the pore size distribution. All the samples vary with the pore size distribution. The Marcellus shale tends to be different in some surface characteristics throughout the three members and within these three members.

Keywords Gas shale · Marcellus shale · Variation

1 Introduction

Gas shale is the fine grain sedimentary rock that has a potential to trap the gas within shale formations [1]. The Marcellus shale is considered as one of the largest unconventional shale-gas reservoirs in the USA [2]. The Marcellus shale (early of mid-Devonian) is distributed throughout the Appalachian basin in the USA [3] and contains 1–17 % TOC [4]. The Marcellus subgroup in New York State is considered

S.M. Balulla · E. Padmanabhan (✉)

Department of Geoscience, Faculty of Geosciences and Petroleum Engineering,
Universiti Teknologi PETRONAS, Tronoh, Perak, Malaysia
e-mail: eswaran_padmanabhan@petronas.com.my

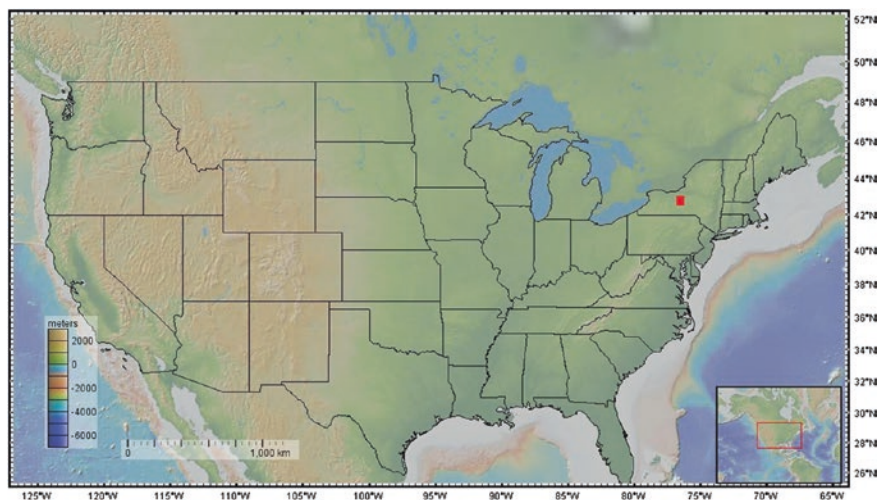


Fig. 1 Location of the study area (indicated as a red box) in the state of New York

as a subgroup of Hamilton Group and comprises three Formations (Union Springs Formation below, and Oatka Creek and Skaneateles) and several members [5, 6]. Marcellus strata are subdivided into three major lithofacies: mudrock facies association, thick synorogenic clastic facies, and carbonate-dominated facies. The aim of this study is to evaluate the variability of some surface characteristics of some different members of the Marcellus shale formation.

2 Materials and Methods

Fourteen samples obtained from a core were used in this study involving three different members (Chittenango, East Berne, and Bakoven) from the Marcellus Formation western New York State Figs. 1 and 2.

Mesoscopic description was done for all the samples using a binocular microscope (OLYMPUS SXZ16).

Some samples were selected for analysis by the XRD powder diffraction method and field emission scanning electron microscope (FESEM) studies. Fourier transform infrared (FTIR) analysis was done using Agilent FTIR-ATR spectrometer to evaluate the distribution of hydrocarbon functional groups. The mercury porosimetry analysis was performed to evaluate the pore size distribution of some selected samples as described below.

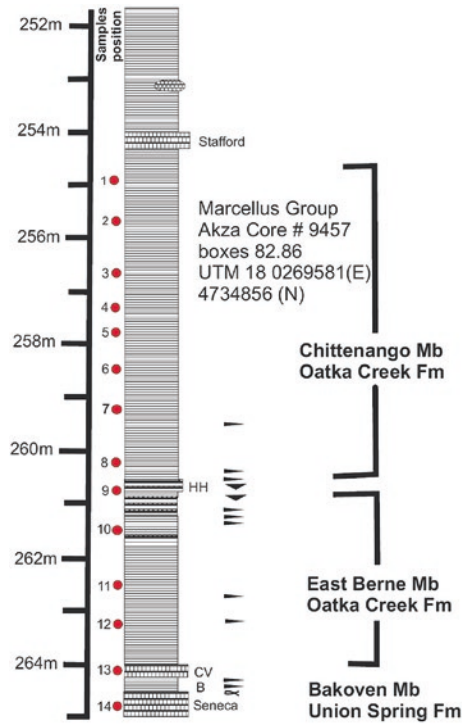


Fig. 2 Well log showing the sample’s position (modified after Ver Straeten et al. [4])

3 Results and Discussion

3.1 Mesoscopic Description

The samples show variation in color from medium gray (N5), medium dark gray (N4), dark gray (N3), and grayish black (N2) to black (N1). All samples have very thin parallel lamination with thickness about 1 mm (Fig. 3a, b).

Quartz is found either in the lamination or as randomly distributed throughout the samples (Fig. 3c, d).

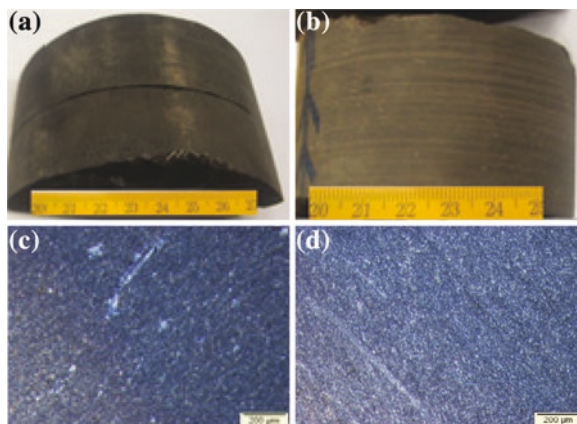


Fig. 3 a, b Laminations in samples. c, d Photographs using a binocular microscope showing heterogeneity in the quartz distribution b: a Isolated patches and b Laminated

3.2 XRD Analysis and FESEM

The Marcellus shale (Chittenango Member) samples contain (Fig. 4) two types of clay minerals. Illite-smectite mixed layer kaolinite as well as non-clay minerals such as quartz which are present as the dominant mineral in these shales. Pyrite and calcite occur in subordinate amount.

The variations in peak height of these minerals may indicate the relative amounts of these minerals in the shale samples.

The SEM analysis of the above selected samples shows the presence of illite, kaolinite, and some non-clay minerals such as quartz and pyrite (Fig. 5).

3.3 FTIR Analysis

The FTIR spectra show that several types of hydrocarbon functional groups exist in these shales (Fig. 6). The spectra were identified using [7]. The Marcellus shale samples from all three members had C–H methyl and C–H methylene aliphatic bond and they have the highest peak intensity. C–H aromatic bonds present in all members. The alcohol O–H stretching bond is absent in one sample from Chittenango member. The sulfur compounds (S–S bond) are absent in two samples from Chittenango and in one from East Berne member. The C=O bonds are absent in only one sample from Chittenango member. C=C ketone compounds were absent in only one sample from East Berne Member. Phosphorous compounds were present in some samples from Chittenango member while they absent in the other two members. Similarly, N–H amine compounds present in two samples from Chittenango Member and East Berne Member.

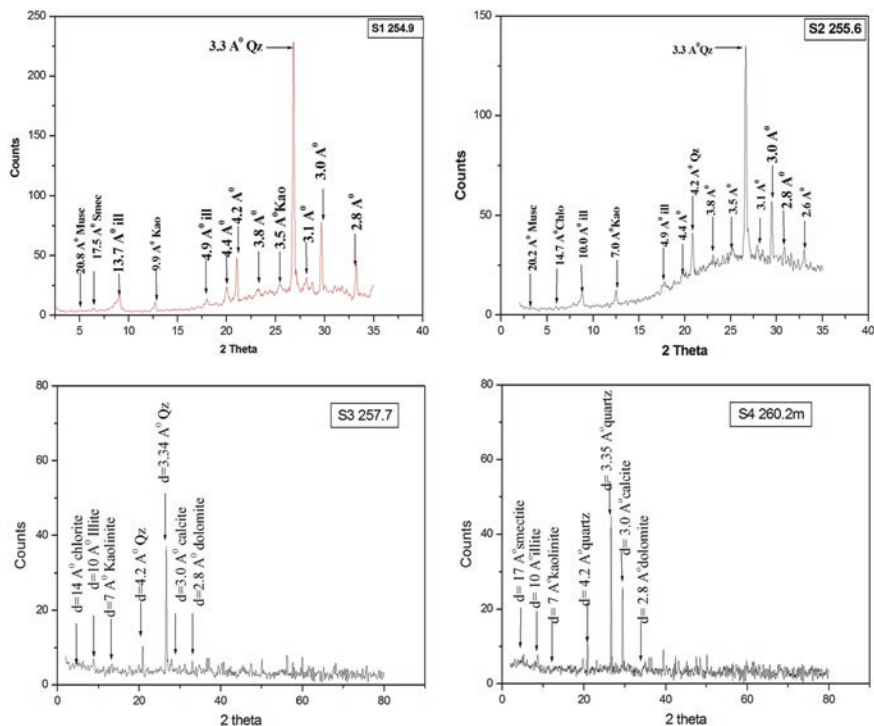
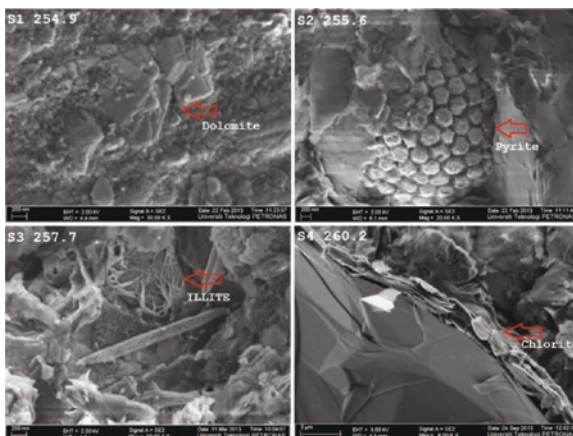


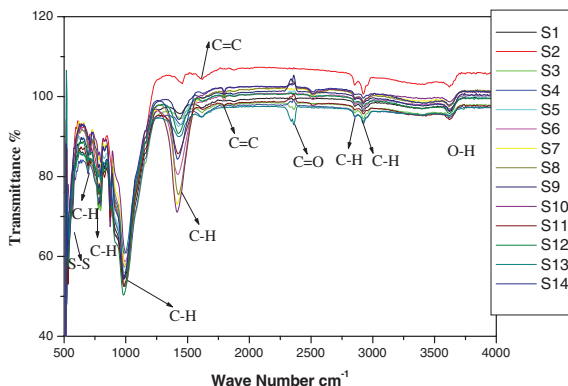
Fig. 4 Selected XRD results showing the minerals present in the samples

Fig. 5 The minerals identified from the SEM micrograph



The FTIR spectra show variations in peak intensities which is partly related to the variations in concentration of the functional groups. The C–H bonds are the highest peak intensities of the other functional group as shown in the FTIR spectra

Fig. 6 FTIR spectra showing the distribution of the hydrocarbon bonds in the different members



indicating possibly high concentrations of these bonds. These vertical variations may indicate complexities in the distribution of hydrocarbon in source rocks.

3.4 Porosity Analysis

Four samples from Chittenango member were selected to be analyzed by mercury porosimetry.

- Sample (1) has a polymodal distribution of pore diameters with a total pore volume $60.96 \text{ mm}^3/\text{g}$, $11.55 \text{ m}^2/\text{g}$ for the total pore surface area, and a maximum pore diameter of 15.48 nm (Fig. 7a).
- Sample (2) has a polymodal distribution of pore diameters (Fig. 7b) with a total pore volume $103.97 \text{ mm}^3/\text{g}$, $13.19 \text{ m}^2/\text{g}$ for the total pore surface area, and a maximum pore diameter of 10.87 nm .
- Sample (3) a pore diameter showing polymodal distribution (Fig. 7c), total pore volume of $148.16 \text{ mm}^3/\text{g}$, total surface area = $28.43 \text{ m}^2/\text{g}$, with a maximum pore diameter of 16.70 nm . This sample is composed of nano pores where 50 % of these pores have a small pore diameter (17 nm). Pores with diameters larger than 340 nm are quite small in number.
- Sample (4) has also a polymodal distribution (Fig. 7d), total pore volume $94 \text{ mm}^3/\text{g}$, total surface area $15.59 \text{ m}^2/\text{g}$, and maximum diameter of pores being 8.64 nm . Pores with diameters of 8 nm are high in occurrence whereas pores with larger diameters occur in small numbers (less than 4%).

The samples show variation in total pore volume, total surface area, and maximum pore diameter.

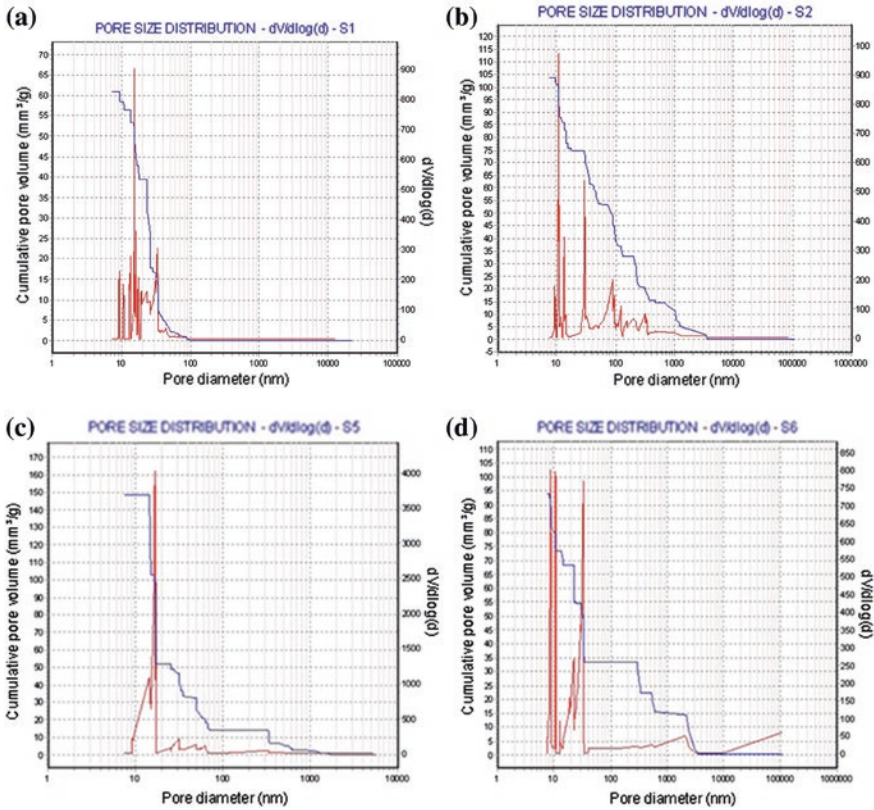


Fig. 7 Pore-size distribution defined by the pore volume from porosimetry analyses

4 Conclusion

The XRD and SEM results indicate that there are variations between the four samples selected from Chittenango members in terms of mineralogy.

All samples showed variation in the distribution of hydrocarbon functional groups which can be attributed to the variation in the concentration of hydrocarbon compound that contain these functional groups.

Results of pore size distribution using mercury porosimetry for four selected samples from Chittenango member show same polymodal distribution for the pore size, but they vary in terms of the value of the sizes of these pores.

Acknowledgment The authors would like to thank UTP graduate assistantship for supporting this study and to Prof. Dr. Jeffery Over from the department of Geological Sciences, Geneseo, NY, USA, for providing the samples.

References

1. (EIA). U.S. Energy Information Administration. "2007 Annual Energy Outlook with Projects to 2030". p. 93. Feb. 2007. [http://www.eia.doe.gov/oiaf/archive/aeo07/pdf/0383\(2007\).pdf](http://www.eia.doe.gov/oiaf/archive/aeo07/pdf/0383(2007).pdf).
2. Wang, G. and Carr, T. R. "Organic-rich Marcellus Shale lithofacies modeling and distribution pattern analysis in the Appalachian Basin". AAPG Bulletin, v. 97, no. 12 (December 2013), pp. 2173–2205.
3. Hall, J. "Third annual report of the Fourth Geological District of the State of New York" New York Geological Survey Annual Report, v. 3. 287-339,
4. Ver Straeten C.E., et al., "The Marcellus subgroup in its type area, Finger Lakes area of New York, and beyond". Unpub report 2011.
5. Ver Straeten C.A., Griffing D.H., and Brett C.E., "The lower part of the Middle Devonian Marcellus "Shale," central to western New York State" Stratigraphy and depositional History. In Brett, C.E., and Scatterday J., Eds., New York State Geological Association, 66th Annual Meeting Guidebook, p. 270-32 (Includes field trip log) 1994.
6. Ver Straeten, C.A., and Brett, C.E. " Pragian to Eifelian strata (mid Lower to lower Middle Devonian), north Appalachian Basin" A stratigraphic revision. North eastern Geology, vol. 28, p. 80-95, 2006. I.S. Jacobs and C.P. Bean, "Fine particles, thin films and exchange anisotropy," in Magnetism, vol. III, G.T. Rado and H. Suhl, Eds. New York: Academic, 1963, pp. 271-350.
7. Stuart, B. 2004. Infrared Spectroscopy: Fundamentals and Applications. John Wiley. 224p.

Preservation of Marine Chemical Signatures in Upper Devonian Carbonates of Kinta Valley, Peninsular Malaysia: Implications for Chemostratigraphy

Haylay Tsegab Gebretsadik, Chow Weng Sum and Aaron W. Hunter

Abstract The Kinta Limestone is an important Silurian to Permian age unit in the Western Belt of Peninsular Malaysia. Diagenetic alteration and thermal alteration, owing to adjacent igneous intrusion, have obscured many primary sedimentary features and primary geochemistry of the Kinta Limestone. Petrographic and geochemical analyses indicate, however, that some locations of this unit may contain textural and chemical indicators of primary marine properties. In particular, nearly pure limestones lacking dolomite and siliciclastic material, and having relatively low Mn/Sr values (1.83–3.14), suggest minor postdepositional alteration and likely preservation of original marine compositions. Those parts of the Kinta Limestone that are relatively unaltered by these criteria may be useful for assembling a data set with chronostratigraphic significance.

Keywords Peninsular Malaysia · Upper Paleozoic · Carbonate · Geochemical

1 Introduction

Peninsular Malaysia is part of the southernmost Southeast Asia mainland. It is divided into three stratigraphic belts, Western, Central, and Eastern, which have differences in stratigraphy, structure, magmatism, and other geophysical signatures

H.T. Gebretsadik (✉) · A.W. Hunter

South East Asia Carbonate Research Laboratory, Department of Geosciences,
Universiti Teknologi PETRONAS, Seri Iskandar, 31750 Tronoh, Perak, Malaysia
e-mail: haylish@gmail.com

C.W. Sum

Department of Geosciences, Universiti Teknologi PETRONAS, Seri Iskandar, 31750 Tronoh,
Perak, Malaysia

A.W. Hunter

Department of Applied Geology, Western Australian School of Mines, Curtin University,
GPO Box U1987, Perth, WA 6845, Australia

[7, 18]. It is characterized by dense networks of streams and rivers [19], which expose older Paleozoic strata. Most of the outcropping Paleozoic strata are limestones, interbedded sandstones, shales, siltstones, slates, phyllites, schists, and quartzites. Many of these rocks have undergone metamorphic and diagenetic alterations [6, 7, 10, 11, 15, 29].

The Kinta Limestone is part of the Western Belt in the northern part of Perak, and it is an area of interest for several reasons. The metamorphic and diagenetic alterations, that have an impact on the stratigraphic complexity, the stanniferous mineralization, the industrial usage of limestone, and heritage values of caves are among some of the reasons which raise the interests of researchers in the past. Kinta Valley is characterized by remnant limestone hills sandwiched by the granitic batholiths of the Kledang in the west and the main range in the east (Fig. 1). The area has been studied by many workers for the last century and a half [12, 14, 20, 21, 25, 26] and the sedimentary sequences have been a subject of intense debate concerning their stratigraphic relationships and geological age. The Kinta Limestone is placed in the stratigraphy lexicon of Peninsular Malaysia to span from Silurian to Permian age [14, 15]. The dating has been made using fossils from former tin mines in the western Kampar [27]. The age of the limestone and associated siliciclastic rocks has been an issue of discussion for many years [11, 14] due to the complexity of the alteration on the limestone which led to inaccurate identification of poorly preserved fossils [27].

The sequence is considered to be recrystallized limestone due to Triassic igneous intrusion [14, 20]. The tectonic setting of the Western Belt is linked to the closure of the paleo-Tethys ocean [10, 17]. Thus, the Kinta lithologies have been subjected to alterations including different types of metamorphism and/or diagenesis because of interaction the continental blocks forming the present peninsular Malaysia, granitic intrusions and related fluids [6, 11, 14, 23, 27, 29]. Due to these alterations, few attempts have been made to collect data to further characterize the Kinta Limestone. For instance, the Kinta Limestone has not been tested for its geochemical characteristics to extract supporting data for the paleontological dating via chemostratigraphy, except for a few oxide analyses conducted to optimize the industrial usage of the Kinta Limestone [11]. There are, however, a few limestone outcrop areas in the valley where the degree of alteration is apparently minimal and sedimentary features are preserved (Fig. 1).

The stratigraphic controversy has been settled with some understanding of the stratigraphy of the Kinta Limestone but without clear consensus concerning the underlying sequence, chronostratigraphic boundaries, and the extent of alterations. As a result, this unit is assigned a tentative age of Silurian to Permian in the stratigraphic column of the peninsula. The age boundaries are not clear, and this makes correlation between outcropping strata impractical. The stratigraphy and postdepositional alterations are challenging subjects and are poorly understood. An attempt to determine using physical and chemical differentiation for the limestones in the peninsula [9] was not successful. This paper investigates whether there is any systematic trend in geochemical compositions of the Kinta Limestone that might indicate the degree of alterations, geochemical characterization of the Kinta Limestone formation might be possible.

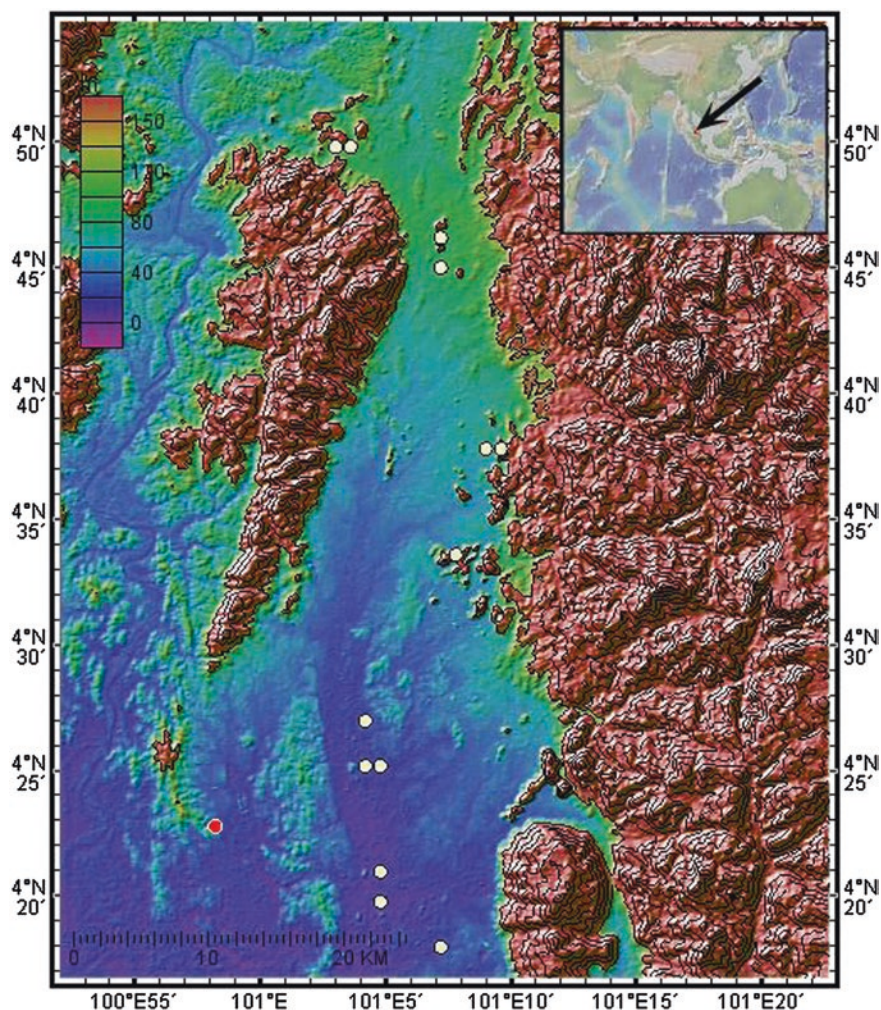


Fig. 1 Location map of the Kinta Valley area in which the *white dots* represent sampling points where accessible outcrops are available. The elevated areas in the east and west are representing the granite intrusions

2 Methods

A stratigraphic section was measured from a cored borehole drilled in the northern part of Kinta Valley (Fig. 2). Additional lithostratigraphic sections were measured in outcrops. The outcrop section includes intercalation of thinly and thickly bedded horizontal to sub-horizontal dark grayish to black limestone. A 78-m-thick section was cored from a vertical borehole which intercepts carbonate mudstone, thin black shale beds, and siltstone. Samples were chosen based on evident lithological

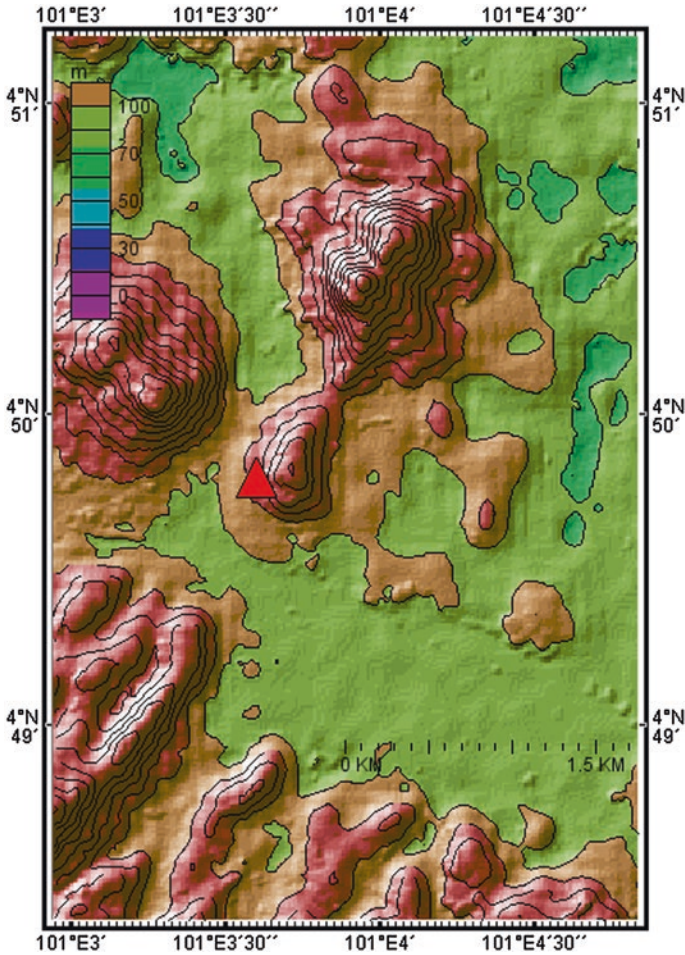
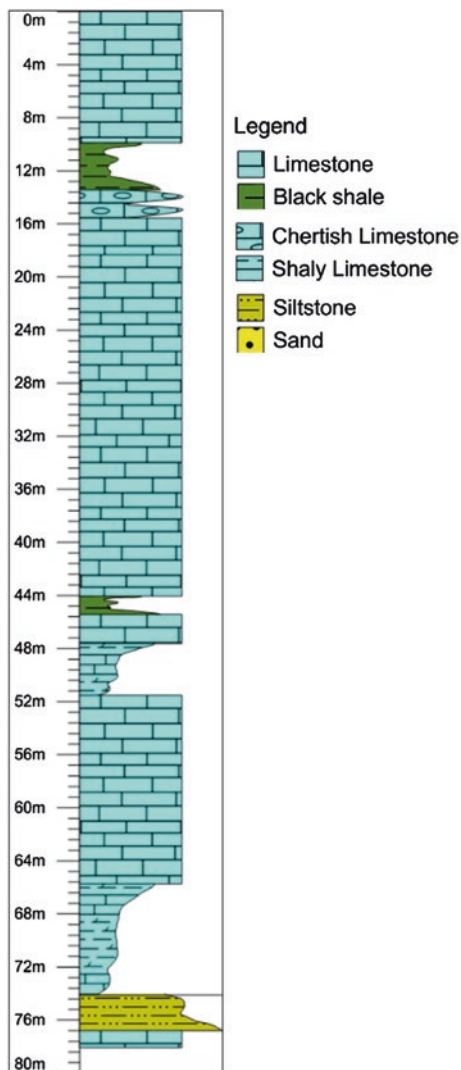


Fig. 2 Drilling site location map where the lithostratigraphic section in Fig. 2 was measured

variations in the cores. Additional samples were collected from almost the entire Kinta Valley for petrographic and geochemical analyses, and a few of them are plotted in Fig. 3 using the global multi-resolution topography synthesis [22].

Thirty-five (35) thin sections were examined and described under transmitted light using a petrographic microscope. Thirty-one (31) samples were analyzed using X-ray powder diffraction (XRD), X-ray fluorescence (XRF), scanning electron microscopy (SEM), and inductively coupled plasma atomic emission spectroscopy (ICP-AES) techniques to extract elemental and mineralogical constituents. The composition of the limestone samples was studied using petrographic microscopy, but also analytical methods such as XDF and XRF, which are particularly

Fig. 3 Lithostratigraphic section from one of boreholes drilled in the northern part of the Kinta Valley



useful for analyzing fine-grained carbonate rocks [5, 28]. Preparation of samples for thin sections and analytical analyses was carried out according to the methods of Tucker [28]. XRD analysis was done using the powderX [3] and EVA DiffracPlus software. The ratio of some key elements was plotted in spreadsheets to identify any systematic relationship and to determine the extent of diagenetic alteration. Interpretation of the data is based on field observations, petrographic descriptions, and geochemical analyses.

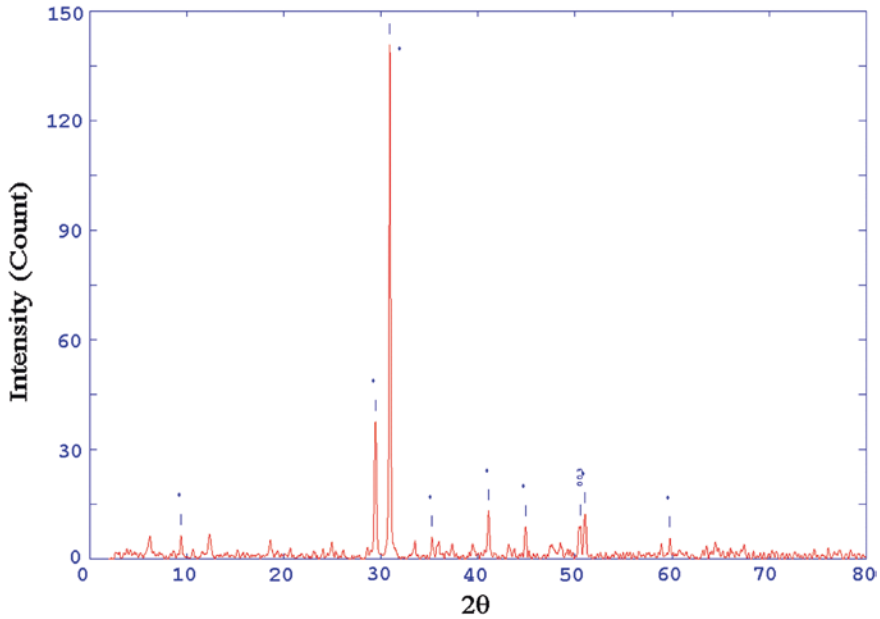


Fig. 4 Mineralogical analysis showing calcite peaks from X-ray diffraction pattern analysis

3 Results and Discussions

The lithostratigraphic section (Fig. 2), geochemical data, and petrographic analyses of limestone from the northern part of Kinta Valley are presented to determine the extent of thermal and diagenetic alterations imposed on the Kinta Limestone. The chemical signature of the Kinta Limestone was investigated to determine whether there are diagenetic and metamorphic proxies for some intervals. The mineralogical composition of the samples is dominated by calcite and by limited occurrences of dolomite (Fig. 4). This was determined in outcrops and in cores based on visual description and simple field tests. Dolomitic intervals were very slow to react to dilute HCl, whereas pure limestone had fast reaction and strong effervescence. Alizarin Red-S stain was also used, and the limestone responded by changing to pinkish orange, whereas a pale mauve color change was observed on the dolomitic sample. This has been confirmed by XRD and thin-section analysis. This is in good agreement with other studies that indicate calcite and dolomite are by far the most common carbonate minerals in ancient carbonate rocks [5]. This approach helped to characterize the fine-grained, light gray to black (Fig. 5), partly altered sedimentary rocks at Sungai Siput, which is part of the Kinta Limestone that yields data suggesting a primary marine chemical composition.

The Kinta Limestone has been partly to completely altered to marble [14]. This alteration is mostly due to low-grade regional metamorphism and diagenesis [8]. Petrographic analyses indicate typical interlocking textures of calcite in the

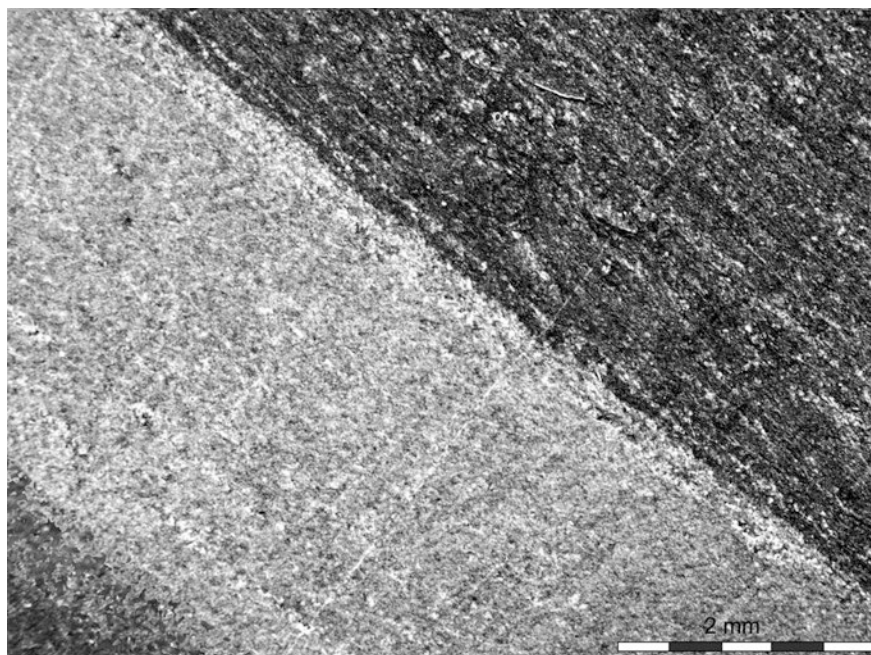


Fig. 5 Micrograph of thinly bedded *light gray* and *black* limestone from the northern Kinta Valley

highly metamorphosed sections (Fig. 6). Recrystallization was also well depicted in microfossil relicts, which were subjected to alteration.

Geochemical results show that there might be temporal and spatial relationships in the chemical signature of the samples. This might be related either to variations in paleoseawater composition or to the effects of the intrusion during the Triassic Period, which resulted in metamorphism. Determining the relationship of compositional variations to geological processes requires comprehensive data collection and analyses, which is beyond the scope of this study. However, we have some ideas for subdividing the monotonous Kinta Limestone based on the chemical signatures of a few elements. This slight systematic variation with time might suggest a reinterpretation of the age of this limestone.

The XRF data indicate that most of the limestone samples contain more than 85 wt% CaO and less than 2.5 wt% SiO₂ (Figs. 7 and 8). This quantitative compositional analysis has also shown slight spatial variation along the valley. However, the overall low silica content in the limestone is an important observation. The pure carbonate rocks indicate there was not much siliciclastic material available during their formation, which suggested that the carbonate rocks in Kinta valley were deposited when there was not much siliciclastic influx into the basin. Thus, the Kinta Limestone might have been deposited in a relatively deepwater setting. This is in good agreement with regional paleogeographic reconstruction of the area of some previous studies. The lack of benthic fauna is another important

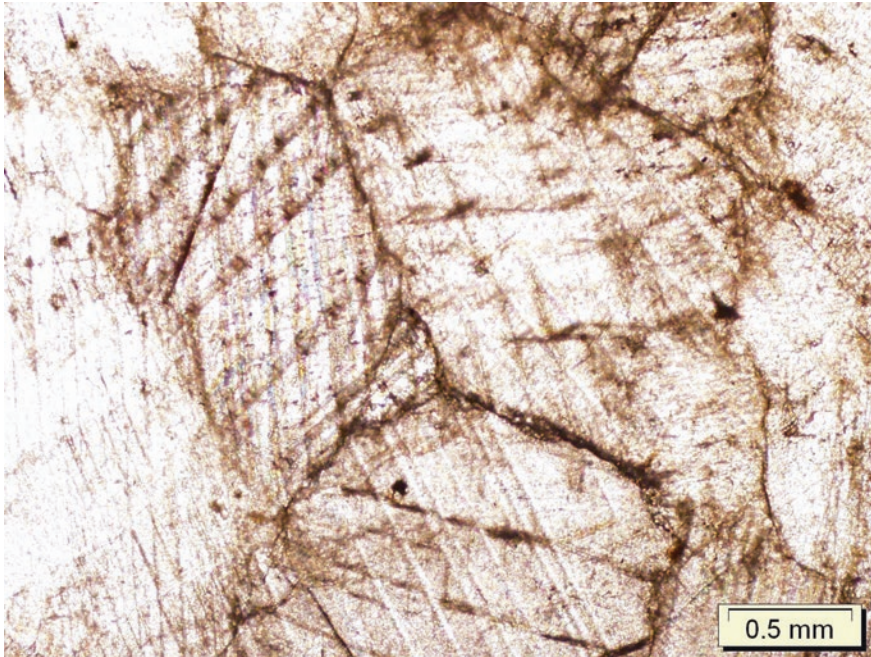


Fig. 6 Micrograph of interlocking texture of the highly metamorphosed sections outcrops in the Kinta Limestone

factor supporting the interpretation that the Kinta Limestone might have been deposited in a deepwater setting.

Sediments that have been subjected to high temperatures and/or pressures, such as those that have undergone deep burial or structural deformation, will be metamorphosed and can no longer be considered sedimentary rocks. However, there is not an absolute boundary between diagenesis and metamorphism [1]. During diagenesis, several cations can replace Ca and Mg in the carbonate group of minerals. The most common are Fe and Mn, which are readily substituted in the hexagonal structure of calcite and dolomite. However, Sr and Ba are also favored by the aragonite trigonal structure [5]. Thus, a variation in these cations might indicate the original mineralogical composition of the rocks or the extent of postdepositional replacement processes.

The main constituent for carbonate sedimentation is extracted from seawater as the skeletal parts of carbonate-secreting organisms [24]. Thus, carbonate sediments and rocks will record paleoseawater composition, provided it is not overprinted by postdepositional events. To investigate the overprint of the primary signature of marine rocks by fresh water requires comparison of some element ratios.

It is well documented that seawater contains very little Mn compared to meteoric water. As a result, a variation in Mn can be used to distinguish samples with a meteoric diagenetic signature from samples that retain their marine signature

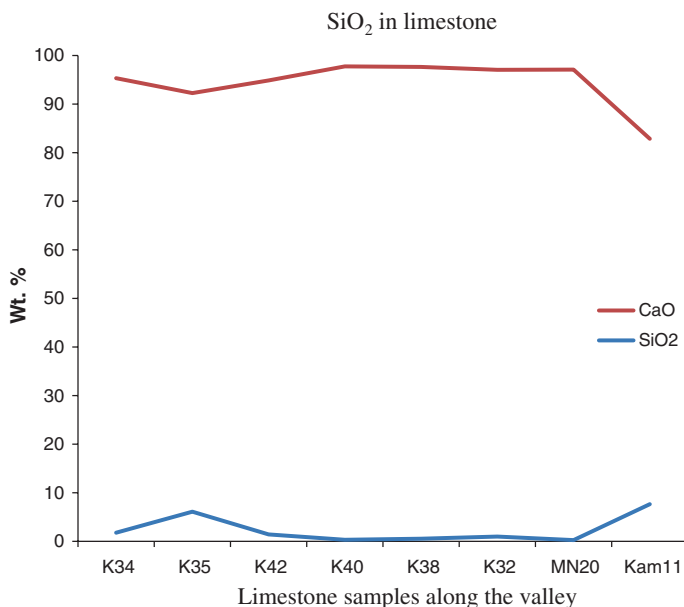


Fig. 7 Silica content of a few limestone samples from the Kinta Limestone formation

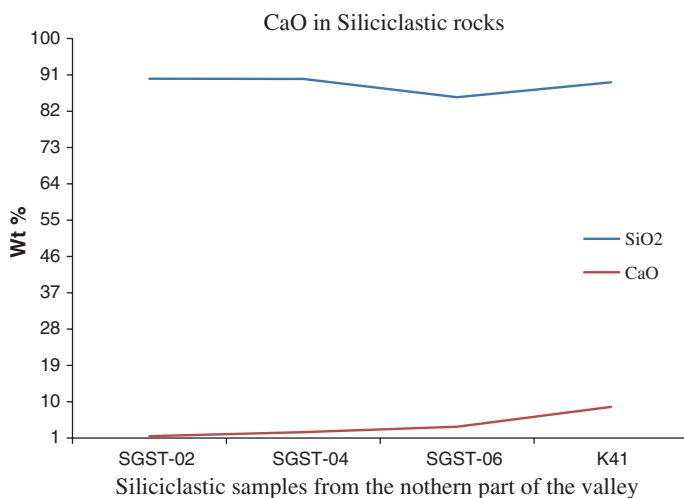


Fig. 8 Calcium oxide content of siliciclastic units from the drilled section in the northern part of the Kinta Valley area

[13]. It is also recognized that significant diagenetic alteration of most carbonates takes place during their exposure to diluted and chemically aggressive meteoric pore waters [2]. Thus, Mn composition has been used to evaluate preservation of

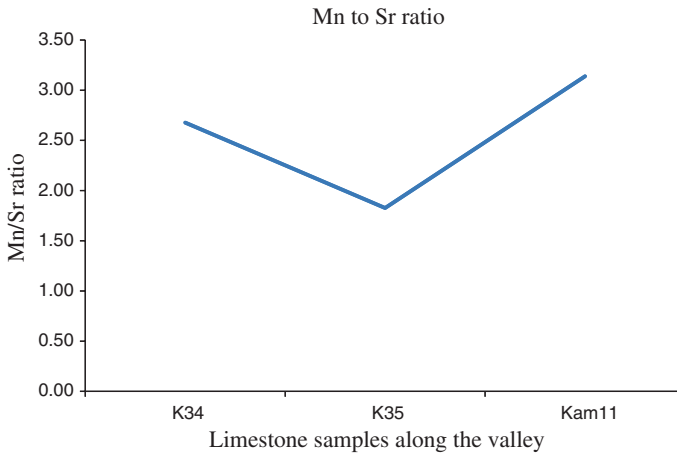


Fig. 9 Mn/Sr ratio for a few selected outcrop samples from the Kinta Limestone. Note that the ratios are below 3 which are considered low and indicating relatively less affected by freshwater diagenesis

primary seawater signatures. In combination with Sr, based on the assumption that samples with high Sr concentrations and low Mn/Sr ratios tend to preserve more primary seawater information, these geochemical data can be used to construct an isotope stratigraphy [16].

The residence time for Sr in seawater is about 4 Ma, which is greater than the seawater mixing time of approximately 1 ka [4]. Thus, variation in the Mn/Sr ratio reflects a change in the Mn content of the marine rock because the denominator is nearly constant for the world ocean. The Mn/Sr ratios of 1.83–3.14 (average = 2.55, $\sigma = 0.66$) for Kinta Limestone indicate that the original marine signature might be preserved (Fig. 9). These compositions approximate the values of <2–3, which were recommended by Kaufman and Knoll [13] for selection of samples that will have preserved marine stable isotope compositions. It is crucial to investigate alteration in the Kinta Limestone using deviation of Mn/Sr from the expected values. It is not appropriate to generalize that the Kinta Limestone is entirely metamorphosed on a regional scale.

4 Conclusions

Petrographic and geochemical data allowed us to choose those samples most likely to have retained an original marine composition. The degree of alteration of Kinta Limestone differs spatially even over a short distances. These chemical complexities have made stratigraphic interpretations difficult. Although clearly affected by fresh water diagenesis in many locations, it is still possible to extract primary marine compositions from these rocks.

Mineralogical analyses have confirmed that the carbonate rocks contain little or no detrital material, and the siliciclastic rocks lack carbonate minerals. Therefore, micropaleontologic dating may be possible whether chemical analyses are used to identify those samples in which the effects of dissolution, cementation, recrystallization, and metamorphism are minimal.

Acknowledgments We thank Universiti Teknologi PETRONAS, South East Asia Carbonate Research Laboratory and International Association of Sedimentologists for financial support and R. P. Major for constructive criticism. We especially appreciate the cooperation and permission granted by Sime Darby Plantation for access to field sites.

References

1. Adams AE, MacKenzie WS (1998) A Color Atlas of Carbonate Sediments & Rocks Under the Microscope. Manson Publishing Limited, Barcelona
2. Boggs S (2009) Petrology of Sedimentary Rocks. 2 edn. Cambridge University Press,
3. Dong C (1999) PowderX: Windows-95-based program for powder X-ray diffraction data processing. *Journal of Applied Crystallography* 32 (4):838. doi:doi:[10.1107/S0021889899003039](https://doi.org/10.1107/S0021889899003039)
4. Emery D, Robinson A (1993) *Inorganic Geochemistry: Application to Petroleum Geology*. Blackwell Scientific Publications, Massachusetts
5. Flügel E (2009) *Microfacies of Carbonate Rocks: Analysis, Interpretation and Application*. Springer,
6. Fontaine H, Ibrahim BA (1995) Biostratigraphy of the Kinta Valley, Perak. *Geological Society of Malaysia* 38:159-172
7. Foo KY The Paleozoic Sedimentary Rocks of Peninsular Malaysia-Stratigraphy and Correlation. In: Workshop on Stratigraphic Correlation of Thailand and Malaysia Thailand, 1983. Geological Society of Thailand, pp 1-19
8. Gebretsadik HT, Aaron W. Hunter, Chow Weng Sum, Pierson BJ Conodonts from the Sungai Siput limestone: its implication to establish a reference section for Paleozoic sequences and dating of the rocks, Perak, Malaysia. In: 3rd International Conference on the Paleontology of South East Asia, Ipoh, Malaysia, 2013. PETRONAS University of Technology (UTP) and the Geological Society of Malaysia (GSM)
9. Hutchison CS (1968) Physical and Chemical Differentiation of West Malaysian Limestone Formations. *Geological Society of Malaysia* 1:45-56
10. Hutchison CS (1994) Gondwana and Cathaysian blocks, palaeotethys sutures and cenozoic tectonics in South-east Asia. *Geologische Rundschau* 83 (2):388-405. doi:[10.1007/bf00210553](https://doi.org/10.1007/bf00210553)
11. Ingham FT, Bradford EF (1960) The geology and Mineral Resources of the Kinta Valley. Geological Survey Headquarters, Perak, Ipoh,
12. Jones CR (1973) The Geology and Mineral resources of the Girk Area, Upper Perak., vol 11. Geological survey West Malaysia district Memoir, New York
13. Kaufman AJ, Knoll AH (1995) Neoproterozoic variations in the C-isotopic composition of seawater: stratigraphic and biogeochemical implications. *Precambrian Research* 73 (1-4):27-49. doi:[http://dx.doi.org/10.1016/0301-9268\(94\)00070-8](http://dx.doi.org/10.1016/0301-9268(94)00070-8)
14. Lee CP (2009) Palaeozoic Stratigraphy. In: Hutchison CS, Tan DNK (eds) *Geology of Peninsular Malaysia*. Geological Society of Malaysia, Kuala Lumpur, pp 55-86
15. Lee CP, Mohd. SL, Kamaludin H, Bahari MN, Rashidah K (2004) *Stratigraphic Lexicon of Malaysia*. Geological Society of Malaysia:3-33
16. Li D, Shields-Zhou GA, Ling H-F, Thirlwall M (2011) Dissolution methods for strontium isotope stratigraphy: Guidelines for the use of bulk carbonate and phosphorite rocks. *Chemical Geology* 290 (3-4):133-144. doi:<http://dx.doi.org/10.1016/j.chemgeo.2011.09.004>

17. Metcalfe I (2000) The Bentong–Raub Suture Zone. *Journal of Asian Earth Sciences* 18 (6):691-712. doi:[10.1016/S1367-9120\(00\)00043-2](https://doi.org/10.1016/S1367-9120(00)00043-2)
18. Metcalfe I (2013) Tectonic evolution of the Malay Peninsula. *Journal of Asian Earth Sciences* (0). doi: <http://dx.doi.org/10.1016/j.jseas.2012.12.011>
19. Raj JK (2009) Geomorphology. In: Hutchison CS, Tan DNK (eds) *Geology of Peninsular Malaysia*. University of Malaya and Geological Society of Malaysia, Kuala Lumpur, pp 5-29
20. Rastall R (1927) *The Limestone of the Kinta Valley, Federated Malay States*. Cambridge Univ Press,
21. Roger AN (1971) characteristics of the Stanniferous Alluvium in the Southern Kinta Valley, West Malaysia. *Geological Society of Malaysia* 4:15-37
22. Ryan WBF, Carbotte SM, Coplan JO, O'Hara S, Melkonian A, Arko R, Weissel RA, Ferrini V, Goodwillie A, Nitsche F (2009) Global multi-resolution topography synthesis. *Geochemistry Geophysics Geosystems* 10 (3):Q03014
23. Savage HEF (1937) *The Geology Of the Neighbourhood of Sungai Siput, Perak, Federated Malay States, With an Account of the Mineral Deposits Geological Survey Department Federated Malay States, Singapore*
24. Schlager W (2005) *Carbonate Sedimentology and Sequence Stratigraphy. Concepts in Sedimentology and Paleontology*, vol 8. SEPM (Society for Sedimentary Geology), Amsterdam, Netherlands
25. Scrivenor JB (1913) The Geological History of the Malay Peninsula. *Quarterly Journal of the Geological Society* 69 (1-4):343-368,NP,369-371. doi:[10.1144/gsl.jgs.1913.069.01-04.22](https://doi.org/10.1144/gsl.jgs.1913.069.01-04.22)
26. Scrivenor JB (1931) *The geology of Malaya*. Macmillan,
27. Suntharalingam T (1968) *Upper Palaeozoic Stratigraphy Of The Area West Of Kampar, Perak*. Geological Society of Malaysia 1:1-15
28. Tucker ME (ed) (1988) *Techniques in Sedimentology*. Blackwell Science Oxford England
29. Wong TW (1991) *Geology and Mineral resources of the Lumut-Teluk Intan area, Perak Darul Ridzuan*. Geological Survey Headquarters,

The Kati Formation: A Review

Hissein A. Alkhali and Chow Weng Sum

Abstract This paper reviews the Kati Formation and provides comprehensive descriptions and an amended stratigraphic name for the Kati Formation. We have reviewed substantial literature on the Paleozoic stratigraphy in the western zone of Peninsular Malaysia and revised the nomenclature of the Kati Formation, changing “Kati Beds” to “Kati Formation” as more information has been available.

Keywords Kati Formation · Paleozoic · Clastic rocks · Seri Iskandar · Arenaceous series

1 Introduction

The Kati Formation constitutes a large portion of the Upper Paleozoic rocks in the western zone of Peninsular Malaysia; it lies between the granites of the Bintang and Kledang ranges and extends southward to Tapah and Teluk Intan. It is exposed in the west and southwest parts of Kinta Valley and the surrounding district of Kuala Kangsar. The rock exposures are very rare in areas that are still mostly covered by dense tropical forests and Quaternary alluvium.

Recently, interests in the Kati Formation has been directed particularly at Seri Iskandar and the Kinta Valley area, where several studies have been conducted with the newly developed idea of “Paleozoic hydrocarbon plays,” e.g., Pierson et al. [24, 25] and Alkhali et al. [2].

H.A. Alkhali (✉)

South East Asia Carbonate Research Laboratory, Department of Geosciences,
Universiti Teknologi Petronas, Bandar Seri Iskandar, 31750 Tronoh, Perak, Malaysia
e-mail: halghali@hotmail.com

C.W. Sum (✉)

Department of Geosciences, Universiti Teknologi Petronas, Bandar Seri Iskandar, 31750
Tronoh, Perak, Malaysia
e-mail: chow_wengsum@petronas.com.my

The Kati Formation, however, was not previously reviewed in detail. This paper updates the knowledge so far reported about Kati Formation to improve the understanding of these clastic rocks, which will be beneficial for future work.

In this paper, we review previous studies of clastic deposits exposed in Kati Formation outcrops. This review is based on previous literature, especially recent contributions from Alkhali et al. [2], in which fieldwork and laboratory analysis were conducted to determine the sedimentological and petrographic properties at near Seri Iskandar, which is the southward extension of the Kati Formation.

2 Paleozoic Formations in the Western Zone

Peninsular Malaysia has traditionally been divided into three zones: western, central, and eastern [4, 6, 11, 12, 20, 21, 23, 31]. Each of these three zones (basins) is characterized by distinctive tectonic, stratigraphy, metamorphism, structure, and sedimentary histories. The western zone is subdivided into the northwestern zone and western zone. The western zone covers a large area stretching from the Perak–Thai border southward to the state of Malacca, whereas the northwestern zone covers Langkawi, Kedah, and Perlis [6]. The Lower Paleozoic rocks are confined to the northwestern zone of the western zone. The Upper Paleozoic rocks are found in all three zones. The geological ages of the rock formations become younger from west to east. The Upper Paleozoic rocks, which crop out along the western zone, are the Silurian to Permian Kinta Limestone, the Terolak Formation, and the Kati Formation in Perak. Along with these are the Lower Palaeozoic Dinding and Hawthornden Schists, the Kuala Lumpur Limestone, and the Carboniferous to Permian Kenny Hill Formation in Selangor (Fig. 1). The limestone and argillites of Kinta Valley are classified as the Kinta Limestone and the Baling Group, respectively, whereas the westerly clastic rocks along the Perak River are grouped under the Kati Formation [6]. The western zone formations are mostly poorly dated because thermal metamorphism has affected the fossils in most of the sequences [1, 6, 21].

In general, Paleozoic clastic formations of the western zone of Peninsular Malaysia are comprised of the Kubang Pasu Formation exposed in Langkawi, Kedah, and Perlis; the Kati Formation in Perak; and the Kenny Hill Formation in Selangor [6, 14, 16, 19, 21]. The western basins include most, if not all, Lower Paleozoic formations and some Upper Paleozoic formations [6].

3 Review of Previous Work

Limited geological investigation of the Kati Formation has been conducted in Kinta Valley and the surrounding areas. The geology of this region was first described and mapped by Scrivenor [28], and one of the best early descriptions of rocks of the Kinta Valley area is those of Scrivenor and Jones [29], particularly in the Dindings area (currently known as Manjung), where they identified three dominant geological units [17, 32].

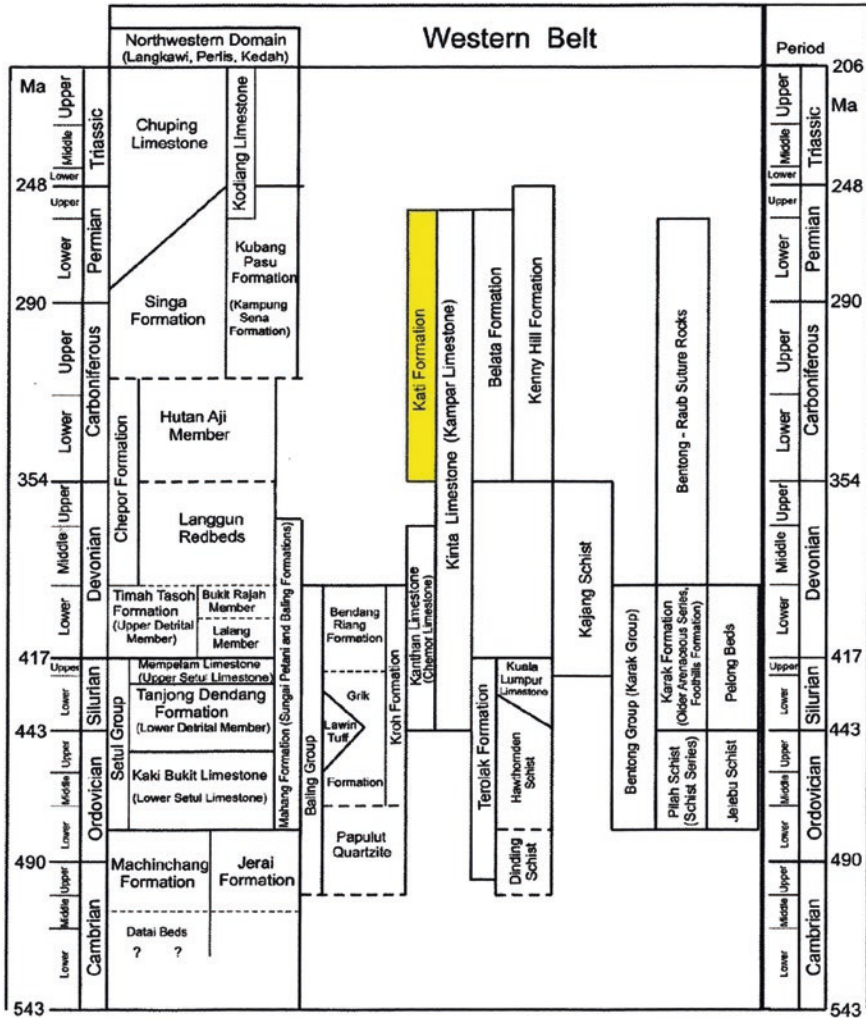


Fig. 1 Stratigraphic chart of Paleozoic sequences of the Western Belt of Peninsular Malaysia. Modified from Lee [21]

Savage [27] conducted investigations in Sungai Siput and the adjacent areas (northern part of Kinta Valley), and he recognized the existence of five distinct stratigraphic units.

Ingham [18] examined the rocks exposed in Tapah and Telok Anson currently known as the Teluk Intan area (southern part of Kinta Valley).

Ingham and Bradford [17] extended the work over to the northeastern part of the Kinta Valley. According to Ingham and Bradford [17], rocks in the Kinta Valley area can be divided into three main series: the calcareous series, the granites and allied rocks, and the arenaceous series.

Foo [5] investigated the Paleozoic exposures in the Kuala Kangsar and Taiping area (northern part of Kinta Valley). Three sedimentary formations were reported: the Pondok Marbles, the Kati Beds, and the Salak Baharu Beds. Wong [32] conducted investigations in the Lumut and Teluk Intan areas (southern part of Kinta Valley) and recognized three sedimentary successions and their metamorphosed equivalents, namely the Kati Beds (the arenaceous and argillaceous series), the Tualang Limestone (part of Kinta Valley Silurian–Permian limestones), and the Gelubi Schists. These units are believed to be contemporaneous and are classified as Carboniferous to Permian age. The Tualang Limestone and Gelubi Schists make up the so-called calcareous series.

Foo [5, 6] and Wong [32] noted that Ingham [18] and Ingham and Bradford [17] described the same formation (arenaceous series) in the west and southwest Kinta Valley area. They based their interpretation on correlation between lithology and structures of arenaceous rocks of the Kuala Kangsar area and the arenaceous series of the west and southwest Kinta Valley area. The Kati Beds (Formation) extend southward to the Seri Iskandar area [2].

4 The Kati Formation

4.1 Name and Distribution

The term “Kati Beds” was introduced by Foo [5] to describe a formation that occurs in the Kuala Kangsar area and extends southward along the western bank of Sungai Perak into Kinta Valley (west and southwest Kinta Valley). This formation lies between the granites of the Bintang and Kledang ranges (Fig. 2) [5, 6, 15, 21, 32]. We have reviewed the literature concerning the Paleozoic stratigraphy in the western zone of Peninsular Malaysia and revised the nomenclature of the Kati Formation, changing “Kati Beds” to “Kati Formation” as more information has been revealed.

Foo [6] renamed Kati Beds to Kati Formation after considering the work of Wong [32] in the Lumut and Teluk Intan areas (no data were presented). Alkhali et al. [2] concluded that their findings are consistent with Foo [6]. The Kati Formation is a lithostratigraphic unit defined by lithological characteristics, and the outcrops at Seri Iskandar fit the definition (Alkhali et al. [3]). Thus, our definition of the Kati Formation follows that of Foo [6] in order to avoid confusion.

4.2 Outcrops (Exposures)

As a generalization, these rocks are poorly exposed, very scarce, and sparsely distributed. Kati Formation outcrops are deeply weathered due to low topographic positions and the tropical climate, an exception being more resistant siliceous metasediments. The existence and position of this formation has been confirmed mainly by boreholes because it is largely located within dense tropical rain forest or is covered by Quaternary alluvium [5, 22, 32].

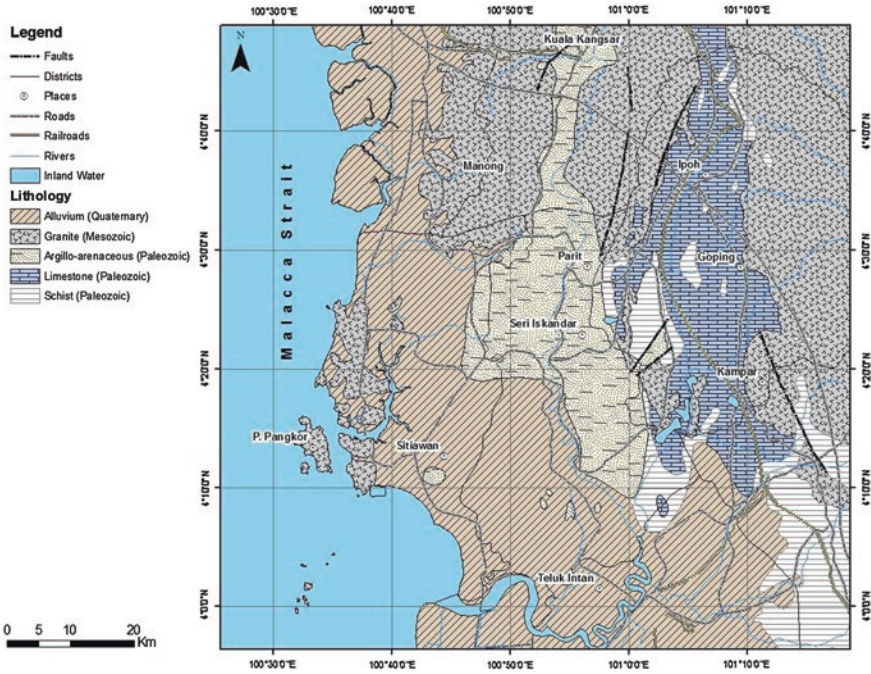


Fig. 2 Geological map of Kinta Valley and the surrounding areas illustrating the distribution of rock units in the western basin (yellow color in the northern and central areas represents the Kati Formation). Based on work by Wong [32], Ingham and Bradford [17], Ingham [18], Foo [5, 6], Gobbett [10], Alkhali et al. [2], Tate et al. [30], and the geological map of Peninsular Malaysia [7]

4.3 Bed Thicknesses

The actual thicknesses of these rocks exposed in the Kuala Kangsar area are very difficult to determine because some of these beds are highly folded [5]. However, at Cangkat Hulu Denak (Lumut and Teluk Intan area), the exposed thickness of the Kati Formation is estimated to be 900 m [32]. At Seri Iskandar, the exposed thickness is estimated to be 780 m [2].

4.4 Lithology

The Kati Formation is generally composed of a predominantly monotonous sequence of interbedded metamorphosed reddish brown carbonaceous shale, mudstones, and sandstones, with minor siltstone “argillaceous and arenaceous rocks” [5, 32]. The siltstone and shale beds are characteristically laminated or thinly banded and vary from gray to dark gray. The thicknesses of sandstone and siltstone beds are in general 7–10 cm, but can reach meters thick. Shale beds are

much thicker, approximately 30 cm, gray to whitish gray, although in some places, secondary staining may produce a pinkish, mottled color to shale and mudstone. Quartzite conglomerate, which is common in some other parts of Peninsular Malaysia, is absent in the Kati Formation [5, 6, 15, 21, 32].

4.5 Contact with Other Formations

Although the Kati Formation can be traced along strike northward between the granites of the Bintang and Kledang ranges, no contact with younger sediments or calcareous rocks was observed apart from Quaternary alluvium [5, 17, 32]. Moreover, because there is no evidence of an unconformity between the Kati Formation and Salak Baharu Beds, the Kati Formation is interpreted as a lateral facies change in the Salak Baharu Beds [5].

4.6 Age

No fossils have been found within the Kati Formation, and a probable Late Paleozoic Carboniferous to Permian age is assigned [5]. Moreover, Foo [5] disagreed with Ingham [18] and Ingham and Bradford [17], believing that the arenaceous series (Kati Formation) is older than the Semanggol Formation in northern Perak, which is Triassic. The Kati Formation was interpreted to be older than the Semanggol Formation based on dissimilarities in the lithology and the style of folding; the Kati Formation is more highly flexured than the Triassic Semanggol Formation [5, 15, 32].

4.7 Metamorphism

The Kati Formation is weakly metamorphosed and not directly affected by regional metamorphism, as thermal metamorphism is largely confined to the far northeastern part of the area [5, 32]. In the vicinity of the granite intrusive, these rocks are metamorphosed to hornfels. A fault contact between the Kati Formation and the granite was observed along Sungai Dal, in Kampong Buaya [5].

4.8 Structural Features

These clastic sequences (arenaceous series) are characterized by the presence of large- and small-scale structures and are locally highly folded into relatively open anticlines and synclines [2, 5, 32]. The most common structural features observed

in Kati Formation outcrops include well-developed faults, joints, veins, infilled joints, and fractures striking approximately N to NNW and dipping 45° – 60° to west or southwest. A relatively open flexural fold of wavelengths varying between 2 and 8 km was also observed in the Lumut and Teluk Intan area [32].

The overall structural style and character of these outcrops suggest that these rocks are structurally complex. It also offers some ideas about the deformational history because these structures show a wide variety of chaotic structure deformation and faults and relatively tight folds. The existence of this complex structural style suggests that these clastic rocks have undergone moderate to strong deformation, probably as a result of a compressional phase or tectonic activity in the Late Triassic at the time when Sibumasu collided with the East Malaya and Indochina blocks. They were not affected by contact metamorphism.

4.9 Sedimentary Structures

From observation on outcrops reported by Wong [32], the most noticeable primary sedimentary structures occurring within the Kati Formation, other than regular bedding, are rhythmic bedding, load structures, flame structures, and flute casts with some graded sandstone beds [5, 6, 32].

4.10 Depositional Environment

Based on our current understanding of the literature and results from the recent study by Alkhali et al. [2], we are in agreement with previous studies of Foo [5] and Wong [32]. The observation and interpretation of sedimentary structures and rock compositions in the clastic sequence of the Kati Formation and the rocks at Seri Iskandar are all consistent with a deep marine slope environment of deposition. The tectonic setting and depositional environment of the Kati Formation suggest it is regionally confined to the slope and basin in the western part of Peninsular Malaysia.

4.11 Provenance (Sediment Source)

The results of petrographic analysis showed that the sandstones are compositionally mature with high quartz/feldspar ratios which probably indicate that these deposits were subjected to significant chemical weathering at the source area or depositional site. The high chemical maturity coupled with the predominant suite of a well-rounded resistate zircon in the heavy minerals would suggest derivation from preexisting sediments. Moreover, the flute casts show a upcurrent direction toward the N-NW. Therefore, it appears that the source areas were located to N-NW and the depositional site in the SSE [32].

4.12 Regional Correlation

There are many similarities both lithologically and stratigraphically between the clastic sediments of the Kubang Pasu Formation in the northwestern zone and the Kenny Hill Formation in Selangor and Kati Formation in west-southwest Kinta Valley [5, 6, 15, 32] (Fig. 3). The Kati Formation is interpreted as equivalent to the Kubang Pasu Formation [6, 15]. Moreover, the Kati Formation can be correlated with the Upper Paleozoic Kenny Hill Formation of the Kuala Lumpur area [32].

After careful review of previous work on clastic deposits of the entire western part of Peninsular Malaysia, it appears that Kati Formation outcrops have been described by only two workers, Foo [5, 6] and Wong [32]. Foo [5] and Wong [32] examined and documented in great detail the sedimentological and petrological characteristic of these rocks, as well as some general structural observations. Moreover, they interpreted the depositional environments based on sedimentary features. However, they did not present any stratigraphic columns (lithologies).

Since the publications of Foo in 1968 and Wong in 1973, and more recent publications in 1990 and 1991, there has been a rapid increase in geological knowledge of Peninsular Malaysia and a considerable amount of work has been published on the geology of Kinta Valley and the surrounding district [8, 9, 12, 13, 26]. These publications contribute to our understanding of the Kati Formation.

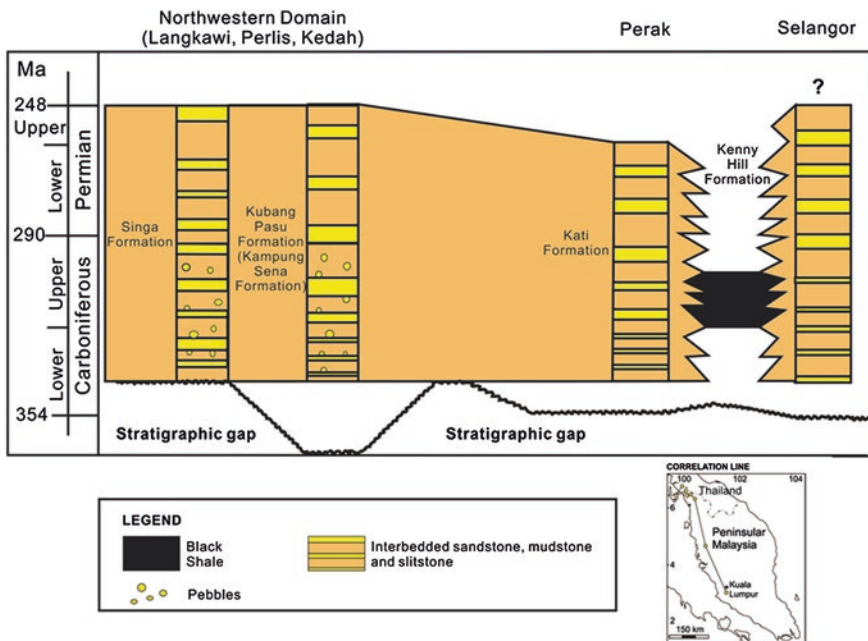


Fig. 3 Stratigraphic correlation of the Paleozoic clastic successions of the Western Belt of Peninsular Malaysia

Acknowledgment This investigation was conducted under the auspices of the South East Asia Carbonate Research Laboratory, Department of Geoscience, Universiti Teknologi Petronas, which is funded principally by Sarawak Shell Berhad.

References

1. Alexander, J. B., 1959, Pre-Tertiary Stratigraphic Succession in Malaya. *Nature*, London, v. 183, p. 203–232.
2. Alkhali, H. A., Chow, W. S., and Pierson, B. J., 2012, Assessment of the Paleozoic clastic deposits of Seri Iskandar as an element of a hydrocarbon system as potential hydrocarbon reservoirs: Proceedings of the Second International Conference on Integrated Petroleum Engineering and Geosciences, June 12–14, 2012 Kuala Lumpur, Malaysia, p.57–58.
3. Alkhali, H. A., and Chow, W. S., in preparation, Sedimentology and hydrocarbon reservoir potential assessment of Paleozoic sandstone of Seri Iskandar, Perak, Malaysia.
4. Aw P. C., 1978. Onshore sedimentary basins of Malaysia, in: ESCAP Atlas of stratigraphy I, United Nations, New York, p.13–31.
5. Foo, K. Y. 1990, Geology and mineral resources of the Taiping-Kuala Kangsar area, Perak Darul Ridzuan. Geological Survey of Malaysia, Map Report 1, 145.
6. Foo, K. Y., 1983, The Palaeozoic sedimentary rocks of Peninsular Malaysia—Stratigraphy and Correlation: Workshop on Stratigraphic Correlation of Thailand and Malaysia, v. 1, Geological Society of Malaysia. p. 1–19.
7. Geological Survey of Malaysia, 1985, Geological Map of Peninsular Malaysia, Scale 1:500,000, 8th ed. Geological Survey of Malaysia.
8. Gobbett, D. J., 1971, Joint pattern and faulting in Kinta, West Malaysia: *Bulletin of the Geological Society of Malaysia*, v. 4, p. 39–47.
9. Gobbett, D. J. and Hutchinson, C. S. (eds.), 1973, *Geology of the Malay Peninsula*: John Wiley & Sons, Inc., New York. 438 p.
10. Gobbett, D. J. 1972, Geological map of Malay Peninsula. Scale 1: 1,000,000: Kuala Lumpur: Geological Society of Malaysia.
11. Hutchison, C. S., 1975, Ophiolite in Southeast Asia: *Geological Society of America Bulletin*, v. 86, p. 797–806.
12. Hutchison, C. S., 1977, Granite emplacement and tectonic subdivision of Peninsular Malaysia: *Bulletin of the Geological Society of Malaysia*, v. 9, p. 187–207.
13. Hutchison, C. S., 1989, Geological evolution of South-East Asia: *Oxford Monographs on Geology and Geophysics* No. 13. Clarendon Press, Oxford, 368 p.
14. Hutchison, C. S., 1994. Gondwanaland and Cathaysian blocks, Palaeotethys sutures and Cenozoic tectonics in South-East Asia. *Geologisches Rundschau*, 82, 388–405.
15. Hutchison, C. S., 2007, Geological Evolution of South-East Asia (2nd Edition), Geological Society of Malaysia, 433 p.
16. Hutchison, C. S., 2009. Tectonic Evolution, Chapter 14, *in* Hutchison, C.S. and Tan, D. N. K. (eds.). *Geology of Peninsular Malaysia*: Geological Society of Malaysia and University of Malaya, Kuala Lumpur, p.309–330.
17. Ingham, F. T. and Bradford E. P., 1960, The geology and mineral resources of the Kinta Valley. Perak: Geological Survey District Memoir 9, Federation of Malaya Geological Survey, Ipoh, 347 p.
18. Ingham, F. T., 1938, The Geology of the neighbourhood of Tapah and Telok Anson, Perak, Federated Malay States, with an Account of the Mineral Deposits.
19. Jasin, B., and Harun, Z., 2011, Lower Carboniferous (Tournaisian) radiolarians from Peninsular Malaysia and their significance, *Bulletin of the Geological Society of Malaysia*, v. 57, p. 47–54.
20. Khoo, T. T., and Tan, B. K., 1983, Geologic evolution of Peninsular Malaysia, Proceedings of a workshop on stratigraphic correlation of Thailand and Malaysia: The Geological Society of Thailand and the Geological Society of Malaysia, p. 253–290.

21. Lee, C. P., 2009, Paleozoic stratigraphy, *in* Hutchison, C. S. and Tan, N. K. (eds), *Geology of Peninsular Malaysia: The University of Malaya and the Geological Society of Malaysia*, 55–86 p.
22. Loh, C. H., 1992, Quaternary geology of the Teluk Intan area, Perak Darul Ridzuan: Geological Survey of Malaysia, *Quaternary Geology Bulletin III*, 52 p.
23. Metcalfe, I., 2000, The Bentong-Raub Suture Zone: *Journal of Asian Earth Sciences*, v. 18, p. 691–712.
24. Pierson, B. J., Kassa, S., Tsegab, H., Kadir, A. A., Chow, W. S., Hunter, A. W., & Zuhar, Z. T. H., 2011, Sedimentology of the Palaeozoic Limestone of the Kinta Valley, Malaysia, *in* First EAGE South-East Asia Regional Geology Workshop—Workshop on Palaeozoic Limestones of South-East Asia and South China, 5–8 December 2011, Ipoh, Malaysia, p.17–20.
25. Pierson, B. J., Askury, A. K, Chow W .S., and Zuhar Z. T., 2009, Paleozoic hydrocarbon plays in and around Peninsular Malaysia: any chance of exploration success?: *Proceedings of the International R&D Forum, Kuala Lumpur*.
26. Rajah, S. S., 1979, The Kinta tin field, Malaysia: *Geological Society of Malaysia Bulletin*; v. 11, p. 36–111.
27. Savage, H. E .F., 1937, The geology of the neighbourhood of Sungei Siput, Perak, Federated Malay State, with an account of the mineral deposits.
28. Scrivenor, J. B, 1913, The geological history of the Malay Peninsula: *Quarterly Journal of the Geological Society*, v. 69(1–4), p. 343–371.
29. Scrivenor, J. B. and Jones, W. R, 1919, The geology of south Perak, north Selangor and the Dindings: Govt. Press, Kuala Lumpur.
30. Tate, R. B., Tan, D. N. K., and Ng, T. F., 2008, *Geological Map of Peninsular Malaysia. Scale 1:1 000 000: Geological Society of Malaysia and University Malaya*.
31. Tjia, H. D., 1999, Geological setting of Peninsula Malaysia, *in* *The Petroleum Geology and Resources of Malaysia: Petronas*, p. 139–170.
32. Wong T. W., 1991, Geology and mineral resources of the Lumut-Teluk Intan area, Perak Darul Ridzuan: Geological Survey of Malaysia, Map Report 3, Geological Survey Laboratory, Ipoh, Perak, 96 p.

Rock Physics Diagnostics and Effective Medium Model of Boonsville Field

Ida Ayu Purnamasari, Wan Ismail Wan Yusoff
and Chow Weng Sum

Abstract Effective medium models can be determined by a vigorous tool which is called as rock physics diagnostics. The function of effective medium model links the elastic properties to reservoir properties, such as porosity, shale volume, or water saturation. This rock physics diagnostic method was applied on the Middle Pennsylvanian formation in the Forth Worth Basin of North-Central Texas to provide such a model. Moreover, the rock physics modeling of reservoir parameters may use an effective medium model in evaluating other reservoir scenarios which are not seen in the wells. Gas-saturated condition on the clean sandstone reservoir was modeled using the effective medium model, obtained in the rock physics diagnostic method. Three models were established for water-saturated rock to gas-saturated, which are the friable sand model, the contact cement model and the constant cement model and Gassmann's theory which is a method for predicting pore fluid from the elastic properties in Boonsville Field. On the velocity–porosity relationship, the constant cement model shows more closely to the velocity.

Keywords Rock Physics Diagnostics · Effective Medium Model · Boonsville Field

I.A. Purnamasari (✉) · W.I.W. Yusoff · C.W. Sum
Geoscience and Petroleum Engineering Department, Universiti Teknologi PETRONAS,
Bandar Seri Iskandar, 31750 Tronoh, Perak, Malaysia
e-mail: purnamasari.ida@live.com

W.I.W. Yusoff
e-mail: wanismail_wanyusoff@petronas.com.my

C.W. Sum
e-mail: chow_wengsum@petronas.com.my

1 Introduction

Rock physics knowledge can be used to examine the elastic properties (P and S wave velocity, density, impedance) and linked it to the reservoir properties such as water saturation, porosity, and shale volume [1]. Rock physics can help in understanding the reservoir parameters. Those parameters are suitable to the seismic wave velocity of the subsurface formation. Thus, in order to lessen the risks of exploration in undrilled areas, rock physics is one of the ways that can be used to predict reservoir properties derived from seismic attributes.

Rock physics laws that link reservoir properties to the elastic rock properties give the connection between seismic impedance and velocity inversion and physical reservoir properties. Often, an earth volume under examination has to be described by more than one rock physics law: Different depth intervals may have distinctively different velocity–porosity trends due to variations in depositional and diagenetic history. When building a rock physics model, one has to single out various velocity–porosity trends from the entire volume of data and assign these separate trends to appropriate depth intervals and depositional sequences. This procedure is called rock physics diagnostics.

For geophysicist, standard log analysis is not the same as well log analysis. Mostly, in order to obtain the well logs, one should estimate the volume of hydrocarbon that can be recovered. Therefore, the area of interest is primarily the producing interval(s). Besides those producing interval(s), the good information of the seismic waves that passed through the rock is one thing that has to be concerned about. Thus, the area of interest is larger and expresses basically everything from the surface.

Effective medium theory and elastic contact theory are some models that can be applied in rock physics. Results of these models will be reviewed and compared to well log data. Rock property analysis and log response of clean sand area were discussed in this paper. The Boonsville field dataset is publicly available from the Bureau of Economic Geology (BEG) at the University of Texas in Austin so that it was chosen for this study. The dataset was generated as part of the Secondary Gas Recovery (SGR) project supported by Gas Research Institute and the US Department of Energy.

The objective of this study is to use appropriate rock physics theories and models to diagnose rock physics trends for given study area. For this study, the rock physics models used are grain contact models for sands.

2 Rock Physics Models

2.1 Gassmann's Theory [3]

Gassmann's theory is the most common tool for fluid substitution. Gassmann's equation gives a relationship between saturated bulk modulus, porosity, dry rock bulk modulus, rock matrix bulk modulus, and pore fluids bulk modulus [4]:

$$K_{\text{sat}} = K_{\text{dry}} + \frac{\left(1 - \frac{K_{\text{dry}}}{K_{\text{m}}}\right)^2}{\frac{\phi}{K_{\text{fl}}} + \frac{(1-\phi)}{K_{\text{m}}} + \frac{K_{\text{dry}}}{K_{\text{m}}^2}} \quad (1)$$

where K_{sat} is the saturated bulk modulus, K_{dry} is dry rock bulk modulus, K_{m} is rock matrix bulk modulus, K_{fl} is pore fluids bulk modulus, and ϕ is porosity. Gassmann's equation assumes the mineral modulus is homogeneous but is free of assumptions to the pore geometry. The basic assumptions about the porous fluid-filled rock are as follows: (1) All pores are connected; (2) all grains have the same physical properties; (3) the pore fluid is homogeneous and fully saturates the pore volume; (4) Gassmann's equation is only valid at low frequencies. The saturated bulk modulus, K_{sat} , can be estimated by using these assumptions and Eq. (1). P and S -wave velocity can be predicted using Eqs. (2) and (3) by knowing the K_{sat} value, [4]:

$$V_P = \sqrt{\frac{K_{\text{sat}} + \frac{4}{3}\mu}{\rho_{\text{b}}}} \quad (2)$$

$$V_S = \sqrt{\frac{\mu}{\rho_{\text{b}}}} \quad (3)$$

where μ and ρ_{b} are the shear modulus and bulk density, respectively.

2.2 The Friable Sand Model or HMHS Model [2]

This model assumes that porosity decreases from the initial critical porosity value due to the deposition of the solid matter away from the grain contacts. This non-contact additional solid matter weakly affects the stiffness of the rock. This porosity reduction for clean sandstone is caused by depositional sorting and packing. The elastic modulus at the critical porosity end point (ϕ_{c}) is given by Hertz–Mindlin (HM) theory [5]. The zero porosity point represents the mineral point. These two points are connected by the unconsolidated line represented mathematically by the modified lower Hashin–Shtrikman (MLHS) bound. The saturated elastic modulus can be calculated using Gassmann's Eq. (1), and then, also V_P and V_S can be obtained using Eqs. (2) and (3).

2.3 The Contact Cement Model [2]

This model assumes that porosity decreases from the initial critical porosity value due to the uniform deposition of cement layers on the surface of the grains. The diagenetic cement dramatically increases the stiffness of the sand by reinforcing the grain contacts.

2.4 *The Constant Cement Model [1]*

The constant cement model is a combination of the friable sand model and the contact cement model, which assumes that the initial porosity reduction from critical porosity is due to contact cement deposition. At some high porosity, this diagenetic process stops, and after that, porosity reduces due to the deposition of the solid phase away from the grain contacts as in the friable sand model. This model is mathematically analogous to the friable sand model except that the high-porosity end point; bulk and shear modulus are calculated at some ϕ_b (cemented porosity) from the contact cement model.

3 Geology of Study Area

The method is applied in the seismic datasets of Bend Conglomerate reservoir system in the SGR Boonsville Field, which is located in the Fort Worth Basin of North-Central Texas (Fig. 1a). The field is one of the largest natural gas fields in the USA that produces gas with some oil, which comes from conglomeratic sandstones deposited during the Atoka Group of the Middle Pennsylvanian Period. A generalized post-Mississippian description of the stratigraphy of the Fort Worth Basin is shown by the stratigraphic column in Fig. 1b. The Bend Conglomerate of Atoka Group is defined as the interval from the base of the Caddo Limestone to the top of the Marble Falls Limestone (Fig. 1c). The target in this field is Vineyard Formation. This level is suspected as gas producing level and as best gas reserve growth potential. The depth of Vineyard Formation ranges from 5,647 to 5,735 ft sub-sea, and the clean sand zone of this level ranges from 5,675 to 5,701 ft (Fig. 2).

4 Results and Discussion

Well log data from Boonsville Field is selected for this study (Fig. 2). The gamma ray log shows the well that contains shale and sands. Three models were established from water-saturated rock into gas-saturated.

Interpolation between the end members and the other members is needed in rock physics modeling. The mineral point which is at zero porosity is the low-porosity end member, while the high-porosity member would depend on the lithology being investigated. Due to the inherent porosity of clay minerals in shales, shales are usually deposited with a higher initial porosity (critical porosity) than sands. This critical porosity defines the high-porosity end member at a given pressure. The elastic stiffness at this porosity is estimated by using the contact theory or some other alternative theory such as Hertz-Mindlin theory. Since the region of interest in Vineyard Formation is a clean sand area, in this study, the critical porosity was defined 40 % for clean sandstones.

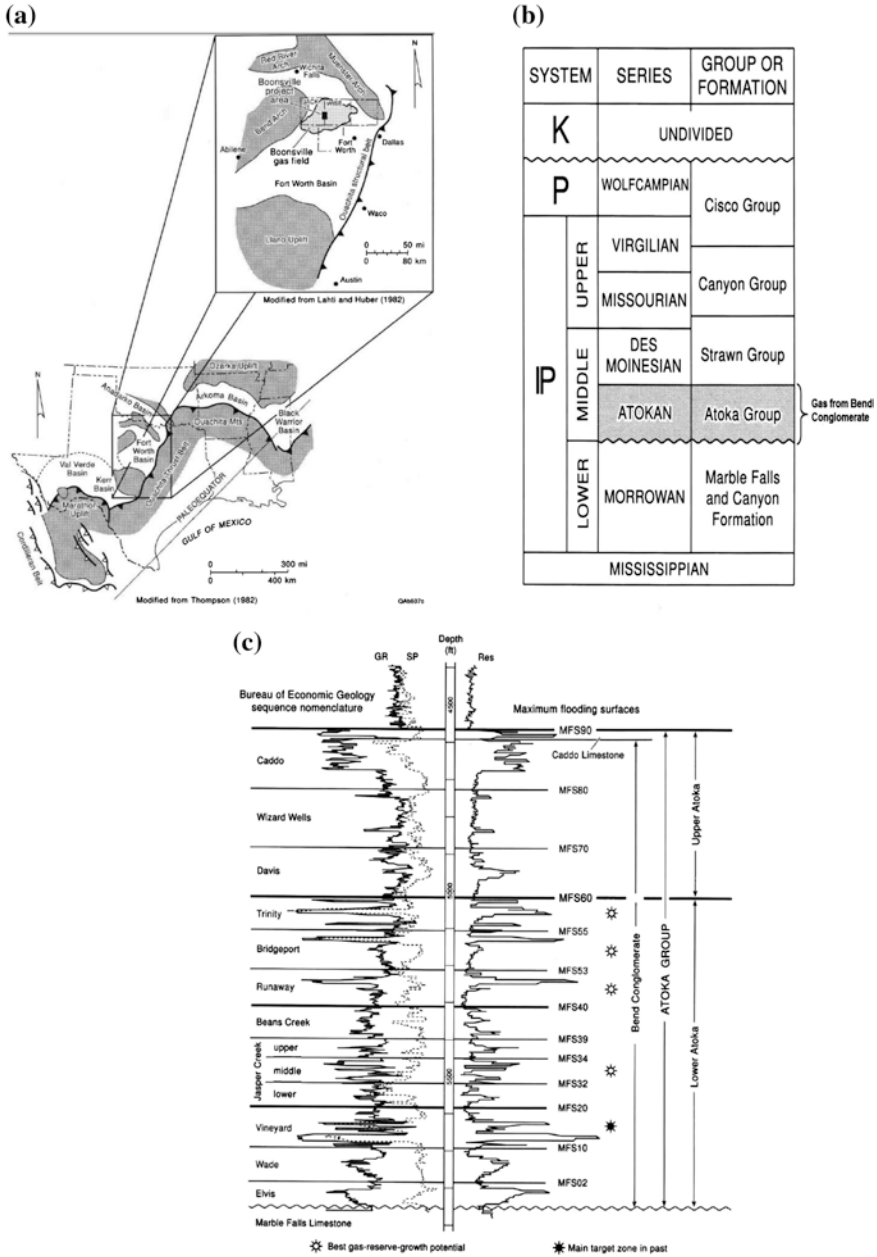


Fig. 1 a Middle Pennsylvanian paleogeographic map showing the Fort Worth basin and other basins related to the Ouachita orogeny and the Boonsville project area. b Generalized post-Mississippian stratigraphic column for the Fort Worth Basin. c Stratigraphic nomenclature used to define Bend Conglomerate Genetic sequences in Boonsville Field

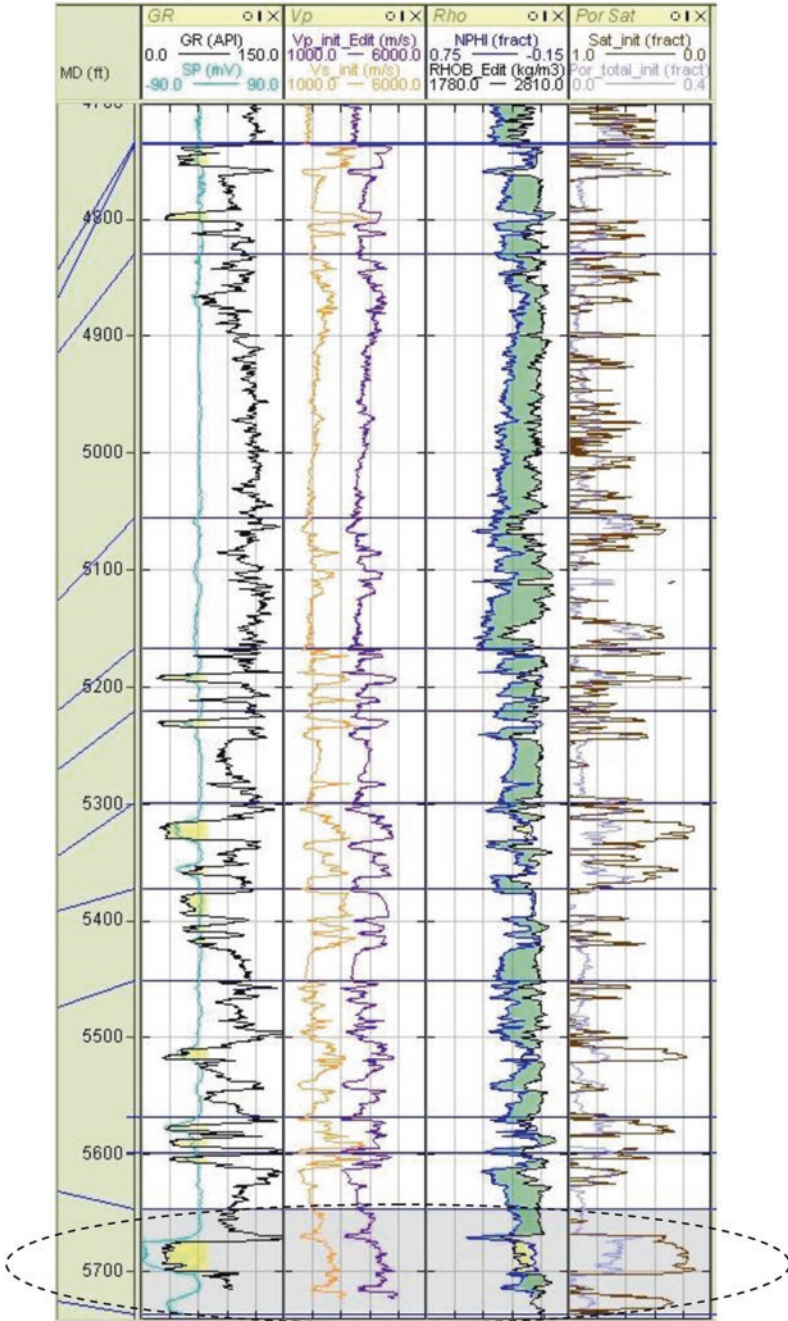


Fig. 2 Log responses of gamma ray, velocities, density, neutron, resistivity, porosity, and water saturation within the depth interval that embodies reservoir in Vineyard Formation. *Dashed line* indicates area of interest

Table 1 Mineral properties are averaged from Mavko et al. [4]

Parameter	Value (GPa)	Parameter	Value
Bulk modulus of clay (Kclay)	17.5	Bulk modulus of gas (Kgas)	7.5 GPa
Shear modulus of clay (μ clay)	7.5	Density of brine	1,060 kg/m ³
Bulk modulus of quartz (Kqtz)	36.6	Density of gas	150 kg/m ³
Shear modulus of quartz (nqtz)	45	Density of quartz	2,650 kg/m ³
Bulk modulus of brine (Kbrine)	2.48	Density of clay	2,300 kg/m ³

Most sands rich in quartz have bulk modulus ranging from 35 to 40 GPa and shear modulus ranging from 35 to 44 GPa [6]. In this paper, a solid bulk modulus and shear modulus for quartz are assumed 36.6 and 45 GPa, respectively, and for clay are 17.5 and 7.5 GPa, respectively. Mixed modulus for both minerals is computed by Voigt–Reuss average. The elastic constants and other parameters used in this study are shown in Table 1.

4.1 Rock Physics Diagnostics and Effective Medium Model Applied to Boonsville Field

Rock physics diagnostics was undertaken to determine an effective medium model. However, before this analysis could be done, Geophysical Well Log Analysis (GWLA) was performed. In addition, since no shear velocity values were measured, a predicted shear curve was derived using Greenberg–Castagna (1992) estimator. Lastly, all curves were normalized to represent a brine-filled reservoir through fluid substitution using Gassmann’s theory [3].

Shear modulus in saturated condition is equal to the dry condition. Now, using Eq. (2), *P*-wave velocity can be calculated for the saturated case. The main input logs were the *P*-wave velocity (V_p), *S*-wave velocity (V_s), and the density (Rho) logs. The main working intervals are focused within the reservoir sandstones.

The gamma ray (black line) and *P*-wave velocity (purple line) log curves for the wells under examination are shown in Fig. 2. In the well, a thick gas-saturated sand interval (the yellow fill inside the dashed line) is marked by very low gamma ray readings (about 33) and quite high velocity (about 4 km/s). This high velocity is suspected to the cementation of the original grains at their contacts.

Herein, several effective medium models were examined. These model lines are superimposed on the velocity–porosity cross-plot (Fig. 3). The three curves represent the contact cement (blue line), constant cement (gray line), and friable sand models (green line). The solid is assumed to be pure quartz, the critical porosity is 40 %, and the initial cement porosity ϕ_b is 37 %. The rock physics diagnostics shown in Fig. 3 indicates that the pay zone sands in the well have small initial contact cementation. Due to the deteriorating sorting, which is smaller grains

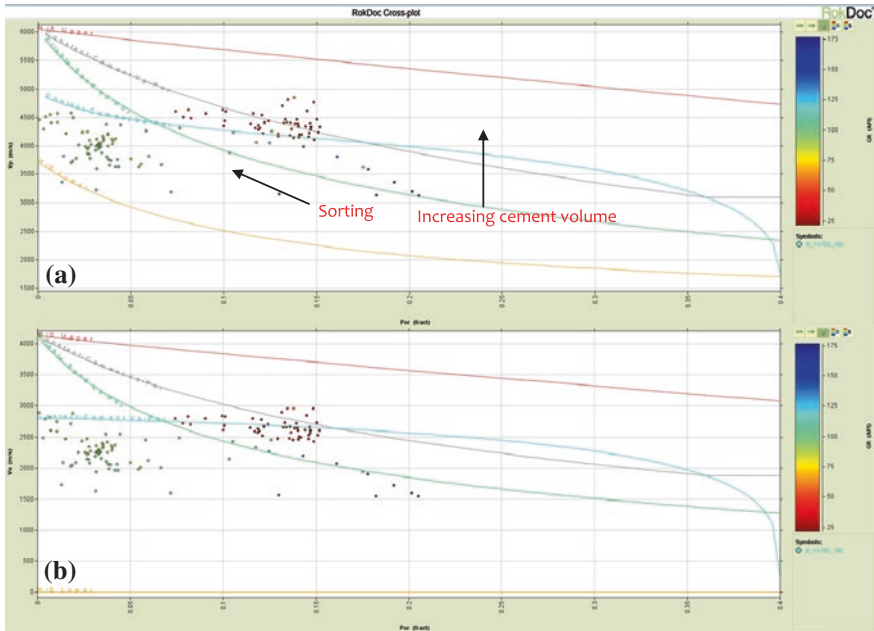


Fig. 3 Velocity–porosity cross-plot. **a** *P*-wave velocity. **b** *S*-wave velocity

falling in the pore space between larger grains with having a large effect on the velocity, porosity had decreased from the initial cement and the model that best fit with the data is the constant cement model.

5 Conclusion

In this study, the application of Gassmann’s theory and contact theories has been tested. Fluid substitution from water-saturated to gas-saturated was performed and compared to the well log response. From the results, it can be concluded that

- The contact cementation can be identified by using rock physics diagnostics based on well log data.
- The contact cement models are the best fit applied for this field that matched with log response.

Acknowledgments We thank the Bureau of Economic Geology for providing access to their 3D seismic and production data.

References

1. Avseth, P., 2000, Combining rock physics and sedimentology for seismic reservoir characterization of North Sea Turbidite Systems: PhD. Thesis, Stanford University.
2. Dvorkin, J.P., Nur, A., 1995, Elasticity of High-Porosity Sandstones: Theory of two North Sea Datasets: SEG Annual Meeting, Conference Paper, p. 890-893.
3. Gassmann, F. 1951. Elastic waves through a packing of spheres. *Geophysics*, 16, 673-685.
4. Mavko, G., Mukerji, T. and Dvorkin, J., 1998, *The Rock Physics Hand Book: Tools for Seismic analysis in a porous media*, Cambridge University Press, Cambridge, U.K.
5. Mindlin, R. D., 1949, Compliance of Elastic Bodies in Contact: *Journal of Applied Mechanics*, 16, 259-268.
6. Smith, T. M., 2011. Practical Seismic Petrophysics: The Effective Use of Log Data for Seismic Analysis. *The Leading Edge*, 30, 1128 – 1141.

Geomechanical Brittleness Estimation Through Simultaneous Pre-stack Inversion

Maman Hermana, Chow Weng Sum and D.P. Ghosh

Abstract Information about mechanical rock properties is an essential understanding when tight reservoir such as in the tight sand plays or oil/gas shale plays will be stimulated using hydro-fracturing technique. Not only for stimulation reservoir, but also the information of brittleness of shale formation also is needed when seal or cap rock of formation is evaluated. The elastic moduli of rock that can be correlated with geomechanical process such as the brittleness, Poisson's ratio, and Young's modulus can be derived from seismic data. In this study, we derived the brittleness, Poisson's ratio, and Young's modulus from seismic data using simultaneous pre-stack inversion. The data used in this work are from Malay basin field. The data consist of well data and seismic data (near stack 5° – 15° , mid-stack 15° – 25° , and far stack 25° – 40°). The data were analyzed and processed to get the compressional velocity, shear velocity, and density volume through simultaneous pre-stack inversion. Poisson's ratio, Young's modulus, and brittleness are calculated afterward. The results show that the compressional wave velocity, shear wave velocity, and density resulted from simultaneous pre-stack inversion are consistent with well log. The shale formation above main reservoir has high Poisson's ratio, high Young's modulus, and low brittleness index.

Keywords Brittleness · Modulus · Pre-stack · Simultaneous inversion

1 Introduction

The trend of oil and gas exploration has moved from conventional reservoir to unconventional reservoir. The coal bed methane (CBM), tight gas sands and shales and the fracture basement reservoir are an alternative unconventional reservoir that

M. Hermana (✉) · C.W. Sum · D.P. Ghosh
Geosciences and Petroleum Engineering Department, Universiti Teknologi Petronas,
Tronoh, Perak, Malaysia
e-mail: mherjody@yahoo.com

would be more interesting in the future. However, all of those reservoirs usually have low permeability and low porosity; hence, the stimulation through hydro-fracturing technique is needed to improve either permeability or porosity in those plays.

The success of hydro-fracturing technique is depending on the geomechanical brittleness of the formation; if the rock in the formation is more brittle, the fracture will more relatively easier to be generated rather than in the rock with more ductile conditions. It could be noted that the information about the brittleness of the rock is very important to support the success in the hydro-fracturing technique.

Brittleness estimation from seismic data in the zone of interest is a new workflow in the fracture reservoir plays. The concept of rock brittleness combines both Poisson's ratio and Young's modulus properties [1, 2]. Chopra et al. [3] estimate the brittleness of formation from seismic data by extracting the Young's modulus and Poisson's ratio from seismic inversion. Koesoemadinata et al. [4] also calculated the Poisson's ratio and Young's modulus from shear impedance, acoustic impedance, and density for shale gas reservoir characterization in Marcellus shale. Estimation of Young's modulus also can be derived from seismic directly by transforming the acoustic impedance and shear impedance into Young's modulus through simple relations.

Not only for hydro-fracturing purposes, but also the information of the brittleness of shale formation is needed when seals of hydrocarbon accumulation in the conventional reservoir are evaluated [5]. Effective seals for hydrocarbon accumulation are thick and ductile; hence, this formation tends to flow plastically under deformation.

This paper discussed how to estimate the geomechanical brittleness index using 3D seismic data through simultaneous inversion technique.

2 Background Theory

During the propagation, the seismic wave will give some stress and strain into medium in the elastic regime of the rock. This fact gives us an opportunity to estimate the elastic properties such as Young's modulus and Poisson's ratio from seismic wave. Young's modulus (E) that representing the stiffness of the rock can be defined in terms of bulk modulus (κ) and Poisson's ratio (σ) as follows:

$$E = 3\kappa (1 - 2\sigma) \quad (1)$$

Meanwhile, the Poisson's ratio can be expressed in terms of compressional (v_p) and shear velocity (v_s) as follows:

$$\sigma = \frac{v_p^2 - 2v_s^2}{2v_p^2 - 2v_s^2} \quad (2)$$

Substitution of κ in terms of velocity and density and σ into Eq. (1) will give the relation of Young’s modulus as follows:

$$E = \rho v_s^2 \frac{(3v_p^2 - 4v_s^2)}{v_p^2 - v_s^2} \tag{3}$$

Equation (3) shows that Young’s modulus can be predicted from seismic data by extracting the compressional velocity (v_p), shear velocity (v_s), and density that can be obtained through seismic inversion.

Brittleness is the measurement of stored energy before failure, and it is function of rock strength, lithology, texture, effective stress, temperature, fluid type, diagenesis, and TOC. The brittleness of the rock can be expressed in the brittleness index (BI) that is based on the calculation of mineral fraction or brittleness average (BA) that is correlated with elastic properties such as Young’s modulus and Poisson’s ratio. In this study, we used brittleness average (BA) to express the brittleness of the formation. The brittleness average can be estimated from normalized Young’s modulus and Poisson’s ratio using the Rick relation:

$$BA = \frac{1}{2} \left(\frac{E - E_{min}}{E_{max} - E_{min}} + \frac{\sigma - \sigma_{max}}{\sigma_{min} - \sigma_{max}} \right) \times 100 \tag{4}$$

where E_{min} and E_{max} are representing the minimum and maximum of Young’s modulus and σ_{min} and σ_{max} are representing the minimum and maximum of Poisson’s ratio which are calculated from the zone being characterized.

3 Available Data and Methodology

The data set used for this study was from Malay Basin field. In this case, the field has a simple anticline closure where the folding and faulting accompany the formation. Convex upward folding of layered sedimentary sequences provides multiple seal interface.

The data consist of partial stack data (near stack 5°–15°, mid-stack 15°–25°, and far stack 25°–40°), well data, and well top. Well log data are used to do feasibility study of zones of interest before the workflow is applied into seismic data. Also, the well data were used in the simultaneous inversion step. The workflow for geomechanical brittleness estimation is shown in Fig. 1.

On well log data, the brittleness average is estimated from shear, sonic, and density log. The analysis also evaluated using the cross-plot between Young’s modulus and Poisson’s ratio colored by the gamma ray log to identify the lithology. To get the volume of geomechanical parameters, we applied the workflow into the simultaneous pre-stack inversion result.

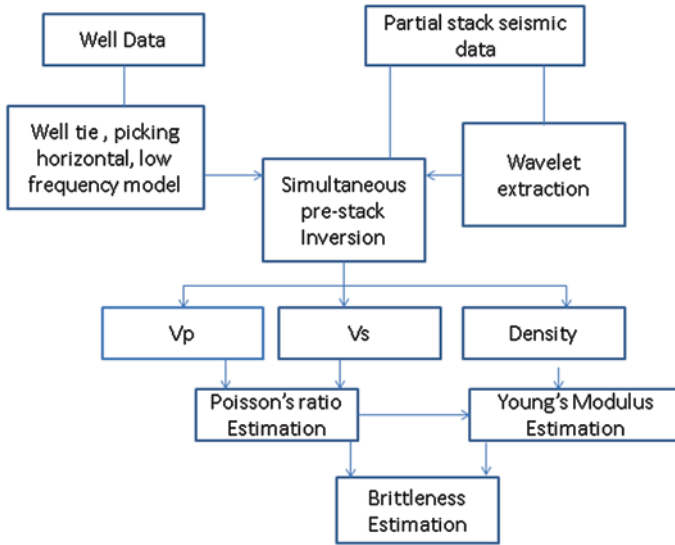


Fig. 1 The workflow of geomechanical properties' estimation from seismic data

4 Results and Discussion

4.1 Feasibility Study on Well Log Data

In the unconventional reservoir case, the porosity are generally completely filled by gas; hence, the seismic data are focused to characterize lithology and mechanical properties, especially the Young's modulus and Poisson's ratio. The feasibility study on well data was performed to analyze the ability of Young's modulus and Poisson's ratio in terms of lithology. Gamma ray log was used to discriminate sand from shale formation. Figure 2 shows the gamma ray log, Young's modulus that was generated from sonic and density log, Poisson's ratio, P-impedance, water saturation, and seismic section panel. In this figure, we can see that the lithology can be identified using Young's modulus. The figure also shows that the lithology change is more clear in the Young's modulus log rather than in the acoustic impedance log.

4.2 Simultaneous Pre-Stack Inversion

Simultaneous inversion is performed on partial stack data that consist of near, mid-, and far stacks. Because the frequency content of the data is quite different between near and far stacks, for this purpose, the individual wavelet was extracted individually for every angle gather stack. The characteristic of the angle stack and

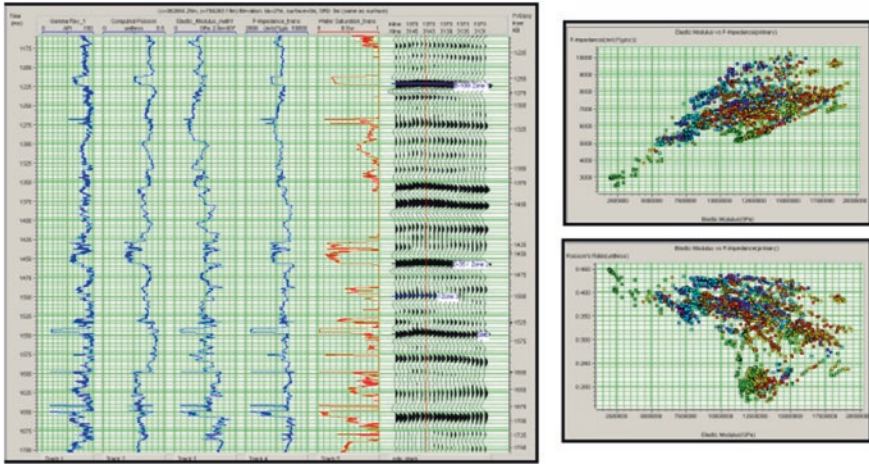


Fig. 2 Elastic parameters, water saturation logs and seismic data (*left*), cross-plot between P-impedance (*up-right*) and Poisson's ratio (*down-right*) versus Young's modulus

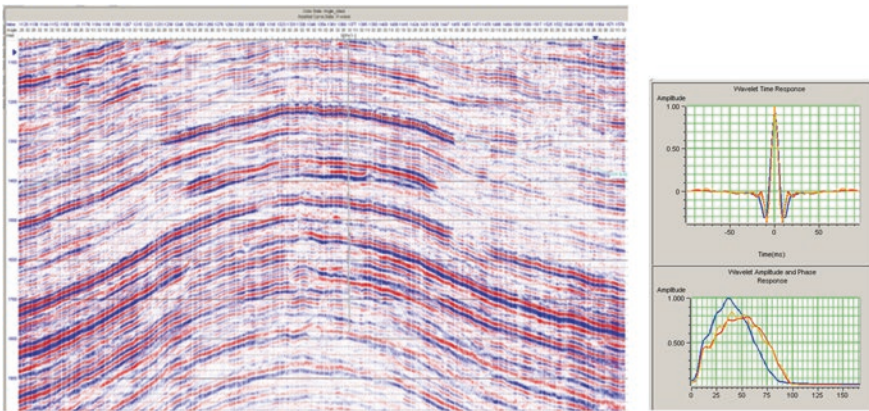


Fig. 3 Angle gather section (*left*) and wavelet (*right*) that was extracted statistically from partial stack (near, mid-, and far)

wavelets is shown in Fig. 3. Low-frequency model for inversion was created from the well data, following the layering boundary of horizon that was picked for the main reservoir formation.

Simultaneous pre-stack inversion produced three seismic volumes of P-wave velocity, S-wave velocity and density (Fig. 4). The result is quite consistent with well log data; hence, the result is able to be used to discriminate the lithology and geomechanical properties. The main reservoir was delineated as low P-impedance compared with the shale in the bottom and in the top of the reservoir.

The anticline structure with the thick shale as a cap rock in the top of the reservoir shows that the area has potential as reservoir.

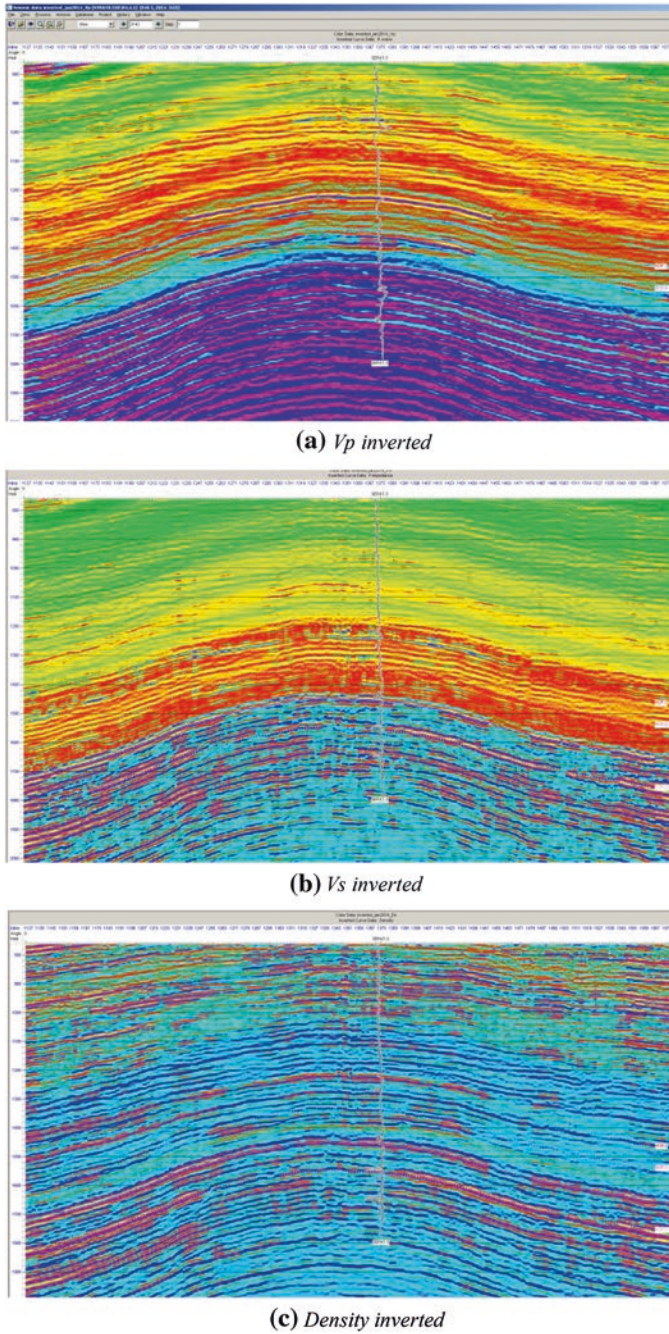
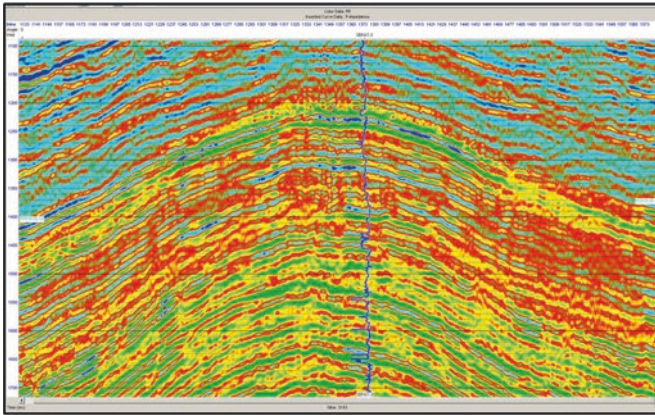
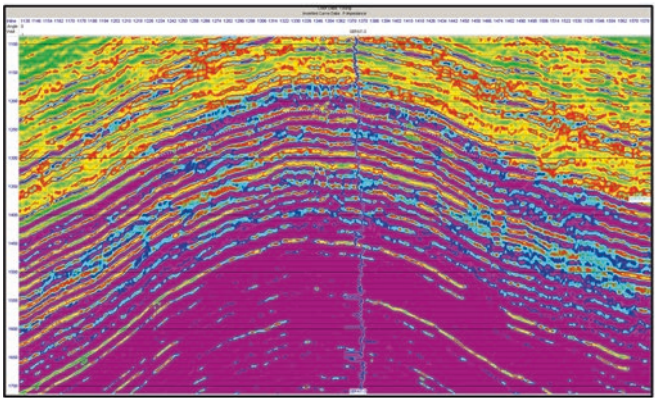


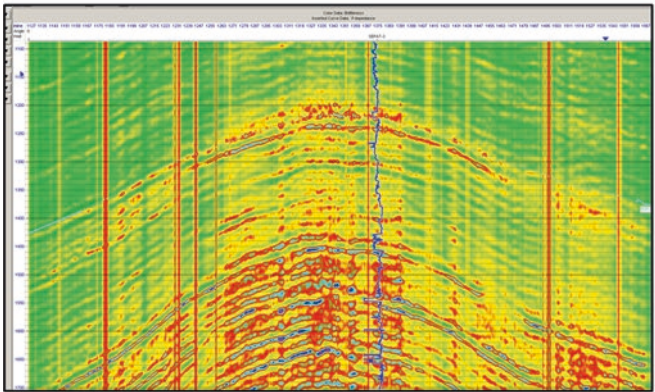
Fig. 4 P-wave velocity section (a), S-wave velocity section (b), and density section (c) resulted from simultaneous pre-stack inversion



(a) Poisson's ratio



(b) Young's modulus



(c) Brittleness

Fig. 5 The section of Poisson's ratio (a), Young's modulus (b), and brittleness (c) are calculated from v_p , v_s , and density

4.3 Geomechanical Brittleness Estimation

Estimation of brittleness based on Eq. (4) needs the information about Poisson's ratio and Young's modulus of formation. The Poisson's ratio and Young's modulus that are generated from simultaneous pre-stack inversion are shown in Fig. 5. In that figure, the main reservoir is shown as low Poisson's ratio area. The shale formation as a cap rock in the top of reservoir has high Poisson's ratio and high Young's modulus. Because the Young's modulus is followed by high Poisson's ratio, it can be predicted that in that formation, the shale is more ductile. Formations will more brittle if the formation has high Young's modulus and low Poisson's ratio. The brittleness as estimated by Eq. (4) is shown in Fig. 5. In this case, the normalization of Young's modulus and Poisson's ratio is performed for whole volume to see variation of the brittleness in the whole volume.

5 Conclusion

The result of simultaneous pre-stack inversion that is performed on pre-stack data has shown the stability and consistent result with well log data. The main reservoir and the cap rock are clearly identified. Not only it can be identified in the P-impedance, but also the lithology changes can be identified in the Young's modulus and Poisson's ratio domain.

Geomechanical brittleness properties that were calculated from Young's modulus and Poisson's ratio are reliable to be used to characterize shale/sand formation. The shale formation in the cap rock of the main reservoir has low brittleness as in the bottom of the reservoir. The shale with low brittleness will be more ductile when stress is performed on that.

References

1. R. Rickman, M. Mullen, E. Petre, B. Grieser, and D. Kundert, "A Practical Use of Shale Petrophysics for Stimulation Design Optimization," *SPE 115258*, 2008.
2. D. Gray, P. Anderson, J. Logel, F. Delbecq, D. Schmidt, and R. Schmid, "Estimation of stress and geomechanical properties using 3D seismic data," *First Break*, vol. 30, no. March, pp. 59–68, 2012.
3. S. Chopra, R. K. Sharma, J. Keay, and K. J. Marfurt, "Shale gas reservoir characterization workflows," *SEG Tech. Progr. Expand. Abstr. 2012*, pp. 1–5, Sep. 2012.
4. A. Koesoemadinata, G. El-kaseeh, N. Banik, J. Dai, M. Egan, and A. Gonzalez, "Seismic reservoir characterization in Marcellus shale Seismic characterization in Marcellus," pp. 3700–3704, 2011.
5. M. W. Downey, "Evaluating Seals for Hydrocarbon Accumulation," *Am. Assoc. Pet. Geol. Bull.*, vol. 68, no. 11.(November), pp. 1752–1763, 1984.

Palynological Zonation of the Paleogene–Neogene Strata of the Kaikang Trough, Muglad Rift Basin, Republic of South Sudan

Omer Babiker Abdelrahim, Mohd Suhaili bin Ismail and Aaron W. Hunter

Abstract Five palynological zones are identified in this Cenozoic-through-Quaternary section based on quantitative specimen counts calculated as absolute abundance. These palynological zones are: K-VI (Paleocene), K-VII (Eocene–Early Oligocene), K-VIII (Late Oligocene–Early Miocene), K-IX (Late Miocene–Pliocene), and K-X (Quaternary).

1 Introduction

Muglad Basin is the largest hydrocarbon-producing continental rift basin discovered in the Republic of the Sudan and the Republic of South Sudan to date. It extends over an area of 120,000 km² and is up to 200 km wide and 800 km long and contains a more than 13-km-thick section of Cretaceous, Cenozoic, and Quaternary continental sediments.

Kaska [1] offered a very low-resolution palynozonation for the Cenozoic to Quaternary sediments of the Muglad Basin, recognizing only two chronostratigraphic zones during the Cenozoic time, Early Paleocene (Zone D), and Late Eocene/Oligocene (Zone E). More recently, [2] offered a revised palynozonation from a limited number of wells that penetrated the Cenozoic to Quaternary section, although they provided no frequency and range charts for the species they used in their investigation [3]. Studied the palynoflora in some parts of Muglad Basin and provided only one zone IV from the Paleocene.

O.B. Abdelrahim (✉) · M.S. bin Ismail
Department of Geosciences, Universiti Teknologi Petronas, 31750 Tronoh,
Perak, Malaysia
e-mail: omer_cpl@hotmail.com

A.W. Hunter
Department of Applied Geology, Curtin University, GPO Box U1987, Perth,
WA 6845, Australia

The purpose of this study is to investigate the Paleogene–Neogene section of the Muglad Basin in the deepest part of this rift basin, the Kaikang Trough. Here, the rapid rate of sedimentation provides opportunity for high-level chronostratigraphic interpretations. We will provide quantitative (absolute abundance) palynological data and distribution information for all palynomorphs.

2 Geologic Setting

The Kaikang Trough is located in the far northern part of the Republic of South Sudan and southwestern part of the Muglad Basin, approximately bounded by latitude $09^{\circ} 17'05''$ and $09^{\circ} 26'00''$ N and longitude $29^{\circ} 05'00''$ and $29^{\circ} 10'00''$ E (Fig. 1).

The Muglad Rift Basin is a part of the Central African Rift System, which formed when the Atlantic Ocean opened during Late Jurassic through Early Cretaceous time [4]. The basin underwent three rifting phases, each of which is related to deposition of specific stratigraphic units. The first rifting phase occurred during Early Cretaceous to Cenozoic time, resulting in deposition of the Abu Gabra and Bentiu formations. The second rifting phase occurred during Late Cretaceous (Turonian–Late Senonian) to Early Cenozoic (Paleocene) time, resulting in deposition of the Darfur Group (Aradeiba, Zerga, Ghazal, and Baraka formations) and Amal Fm. The third rifting phase occurred during Late Cenozoic time and resulted in deposition of the Korodofan Group, the lower part of which is represented by the Nayil and Tendi formations (Eocene/Early Miocene), and the upper part is represented by the Adok and Zeraf formations (Late Miocene/Pleistocene) [5].

3 Methodology

Samples were analyzed using standard palynological sample preparation technique adopted and used at Central Petroleum Laboratories, Sudan; this includes the following steps:

A weight of 35–50 g of the samples was coarsely crushed to a suitable grain size, followed by treatment with con. hydrochloric (HCL) 35–37 % acid, then treatment with con. hydrofluoric (HF) 40–48 % acid. Zinc chloride ($ZnCl_2$) and zinc bromide ($ZnBr_2$) are then used as heavy liquid separator. The resulting residue sieved under 10- μ m-mesh sieve with the aid of ultrasonic bath. Mounting media Petroboxy® resin used for slides pasting and consequently examined under transmitted light microscope of an Olympus BX43. Microscope coordinates are used to record the location of the identified taxa. Photographic documentation performed using an Olympus Camera DP72 digital photographic system. All slides are permanently kept at Petroleum Geoscience Department, Universiti Teknologi Petronas.

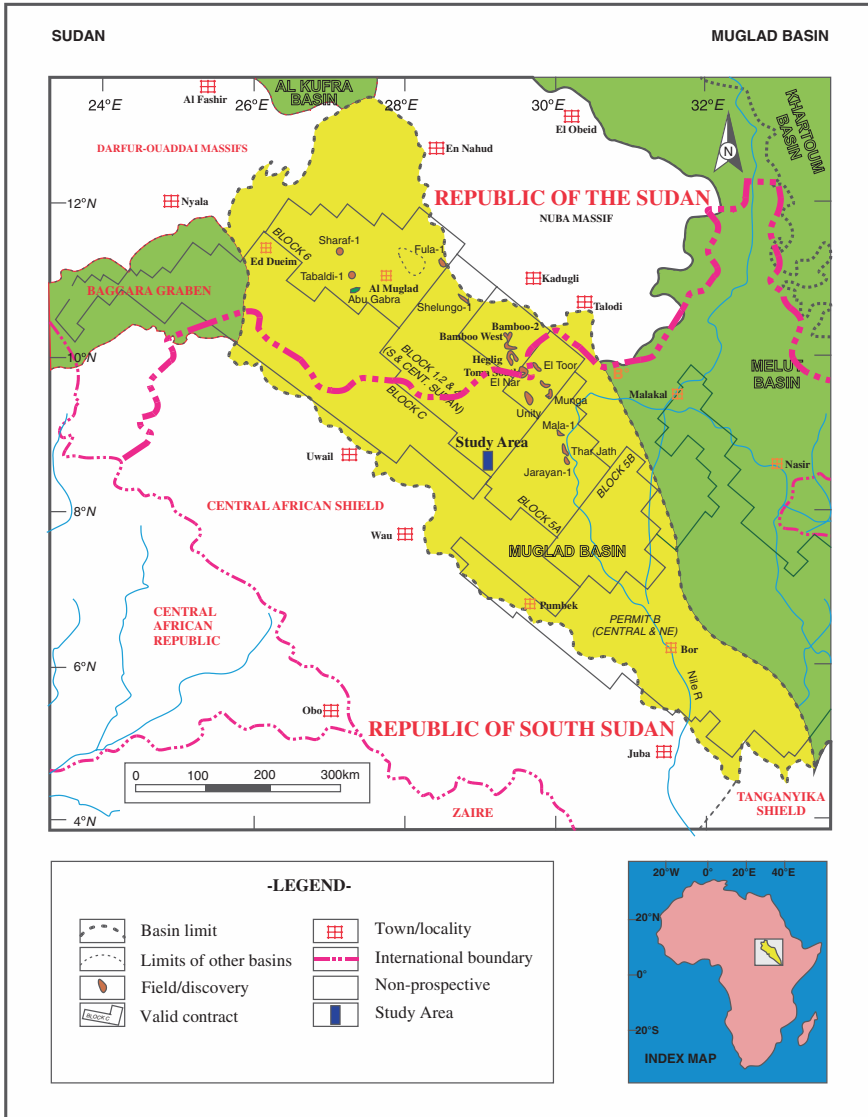


Fig. 1 Location map and basin outline for the Muglad Basin (in yellow), with political boundaries. Note study area in blue

4 Results

Five palynological zones are identified in this Cenozoic-through-Quaternary section based on quantitative specimen counts calculated as absolute abundance. These palynological zones are: K-VI (Paleocene), K-VII (Eocene–Early

PERIOD		AGE	LITHOSTRAT	LITHOLOGY	Palynozonation in the Kaikang Trough
QUATERNARY			Umm Ruwaba	[Yellow]	K-X
			Zeraf		
TERTIARY	PALAEOGENE	Pliocene	Adok	[Black horizontal stripes]	K-IX
		Miocene	Tendi	[Yellow]	
		Oligocene	Nayil	[Black horizontal stripes]	K-VIII
		Eocene		[Yellow]	K-VII
		Paleocene	Amal	[Black horizontal stripes]	K-VI
				[Yellow]	
MESOZOIC	LATE CRETACEOUS	Maastrichtian	Baraka	[Black horizontal stripes]	K-V
		Campanian	Ghazal	[Yellow]	K-IV
			Zerga		
		Santonian	Aradeiba	[Yellow]	K-III
	Turonian				
	EARLY CRETACEOUS	Albian	Upper Bentiu	[Yellow]	K-II
					K-I
		Aptian	Lower Bentiu	[Yellow]	[Black and white small squares]
Neocomian-Barremian		Abu Gabra	[Black horizontal stripes]		

Fig. 2 Mesozoic, Cenozoic, and Quaternary stratigraphic section for the study area with palynozonation developed by this study. Lithology marked in yellow is sandstone, lithology marked in black horizontal stripes in clay and shale, and the area in black and white small squares not reached by drilling

Oligocene), K-VIII (Late Oligocene-Early Miocene), K-IX (Late Miocene–Pliocene), and K-X (Quaternary) (Fig. 2). As it has been demonstrated by [6], Cenozoic sequences have few age restricted palynomorphs, limited extinctions, and few evolutionary events. The use of the qualitative (measurement of adopted biostratigraphic scheme) method of presence and absence of taxa, as is commonly used by the petroleum industry, provides insufficient resolution to subdivide the thick Cenozoic sequence of the Muglad Basin in general and the Kaikang Trough in particular. Greater age resolution will be needed for the next stage of this study: sequence stratigraphy and depositional environment interpretations.

5 Conclusions

This initial stage of this palynological study of the Muglad Basin has increased the age resolution in this stratigraphic section. Greater age resolution will be need as this study progresses.

Acknowledgments Funding for this study was provided by Ministry of Petroleum Sudan, Central Petroleum Laboratories, and a Petronas Scholarship. We are grateful for access to the facilities of the Geoscience Department, Universiti Teknologi Petronas.

References

1. H. V. Kaska, "A spore and pollen zonation of Early Cretaceous to Tertiary nonmarine sediments of Central Suda," *Palynology*, v. 13, pp. 79-90, 1989.
2. D. T. Stead and M. Z. Awad, "Palynological zonation of Cenozoic and nonmarine sediments, Muglad Basin, Sudan," *The Micropaleontology Society Special Publication*, pp. 161–178, 2005.
3. A. Eisawi, and E. Schrank, "Upper Cretaceous to Neogene palynology of the Melut Basin, Southeast Sudan," *Palynology*, v. 32, pp. 101–129, 2008.
4. S. E. Browne, and J. D. Fairhead, "Gravity studies in Sudan by the University of Leeds (UK), in collaboration with the Geological and Mineral Resources Department, Sudan 1979–1983.
5. T. J. Schull, "Rift basins of interior Sudan: petroleum exploration and discovery," *American Association of Petroleum Geologists Bulletin*, v. 72, pp. 1128–1142, 1988.
6. R. J. Morley, "Tertiary stratigraphic palynology in Southeast Asia: current status and new directions," *Geological Society of Malaysia Bulletin*, v. 28, pp. 1–36, 1989

The Shallow Marine Succession of Begrih Formation (Pliocene), Mukah Area, Sarawak: Facies, Stratigraphic Characteristics, and Paleoenvironmental Interpretation

Muhammad Murtaza, Abdul Hadi Abdul Rahman and Chow Weng Sum

Abstract This work presents the detailed facies analysis of the Begrih Formation exposed along the Mukah–Selangau road, Sarawak, East Malaysia. The Begrih Formation shows a variety of sedimentary facies in terms of composition, sedimentary structures, bed geometry, and microfossils. Fifteen sedimentary facies from seven (07) outcrops of Begrih Formation have been identified and interpreted. These sedimentary facies are categorized into three main types depending on the major lithology type. (1) Mud-dominated unit: laminated mudstone/shale (Msl), mudstone with planar and lenticular sandstone/siltstone laminations (Mpl), and fossiliferous mudstone (Mf); (2) Sandstone/Siltstone-dominated facies: trough cross-stratified sandstone (Sts), planar-laminated sandstone and mudstone (Slm), rhythmically bedded sandstone and mudstone (Srh), hummocky cross-stratified sandstone (Shs), hummocky-stratified sandstone with mudstone (Shsm), ripple-laminated sandstone and mudstone (Srp), flaser-bedded sandstone (Sfl), and bioturbated sandstone (Sb); and (3) Conglomerate: massive conglomerates (Gm), trough cross-bedded pebbly conglomerate (Gpt), bioturbated conglomerate (Gb), and coal facies. These fifteen facies are grouped into seven facies association; (1) Shelf and lower offshore, (2) Upper offshore, (3) Lower to middle shoreface, (4) Upper shoreface, (5) Foreshore, (6) Lagoonal facies, and (7) Backshore/fluvial facies. The pattern of facies and presence of distinct foraminifera species imply that these facies were deposited in the shallow marine setting with pronounced storms, wave, fluvial, and tidal influence along the paleo-margin.

Keywords Begrih · Facies · Mukah · Shallow marine · Coal

M. Murtaza (✉) · A.H.A. Rahman · C.W. Sum
Faculty of Geosciences and Petroleum Engineering, Universiti Teknologi PETRONAS,
Bandar Seri Iskandar, 31750 Tronoh, Perak, Malaysia
e-mail: murtaza_k@hotmail.com

1 Introduction

This work presents the detailed facies analysis of the Begrih Formation exposed along the Mukah–Selangau road, Sarawak, East Malaysia (Fig. 1a). The study area is underlain by a succession of coal-bearing molasse deposits of Balingian Formation (Upper Miocene), Begrih Formation (Pliocene), and Liang Formation (Late Pliocene-Pleistocene). These Neogene Formations unconformably overlie the Upper Cretaceous to Eocene Belaga Formation of Rajang Group.

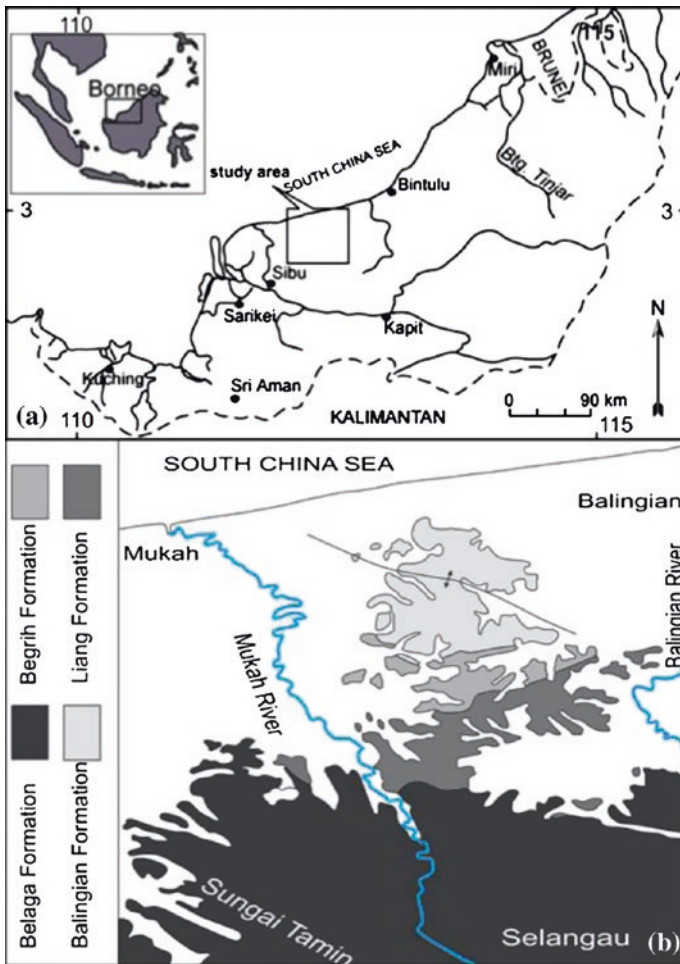


Fig. 1 Map showing the location of the study area. **a** Regional map of the Sarawak showing the study area in Mukah district, Central Sarawak. **b** Close-up map showing the extension of Balingian Formation, Begrih Formation, and Liang Formation exposed in study area

The initial reported geological studies in Mukah–Balingian area were accomplished the geological survey department (British territories in Borneo) with the cooperation from oil companies, which were hunting for oil and gas in early and mid 1900s [1]. Leichti et al. [1] defined and studied the exposed rocks in the area. The first geological map of the area, showing this Tertiary succession (Balingian, Begrih, and Liang Formations) is unconformably resting on deep-sea turbiditic sequence of Belaga Formation [2]. De Silva [3] described all the formations exposed in Mukah–Balingian area and combined Begrih and Liang Formations, describing them a single formation without any unconformity and named it as Begrih–Liang Formation. The Begrih Formation that is the focus of the study outcrops over 20 square miles between the Balingian and Mukah rivers along the coast of Sarawak [1] (Fig. 1b).

2 Regional History and Stratigraphy

Sarawak basin is an Upper Eocene to Recent sedimentary basin unconformably overlying the deformed Rajang Group. Late Eocene collision of Luconia block with the West Borneo Basement and the closure of the Rajang Sea or remnant ocean basin [4] resulted in the creation of Sarawak foreland basin [5, 6].

On the basis of geological history, structural complexity, and stratigraphy, the Sarawak province can be divided into three tectonostratigraphic zones: the Kuching Zone, the Sibul Zone, and the Miri Zone [7] (Fig. 2). The northward extension of the West Borneo Basement in Sarawak is the Kuching Zone. The age of the formations in this zone ranges from Upper Carboniferous (Kerait Formation) to Middle Miocene (Plateau Formation). The boundary between the Kuching Zone and the Sibul Zone is marked by the Lupar Line, which is a NW-trending tectonic mélange formed during the Eocene [8, 9].

The Sibul Zone is predominantly underlain by the Rajang Group that consists of intensely folded and low-grade metamorphosed Late Cretaceous to Eocene turbidites [10]. These rocks were uplifted as a result of closure of Rajang Sea in Late to Middle Eocene [11, 12]. Outliers of the overlying Oligo-Miocene Nyalau Formation also occur in some parts of the Sibul Zone.

Tatau–Mersing Line represents the junction between the Sibul Zone and the Miri Zone (Fig. 2). The Sibul Zone is structurally a complex zone consisting of Paleocene to Eocene ophiolitic rocks, while Miri Zone represents younger gentle dipping strata without structural ambiguity as compared with Sibul Zone [13]. Stratigraphically, the Miri Zone is divided in Central Sarawak and North Sarawak in the onshore area. Tatau–Mersing line also represents a major unconformity between the Rajang Group and overlying Upper Eocene–Recent Sediments in the Miri Zone.

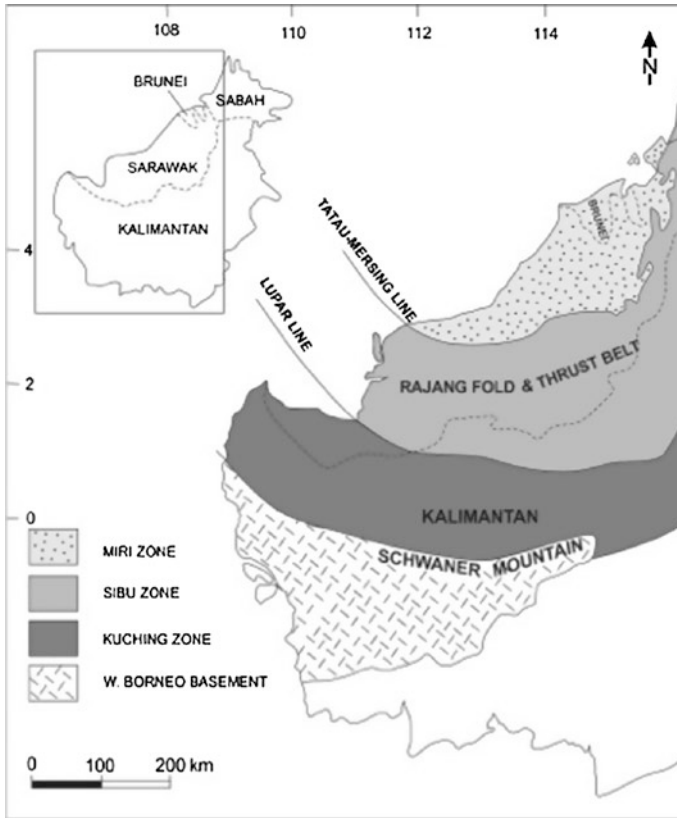


Fig. 2 A map illustrating the onshore structural subdivision of Sarawak (based on Liechti et al. [1] and Madon [7])

3 Lithofacies Analyses of Begrih Formation

The Begrih Formation shows a variety of sedimentary facies in terms of composition, sedimentary structures, bed geometry, and microfossils. Fifteen sedimentary facies from eight (8) outcrops (Fig. 8) of Begrih Formation have been analyzed and interpreted. These sedimentary facies are categorized into four (4) main types depending on the major lithology type.

1. Mud-dominated units
 - I. F1—Laminated mudstone (Ml)
 - II. F2—Lenticular-bedded mudstone (Ms)
 - III. F3—Fossiliferous massive mudstone (Mf)
2. Sandstone-dominated facies
 - I. F4—Trough cross-stratified sandstone (Sts)

- II. F5—Planar-laminated sandstone and mudstone (Slm)
 - III. F6—Rhythmically bedded sandstone and mudstone (Srh)
 - IV. F7—Thick hummocky cross-stratified sandstone (Shc)
 - V. F8—Thin hummocky-stratified sandstone with mudstone (Shsm)
 - VI. F9—Ripple cross-laminated sandstone and mudstone (Spr)
 - VII. F10—Flaser-bedded sandstone (Sfl)
 - VIII. F11—Bioturbated sandstone (Sb)
3. Conglomerate:
- I. F12—Pebbly conglomerates (Gm),
 - II. F13—Trough cross-bedded pebbly conglomerate (Gpt),
 - III. F14—Bioturbated conglomerate (Gb)
4. F15—Coal

3.1 F1—Laminated Mudstone

Description: Facies F1 was identified at four outcrops (BL-2, BL-3, BL-4, and BL-6) (Fig. 8). The thickness of this facies range from a few centimeters to 2 m in some exposed sections. It has mostly irregular basal and top contact with the sandstone-dominated facies (HCS sandstone etc.).

The F1—laminated mudstone/shale (Msl) consists of light to dark gray laminated (1–2 mm) mudstone and massive gley-mud horizons. Various parts of weathered outcrop show fissility in the sequence. At two locations, these facies show thin horizons of erosive-based, medium to coarse-grained, thin to medium beds of sandstone and matrix-supported conglomerates. These facies have rare siltstone/fine sandstone lamination as compared with the other mudstone facies having prominent laminations and thin beds.

The interbedded sandstone layers/lenses are sparsely bioturbated with *Paleophycus* (Pa), *Planolites* (Pl), and *Ophiomorpha* (Oph) burrows. Generally, trace fossils are not observed in this facies. Foraminiferal analyses of four (04) samples were done. The two samples for BG-2 (2BG 9/1, BG 9/2) were barren and were devoid of any foraminifera. The samples from BG-3 (BG 10/1, BG 10/2) lack environmentally diagnostic taxa. Rare to few arenaceous and calcareous forms were identified (Fig. 9).

Interpretation: F1 reflects deposition of fine material in low-energy setting in the absence of waves and currents [14, 15]. The absence of bioturbation, dark gray color, and having substantial thickness suggest oxygen-depleted conditions [16]. The absence of oscillatory structures indicates that the deposition occurs below storm wave base (SWB). The lower offshore and shelf mudstones reflect relatively constant deposition over an extended period of time. F1 is interpreted to be deposited in a lower offshore to shelf environment. The presence of few calcareous foraminifera also suggest stressed marine conditions.

3.2 F2—*Lenticular-bedded Mudstone (Ms)*

Description: F2 was encountered in BG-2, BG-3, and BG-4 (Fig. 8). The thickness of this facies ranges from few centimeters (BG-2) to over 8 m (BG-3). This facies is mostly associated with the hummocky-stratified sandstone (erosive top contact) and laminated mudstone facies (transitional) (BG-3), HCS sandstone (BG-4), and thick flaser-bedded sandstone (BG-2).

The facies consists of laminated mudstone with varying ratio of sandstone/siltstone lenses. The laminated sandstone/siltstone layers are less than 5 mm, and it also contains carbonaceous flakes and thin lamination at some exposed horizons. The thin laminations of fine to very fine sandstone/siltstone are not extensive. This facies also bears nodules and nodular layers (2–10 cm). Rare bioturbation is recorded.

Interpretation: The presence of fine sandy/siltstone thin lamination incorporated in mudstone and shale suggests deposition in low-energy environments [14, 15]. During high-energy storm events, waves erode and rework the nearshore area [17, 18]. Fine-grained sandstone/siltstone is further transported seaward in suspension by waves and currents. Transport capacity of waves and currents decreases basinward, and as a result, very fine-grained silt and sand is deposited as thin, sandy laminae within the overall mud-prone environment [19].

3.3 F3—*Fossiliferous Mudstone (Mf)*

Description: This facies was identified at BG-5 and BG-7. The thicknesses of this facies vary from four (4) to five (5) meter. It has sharp and slightly irregular basal contact with the sandstone facies and gradual upper contact with the coal facies. F3 is intensely bioturbated, homogeneously mixed.

This F3 facies (Mf) is composed of light to dark gray, homogenized, structureless mudstone with varying amount of siltstone/very fine sandstone. At BG-5, the base of the exposed unit is dominated by silty mudstone. The amount of siltstone contents decreases upward and gradually changes into pure mud containing carbonaceous lamination and rootlets on top. These carbonaceous laminations are abundant toward the top, below the thin coal facies. This facies also displays thin, fine sandstone beds at the base of BG-7. F3 bears bivalves, gastropods, and other broken fragments of the calcareous body fossils (Fig. 5a). The body fossils are filled with muddy material, but outer shells of these organisms are well preserved (Fig. 5e, f). Palynological analyses reveal that this facies is characterized by the common occurrence of *Rhizophora*, *Avicennia*, and the other mangrove taxa (Fig. 6), averaging about 35.6%. *Blumeodendron*, *Cycas*, and *Palmae* pollen which represents the lowland/peatland group shows a distinct value in this interval. The fern spores are present in moderate amounts, with the occurrence of 10%.

Interpretation: Muddy deposits indicate deposition within quiet, low-energy depositional environments [20–22]. The complete bioturbation, presence of bivalves, and gastropods in lower part of the facies suggest that the deposition occurs in overall low-energy environments with plenty of oxygen. The presence of mangrove taxa (*Rhizophora*, *Avicennia* etc.) with peatland flora (*Blumeodendron*, *Cycas*, and *Palmae* pollen) also suggests marginal marine environment with both saline as well as fresh water influence, respectively. The facies F3 may suggest a brackish lagoonal setting with occasional fresh water input.

3.4 F4—Trough Cross-stratified Sandstone (Sts)

Description: This facies was identified at outcrops BG-1, BG-2, and BG-5. The thickness of this facies ranges from 0.5 to 1.7 m (BG-5). At BG-1, it is encountered in between the massive conglomerate facies. F4 forms a multistoried sandstones with rip-up mud clasts and trough cross-bedding (Fig. 5e). At BG-2 and BG-5, the bedding is thin relative to BG-2. The individual packages of TCB sandstone in BG-2 are separated by thin mud beds (2–4 cm). It pinches out in the north direction of the outcrop in BG-2.

The facies (Sts) consist of light gray to dark gray, reddish- and gray-colored, medium to coarse-grained, with mostly shows erosive-based, thin to thick-bedded, high to low angle trough cross-stratified sandstone interbedded with thin mudstone horizons. Medium to coarse-grained units also bear pebbles floating throughout the extent of exposed boundaries. Mud chip is present along the trough cross-foresets (Fig. 4c). The interval of mudstone ranges from few centimeters (1–5 cm) with some discontinuous patches of mud. The F4 is devoid of any trace and body fossils.

Interpretation: Trough cross-stratifications occur in many different settings, from fluvial environment to shallow marine areas. In shallow marine setting, the trough cross-stratification denotes high-energy environments, probably rip-up and long-shore currents in the shoreface area [20, 23, 24]. The interpretation solely depends on the associated facies [25]. In general, F4 reflects strong unidirectional currents. Here, F4 is interpreted to be of fluvial origin.

3.5 F5—Planar-Laminated Sandstone and Mudstone (S_{lm})

Description: The F5 was not identified anywhere except BG-8 where its thickness is 0.5 m (Fig. 8). Although parallel-laminated sandstone are included in other facies, some sequences have entirely planar-laminated sandstone beds separated by 2 cm parallel-laminated mud having carbonaceous contents (BG-8). The basal contact of the F5 in BG-8 was not observed, while top contact is gradational with the facies F9. These facies represent the most southward-exposed sequence of Begrih Formation.

This F5 facies (S_{lm}) consist of gray to dark gray- and yellowish-colored, fine to medium-grained, well-sorted, medium-bedded sandstone with parallel laminations.

Trace fossils distribution is limited to rare *Planolites*, *Paleophycus* burrows, and rare *Skolithos* burrows.

Interpretation: The planar-laminated sandstone beds indicate swash and backwash processes, while the mud interbeds specify slack water condition during high tide [15, 25]. The shoreline migrates landward and seaward, during high and low tide periods, respectively. The sparse bioturbation also suggests high-energy currents prevailed during deposition of this sand-variant facies. This facies is interpreted to be deposited in tidal influence.

3.6 F6—Rhythmically Bedded Sandstone and Mudstone (S_{rh})

Description: The F6 was encountered at outcrops BG-2, BG-4, and BG-8 (Fig. 8). The thickness of F6 ranges from one (01) to three (03) meters. This facies has sharp contact with F1 and F2. The facies F6 is laterally continuous, but local variation in lithology and bioturbation is visible in all the exposures. Most of the thin sandstone beds are laterally continuous, otherwise form lenticular bedding.

This facies (S_{rh}) is composed of yellowish to gray, thickly laminated and thin-bedded, moderately to well-sorted fine sandstone. Sedimentary structures include both asymmetric and symmetric ripples and ripple cross-lamination, tabular cross-lamination, and wavy to lenticular bedding with occasional thin laminations of carbonaceous material in mud part. Mudstones are commonly clay-rich, though silt-rich intervals occur locally. Few sandstone beds show parallel laminations with mudstone couplets.

Bioturbation is rare in the coarser part of F6, though some unit contains *Ophiomorpha*, *Paleophycus*, *Arenocolites*, and *Terebellina*. The lenticular- and wavy-bedded sandstone and mudstone have abundant trace fossils; *Terebellina* (Tr), *Thalassinoides* (Th), *Teichichnus* (Te), *Paleophycus* (Pa), *Skolithos* (Sk), and *Conichnus* (Co?) (Fig. 3e). Body fossils are not observed.

Interpretation: The facies F6 represents deposition in alternating high-/low-energy conditions with mud deposition during slack water periods. The heterolithic bedding usually indicates strong tidal influence and ranges from intertidal to subtidal environment of deposition [26]. Presence of symmetrical and asymmetrical ripples indicates persistent wave action, resulted from combined flows [15]. Bioturbation may suggest brackish water conditions.

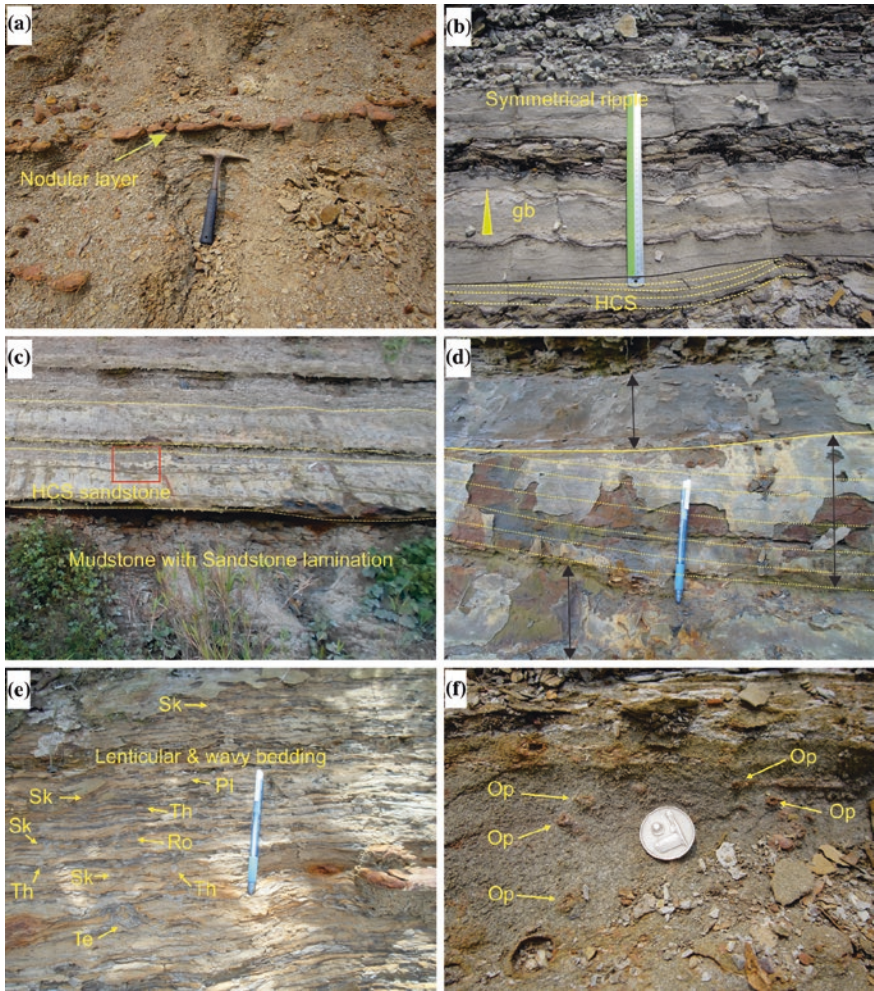


Fig. 3 Photographs of the different facies belonging to Begrih Formation. **a** Photograph showing the discontinuous nodular layer in the siltstone to fine sandstone laminated mudstone facies. **b** Hummocky cross-stratified sandstone and mudstone. Note the HCS in lower part of the picture. In the middle is the graded bedded sandstone. The top of the picture shows discontinuous symmetrical ripples with cross-lamination (combined flow?). **c** Hummocky cross-stratified sandstone and mudstone with sandstone laminations. Note the hummocky bed form, higher order erosive surface. Red rectangle denotes figure **d**. **d** Internal geometry of the hummocky cross-stratified sandstone. The arrowed lines show the thickness of individual beds. The yellow line shows low-angle cross-bedding. **e** Rhythmically bedded/laminated sandstone and mudstone, consisting of alternating centimeters thick wavy and lenticular-bedded sandstone and mud layers. Moderate bioturbation with *Skolithos* (Sk), *Planolites* (Pl), *Rosselia* (Ro), *Teichichnus* (Te), and *Thalassinoides* (Th). **f** Fine-grained, bioturbated, medium-bedded horizon of rhythmically bedded/laminated sandstone and mudstone with *Ophiomorpha* burrows

3.7 F7—*Thick Hummocky Cross-stratified Sandstone (Shs)*

Description: F7 was identified at outcrops at BG-2 and BG-4 (Figs. 8 and 3c, d). This facies is associated with laminated mudstone/shale facies having erosive basal contact and uneven top contact. At BL-4, this facies shows composite thick amalgamated beds of 60 and 70 cm separated by 10-cm mud bed. At both the outcrops, F7 shows good lateral continuity (max. 15–20 m). Internally, they are marked by scoured surfaces and mud partings. Mudstone partings (0.3–5 cm) are occasionally present between some hummocky-stratified units. The individual bed is formed by thinner packages of hummocky beds of 20–50 cm thick. The thick individual hummocky beds commonly show lateral pinching out.

The F7 (Shs) facies is composed of dark gray-colored, well-sorted, fine-grained sandstone. In BL-4, this facies is represented by two hummocky cross-stratified beds, which are separated by 10 cm laminated mudstone beds (Fig. 3c). Hummocky cross-stratification occurs throughout the whole beds with individual laminae less than 0.5 cm (Fig. 3d). Trace fossils and body fossils are absent.

Interpretation: Hummocky cross-stratification in F7 represents storm event beds in an overall muddy environment, deposited between fair-weather wave base (FWWB) and storm wave base (SWB) [27, 28]. During fair-weather conditions, the area experiences relatively low-energy conditions with continuous deposition of mud from suspension.

3.8 F8—*Thin Hummocky-Stratified Sandstone with Mudstone (Shsm)*

Description: The facies F8 was encountered at four outcrops (BG-2, 3, 6, and 7). Thickness of this unit ranges from 0.5 to 1 m (BG-6). The hummocky horizons are continuous laterally with variation in thickness. This facies has mostly sharp and erosive contact with F1 and F2, while top contact is slight irregular. This facies is different from the hummocky cross-stratified sandstone in size of hummocky cross-stratification, sandstone contents, bedding thickness, and introduction of mud and rippled horizon.

This facies (Shsm) consist of light gray to gray, fine to very fine-grained, sharp-based, hummocky cross-stratified sandstone interbedded with mudstone. The clay content dominates in this facies, with parallel laminations and often symmetrical to near-symmetrical ripples at the top (Fig. 3b). Body fossils are not observed, while few trace fossils of *Paleophycus* (Pa), *Planolites* (Pl), and *Skolithos* (Sk) were spotted.

Interpretation: F8 represents distal storm event beds in an overall muddy environment, deposited above fair-weather wave base (FWWB) [27, 28]. During fair-weather conditions, the area experiences relatively mixed-energy conditions with continuous deposition of mud from suspension and wave actions. The intense storm activity caused abrupt increase in wave energy and the deposition of HCS and wave rippled sandstone beds in an overall muddy environment.

3.9 F9—Ripple-Laminated Sandstone and Mudstone (Srp)

Description: The F9 was only identified at outcrop BL-8 where its overall thickness reaches up to 3 m. The basal contact with the F8 is transitional, while upper contact is not exposed. F9 shows good lateral continuity across the whole outcrops (Approx. 30 m).

F9 facies consists of light gray, tabular cross-bedded and ripple (symmetrical and asymmetrical) cross-laminated (Fig. 4d, e), bidirectional cross-stratified (Fig. 4e), well-sorted, fine-grained sandstone and siltstone with thin wavy clay laminations and thin clay beds having laths of carbonaceous material. Sandstone beds are 4–15 cm thick. Mudstone intervals are 1–2 cm along the rippled surfaces or in the form of parallel laminations. Tabular cross-bedding is common, but some beds have small low-angle cross-laminations having carbonaceous material covering the consecutive laminae foresets, climbing ripples (Fig. 4f), and current ripples cross-laminations. Symmetrical and asymmetrical ripples are preserved on the top of the sandstone beds with some of the rippled surfaces are eroded by parallel lamination sandstone beds (Fig. 4e). Ripples amplitude 1–4 cm with wavelength range of 7–12 cm. Thinning- and fining-upward intervals are common with individual set enveloped by thin laminated mud with carbonaceous material. Facies F9 is slightly bioturbated with few trace fossils of *Paleophycus* (Pa) and *Planolites* (Pl) (Fig. 4f). Body fossils are absent.

Interpretation: The ripple cross-laminations and climbing ripples denote high sediment input and agitated water body under the influence of wave and current. Bidirectional cross-lamination indicates reverse flow in tidal settings. While carbonaceous material incorporated in thin mud beds and minor mud and carbonaceous material along the foresets of cross-laminae indicates low-energy interval.

3.10 F10—Flaser-Bedded Sandstone (Sfl)

Description: The F10 was only identified at outcrop BL-2 where its thickness is 0.8 m. It has transitional basal contact with the underlying F7 while upper slightly irregular contact with the overlying F1 and F4. F10 shows good lateral continuity in the outcrop.

F10 (Sf) is composed of yellow-colored, fine-grained, well-sorted sandstone with irregular, discontinuous mudstone (clay-rich), beds, and few scours surfaces with mud lining. It also bears very thin laminations of carbonaceous material and mud. This facies is associated with rhythmically laminated sandstone and mudstone and laminated mud/shale. Trace fossils include *Skolithos* (Sk), and *Paleophycus* (Pa) burrows.

Interpretation: Facies F10 indicates transition into environment characterized by an increased in effect of wave action above fair-weather waves base, which results in lower preservation potential of mud deposits and having higher proportions of sandstone fraction. On the bases of associated facies, F10 is interpreted to be deposited in transition zone between upper offshore and shoreface facies.

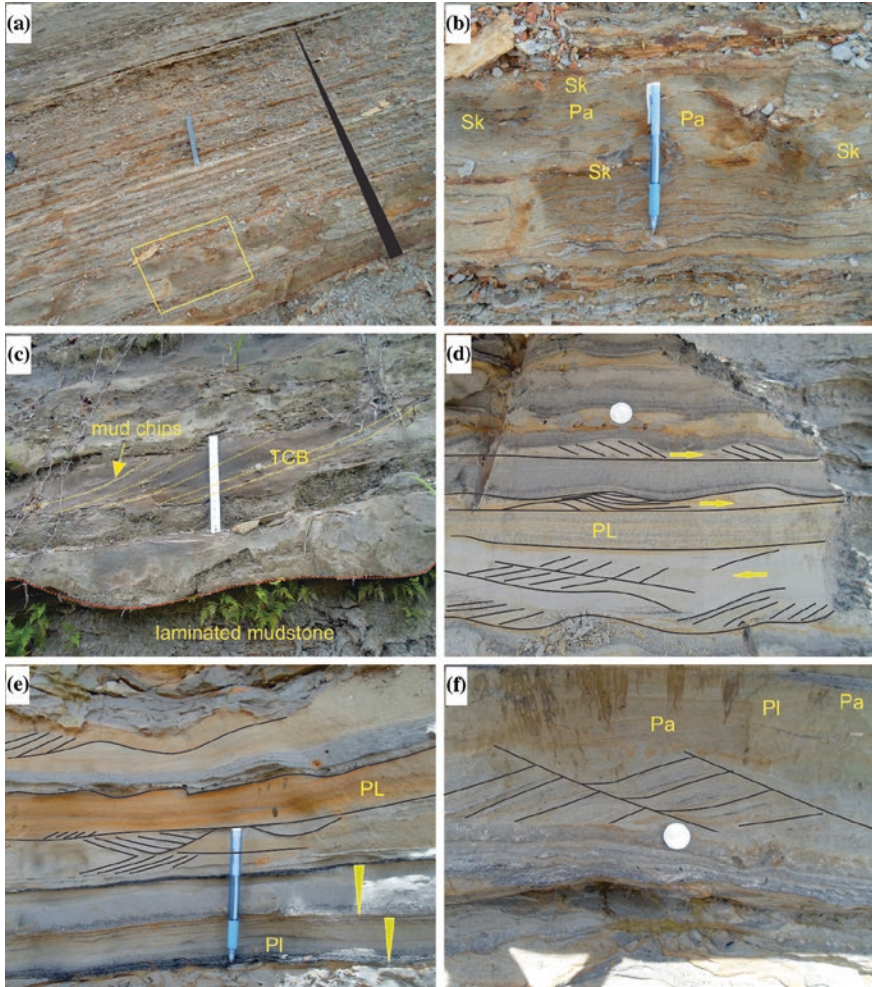


Fig. 4 Photographs of the different facies belonging to Begrih Formation. **a** Planar-bedded sandstone with sub-ordinate mudstone (clay-rich) and brown nodules and nodular layers. Lower erosive contact with laminated mudstone unit. Note the thinning-upward sequence. The *rectangle* refers to figure **b**. **b** Thick beds of sandstone with discontinuous clay and carbonaceous laminations. Burrows include *Skolithos* (Sk) and *Paleophycus* (Pa). **c** Trough cross-bedded sandstone with mud chip along the foresets. Note the erosive basal contact with the laminated mudstone. **d** Rippled-laminated sandstone and mudstone. *Arrow* shows the flow direction and resultant cross-laminated ripples. Lower part contains climbing ripples but in opposite direction of upper ripples. Parallel-laminated (PL) thin bed in the middle. **e** Part of ripple-laminated sandstone and mudstone with coarsening upward beds (reverse grading), bidirectional laminations, ripples crest eroded by parallel-laminated fine-grained sandstone bed. *Planolites* burrows above the carbogilite/silt lamination. **f** Climbing ripples from rippled cross-bedded/laminated sandstone and mudstone. Burrows include *Paleophycus* (Pa), *Planolites* (Pl)

3.11 F11—*Bioturbated Sandstone (Sb)*

Description: The facies F11 was identified at outcrop BG-3 and BG-7. F11 is associated with F1 and F2 in BG-3 where its thickness is 12–20 cm. F11 is laterally continuous with obliterated original sedimentary fabric. The sandstone beds are fully homogenized.

This facies consists of light gray, gray, and yellowish, fine to medium-grained, severely bioturbated sandstone beds having original fabric partially or fully destroyed. The thickness of this facies vary from 12 to 20 cm (BG-3). No individual trace fossil can be identified due to intense bioturbation. Body fossils are also absent.

Interpretations: This facies is deposited in low-energy area primarily from suspension with some sporadic higher sand influx due to storms. The complete mixing of the sandstone suggests very slow sedimentation rate which allowed organism to mix it thoroughly. Bioturbated units can be deposited in low-energy open marine depositional environments, sporadically influenced by storm deposits [15].

3.12 F12—*Pebbly Conglomerates (Gp)*

Description: The facies F12 was identified at the outcrop BG-1. The base of the Begrih Formation holds distinctive massive 3.5-m conglomerate with very erosive lower contact and uneven upper contact. The composite thickness of F12 reaches up to 3.5 m in the BG-1. This facies is characterized by wavy interbedding of mudstone and conglomerate beds, with fine sandstone intervals and thin discontinuous mudstone beds at the top of the outcrop. Most of the other conglomerates encountered in the Begrih Formation have thickness range from 10 to 65 cm having sheet-like geometries.

This facies (Gp) consists of yellowish brown, grayish, thin to thick-bedded (0.1–2.5 m), structureless, erosive-based, poorly sorted conglomerate and fining-upward, moderately sorted, medium to coarse-grained trough cross-stratified sandstone. Conglomerates are either grain and/or matrix-supported (Fig. 5d, f). Thin conglomerate beds also occur in the mudstone facies with other coarse sandstone beds. The clasts are randomly oriented and range from angular quartz, coal clast to well-rounded clast of sedimentary origin. The matrix of conglomerate consists of fine to coarse sandstone and mudstone. It is devoid of any trace and body fossil.

Interpretation: The facies characteristics of Gm reflect strong unidirectional currents. Coarser fraction of the sediment stays near the base in sandy and pebbly sediment laden flow. Thick conglomerates (pebbly) can be product of high-density sandy and pebbly turbidity currents [29]. The absence of any marine trace or body fossils supports non-marine, freshwater deposition.

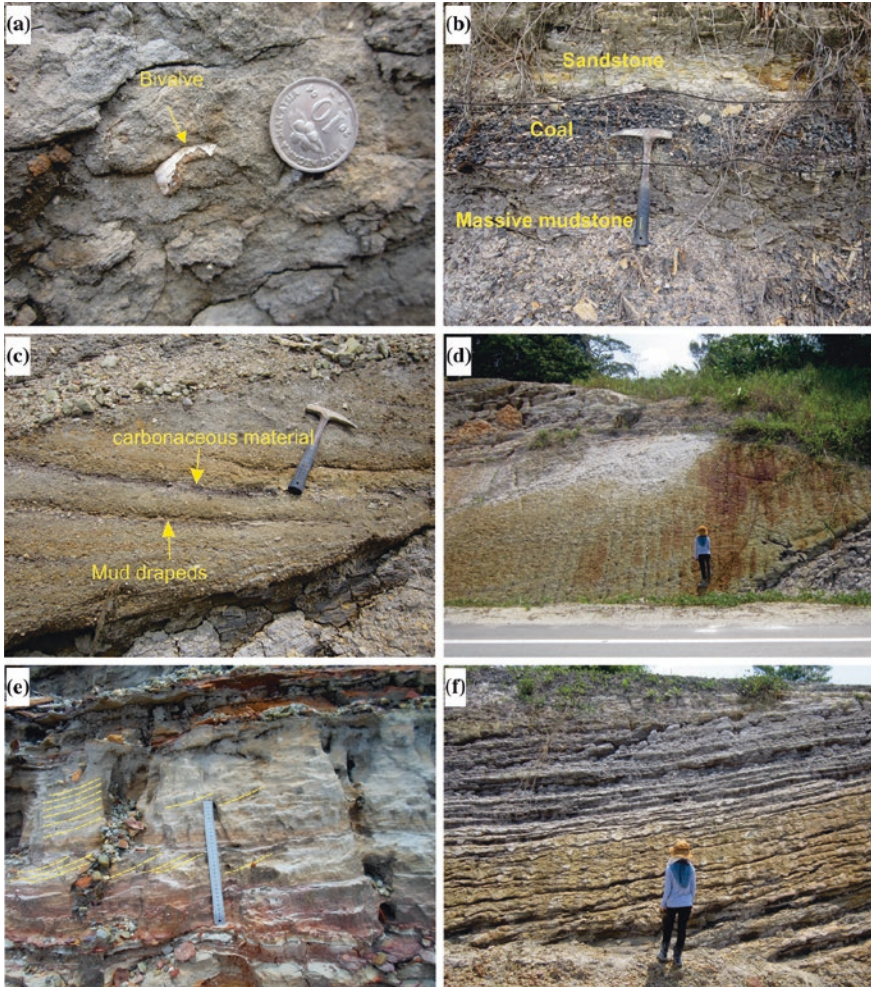


Fig. 5 Photographs of the different facies belonging to Begrih Formation. **a** Fossiliferous mudstone (silt-rich) bearing a bivalve shell fragment. This unit is fully bioturbated having original fabric destroyed or partly altered. **b** Coal layer having upper erosive contact with white, yellowish (leached) sandstone and lower gradual contact with the massive rootletted mudstone. The lower contact is marked carbonaceous material and rootletted mudstone. **c** Pebbly trough cross-bedded sandstone with mud drapes and carbonaceous material along the cross-bed foresets. **d** Thick massive conglomerate (3.5 m) at the lower part of the Begrih Formation. Irregular coal body at the lower contact above the mudstone. **e** Trough cross-laminated medium to thick-bedded sandstone. Individual beds are separated by clay-rich thin mudstone beds. Abundant mud chips and rip-up mud clast in the reddish horizon. **f** Alternating conglomerate and gley mudstone wavy bedding on top of the BG-1. Thinning-upward sequence of conglomerate as mud contents increases upward

3.13 F13—Trough Cross-bedded Pebbly Conglomerate (Gpt)

Description: This facies was identified at outcrops at outcrops BG-3 and BG-4. The thickness of this facies is 35 cm (BG-3) and 30 cm (BG-4). Intervals of very fine silty sandstone with mud drapes and carbonaceous material along the cross-bedding foresets are observed. The thickness of this facies changes laterally with some beds pinching out. This facies has sharp and erosive basal contact with F1, while top contact is also sharp and slightly irregular along some parts of exposure.

The F13 facies consists of gray to dark gray, erosive-based, pebbly conglomerates with large trough cross-bedding (Fig. 5c). Trough cross-beddings have tangential lower contact with the mud layer at outcrop BG-3 (Fig. 5c). The clasts are mostly of pebble size with angular (quartz and feldspar) and some well-rounded sedimentary fragment. Trace fossils and body fossils are absent.

Interpretation: The F13 facies represents strong unidirectional currents. The pebbly conglomerate with trough cross-bedding is usually associated with strong unidirectional currents. The enveloping mudstone reflects calm condition which favored the deposition of mud, while F13 suggest some catastrophic event. The F13 may be the product of high-density sandy and pebbly turbidity currents [29]. F13 shows close relationship to other interpreted shallow marine facies (F1). F13 is interpreted to be deposited by major typhoon which was generated in open marine setting. Besides reducing condition, the high rate of sedimentation and coarse fraction, halt the biological activities in any rock strata. The occurrence and type of bioturbation are controlled by grain size of the sedimentary rocks [30].

3.14 F14—Bioturbated Conglomerate (Gb)

Description: The facies F14 was only exposed at BG-6. The coarse pebbly sandstone and conglomerate beds thickness range is 5–60 cm. The basal contact is sharp and erosive, while top contact with the F1 facies is sharp and irregular. Internally, the facies F14 is marked by several scoured surfaces and mud partings. The sandstone and conglomerates are interbedded and contain large mud chips. The upper part of F14 is generally sandy, thus forming fining-upward unit.

F14 facies (Gb) consists of dark gray, with yellowish patches, matrix-supported pebbly conglomerates and interbedded pebbly, medium to coarse sandstones and laminated mudstone (F1). The interbedded mudstone thickness ranges from 5 to 30 cm. Bioturbation is common in F14. The bioturbation is directly related to the grain size at the outcrop. Medium to coarse part of the sandstone is more bioturbated as compared to part having coarser fraction (pebbles). Some of the burrows were identified as *Ophiomorpha* (Op).

Interpretation: The type of grains and grain size is the controlling factor on the occurrence of bioturbation in sedimentary units [30]. The rare occurrence of the *Ophiomorpha* burrows in pebbly part suggests that strong current or waves (?) deposited the pebbly fraction. These strong currents and coarser fraction did not allow suitable substrate and time for biological activities. After the initial strong phase, the flow lost energy and sand fraction were allowed to settle down and burrowing activities took place. The characteristic and association of this facies imply that F14 was deposited high-energy seaward directed current as result of major storms. The bioturbation also suggests marine setting, with plenty of oxygen available for organism to thrive.

3.15 F15—Coal

Description: In Begrih Formation, F15 was only exposed at BG-5. The thickness of the coal layer is only 20 cm. F15 shows a gradual lower contact with the underlying massive rootletted mudstone. The top contact with the overlying sandstone is slightly erosive.

The facies F15 (C) consists of fractured black coal (Fig. 5b). The carbonaceous material is introduced from the middle of the unit, which increases upward. It has some carbogillite horizon on the lower surface that is 2–3 cm thick (Fig. 5).

Palynological analyses reveal that the coal facies (F15) yielded moderate pollen and spore assemblages. In general, the mangrove species are characterized by *Bruguiera*, *Florschuetzia*, *Acrostichum aureum*, *Excoecaria aggulocha*, *Nypa*, *Avicennia*, and *Oncosperma* which constitute 37.6 % of the total pollen counts. The pollen derived from lowland/peatland source such as *Dactylocladus*, *Blumeodendron*, and *Stemonorus* shows value of 32.1 % from the total pollen content (Fig. 6).

Interpretation: Coals are usually deposited as a result of in situ accumulation of plant material and organic matter in reducing waterlogged conditions, where the rate of accumulation is more than the rate of decomposition. The palynological analyses show both the mangrove and lowland/peatland assemblages of pollen and spores with slight abundance of mangrove species. The presence of mangrove species found in the coal suggests that plant material accumulated in the area with pronounced marine influence, while lowland species suggest input of fresh water.

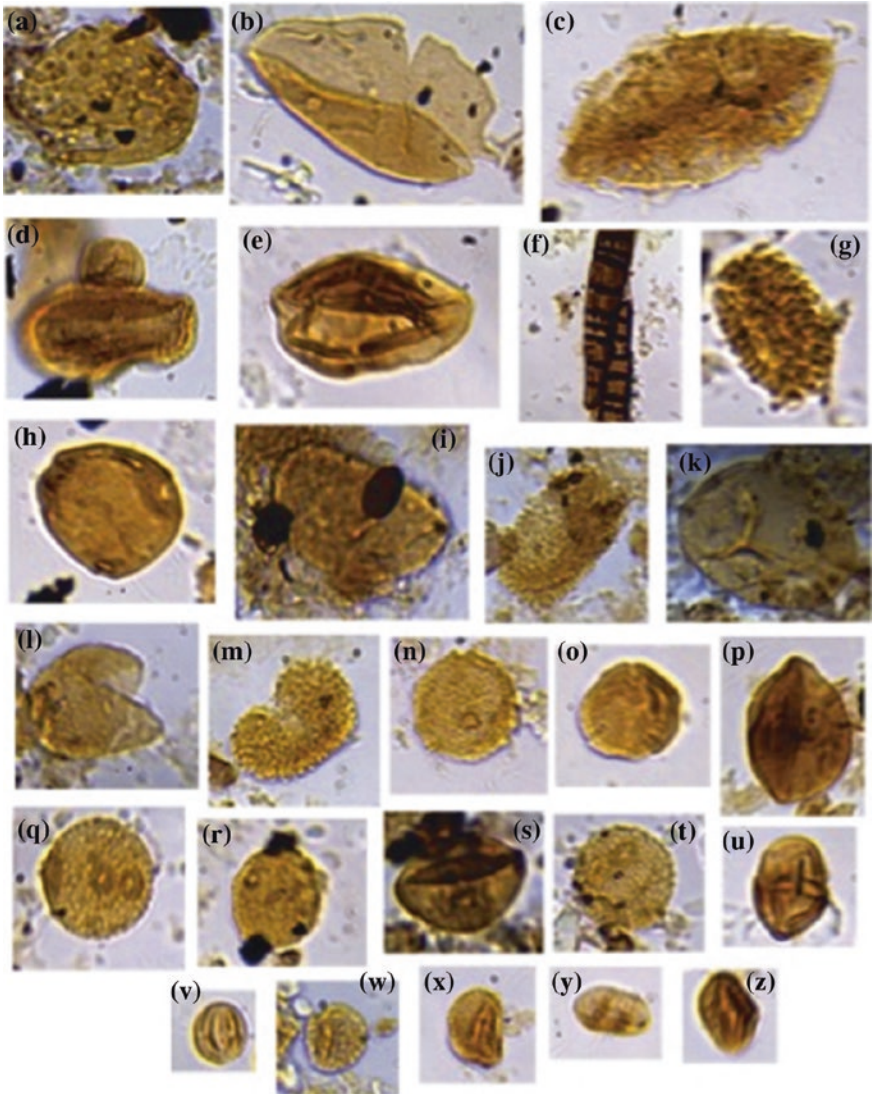


Fig. 6 a *Stenochlaena usmensis*. b *Magnolia*. c *Dinoflagellate*. d *Calophyllum* (Big). *Rhizophora* (Small). e *Polypodium*. f *Fungus*. g *Ilex*. h *Casuarina*. i *Asplenium*. j *Oncosperma*. k *Acrostichum aureum*. l *Metroxylon*. m *Oncosperma*. n *Canthium*. o *Brownlowia*. p *Florschuetzia semilobata*. q *Cephalomappa*. r *Cephalomappa*. s *Florschuetzia levipoli*. t *Cephalomappa*. (4 pores) u *Rhizophora*. v *Dactylocladus*. w *Blumeodendron*. x *Aecenia*. y *Lithocarpus*. z *Campnosperma*

4 Facies Association of Begrih Formation

Section 3 and Figs. 3, 4 and 5 provide detailed information regarding each facies in the study area. The described fifteen facies (15) are grouped into seven (07) facies association (Figs. 7 and 8).

1. FA1—Lower offshore and shelf facies
2. FA2—Upper offshore
3. FA3—Lower to middle shoreface
4. FA4—Upper shoreface
5. FA5—Foreshore facies
6. FA6—Lagoonal facies
7. FA7—Backshore/Fluvial facies

4.1 FA1—Lower Offshore and Shelf Facies

The lower offshore facies association is dominated by muddy facies (Figs. 7 and 8). The very fine-grained character of these facies suggests a very low-energy setting, which allowed sediment fall-out from suspension [14, 15]. The thin pebbly sandstone, conglomeratic beds and bioturbated thin beds of fine

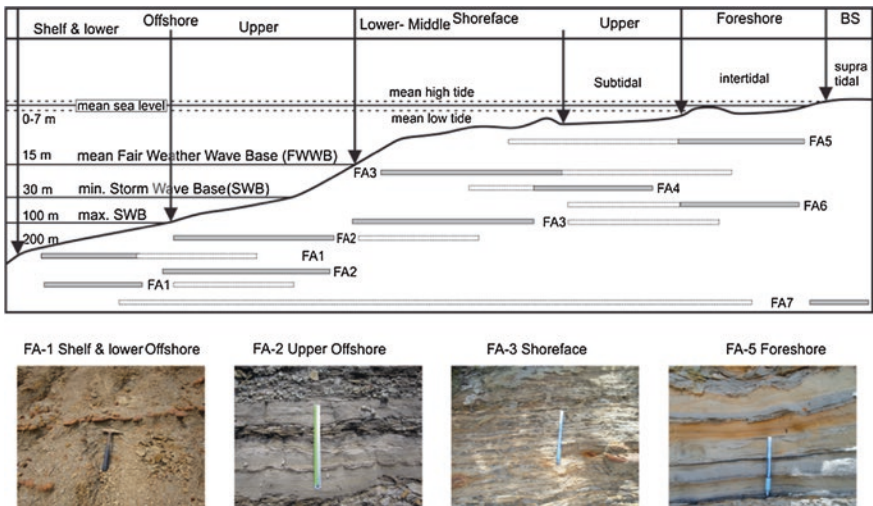


Fig. 7 Schematic depositional profile of the Begrih Formation. The partition of the depositional profile follows the model of Pemberton and Wightman [33], modified by Nagel et al. [31] according to Taiwan orogeny. The sedimentary facies and facies association are assigned on the basis of sedimentary structure, trace fossil distribution. *Photograph* showing the interpreted facies and facies association identified in the study area

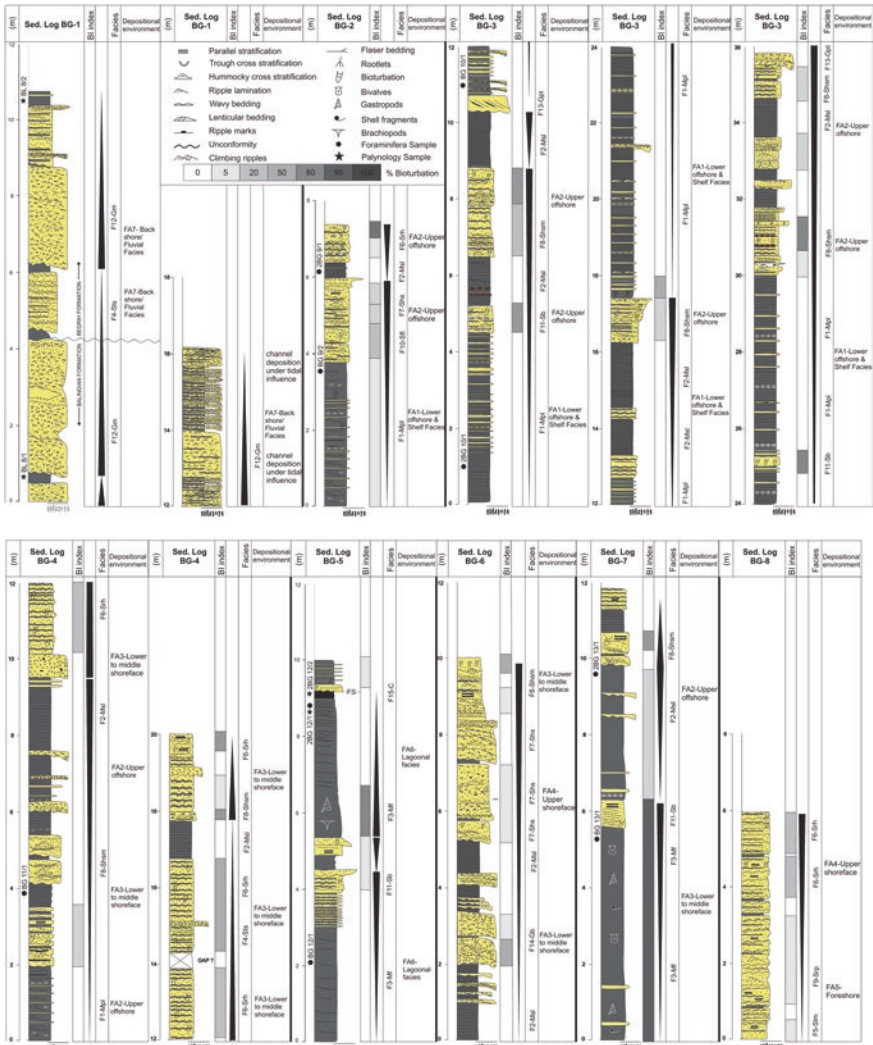


Fig. 8 Compilation of all the outcrops of Begrih Formation revealing individual facies and facies association

sandstone may represent deposits of event flow in the offshore area as a result of flooding in the rivers along with big major storms/typhoons. These rare events might be the cause for deposition of coarser unit within offshore deposits [31]. It might be result of turbidity currents induced by strong storms [15] which transport this coarser material over offshore fine fraction. The shale and laminated mudstone without sandstone/siltstone laminations is interpreted to be deposited below storm wave base.

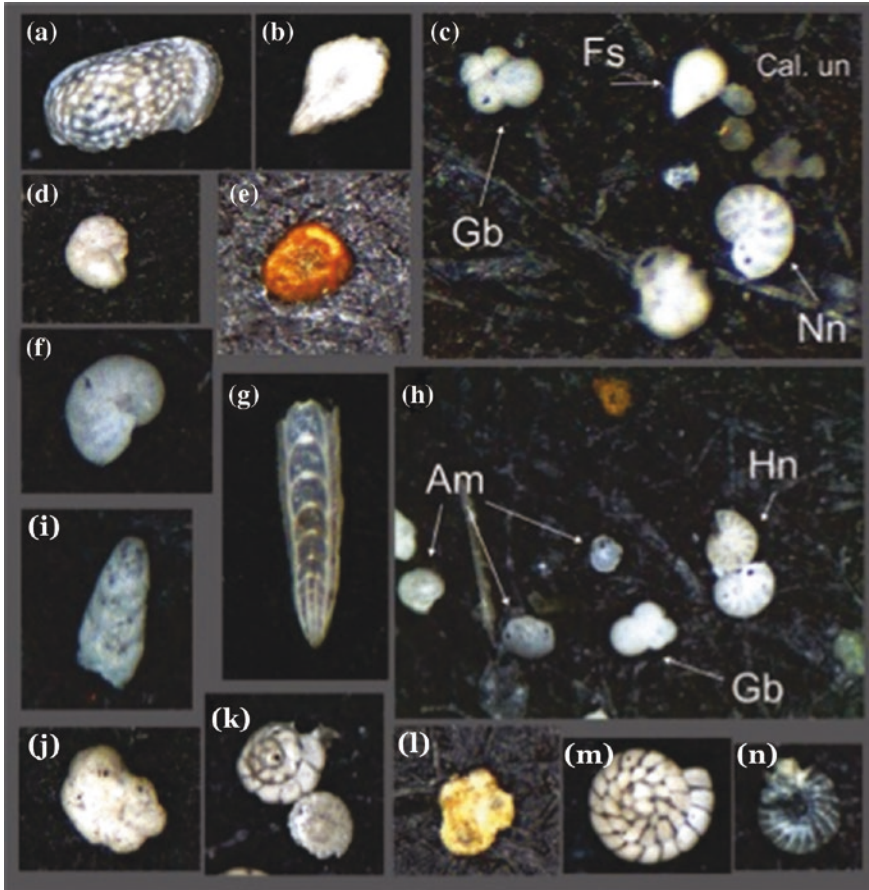


Fig. 9 (X.40 magnification) **a** *Ostracod*. **b** Calcareous undifferentiated. **c** *Globogerina buliades* (gb) *Fissurina* (Fs) *Nonian* (Nn). **d** *Trochammina*. **e** *Haplophragmoides* sp. **f** *Anomalina* sp. **g** *Frondicularia*. **h** *Ammonia* sp. (Am), *Globogerina buliades* (Gb), *Hanzawaia* (Hn). **i** *Loxostomun* sp. **j** *Haplophragmoides* sp. **k** *Ammonia* sp. **l** *Trochammina*. **m** *Ammonia beccarii*. **n** *Elphidium*

4.2 FA2—Upper Offshore

The upper offshore facies association comprises fining-upward succession. It is dominated by muddy deposits in the base, which grades into thin-bedded hummocky cross-stratified sandstone and mudstone. In few sections, the muddy deposits are also interbedded with bioturbated sandstone (F11-Sb) facies (Figs. 7 and 8). The muddy units of FA-2 represent suspended sediment fall-out in a low-energy setting [15]. The thin-bedded hummocky cross-stratified sandstone and mudstone having oscillatory-generated structures indicate repetition of less frequent and low-energy storm events below fair-weather wave base but well above storm-wave

base [14, 15, 27, 32]. Trace fossil assemblage is of *Skolithos* ichnofacies that are restricted to the sandstone beds. Mostly, these *Skolithos* ichnofacies in combination with *cruziana* ichnofacies are indicative of offshore sedimentation [33].

4.3 FA3—Lower to Middle Shoreface

Lower to middle shoreface facies association is dominated by gray, sharp- and erosive-based, thick-bedded, fine to medium-grained, well-sorted sandstone with hummocky cross-stratification and heterolithic (F6-Srh) facies (Figs. 7 and 8).

This facies association is interpreted to represent lower to middle shoreface (Figs. 7 and 8). Thick, amalgamated hummocky cross-stratified beds are interpreted as storm beds, above the fair-weather base and record high-energy oscillatory and combined flows during repeated storms [15] in proximal storm range [32]. Continued wave erosion removed mud layers between sandstone beds, with the exception of locally preserved residual thin mud laminations [14, 34]. The relative decrease in proportion of mudstone interbeds in the F10 (BG-2) suggests deposition above fair-weather wave base and continuous water agitation [15]. It is also indicated by presence of flaser-bedded sandstone beds, which indicate persistent wave action [31]. The heterolithic facies in FA-3 are interpreted to be results of deposition in oscillatory and occasionally combined flow in lower to middle shoreface during fair-weather conditions [26].

4.4 FA4—Upper Shoreface

The upper shoreface facies association comprises of thin to thick-bedded, medium to coarse-grained, trough cross-stratified, sandstone and pebbly sandstones. The upper shoreface represents energetic intervals, relative to lower shoreface deposits (Figs. 7 and 8). Trough cross-stratification represents migration of bars and dunes along the shoreline due to either rip currents or longshore currents in the upper shoreface [20, 23, 24]. The coarser fraction along with sparse or lack of bioturbation also suggests deposition in agitated high-energy conditions [33]. The type of grains and grain size is the controlling factor on the occurrence of bioturbation in sedimentary units [30]. The strong currents and coarser fraction during the high-energy interval in upper shoreface did not allow suitable substrate and time for biological activities.

4.5 FA5—Foreshore Facies

The foreshore facies association (FA-5) consists of two distinct facies (F9- Srp and F5-Slm) that are interpreted to represent foreshore deposits (Figs. 7 and 8). FA5

denotes deposition between mean low and mean high tide [25]. Thin to medium-bedded sandstone with ripple cross-laminations and climbing ripples denote the agitated water body under the influence of wave and current. Bidirectional cross-lamination indicates reverse flow in tidal settings. Carbonaceous material incorporated in thin mud beds and minor mud and carbonaceous material along the foresets of cross-laminae indicate low-energy interval. However, high-energy conditions also prevail due to intense swash and backwash process [15, 25] indicated by parallel lamination eroding the underlying crests of the ripples top. These facies record the interplay of tidal and wave actions within the shallow foreshore area.

4.6 FA6—Lagoonal Facies

The lagoonal facies association consists of overall fining-upward succession of fossiliferous mudstone, capped by coal facies (Fig. 8). The sandy interval in the middle of the BL-5 indicates some turbulent episode in generally quiet setting. The presence of rootlets and coal indicates swampy/marshy area [35]. The muddy fraction and mixed fine-grained material suggest that these facies were deposited in very low-energy condition with slow sedimentation rate. The low-energy conditions are also favored by complete mixing of the units as a result of bioturbation. The presence of bivalve and brachiopods in the base of the mudstone beds suggests that the initial phase of lagoon was dominated by presence of these organisms. Due to prolonged prevailing condition, the area was covered by marshes along the periphery of the lagoon. The coal bed is as a result of waterlogged conditions in this lagoon. This is also supported by presence of rare marsh forms *Haplophragmoides* sp., *Haplophragmoides* sp., along with *Trochammina* sp (Fig. 9).

4.7 FA7—Backshore/Fluvial Facies

The backshore/fluvial facies association consists of fining-upward succession of massive conglomerate, cross-bedded sandstone and mudstone. The conglomerate and trough cross-bedded sandstones are separated by disorganized mud deposits. The conglomerate having very coarse sediments reflects strong currents deposited these units. The associated interlayered sandstones are interpreted to be deposited by reduced flow conditions reflected by grain size and trough cross-stratification. Erosive bases and fining-upward trends having trough cross-stratifications with abundant mud rip-up clast reflects migration of dune in fluvial channels [15, 25, 36, 37]. The associated mud horizons are interpreted to be deposited as overbank deposits during reduced flow conditions or it may indicate some tidal influence on the channel facies. The pinching of the sandstone beds along the lower conglomerate bed in Begrih Formation reveals shadow zone/barrier in high-energy braided stream. The overall succession in BG-1 may suggest subsiding basin margin due to tectonic activity.

5 Depositional Setting and Paleogeography

The marginal marine successions are very complex having interplay of wave, tides, and fluvial influence on the deposits. The Begrih Formation is exposed between the older Balingian Formation and younger Liang Formation in the study area. The Begrih Formation is characterized by presence of fluvial-dominated units, overlain by wave and storms dominated deposits interbedded with offshore mud-prone facies. The base of the Begrih Formation is represented by massive conglomerate and trough cross-stratified sandstone of fluvial origin (backshore/fluvial facies). Trough cross-stratified sandstones and conglomerates have negligible bioturbation usually represent falling stage or early transgressive stage deposits [22, 37]. The conglomerates and sandstones in the base of the formation represent remnant of braided river of the regressive phase (major uplift) followed by transgression in the sub-basin. The coarser fraction of the feeding river that was dumped in low areas reflects major regressive phase dominated by low sinuosity fluvial deposits in the sub-basin. This is consistent with the Madon [7] who suggested that the Sarawak continental shelf continued to prograde from Middle Miocene to Early Pliocene times with the coastal fluviomarine sediments. Previously reconstructed paleogeographic evolution of Sarawak continental margin also suggests that during the Early Pliocene, most of area along the present coast was dominated by lower coastal plains deposits [38]. Our data suggest that shallow marine condition prevailed in this area, during the Pliocene age.

The change from alluvial plain or fluvially dominated coastal plain deposits in the lower part of the Begrih Formation to dominantly shallow marine deposits in

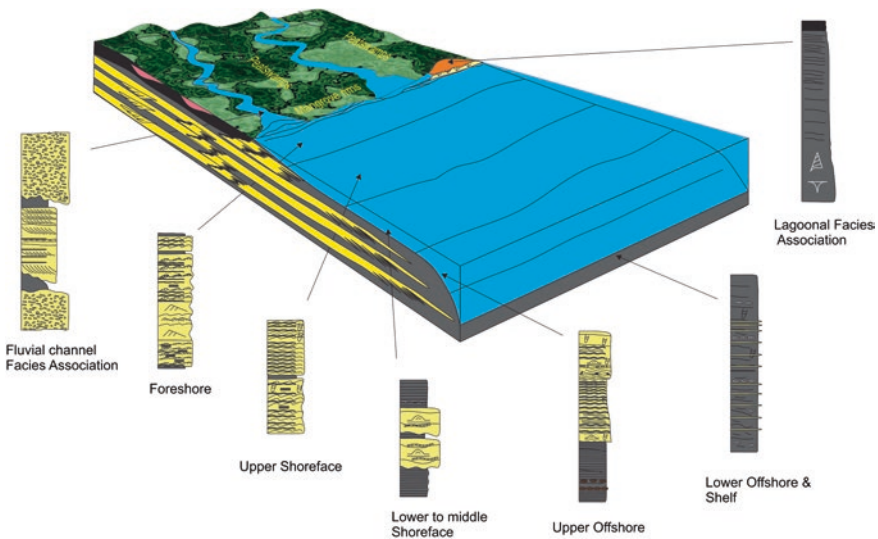


Fig. 10 Depositional setting of the Begrih Formation

the middle and upper part of the Pliocene succession indicates large-scale relative sea-level rise or regional subsidence contributed in the creation of accommodation space. In vertical sequence, the lower fluvial deposit overlies sandstone and conglomerate units interbedded with the mud represents fining- and thinning-upward sequence. The rocks encountered in BG-2 to BG-4 consist of storm and wave dominated units ranging from foreshore to offshore and shelf facies. The shallow marine facies are scattered in such manner that it shows fluctuation in relative sea level during the deposition of Begrih Formation. BG-5 shows fully bioturbated silty mudstone with coal capping the sequence. The presence of *Haplophragmoides* sp (Fig. 9) indicates that marsh conditions prevail during the deposition of mud and overlying coal. The overall paleogeography of the Mukah–Balingian sub-basin during Pliocene is depicted in Fig. 10, revealing relative sea level rise and subsequent facies deposition in the shallow marine setting during Pliocene age.

6 Conclusion

1. Sedimentological, palynological, and micropaleontological (Foraminifera) data were integrated for Begrih Formation. Fifteen (15) sedimentary facies from eight (08) outcrops of Begrih Formation have been identified and interpreted.
2. These sedimentary facies are categorized into four main types depending on the major lithology type.
 - (a) Mud-dominated unit: F1—laminated mudstone/shale (Msl), F2—lenticular-bedded mudstone (MI), and F3—fossiliferous mudstone (Mf);
 - (b) Sandstone/Siltstone-dominated Facies: F4—trough cross-stratified sandstone (Sts), F5—planar-laminated sandstone and mudstone (SIm), F6—rhythmically bedded sandstone and mudstone (Srh), F7—thick hummocky cross-stratified sandstone (Shs), F8—thin hummocky cross-stratified sandstone with mudstone (Shsm), F9—ripple-laminated sandstone and mudstone (Srp), F10—flaser-bedded sandstone (Sfl), and F11—bioturbated sandstone (Sb);
 - (c) Conglomerate: F12—pebbly conglomerates (Gm), F13—trough cross-bedded pebbly conglomerate (Gpt), and F14—bioturbated conglomerate (Gb); and
 - (d) F15—Coal facies.
3. The evaluated facies were grouped into seven facies association; (1) FA1-shelf and lower offshore. (2) FA2-upper offshore. (3) FA3-lower to middle shoreface. (4) FA4-upper shoreface. (5) FA5-foreshore. (6) FA6-lagoonal facies. (7) FA7-backshore/fluvial facies.
4. The pattern of facies and presence of foraminifer's species imply that these facies were deposited in the overall shallowing and sandying upward succession, with pronounced storms, wave, tidal, and fluvial influence along the paleo-margin.

References

1. Liechti, P., Roe, R. W. & Haile, N. S., 1960. Geology of Sarawak, Brunei and Western North Borneo, British Borneo Geological Survey Bulletin, 3, 1960.
2. Wolfenden, E.B., 1960. The geology and mineral resources of the Lower Rajang Valley and adjoining areas, Sarawak. Memoir, 11. Geological Survey of British Borneo 167p.
3. De Silva, S. 1986b. Stratigraphy of south Mukah–Balingian region, Sarawak. Newsl. Geol. Soc. Malaysia, 12 (5), p. 215–219.
4. Dickinson, W.R., 1974. Plate tectonics and sedimentation. Soc. Economic Paleontologists and Mineralogists Special Publ., 22:1-27p.
5. Hazebroek, H.P. and Tan, D.N.K., 1993. Tertiary tectonic evolution of the NW Sabah continental Margin. In: The, G. H., ed., Proceedings of the symposium on Tectonic Framework and Energy Resources of the Western Margin of Pacific Basin. Bulletin of the Geological Society of Malaysia, 33, 195-210p.
6. Hazebroek, H.P., Tan, D.N.K. and Swinburn, P, 1994. Tertiary evolution of the offshore Sarawak and Sabah Basins, NW Borneo. American Association of Petroleum Geologist Bulletin, 78, 1144-1145p.
7. Madon, M., 1999. Chapter 5 In: The Petroleum Geology and Resources of Malaysia, ISBN 983-9738-10-0, 275-286 p.
8. Tan, D.N.K., 1982. The Lubok Antu Melange, Lupar Valley, west Sarawak: A lower Tertiary subduction complex. *Geol. Soc. Malay. Bull*, 15, 31^6.
9. Haile, N.S., Lam, S.K. and Banda, R.M., 1994. Relationship of gabbro and pillow lavas in the Lupar Formation, West Sarawak; implications for interpretation of the Lubok Antu Melange and the Lupar Line. Bulletin of the Geological Society of Malaysia, 36, 1-9.
10. Haile, N.S., 1969. Geosynclinal theory and the organizational pattern of the Northwest Borneo Geosyncline. Quarterly Journal of the Geological Society of London, 124, 171-194p.
11. Williams, P. R., and Harahap, B. H., 1987). Preliminary geochemical and age data from post-subduction intrusive rocks, northwest Borneo. *Australian Journal of Earth Sciences*, 34(4), 405-415.
12. Hutchison, C.S., 2005. Geology of North West Borneo, Sarawak, Brunei and Sabah. Elsevier, UK, p 67-80.
13. Hutchison, C.S., 1989. Geological Evolution of South-East Asia. Oxford monographs on Geology and Geophysics, no. 13, Clarendon Press, Oxford.
14. Buatois, L.A. and Ma'ngano, M.G. (2003) Sedimentary facies and depositional evolution of the Upper Cambrian to Lower Ordovician Santa Rosita Formation in northwest Argentina. *J. S. Am. Earth Sci.*, 16, 343–363.
15. Buatois, L. A., Santiago, N., Herrera, M., Plink-Bjorklund, P. I. R. E. T., Steel, R., Espin, M., & Parra, K. (2012). Sedimentological and ichnological signatures of changes in wave, river and tidal influence along a Neogene tropical deltaic shoreline. *Sedimentology*, 59(5), 1568-1612.
16. Potter, P.E., Maynard, J.B. and Depetris, P.J. 2005. Mud & Mudstones: Introduction and Overview. Springer-Verlag, Berlin, 297 p.
17. Niedoroda, A.W., Swift, D.J.P., Hopkins, T.S. and MA, C.M. 1984. Shoreface Morphodynamics on Wave-Dominated Coasts. *Marine Geology*, 60: 331.
18. Walker, R.G. and Plint, A.G. 1992. Wave- and Storm-Dominated Shallow Marine Systems. In: *Facies Models: Response to Sea-Level Change* (Eds R.G. Walker and D.P. James), pp. 219. Geological Association of Canada.
19. Johnson, H.D. and Baldwin, C.T. 1996. Shallow clastic seas. In: *Sedimentary Environments: Processes, Facies and Stratigraphy* (Ed H.G. Reading), pp. 232.
20. Reineck, H.E. and Singh, I.B., 1980. *Depositional sedimentary environments*. Berlin, Heidelberg, New York, Springer Verlag, 549 pp.
21. Nio, S.D. and Yang, C.S., 1991. Diagnostic attributes of clastic tidal deposits; a review. In: *Clastic tidal sedimentology* (Eds D.G. Smith, B.A. Zaitlin, G.E. Reinson and R.A. Rahmani), *Memoir*, 16, pp. 3. Canadian Society of Petroleum Geologists.

22. Dalrymple, R. 1992. Tidal depositional systems. In: *Facies Models: Response to Sea-Level Change* (Eds R.G. Walker and N.P. James), Geological Association of Canada, pp. 195.
23. Clifton, H.E., Phillips, R.L. and Hunter, R.E. 1971. Depositional structures and processes in the non-barred high-energy nearshore. *Journal of Sedimentary Petrology*, 41: 651.
24. Collinson, J.D. and Thompson, D.B., 1989. *Sedimentary Structures*. Unwin Hyman Ltd, 207 pp.
25. Collinson, J.D. 1996. Alluvial sediments. In: *Sedimentary Environments: Processes, Facies and Stratigraphy* (Ed H.G. Reading), pp. 37.
26. García-García, F., De Gea, G. A., & Ruiz-Ortiz, P. A. (2011). Detached forced-regressive shoreface wedges at the Southern Iberian continental palaeomargin (Early Cretaceous, Betic Cordillera, S Spain). *Sedimentary Geology*, 236(3), 197-210.
27. Dott, R.H. Jr and Bourgeois, J. (1982) Hummocky stratification: significance of his variable bedding sequences. *Geol. Soc. Am. Bull.*, 93, 663.
28. Swift, D.J.P., Figueiredo, A.G., Freeland, G.L. and Oertel, G.F. 1983. Hummocky cross-stratification and megaripples - a geological double-standard. *Journal of Sedimentary Petrology*, 53: 1295.
29. Buatois, L.A. and Medina, F.J. 1993. Stratigraphy and depositional setting of the Lagrelius Point Formation from the Lower Cretaceous of James Ross Island, Antarctica. *Antarctic Science*, 5, 379–388.
30. Dashtgard, S. E., Gingras, M. K., & Pemberton, S. G. (2008). Grain-size controls on the occurrence of bioturbation. *Palaeogeography, Palaeoclimatology, Palaeoecology*, 257(1), 224-243.
31. Castellort, S., Nagel, S., Mouthereau, F., Lin, A. T. S., Wetzel, A., Kaus, B., ... & Chiu, W. Y. (2011). Sedimentology of early Pliocene sandstones in the south-western Taiwan foreland: Implications for basin physiography in the early stages of collision. *Journal of Asian Earth Sciences*, 40(1), 52-71.
32. Cheel, R.J. and Leckie, D.A. (1993). Hummocky cross-stratification. *Sedimentology Review*, 1, 103–122.
33. Pemberton, S.G. and Wightman, D.M. (1992) Ichnological characteristics of brackish water deposits. In: *Applications of Ichnology to Petroleum Exploration – A Core Workshop* (Ed. S.G. Pemberton), SEPM Core Workshop, 17, 141–167.
34. Brenchley, P.J., Pickerill, R.K. and Stromberg, S.G. (1993) The role of wave reworking on the architecture of storm sand- stone facies, Bell Island Group (Lower Ordovician), eastern Newfoundland. *Sedimentology*, 40, 359–382.
35. Retallack, G.J., 1997, *A Color Guide to Paleosols*. John Wiley & Sons, Chichester, 175 p.
36. Miall, A.D. 1992. Alluvial deposits. In: *Facies Models: Response to Sea-Level Change* (Eds R.G. Walker and N.P. James), Geological Association of Canada. 119 pp.
37. Zaitlin, B.A., Dalrymple, R.W. and Boyd, R., 1994. The stratigraphic organization of incised-valley systems associated with relative sea-level change. In: *Incised-valley systems; origin and sedimentary sequences*. (Eds R. Dalrymple, R. Boyd and B.A. Zaitlin), *Society for Sedimentary Geology. Special Publication*, 51, pp. 45.
38. Taylor, G., Powell, C., Newall, M. and Ngau, A., 1997. Petronas and Sarawak Shell Berhad Joint Regional Study of the Pre-Carbonate Clastics, Central Luconia Province, Offshore Sarawak. Unpublished report (Madon, 1999).

Part VI
Advanced Geological Concepts in
Carbonates and Sedimentary Basins

Application of Wireline Logs in the Determination of Fluvial Deposits of the Reservoir Interval of Bentiu Formation (Albian–Cenomanian) Muglad Basin Sudan

Ahmed Ali Hassan Taha, Abdul Hadi Abd Rahman
and Wan Ismail bin Wan Yusoff

Abstract This paper discusses the application of wireline logs in the determination of depositional environment. A suite of wireline logs from the well A38 is collected from the Ministry of petroleum in Sudan and consists of GR, SP, R, Rs, RMSL, CNC, ZDEN, and DT, which comprise the materials for this study. Petrel software was used to display these logs. Bentiu formation which is a main reservoir interval in the well A38 is the main target of this study; it is divided into Bentiu I, Bentiu 2, and Bentiu 3. Wireline log signatures and lithology log show that these intervals composed mainly of sandstone intercalated with mudstone and siltstone. The sandstones rang in grain size from fine to coarse, predominantly medium grains, and GR signatures show coarsened-up and fining-up patterns indicating fluvial deposit. GR pattern, neutron–density separation, resistivity, and sonic and lithology logs indicate the interval was deposited in a fluvial environment, mainly crevasse splay, flood plain, channel fill, and point bars.

Keywords Bentiu formation · Wireline log · Muglad basin · Fluvial deposits

1 Introduction

Bentiu formation is the main reservoir interval within the Muglad basin of the Sudan [1]. Muglad basin is the largest among the central African rift system members (CARS); part of it is situated in south of Sudan Republic and the other half situated in the North of the South Sudan Republic; it extends for about 1,200 km in its length and more than 300 km in its width; it trends northwest–southeast. Figure 1 shows the location of the Muglad basin.

A.A.H. Taha (✉) · A.H.A. Rahman · W.I.b.W. Yusoff
Geosciences Department, Universiti Teknologi Petronas, Tronoh, Malaysia
e-mail: Ahmedtaha75@yahoo.com

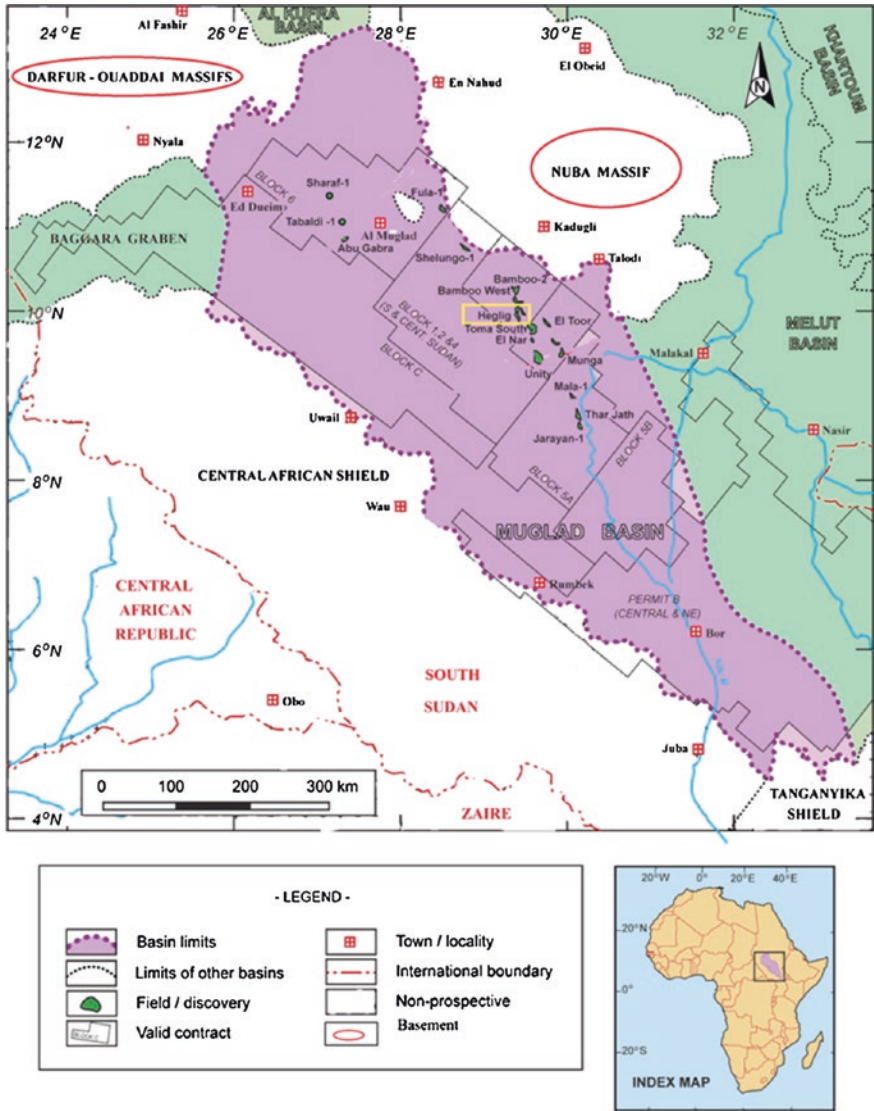


Fig. 1 Muglad basin location modified after IHS energy

Bentiu formation whose depositional environment was interpreted as fluvial environment represents the main reservoir interval of the Muglad basin, and it consists mainly of sandstones interbedded with claystones and mudstones.

The interpretation of wireline logs as subsurface techniques is now widely used in sedimentology. A wide range of physical parameters can be measured using different suites of tools lowered down a hydrocarbon exploration borehole.

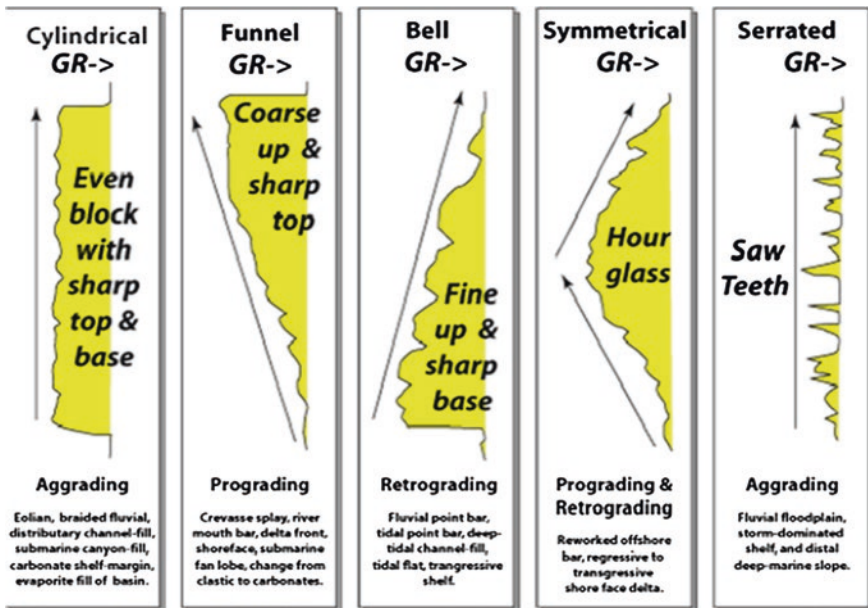


Fig. 2 Environmental interpretations of gamma log patterns (after Sanchez and Le Roux [6]) (base on Cant 1992)

These give information on lithology, porosity, oil, and water saturation [2–4]. Depositional environment and facies could also be inferred from certain suites of wireline logs. Geophysical logs not only provide a complete vertical profile of the borehole, but also rapidly yield to the trained interpreter curve shapes and features representative of depositional facies. Some of these features include fining upward sequences, coarsening upward sequences, and uniform sequences which result from unique depositional processes. For example, gamma ray log shapes are often used by geologists to determine sandstone grain size, trends, and hence depositional environment and facies (Fig. 2).

This study uses a suite of well logs from well A38 in one of the largest oil fields in Muglad basin in Sudan; the log suite consists of gamma ray, resistivity, neutron, density, and sonic logs. The purpose of this study is to infer the different facies and to interpret the depositional environment along the reservoir interval of Bentiu formation of the Muglad basin.

2 Materials and Methods

A gamma ray, resistivity, neutron, density, and sonic are the principle logs collected from the Ministry of Petroleum in Sudan in the form of LAS files and comprise the core materials for this study.

The LAS files are imported on selection into Petrel software for the display of the logs on Petrel first explorer window, after inserting a new well folder where LAS files are imported on selection. Gamma ray is a record of a formation's radioactivity; in its simple form, Gamma ray can be used to correlate, to suggest facies and sequences, and definitely to identify lithology (shaliness). Resistivity is the measurement of a formation's resistivity. Resistivity log is mainly used to find hydrocarbon, and it can also contribute to lithology, texture, facies, overpressure, and source rock aspects. Neutron log is principally a measure of formation water content; it is an important porosity indicator and also is a very good lithology indicator when accompanied with density log. The density log is the continuous record of formation's bulk density. Quantitatively, the density log is used to calculate porosity and indirectly hydrocarbon density. When combined with neutron

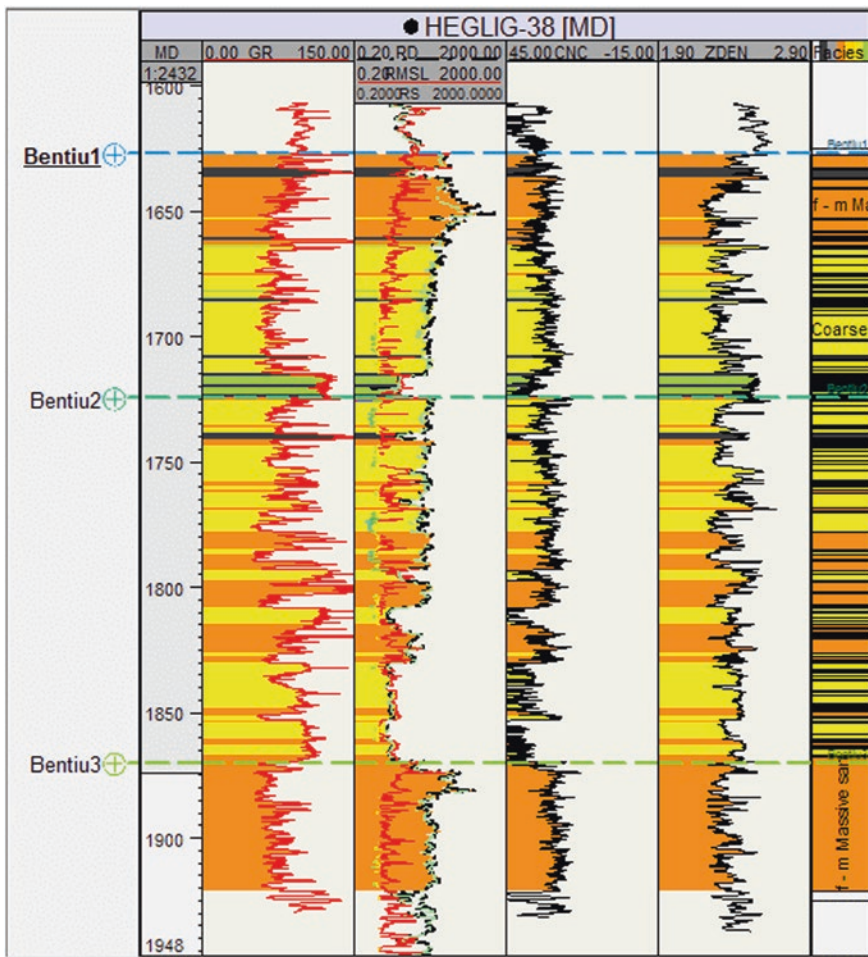


Fig. 3 Section shows well logs of the well A38 indicating well tops of Bentiu 2, Bentiu 2, and Bentiu 3

log, it gives a good lithology indicator. Finally, sonic log measures travel transit time of a formation. Quantitatively, the sonic log is used to evaluate porosity in a liquid-filled hole. For geologists, the sonic log is sensitive to subtle textural variations in both sands and shales. It can help to identify lithology and help to indicate source rocks.

3 Results and Discussion

The Bentiu formation comprises the main reservoir interval in the study area and is characterized by stacking successions of thick, amalgamated cross-bedded sandstones, and intervening extensive laterally thinner mudrock intervals, [5]. In well A38, Bentiu formation is considered to be the principle reservoir horizon; it consists of about 302-meter-thick pile of non-marine sediments, mainly sandstone interbedded with siltstones and claystones. Well tops Bentiu 1, Bentiu 2, and Bentiu 3 are well documented on the well (Fig. 3).

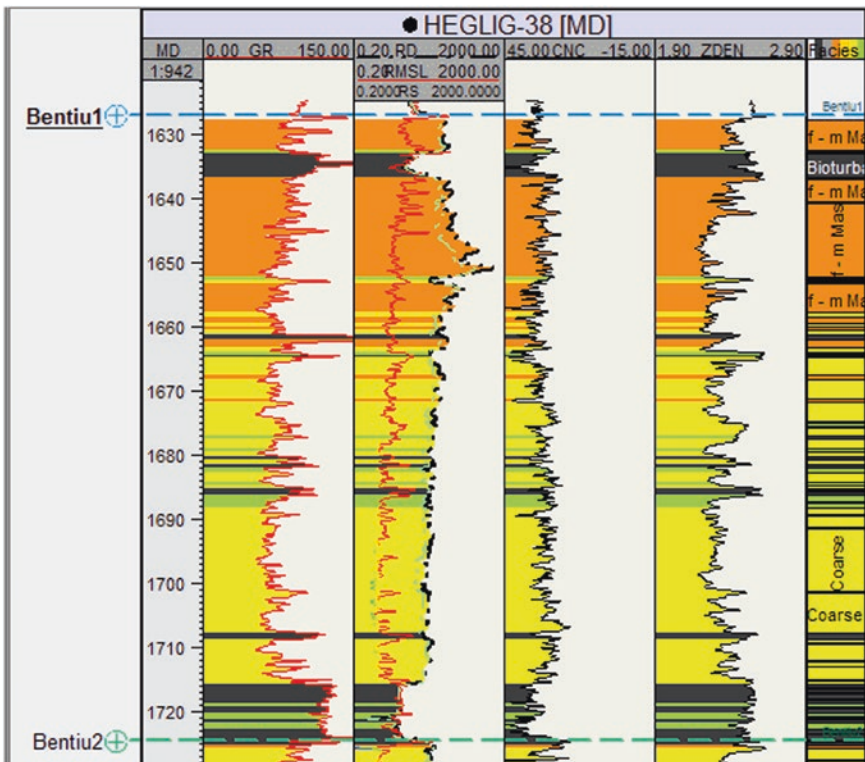


Fig. 4 Section shows Bentiu 1 interval

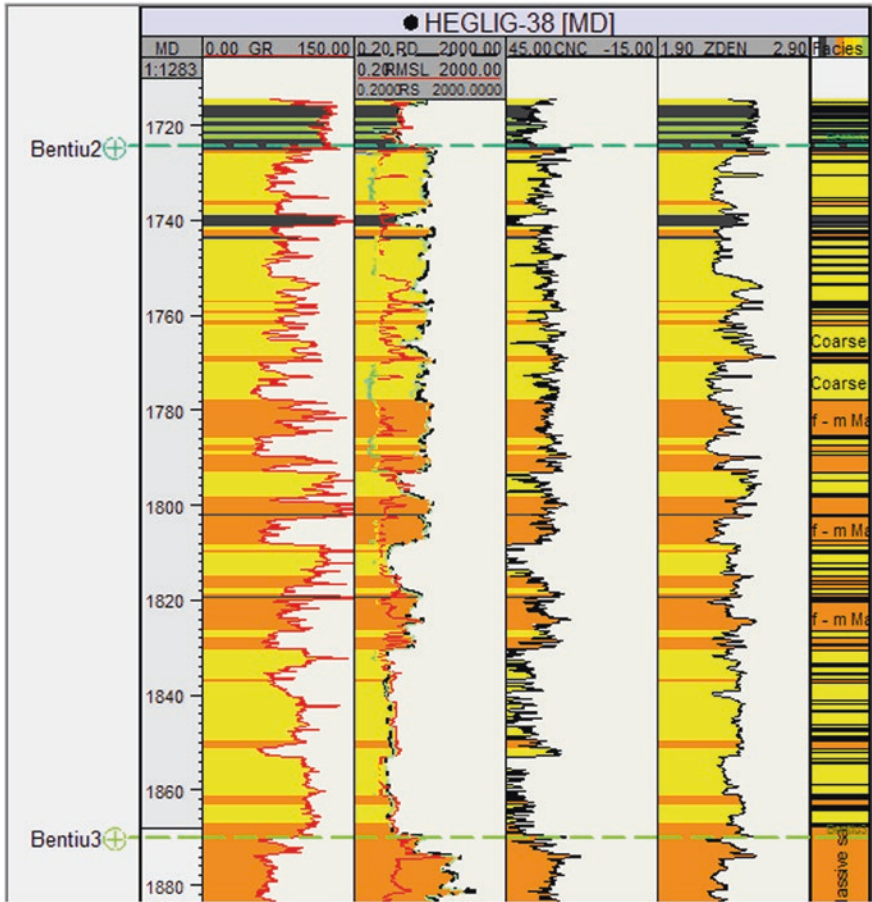


Fig. 5 Section shows Bentiu 2 interval

Bentiu 1 consists of about 96-meter-thick sandstone with minor intercalation of siltstone and claystones; the sandstone ranges in grain size from coarse, medium to fine grains; majority is medium grains. The intercalation of shale is mainly concentrated in the lower part having a thickness of about 14 m; this clearly manifested in high GR readings and very large separation of neutron–density logs and low resistivity readings. Generally, GR shows low to medium readings, indicating the presence of clean sandstone that conformed with neutron–density curve falling close to each other, but at some intervals, high GR readings are recorded, indicating the presence of shale that conformed with large separation of neutron–density log and constant resistivity log. GR shapes show coarsening upward sequences as well as fining upward sequences, indicating crevasse splay and point bar fluvial environment, respectively, Fig. 4 shows Bentiu 1 section with a suite of logs comprising of GR, SP, R, Rs, RSL, CNC, ZDEN, DT, and lithology logs.

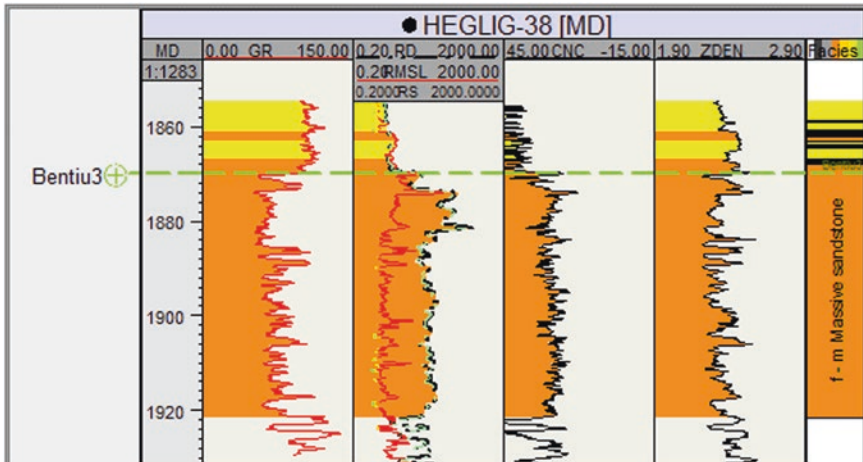


Fig. 6 Section shows Bentiu 3 interval

Bentiu 2 consists of about 146-meter-thick sandstone interbedded with shale; the sandstone ranges in grain size from fine to medium, occasionally coarse grained, and predominantly medium grained; the shale intercalation is predominant in different parts of the section indicated by the high GR value conformed with wide separation of neutron–density logs and low resistivity readings; GR shows fining upward pattern in most parts of the section, indicating deposition in crevasse splay or flood plain environment. Figure 5 shows Bentiu 2 section with a suite of logs comprising of GR, SP, R, Rs, RMSL, CNC, ZDEN, DT, and lithology logs

Bentiu 3 consists of about 60-meter-thick sandstone interval, mostly medium grained and occasionally coarse grained and intercalated with minor shales. GR signature mostly shows coarsening up pattern that is clear from the low GR readings and conformed with neutron–density curves falling close to each other and high resistivity readings; this indicates depositional environment along channel as a channel fill or point bar. Figure 6 shows Bentiu 3 section with a suite of logs comprising of GR, SP, R, Rs, RMSL, CNC, ZDEN, DT, and lithology logs.

4 Conclusion

Bentiu formation is a main reservoir interval in the well A38, it has a thickness of 302 m, and it consists of Bentiu 1, Bentiu 2, and Bentiu 3, and all of them being deposited in a fluvial environment. Bentiu 1 has a thickness of 96 m and mainly consists of medium-to-fine grain sandstone, occasionally coarse grain, and predominantly medium grain. GR shapes show coarsening upward sequences as well as fining upward sequences. GR, neutron–density, and resistivity signatures indicate crevasse splay or point bar fluvial environment. Bentiu 2 comprises about

146 m of thick sandstone interbedded with shale. The sandstone range in grain size from fine to medium, occasionally coarse grained, and predominately medium grained; the shale intercalation is predominant in different parts of the section. High GR values conformed with wide separation of neutron–density logs and low resistivity readings; GR shows fining upward pattern in most parts of the section, indicating deposition in crevasse splay or flood plain environment. Bentiu 3 consists of about 60-meter-thick sandstone interval, mostly medium grained, occasionally coarse grained, and intercalated with minor shales. GR signature mostly shows coarsening upward pattern that is clear from the low GR readings and conformed by neutron–density curves falling close to each other and high resistivity readings; this indicates depositional environment along channel as a channel fill or point bar.

Acknowledgment The author likes to thank Ministry of Petroleum (Sudan) for providing data for this study. Thanks is due to university Teknologi Petronas for providing the opportunity for this work to be published.

References

1. T. J. Schull, "Rift basins of interior Sudan: petroleum exploration and discovery," *AAPG bulletin*, vol. 72, pp. 1128-1142, 1988.
2. D. J. Cant, "Subsurface facies analysis. In Facies Model (Ed.by R.G. Walker)." *Geoscience*, pp. 195–218, 1992.
3. P. A. Allen, JR, "Basin analysis: Principles and applications, 1990," *British Petroleum Company pic., London*, 1990.
4. D. Emery and K. Myers, "Sequence stratigraphy, 1996," *London, Uxbridge*, p. 297.
5. A. Yagoub, "Structural and Stratigraphical Significance of Reservoirin Heglig Field (Sudan)," *Journal of Science and Technology*, vol. 11, p. 2, 2010.
6. J. A. Sanchez and J. P. Le Roux, 2003, Mesozoic sedimentation on an isolated platform at the eastern entrance to the Strait of Magellan, Tierra del Fuego (Chile). *Revista geológica de Chile*, 30(2), pp. 143–157.

Construction in Terrain with Subsurface Karstic Limestone Bedrock

Chow Weng Sum, A.H. bin Abdul Rahman, Khor Wei Chung and Solomon Kassa

Abstract About 80 % of the Kinta Valley and 40 % of the Kuala Lumpur area, both of which are densely populated, are underlain by limestone bedrock. Dissolution of the limestone bedrock by the slightly acidic rainwater which seeps into the bedrock along discontinuities gives rise to a subsurface karstic morphology with features like steep pinnacles and deep troughs, overhangs, boulder floaters, an intricate network of cavities beneath the bedrock surface and sinkholes. At the interface between the bedrock and the overlying soil, there is a pocket of very soft, compressible soil with zero SPT value. All these features and characteristics pose a big challenge to engineers in the design of foundation of buildings. To obtain a comprehensive profile of the karstic bedrock, it would be prudent to conduct an integrated geophysical survey utilizing georadar, seismic and resistivity methods complemented with a few boreholes for ground truthing.

Keywords Buried karsts · Geotechnical problems · Karstic features · Kinta Valley · Kuala Lumpur

1 Introduction

About 80 % of the Kinta Valley (Fig. 1) and 40 % of the Kuala Lumpur (Fig. 2) area, both of which are densely populated, are underlain by limestone bedrock [1, 2]. Due to the humid tropical climate in Malaysia, the rainfall is slightly acidic, and when

C.W. Sum (✉) · A.H. bin Abdul Rahman · K.W. Chung · S. Kassa
Universiti Teknologi PETRONAS, Tronoh, Malaysia
e-mail: chow_wengsum@petronas.com.my

A.H. bin Abdul Rahman
e-mail: hadi_rahman@petronas.com.my

K.W. Chung
e-mail: weichung.khor@petronas.com.my

S. Kassa
e-mail: solkas4@gmail.com

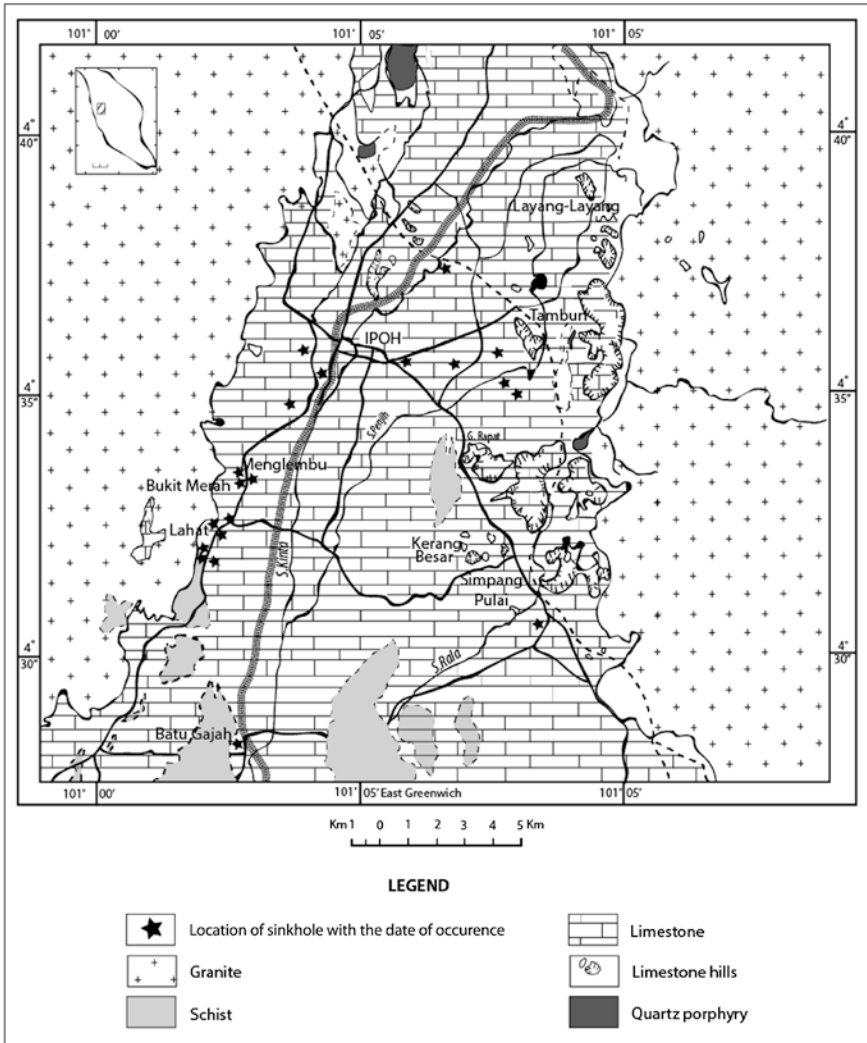


Fig. 1 Geology of the Kinta Valley [1]

it seeps into the ground, the limestone bedrock undergoes natural dissolution which gives rise to a karstic landscape characterized by steep cliff faces which formed sub-vertical pinnacles and deep troughs. These karstic profiles pose a lot of problems to engineers when the foundation for a building is being designed and in rare cases, the layout of the building has to be re-sited.

Subsurface karstic features which pose problems to the design of foundation include overhangs, narrow pinnacle tops, boulder floaters and cavities just beneath the bedrock surface [3].



Fig. 2 Geology of the Kuala Lumpur area [3]

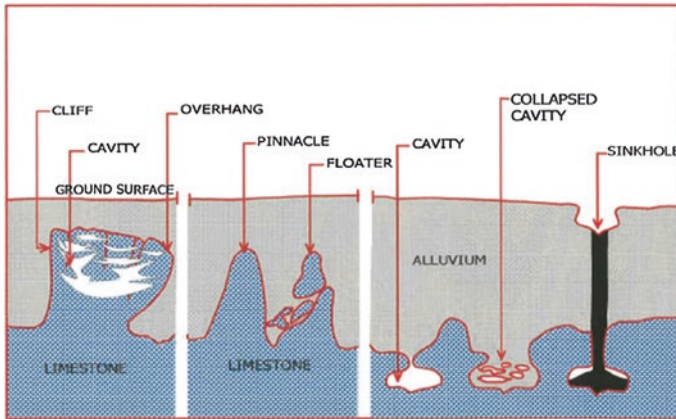


Fig. 3 Some features of karstic limestone bedrock [3]

2 Karstic Features of Buried Karsts

The acidic surface run-off which seeps into the soil cover and thence to the bedrock would seep along planes of weaknesses such as joints, faults and sheared zones. Dissolution of the limestone bedrock along these discontinuity planes often results in the formation of karstic features such as steep pinnacles and deep troughs. Other features which can be found include overhangs, boulder floaters and cavities with thin roofs just below the bedrock surface or collapsed roofs over sinkholes (Fig. 3).

3 Geotechnical Problems Posed by Subsurface Karstic Features

The karstic features mentioned above may pose severe geotechnical problems to engineers in their design of foundation for civil structures. The foundation of buildings which often rests on concrete or steel piles is driven to rest on the karstic bedrock. Piles which are driven may be founded on the tips of pinnacles. Over time, these piles may slip. Piles which are founded on the steep sides of the pinnacles may suffer deviation. Piles which are founded over or close to sinkholes may experience settlement problems and may fall into or drag towards the sinkhole. Piles which are founded on overhangs may experience an overhang failure where the overhang may detach from the main rock body [4]. Piles founded on top of the boulder floaters may suffer settlement problems if the soil beneath the floaters has low bearing capacities.

4 Soil Over Limestone Bedrock

The strength of the soil overlying the karstic bedrock depends on its inherent characteristics such as its intensity of compaction and its degree of friction, its grain size and cohesion, density and moisture content. Standard penetration tests (SPT) conducted on the soils would invariably record some degree of bearing strength, varying from low to high, unless the soil is composed of slime, where its SPT value is zero [5] as may be the case if the soil is a by-product of the tin mining activities. However, in terrain underlain by limestone bedrock, a peculiar phenomenon is observed whereby just above the karstic bedrock surface, there is always a pocket of very weak, compressible soil, with some reaching up to 15 m thick. This pocket of soil has zero SPT value, meaning that the SPT rod would sink under its own weight. Piles which found on the more compact soils above this pocket of very weak soil may experience some degree of settlement [3].

5 Zone of Cavities Beneath Surface of Limestone Bedrock

Compilation of borehole data in the Kinta Valley and Kuala Lumpur area has shown that cavities and caverns invariably are found in the limestone bedrock. This attests to the solubility of limestone in even slightly acidic waters. In areas where the limestone is dolomitized, there are less cavities as dolomite is not soluble in acidic waters. Cavities in limestone bedrock are a major concern of engineers when planning or designing the foundation of buildings. These cavities may occur at various depths and are of various sizes. Borehole data assessment in the Ipoh area in the Kinta Valley showed that the cavities are mostly less than 3 m in size [6]. A majority of the cavities are less than 1 m in size. The formation of these cavities is affected by the fluctuations of the groundwater table. It was observed that the cavities are developed mostly within the zone of groundwater fluctuation. As such, it would be reasonable to assume that below the lowest groundwater level, there would be little or no cavities. Such an assumption may be proven if a comprehensive and systematic analysis of all the existing borehole data is carried out.

If the piles rest over a thin roof with cavities beneath the bedrock, only limited loads may be supported by the roof. Even if a single pile can be supported safely on this thin roof, the rock slab may still fail if there are a number of piles founded on the top of the roof simultaneously.

6 Detection of Subsurface Karstic Profile

Studies of subsurface limestone bedrock profile in the Kinta Valley and Kuala Lumpur area showed that it is not uncommon to have more than one karstic feature such as pinnacles, troughs, overhangs, boulder floaters, sinkholes and cavities

at a site. The profile may change drastically, with pinnacles plunging a height of 50 m within a short distance to form troughs. As such, it is not easy to interpret bedrock profile from borehole records unless there are sufficient boreholes within the site. There are suggestions to have drill holes spaced as close as 10–15 m apart in order to have a comprehensive bedrock profile. However, the cost for such implementation would be astronomical. A better and cheaper solution would be to utilize a combination of geophysical techniques such as, georadar, microgravity, transient electromagnetic, seismic and resistivity to get the bedrock profile and drilling a few boreholes for ground truthing [1].

7 Conclusion

The complex subsurface karstic profile of limestone bedrock poses a challenge to engineers in the design of foundation for buildings. The karstic profile may exist as steep pinnacles, overhangs, boulder floaters, or may have a network of cavities just beneath the bedrock surface. The existence of a pocket of very soft, compressible soil with zero SPT values near the interface between the limestone bedrock and the overlying soil makes it a challenge in foundation design as due consideration for settlement has to be accorded.

To obtain a comprehensive karstic bedrock profile, it would be prudent to utilize a combination of geophysical techniques such as georadar, seismic and resistivity followed by having a few boreholes for ground truthing.

References

1. Chow Weng Sum, Jamaludin Othman & P. Loganathan., 1995. Geotechnical Problems in Limestone Terrain With Emphasis On Cavities And Sinkholes. Minerals & Geoscience Department Unpublished Report E(F) 7/95
2. Yeap Ee Beng, 1985. Irregular Topography Of The Subsurface Carbonate Bedrock In The Kuala Lumpur Area. Proceedings of the Eighth Southeast Asian Geotechnical Conference, pp 4-1 to 4-12
3. Chan, S.F. & Hong, L.P., 1985. Pile Foundations In Limestone Areas Of Malaysia. Proceedings of the Eighth Southeast Asian Geotechnical Conference, pp 4-17 to 4-28
4. Mitchell, J.M., 1985. Foundations For The Pan Pacific Hotel On Pinnacled And Cavernous Limestone. Proceedings of the Eighth Southeast Asian Geotechnical Conference, pp 4-29 to 4-44.
5. Chow Weng Sum., 1998. Studies Of Slurry Slime In Mined-Out Ponds, Kinta Valley, Peninsular Malaysia, For The Purpose Of Reclamation. Universiti Malaya Unpublished PhD Thesis.
6. Tan Boon-Kong., n.d. Environmental Geology Of Limestone In Malaysia. Unpublished Report.

Evaluation of Pore Network Variation in a Carbonate Rock from Onshore Sarawak, Malaysia

S. Andriamihaja and E. Padmanabhan

Abstract Due to its heterogeneities, the evaluation and characterization of carbonate reservoir rocks are always challenging in the petroleum industry. Therefore, in order to optimize the recovery of hydrocarbons in carbonate reservoirs, the pore network needs to be properly understood. In this research, 282 digital thin sections from computer tomography (CT) scan of carbonate rock from Subis Limestone in Sarawak were processed and analyzed in order to determine pore type variation, pore size, pore shape, pore distribution, and pore connectivity. The studied core plug of limestone shows vuggy pores with an average porosity of 9.25 % varying from 5.98 to 12.3 % within the 282 slices. This results show that using 3D CT scan modeling enhances the accuracy of pore classification and pore quantification as large amount of input data are used leading to more reliable output.

Keywords Carbonate pore networks · CT scan · Porosity

1 Introduction

In the petroleum industry, clastic and carbonate rocks are the main reservoir types in most of the world's hydrocarbon fields. Based on Schlumberger market analysis in 2007 [1], 60 % of world oil and 40 % of world gas are in carbonate reservoir types. The reservoir properties of carbonates are more challenging to predict and to define than clastic reservoir as they are formed by biological precipitation under marine conditions [2–4]. This formation of carbonate rock and the diagenetic effect leads to heterogeneities and complexities of the rock fabrics and their pore systems.

S. Andriamihaja · E. Padmanabhan (✉)
Department of Geosciences, Universiti Teknologi PETRONAS, Tronoh, Malaysia
e-mail: Eswaran_padmanabhan@petronas.com.my

Choquette and Pray [5] developed a pore type classification related to sedimentological fabric using optical thin section. Another pore classification that is widely used was developed by [6–8] based on thin section analysis. In 1995, [7] defined two pore types which are interparticle pore space and vuggy pore space. The first category is based on fabric (grain size, sorting, crystals), whereas the second category is based on vug interconnectivity. Compared to Choquette and Pray classification, this system takes into account mainly the pore geometries and flow parameters within the reservoir.

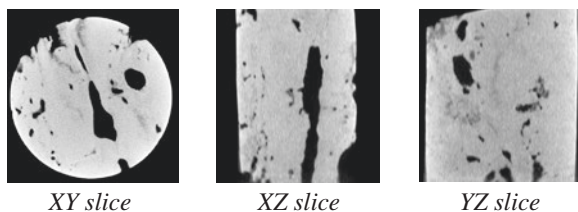
Recently, [9] developed a new pore type classification system based on previous pore classification systems which combine sedimentological, diagenetical features and flow-related properties. As the research on carbonate evolves through time, [10] developed a carbonate rock classification based on rock contents (grain, mud, and cement) and pore geometries in order to use it in pore-scale modeling.

In terms of quantitative analysis of pore system within the carbonate rocks, [11] developed a new method to quantify the macro- and microporosity of carbonate pore system. [12] used the techniques of thin section, pore–permeability relationship, and pore throat size and distribution in order to characterize the heterogeneity of carbonate reservoir in South East Kuwait.

With the evolution of technology, [13] have reviewed the development of X-ray CT scan as a geoscience tool. Arns et al. [14] characterized pore systems in carbonate sample using μ CT scan. Knackstedt et al. [15] and Abraham et al. [18] used pore network model of carbonate sample from μ CT at low and high resolutions and combined them with MICP to predict petrophysical and productivity properties. Youssef et al. [16] combined analysis and the partitioning pore space method on sandstone and carbonate, in order to describe the geometry and the topology of pore network. Vik et al. [17] characterized vuggy carbonates in order to establish a basis for estimating fluid flow and oil recovery efficiency in the rock type. Qajar et al. [19] have used μ -computed tomography images to analyze qualitatively and quantitatively the evolution of meso/micropores of carbonates caused by chemical dissolution.

These previous researches on carbonate pores and the technology used to evaluate the pores raise the issue of pore configuration variation in 3D (Fig. 1). μ CT scan and the derived pore networks have mainly been used in multiphase flow modeling and simulation of hydrocarbon. In order to optimize the recovery of hydrocarbon within carbonate reservoir, the pore network behavior and development need to be understood. Therefore, this research seeks to investigate pore network variation in all spatial directions.

Fig. 1 Change in pore configuration in three different directions



2 Materials and Methods

The sample used for this study is carbonate rock collected from Subis Limestone Formation in Balingian Province in Sarawak basin. This carbonate rock is formed in shallow marine environment as an extensive reef [20], caused by an uplift during Early Miocene [21]. A core plug of 2.5 cm diameter and 3.5 cm length from main sample is scanned with InSpeXio Microfocus CT system.

Pore individualization and analysis consist of extracting the pore systems from the material, using the threshold value defined earlier. The pore analysis approach can be subdivided into two categories:

- Qualitative pore analysis which includes pore type classification and pore shape. This analysis is carried out by using the classification developed by [7]. This classification is used because it is more descriptive and takes into account the pore size distribution controlling the permeability and the saturation.
- Quantitative pore analysis including total porosity and pore size.

3 Results and Discussion

3.1 Qualitative Analysis

3.1.1 Pore Classification

By individualizing the pore system from the matrix (grains and cements), 253 individual pores are identified (Fig. 2a). Based on Lucia classification, the analysis of pore space slice by slice through 282 slices in XY plane shows that most of these individual pores are touching vuggy pores because they are larger than the grain size and form an interconnected pore system. The pore type of the sample is mainly “solution-enlarged fracture” type within the three axes (X; Y; Z) (Fig. 2b). From a series of slices of core plug sample, pore classification can be done accurately as several digital slice images are involved in the analysis. The dominant

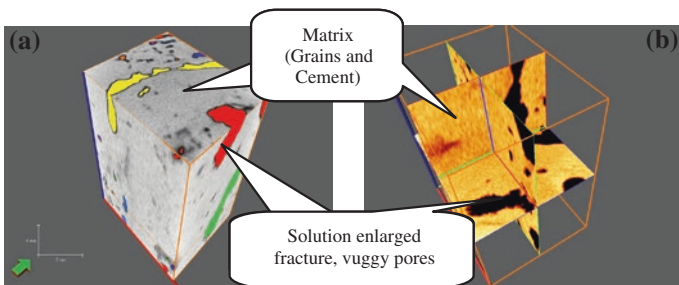


Fig. 2 a 3D model showing individual pores and b X, Y, Z random slice showing pore type

pore type is defined by the number of slices with the dominant pore being the pore type that is dominant for each slice.

3.1.2 Pore Shape Development

The shape development of vuggy pores is studied along XY , XZ , and YZ planes. Within XY plane, there is an irregular variation of the pore as the number of slice increases along the Z -axis. From slice 105, the pore starts to be split into three smaller pores (Fig. 3 a, b and c).

Within YZ plane, three different pores are identified with different and irregular shapes in slice 90 (Fig. 4a). In slice 92 (Fig. 4b), as the slice number varies parallel to X -axis, the circular shape of pore 1 does not change. However, after 2 slices (Fig. 4b), the elongated pore 2 is closed (Fig. 4c), whereas the single pore 3 is split into four irregular pores.

3.1.3 Pore Connectivity

The analysis of pore connectivity for each slice within the carbonate core plug shows that the pores are poorly distributed and connected within 2D plane. It is observed that the pores are connected in all directions (Fig. 5). The analysis shows that among 253 studied vuggy pores, 104 pores are connected based on the defined threshold length value of 10 mm.



Fig. 3 Pore shape variation within XY plane at **a** slice 100; **b** slice 105; and **c** slice 110

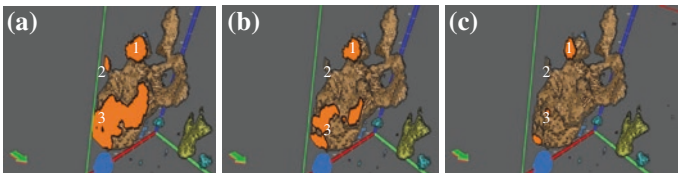


Fig. 4 Pore shape variation within YZ plane at **a** slice 90; **b** slice 92; **c** slice 94

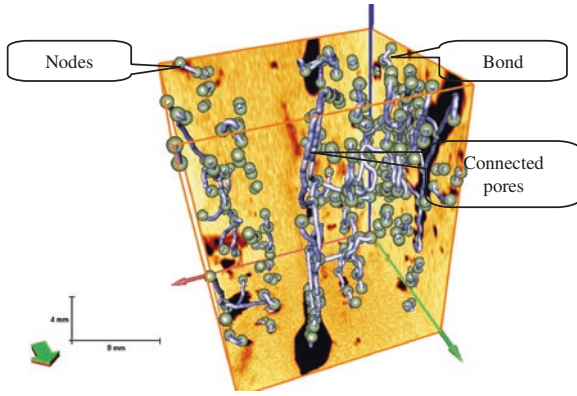


Fig. 5 Variation in connectivities of pores in 3D

3.2 Quantitative Analysis

3.2.1 Porosity Calculation

The porosity of the core plug sample varies from 5.98 % in slice 170 (Fig. 6a) to 12.3 % in slice 281 (Fig. 6b) with an average of 9.06 %. As observed from porosity distribution (Fig. 7) within the 282 slices, the porosity varies significantly from slice to slice.

Compared to porosity obtained from routine thin section, the porosity from digital image is more reliable due to the large amount of digital thin sections used to deduce the porosity.

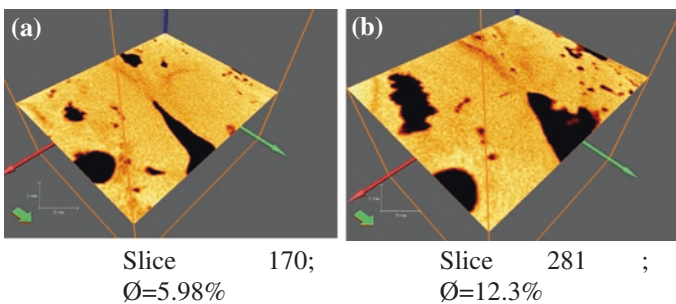


Fig. 6 Porosity variation between slices. a Slice 170; $\varnothing = 5.98\%$, b. slice 281; $\varnothing = 12.3\%$

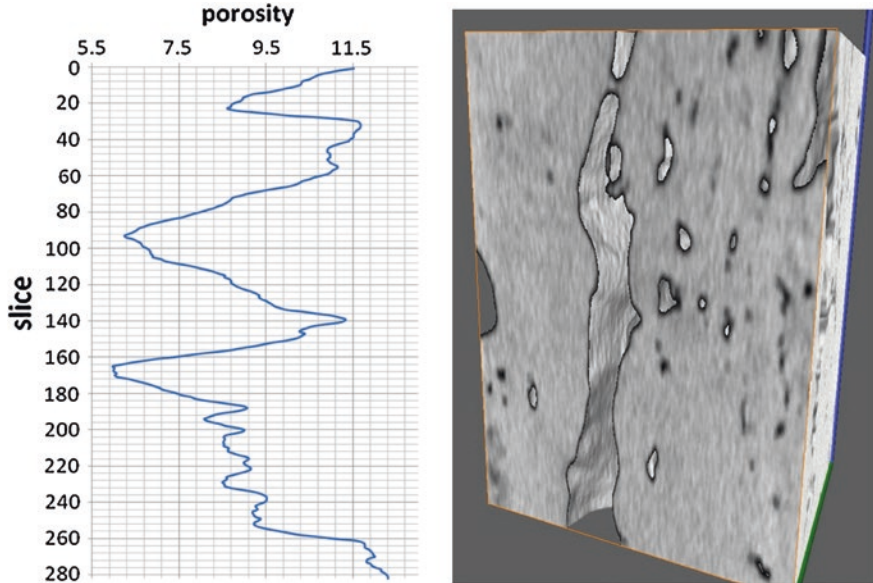


Fig. 7 Calculated porosity variation with depth in the core plug

4 Conclusion

3D modeling and analysis using CT scan is a complementary method to evaluate carbonate pore network. From the results, we can conclude that using the CT scan method to classify the pore type is more accurate because large amount of digital thin sections (282 slices) can be used compared to routine thin sections. Every slice of the carbonate core plug sample shows a dominance of touching vuggy pores (solution-enlarged fracture) based on Lucia's classification. These pores have irregular shapes and develop randomly in all directions from slice to slice and plane to plane.

Acknowledgments This study is supported through a YUTP grant awarded to Dr. Eswaran Padmanabhan.

References

1. Schlumberger, 2008. Carbonate reservoir, Meeting unique challenges to maximize recovery, Schlumberger, pp 1–16
2. Milliman, J. D., 1974a. Marine Carbonates. Springer-Verlag Berlin, 375 pp.
3. Wilson, J. L., 1975. Carbonate Facies in Geologic History. Springer-Verlag New York, 471 pp.
4. Sellwood, B. W., 1978. Shallow-water carbonates environments. In: H. G. Reading (Ed.), Sedimentary Environments and Facies. Elsevier New York, pp. 259–313.

5. Choquette, P. W., and L. C. Pray, 1970, Geologic nomenclature and classification of porosity in sedimentary carbonates: AAPG Bulletin, v. 54, no. 2, p. 207–250.
6. Lucia, F. J., 1983. Petrophysical parameters estimated from visual descriptions of carbonate rocks: A field classification of carbonate pore space: Journal of Petroleum Technology, v. 216, p. 221–224.
7. Lucia, F. J., 1995. Rock-fabric/petrophysical classification of carbonate pore space for reservoir characterization: AAPG Bulletin, v. 79, no. 9, p. 1275– 1300.
8. Lucia, F. J., 1999. Carbonate reservoir characterization: Berlin, Springer-Verlag, 226 p.
9. Lønøy, A. 2006. Making Sense of Carbonate Pore Systems. AAPG Bull. 90 (9): 1381-1405.
10. Mousavi, M., Prodanović, M., Jacobi, D., 2013. New Classification of Carbonate Rocks for Process-Based Pore-Scale Modeling : SPE Journal (SPE 163073) p243-263
11. Anselmetti, F.S., Luthi S., and Eberli G.P., 1998. Quantitative Characterization of Carbonate Pore Systems by Digital Image Analysis: AAPG Bulletin, V. 82, No. 10, P. 1815–1836.
12. Turkey, S., Al –Kanderi J., Kumar, P., Al –Alawi, G., Al –Hashmi, S., Al –Harthy, A., Al –Raisi, M., 2012. Rock Typing and Characterization of Carbonate Reservoirs: A case Study from South East Kuwait., paper SPE 163294, presented at SPE International Petroleum Conference and Exhibition, Kuwait
13. Kayser, A., Knackstedt, M., Ziauddin, M., 2006: A Closer Look at Pore Geometry, Oilfield Review p 4-13
14. Arns C.H., Limaye A., Sakellariou A., Senden T.J., Sheppard A.P., Sok R.M., Pinczewski W.V., Bakke S., Berge L.I., Øren P.-E., Knackstedt, M.A., 2004,. Pore Scale Characterization using X-ray microtomography, SPE. pp 1-11.
15. Knackstedt, M.A., Arns, C. H., Ghous, A., Sakellariou, A., Senden, T. J., A.P. Sheppard, A.P., Sok, R. M., Nguyen, V., Pinczewski, W. V., 2006 : 3D imaging and characterization of the pore space of carbonate core; implications to single and two phase flow properties, SPWLA 47th Annual Logging Symposium, p1 -15.
16. Youssef S., Rosenberg E., Gland N., Bekri S., Vizika O. (2007a) Quantitative 3D characterisation of the pore space of real rocks: improved μ -CT resolution and pore extraction methodology, *Paper SCA 2007-17* presented at the International symposium of the Society of Core Analysts, Calgary, Canada, 10-12 September.
17. Vik, B., Djurhuss, K., Spildo, K., Skauge, A., 2007: Characterization of vuggy carbonates, SPE /EAGE Reservoir Characterization and Simulation Conference, Abu Dhabi, SPE 111434, p1-9.
18. Abraham S., Clark B.S., Taha Al – Dayyaani, Amos Nu, 2009: Computations of porosity and permeability of sparic carbonate using multi-scale CT images, prepared for International Symposium of the Society of Core Analysts.
19. Qajar, J., Francois, N., Arns, C.H., 2013: Microtomographic Characterization of Dissolution-Induced Local Porosity Changes Including Fine Migration in Carbonate Rock, SPE Journal, p 545 - 562.
20. Tjia, H.D., 1999: The Petroleum Geology and Resources of Malaysia, Chapter 26, p 628.
21. Madon, M.B.Hj., Abolins P.,1999: The Petroleum Geology and Resources of Malaysia, Chapter 14, p 349.

Comparison of Different Rock Physics Models to Evaluate the Impact of Pore Types on Velocity—Porosity Relationship in Carbonates of Central Luconia Sarawak

Luluan A. Lubis, Sara Bashah and Deva P. Ghosh

Abstract It has been documented that carbonate contributes to the most hydrocarbon resources worldwide. For rigorous reservoir characterization and performance prediction from seismic, the exact interpretation of geophysical response of different carbonate pore types is crucial. In this study, we test a number of empirical models, such as the Wyllie time-average and Raymer's velocity-porosity equation, as well as physics-based effective-medium models, such as differential effective-medium theory, against the published datasets from Central Luconia. We find that for certain ranges of inclusion concentration and porosity, the empirical equations (Wyllie's and Raymer's) fail. At the same time, an effective-medium model, such as differential effective medium (DEM), appears to be consistently valid if the aspect ratio is selected appropriately and then held constant for the entire concentration or porosity range. The intention of this work is to set a consistent rigorous foundation for modeling of the elastic properties of carbonate rocks, with the ultimate goal of consistent interpretation of log and seismic data for carbonate rock properties and texture.

Keywords Carbonate · Elastic properties · Pore types · Rock physics models

1 Introduction

The Central Luconia Province is an broad and stable continental shelf, characterized by extensive development of Late Miocene carbonates. About 56 carbonate buildups are proven to contain commercial quantities of non-associated gas in carbonate reservoirs. The Central Luconia Province contains about 40 % of the total non-associated gas reserves of Malaysia [1].

L.A. Lubis (✉) · S. Bashah · D.P. Ghosh
Geosciences Department, Universiti Teknologi PETRONAS, Tronoh, Malaysia
e-mail: luluan.lubis@gmail.com

As distinct from sandstones, in carbonate systems, the combined effect of variations in depositional facies, rock texture, mineralogy, and diagenetic alteration plays a key role in controlling the variations in sonic velocities and acoustic impedance, which makes the seismic response of these rocks hard to interpret and understand [2]. Carbonate pore types are considered the key factor causing significant variations in permeability and elastic properties [3].

This paper seeks to analyze the published laboratory measurements data of elastic properties on reservoir carbonate samples in offshore Sarawak [2] and evaluate the appropriate rock physics models that can be possibly used in log analyses and quantitative seismic interpretation. In this study, we test a number of empirical models, such as the Wyllie time-average and Raymer's velocity-porosity equation, as well as physics-based effective-medium models, such as differential effective-medium theory, against the published datasets from Central Luconia.

2 Methodology

2.1 Empirical Relationships

On the elastic properties of sedimentary rocks, laboratory measurements have often presented that simple empirical relationship can be used for describing the elastic properties. A P-wave transducer were arranged to measure V_p velocities. The approached of these relationships by a formula expressed below:

$$\frac{1}{V_p} = \frac{\phi}{V_{pf}} + \frac{1 - \phi}{V_{ps}}$$

where V_p is P-wave through the rock matrix, V_{pf} is P-wave through the pore fluid, and V_{ps} is P-wave through the mineral material, P-wave is from sonic velocity. The velocity is expressed on the formula:

$$V_p = \sqrt{\frac{(K + 4/3\mu)}{\rho}}$$

The explanation of the Wyllie formula is that the total passage or transit time is the total of the passage time of the elastic wave through the mineral and the passage time through the pore fluid. For this reason, the Wyllie is often described as the time-average equation.

The improvement of Wyllie's empirical equation for low porosities is suggested by Raymer et al. [7], which is expressed on the formula below:

$$V_p = (1 - \phi)^2 V_{ps} + \phi V_{pf}, \quad \phi < 37\%$$

2.2 Differential Effective Medium

The combined effect of variations in depositional facies and diagenetic alteration occurred during intense geological processes initiating carbonate rocks to develop wide variations of pore types, for example interparticle, intercrystal, moldic, vuggy, intraframe, and microcracks pore types [8]. Although this classification is useful for describing petrophysical properties, connecting these microstructures and trends toward studying geophysical responses and seismic inversion remains very challenging. From previous geoscientists' observation, normally, vuggy pores are very rigid and less affected by seismic wave propagation, while cracks are effective to reduce velocities in carbonates due to increased porosity [3]. Xu and White (1995) model for shaley sandstones can be extended to predict velocities in carbonate rocks, as demonstrated by Xu and Payne [9]. Following Xu and Payne's rock physics modeling approach for carbonates, the minerals present were modeled and mixed using Voigt–Reuss–Hill (VRH averages). Differential effective medium (DEM) scheme is used to calculate the dry (no fluid) bulk and shear moduli for altered geophysical pore types represented by the pore aspect ratio.

There are three (3) geophysical pore types used to abstractly represent or act for seismic velocities in carbonate rocks. The representative for these models is shown in Fig. 1: (a) the reference pore types, which deliberated as the main pore type in carbonate sedimentary rocks, the pore types considered as mainly of interparticle pores, (b) the stiff pore types, which deliberated as vuggy and moldic pore types, these type of pores formed as a result of fossil and grains chambers which were dissolved, (c) the cracks pore types, which can take place due to solution collapse, faulting and differential compaction in carbonate sedimentary rocks [9]. For the model, each individual pore type component is incrementally added to the rock matrix and used to calculate the elastic properties of the subsequent effective medium. The flexibility of the Xu-Payne model is the components of each individual pores can be included into

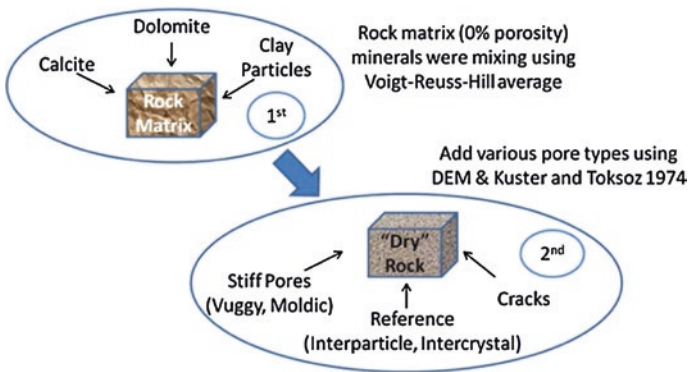
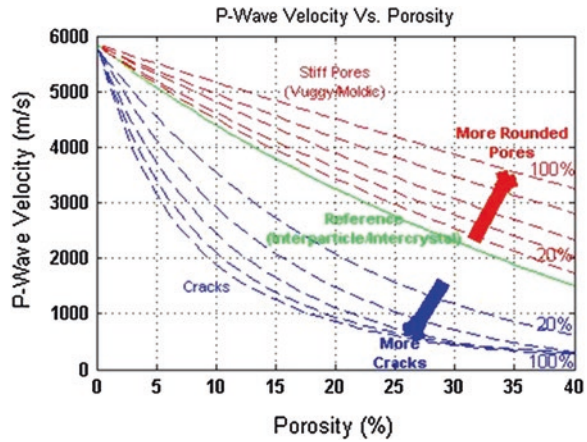


Fig. 1 DEM results for different percentage pore types on P-wave velocity

Fig. 2 DEM (modified from Xu et al. [3]) to build carbonate rock physics model in our study



the model such either that the pores are in perfect fluid connectivity with the remaining pore space, or the pores are isolated. The cross-plot of velocity with porosity is used to calibrate the pore space model created [9].

Figure 2 shows how we create our carbonate rock physics model on dry rock (no fluids). The first step is using a mixing law (the Voigt–Reuss–Hill average) to mix the minerals which are present in the rock. The dominant minerals for carbonate rocks are usually calcite and dolomite. Last step is to incorporate differential effective media theory and Kuster-Toksoz (1974) theory to include type of pores (Moldic, Interparticle, and Microcracks) and take into account the mechanical interaction between pores. The result of the calculation is the effective elastic properties of dry rock.

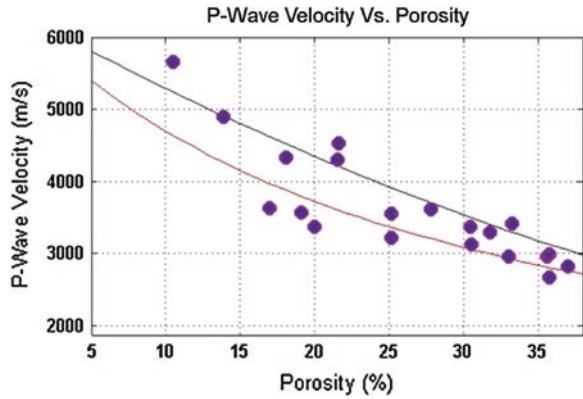
Figure 1 shows the predicted effect of pore type on P-wave velocity, and the reference line for mixed minerals which contains interparticle and intercrystal pore types is also incorporated on the plot.

On the figure above, the solid matrix was assumed with dominant mineral in calcite plus clay particles. The average Voigt–Reuss–Hill was used to calculate the minerals average of carbonate rocks for P-wave velocity. The reference represents a system with interparticle or intercrystal pore types. The curves below the reference curve represent systems with increasing percentage of cracks pore type. The curves above the reference curve represent systems with increasing percentage of stiff pore (vuggy/moldic).

3 Results and Discussions

The dataset is a velocity-porosity dataset for carbonate samples in offshore Sarawak [2]. Ultrasonic P-wave velocities were measured. A single P-wave velocities with a transducer arrangement that propagated V_p -waves. The ultrasonic pulse

Fig. 3 Purple dots are P-wave velocities from laboratory measurement [2]. Black and red lines are Raymer's and Wyllie's empirical relationship lines



produces a frequency around 800 kHz. In Fig. 3, we compare the measured V_p with the Wyllie's and Raymer's empirical relationship.

The velocity–porosity plot from laboratory measurement shows an inverse trend which the increasing of porosity produces a decreasing trend in velocity (Fig. 3). The laboratory measurement values show a scatter distribution around the inverse trend correlation in the diagram. The velocity differences at equal value of porosity is triggered by the ability of carbonates to form special fabrics with pore types, and cements can enhance the elastic properties of a carbonate rock without filling all the pore spaces. Consequently, measured velocities are higher than the velocity predicted by the time-average equation [5].

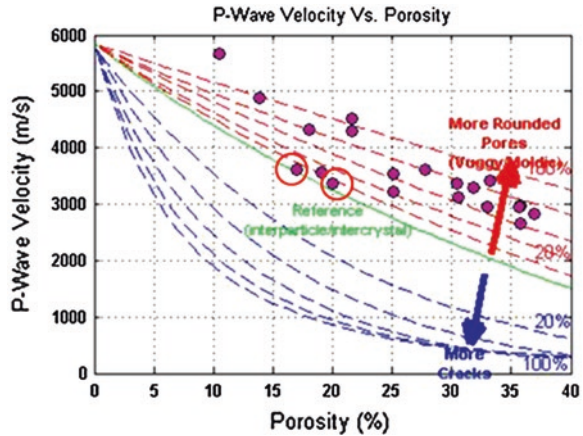
The interpretation of Wyllie's expression is that the total transit time is the sum of the transit time in the mineral (calcite and dolomite) plus the transit time in the pore fluid (water). The weak relationship between porosity and velocity in carbonates can be related to specific pore types resulting in different characteristic and elastic properties. At given porosity values, velocity shows different values.

Raymer's relationship which is the extended of Wyllie's over predicts most of the data in the whole range of porosity. From Fig. 3, we can see most of the dataset is below the Raymer's line.

On the last test, we compare the physics-based effective-medium models, DEM, with the experimental V_p dataset. We examined pore type effect on elastic properties and calibrate the pore geometry related parameters in effective-medium-based model.

Green line gives the best fit using Xu-Payne model with pore aspect ratio of 0.15. Red and blue dashed lines give the best fit with aspect ratio of 0.8 and 0.02, respectively. From the plot, we can observe that the dominant pore types from 20 core plugs (magenta dots) are stiff pores (vuggy/moldic). There are two data which, refer to red circles on Fig. 4, align with the reference plot (interparticle/intercrystal) pore types.

Fig. 4 Magenta dots are P-wave velocities from laboratory measurement [2]. Red and blue dashed lines indicate vuggy give the best fit with aspect ratio of 0.8 and 0.02, respectively



4 Conclusions

The purpose of the discussion put forward in this paper is to pay homage to the traditional rock physics velocity transforms by comparing them to rigorous effective-medium models. Both types of transforms are tested on carbonate dataset in offshore Sarawak to demonstrate the use of elastic properties and pore type classification prediction on carbonate rock. The traditional empirical relationship (Wyllie's and Raymer's) are somewhat still applicable for some fundamental analysis. Nevertheless, a rigorous inclusion theory, such as DEM, provides results that are applicable for the classification of the pore types in carbonate rock.

We use the DEM approach that takes into account three defined geophysical pore types and shown the possibility to bridge them to the bigger scale such as log and seismic responses. A more comprehensive study that includes more samples with various pore types and similar porosity values need to be carried out. This can be done (if the core samples are not available) on digital rock images of cuttings and sidewall core plugs which cannot be used to properly on the laboratory for measurement. This approach is practical, easily repeatable (in real time) and can be used as an alternative method when core plug is not available. The possibility to use this method on chips, cuttings, and rotary sidewall cores that routinely available from wells is also aligned to obtain elastic properties distribution information since these samples give good sampling intervals which almost cover whole depth of the wells.

Acknowledgments Paper for ICIPEG 2014 submitted on January 23, 2014. This work was supported in part by the 28/2012 University Research Internal Funding (URIF). We would like to acknowledge Shell Sarawak and Universiti Teknologi PETRONAS (UTP) for allowing us to work on this project. The data were provided by the SEACARL Laboratory in UTP.

References

1. Ali, M.Y. and Abolins, P., Central Luconia in The Petroleum Geology and Resources of Malaysia, 1999.
2. Bashah, N.S.I. and Pierson, B., Quantification of pore structure in a Miocene Carbonate Build-up Central Luconia, Sarawak and its relationship to sonic velocity, IPTC, Thailand, February 2012.
3. Eberli, G.P, Baechle G.T, Anselmetti, F.S and Incze, M.L., Factors Controlling Elastic Properties in Carbonate Sediments and Rocks, The Leading Edge, July 2003, p. 665–660.
4. Wyllie, M., Gregory, A., and Gardner, G., Elastic wave velocities in heterogeneous and porous media, *Geophysics*, 21, 41–70, 1956.
5. Wyllie, M., Gregory, A., and Gardner, G., An experimental investigation of factors affecting elastic wave velocities in porous media, *Geophysics*, 23, 459–493, 1958.
6. Wyllie, M., Gregory, A., and Gardner, G., “Studies of elastic wave attenuation in porous media”, *Geophysics*, 27, 569–589, 1963.
7. Raymer, L. L., Hunt, E. R., and Gardner, J. S., An improved sonic transit time to porosity transform, 21st Ann. Logging Symp., Soc. Prof. Well Log Analysts, paper P. 1980.
8. Lucia, F. J., Carbonate reservoir characterization, Berlin, Springer-Verlag, 1999, 226 p.
9. Xu, S. and Payne, M.A. Modeling elastic properties in carbonate rock, The Leading Edge, January 2009, p. 66-74.

Presence of Oleanane in Oil also as Evidence of Contamination

Swapan Kumar Bhattacharya, Syed Mohammad Ibad Mahmoodi
and Fawzia Hussein Ali Abdulla

Abstract Presence of oleanane in crude oil is now considered as the age indicator of source deposition assuming the biomarker has been migrated with oil from the source rock. Possibility of contamination of the same biomarker in reservoir has so far been ignored. In this work, attempt has been made to see the possibility of reservoir contamination of $18\alpha(\text{H})$ -Oleanane in crude oil. A mixture of standard oleanane with saline water is first used to saturate a core, and then gasoline (free of oleanane) is used to displace the water in the core. Extracted gasoline from the core is then analyzed to check the presence of oleanane. Results show appreciable concentration in the extracted gasoline suggesting gasoline can be contaminated with oleanane if reservoir is deposited in oleanane-rich water.

Keywords $18\alpha(\text{H})$ -Oleanane · Age indicator · Biomarker · Source rock · Contamination

1 Introduction

Biomarkers are normally utilized in petroleum geochemistry to identify the stratigraphic origin of crude oil and thermal maturity of associated source rock [1]. In petroleum geochemistry, biomarkers are most useful to understand generation and thermal maturity of petroleum [2]. Biomarkers are helpful for the reason that they keep all or most of original carbon skeleton of the original natural product and this structural resemblance reveals further information concerning their origins than other compounds. Whereas proteins and carbohydrate structures are

S.K. Bhattacharya (✉) · S.M.I. Mahmoodi
Petroleum Geoscience Department, Universiti Teknologi Petronas,
Bandar Seri Iskandar, 31750 Tronoh, Perak Darul Ridzuan, Malaysia
e-mail: Swapan_b@petronas.com.my

F.H.A. Abdulla
Earth and Environmental Science Department, Kuwait University, Kuwait, Kuwait

destroyed during diagenesis, but biomarkers are not destroyed. The alteration of an enormous number of the precursor biochemical compounds from existing organisms into biomarkers produces a vast suite of compounds in crude oils that have different structures. Further, due to the extensive diversity of geological conditions and ages under which oil has been created, each crude oil reveals an essentially unique biomarker [3]. Among them, the efficient utilization of $18\alpha(\text{H})$ -Oleanane biomarker as age indicator for source deposition is of great significance.

Relative concentration of oleanane in crude oil indicates the diversification of angiosperm lineage due to occurrence of angiosperm fragments or molecules that have migrated from the source plant material. Thus, the presence of this compound suggests the occurrence of angiosperm and angiosperms came to dominate the world flora since the Early-Late Cretaceous [4–7]. Therefore, nowadays, most of geologist or geochemist assumes $18\alpha(\text{H})$ -Oleanane as Tertiary-Cretaceous age indicator of source deposition.

Presence of oleanane in source rock indicates lot of information, but all applications regarding source rock become accurate if oleanane truly found in source rock instead of reservoir rock. In case, if oleanane contaminates oil in the reservoir then the age inference for source rock becomes totally wrong and misleading.

There is a long list of works that concludes Tertiary age of the source rock using high Oleanane index in the oil [8–24]. However, till date, it has not been confirmed that oleanane in oil is migrated from the source rock. It has also not tested if this biomarker can be incorporated in the reservoir.

Present work is focused to test whether oleanane in the reservoir can contaminate trapped oil or not.

2 Methodology

Synthetic core with measurable porosity and permeability has been used to test the possibility of contamination of petroleum oil with $18\alpha(\text{H})$ -Oleanane. First, a mixture of saline water and oleanane is injected into core. When core was saturated with the solution mixture, we added gasoline into core. This gasoline displaced already present water mixture of $18\alpha(\text{H})$ -Oleanane (Fig. 1). The displaced gasoline is then tested with GC-MS following the same earlier procedure to test the presence of oleanane.

3 Results

In Fig. 2, it is shown that the standard of $18\alpha(\text{H})$ -Oleanane has been detected at retention time 50.64 with 70,000 ppm abundance. As discussed earlier, after core flooding, the fluid is analyzed using GC-MS. As shown in Fig. 3, the occurrence of $18\alpha(\text{H})$ -Oleanane can be seen at retention time 50.64 with abundance range of 800 ppm.

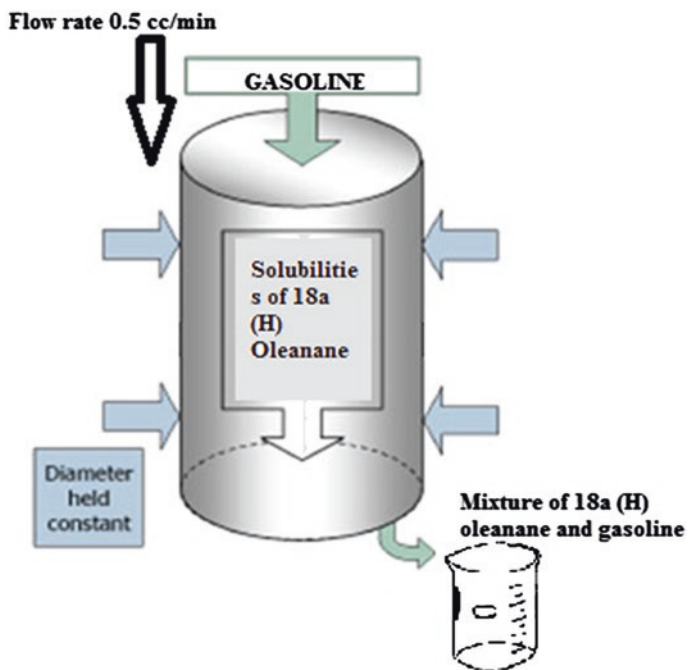


Fig. 1 Gasoline displace 18α(H)-Oleanane

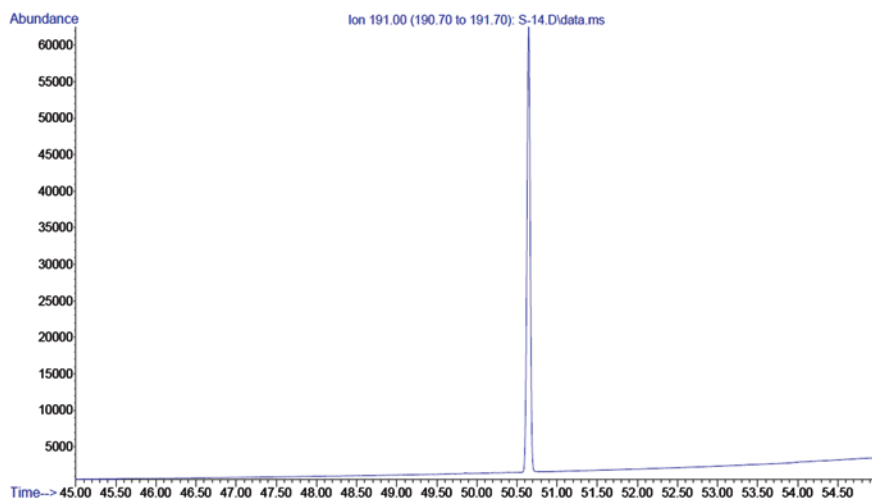


Fig. 2 m/z 191 of 18α(H)-Oleanane

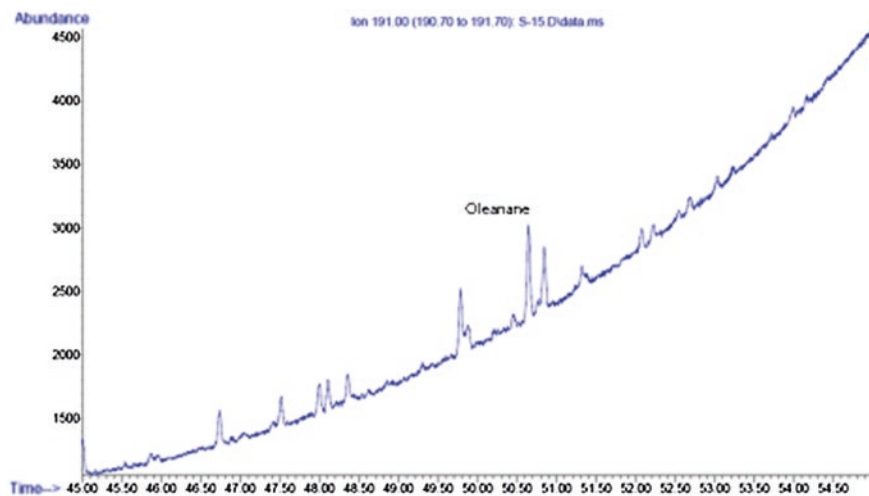


Fig. 3 m/z 191 of core gasoline sample

Fig. 4 Comparison of $18\alpha(\text{H})$ -Oleanane, gasoline, and core gasoline at retention time 50.64

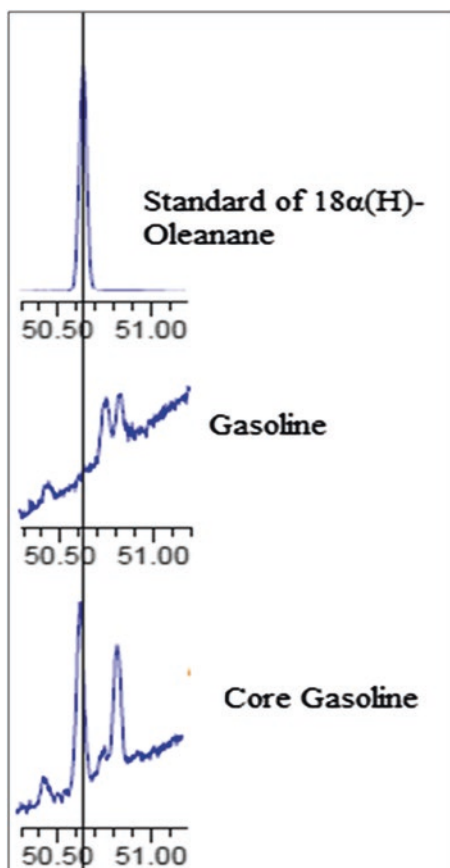
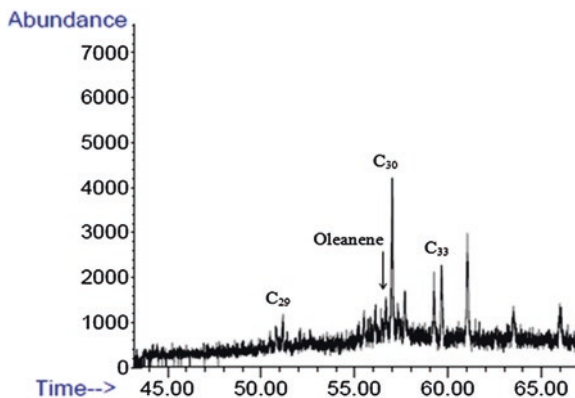


Fig. 5 Ligustrum lucidum in Gasoline



In Fig. 4, we combine $18\alpha(\text{H})$ -Oleanane, gasoline, and core gasoline sample. It indicates that at retention time 50.64, standard of $18\alpha(\text{H})$ -Oleanane and core gasoline sample shows peaks, while gasoline does not have any peak at this retention time.

Attempt has also been used to test whether $18\alpha(\text{H})$ -Oleanane can contaminate gasoline directly from the ligustrum lucidum source. However, we know that $18\alpha(\text{H})$ -Oleanane is generated from the source only after diagenesis. The present study thus focuses to check whether oleanene from ligustrum lucidum is soluble in gasoline or not.

Result suggests that oleanene from ligustrum lucidum can also contaminate gasoline (Fig. 5). Thus, it is possible that trapped oil in the reservoir can also be contaminated from the oleanane source.

4 Conclusions

Based on the above results and discussions, it is therefore concluded that:

1. $18\alpha(\text{H})$ -Oleanane can be introduced in oil as contamination in the reservoir. Therefore, presence of such $18\alpha(\text{H})$ -Oleanane in oil neither indicates the tertiary-cretaceous age nor indicates the terrestrial input of the source rock.
2. As on today, the presence of $18\alpha(\text{H})$ -Oleanane in oil is believed as a source indicator of oil field. However, our study reveals that the presence of oleanane always may not be right age indicator for the source of the oils.

5 Recommendation

1. Since oleanene can be converted to oleanane by diagenesis [25], the experiment can follow those natural conditions of diagenesis and migration to confirm the contamination of oleanane in reservoir.
2. From this analysis, it is apparent that oleanane is not reliable for age of source deposition. This needs to be checked for other biomarkers that previously considered or used as age indicator of source oil.

References

1. D. M. J. S. R. L. Ian M. Head, "Biological activity in the deep subsurface and the origin of heavy oil," *Nature*, pp. 1-36, 2003.
2. J. H. Hunt, *Petroleum Geochemistry and Geology*, 1996.
3. Z. Wang, Fingas, M., Yang, C., Hollebone, B., Peng, X., "Biomarker fingerprinting: Application and limitations for source identification and correlation of oils and petroleum products," presented at the Environment Canada Arctic and Marine Oil Spill Program Technical Seminar (AMOP) Proceedings, 2004.
4. J. D. J. Michael Moldowan, Bradley J. Huizinga, Frederick J. Fago, Leo J. Hickey, Torren M. Peakman, David Winship Taylor, "The molecular fossil record of oleanane and its relation to angiosperms," *Science*, vol. 265, pp. 768-771, 1994.
5. M. Stefanova, J. Kortenski, A. Zdravkov, and S. Marinov, "Paleoenvironmental settings of the Sofia lignite basin: Insights from coal petrography and molecular indicators," *International Journal of Coal Geology*.
6. G. Hassanzade, M. Kobraei, A. Ahanjan, R. B. Tirtashi, M. Rashidi, and M. Khaleghi, "Petroleum System Analysis Using Geochemical Studies, Isotope and 1D Basin Modeling in Hendijan Oil Field, SW Iran," presented at the International Petroleum Technology Conference, Bangkok, Thailand, 2011.
7. T. Gentzis, "Geochemical characterization of an oil seep from the Bagua Basin, north-central Peru," *International Journal of Coal Geology*, vol. 108, pp. 18-26, 3/30/ 2013.
8. W. S. El Diasty and J. M. Moldowan, "The Western Desert versus Nile Delta: A comparative molecular biomarker study," *Marine and Petroleum Geology*, vol. 46, pp. 319-334, 9// 2013.
9. F. Hoş-Çebi and S. Korkmaz, "Organic geochemistry and depositional environments of Eocene coals in northern Anatolia, Turkey," *Fuel*, vol. 113, pp. 481-496, 11// 2013.
10. B. O. Ekpo, N. Essien, E. P. Fubara, U. J. Ibok, E. J. Ukpabio, and H. Wehner, "Petroleum geochemistry of Cretaceous outcrops from the Calabar Flank, southeastern Nigeria," *Marine and Petroleum Geology*, vol. 48, pp. 171-185, 12// 2013.
11. D. Oppo, R. Capozzi, and V. Picotti, "A new model of the petroleum system in the Northern Apennines, Italy," *Marine and Petroleum Geology*, vol. 48, pp. 57-76, 12// 2013.
12. J. E. Cortes, J. E. Niño, J. A. Polo, A. G. Tobo, C. Gonzalez, and S. C. Siachoque, "Molecular organic geochemistry of the Apiay field in the Llanos basin, Colombia," *Journal of South American Earth Sciences*, vol. 47, pp. 166-178, 11// 2013.
13. M. Ahmed, H. Volk, T. Allan, and D. Holland, "Origin of oils in the Eastern Papuan Basin, Papua New Guinea," *Organic Geochemistry*, vol. 53, pp. 137-152, 12// 2012.
14. A. Reitz, T. Pape, M. Haeckel, M. Schmidt, U. Berner, F. Scholz, et al., "Sources of fluids and gases expelled at cold seeps offshore Georgia, eastern Black Sea," *Geochimica et Cosmochimica Acta*, vol. 75, pp. 3250-3268, 6/1/ 2011.
15. M. H. Hakimi, W. H. Abdullah, and M. R. Shalaby, "Organic geochemical characteristics of crude oils from the Masila Basin, eastern Yemen," *Organic Geochemistry*, vol. 42, pp. 465-476, 6// 2011.
16. Q. Abeer, D. Leythaeuser, and R. Littke, "Geochemistry, origin and correlation of crude oils in Lower Cretaceous sedimentary sequences of the southern Mesopotamian Basin, southern Iraq," *Organic Geochemistry*, vol. 46, pp. 113-126, 5// 2012.
17. E. P. F. Bassey O. Ekpo, Okon D. Ekpa and Hab L. Marynowski, "Distributions of Fossil Fuel Biomarkers in Sediments as Proxies for Petroleum Contamination of Coastal Environment of the Niger Delta, Southeastern Nigeria," *Journal of Applied Sciences in Environmental Sanitation*, vol. 7, pp. 75-86, 2012.
18. H. I. Petersen, H. P. Nytoft, M. B. W. Fyhn, N. T. Dau, H. T. Huong, J. r. A. Bojesen-Koefoed, et al., "Oil and Condensate Types In Cenozoic Basins Offshore Vietnam: Composition And Derivation," presented at the International Petroleum Technology Conference, Bangkok, Thailand, 2011.

19. M. Alberdi and L. López, "Biomarker 18 α (H)-oleanane: a geochemical tool to assess Venezuelan petroleum systems," *Journal of South American Earth Sciences*, vol. 13, pp. 751-759, 2000.
20. L. I. Dzou, A. G. Holba, J. C. Ramón, J. M. Moldowan, and D. Zinniker, "Application of new diterpane biomarkers to source, biodegradation and mixing effects on Central Llanos Basin oils, Colombia," *Organic Geochemistry*, vol. 30, pp. 515-534, 1999.
21. C. F. Hoffmann, A. S. Mackenzie, C. A. Lewis, J. R. Maxwell, J. L. Oudin, B. Durand, *et al.*, "A biological marker study of coals, shales and oils from the Mahakam Delta, Kalimantan, Indonesia," *Chemical Geology*, vol. 42, pp. 1-23, 1984.
22. C. M. Ekweozor and O. T. Udo, "The oleananes: Origin, maturation and limits of occurrence in Southern Nigeria sedimentary basins," *Organic Geochemistry*, vol. 13, pp. 131-140, 1988.
23. J. A. Curiale, "The petroleum geochemistry of Canadian Beaufort Tertiary "non-marine" oils," *Chemical Geology*, vol. 93, pp. 21-45, 1991.
24. S. D. Killips, M. S. Massoud, and A. C. Scott, "Biomarker characterisation of an oil and its possible source rock from offshore Korea Bay Basin," *Applied Geochemistry*, vol. 6, pp. 143-157, 1991.
25. H. L. T. Haven and J. Rullkötter, "The diagenetic fate of taraxer-14-ene and oleanene isomers," *Geochimica et Cosmochimica Acta*, vol. 52, pp. 2543-2548, // 1988.